



# Development of an ultrashort and intense collisional OFI plasma-based soft X-ray laser

Adrien Depresseux

## ► To cite this version:

Adrien Depresseux. Development of an ultrashort and intense collisional OFI plasma-based soft X-ray laser. Physics [physics]. Ecole Polytechnique, 2015. English. NNT: . tel-01233246

**HAL Id: tel-01233246**

**<https://pastel.hal.science/tel-01233246>**

Submitted on 24 Nov 2015

**HAL** is a multi-disciplinary open access archive for the deposit and dissemination of scientific research documents, whether they are published or not. The documents may come from teaching and research institutions in France or abroad, or from public or private research centers.

L'archive ouverte pluridisciplinaire **HAL**, est destinée au dépôt et à la diffusion de documents scientifiques de niveau recherche, publiés ou non, émanant des établissements d'enseignement et de recherche français ou étrangers, des laboratoires publics ou privés.

Copyright

# Development of an ultrashort and intense collisional OFI plasma-based soft X-ray laser

## THÈSE

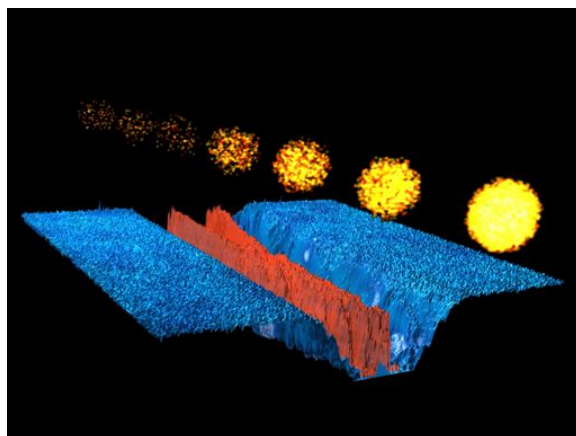
présentée et soutenue publiquement le 1er octobre 2015

pour l'obtention du

Doctorat de l'École Polytechnique

par

Adrien Depresseux



### Composition du jury

<i>Rapporteurs :</i>	Annie KLISNICK	ISMO, Orsay
	Fabien QUÉRÉ	CEA, Saclay
<i>Examineurs :</i>	Manuel JOFFRE	LOB, Palaiseau
	Bedřich RUS	FZU, Prague
	Olivier GUILBAUD	LPGP, Orsay
<i>Directeur de thèse :</i>	Stéphane SEBBAN	LOA, Palaiseau



Cover - courtesy of Agustin Lifschitz.

« С одной логикой нельзя через натуру перескочить! Логика предугадает три случая, а их миллион! Отрезать весь миллион и все на один вопрос о комфорте свети! Самое легкое разрешение задачи! Соблазительно ясно, и думать не надо!

Главное - думать не надо! Вся жизненная тайна на двух печатных листках умещается! »

Фёдор Михайлович Достоевский, *Преступление и Наказание*. Часть 3, глава 5, 1866.

« You can't skip over nature by logic! Logic presupposes three possibilities, but there are millions! Cut away a million, and reduce it all to the question of comfort! That's the easiest solution of the problem! It's seductively clear and you musn't think about it. That's the great thing, you mustn't think! The whole secret of life in two pages of print! »

Fyodor Mikhailovich Dostoyevsky, *Crime and Punishment*. Part 3, Chap. V, 1866.



## Acknowledgements

The three years of my PhD program laid an important milestone regarding both my skills and personal fulfillment. Although being individual, this thesis work has been strongly rooted in a cooperative work and thus would not have been possible without the collaboration, support and advice of numerous people.

First, I would like to express my deep gratitude to my PhD advisor, Stéphane Sebban, who carefully introduced me to the new experimental and theoretical environment, and whose numerous contributions turned out essential to the success of this thesis. Throughout those years, I highly benefited from his overarching knowledge of the mainsprings of plasma-based soft X-ray lasers, but also from his comprehensive know-how, ingenuity, ubiquitous and constant support, as well as his fruitful advice. Moreover, I strongly appreciated the balance between his leadership, which defined the framework and main directions of my work, and the freedom and trust he granted me, which enabled building up my own experience. In addition to his expertise, I deeply enjoyed his availability, untiring motivation and his unfailing good mood, which altogether had a great impact on the positive course of my work.

My acknowledgements are then devoted to Julien Gautier for his remarkable availability, dynamism, backing, kindness and very good mood. I would also like to warmly thank Fabien Tissandier. As the previous PhD student in the team, he gave me useful feedbacks, provided me numerous valuable insights into the field of study and kindly supported me. I am also thankful to the leader of my FLEX group, Philippe Zeitoun for his support and enlightening discussions.

The experimental work has been strongly tied to the collaboration with the laser team members, Jean-Philippe Goddet and Amar Tafzi, whose diligence was highly appreciated.

I acknowledge the numerous and various help and contributions from the main collaborators and co-authors. To this regard, I would like to praise Eduardo Oliva and Gilles Maynard, who developed numerical tools to model the complex underlying physics introduced hereby. I am strongly grateful for their valuable cooperation and discussions to explain observed phenomena. I particularly appreciated the availability, heed and assistance from Eduardo Oliva.

Then, I thank Hyung Taek Kim and Kyung Hwan Lee for their worthwhile contributions to the collaborative work. I want to warmly thank the former collaborator for his warm welcome when I visited APRI petawatt laser facilities in Gwangju late 2012.

I also want to pay special tribute to Jaroslav Neidl, Mickaella Kozlova and Viktoriia E. Nefedova for their rewarding collaborative efforts during joint experiments.

As strong collaboration links prevail between FLEX and SPL teams, I would like to fervently thank members of both teams, particularly Guillaume Lambert, Agustin Lifschitz, Kim Ta Phuoc, Cédric Thauray, Alessandro Flacco and the SPL group leader Victor Malka. My thanks are also devoted to Boris Vodungbo for his support and cooperation efforts and contributions. Additionally, I wish to show gratitude to the director of LOA, Antoine Rousse, who welcomed me and strives to improve the laboratory visibility and working environment.

I feel also indebted to people responsible for the technical support, whose contribution allowed a smooth operation of the experimental facilities. First and for all, I deeply thank members of the mechanical shop: Jean-Loup Charles and Michael Martinez. I would like to particularly cheer the kindness, experience and diligence of Jean-Loup Charles, which substantially impacted on my work.

Then, I thank Pascal Rousseau, Thierry Lefrou and Gregory Iaquaniello, who took care of automation and vacuum systems in «Salle Jaune» experimental facilities.

I wish also to thank the past and present students as well as post-docs, with whom I shared

my office for the conversations and contributions to a nice working environment: Emilien Guillaume, Andreas Doepp, Rémy Léhé, Igor Andryash, Benjamin Vauzour, Lu Li, Benoît Mahieu, Florian Mollica, Antoine Doche and Loann Pommarel. I would like to show a special esteem to my friend Emilien Guillaume, whose thesis work also took place in «Salle Jaune» within the same time window. I thoroughly appreciated sharing our individual PhD experience enjoyed his good mood, readiness to help, his continuous moral support as well as numerous beneficial dissuasions.

I also want to show gratitude to François Sylla, CEO of the SourceLab laboratory spinoff, who supported efforts to develop high-density gas targetery.

I want to warmly thank the members of secretary team – Patricia Touillier, Sandrine Tricaud, Octavie Verdun, Carole Gratpanche and Lucie Huguet – for their efficiency, kindness and strong commitment to help and smooth out paperwork.

At last, I would want also to thank the jury members for their time and careful review of my manuscript, as well as for their remarks and the fruitful discussions they initiated.

Finally, I would want to thank my family for its strong moral backing all over those years and also, without which all my academic course until the last steps of this PhD would not have been possible.

# Contents

<b>Introduction</b>	<b>1</b>
<b>Chapter 1 Introduction to coherent soft X-ray sources</b>	<b>5</b>
1.1 Coherent soft X-ray sources . . . . .	6
1.1.1 Synchrotron radiation . . . . .	6
1.1.2 High-harmonic generation . . . . .	8
1.2 Plasma-based soft X-ray lasers . . . . .	12
1.2.1 Population inversion in a plasma . . . . .	12
1.2.2 Overview of the development of collisional soft X-ray lasers . . . . .	17
1.3 Seeded collisionally-pumped OFI plasma-based soft X-ray laser chain . . . . .	23
1.3.1 Source performances and limitations . . . . .	23
1.3.2 Prospective applications . . . . .	28
1.4 Conclusion . . . . .	30
<b>Chapter 2 Physical processes in seeded collisional OFI plasma-based soft X-ray lasers</b>	<b>31</b>
2.1 Laser-plasma interaction using an ultrashort pulse . . . . .	32
2.1.1 Types of ionization . . . . .	32
2.1.2 The « Optical Field Ionization regime » regime: ionization rate . . . . .	37
2.1.3 Energy distribution of electrons and ions . . . . .	40
2.2 Plasma kinetics . . . . .	44
2.2.1 Atomic processes . . . . .	44
2.2.2 Evolution of electrons' and ions' temperature . . . . .	47
2.3 Population inversion, gain and radiative transfer . . . . .	52
2.3.1 Laser effect in the soft X-ray range . . . . .	52
2.3.2 Gain dynamics . . . . .	57
2.3.3 Saturation intensity . . . . .	62
2.4 Propagation of an ultrashort infrared pulse in plasmas . . . . .	63
2.4.1 Propagation equation . . . . .	63

2.4.2	Beam refraction . . . . .	67
2.5	Modeling the amplification of HH by a plasma amplifier . . . . .	72
2.5.1	Field equations . . . . .	73
2.5.2	Atomic description . . . . .	74
2.5.3	Amplification of a HH seed pulse . . . . .	76
2.6	Conclusion . . . . .	78
<b>Chapter 3 Modeling of a high-density krypton plasma waveguide</b>		<b>79</b>
3.1	State of the art of waveguiding techniques of high-intensity laser pulses . . . . .	80
3.1.1	Relativistic self-guiding . . . . .	80
3.1.2	Capillary discharge plasma waveguide . . . . .	81
3.1.3	Hollow capillary tube . . . . .	82
3.1.4	Optically-preformed plasma waveguide using the «ignitor-heater » technique	83
3.2	Numerical modeling of plasma waveguiding . . . . .	89
3.2.1	Waveguiding conditions . . . . .	90
3.2.2	Numerical model . . . . .	94
3.2.3	Numerical investigation of a range of parameters . . . . .	100
3.3	Conclusion . . . . .	107
<b>Chapter 4 Experimental investigation of a high-density soft X-ray plasma amplifier</b>		<b>109</b>
4.1	Experimental arrangement . . . . .	110
4.1.1	«Salle Jaune» experimental installations . . . . .	110
4.1.2	Experimental setup . . . . .	113
4.2	Elongated high-density gas jet target . . . . .	115
4.2.1	Design of a rectangular nozzle . . . . .	115
4.2.2	Experimental characterization of rectangular slit nozzles . . . . .	118
4.3	Diagnostics . . . . .	122
4.3.1	Waveguide diagnostics . . . . .	122
4.3.2	Soft X-ray diagnostics . . . . .	124
4.4	Experimental results . . . . .	125
4.4.1	Characterization of the plasma waveguide . . . . .	125
4.4.2	Guiding efficiency . . . . .	132
4.4.3	Characterization of the soft X-ray laser emission . . . . .	135
4.4.4	Correlation between waveguiding quality and SXRL signal strength . . .	142
4.5	Conclusion . . . . .	145

---

<b>Chapter 5 Characterization of a high-density HH-seeded plasma-based soft X-ray laser</b>	<b>147</b>
5.1 Development of the HH-seeded soft-X-ray laser at 32.8 nm . . . . .	148
5.1.1 Experimental setup . . . . .	149
5.1.2 Spectra . . . . .	153
5.1.3 Far-field Energy distribution and output energy . . . . .	154
5.1.4 Seeding signal strength level . . . . .	157
5.2 Gain dynamics measurement . . . . .	159
5.3 Maxwell-Bloch modeling . . . . .	162
5.3.1 Temporal structure of the amplified HH field . . . . .	163
5.3.2 Regimes of amplification of the resonant HH field . . . . .	165
5.3.3 SXRL pulse buildup . . . . .	166
5.3.4 Final SXRL pulse duration and discussion . . . . .	169
5.4 Extracted energy . . . . .	175
5.5 Conclusion . . . . .	176
<b>Chapter 6 Control of the polarization of plasma-based soft X-ray lasers</b>	<b>177</b>
6.1 Existing circularly-polarized soft X-ray sources . . . . .	178
6.1.1 Synchrotrons and Free Electron Lasers (FELs) . . . . .	178
6.1.2 High-harmonic sources . . . . .	178
6.2 Efficient scheme for a circularly-polarized plasma-based soft X-ray laser . . . . .	179
6.2.1 Experimental setup . . . . .	179
6.2.2 Four mirror-phase shifter . . . . .	180
6.2.3 Rotating analyzer . . . . .	184
6.2.4 Measurement of the SXRL polarization . . . . .	185
6.2.5 Output beam profile & energy . . . . .	189
6.3 Maxwell-Bloch model of amplification of polarized radiation . . . . .	190
6.3.1 Adaptation of equations to various states of polarization . . . . .	190
6.3.2 Final energy and duration of the circularly polarized soft X-ray laser . . . . .	193
6.3.3 Polarization of the amplified HH signal . . . . .	199
6.4 Conclusion . . . . .	201
<b>Conclusion</b>	<b>203</b>
<b>Appendixs</b>	<b>209</b>
<b>Appendix A OFIKinRad atomic code</b>	<b>209</b>



<b>Appendix B Laser spectral lineshape</b>	<b>213</b>
<b>Appendix C Focusing light by means of an axicon lens</b>	<b>215</b>
<b>Appendix D Design of elongated rectangular slit nozzles</b>	<b>219</b>
<b>Appendix E Gas and plasma density diagnostics</b>	<b>227</b>
<b>Appendix F Polarization state recovery</b>	<b>233</b>
<b>Appendix G List of publications and conference contributions</b>	<b>237</b>

# Introduction

Over sixty years have elapsed since the first demonstration of laser operation. The development and utilization of the properties of those coherent sources proved to be a breeding ground for various innovations and led to significant breakthroughs in a wide scope of domains, from biology, chemistry and material sciences to industry. Stimulated emission, underpinning the laser operation, was first achieved in the microwaves domain by Townes in 1953 [Gordon et al., 1954] and then extended into the light spectrum by Prokhorov and Basov in 1958 [Basov and Prokhorov, 1958], before being experimentally demonstrated two years later by Maiman [Maiman, 1960].

The development of such sources in the soft X-ray range arouses great interest since they allow applying the powerful coherent imaging techniques at low wavelengths, where very high spatial resolutions and tiny focal spots are promised. Although the declension of laser wavelengths has rapidly stretched from the infrared to the ultraviolet domain, notably thanks to the advent of nonlinear optics, the development of lasers in the soft X-ray range was substantially slower. Indeed, limitations intrinsic to this wavelength range turn the architecture using conventional "active media" in a resonant cavity inappropriate. In this perspective, other methods have been envisioned to overcome those bottlenecks and **plasmas** turn out suitable media to achieve this.

Plasma-based soft X-ray lasers are achieved through laser-plasma interaction in a solid or a gas. The emission of coherent light results from a two-step process. First, a significant population of so-called « **lasing ions** », which display atomic transitions suitable for emitting in the soft X-ray range, is generated. Secondly, this transition is « **pumped** » in order to promote stimulated emission, whose properties determine the coherence of emitted light. Since such plasmas exhibit high-gain coefficients, amplification of coherent light over a single pass proves to be a viable approach.

Aside from being compact and rather inexpensive, plasma-based soft X-ray lasers turn out enticing since they can emit a large number of photons in one single pulse [Rus et al., 2002] (up to  $10^{15}$ ). Indeed, laser operation can be observed in two regimes. One regime is called the « **ASE** » (Amplification of Spontaneous Emission) mode, where the plasma amplifies its own « noise », stemming from spontaneous de-excitations from the upper to the lower level of the laser transition. By comparison, the « **seeded** » regime is implemented through the plasma amplification of an external coherent signal, whose wavelength is tuned to the laser transition of the plasma.

Successful work has been carried out over more than one decade at Laboratoire d'Optique Appliquée, which notably lead to the implementation of a soft X-ray laser chain with a plasma amplifier and an oscillator with a high-harmonic source [Zeitoun et al., 2004]. The seeded regime allows a dramatic improvement of the spatial properties of emitted radiation, such as the beam divergence and wavefront [Goddet et al., 2009], compared to ASE. Moreover, such sources exhibit

a very narrow linewidth and are intrinsically jitter-free.

Compared to other types of sources delivering coherent photons, such as Free Electron Lasers (FELs) or high-harmonic sources, plasma-based soft X-ray lasers find a niche for multiple applications by retaining their own advantages.

Besides those merits, four main elements affect the competitiveness of the source. First, the **duration** of plasma-based soft X-ray emission has been limited to date to the picosecond range, thus making the source unsuitable to probe the ultrafast dynamics of phenomena or for applications requiring high intensities on target. Therefore, the reduction in duration of emission appears as a new challenge to enhance the capabilities of plasma-based soft X-ray lasers.

Secondly, applications like soft X-ray coherent diffraction requires a significant number of photons. High-harmonic seeded plasma-based soft X-ray lasers display very good focusability. However, the available **photon yield** is still moderate and demonstrated energies remain below the 1  $\mu\text{J}$  level to date. Indeed, a great amount of emitted photons are part of ASE and worthwhile efforts are thus needed to improve the extraction of the plasma amplifier gain by the amplified high-harmonic pulse.

Third, the **polarization** of the source has been either undefined or restricted to linear polarization. Namely, circular polarization widens the potential of conventional nanometer-scale resolution probing sources and proves to be an extremely valuable tool to investigate a wide range of phenomena from biology to material science, including dichroism and chirality. Hence, controlling the state of polarization turns out to be a new milestone in the development of plasma-based soft X-ray lasers.

At last, the resolution that can be expected from probing techniques using a coherent source is given by the operated wavelength. Indeed, the collisional pumping scheme is only efficient in the soft X-ray range. Thus, one has to resort to other pumping schemes to reach a **shorter wavelength**.

This manuscript summarizes the work, which aimed at addressing the first two development foci and partially the third one, while the perspective of reducing the operated wavelength lies beyond the scope of this thesis. The work was centered on the development of a collisionally-pumped OFI plasma-based soft X-ray laser with krypton, which emits at 32.8 nm. The outline of the manuscript is the following:

Chapter 1 presents the scientific landscape surrounding the development of collisionally-pumped OFI plasma-based soft X-ray lasers, and the challenges associated with the implementation of laser action in the soft X-ray range.

Chapter 2 introduces the theoretical principles, which underpin the physics of such lasers operating in a seeded regime. A description of the laser transition pumping process, the plasma kinetics, the propagation of the driving laser pulse and the radiative transfer is presented. This section also introduces the principle of an innovative technique, named « *Collisional Ionization Gating* », which was used to demonstrate femtosecond duration from plasma-based soft X-ray laser emission. This method constitutes the fulcrum upon which the experimental data in chapter 3, 4 & 5 are based.

Chapter 3 presents an optical waveguiding technique used to overcome challenges associated with the requirements of the « *Collisional Ionization Gating* » technique. The critical parameters for efficient waveguiding are stated and their relative importance discussed using a numerical model.

Chapter 4 describes the experimental characterization of elongated plasma amplifiers imple-

---

menting the aforementioned waveguiding technique. The guiding quality of the driving laser pulse and its correlation with the laser signal strength are discussed.

Chapter 5 shows the experimental investigation of an ultrashort plasma-based soft X-ray laser. The seeding technique was employed to probe the gain dynamics of the plasma amplifier, but also to generate nearly-collimated high-quality beams. A time-dependent Maxwell-Bloch code has been used to derive the duration of the emitted soft X-ray laser pulses.

Finally, chapter 6 reports the demonstration of an efficient architecture used to achieve a high-harmonic-seeded circularly polarized soft X-ray laser. An existing Maxwell-Bloch code was modified to describe the amplification of a polarized seeding resonant field and corroborate the experimental observations.



# Chapter 1

## Introduction to coherent soft X-ray sources

Coherent soft X-ray sources have aroused great interest for many years since they open the way to a wide scope of innovative and multi-disciplinary application fields. The main advantages of those sources involve the achievable high-resolution for imaging, the focusability over small dimensions and the possibility to investigate previously unexplored areas in physics requiring energetic photons. Amid existing coherent soft X-ray sources, one can distinguish sources obtained from synchrotron radiation and laser-driven sources. The latter include high-harmonic and plasma-based soft X-ray lasers.

The development of the source performances is focused on the increase of the photon yield, the reduction of the duration of emission, the control of the field polarization, the enhancement of the wavefront quality, the increase of the repetition rate, as well as the improvement of both spatial and temporal coherence.

### Contents

---

<b>1.1 Coherent soft X-ray sources</b>	<b>6</b>
1.1.1 Synchrotron radiation	6
1.1.2 High-harmonic generation	8
<b>1.2 Plasma-based soft X-ray lasers</b>	<b>12</b>
1.2.1 Population inversion in a plasma	12
1.2.2 Overview of the development of collisional soft X-ray lasers	17
<b>1.3 Seeded collisionally-pumped OFI plasma-based soft X-ray laser chain</b>	<b>23</b>
1.3.1 Source performances and limitations	23
1.3.2 Prospective applications	28
<b>1.4 Conclusion</b>	<b>30</b>

---

## 1.1 Coherent soft X-ray sources

### 1.1.1 Synchrotron radiation

**Synchrotron sources.** A synchrotron is a large-scale facility used to stock particles, which are accelerated by an electric field and maintained on fixed circular trajectories thanks to powerful magnets adapted to their energies in a synchronous way (see fig. 1.1). The oscillation of particles accelerated up to relativistic speeds results in the emission of photons from the infrared to the hard X-ray range. More specifically, a strong Doppler shift due to the particles' speed allows reaching the X-ray range. This facility is able to provide energetic beams but the coherence of radiation is very low. Nowadays, a dozen of facilities of this type exist, from ESRF and SOLEIL in France, BESSY in Germany, to APS and Spring-8 in USA and Japan respectively. Those sources are attractive because of high repetition rates (as high as a few tens of MHz), high brilliances (as high as  $10^{20} \text{photons/s/mrad}^2/\text{mm}^2/(0.1\% \text{bandwidth})$  demonstrated at ESRF - 3rd generation), a natural narrow angular collimation and a wide range of available wavelengths (photon energy tunability from the very far infrared (a few THz) to the hard X-ray range (0.1 nm)). However, the statistical processes caused by the emission of synchrotron radiation limits the minimum pulse duration (a few tens of picoseconds).



Figure 1.1: Schematic of SOLEIL synchrotron, Saint-Aubin, France. The emitted light is collected at different locations of the ring.

**Free Electron Lasers (FELs).** While initially centered on the development of sources in the hard X-ray range, the demonstration of emission of soft X-ray photons from FELs is more recent. By contrast to synchrotrons, the principle of FELs is to obtain coherent light from synchrotron radiation through its interaction in an undulator with the electron beam producing this synchrotron radiation. The undulator is illustrated in fig. 1.2 consists in a periodic structure of magnets, which compels electrons to oscillate transversely to emit radiation.

Coherent photons are obtained from SASE effect (Self-Amplified Spontaneous Emission). An electron bunch with a uniform density distribution is first accelerated to relativistic speeds and then injected into the undulator. The deviation from the magnetic field causes the electrons to wiggle and emit synchrotron radiation within a certain energy bandwidth. The emitted photons travel slightly faster than the electrons and interact with them within each magnetic field period of the undulator. Depending on the phase to each other, electrons are either accelerated or

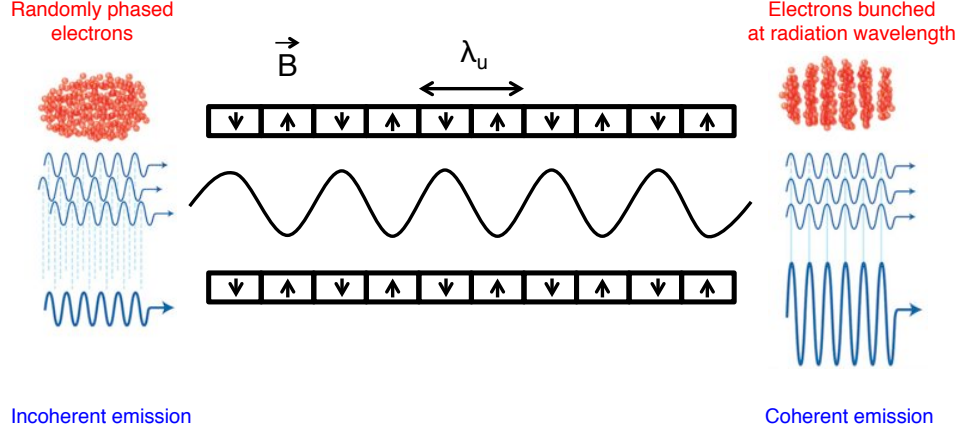


Figure 1.2: Schematic of the structure of magnets used to generate XFEL radiation [McNeil and Thompson, 2010].

decelerated, which prompts faster electrons to catch up with slower ones. Thereby the electron bunch density is periodically modulated by the radiation, creating a so-called "microbunching" effect. Then, the structured electron beam amplifies only certain photon energies. The microbunch structuring causes photons to have very similar phase, thus leading to quasi-coherent FEL emission. The wavelength of the emitted radiation at the resonance depends on the electron energy, as well as on the magnitude and periodicity of the undulator field according to the relation [Dattoli et al., 1993]:

$$\lambda_p^{em} = \frac{\lambda_u}{2p\gamma}(1 + \kappa^2) \quad (1.1)$$

where  $\lambda_u$  is the undulator period,  $\gamma$  is the relativistic factor and  $\kappa$  is the so-called undulator parameter which is proportional to the magnetic field inside the undulator. The number  $p$  is the order of the so-called emitted non-linear harmonics. Their intensity decreases sharply as  $p$  is increased.

Among existing sources, the most emblematic is probably LCLS (Linac Coherent Light Source) in Stanford, California [Emma et al., 2010]. The facility, opened in 2009, is able to emit very bright beams at wavelengths ranging from 0.14 nm to 2.3 nm. Three millijoule beams of a few femtoseconds duration have been demonstrated. Other facilities include European XFEL in Germany [Schwartz, 2004] and SCSS (Spring-8 Compact SASE Source) in Japan [Shintake, 2006]. In the soft X-ray range, FLASH facility in Hamburg [Tiedtke et al., 2009] provides  $\mu$ J level pulses of a few tens of fs in the wavelength range between 3 and 30 nm.

The lack of temporal coherence due to a noisy initial process is encountered with SASE XFELs. To overcome this problem, the injection seeding technique has been successfully implemented [Lambert et al., 2008] with a laser tuned to the resonance of the XFEL. This method is at the heart of this thesis work and will be more precisely introduced in chapter 2. A temporally coherent seed, such as high-harmonic (HH) is injected into the XFEL and gets coherently amplified. The output beam quality is characterized by the initial good properties of the seed. Furthermore, because the saturation regime is more quickly reached, the technique allows the use of shorter undulators for an equivalent amount of output photons. In the harder X-ray range where the availability of such seed is lacking, a self-seeding technique has been implemented by seeding the laser with its own beam. [Amann et al., 2012]. Unprecedented intensity and



monochromaticity was demonstrated, which allows pioneering innovative experiments involving manipulating atoms and imaging molecules.

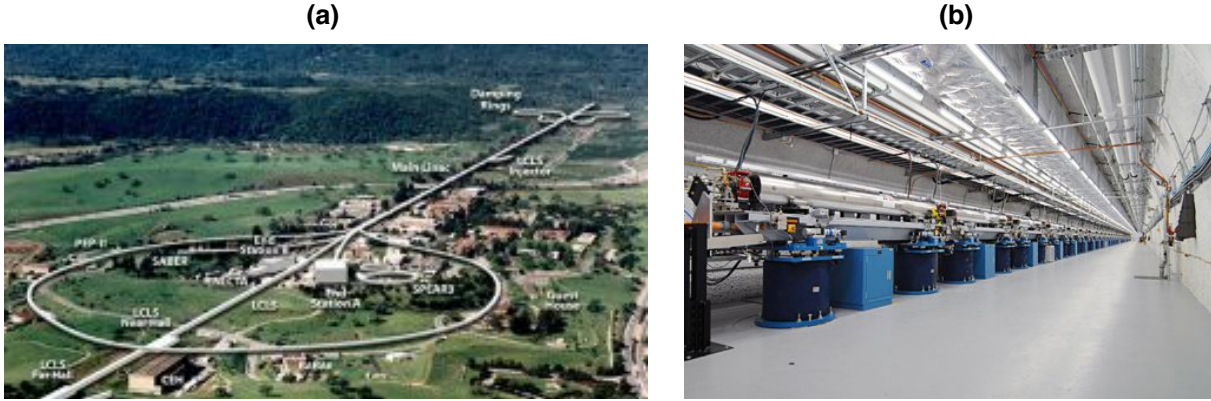


Figure 1.3: (a) Overview of LCLS facilities. (b) Undulators' hall used to generate X-rays (the whole length exceeds 130 m).

However, while displaying excellent beam properties, those facilities featuring a linear accelerator and undulators are very large (see fig. 1.3) and expensive both to build and operate. In this perspective, laser-driven sources, such as high-harmonics and plasma-based soft X-ray lasers turn out attractive alternatives.

### 1.1.2 High-harmonic generation

High-harmonic (HH) generation results from the coherent and nonlinear response of individual atoms under a strong electric field. High-harmonic radiation is obtained by focusing an intense beam (with an intensity in the order of  $10^{13} - 10^{14} \text{ W/cm}^2$ ) into a target consisting of molecules [Lynga et al., 1996], atomic clusters [de Aldana and Roso, 2001], a gas [L'huillier et al., 1991] or a solid [Gibbon, 1996]. The resulting is composed of a set of frequencies, which are multiples of the frequency of the driving laser.

#### High-harmonic generation in solid targets

When an intense laser pulse interacts with an optically-polished solid target, a dense plasma, which acts as a mirror is generated. This so-called "plasma mirror" reflects the high-intensity laser pulse and its non-linear temporal response can lead to the emission of high-order harmonics in the form of a train of attosecond pulses [Nomura et al., 2009]. An illustration of this process is presented in fig. 1.4(1).

The first demonstration of high-harmonic generation (HHG) on solid targets was pioneered in the late 70s and early 80s [Burnett, 1977; Carman et al., 1981] thanks to intense nanosecond  $\text{CO}_2$  lasers at  $10.6 \mu\text{m}$  focused on solid targets, which then turned into plasmas over the interaction. The development of those sources stalled at the expense of HHG in gases, where more accessible interaction regimes were then available.

However, the recent advances in laser technology combined with the introduction of powerful numerical simulation tools have prompted research on HHG in plasmas to gain momentum. The most efficient way for HHG in plasmas is achieved by focusing an intense laser pulse of a few 10s of fs onto an initially solid target.

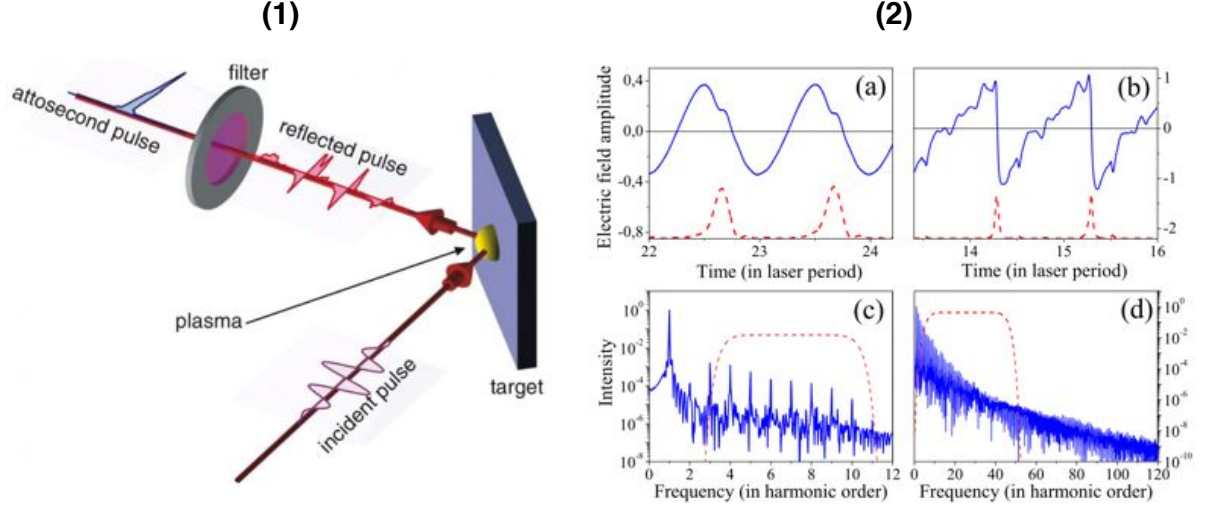


Figure 1.4: (1) Illustration of HHG on plasma mirrors. (2) Results from Particle-In-Cell simulations of such HHG showing the electric field ((a) & (b)) and the corresponding spectra ((c) & (d)). The cases (a) & (c) correspond to a regime where CWE dominates, whereas (b) & (d) show similar data but when ROM dominates. The red dashed curves in (a) and (b) show the intensity profiles of the trains of attosecond pulses obtained when filtering groups of harmonics in the spectra (red dashed lines in (c) and (d)) [Thaury and Quéré, 2010].

Two dominant mechanisms of HHG can be identified in case of ultrashort laser pulses: Coherent Wake Emission (CWE) [Quéré et al., 2006] and the Relativistic Oscillating Mirror (ROM) [Lichters et al., 1996]. Those mechanisms occur in different regimes and lead to very different distortions of the reflected field, and to very different harmonic spectra (fig. 1.4(2) (c) & (d)). Indeed, the periodic temporal distortion of the reflected wave is associated with the emission of high-harmonic pulses, which prove to be the "signature" of the laser-plasma interaction (blue curves in (fig. 1.4(2) (a) & (b))).

In case of infrared driving laser pulses, CWE becomes efficient at moderate intensities of a few  $10^{15} \text{ W/cm}^2$ . In this process, harmonics are emitted by plasma oscillations excited in the sharp density gradient at the plasma surface. These plasma oscillations are triggered in the wake of returning bunches of fast electrons (the so-called "Brunel electrons") [Brunel, 1987] generated by the laser field. Because this process occurs periodically once every laser optical cycle, the spectrum of the HHG emission consists in harmonics of the laser frequency. The fig. 1.4(2) (a) & (c) shows that the emission spectrum is extended up to the maximum plasma frequency  $\omega_p^{max}$ . Data correspond to a vector potential  $a_0 = 0.2$  and  $\omega_p^{max} = 10\omega_{laser}$ .

The ROM process occurs for intensities above a few  $10^{18} \text{ W/cm}^2$ . In this case, outgoing jets of electrons at the plasma mirror surface are accelerated by the laser field up to relativistic velocities. This oscillating mirror gives rise to a periodic Doppler shift of the reflected beam, and thus to HHG of the incident frequency. The fig. 1.4(2) (b) & (d) illustrate this process in case of  $a_0 = 5$  and  $\omega_p^{max} = 15\omega_{laser}$ .

Beyond  $\omega_p^{max}$ , ROM is the dominant source of HHG, whereas below  $\omega_p^{max}$ , both CWR and ROM coexists and their relative contribution depends on the laser intensity.

HHG on plasmas has been successfully developed, either as a tool to better understand non-linear interaction, on which the harmonic signal provides information, or as a way to obtain collimated beams of coherent light at short wavelengths. Among recent developments, we can cite

the generation of isolated attosecond pulses (the so-called "attosecond lighthouses"), by rotating the instantaneous wavefront direction of an intense few-cycle laser driving field [Wheeler et al., 2012].

Finally, the possibility to operate at high-repetition rates offer significant prospects for further developments.

### High-harmonic generation in gas targets

HHG in gases was first demonstrated in 1967 [New and Ward, 1967] with the 3rd order. The use of driving lasers with higher intensities led to the observation of ever increasing HH orders. In 1997, the 300th order has been observed in helium [Chang et al., 1997]. Increased generation efficiencies were pioneered implementing phase-matching [Seres et al., 2005; Takahashi et al., 2007] or quasi-phase matching schemes [Zhang et al., 2007; Zepf et al., 2007]. Other architectures used a so-called "two-colors" scheme, boosting the frequency conversion efficiency by tuning the HH lines to ion resonances [Elouga Bom et al., 2009].

In case of a gas target, the generation of HH can be understood from both microscopic and macroscopic points of view. The microscopic approach is about the individual response of an atom under a strong field, whereas the macroscopic one is related to the phase relationship between the emitters, which is imposed by the laser field.

**Microscopically**, the behavior of individual atoms can be described with a semi-classical model [Corkum, 1993], as illustrated in fig. 1.5. From a very simple overview, the emission arises from the absorption by an atom of  $n$  incoming photons of energy  $E$  and the subsequent emission of one photon of energy  $nE$ . Following interaction with the intense laser field, the atom is ionized and an electron can free from the Coulomb potential barrier by tunneling effect. Ionization occurs twice over an optical cycle (because of maxima and minima of the electric field over a period). Then, the stripped electron is being accelerated by the laser electric field. Under linear polarization, the change of sign of the electric field within an optical period causes the electron to turn back in the same direction in which it was accelerated. When approaching the atom nucleus, the electron can recombine with its parent ion. Within this last step, high-harmonic radiation is emitted with a photon energy:

$$E_{\text{photon}}^{HH} = U_I + E_k \quad (1.2)$$

where  $U_I$  is the atomic ionization potential and  $E_k$  is the kinetic energy gained by the electron by its acceleration.

**Macroscopically**, multiple atoms emit HH radiation in the zone of interaction. The electromagnetic fields emitted by the dipole can interfere constructively and therefore add up constructively. A good phase-matching condition is then needed to efficiently generate a HH signal. Appropriate conditions [Durfée et al., 1999] for generation can be met adjusting the energy, duration and focal spot position of the driving laser, but also on the gas pressure along with the Gouy phase by adapting the aperture of the laser driver beam.

The spectrum of emission depends on the used targets and is characterized by a discrete emission, where the signal is confined around frequencies corresponding to an odd multiple of the driving laser frequency. The spectrum displays a rapidly decaying amplitude at the lowest orders, then a bandwidth with a set of fairly intense HH frequencies and finally a sharp cut at the highest energies. According to the quantum approach to describe HHG (Lewenstein model), the cutting energy is determined by the atomic ionization ( $U_I$ ) and ponderomotive ( $U_p$ ) potentials. The maximum energy of HH photons is:

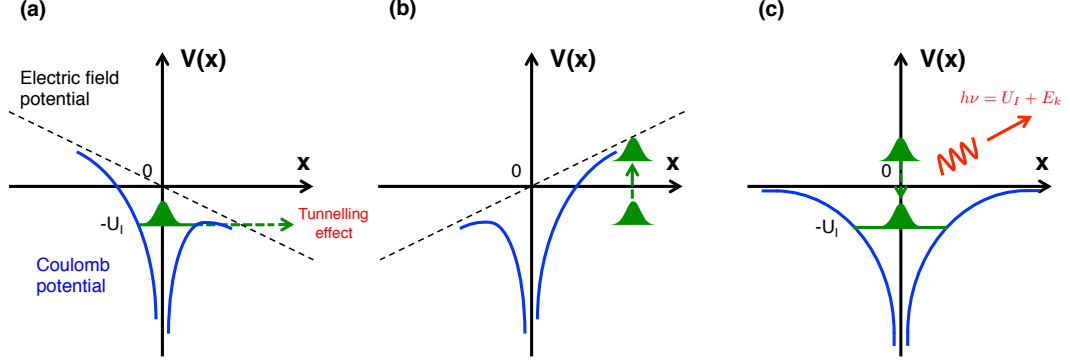


Figure 1.5: Three-step high-harmonic generation process. (a) Tunnel ionization. (b) Acceleration of the electron by the laser field. (c) Radiative recombination on the ground state with emission of a photon.

$$U_{\text{photon}}^{\text{max}} \approx 1.3U_I + \alpha U_p \quad (1.3)$$

with  $\alpha = 3.17$  [Lewenstein et al., 1994]. The odd HH generation in a gas is explained by the fact that, during dipole interaction, the absorption of a pair number of photons cannot lead to the simultaneous conservation of energy and momentum. Such an emission spectrum is illustrated in fig. 1.6a in case of argon.

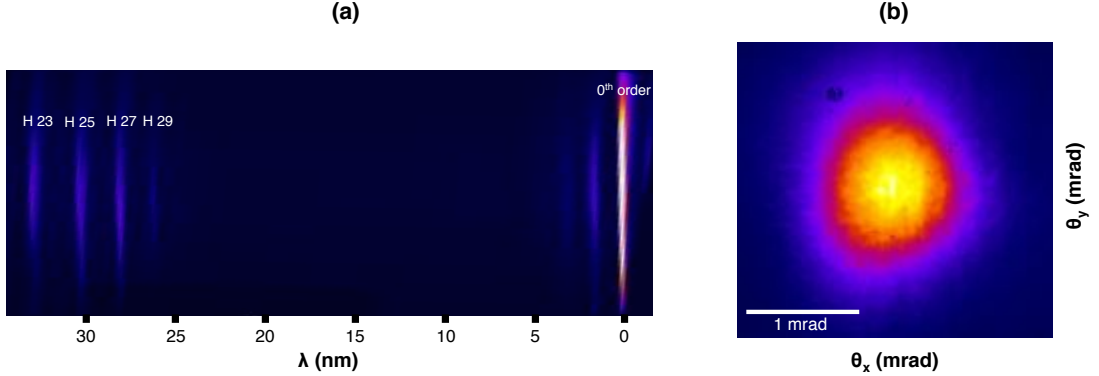


Figure 1.6: (a) Spectrum of HHG obtained from argon irradiated by an ultrashort IR pulse of intensity  $10^{15} \text{ W/cm}^2$ . (b) Low divergence far-field profile of the HH beam.

Aside from being compact and inexpensive, high-harmonic sources display a wealth of attractive features. Regarding **spatial properties**, those sources exhibit highly collimated beams [Ditmire et al., 1996] (fig. 1.6b) and a nearly diffraction-limited wavefront [Gautier et al., 2008]. The emitted radiation is fully polarized and the state of **polarization** can be tuned [Fleischer et al., 2014]. From a **spectral** point of view, HH emission has been demonstrated over a very wide range of wavelengths and down to the so-called "water window" with neon, and helium at energies of 300 eV and 450 eV respectively [Takahashi et al., 2008]. Furthermore, their wavelength is tunable. Finally, short **duration** pulses are demonstrated down to the attosecond range ( $10^{-18} \text{ s}$ ) [Paul et al., 2001].

The main limitation of HH sources is linked to the **photon yield**. Indeed, challenges are met to keep the coherence between the driving field and the generated HH signal over a large distance. Larger interaction volumes can be implemented using long focal length optics but

the intrinsically limited coherence length prevents significant enhancement in the photon yield. In this perspective, HH-seeded plasma-based amplifiers provide an appropriate solution to this challenge.

## 1.2 Plasma-based soft X-ray lasers

Since the first experimental demonstration of laser effect in ruby in 1960 at a wavelength of 694.3 nm [Maiman, 1960], significant research efforts have been made to widen the scope of operating wavelengths. In 1972, it had been shown for the first time that, in case of laser-driven plasmas, stimulated emission can significantly contribute to the enhancement of certain spectral lines in the soft X-ray domain [Jaeglé et al., 1971].

The laser effect hinges on the **population inversion** between two energy levels of an element atomic transition. In this configuration, stimulated emission is promoted and leads to the generation of coherent photons, whose properties characterize laser emission. Extending the operating range of lasers in the soft X-ray range faces two main difficulties.

First, a large energy gap between the atomic levels of the laser transition, corresponding to the emission of soft X-ray photons, is required. Energies of a few tens to hundreds of electron-volts (eV) are therefore needed. The fact that binding energies of solids or molecules only reach at best a few eV illustrates the unfeasibility of the approach using conventional active media. The solution consists in resorting to plasmas populated with **multi-charged ions**, which display those energetic transitions. Lasing in the soft X-ray range requires strong plasma ionization as the energy difference between two levels of a transition gets larger with the increasing charge of the nucleus.

Second, traditional lasers operating in the visible to IR use resonant optical cavities to amplify radiation over multiple passes. This architecture is irrelevant in the soft X-ray range because of the lack of very high-reflectance mirrors at those wavelengths. Moreover, in most cases, the gain lifetime of plasma active media is too short to allow amplification over numerous passes. But, fortunately, high gains are promised, which turns **one-pass amplification** practical.

Radiation from such soft X-ray laser plasmas is characterized by *Amplified Spontaneous Emission* (ASE). In this regime, the bound electrons populating the upper excited level of the laser transition tend to de-excite spontaneously and emit photons at the transition wavelength. This initiates a coherent amplification of those photons by the plasma through stimulated emission. Because of the stochastic nature of spontaneous emission, the resulting emission is weakly spatially coherent. We will see in chapter 2 & chapter 5 that the emission properties can be greatly enhanced resorting to the so-called « **seeding technique** ».

### 1.2.1 Population inversion in a plasma

Achieving a population inversion is carried out through a **pumping process**, which populates the excited levels of bound electrons of multi-charged ions and allows, as showed in section 2.3.1, a larger population in the upper level than in the lower level of the laser transition.

Two main schemes have been proposed and experimentally investigated to yield a population inversion: the **recombination** and the **collisional** pumping schemes. The fig. 1.7 shows the ion species and the range of wavelength they can operate respectively. Besides, a inner-shell ionization scheme has been pioneered.



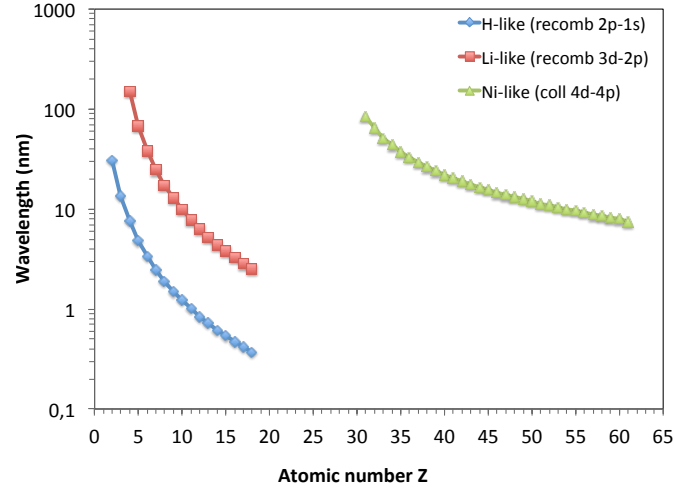


Figure 1.7: Envisioned ion species and their lasing wavelengths regarding recombination (H-like and Li-like ions) and collisional (Ni-like ions) pumping schemes.

### Inner-shell ionization

This scheme was first proposed by Duguay et Rentzepis in 1967 [Duguay and Rentzepis, 1967]. Its principle is depicted in fig. 1.8 and relies on photoionization of a plasma, which occurs when the energy of an incoming photon is equal or greater than the binding energy of the electron bound to the atom. This process involves the absorption of the photon by the atom, which results in freeing an electron. By contrast to recombination and collisional pumping schemes, inner-shell ionization involves the removal of an electron from the atom inner-shell. This process occurs for high energy incoming photons in the wavelength range of X-rays and for a short duration pulse. The hole created by the removal of an inner-shell electron from shell K is then being occupied through the de-excitation of an electron from the outer-shells, which results in the emission of a high-energy photon.

In this pumping scheme (fig. 1.8), the lower level of the laser transition is the ground level of the ion. The resulting emission in the soft X-ray is transient and ultrashort for two reasons. First, multiple processes, such as collisional ionization of a lower charged ion, populate the lower level of the laser transition and hence reduce the lifetime of the population inversion. Second, the Auger de-excitation depopulates the upper level of the laser transition. This de-excitation is a non-radiative process and the radiated energy is transferred to a bound electron, which is then freed. The Auger effect is ultrafast and also leads to a reduction of the time window, in which a population inversion is achieved.

The population inversion requires drastic conditions for the pump beam. The pumping pulse should be sufficiently intense and ultrashort in order to minimize the occurrence of Auger ionization for the upper level, and the population of the lower level. Another hurdle in the implementation of this pumping scheme is linked to the synchronization of amplified emission with the generation of the amplifying plasma. Experimental approaches resorted to the use of X-ray Free Electron Lasers as a pump beam [Zhao et al., 2008; Rohringer et al., 2012] or the use of betatron emission [Ribière et al., 2010].

Despite the difficulties deeply associated to its principle of operation, inner-shell ionization pumping features many advantages, such as the possibility of amplifying very short wavelengths [Kapteyn, 1992] ( $\approx 1.5$  nm for  $Z = 10$ ) over ultrashort durations ( $\lesssim 100$  fs) thanks to light species

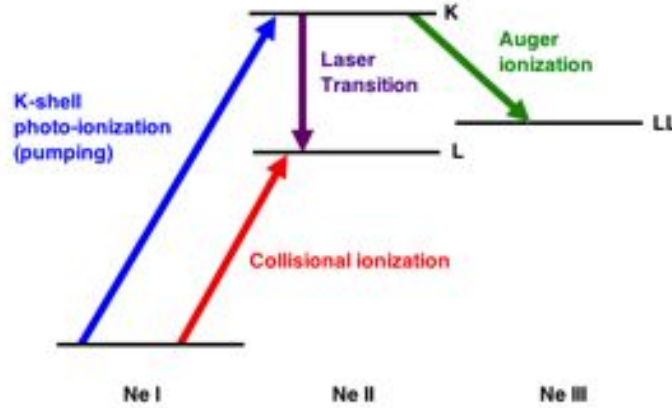


Figure 1.8: Principle of the X-ray lasing scheme using inner-shell photo-ionization illustrated in the particular case of neon. The X-ray pump can be generated by the interaction of an IR laser with a plasma or from FEL emission. The amplified wavelength corresponds to a few nanometers.

( $Z = 10$ ). Furthermore, the required pump energy is quite small when considering the very short amplified wavelength [Eder et al., 1994].

### Recombination pumping scheme

The theoretical model of plasma recombination pumping scheme has been introduced by Gudzenko and Shelepin in 1965 in case of hydrogen [Gudzenko and Shelepin, 1965] and has been then extended for hydrogen-like [Seely et al., 1985] and lithium-like [Jaeglé et al., 1986] species. The principle of this process is illustrated in fig. 1.9. It consists in generating a dense highly ionized (of charge  $Z+1$ ) plasma. In those conditions, some recombination mechanisms preferentially populating the excited states of the ion of charge  $Z$  can be promoted. Thus, ultrafast de-excitation via radiative collisional cascade towards the lower excited levels of this ion allows building up a population inversion.

The resulting laser effect occurs for H-like transitions  $3d \mapsto 2p$  or Li-like  $5f \mapsto 3d$  or  $4f \mapsto 3d$  transitions (fig. 1.9). In both cases, those schemes are characterized by a strong spontaneous emission rate for the lower level of the laser transition, whereas the upper level is pumped by radiative cascades from highly charged atomic levels. The latter have been earlier populated by collisional recombinations from the fully ionized continuum (case of H-like transitions) or by collisional and dielectronic recombinations from the He-like ground state (case of Li-like transitions). Those mechanisms were highlighted for the Balmer line of C VI by theoretical [Pert, 1976] and experimental [Pert, 1976] works. We can notice that the laser effect cannot take place with the ground state as the lower level, because the collisional ionization of the plasma contributes to build up a significant population of the ground level.

The advantages of this X-ray lasing scheme lie in the intrinsic ultrashort nature of the laser transition (down to a few tens of femtoseconds), as well as in its ability to be operated for short wavelengths (shorter than those induced between the excited levels) that can reach the so-called « water window » (between 2.34 and 4.4 nm), for which numerous applications in biology can be envisioned.

Nevertheless, the challenges associated with the implementation of such a scheme are numerous [Zeitoun, 1994]. The experimentally demonstrated gains are weak. In case of H-like lithium

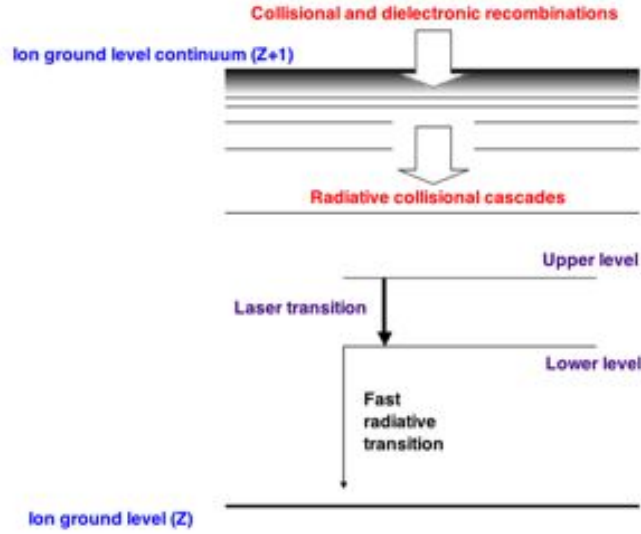


Figure 1.9: Principle of the recombination pumping scheme.

emitting at 13.5 nm, the gain was reported to be less than  $10 \text{ cm}^{-1}$ . Besides, saturation regime has not yet been achieved. Actually, this lasing scheme requires drastic experimental conditions. The first difficulty is to use ultra-intense [Penetrante and Bardsley, 1991] pulses to generate fully ionized species in case of H-like ions or He-like species in case of Li-like ions. Secondly, obtaining a population inversion is based on ultrafast emptying of the lower level of the laser transition via a radiative transition, and first of all on a high collisional recombination rate to populate the upper level. The latter rate varies as a function of  $n_e^3/T_e$  with  $n_e$  the electron density and  $T_e$  the electron temperature. Thus, appropriate conditions are met for an electron density of  $10^{21} \text{ cm}^{-3}$  and an electron temperature limited to a few tens of eV. However, the ionization mechanisms of solid and gas targets are strongly relying on collisions, which leads to a significant plasma heating. In this view, the previously stated conditions appear contradicting.

Nevertheless, techniques were proposed to reach those stringent thermodynamic requirements. The use of ultrashort driving laser pulses (a few 10s of fs) allows strongly ionizing the medium through tunneling effect, which limits plasma heating. However, this is far from sufficient and this should be combined to techniques enabling ultrafast cooling of the plasma [Pert, 1976]. In this perspective, the proposed methods include the electromagnetic confinement of the plasma [Suckewer et al., 1985] to increase the radiative losses, the increase of the thermal conduction via wall contact [Kim et al., 1989], or the use of a gas mixture with low Z species (hydrogen for example).

The prospective laser transitions for this scheme are the  $3d_{5/2} \mapsto 2p_{3/2}$  transition at 9.81 nm for lithium-like neon [Eder et al., 1991] where a maximal theoretical gain of  $g_{max} = 130 \text{ cm}^{-1}$  is computed for  $n_e = 5 \times 10^{20} \text{ cm}^{-3}$  and  $T_e = 40 \text{ eV}$ ; as well as two transitions for hydrogen-like nitrogen [Hulin, 2001]: the  $2p_{3/2} \mapsto 1s_{1/2}$  transition at 2.48 nm ( $g_{max} = 1100 \text{ cm}^{-1}$  for  $n_e = 6 \times 10^{20} \text{ cm}^{-3}$  and  $T_e = 15 \text{ eV}$ ) and the  $3d_{5/2} \mapsto 2p_{3/2}$  transition at 13.39 nm ( $g_{max} = 190 \text{ cm}^{-1}$  for  $n_e = 10^{20} \text{ cm}^{-3}$  and  $T_e = 20 \text{ eV}$ ).





et al., 1992]. The collisional scheme is the most widely used and yields high gains. This scheme requires hot and dense plasma, which therefore turns easy to implement. Available wavelengths with this pumping scheme spread from 3 to 60 nm. This architecture has been mainly achieved by irradiating solid or gas targets with lasers, but also by electric discharge.

Amid the various considered plasma pumping schemes [Daido, 2002], the **collisional** pumping scheme proved to be the most successful one since it turned out robust, demonstrated high gains and was the only one, which allowed to reach the saturation regime. This thesis is focused on the implementation of the **collisional pumping** scheme in a krypton plasma.

### 1.2.2 Overview of the development of collisional soft X-ray lasers

Since the mid-90s, most developments of soft X-ray lasers focused on the collisional pumping scheme. Various techniques to implement this scheme have been developed and their timeline has been strongly impacted by the parallel progresses on driving lasers.

#### Quasi-Steady State (QSS) pumping

The first soft X-ray lasers taking advantage of collisional excitation were achieved using fusion-class laser facilities using high-energy (a few hundreds of Joules) and long duration (a few nanoseconds). The excitation scheme is known as Quasi Steady State (QSS) pumping. In this pumping scheme, the population of the energy levels of the plasma lasing ions reaches an equilibrium. The maiden run of this scheme was demonstrated in 1985 at LLNL (Lawrence Livermore National Laboratory) [Matthews et al., 1985]. Those lasers deliver pulses of a few mJ with a duration of about 100 ps. First plasma-based soft X-ray lasers exhibiting high a gain-length product were demonstrated in 1985 at 20.6 nm [Matthews et al., 1985] and 18.2 nm [Suckewer et al., 1985]. This experiment was carried out using the then most powerful laser delivering kJ-class pulses.

Rather long media are obtained focusing the laser beams onto a focal line using a cylindrical lens or an off-axis spherical mirror, as illustrated in fig. 1.11. The long duration of the pump pulse allows for a significant inverse-Bremsstrahlung heated electrons, which are used to pump the laser transition of a multi-charged ion.

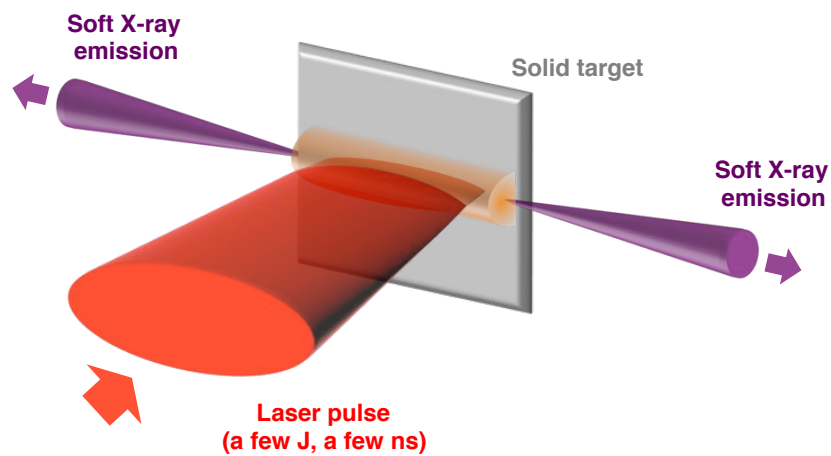


Figure 1.11: Illustration of the QSS pumping principle.

This regime allowed achieving very short wavelength, such as 3.56 nm in case of Ni-like gold [McGowan et al., 1992a]. However, the reported gain coefficients were very low ( $2 \text{ cm}^{-1}$ ). The use of shorter pulse duration driving lasers ( $\sim 100 \text{ ps}$ ) made it possible to reach higher ionization degrees and higher electron temperatures, which lead to higher gain coefficients. In those conditions, saturated amplification was demonstrated for Ni-like silver at 13.9 nm [Zhang et al., 1997] and Ni-like tin at 11.9 nm [Ros, 1999].

Further developments allowed generating lower wavelengths and included the use of a pre-pulse, which enabled reaching saturation. Considering the fairly long lifetime of the amplifying medium, this type of laser can operate in a double-pass configuration, which allows increasing the energy of the emitted pulse and improving the optical quality of the beam without any additional pump energy. This architecture was successfully implemented at PALS (Prague Asterix Laser System) facilities. This installation operates a Ne-like Zn QSS soft X-ray laser emitting at 21.2 nm thanks to a driving laser using a half multi-pass laser cavity [Ceglio et al., 1988]. The system delivers pulses of a few mJ per pulse with a duration of about 100 ps.

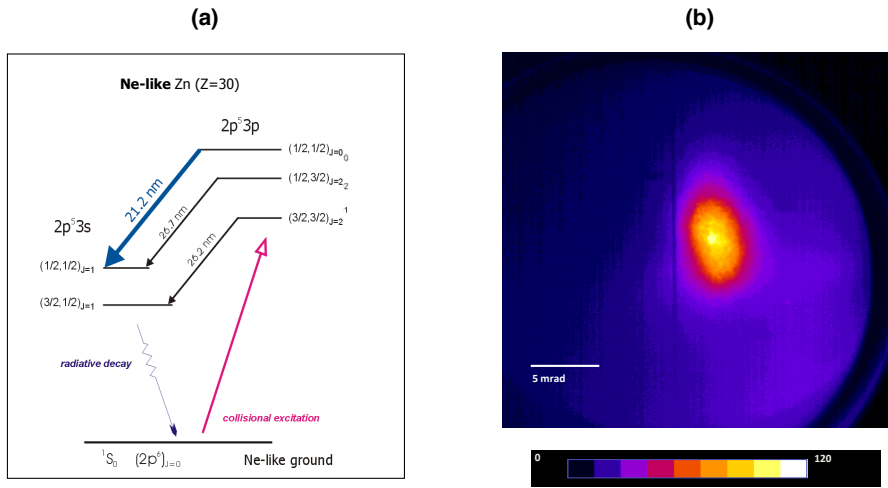


Figure 1.12: (a) Laser pumping scheme of the Ne-like Zn QSS laser operated at PALS. (b) Profile of the beam displaying a  $3.5 \times 5.5 \text{ mrad}$  divergence, an energy of 4 mJ per pulse (about  $10^{14}$  photons) and a pulse duration of 150 ps.

However, this scheme faces strong limitations because refraction effects prevent from increasing laser intensities and reaching saturation. The use of a pre-pulse can help overcoming this problem by creating a weakly ionized pre-plasma allowing a lower electron density gradient and improving the absorption of the main long pulse [Rus et al., 1997]. A few cm long plasma amplifiers can thus be created. Besides, a two-filament technique was implemented to balance refraction and reach saturation [Lewis et al., 1992].

Numerical and experimental studies showed that the use of shorter pulses (less than 100 ps) leads to more favorable conditions for the collisional pumping scheme. Indeed, a faster pumping process allows higher plasma heating on the timescale when the relevant multi-charge ions are generated. As a consequence, this results in higher amplification of X-rays and reducing the energy required to achieve the plasma amplifier.

The main drawbacks of this pumping scheme are related to their very low repetition rate and the high cost of high-energy laser installations. Moreover, the demonstrated pulse durations are long and lie in the range of one hundred to a few nanoseconds.

### Transient pumping

Following the development of QSS lasers, a so-called "transient" pumping scheme has been introduced. Actually, the emergence of CPA (Chirped Pulse Amplification) techniques to deliver ultrashort and ultra-intense pulses for the driving laser led to the development of the transient pumping scheme.

The principle of this scheme is illustrated in fig. 1.13 and consists in decoupling the generation of lasing ions and the pumping of their laser transition. In this purpose, a long pulse and a short pulse are used. The long pulse (several hundreds of picoseconds) of moderate intensity (about  $10^{12} \text{ W/cm}^2$ ) is used to generate Ne-like or Ni-like ions at a relatively low electron temperature. This plasma is then irradiated by a short pulse (several picoseconds) of high intensity (about  $10^{15} \text{ W/cm}^2$ ). The free electrons are then heated and collide with ions to promote the bound electrons of the ion ground level to the upper level of the laser transition. A population inversion can therefore be generated. Soft X-ray emission is then observed in the direction of the progressive wave [Kuba et al., 2000]. This method uses a grazing incidence geometry to deposit energy step by step over a long length to allow photons to be effectively amplified as they propagate, despite the short duration of the gain (a few picoseconds).

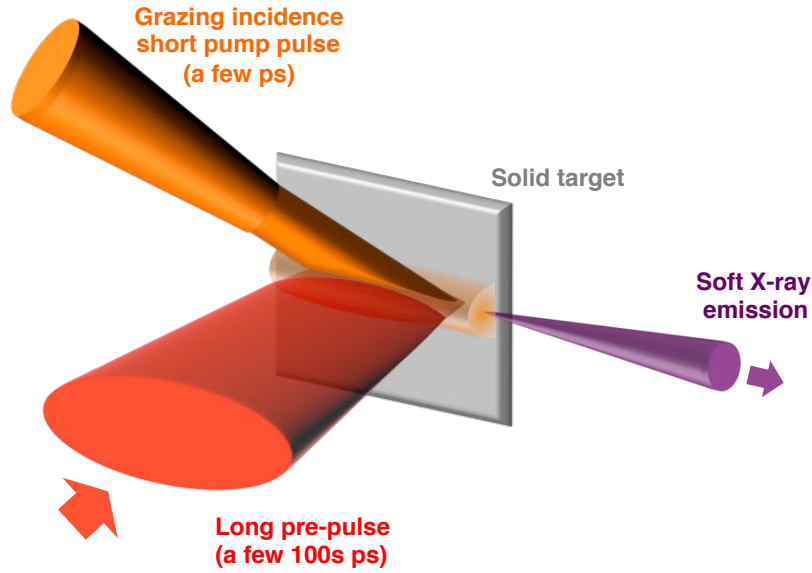


Figure 1.13: Illustration of the QSS pumping principle.

This pumping scheme is called *transient* because, contrary to the QSS process, this excitation scheme allows substantial gain to be achieved whereas the population of atomic levels did not have time to reach their equilibrium. The lifetime of the pumping process is significantly inferior to the characteristic timescale of the plasma ionization. While typical gains with the QSS scheme are about  $5 \text{ cm}^{-1}$ , the transient pumping method yields gains of about  $50 \text{ cm}^{-1}$ .

Besides, compared to the QSS pumping scheme, this technique allowed a significant reduction of the required energy to generate lasing ion species. This scheme was first proposed in 1989 [Afanasev and Shlyaptsev, 1989] and then first demonstrated experimentally in 1995 [Nickles et al., 1997] with Ne-like Ti. This operation has been achieved then with other Ne-like and Ni-like species [Kuba et al., 2000; Dunn et al., 1998], while the saturation regime was first realized with Ne-like Ge using an inhomogeneous wave [Kalashnikov et al., 1998].

The fig. 1.14 shows the demonstration of lasing action by the team of J.J. Rocca down to the range of 10 nm [Wang et al., 2005].

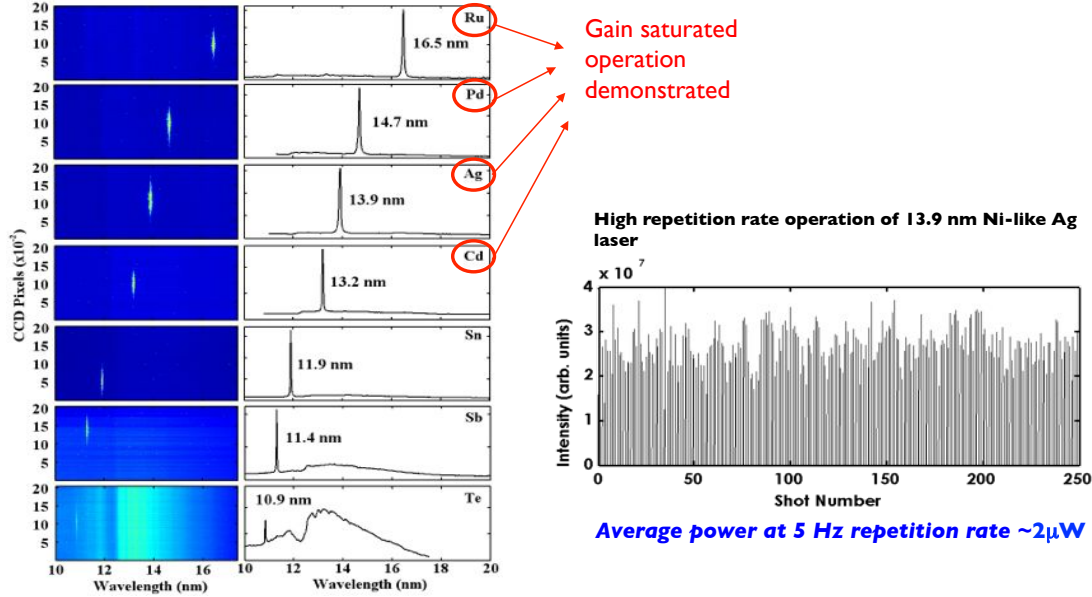


Figure 1.14: Experimental spectra of lasing action obtained from Ni-like species from rubidium to tellurium. Very good shot-to-shot stability is observed [Wang et al., 2005].

Moreover, higher repetition rates (about 10 Hz) can be reached. A *Grazing Incidence Pumping* (GRIP) technique has been more recently introduced [Keenan et al., 2005]. The short pulse responsible for the laser transition pumping is focused at grazing incidence onto the target. This configuration takes advantage of the short pulse refraction to improve the coupling between the pre-plasma and the pump. This setup allows operation at rates up to 10 Hz. A variant, dubbed DGRIP (Double-pulse Grazing Incidence Pumping), improves the beam stability and the repetition rate. It has been demonstrated at LASERIX facility with 10 Hz laser at 18.9 nm with energies surpassing  $2 \mu\text{J}$  [Zimmer et al., 2010]. Other such facilities are operated at JAEA (Japan Atomic Energy Agency) in Japan [Ochi et al., 2007] and at GIST (Gwangju Institute of Science and Technology) in South Korea [Kim et al., 2008].

The transient scheme was initially demonstrated on solid targets, but it has been extended to gas ones with a first experiment in 2002 using Ni-like Xe emitting at 9.98 nm [Lu et al., 2002].

The spatial profile of output soft X-ray laser emission is strongly inhomogeneous. Similarly to the emission from QSS soft X-ray lasers, the temporal coherence is high, whereas its spatial coherence is low. The advent of the transient pumping scheme allowed a significant reduction of the duration of emission, compared to the QSS scheme. The shortest duration demonstrated for transient soft X-ray lasers yielded 2 picoseconds [Klisnick et al., 2002]. Those QSS pumped soft X-ray lasers now operate at electron densities of a few  $10^{20} \text{ cm}^{-3}$ . An improvement of the spatial coherence of the source has been demonstrated by resorting to a seeding technique [Wang et al., 2008]. In this case, pulse durations as short as 1 ps have been measured [Wang et al., 2014].

### OFI collisional pumping

This pumping scheme is used in this thesis work. The use of ultrashort and intense driving lasers (of duration below 100 fs) is relatively recent and was motivated by the availability of higher repetition rate laser systems based on Ti:sapphire technology and delivering ultrashort and intense pulses. The OFI plasma-based soft X-ray laser scheme was first proposed in 1989 [Corkum et al., 1989]. This scheme was described theoretically in 1994 [Lemoff et al., 1994] and demonstrated experimentally shortly thereafter [Lemoff et al., 1995] with a lasing line at 41.8 nm obtained from a xenon plasma column. However, while opening the high repetition rate sources, the lack of proper understanding of the physics of interaction at the time delayed the development of those sources. A saturated amplifier in the xenon was only achieved in the early 2000s [Sebban et al., 2001] and shortly after in krypton [Sebban et al., 2002] at 32.8 nm.

This scheme is illustrated in fig. 1.15 and is implemented focusing an ultrashort (a few 10s of fs) high-intensity (over  $10^{17} \text{ W/cm}^2$ ) infrared pulse into a gas [Sebban et al., 2002] target. Contrary to QSS and transient pumping geometries, the plasma amplifier is generated longitudinally as the intense IR pulse propagates. The interaction between an ultrashort and intense laser pulse with a plasma induces the so-called "optical field ionization" (OFI) of atoms. This process results in successively stripping electrons within the very strong electric field, till getting highly charged ions, displaying transitions with energy gaps corresponding to the soft X-ray range. Subsequently, collisions of hot electrons with multi-charged ions allow pumping the laser transition.

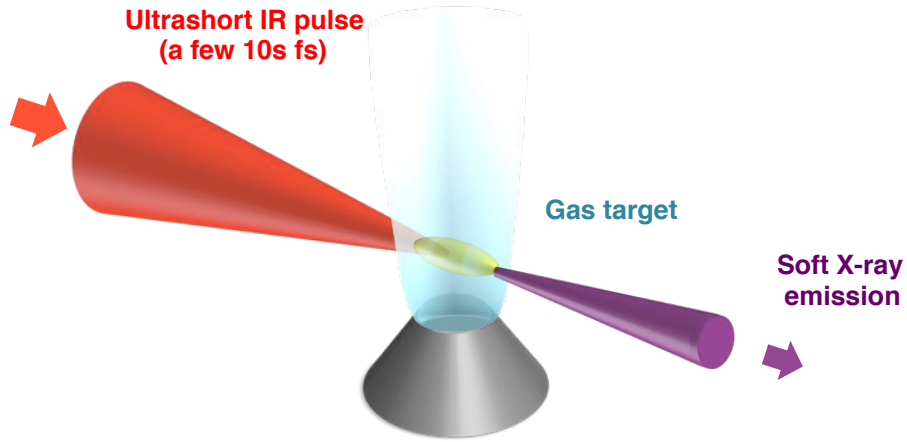


Figure 1.15: Illustration of the OFI pumping scheme.

For OFI plasma amplifiers, lasing species are ion species exhibiting a full atomic sub-shell. Those elements prove stable and "resistant" to further over ionization. This overionization can come from OFI or ongoing collisional ionization initialed by the significant generation of hot electrons, which turns vital for pumping the laser transition. Hence, the stability of those species will maximize the fraction of ions that may be effectively pumped and then emit in the soft X-ray range. Eight times-ionized neon, xenon and argon prove to be very stable species. Their lasing transitions are summed up in table 1.1 and the four-level pumping scheme is illustrated in fig. 1.16.

Amid the advantages of this approach, the generation of the lasing ions population and pumping are implemented with the same ultrashort laser pulse, thus making the approach

Ion	A Pd-like Xe (n=4)	Ni-like Kr (n=3)	Ne-like Ar (n=2)
Transition	5d-5p	4d-4p	3p-3s
Wavelength	41.8 nm	32.8 nm	47.8 nm

Table 1.1: Transitions of common OFI plasma-based soft X-ray lasers

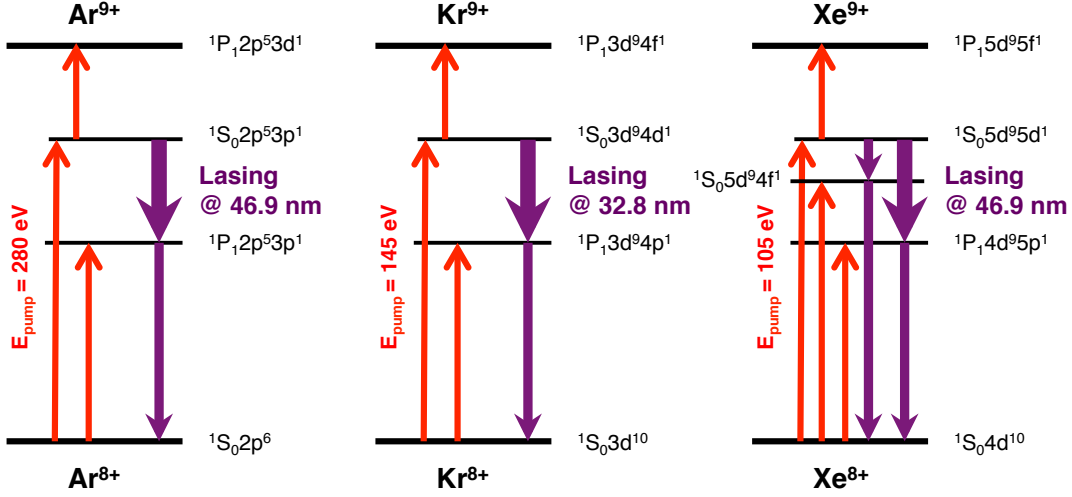


Figure 1.16: Simplified scheme of the laser transition levels associated with ions  $\text{Ar}^{8+}$ ,  $\text{Kr}^{8+}$  and  $\text{Xe}^{8+}$ . Red arrows stand for populating processes resulting from electron-ion collisions. Purple arrows denote the radiative transitions. Electron energies for pumping the upper levels of the laser transitions are presented in eV.

more simple, compared to transient [Afanasev and Shlyaptsev, 1989] and quasi-steady state (QSS) [Kungwirth, 2001] plasma-based soft X-ray lasers. Such low energy requirements can be provided by tabletop laser drivers implementing CPA techniques.

The gain of such OFI plasma amplifiers depends on the electron density, the propagation of the driving laser and its polarization, which impacts the heating of electrons and thus the efficiency of pumping. Those sources have been demonstrated at high repetition rates reaching 10 Hz and yielding pulses of a few picoseconds with energies of several 100s of nJ [Bettaibi, 2005].

Waveguiding the driving pulse using hollow capillary tubes [Mocek et al., 2004] or plasma capillary discharge waveguides [Butler et al., 2003] allowed increasing the length of the amplifying medium and thus a boost of the photon yield. More recently, the demonstration of high-density plasma waveguides [Chou et al., 2007; Lin et al., 2007] opened promising prospects. The work of this thesis comes in line with those developments.

### Electric discharge pumping

In parallel to laser-driven plasma-based soft X-ray lasers, an alternative to achieve collisional pumping relies upon the use of electric discharges. This work has been successfully led by the team of J. Rocca from 1985.

The first demonstration of a soft X-ray laser operating with this principle was performed at CSU in 1994 [Rocca et al., 1994; Vinogradov and Rocca, 2003]. In this scheme, the gas confined



in a capillary tube and a very high electric current (a few kA) with a very steep rising edge (a few 10s of ns) generates a significant population of lasing ions. The Ohm heating process is yielding heat electrons, which then pump the lasing ion laser transition through collisional excitation. The main virtues of those lasers are related to their ability to run at fairly high frequency (4 Hz) and deliver high energy pulses (a few mJ). Those characteristics were reached in Ne-like Ar emitting at 46.9 nm [Macchietto et al., 1999]. However, this scheme makes it difficult to reach shorter wavelengths as this would require higher currents, which lead to instabilities rapidly degrading the uniformity of the plasma required to efficiently amplify photons. Moreover, the duration of those pulses is restricted to the nanosecond range.

The system is illustrated in fig. 1.17 and consists of a gas confined in a few cm long capillary tube. Lasing action was obtained through the direct excitation of the plasma medium by a pulsed discharge. This setup benefits from the efficient deposition of electrical energy into a plasma. A very high intensity (a few kA) is sent via conducting plates at the extremities of the tube. A very fast, low-impedance electrical discharge is generated and creates a uniform plasma. This extreme ultraviolet laser delivers pulses of a few mJ at high repetition rates (10Hz) with about 100 ns pulse duration. It successfully operates the 3p-3s atomic transition of  $Ar^{8+}$  at 46.9 nm with argon.

In order to implement such a few cm-long emitting plasma, a capillary discharge waveguide is achieved (see section 3.1.2) the lasing ions are mixed with hydrogen.

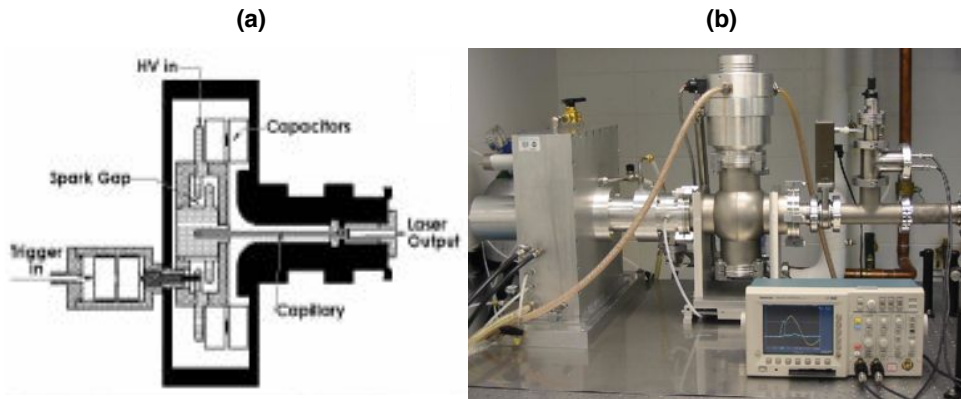


Figure 1.17: Capillary discharge EUV laser developed at CSU operating at 46.9 nm. (a) Principle. (b) Experimental setup (Colorado State University).

Nevertheless, this type of soft X-ray laser is limited to both long wavelengths and pulse duration (about 1 ns). But the compactness of the system, the large available energy (mJ) and its operating rate (10 Hz) turn it into an remarkable source.

## 1.3 Seeded collisionally-pumped OFI plasma-based soft X-ray laser chain

### 1.3.1 Source performances and limitations

In the same way as QSS and transient soft X-ray lasers, collisional OFI plasma-based soft X-ray lasers display an inhomogeneous spatial profile of emission, which limits the range of potential applications. These emission features are due to the fact that ASE corresponds to the amplification the plasma own "noise", made of incoherent spontaneous emission.



However, aside from being compact and rather inexpensive, plasma-based soft X-ray lasers turn out enticing since they can emit a large number of photons in one single pulse [Rus et al., 2002] (up to  $10^{15}$  photons) within a very short line width ( $d\nu/\nu \sim 10^{-5}$ ).

The low coherence of those sources lead to envision the plasma, not as a source in itself, but as an amplifier in a soft X-ray laser chain where an external coherent source is used to seed the plasma. The « seeding architecture » has been proposed by T. Ditmire and then demonstrated at Laboratoire d'Optique Appliquée in case of collisional OFI amplifiers using a high-harmonic source as a seed. Such an experimental setup is illustrated in fig. 1.18. Those sources exhibit high-quality optical properties and adjustable linear polarization [Zeitoun et al., 2004]. More recently, this geometry has also been adopted regarding transient plasma-based soft X-ray lasers and showed similar beam quality improvements [Wang et al., 2008]. However, the amplified high-harmonic energy remained quite low ( $100 \mu\text{J}$ ) because of a rather small gain region induced by the plasma hydrodynamics [Oliva et al., 2009].

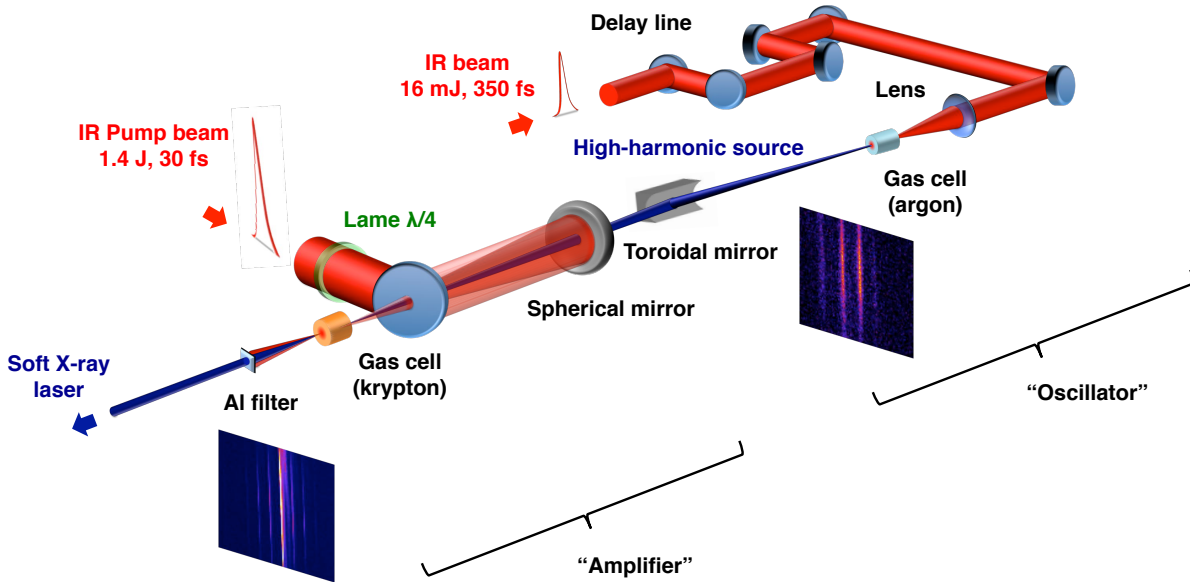


Figure 1.18: Architecture of a soft X-ray laser chain comprising an "oscillator" (high-harmonic source) and an "amplifier" (plasma).

The following paragraphs summarize the previous achievements regarding a HH-seeded collisionally pumped OFI krypton plasma-based soft X-ray laser. The results presented in this thesis are built upon those previous achievements.

**Beam spatial quality.** The fig. 1.19 illustrates the spatial profiles of a plasma-based soft X-ray laser emission obtained with krypton at pressure of 50 mbar using a pump beam intensity of  $10^{18} \text{ W/cm}^2$ . The Gaussian-like far-field profile and the low divergence of the high-harmonic beam are maintained over the amplification in the plasma.

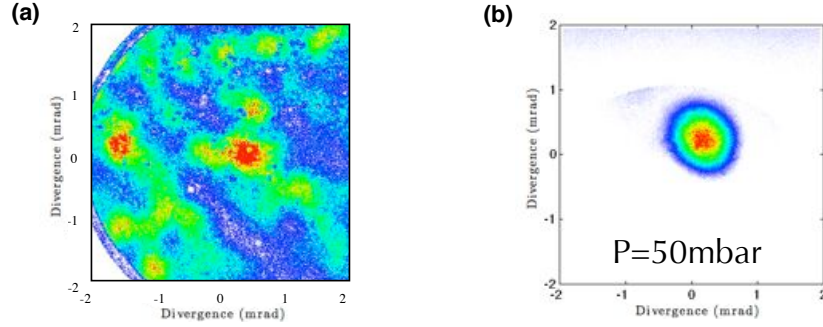


Figure 1.19: (a) Energy distribution of the amplified spontaneous emission. (b) Energy distribution of the soft X-ray plasma-based X-ray laser (in case of krypton-filled cell) [Tissandier, 2011].

**Beam wavefront quality.** As far as the spatial wavefront is concerned, the HH beam exhibits a near-diffraction wavefront [Gautier et al., 2008] and those attractive characteristics are preserved when being amplified by the plasma [Goddet et al., 2009]. The fig. 1.20 shows the phase deformations are even reduced over propagation. While a  $\lambda/2.5$  quadratic normal shift of the wavefront deformations has been measured for HH, it was found to reach  $\lambda/11$  for the seeded soft X-ray laser signal. This nearly corresponds to the diffraction limit according to the Maréchal criterion [Born and Wolf, 1959], for which  $\Delta\lambda_{RMS} = \lambda/14$ .

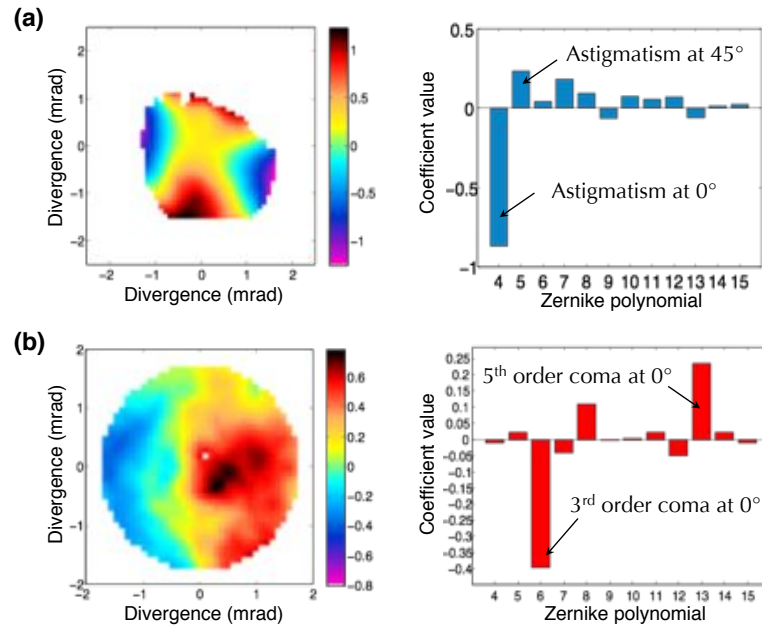


Figure 1.20: (a) Wavefront of the high-harmonic signal. (b) Wavefront of the HH-seeded soft X-ray laser. [Tissandier et al., 2010b]. Aberrations get corrected thanks to spatial filtering in the plasma amplifier.

Those excellent properties promise very good soft X-ray focusing characteristics, which are essential to minimize losses and maximize on-target intensity.

**Emission spatial coherence.** Regarding the source coherence, the HH-seeded plasma-based soft X-ray lasers display excellent features. It keeps the very good spatial coherence of HH [Ditmire et al., 1996]. The fig. 1.21 illustrates this result with a Young slit experiment with adjustable slit separation. A system of fringes is observed with a contrast depending on the spatial coherence between the interfering secondary sources defined by the slits. The amplified spontaneous emission is mostly incoherent because of the stochastic nature of spontaneous emission. This translates into a rather large cone of emission of a few tens of milliradians. By contrast, the HH and HH-seeded SXRL emissions are spatially coherent and have a divergence in the order of 1 mrad (see fig. 1.19).

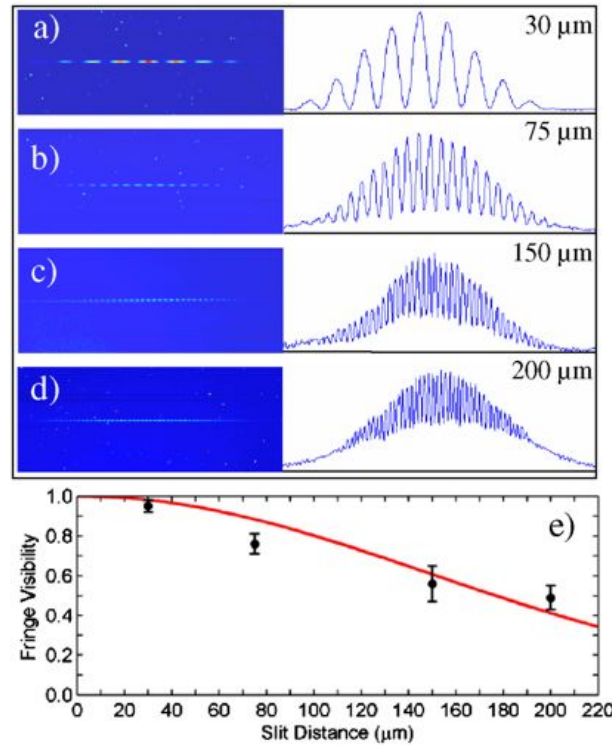


Figure 1.21: Results of Young slit pair interference experiment for the output of a seeded laser amplifier emitting at 32.6 nm. (a) - (d) Interferograms for different slit separation. (e) Plot of the degree of coherence as a function of the slit separation [Wang et al., 2006].

**Emission temporal coherence.** The temporal coherence is related to the spectral linewidth of the source and characterizes the timescale on which photons are found to have a defined phase relationship between each other. It can be measured using a varying optical path difference interferometer consisting of a Fresnel double mirror system with slanted angles [Joyeux et al., 1995]. This system introduces a tunable time delay between two parts of the same source, which then interfere and yield a system of fringes whose contrast depends on the temporal coherence of the source. The fig. 1.22 illustrates those results for both ASE and the amplified HH signals in case of a collisional OFI krypton plasma at 30 mbar. As expected the fringe visibility decreases

as the delay increases. The coherence time  $\tau_c$  of the pulses, defined by the time difference at which the visibility is decreased by a factor  $1/e$ , is not the same for the two cases investigated. It was estimated as  $5.1 \pm 0.2$  ps for the seeded SXRL pulse and slightly larger at  $5.5 \pm 0.3$  ps for the ASE SXRL pulse. According to the Wiener-Khinchin theorem, the evolution of the fringe visibility with the delay is the Fourier transform of the spectral density of the source. The spectral profiles have been calculated from the fitted visibility variations, and correspond to spectral Voigt profiles with a full width at half-maximum (FWHM) of  $\Delta\nu = 89 \pm 6$  GHz ( $\Delta\lambda = 3.2 \pm 0.2 \cdot 10^{-13}$  m) for the seeded SXRL and  $\Delta\nu = 75 \pm 8$  GHz ( $\Delta\lambda = 2.7 \pm 0.3 \cdot 10^{-13}$  m) for the ASE. We can notice that the linewidth of the amplified HH is slightly larger than the ASE linewidth. Indeed, the initial linewidth of the HH signal is far larger than the laser transition linewidth. The plasma amplifier gain leads to a sharp narrowing of the amplified HH signal [Tissandier et al., 2010a].

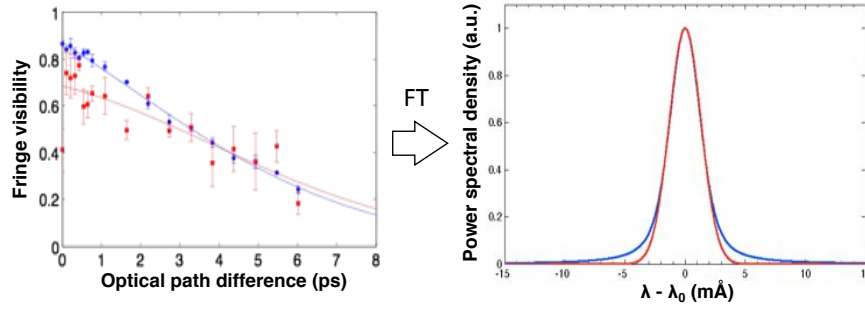


Figure 1.22: Temporal coherence in case of ASE (red) and HH-seeded soft X-ray laser (blue) [Tissandier et al., 2010a].

The source has been demonstrated to be Fourier-limited [Guilbaud et al., 2010] thanks to a measurement of the temporal coherence and the gain dynamics yielding the same value of 5 ps.

**Pulse duration.** Plasma-based soft X-ray lasers have been limited to the picosecond range [Klisnick et al., 2002; Wang et al., 2008] for more than one decade, consequently restricting the field of applications.

In 2005, the "seeding technique" was used to measure the time evolution of the gain of a soft x-ray laser amplifier [Mocek et al., 2005]. The HH seed pulse was injected into the plasma at different delays with respect to the plasma generation. Strong amplification was observed when the seed pulse is synchronized with the gain period. The fig. 1.23 illustrates those measurements, which were done with a  $Xe^{8+}$  plasma emitting at 41.8 nm. The study was carried out for low electron densities ranging from 5 to 25 Torr and showed a significant reduction of the time window, in which amplification takes place. This behavior is expected to affect the pulse duration in the similar way.

The main objective of this thesis was to explore the gain dynamics and the amplification regime of the seeded high-harmonic when operating significantly higher gas densities. Indeed, as the pulses emitted from OFI collisionally-pumped SXRLs are Fourier-limited, a broadening of the soft X-ray laser linewidth resulting from an increase of the electron density paves the way for generating ultrashort pulses.

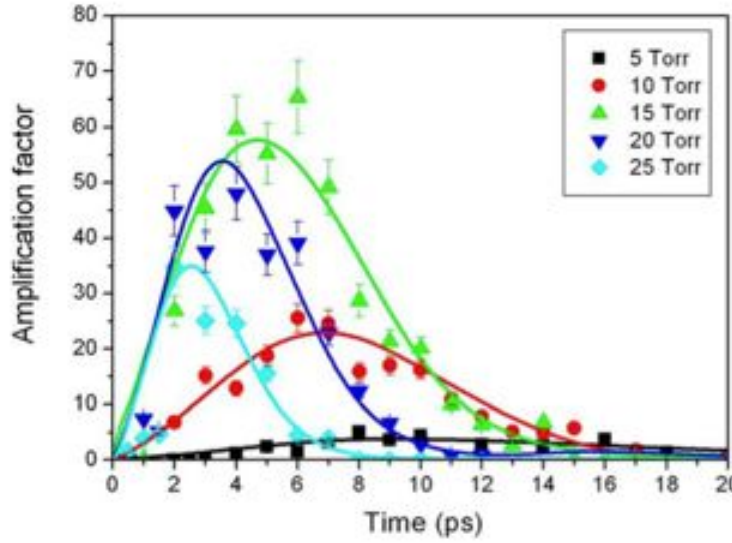


Figure 1.23: Measured amplification factor of the seeded  $\text{Xe}^{8+}$  laser for various gas pressures, as a function of the delay between the SXRL plasma generation and seed pulse injection [Mocek et al., 2005].

**Polarization.** Additionally, the polarization of HH-seeded plasma-based soft X-ray lasers has been restricted to linear polarization [Zeitoun et al., 2004]. Another focus of this thesis has been associated with the development of a circularly polarized plasma-based soft X-ray laser.

### 1.3.2 Prospective applications

The development of ultrashort plasma-based soft X-ray lasers, as well as the control of their polarization open new prospects for those sources and promise the ability to carry out research, at the laboratory-scale, in areas that were previously restricted to the XFEL community.

#### Time-resolved nanometer-scale applications

The development of intense ultrashort coherent X-ray pulses has granted scientists a very useful access to a wide range of research areas. A first application involves the use of the intense X-ray radiation to create previously unexplored exotic states of matter [Liu et al., 2014]. Matter interaction light in the soft X-ray range is dominated by photoionization. When subjected to ultrashort and intense coherent soft X-ray radiation, electrons are suddenly removed from molecules and leave them in a so-called "super-excited state", where coupled electronic and nuclear dynamics are ultrafast. Probing those photoionization-driven dynamic phenomena is possible thanks to advanced coincident molecular imaging techniques [Gagnon et al., 2008]. Secondly, those sources make also possible to get an insight into the ultrafast dynamics in matter. Thanks to times scales relevant to atomic or molecular dynamics, ultrashort coherent X-ray sources allow monitoring transient elementary processes in atomic or biology occurring on the femtosecond timescales. Applications include ultrafast [Vodungbo et al., 2012] and molecular physics [Zhou et al., 2008]. Finally, those intense soft X-ray sources also help pioneering high-contrast imaging at nano-meter spatial resolutions, notably opening prospects in biomedicine. When combined with new diffractive imaging techniques using iterative phase retrieval algorithms, those sources make wavelength-limited nano-imaging possible. Furthermore, intense pulses allow for the possibility to perform single-shot measurements, using for instance coherent

diffraction imaging techniques [Raines et al., 2010]. Apart from saving time, those techniques are essential when it comes to studying rapidly degrading biological samples. Furthermore, when subjected to such intense radiation, samples may be destroyed and the use of femtosecond-scale sources allows imaging those samples right before their destruction.

Those innovations were mostly driven by the development of expensive and large-scale facilities such as synchrotron and FELs, thus restricting their access and flexibility of use for laboratory-scale research. In this perspective, the advent of compact high-harmonic sources provide competitive tools to investigate space- and time-resolved phenomena. On their side, when seeded with HH, plasma-based soft X-ray lasers benefit from the many merits (spatial and temporal coherence, diffraction-limited wavefront) of HH while providing far more energetic pulses. One drawback is the impossibility of tuning the source wavelength but the sources still proves relevant for material and molecular structures imaging. The main drawback of HH-seeded plasma-based soft X-ray sources is that amplification of HH is performed at the expense of the soft X-ray emission final duration. For more than a decade, the duration of these sources has been limited to the picosecond range [Wang et al., 2008]. We will show that the introduced technique, named *Collisional Ionization Gating* allows breaking this duration barrier.

### Applications of polarized soft X-ray sources

Areas of applications for circularly-polarized coherent X-ray sources involve dichroism in various materials. For instance, unequal absorption of right- and left-handed circular polarization allows investigating folding and binding structures of proteins [Greenfield, 2006]. Hence, the structure of molecules can be revealed and their conformational changes due to the environment, interactions or mutations monitored.

Circularly polarized soft X-ray radiation finds also fruitful applications in the study of magnetic domains at nanometre-scale spatial resolutions. The magnetic contrast arises from the dependence of the X-ray absorption cross section at inner-shell absorption edges of aligned magnetic atoms on the relative orientation of the photon spin and the local magnetization direction. In this framework, the detection of the X-ray Magnetic Circular Dichroism (XMCD) [Schutz et al., 1987] proved to be extremely useful to study the magnetic properties of atoms, such as their spin and orbital magnetic moment. Moreover, the use of ultrashort pulse allows unveiling ultrafast magnetization and demagnetization dynamics in matter [Vodungbo et al., 2012; Stoll et al., 2004].

One burgeoning subject is related to the observation of chiral structures, notably in biology. Samples are said to be chiral when their configuration cannot coincide with their mirror image by any sequence of translations and rotations. Chiral properties turned to be of keen interest regarding molecules [Contini et al., 2012], crystals [Zhang et al., 2013], clusters [Micali et al., 2012], nanoparticles [Zhang et al., 2014] or metamaterials [Kuwata-Gonokami et al., 2005]. Those features can be reported studying the difference in optical response of the substance to left- or right-handed circularly polarized light. The fig. 1.24 illustrates quadrupole helix structure domains in  $DyFe_3(BO_3)_4$ . Probing such a material with circular polarization of variable helicity leads to intensity maps portraying the material specific helix structure [Usui et al., 2014].

The development of compact and rather inexpensive plasma-based soft X-ray lasers proved attractive since they promise a high number of photons per shot [Rus et al., 2002] combined with excellent optical [Goddet et al., 2009], previously only available in large-scale facilities [Ackerman et al., 2007]. The development of an efficient photon-rich circularly-polarized plasma-based source paves the way for single-shot measurements of various polarization-sensitive phenomena. Aside from a quicker measurement time, the opportunity to carry out single-shot imaging



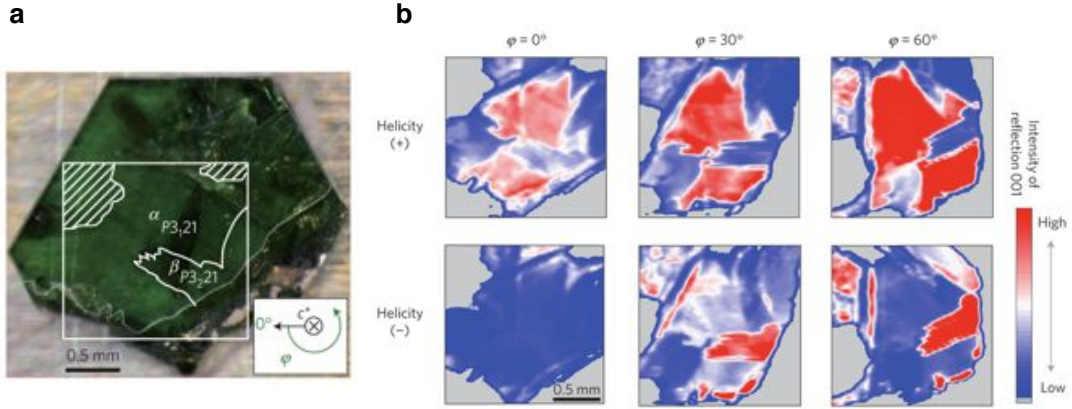


Figure 1.24: (a) Sample of  $DyFe_3(BO_3)_4$ . (b) Helicity-dependent back-reflection intensity maps for different azimuthal angles of the sample.

can be particularly appreciable when considering rapidly degrading biological samples. Imaging techniques could envisage single-shot holography [Eisebitt et al., 2004]. Another potential application of the source can be pump-probe experiments, such as X-ray crystallography [Boutet et al., 2012], because of the source intrinsic absence of jitter.

## 1.4 Conclusion

The development of high-performance coherent soft X-ray sources is nowadays mainly driven by the synchrotron scientific community, as XFELs provide very high-brilliance beams, which foster many breakthroughs in chemistry, biology, non-linear optics or the creation and study of previously unexplored states of matter. However, those sources are very large and expensive, thus limiting their availability for laboratory-scale research. In this perspective, being compact and cheaper, laser-driven soft X-ray sources appear as worthwhile alternatives.

While keeping their own intrinsic advantages, the development of HH-seeded plasma-based soft X-ray lasers turns out enticing since it allows approaching performances of large-scale facilities in some parameters. However, the fairly long duration of the emitted pulses (a few picoseconds), the modest output energy (a few 100s of nJ) and the restriction to linear polarization limit the scope of potential applications. The work of this thesis mainly aimed at pushing back those limitations introducing a technique to substantially reduce the pulse duration while boosting the output energy. Besides, work has been carried out to extend tune the polarization of plasma-based soft X-ray lasers to circular polarization.

# Chapter 2

## Physical processes in seeded collisional OFI plasma-based soft X-ray lasers

This chapter summarizes the main underlying theoretical principles behind lasing action in collisionally-pumped Optical Field Ionized (OFI) plasma-based soft X-ray lasers. OFI plasmas are achieved by focusing an ultra-short and intense infrared laser pulse ( $\approx 10^{18} \text{W/cm}^2$ ) into a gas column and thus promptly generating a sizable population of lasing ions within the intense IR laser field, which are then pumped through collisional excitation. The seeding of the plasma amplifier by a high-harmonic signal is described as well as the associated radiative transfer.

### Contents

---

<b>2.1</b>	<b>Laser-plasma interaction using an ultrashort pulse</b>	<b>32</b>
2.1.1	Types of ionization	32
2.1.2	The « Optical Field Ionization regime » regime: ionization rate	37
2.1.3	Energy distribution of electrons and ions	40
<b>2.2</b>	<b>Plasma kinetics</b>	<b>44</b>
2.2.1	Atomic processes	44
2.2.2	Evolution of electrons' and ions' temperature	47
<b>2.3</b>	<b>Population inversion, gain and radiative transfer</b>	<b>52</b>
2.3.1	Laser effect in the soft X-ray range	52
2.3.2	Gain dynamics	57
2.3.3	Saturation intensity	62
<b>2.4</b>	<b>Propagation of an ultrashort infrared pulse in plasmas</b>	<b>63</b>
2.4.1	Propagation equation	63
2.4.2	Beam refraction	67
<b>2.5</b>	<b>Modeling the amplification of HH by a plasma amplifier</b>	<b>72</b>
2.5.1	Field equations	73
2.5.2	Atomic description	74
2.5.3	Amplification of a HH seed pulse	76
<b>2.6</b>	<b>Conclusion</b>	<b>78</b>

---



## 2.1 Laser-plasma interaction using an ultrashort pulse

### 2.1.1 Types of ionization

To generate photons of energies in the soft X-ray range, one needs to create highly charged ions. In the case of OFI plasma-based lasers, the interaction medium is implemented by focusing an intense pulse of tens of femtoseconds duration with a high intensity ( $> 10^{16} \text{ W.cm}^{-3}$ ) into an ideal gas. In this part, the different mechanisms leading to the generation of a plasma of highly charged ions are presented.

Considering the simple Bohr model, the intensity of the laser field has to match the binding strength of the electron to the atom, in order to strip it from the atom's orbitals. For *low field strengths*, ionization occurs only if the absorbed photon energy exceeds the atom's ionization potential. This process depends on the laser intensity and the atom cross section. For *high field strengths* comparable to the atomic intensity, non-linear processes occur. The most important processes are multi-photon [Becker and Faisal, 2005], tunnel [Popov, 2004] and suppression-barrier [Delone and Krainov, 1998] ionization.

The amount of generated free electrons and conversely the population and charge of ions depend on the ionization potentials of different types of atoms, the laser intensity and its wavelength. Here, we will concentrate only on the laser field strength i.e the intensity. But, in the next part, we will see that the field components play an essential role in the electrodynamics of atomic system, which impacts the pumping process of the ion's transitions.

Electrons are trapped in the Coulomb potential that links them to the atom nucleus. Depending on the laser intensity undergone by the atom, the potential barrier can be either suppressed or lowered. For barrier-suppression ionization, the laser field should be very strong to leave free electrons. When the laser field is less intense, the potential barrier gets distorted and electrons can also be freed by tunnel ionization. This latter case corresponds to the so-called optical field ionization (OFI).

In 1965, Keldysh pioneered the theory of ionization for strong field interaction. This study showed that tunnel and barrier-suppression ionization are two limit cases of the same phenomenon, which corresponds to the non-linear ionization. Keldysh distinguishes two regimes, defining a parameter  $\gamma$ , such that [Keldysh, 1965]:

$$\gamma = \sqrt{\frac{U_I}{2U_p}} \quad (2.1)$$

where  $U_p$  is the ionization potential of the material and  $U_p$  the ponderomotive potential, defined as the free electron quiver energy. This corresponds to the average kinetic energy of the free electron oscillating in the laser field.

$$U_p = \frac{e^2 \mu_0}{8\pi^2 m_e c} I \lambda^2 \quad (2.2)$$

where  $e$ ,  $\mu_0$ ,  $m_e$ ,  $c$ ,  $I$  and  $\lambda$  are respectively, the electron charge, the vacuum permeability, the speed of light in vacuum, the laser intensity and its wavelength. In the low frequency and high intensity limit ( $\gamma \ll 1$ ), tunnel ionization and barrier-suppression ionization will occur. When  $\gamma \gg 1$ , multiphoton ionization occurs. Experimentally, a mixture of both regimes is observed, as no sharp frontier exists between those ionization phenomena.

• **Multi-photon ionization:**

Considering the interaction of a moderate intensity field with matter, photoelectric effect from a unique photon is impossible, as the material ionization potential is usually much greater than the laser photon energy. Actually, transitions between free or bound atomic levels are in the range of a few eV to tens of eV. High-power lasers are usually operating in the infrared wavelength range (Ti:Sapphire), where photon energies are below the eV threshold. Hence, those photons cannot ionize atoms or ions.

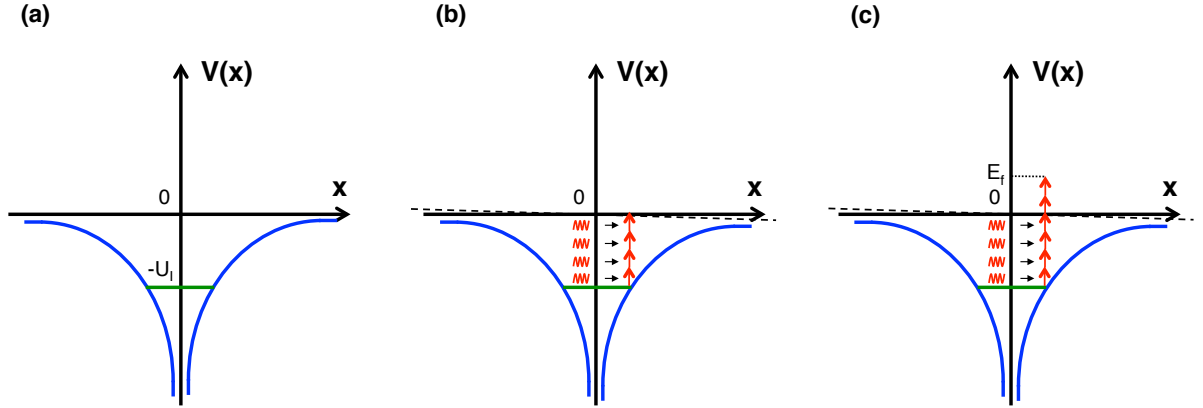


Figure 2.1: (a) Coulomb potential of an unperturbed ion. The trapped electron has a binding energy  $U_I$ . (b) Illustration of multi-photon ionization. An electron can simultaneously absorb  $n$  photons of energy  $\hbar\omega$ . Electrons are released with minimal kinetic energy. (c) In Above-threshold Ionization (ATI), the electron is stripped through multi-photon ionization but absorbs more photons than required to be freed and thus retains a non-negligible momentum.

However, laser-induced breakdown is observed at moderated intensities. This phenomenon is enabled by the simultaneous contributions of several photons to ionization, as illustrated in fig. 2.1. We can notice that the atomic binding potential remains undisturbed by the laser field. *Multi-photon ionization* predominates at field intensities between  $10^{11}$  and  $10^{13} \text{ W.cm}^{-3}$  [Agostini et al., 1968]. Its efficiency depends on the intensity of laser radiation, which rises as the flux of photons crossing a given surface increases. The probability of multi-photon ionization increases with the "photon density".

Resulting from ionization thanks to a large number of absorbed photons, the final kinetic energy of the electrons is given by the Einstein formula:

$$E_f = n\hbar\omega - U_I \quad (2.3)$$

where  $n$  is the number of absorbed photons needed for multi-photon ionization,  $\omega$  the laser frequency and  $U_I$ , the binding energy.

The rate of multi-photon ionization is proportional to the field strength:

$$\rho_{MFI} \propto E^{2N_{ph}} \quad (2.4)$$

where  $N_{ph}$  is the number of absorbed photons.

Similarly, an electron can absorb more photons than strictly necessary to free it from the atom. This process is known as *Above Threshold Ionization (ATI)* [Agostini et al., 1968].

$$E_f = (n + s)\hbar\omega - U_I \quad (2.5)$$

where  $s$  is the excess number of photons absorbed. This process takes place in the field of the parent ion and thus, conserves the momentum. Considering an initially immobile electron, its motion is governed, under a laser field by the equation:

$$\frac{d\mathbf{v}}{dt}(t) = -\frac{e}{m_e}\mathbf{E}(t) \quad (2.6)$$

For a field polarization defined by the parameter  $\phi$  ( $\phi = 0$ : linear /  $\phi = 1/2$ : circular), the transverse field components are written:

$$E_x = \sqrt{\frac{2I\phi}{\epsilon_0 c}} \quad \text{and} \quad E_y = \sqrt{\frac{2I(1-\phi)}{\epsilon_0 c}} \quad (2.7)$$

The term  $\phi$  describes the dependence on the laser field polarization.  $\phi=0$  or  $1/2$  corresponds to linear and circular polarization respectively. Under a laser electric field  $E_0$  of frequency  $\omega$ , the electron of mass  $m_e$  oscillates and gets a kinetic energy given by:

$$E_{ATI} = \frac{e^2 E_0^2}{2m_e \omega^2} [\phi \cos^2(\omega t) + (1 - \phi) \sin^2(\omega t)] \quad (2.8)$$

The magnetic effects are here neglected.

- **Barrier-suppression and tunnel ionization:**

This regime corresponds to the low frequency-high intensity limit of the Keldysh parameter defined in the relation eq. (2.1). At higher laser intensities ( $> 10^{13} \text{W.cm}^{-2}$ ), the field is strong enough to significantly distort the Coulomb potential. This strong laser field reaches the order of magnitude of the electron-atom binding potential and thus a perturbative approach, as considered for multi-photon ionization, is no more possible.

A quasi-static treatment can be used here because the laser frequency is far smaller than the atomic frequency. This corresponds to the case where the laser photon energy is very small compared to the atomic transition energy. In this case, we can consider that the electron could respond adiabatically to the applied laser potential. Hence, the laser field  $E$  can be considered to be static.

The *barrier-suppression ionization* (BSI) regime corresponds to an extreme case where the laser intensity is very high and therefore allows an electron to be directly freed. This can be simply described for an atom of hydrogen. The required intensity to strip the electron is easily derived from the Bohr model for an electron of charge  $e$  and mass  $m_e$ , placed on an atom orbit of radius:

$$r_a = \frac{\hbar^2}{m_e e^2} \approx 0.53 \times 10^{-13} \text{m} \quad (2.9)$$

$r_a$  is the Bohr radius and the bound electron is subjected to the Coulomb potential  $E_a$ :

$$E_a = \frac{1}{4\pi\epsilon_0} \frac{e}{r_a^2} \approx 5.1 \times 10^9 \text{V/cm} \quad (2.10)$$

where  $\epsilon_0$  is the vacuum permittivity. Therefore, the intensity required to free an electron must be at least equal to the intensity:

$$I_a = \frac{1}{2}\epsilon_0 c E_a \approx 3.45 \times 10^{16} \text{ W.cm}^{-2} \quad (2.11)$$

The BSI model can be generalized to H-like atoms superimposing an external static field to the nucleus potential [Bethe and Salpeter, 1957]. An effective charge can be defined as:

$$Z^* = \sqrt{\frac{U_I}{U_H}} \quad (2.12)$$

with  $U_I$ , the ionization potential of the atom or ion, and  $U_H = 13.6 \text{ eV}$  the ionization potential of hydrogen. Therefore, the Coulomb potential  $V$  describing the contributions of the atom and laser fields can be written:

$$V(x) = -\frac{Ze^2}{x} - eEx \quad (2.13)$$

The distortion leading to freeing an electron from the Coulomb potential is illustrated in fig. 2.2 c).

Imposing the maximum value of  $V$ , obtained from stating  $(\partial V / \partial x)_{x=x_{max}} = 0$ , equal to the ionization potential, the value of the field needed to free an electron can be obtained:

$$E_{BSI} = \frac{U_I^2}{4Z^*e^3} \quad (2.14)$$

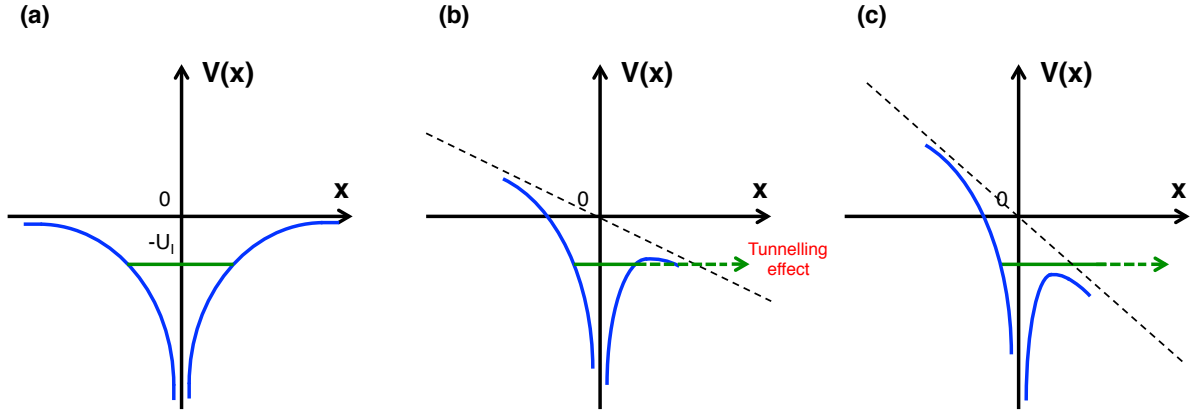


Figure 2.2: (a) Coulomb potential of an unperturbed ion. The trapped electron has a binding energy  $U_I$ . (b) Illustration of tunnel ionization. When the laser field strength is approaching the binding potential, tunneling effect can occur and lead to a release of electrons. (c) Barrier-suppression ionization happens for higher field strength for which the potential barrier is completely lowered.

From equation eq. (2.14), a threshold intensity for BSI to happen can be derived in case of linear polarization [Augst et al., 1991]:

$$I_{BSI}^{lin} \approx \frac{4 \times 10^9}{Z^{*2}} U_I^4 [\text{eV}] \quad [\text{W.cm}^{-2}] \quad (2.15)$$

Z	Ground levels	$U_I[eV]$	$I_{BSI}[W.cm^{-2}]$
Kr I	$[Ar]3d^{10}4s^24p^6$	14.00	$3.10 \times 10^{14}$
Kr II	$[Ar]3d^{10}4s^24p^5$	24.36	$7.00 \times 10^{14}$
Kr III	$[Ar]3d^{10}4s^24p^4$	35.67	$1.44 \times 10^{15}$
Kr IV	$[Ar]3d^{10}4s^24p^3$	50.85	$3.34 \times 10^{15}$
Kr V	$[Ar]3d^{10}4s^24p^2$	64.69	$5.60 \times 10^{15}$
Kr VI	$[Ar]3d^{10}4s^24p^1$	78.49	$8.43 \times 10^{15}$
Kr VII	$[Ar]3d^{10}4s^2$	109.13	$2.32 \times 10^{16}$
Kr VIII	$[Ar]3d^{10}4s^1$	125.80	$3.13 \times 10^{16}$
Kr IX	$[Ar]3d^{10}$	233.00	$2.91 \times 10^{17}$
Kr X	$[Ar]3d^9$	268.20	$4.14 \times 10^{17}$

Table 2.1: Ionization energies (source: NIST database) and required barrier-suppression intensities for the 10 first ionized states of krypton. Ground levels are expressed as a function of the electronic configuration of argon:  $[Ar] = 1s^2 2s^2 2p^6 3s^2 3p^6$ .

For circular polarization, the intensity threshold is twice the value reported in relation eq. (2.15). It should be noted that Stark effect at those high intensities ( $> 10^{14} W.cm^{-2}$ ) is non-negligible and modifies (a few eV) the ionization potential. However, the formula eq. (2.15) turns relevant to assess the required laser intensity to created lasing ions.

In case of krypton, the table 2.1 gives the ionization potentials as well as the threshold intensities for barrier-suppression ionization  $I_{BSI}$  for various ion species in case of a circularly polarized field.

These conditions for strong field can be interpreted by a laser period of oscillation greater than the characteristic time for an electron to cross the potential barrier. The  $\gamma$  perimeter can also be expressed as the ratio between two frequencies:

$$\gamma = \frac{\omega_0}{\omega_I} \quad (2.16)$$

where  $\omega_0$  is the laser frequency and  $\omega_I$  a characteristic frequency corresponding to the average time  $\tau$  for an electron to cross the potential barrier of length  $l$ :

$$\tau = l/v \quad \text{with} \quad l = \frac{U_I}{eE} \quad \text{and} \quad v = \sqrt{\frac{2U_I}{m_e}} \quad (2.17)$$

where  $e$  is the elementary charge and  $v$  the average speed of an electron. Hence,

$$\omega_I = \frac{eE}{\sqrt{2m_e U_I}} \quad (2.18)$$

and then, the  $\gamma$  parameter reads:

$$\gamma = \omega_0 \frac{\sqrt{2m_e U_I}}{eE} \quad (2.19)$$

The *tunnel ionization* occurs for lower intensities than those required for BSI and its principle is depicted in fig. 2.2 b. This process is dominant for low frequencies and intensities

roughly between  $10^{14}$  and  $10^{15} \text{ W/cm}^{-2}$ . In the Keldysh model, its rate increases in an exponential way with the field:

$$\rho_{\text{tunnel}} \propto \exp\left(\frac{U_I^{3/2}}{E}\right) \quad (2.20)$$

### 2.1.2 The « Optical Field Ionization regime » regime: ionization rate

The Optical Field Ionization (OFI) regime for creating a highly charged plasma uses high-intensity pulses with a duration far greater than atomic timescale ( $2.419 \times 10^{-17} \text{ s}$ ). Therefore, one can consider a quasi-static laser field at the first moments of laser-plasma interaction. The Keldysh parameter is quite large and multi-photon ionization dominates. However, because the intensity is rather low and the ionization energy is far bigger than photon energy, the ionization rate is moderate. Then, as the intensity rapidly surges with time, the probability of tunnel ionization soars and a lot of electrons are generated, before finally reaching the BSI regime when the intensity reaches its peak. Globally, tunnel ionization dominates in OFI plasmas.

The tunnel ionization rates were first calculated in case of static laser field in 1966 [Smirnov and Chibisov, 1966; Perelomov et al., 1966]. Derived from Ammosov-Delone-Krainov theory (ADK) [Ammosov et al., 1986], the tunnel ionization rates were later corrected. The ADK theory evaluates the OFI rate of the quantum system solving the Schrödinger equation involving parabolic coordinates and using the asymptotic form of the wave-function in semiclassical approximation. The tunnel ionization rate for an atom whose electronic configuration is determined by  $(n, l, m)$  (respectively the main, orbital and magnetic quantum numbers) is [Pert, 1999]:

$$W_{ADK}^0 = \frac{\omega_a}{2} C_{n^*l}^2 \frac{U_I}{U_H} f(l, m) U_I \left[ 2 \left( \frac{U_I}{U_H} \right)^{3/2} \frac{E_a}{E} \right]^{2n^* - |m| - 1} \exp \left[ -\frac{2}{3} \left( \frac{U_I}{U_H} \right)^{3/2} \frac{E_a}{E} \right] \quad (2.21)$$

where  $U_I$  and  $U_H$  are the ionization energies for the ion under consideration and hydrogen respectively,  $E_a$  the atomic field strength and  $\omega_a$  the atomic frequency:

$$\omega_a = \frac{e^4 m_e}{\hbar^3} \approx 4 \times 10^{16} \text{ s}^{-1} \quad (2.22)$$

$n^*$  is the effective main quantum number, defined for an ion of charge  $Z-1$ , as:

$$n^* = Z \sqrt{\frac{U_H}{U_I}} \quad (2.23)$$

The  $C_{n^*l}$  and  $f(l, m)$  coefficients from the ADK treatment are written [Ammosov et al., 1986]:

$$C_{n^*l} = \left( \frac{2e}{n^*} \right)^{n^*} \times \frac{1}{\sqrt{2\pi n^*}} \quad (2.24)$$

and,

$$f(l, m) = \frac{(2l+1)(l+|m|)!}{2^{|m|} |m|! (l-|m|)!} \quad (2.25)$$

The expression of the rate of tunnel ionization in equation eq. (2.21) is valid under a static field. When considering a varying field, one can consider the instantaneous rate eq. (2.21) valid at each instant  $t$ . Besides, the polarization of the field has also to be taken into account. A transverse field propagating along  $z$  can be written:

$$\mathbf{E}(\mathbf{z}, t) = E(z) [\cos(\omega_0 t) \mathbf{x} + \phi \times \sin(\omega_0 t) \mathbf{y}] \quad (2.26)$$

where  $\phi$  is a parameter, ranging from 0 to 1, linked to the field intensity and describing the polarization. Under those conditions, the field components  $E_x$  and  $E_y$  can be written as a function of the intensity:

$$E_x = \sqrt{\frac{2I\phi}{\epsilon_0 c}} \quad \text{and} \quad E_y = \sqrt{\frac{2I(1-\phi)}{\epsilon_0 c}} \quad (2.27)$$

For the general case of an elliptical polarization, the rate of tunnel ionization can be linked to the equation eq. (2.21):

$$W_{ADK} = \sqrt{\frac{2}{\phi(\phi+1)}} \exp\left[-\frac{1-\phi}{3\phi} \frac{Z^3}{n^* E}\right] B\left[\frac{1-\phi}{3\phi} \frac{Z^3}{n^* E}\right] W_{ADK}^0 \quad (2.28)$$

When comparing linear and circular polarization cases, the corresponding rates are linked through the following formula:

$$\frac{W_{ADK}^{circ}}{W_{ADK}^{lin}} = \sqrt{\frac{\pi Z^3}{En^*}} \quad (2.29)$$

where the field strength  $E$  is expressed in atomic units. We can notice that, in case of circular polarization, the rate of tunnel ionization is significantly greater compared to linear polarization.

In plasma generation, thanks to an intense field, the ions are created in the rising edge of the ultrashort pulse, i.e. within a few tens of femtoseconds. In the ADK model, electrons are assumed to be stripped one after another. Hence, all intermediary ion charges are being generated within the field. The evolution of ions' populations as the field is increased can therefore be computed as well as the evolution of the ionization degree:

$$\begin{cases} \frac{d\rho_0}{dI} = -W_{ADK}^{(0)}(I)\rho_0(I) \\ \frac{d\rho_k}{dI} = -W_{ADK}^{(k)}(I)\rho_k(I) + W_{ADK}^{(k-1)}(I)\rho_{k-1}(I) \end{cases} \quad (2.30)$$

where  $W_{ADK}^{(k)}$  and  $\rho_k$  are respectively the tunnel ionization rates and density in case of an ion ionized  $k$  times. The ionization rates follow the field strength and increase exponentially. The terms  $W_{ADK}^{(k)}$  are significant only in the intensity window whose lower limit is their intensity threshold  $I_{BSI}$  and upper limit defined when the  $k$ -times ionized ion gets overionized.

The 0-D numerical code *OFI-adk* (G. Maynard, LPGP, Orsay) solves the tunnel rate equations eq. (2.30).

The fig. 2.3 shows the evolution of the ionization degree of krypton under an intense field. The large range of intensities where the  $Kr^{8+}$  is present is illustrated in fig. 2.3 (b). The ion exists between  $2 \times 10^{16} W.cm^{-2}$  and  $2 \times 10^{17} W.cm^{-2}$ , i.e. remarkably over one order of magnitude in intensity. This is explained by the ion stability because its  $n=3$  electron shell is complete. The distribution of field intensity in the interaction medium will be non-homogeneous due to propagation. Hence, the ion stability promises to efficiently fill the interaction medium with

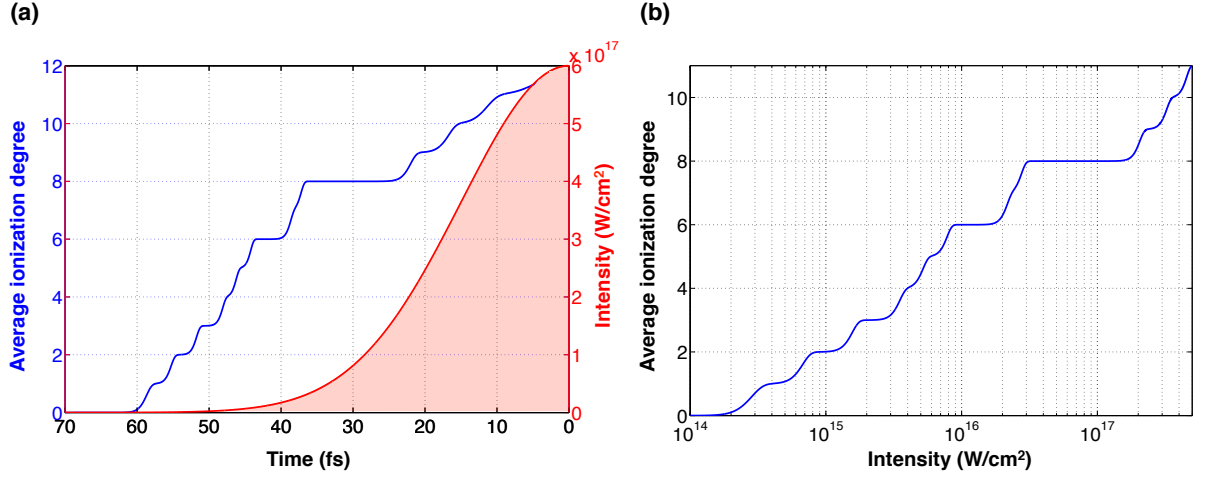


Figure 2.3: (a) Evolution of the average ionization degree within the field. The pulse duration and intensity are respectively 35 fs and  $6 \times 10^{17} \text{ W/cm}^2$ . (b) Average ionization degree as a function of the instantaneous pulse intensity.

$\text{Kr}^{8+}$  lasing ions.

The fig. 2.4 reports the successive creation and depletion of ion species through tunnel ionization and overionization of a krypton gas subjected to an ultrashort IR pulse of intensity  $6 \times 10^{17} \text{ W.cm}^{-2}$ .

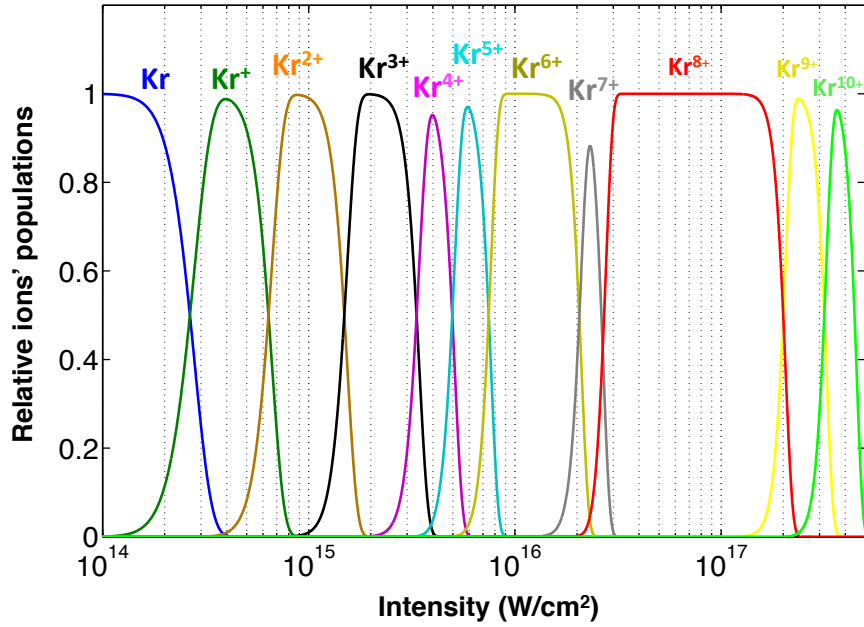


Figure 2.4: Evolution of krypton ionization states within the ultrashort intense field. The pulse duration and intensity are respectively 35 fs and  $6 \times 10^{17} \text{ W.cm}^{-2}$ .





upper level and the fundamental level. As far as  $Kr^{8+}$  is concerned, hot electrons of 145 eV minimal energy should be generated.

**Heating processes.** As previously reported, the generation of hot electrons is pivotal to the efficient collisional pumping of lasing ions transitions. In the following, the most important plasma heating processes are discussed.

- Above-threshold ionization (ATI):

In ATI process, the electron absorbs more photons than required to be freed from the atom or the ion. This leaves the free electron with significant momentum. The polarization of the field of the pumping beam has a decisive impact on the temperature of the electrons generated through optical field ionization.

To optimize collisional pumping in an OFI plasma, the driving pulse should be circularly polarized to produce hot electrons able to excite the lasing ions and yield a population inversion between the desired levels.

The equation eq. (2.8) gives the kinetic energy of electrons considering a field with a polarization defined by the parameter  $\phi$ . In the considered model, electrons are assumed to be stripped independently and only subjected to the laser electric field. The ion field is overlooked. Moreover, secondary collisions of electrons with their parent ions are neglected.

When  $\phi = 1/2$  (circular polarization), the kinetic energy is equal to:

$$E_{ATI}^{circ} = \frac{e^2 E_0}{4m_e \omega^2} \quad (2.31)$$

Regarding linear polarization ( $\phi = 0$ ), the gained kinetic energy is:

$$E_{ATI}^{lin} = \frac{e^2 E_0}{2m_e \omega^2} \sin^2(\omega t) \quad (2.32)$$

When subjected to a linearly polarized field, the kinetic energy gained by a free electron is maximized when the the field  $E(t)$  is minimized (eq. (2.32) and eq. (2.7)). However, the tunnel ionization rate is maximized when the field strength is maximized (eq. (2.21)). This explains why heating of electrons is less efficient with linear polarization. By contrast, with a circularly polarized field, the kinetic energy gained by a free electron is constant over an optical period. The velocity of accelerated electrons will be therefore far higher and thus the heating.

The ATI heating process scales as  $\lambda^2$ , hence long wavelengths (generally 800 nm Ti:Sapphire lasers) are desirable for collisional pumping schemes. Such optical field ionization with circular polarization generates a plasma of cold ions and produces hot free electrons with the required energy to efficiently excite of bound electrons.

- Inverse-bremsstrahlung:

Inverse-bremsstrahlung heating [Pert, 1995] is also known as collisional heating. When colliding with an ion, an oscillating electron can absorb a photon. This absorbed energy is converted into heating. In an equivalent way, an electron undergoing an elastic collision with an ion will have its motion direction altered. Then, a portion of quiver energy will be

transferred into thermal energy. Electrons hence absorb energy from the electromagnetic field to conserve angular momentum in the presence of ions. This is the reverse process of bremsstrahlung emission of radiation, where electrons get slowed and deflected in the presence of the ion field and then emit photons.

The rate of energy absorption by electrons from an electromagnetic field can be determined from the "impact approximation". This approximation is discussed by Pert [Pert, 1995] and is valid for long wavelengths, where the scattering time is short compared to the period of the electromagnetic wave. Considering classical collisions, the momentum transfer is:

$$\sigma_{IB} = 2\pi \left( \frac{Ze^2}{m_e} \right)^2 \frac{1}{v_e^4} \ln \left( 1 + \frac{\nu^6}{(Ze^2\omega_0/m_e)^2} \right) \quad (2.33)$$

Because the timescale on which collisions occur is shorter compared to the period of the electromagnetic wave and as the field contains a number of periods, the cross section should be integrated to take account of multiple collisions and the laser pulse duration. Doing so yields the absorption rate [Pert, 1995]:

$$\rho_{IB} = 4m_en_i \left( \frac{Ze^2}{m_e} \right)^2 \frac{1}{v_q} \ln(\Delta) \left( \frac{1}{2} \ln(4x) + \frac{1}{2} \gamma + \ln(2) - 1 \right) \quad (2.34)$$

where  $\gamma \approx 0.577$  is the Euler-Mascheroni constant,  $v_q$  the electron velocity after collision,

$$v_q = \frac{eE}{m_e\omega_0} \quad (2.35)$$

x the ratio of quiver energy to thermal:

$$x = \frac{m_ev_q^2}{2k_BT_e} \quad (2.36)$$

and

$$\Delta = \frac{8(k_BT_e)^3}{Z^2e^4\omega_0^2m_e} \quad (2.37)$$

The heating induced by inverse-bremsstrahlung effect depends on the density of ions and the laser pulse duration. The absorption rate is calculated from the momentum transfer cross section. It was shown that inverse-bremsstrahlung heating has a negligible contribution when compared to ATI heating [Sebban et al., 2003]. The collisional processes, along with the intensity and polarization of the field determine the profiles of the electron energy distributions. These distributions are calculated using Fokker-Planck equations following the method introduced by Pert in 1999 [Pert, 1999]. Then, their relaxation over time will be considered in the following section about plasma kinetics.

- Relativistic effects:

The previously described OFI and ATI processes do not take into account relativistic effects, which occur in the presence of an ultra intense field in the intensity range of  $10^{18} \text{ W/cm}^2$ . This contribution has been described [Smirnov and Krainov, 1998] in case

of linearly polarized fields and tunnelling of relativistic electrons was found to be negligible. However, this is no more the case considering a circularly polarized field [Krainov, 1999], but the contribution remains small. Compared to classical calculations, the peak of electron energy distribution is found to be shifted by the following factor:

$$f_{rel} = \sqrt{1 + \frac{e^2 \lambda^2 I}{8\pi m_e^2 c^5 \epsilon_0}} \quad (2.38)$$

where  $I$  is the laser intensity. Considering pumping with 800 nm Ti-Sapphire lasers, the resulting electron energy distribution gets shifted by a few eV compared to classical predictions.

**Electron energy distribution.** The energy distribution of electrons is mainly due to the kinetic energy that the circularly-polarized field confers to electrons freed essentially through tunnel ionization. The fig. 2.6. These results are given by the OFIKinRad plasma kinetic code (see Appendix A). The integral of the energy distribution of electrons has been normalized to 1. For the linearly polarized case (blue curve), the electron population follows a Maxwell distribution in energy. In the circularly polarized case (red curve), the energy distribution has a complex shape and is shifted towards higher electron temperatures. The different peaks correspond to various charge states of krypton. Reminding that the minimal temperature of electrons to pump the  $Kr^{8+}$  transition at 32.8 nm is 145eV, we see the linearly polarized field produces only a few electrons having the required energy. Only 8% of produced electrons will be able to pump the laser transition. By contrast, the circularly polarized field allows the generation of hotter electrons. The figure reports 70 % of produced electrons with an energy higher than 145 eV.

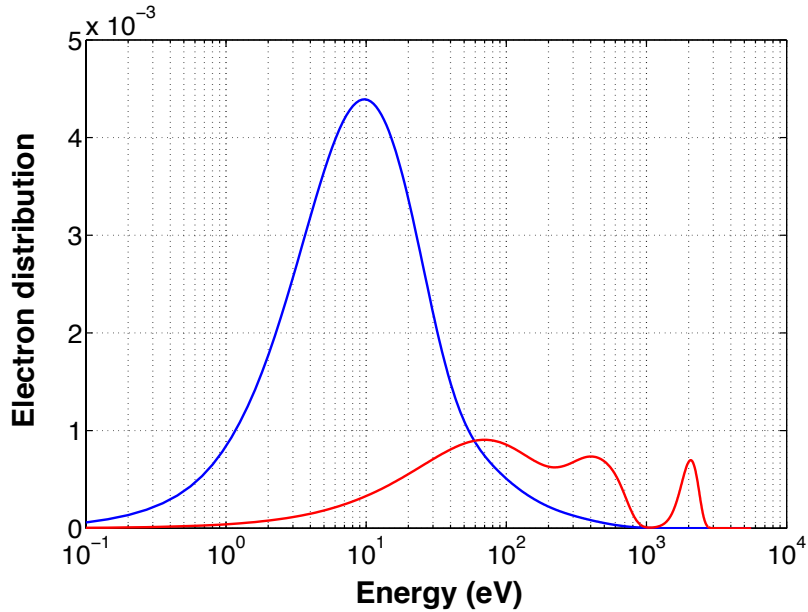


Figure 2.6: Electron energy distribution in case of a linear (blue) and circular (red) fields for a gas cell with 30 mbar of krypton ( $n_{at} = 7.4 \times 10^{17} \text{ cm}^{-3}$ ). The pump beam intensity is  $6 \times 10^{17} \text{ W/cm}^2$ .

**Energy distribution of ions.** Similarly to electron heating, the electromagnetic field confers ions kinetic energy. The initial distribution of velocities of atoms in the gas is a maxwellian function depending of the gas temperature. In a simplified model, the motion of ions and electrons under an electric field  $E$  is:

$$\frac{d\mathbf{v}_i}{dt}(t) = \frac{Ze}{m_i}\mathbf{E}(t) \quad \text{and} \quad \frac{d\mathbf{v}}{dt}(t) = -\frac{e}{m_e}\mathbf{E}(t) \quad (2.39)$$

Thus, the speed of ions can be expressed from the electron velocity:

$$\mathbf{v}_i = -Z\frac{m_e}{m_i}\mathbf{v}_e \quad (2.40)$$

As  $m_e/m_i$  is very small ( $7 \times 10^{-6}$  in case of krypton), the ions will virtually acquire no velocity. The ion energy distribution keeps a Maxwell distribution profile after optical field ionization, while being shifted towards higher energies. Typically, in OFI plasmas, ion temperature is a few eV for gas densities in the range of  $10^{18} \text{ cm}^{-3}$ . A study showed [Maynard et al., 2007] that OFI-induced heating of ions is limited to only 9 meV.

## 2.2 Plasma kinetics

This section presents the temporal evolution of electrons and ions temperature, as well as the plasma amplifier gain after optical field ionization. Because OFI occurs on very short timescales (tens of femtoseconds) compared to the plasma kinetics characteristic time (picosecond range), one can treat the state of the plasma resulting from OFI (previous section) and its evolution separately.

### 2.2.1 Atomic processes

The electron and ion kinetics is determined by a number of atomic processes. In OFI plasmas, the electron temperature is high whereas ions are cold. Collisions between ions and electrons will therefore lead to energy transfer between those two species and therefore modify their respective temperatures. Besides, plasma hydrodynamics after ionization is characterized by an ambipolar diffusion of species. Thus, a hydrodynamic transfer of heat from the plasma hottest zones to the coolest ones occurs. Moreover, the ponderomotive force resulting from laser-plasma interaction leads to charge separation and oscillation of particles within the field. This also affects the plasma temperature.

**Electron-ion thermalization.** The interactions between ions and electrons lead to an energy exchange, such that both species tend towards thermal equilibrium. The state of OFI plasmas are essentially determined by Coulomb interactions between charged particles. The Debye sphere characterizes the volume of influence of a particle Coulomb potential. Its radius is determined by the Debye length:

$$\lambda_D = \sqrt{\frac{\epsilon_0 k_B T_e}{n_e e^2}} \quad \text{when} \quad T_e \gg T_i \quad (2.41)$$

When considering hot electron temperatures, the Debye length is big and the number of particles in the Debye sphere, which can interact with each other, is high.

A collision cross section can be introduced to apprehend the electron-ion collision rate. Because the mean distance between particles is very low compared to the Debye length, one

can consider a uniform Coulomb potential applying to all particles. In these conditions, the electron-ion collision cross section can be derived from the Rutherford formula, considering an electron with solid angle  $\Omega$  and a speed  $v_e$  colliding with an immobile ion of "infinite" mass.

$$\frac{d\sigma_{ei}}{d\Omega} = \frac{1}{4} \left( \frac{Ze^2}{m_e v_e^2} \right)^2 \frac{1}{\sin^4(\theta/2)} \quad \text{with} \quad d\Omega = 2\pi \sin\theta d\theta \quad (2.42)$$

The total cross section then reads:

$$\sigma_{ei} = \int \frac{d\sigma_{ei}}{d\Omega} d\Omega = \frac{\pi}{2} \left( \frac{Ze^2}{m_e v_e^2} \right)^2 \int_0^\pi \frac{\sin\theta}{\sin^4(\theta/2)} d\theta \quad (2.43)$$

An average collision frequency  $\overline{\nu_{ei}}$  can be derived from the equation eq. (2.43). It corresponds to the number of collisions between two particles per second.

$$\overline{\nu_{ei}} = n_i < \sigma_{ei} v_e > \quad (2.44)$$

$n_i$  is the ion density. Averaging over the electron speed is necessary to take into account the distribution of speeds. A calculation [Delacroix, 1994] of this quantity yields:

$$\overline{\nu_{ei}} = \frac{\sqrt{2}}{16\pi\epsilon_0^2} \frac{e^4}{\sqrt{m_e}} \frac{n_e Z}{(k_B T_e)^{3/2}} \ln\Lambda \quad (2.45)$$

with  $\Lambda$ , the Coulomb logarithm. It is a parameter defined as the ratio between the Debye length and the minimal distance between the two particles:

$$\Lambda = 8\pi\epsilon_0^{3/2} \frac{(k_B T_e)^{3/2}}{Z\sqrt{n_e}} \quad (2.46)$$

Considering electrons and ions have Maxwell energy distributions, electrons and ions thermalize themselves with their respective temperatures  $T_e$  and  $T_i$ :

$$\frac{dT_i}{dt} = -\frac{dT_e}{dt} = -\frac{T_i - T_e}{\tau_{ei}} \quad (2.47)$$

where  $\tau_{ei}$  is the electron-ion equilibration time, defined as [Spitzer, 1962]:

$$\tau_{ei} = \frac{3m_e m_i k / B^{3/2}}{8\sqrt{2\pi} n_i Z^2 e^4 \ln(\Lambda)} \left( \frac{T_i}{m_i} + \frac{T_e}{m_e} \right)^{3/2} \quad (2.48)$$

Therefore, combining equations eq. (2.47) and eq. (2.47) in the case where  $T_i \ll T_e$  yields:

$$\frac{dT_i}{dt} = \frac{8}{3} \sqrt{2\pi} \ln(\Lambda) \frac{n_e e^4}{\sqrt{m_e k_B T_e}} \frac{m_e}{m_i} \left( 1 - \frac{T_i}{T_e} \right) \quad (2.49)$$

Spitzer defined a self-collision time [Spitzer, 1962], which gives an assessment of the time taken to remove any anisotropy from the group of electrons and therefore achieve equilibration. At equilibrium, the energy distribution takes a Maxwell distribution shape.

$$\tau_c = \frac{(3m^{1/3} k_B T)^{3/2}}{5.712\pi n e^4 Z^4 \ln(\Lambda)} \quad (2.50)$$

We can notice that  $\tau_{ci} > \tau_{ce}$ , which means electrons reach equilibrium more rapidly than ions.

**Plasma hydrodynamics.** Apart from electron-ion collisions and their resulting exchange of energy, the hydrodynamics of the laser produced plasma plays a role in the evolution of the temperature of plasma species. Because of the large difference of mass between ions and electrons, electrons are diffusing far quicker than ions. The electron and ion species diffuse at velocities corresponding to their respective temperatures. In OFI plasmas, ions are relatively cold whereas electrons are hot. In those conditions, electrons leave the interaction volume rapidly at a average speed of  $v_e = \sqrt{k_B T_e / m_e}$ . They leave behind them a zone with a positive charge density. Because of the charge separation, an electric field is induced, which slows down electrons and tends to accelerate ions. Therefore, an equilibrium is reached where electrons and ions diffuse at a speed far smaller than the initial electron speed but significantly greater than the ion velocity. This speed is known as the ambipolar diffusion speed  $v_{ad}$ :

$$v_{ad} = \sqrt{\frac{k_B T_e}{m_i}} \quad (2.51)$$

This speed is valid for the initial times of the plasma expansion, when the density gradients are steep. Over longer timescales, the plasma expansion speed is governed by the plasma hydrodynamics. When considering laser-induced plasmas, the plasma hydrodynamics are due to the ions and electrons pressures. The equations of state in the case of ideal gases including ionization are:

$$\begin{cases} P_e = n_e(\gamma_e - 1)\mathcal{E}_e \\ P_i = n_i(\gamma_i - 1)\mathcal{E}_i \end{cases} \quad (2.52)$$

where  $\mathcal{E}_e$  and  $\mathcal{E}_i$  are electrons and ions energies respectively, and  $\gamma_e = \gamma_i = 5/2$ , the ratio of specific heats. The electron and ion densities are related by  $n_e = Z^* n_i$ , where  $Z^*$  is the mean ion charge. Assuming Maxwell energy distributions, the temperature of the two species are given by:

$$T_{e/i} = \frac{2}{3k_B} \mathcal{E}_{e/i} \quad (2.53)$$

Experiments and numerical calculations [Dunne et al., 1994] in case of linearly polarized light in recombination schemes showed that a significant plasma expansion takes a few hundreds of picoseconds. Although OFI plasmas produce far hotter electrons, the plasma effects on the evolution of temperature are not significant, even at high densities. This is due to the fact that this contribution occurs on far longer timescales compared to the gain lifetime, and hence is not expected to have a dominating effect on soft X-ray emission.

**Influence of ponderomotive force.** The interaction of an ultrashort and intense IR pulse with a plasma induces longitudinal fields. Those excited plasma fields are in the order of a few GV/cm and are used in electron acceleration schemes. An energy transfer between those fields and ions can occur. The radiate pressure from the intense IR pulse leads to electrostatic perturbations in the plasma and generates a ponderomotive force, which contributes to expel electrons from the optical axis where the laser intensity is high.

In case of an electromagnetic wave defined as:  $E(t) = E_0 \cos(\omega_0 t)$ , the ponderomotive force per unit volume reads [Landau and Lifchitz, 1969]:

$$F_p = -\frac{\omega_p^2}{16\pi\omega_0} \nabla E_0^2 \quad (2.54)$$

where  $\omega_p = \sqrt{4\pi n_e^2/m_e}$  is the plasma frequency.

This force applying to ions and electrons are different and relate through the following relation [Eliezer, 2002]:

$$\frac{F_{pi}}{m_e} = \frac{F_{pe}}{m_i} \quad (2.55)$$

The equation eq. (2.55) shows the ponderomotive force that ions undergo is very weak compared to that on electrons. As far as electrons are concerned, they get displaced, which contributes to plasma collective effects affecting their temperature.

## 2.2.2 Evolution of electrons' and ions' temperature

The plasma kinetics is described using the OFIKinRad atomic code (see Appendix A). The algorithm allows modeling the plasma amplifier in one point in the space notably in terms of atomic populations and gain with respect to key parameters, such as gas pressure, laser intensity and field polarization. This code only observes the temporal dependence and does not take into account the plasma hydrodynamic expansion and its radiative losses.

### Evolution of electrons' temperature

**Electron kinetics.** The previously discussed sources of heating produce an electron energy distribution, upon which subsequent atomic physical processes will depend. Electron heating in OFI plasmas is mainly dominated by ATI and to a lesser extent inverse-bremsstrahlung heating (at high densities). The electron energy distribution is assumed to be thermal and it can therefore be treated with a Maxwell-Boltzmann distribution of characteristic temperature  $T_e$ . This approximation is relevant locally. A 0D approach can therefore be undertaken considering the different parts of the plasma are in local thermal equilibrium. There are two main approaches in modeling electron energy distributions. One is a Monte-Carlo method [Pert, 1999] and considers binary collisions in a statistical sample. The other, called Fokker-Planck method [Pert, 2001], is based on Boltzmann equations with a collisional term. The first one fails to properly describe the high energy tail of hot electron distributions and turns out noisy when a large number of particles is considered. The Fokker-Planck method is computationally much faster and more accurate.

The Fokker-Planck equation for an electron energy distribution  $f(\mathcal{E}, \mathbf{r}, t)$  reads:

$$\frac{\partial f}{\partial t} + \mathbf{v}_e \frac{\partial f}{\partial \mathbf{r}} - \frac{e}{m_e} (\mathbf{E} + \mathbf{v} \times \mathbf{B}) \frac{\partial f}{\partial \mathbf{v}_e} = S_e + C_{ei} + C_{ee} \quad (2.56)$$

This equation is defined as a function of time  $t$  and position  $\mathbf{r}$  where  $S_e$  is a source term, derived from ionization processes, and  $C_{ei}$  and  $C_{ee}$  the electron-ion and electron-electron collision terms respectively. The rate of collision strongly depends on the initial electron energy distribution. The knowledge of the temporal dependence of this rate is very important since it affects the evolution of atomic populations over time. The inelastic electron-ion collisions modify the average energy of electrons, whereas the electron-electron collisions are elastic and impact the energy distribution while maintaining the energy level. The collision terms are determined [Rosenbluth et al., 1957; Pert, 2001] taking into account a diffusion term and a frictional term slowing down the electrons.

The fig. 2.7 gives the temporal evolution of the average ionization degree obtained from the OFIKinRad code in case of a 30 mbar krypton gas cell with laser intensity of  $5 \times 10^{17} \text{ W/cm}^2$  in



circular polarization. This evolution takes place after OFI and reports the effects of collisional ionization, which results in an increase of the average ionization degree. The rate of increase gets lower as time elapses because electron energy decreases and higher charge states are more difficult to ionize. The curve gives the time window, within which amplification can take place thanks to the presence of  $Kr^{8+}$  ions. Its lifetime is about 9 ps in those conditions.

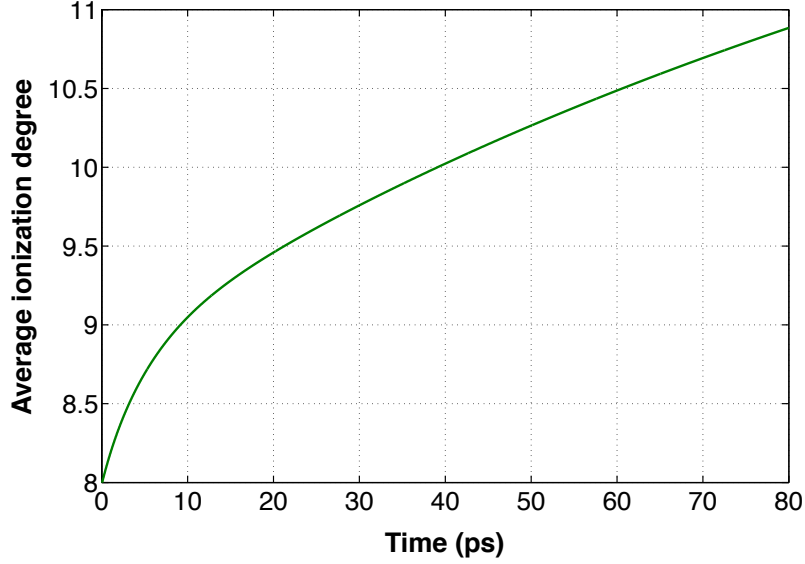


Figure 2.7: Temporal evolution of the average ionization degree right after OFI occurring within a few tens of femtoseconds. Data are shown considering a gas cell with 30 mbar of krypton.

The fig. 2.8 shows the evolution of the electron temperature. It decreases monolithically mainly because collisions are responsible for energy transfers with cooler ions.

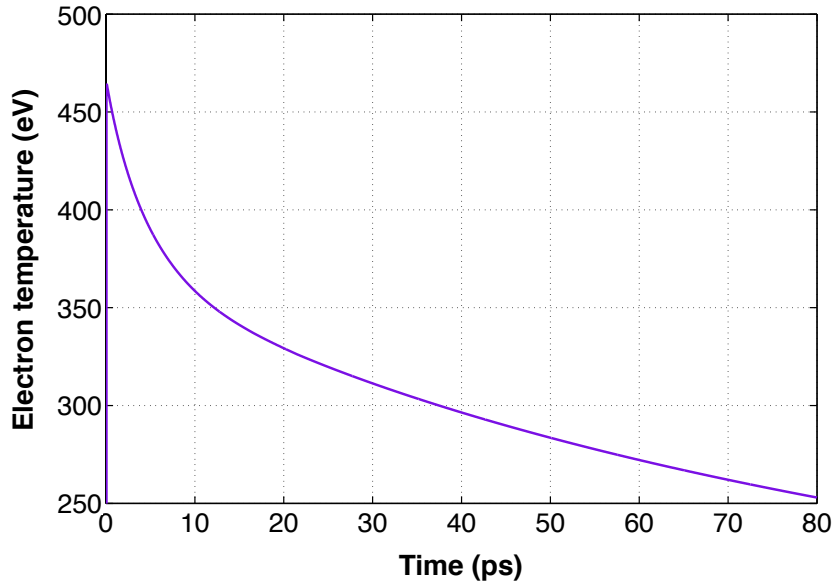


Figure 2.8: Temporal evolution of the electron temperature following OFI in case of a gas cell with 30 mbar of krypton.

The fig. 2.9 reports the temporal evolution of the energy distribution of electrons in case of a circularly polarized field. The profile tends to a Maxwell distribution as electrons and ions exchange energy and subsequently thermalize. This distribution profile is reached about 30 ps right after ionization, which amounts to a far longer timescale compared to the  $Kr^{8+}$  lasing ion lifetime.

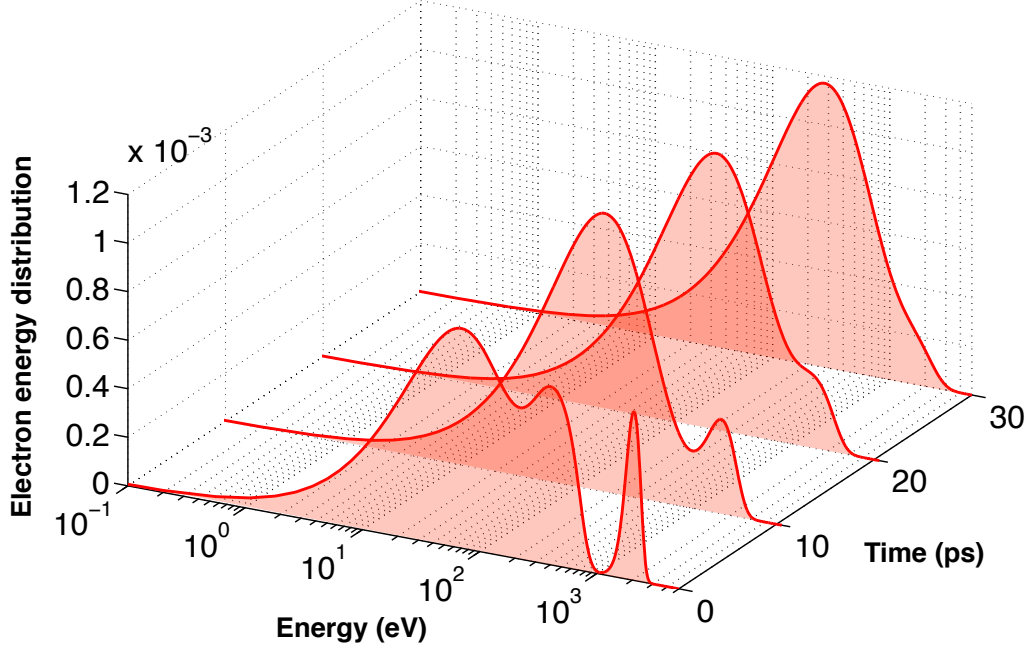


Figure 2.9: Temporal evolution of the normalized electron energy distribution in case of a gas cell with 30 mbar of krypton.

### Evolution of ions' temperature

In this part, the contributions of the previously discussed energy transfer mechanisms to ion heating are discussed. Those elements have been studied [Maynard et al., 2007] and showed that, in case of OFI plasmas, ion-ion coupling turns out to have the main impact on the ion temperature during the soft X-ray emission time window, i.e. a few picoseconds.

**Electron-ion collisions.** The evolution of ions temperature due to the collision with hot electrons is given by the Spitzer formula with the relations eq. (2.47) and eq. (2.48). Considering  $T_i \ll T_e$ , we can write:

$$\begin{cases} \frac{dT_i}{dt} = \nu_{ei} T_e \\ \nu_{ei}[s^{-1}] = 3.2 \times 10^{-9} \frac{Z^2 n_e [cm^{-3}] \ln(\Lambda)}{M} \sqrt{T_e [eV]} \end{cases} \quad (2.57)$$

where  $M$  is the atomic mass number,  $Z$  the ion charge and  $\ln(\Lambda) \approx 10$ . When considering a krypton gas cell of 30 mbar, this contribution to the heating of ions amounts to less than 10 meV over the soft X-ray emission timescale.

**Plasma hydrodynamics.** The plasma hydrodynamic expansion takes place through the ambipolar diffusion with a velocity of the order of  $\sqrt{ZT_e/M}$ . Considering the hottest electrons, this velocity is only  $10^{-3} \mu\text{m/ps}$  [Maynard et al., 2007] and can therefore be neglected when compared to the size of OFI plasmas, i.e. in the order of tens of  $\mu\text{m}$ .

**Wake and ponderomotive effects.** The ions sitting in the wake of the IR pulse gain a kinetic energy equal to [Maynard et al., 2007]:

$$E_{ion}^{wake} = \frac{1}{2} \frac{Q^2}{2M} v_{osc}^2 \quad [a.u.] \quad (2.58)$$

This formula is expressed in atomic units [a.u.], where  $v_{osc}$  is the electron quiver velocity. Numerical simulations [Andreev et al., 2002] were performed for the interaction between an ultrashort IR pulse in a gas, taking account of the plasma hydrodynamics in a "cool fluid" approximation. This contribution is limited to a few meV.

The ions are also subjected to the transverse ponderomotive force. The same simulations showed this contribution can also be neglected. From the equation eq. (2.54), considering a Gaussian pulse of duration  $\tau$ , the kinetic energy gained by ions is:

$$E_{ion}^{pond.} \approx \frac{1}{32} \frac{Z^2 m_e}{M} \left( \frac{c\tau}{w_0} a_0^2 \right)^2 m_e c^2 \quad [a.u.] \quad (2.59)$$

where  $a_0$  is the electric field vector potential (related to the pulse intensity) and  $w_0$  the pulse radius.

All in all, within the soft X-ray emission timescale of a few picoseconds, electrons and plasma effects don't have the time to heat the ions significantly. Moreover, in OFI plasmas, electrons are "too hot" compared to ions to be able to somewhat heat them. Indeed, the formula eq. (2.49) shows, counter-intuitively, that the proclivity of electrons to heat ions is lower when their temperature is bigger.

**Ion-ion coupling.** In OFI plasmas, ion heating is actually mainly due to the initial coupling effects between ions. Because of the high electron temperature, the Debye length is much larger than the average distance between two ions. In these conditions, a One Component Plasma (OCP) model [Fortov et al., 2006], in which the electrons are supposed to form a frozen neutralizing background, can be applied to describe the properties of the plasma ions. The ion-ion coupling is determined by the coupling parameter  $\Gamma$ , defined as the ratio between the average Coulomb potential energy and the ion kinetic energy:

$$\Gamma = \frac{Z^2}{< r_{ii} > T_i} \quad (2.60)$$

where  $r_{ii}$  is the mean distance between ions and  $Z=8$  in case of a  $Kr^{8+}$  amplifier. For a krypton gas cell of 30 mbar, the coupling parameter is about 400, which means the plasma is highly correlated.

The initial pair correlation between the ions is strongly out of equilibrium, which leads to an excess of potential energy. Thus, the system should relax by transferring a part of its potential

energy to the kinetic one. A rough estimate of the equilibrium temperature can be calculated within the harmonic oscillator model. It has been shown the ratio  $\Gamma/\Gamma_0$ , where  $\Gamma_0$  is the initial value, tends to the asymptotic number of 2.23 [Maynard et al., 2007]. Hence,

$$\Gamma_\infty = \frac{Ze^2}{\langle r_{ii} \rangle T_i^f} = 2.23 \quad \Rightarrow \quad T_i^f = 0.45 \frac{Z^2}{\langle r_{ii} \rangle} \quad [a.u.] \quad (2.61)$$

This calculation is valid for  $\Gamma_0 \gg 1$ . Because there is only one ion in the sphere of radius  $r_{ii}$ , one can write for krypton ion density  $n_i$  in  $[cm^{-3}]$ :

$$\frac{4}{3}\pi \langle r_{ii} \rangle n_i = 1 \quad (2.62)$$

Therefore, one can derive from the previous relations:

$$\langle r_{ii} \rangle = \frac{1.18 \times 10^8}{n_i^{1/3}} \quad [a.u.] \quad \text{and} \quad T_i^f \approx \frac{783.688}{\langle r_{ii} \rangle} \quad [eV] \quad (2.63)$$

The relations eq. (2.63) lead to:

$$T_i^f \approx 7.489 \times n_i^{1/3} \quad [cm^{-3}] \quad (2.64)$$

The fig. 2.10 illustrates the evolution of the final ion temperature due to ion-ion coupling effects in case of krypton as a function of the neutral density of the krypton plasma. For a 30 mbar krypton gas cell, which corresponds to a neutral atomic density of  $7.4 \times 10^{17} cm^{-3}$ , the final ion temperature reaches about 6.7 eV.

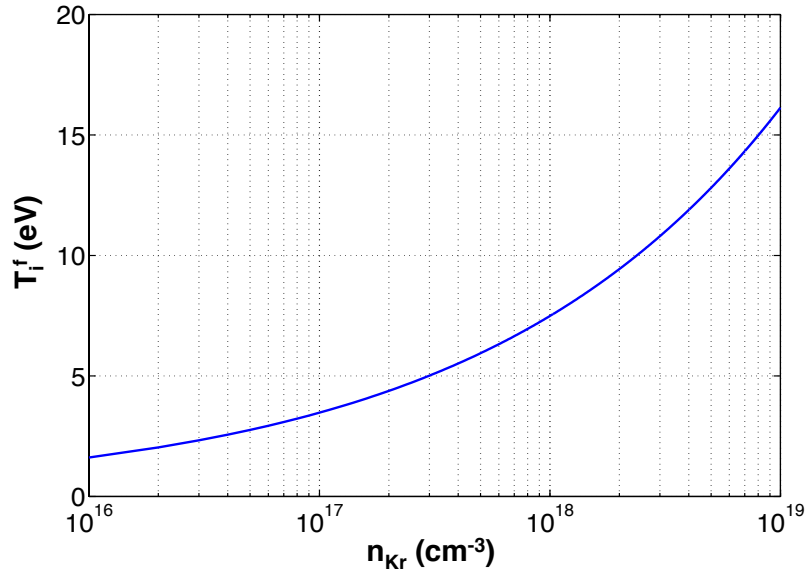


Figure 2.10: Evolution of the final ion temperature due to ion-ion coupling effects with respect to the neutral krypton gas density.

The ion relaxation timescale is given by the period at which kinetic energy oscillates, i.e. half the plasma period and keeps at least one order of magnitude below the soft X-ray emission duration.

## 2.3 Population inversion, gain and radiative transfer

### 2.3.1 Laser effect in the soft X-ray range

#### Laser operation

Laser effect is based on the amplification of stimulated emission of electromagnetic radiation. When being excited, electrons bound to atoms take discrete positions in orbitals, which correspond to specific energy levels governed by quantum theory. Considering a simple two-level system, as illustrated in fig. 2.11, three processes can occur.

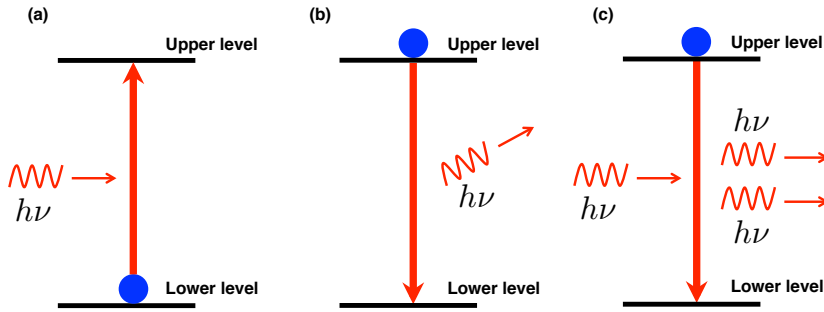


Figure 2.11: (a) Absorption. (b) Spontaneous emission. (c) Stimulated emission. The energy discrepancy between the lower and the upper level is  $E = h\nu$ .

Transitions can only occur between discrete transition levels. When lying in the lower level, bound electrons can **absorb** an incident quantum of energy and be promoted to the upper level. When lying in the upper level, two processes can occur. First, excited bound electrons tend to naturally de-excite and emit a photon to minimize their energy and come back to equilibrium. We talk about **"spontaneous emission"**. The emission is stochastic under temporal and spatial considerations. Secondly, being subjected to a quantum of energy corresponding to the energy difference between the upper and lower levels, the electron de-excites and emits a photon identical to the incident photon in phase, energy, frequency and polarization. We talk about **"stimulated emission"**. Compared to spontaneous emission, the characteristics of stimulated emission can be apprehended by the notion of light coherence, which leads to intrinsic properties of laser light.

The amplification process was first described by Einstein in 1917 [Einstein, 1917]. Assuming that electrons are in thermal equilibrium, the ratio of populations between the upper and lower levels is given by the Boltzmann equation:

$$\frac{N_u}{N_l} = \frac{g_u}{g_l} \exp\left(-\frac{h\nu}{k_B T}\right) \quad (2.65)$$

where  $N_u$  and  $N_l$  are respectively, the populations of atoms in the upper and lower levels, and  $g_u$  and  $g_l$ , the associated degeneracy factors. The coefficient  $k_B$  is the Boltzmann constant,  $h\nu = E_u - E_l$  (with  $h$ , the Planck's constant) and  $T$  is the temperature at equilibrium. Taking all three processes described in fig. 2.11, the rate equation governing the population of the upper level is:

$$\frac{dN_u}{dt} = \underbrace{B_{lu}U_\nu N_l}_{\text{absorption}} - \underbrace{B_{ul}U_\nu N_u}_{\text{stimulated emission}} - \underbrace{A_{ul}N_u}_{\text{spontaneous emission}} \quad (2.66)$$

In equation eq. (2.66),  $U_\nu$  is the spectral energy density in  $J.m^{-3}.Hz^{-1}$ . It corresponds to an energy per unit volume within a spectral interval  $d\nu$ . Namely, laser emission occurs at a defined frequency within a linewidth (see Section section 2.3.1). The total intensity  $I$  can thus be defined integrating the spectral intensity  $I_\nu$  ( $W.m^2.Hz^{-1}$ ) over the emission spectral lineshape:

$$I = \int I_\nu S(\nu) d\nu \quad \text{with} \quad I_\nu = c \times U_\nu \quad \text{and} \quad \int S(\nu) d\nu = 1 \quad (2.67)$$

with  $c$ , the speed of light and  $S(\nu)$ , the normalized spectral profile of the emission linewidth. The term  $B_{lu}U_\nu N_l$  corresponds to the absorption of an incident photon of energy  $h\nu$  by an atom lying in the lower level.  $B_{ul}U_\nu N_u$  denotes the stimulation of the decay of an atom in the upper level down to the lower level by an incident photon. Finally,  $A_{ul}N_u$  denotes the spontaneous emission rate, where  $A_{ul}$  is the absorption Einstein coefficient, whose expression is given by [Louisell, 1973]:

$$A_{ul} = \frac{8\pi^2 e^2}{3\epsilon_0 c^3 \hbar} \frac{g_l}{g_u} \nu^3 |d_{ul}|^2 \quad (2.68)$$

where  $d_{ul}$  is the transition dipole moment of the atom. This term is related to the so-called oscillator strength associated to a particular atomic transition. It can be shown that [Hawkes and Latimer, 1995]:

$$g_u B_{ul} = g_l B_{lu} = B \quad (2.69)$$

Considering a system in stationary equilibrium, we can write

$$B_{lu}U_\nu N_l = B_{ul}U_\nu N_u + A_{ul}N_u \quad (2.70)$$

Hence, taking into account the relation eq. (2.65), the ratio between spontaneous and stimulated emission is:

$$\frac{A}{BU_\nu} = \exp\left(\frac{h\nu}{k_B T}\right) - 1 \quad (2.71)$$

This relation in a simplified case illustrates the **challenge** associated with achieving laser action down to the **soft X-ray range**. In equation eq. (2.71), spontaneous emission indeed outpaces stimulated emission when  $\nu$  increases. Hence, implementing a population inversion gets tricky and conventional laser techniques in the visible and IR ranges cannot be adapted to far shorter wavelengths.

The population inversion is satisfied when, taking into account the degeneracy factors, the population of the upper level is bigger compared to the lower level. This translates into a non-equilibrium state of the atomic level system with initial conditions defined by:

$$\frac{N_u}{g_u} > \frac{N_l}{g_l} \quad (2.72)$$

If we consider a uniform gain medium with a cylindrical shape, a radiative transfer equation in terms of spectral intensity ( $W.cm^{-2}.Hz^{-1}$ ) can be derived from the rate equation eq. (2.66) :

$$\frac{dI_\nu}{dz} + \frac{1}{c} \frac{dI_\nu}{dt} = B_{ul}(\nu)g_u \left( \frac{N_u}{g_u} - \frac{N_l}{g_l} \right) h\nu \frac{I_\nu S(\nu)}{c} + N_u A_{ul}(\nu) S(\nu) h\nu \frac{\Omega}{4\pi} \quad (2.73)$$

The first term of the right-hand side of equation eq. (2.73) corresponds to the stimulated emission and absorption. This term contributes to coherent amplification of light. The second term represents the fraction of spontaneous emission irradiated within a solid angle  $\Omega$ , which corresponds to emission within a cylindrical medium. Defined in fig. 2.12, this solid angle can be written:

$$\Omega = \frac{\pi d^2}{4(L-z)^2} \quad (2.74)$$

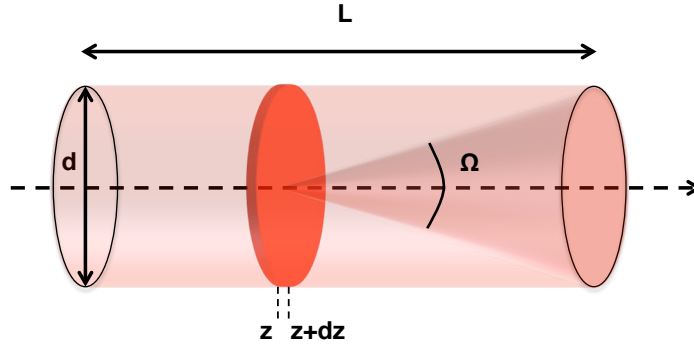


Figure 2.12: Schematic of a cylindrical gain medium.

The following relation determines the **population inversion** between the laser transition levels:

$$\Delta N = \frac{N_u}{g_u} - \frac{N_l}{g_l} \quad (2.75)$$

A **gain coefficient**  $g(\nu)$  and **emissivity**  $j(\nu)$  can then be defined:

$$\begin{cases} g(\nu) = N_u \sigma_{stim}(\nu) - N_l \sigma_{stim}(\nu) = \sigma_{stim}(\nu) \Delta N \\ j(\nu) = N_u h\nu A_{ul}(\nu) S(\nu) \frac{\Omega}{4\pi} \end{cases} \quad (2.76)$$

where  $\sigma_{stim}(\nu)$  and  $\sigma_{abs}(\nu)$  are the cross sections, respectively for stimulated emission and absorption. The stimulated emission cross section is defined by:

$$\sigma_{stim}(\nu) = \frac{h\nu}{c} B_{ul} g_u S(\nu) \quad (2.77)$$

Therefore, equation eq. (2.73) simplifies to:

$$\frac{dI_\nu}{dz}(z) + \frac{1}{c} \frac{dI_\nu}{dt}(z) = g(\nu) I_\nu(z) + j(\nu) \quad (2.78)$$

If we assume the gain and the emissivity are constant over the propagation direction within the cylindrical gain medium, the equation eq. (2.78) can be easily integrated and the spectral intensity then reads:

$$I_\nu(z) = \frac{j}{g} (e^{gz} - 1) + I_{\nu 0} e^{gz} \quad (2.79)$$

where  $I_{\nu 0} = I_\nu(z = 0)$  is given by the initial conditions. In the amplification of spontaneous emission (ASE) regime, where the plasma amplifies its own noise, only the term  $\frac{j}{g} (e^{gz} - 1)$  holds

in the right-hand side of the expression eq. (2.79). In case of injection seeding of the amplifier, an additional term  $I_{\nu 0}$  adds up and gets amplified over propagation in the plasma.

The expression of intensity buildup in equation eq. (2.79) is only valid for low values of intensities. In this case, a so-called "low-signal gain" is defined. Considering an inhomogeneous Doppler broadening of the line shape (where  $S(\nu_0) = 1/\Delta\nu_{FWHM}$  with  $\Delta\nu_{FWHM}$ , the full width at half-maximum (FWHM)), its value defined at the centre of the emission line width is:

$$g_0 = \frac{h\nu}{c\Delta\nu_{FWHM}} B_{ul} g_u \Delta N \quad (2.80)$$

Assuming a spectral integration over a Gaussian lineshape, the intensity of the lasing line is given by the Linford formula [Linford et al., 1974]:

$$I(L) = \frac{1}{2} \sqrt{\frac{\pi}{\ln 2}} \Delta\nu_{Gauss} \frac{j_0 (e^{g_0 L} - 1)^{3/2}}{g_0 \sqrt{g_0 L e^{g_0 L}}} \quad (2.81)$$

Considering a Lorentzian line shape, the equation takes the form:

$$I(L) = \frac{\sqrt{\pi}}{2} \Delta\nu_{Lorentz} \frac{j_0 (e^{g_0 L} - 1)^{3/2}}{g_0 \sqrt{g_0 L e^{g_0 L}}} \quad (2.82)$$

A generalized formula taking into account a position-dependent gain coefficient and the different values of spontaneous and stimulated linewidths for either Gaussian or Lorentzian line shapes has also been derived [Tommasini and Fill, 2000] and fits better experimental conditions.

When intensity increases to a certain level, the population of the upper level of the laser transition depletes because of strong stimulated emission. The population inversion, and thus the gain, dwindles. The amplification of signal ceases increasing exponentially and reaches the "saturation" regime, from which intensity linearly increases. This behavior is illustrated in fig. 2.13.

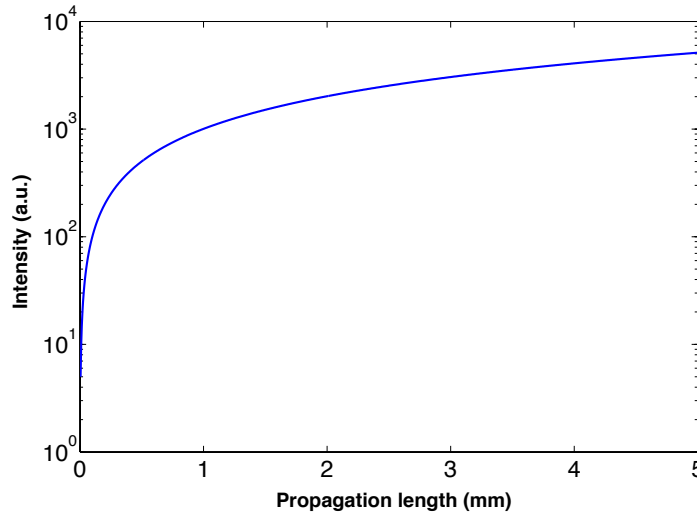


Figure 2.13: Saturation behavior of the amplified emission in case of ASE. The signal surges exponentially at the beginning and depletes the population inversion, which reduces the gain and results in saturation of amplification, from where the signal grows linearly.



It can be shown that, in a quasi-stationary regime, the population inversion decreases with intensity in the following way:

$$\Delta N = \frac{\Delta N_0}{1 + \frac{I}{I_{sat}}} \quad (2.83)$$

where  $\Delta N_0$  is the initial population inversion, right after pumping,  $I = \int_{-\infty}^{\infty} I_{\nu} S(\nu) d\nu$  and  $I_{sat}$ , the saturation intensity that can be expressed as:

$$I_{sat} = \frac{h\nu_0}{\sigma_{stim}(\nu)\tau_u} \quad (2.84)$$

where  $\tau_u$  is the recovery time of the population inversion. It only depends on the depletion rate of the transition upper level.

As a consequence, the profile of the gain will follow the formula:

$$g = \frac{g_0}{1 + \frac{I}{I_{sat}}} \quad (2.85)$$

The saturation length decreases as the gain increases and has the following expression:

$$L_{sat} = \frac{1}{g_0} \ln \left( \frac{4\pi\Delta N}{\Omega B_{ul} N_u \tau_u} \right) \quad (2.86)$$

## Spectral linewidth

As previously reported, both emissivity and gain coefficients depend on the spectral lineshape of emission. The lineshape  $S(\nu)$  is such that:

$$\int_{-\infty}^{\infty} S(\nu) d\nu = 1 \quad (2.87)$$

The spectral profile of the emission line depends on plasma properties and ongoing broadening mechanisms accompanying emission. Four main sources of line broadening exist [Griem, 1974]:

1. The natural broadening, which defines the minimal linewidth. It is linked to the non-infinite lifetime of the radiative upper level.
2. The Doppler effect. Heating of ions causes frequency shifts of the central emission frequency in the laboratory frame of reference.
3. Collisions of ions mainly with electrons, which limit the lifetime of the radiative upper level.
4. Stark broadening. The variations of local electrostatic fields due to neighboring ions leads to a shift and a split of energy levels.

Those broadening mechanisms can be divided into two categories: homogeneous or inhomogeneous broadening. The homogeneous mechanism includes the so-called natural broadening, given by spontaneous emission rates, and the collisional broadening. The Doppler and Stark broadening effects are inhomogeneous mechanisms. Some alterations of the profile may be due to ion turbulence and additional ion-ion interactions [Griem, 1986].

Their impact on the laser lineshape is discussed in Appendix B. At low atomic densities corresponding to a krypton pressure of 30 mbar, the total broadening can be assessed to be  $\Delta\nu = 2.4 \times 10^{11}$  Hz (using OFIKinRad code). Spectral gain narrowing leads to a reduction of this value to about  $7.5 \times 10^{10}$  Hz ( $\Delta\lambda = 2.7 \pm 0.3 \cdot 10^{-13}$  m) [Tissandier et al., 2010a] considering a 5 mm-long  $Kr^{8+}$  plasma amplifier. This effect is found to be broadly inversely proportional to the gain-length product.

The group of Koch proposed in 1994 a description [Koch et al., 1994] of the evolution of the lineshape with amplification in case of Ne-like selenium emitting at 20.6 and 18.2 nm. The unidimensional radiative transfer equation was obtained in case of ASE and under stationary conditions:

$$\frac{dI_\nu(z)}{dz} = \frac{j_0}{S_V(\nu_0)} \left[ 1 + \frac{g_0 I_\nu(z)}{j_0} \right] \int_0^\infty \frac{S_D(u) S_L(\nu, u)}{1 + \frac{1}{I_{sat}} \int I(v, z) S_L(v, u) dv} du \quad (2.88)$$

where  $j_0$  and  $g_0$  are respectively the values of emissivity and gain in the centre of the the lineshape in a small signal regime.

A narrowing of the lineshape is reported in the first propagation lengths, because of strong amplification. However, contrary to experimental observations, no traces of line re-broadening due to saturation effects is found. Moreover, the homogeneous model does not take into account the variations of ions velocities because of collisions. Ions are supposed to have a constant velocity over the characteristic timescale of the radiative process. A more thorough model of radiative transfer is discussed in section 2.5.

A recent work [Calisti et al., 2013] presented a detailed analysis of the various broadening processes affecting the intrinsic profile of the Ni-like Ag soft X-ray laser line over an extended range of plasma parameters, such as the electron density, electron and ion temperatures. The impact of ionic correlations on the emission lineshape is investigated in case of transient and QSS pumping schemes.

As a consequence from a spectral perspective, the operation of high-density plasma amplifiers promises a reduction of the Fourier-limited pulse duration, as an enhancement of the rate of collisions will broaden the laser emission lineshape.

### 2.3.2 Gain dynamics

As previously reported, the gain coefficient is directly proportional to the population inversion following the collisional excitation of  $Kr^{8+}$  ions. The fig. 2.14 illustrates the temporal evolution of the gain in case of krypton gas cell with a pressure of 30 mbar ( $n_{Kr} = 7.4 \times 10^{17} cm^{-3}$ ) and a pump intensity  $I = 5 \times 10^{17} W/cm^2$ . The gain profile features an asymmetric behavior with a sharp increase during the first moments up to a maximum value and a rather long end tail. Because of electron-ion collisions, the 4d-4p transition of  $Kr^{8+}$  is excited and the populations soars right after OFI. The gain reaches a maximum value of about  $170 cm^{-1}$  at 2.3 ps, when the populations of the upper and lower levels are in quasi-equilibrium. The subsequent drop is primarily explained by the depletion of  $Kr^{8+}$  lasing ion species, as reported in fig. 2.7. The gain duration is therefore limited by the lasing ions lifetime. The  $Kr^{8+}$  exhausts less than 10 ps right after its creation. It should also be pointed that the heat transfer to cooler regions of the plasma also leads to a reduction of the collisional excitation rate that pumps the laser transition.

As aforementioned, the electron-ion thermalization is effective on the timescale of a few picoseconds, which is longer than the gain lifetime during which lasing occurs. Thus, this electron cooling process is not affecting the gain dynamics too much. Over-ionization of the  $Kr^{8+}$  lasing ion species is mainly responsible for the gain duration.

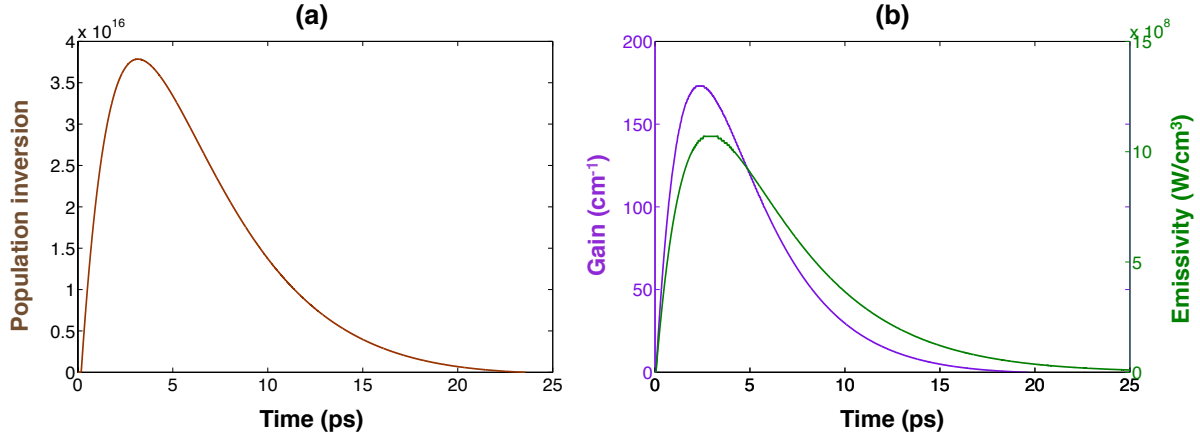


Figure 2.14: (a) Dynamics of the population inversion of the  $3d^9 4d_{J=0} \mapsto 3d^9 4p_{J=1}$  laser transition. (b) Temporal evolution of the gain (magenta) and emissivity (green) in case of a krypton gas cell of 30 mbar.

The fig. 2.14 shows the temporal evolution of emissivity in the low signal regime. Emissivity is proportional to population inversion and its behavior is very similar to the gain dynamics. The fast rise of the collisional excitation rate leads to a strong pumping of the emitting ions.

### Towards ultrashort pulse duration

The duration of the pulses emitted from a plasma amplifier is shorter than the gain lifetime and its fundamental limitation is governed by the Fourier transform of the pulse spectral line width. Collisionally-pumped plasma-based lasers are generally characterized by an intrinsic very narrow line width of the atomic laser transition (in the order of  $\Delta\nu/\nu \sim 10^{-5}$ ), which therefore limits their abilities to deliver ultrashort emission. Recent works demonstrated durations of emitted soft X-ray pulses between 1 and 2 picoseconds [Sebban et al., 2004; Wang et al., 2008].

To overcome this constraint, recent numerical calculations [Oliva et al., 2012] proposed a transposition of chirped pulse amplification technique to the soft X-ray range. By stretching a femtosecond HH seed to duration close to the gain lifetime, this would allow continuously and coherently extracting the energy stored in the plasma. After compressing the amplified seed, this scheme theoretically inferred SXRL pulses as short as 200 fs but has not been experimentally demonstrated so far. Other research directions have been considered to bring SXRL in the ultrafast domain, mainly based on straightforward approach capitalizing on intrinsically femtosecond population inversion schemes. The so-called recombination scheme in plasmas is an attractive candidate [Korobkin et al., 1996] (see section 1.2.1), nevertheless it requires drastic plasma conditions, which have not been implemented to date. More recently, the inner-shell ionization scheme has demonstrated an ultrafast capability in the keV range, however this scheme requires a very intense hard X-ray pump to work efficiently [Rohringer et al., 2012; Kapteyn, 1992] (see section 1.2.1).

An alternative approach is based on the **Collisional Ionization Gating** (CIG) of the gain media [Depresseux et al., 2015b]. This method allows reducing the time window in which the lasing action takes place by quenching the lifetime of the lasing ions and therefore the gain duration. In the collisionally-pumped OFI scheme, the amplifier lifetime strongly depends on the depletion rate of the lasing ion population [Lin et al., 2009] due to collisional ionization during the lasing process. As a consequence, a reduction in the emission duration can be expected

by favoring the electron-ion collision rate in order to over-ionize the medium and interrupt the lasing effect. The electron density of the plasma amplifier exactly allows tuning the collisional ionization rate.

**Gain quenching.** The temporal dependence of the amplifier gain coefficient is displayed in fig. 2.15, which illustrates the continuous trend of gain lifetime reduction as the electron density is increased for a set of five electron densities ranging from  $3 \times 10^{18} \text{cm}^{-3}$  to  $4 \times 10^{20} \text{cm}^{-3}$ . The increase in electron density results in a steeper rise, an increased value and a shorter lifetime of the gain coefficient. The data are computed using the OFIKinRad code (see Appendix A).

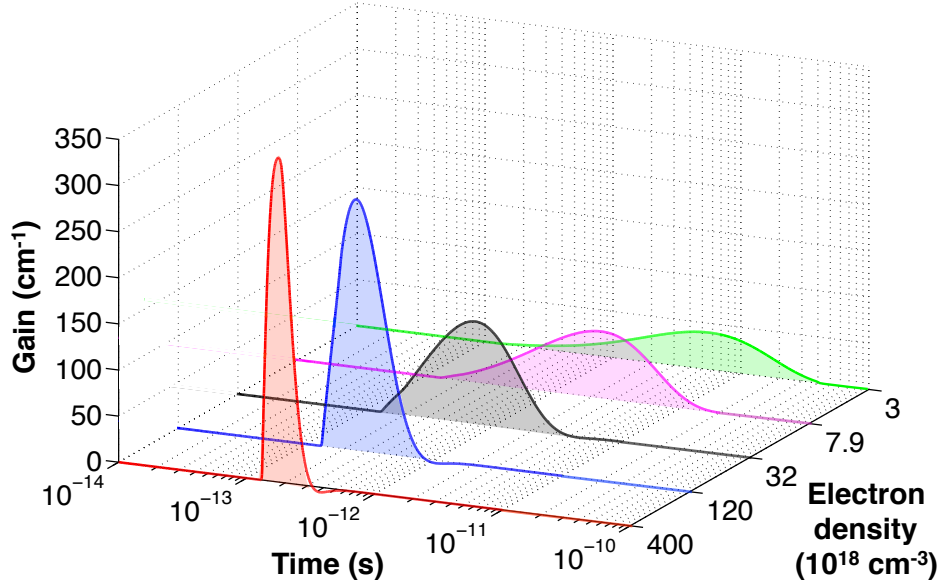


Figure 2.15: Temporal profiles of the gain coefficient for a  $Kr^{8+}$  plasma amplifier in case of electron densities  $n_e = 3 \times 10^{18} \text{cm}^{-3}$ ,  $n_e = 7.9 \times 10^{18} \text{cm}^{-3}$ ,  $n_e = 3.2 \times 10^{19} \text{cm}^{-3}$ ,  $n_e = 1.2 \times 10^{20} \text{cm}^{-3}$  and  $n_e = 4 \times 10^{20} \text{cm}^{-3}$

To explain this behavior, the fig. 2.16 shows the correlation between the collisional ionization rate and gain lifetime for a set of three electron densities:  $n_e = 6 \times 10^{18} \text{cm}^{-3}$  (green),  $n_e = 1.2 \times 10^{20} \text{cm}^{-3}$  (blue) and  $n_e = 4 \times 10^{20} \text{cm}^{-3}$  (red). The solid curve displays the gain temporal profile whereas the dashed line illustrates the evolution over time of the average ionization degree in the plasma amplifier. For the latter curve, we can distinguish two regimes. The first regime is delimited by the grey-tinted area and corresponds to the tunnel ionization that takes place over a few tens of femtoseconds within the ultra intense IR laser field. Experimentally, the pump beam duration is 30 fs FWHM for an on-target intensity of  $3 \times 10^{18} \text{W/cm}^2$ , which allows generating a significant portion of  $Kr^{8+}$  ions. The second regime occurs right after the passage of the IR pulse and is characterized by the long-duration collisional ionization of the medium. Although electron collisions with the  $Kr^{8+}$  ion contribute to build up a population inversion of the laser transition, they also lead to the over-ionization of this ion. The average ionization degree increases more and more over time because the collision of electrons with ions generates even more electrons that then collide with ions.

The yellow-tinted zone illustrates the lifetime of  $Kr^{8+}$  lasing ions. The range of average ionization values from 8 to 9 (materialized by the yellow-tinted area) defines a time window, in

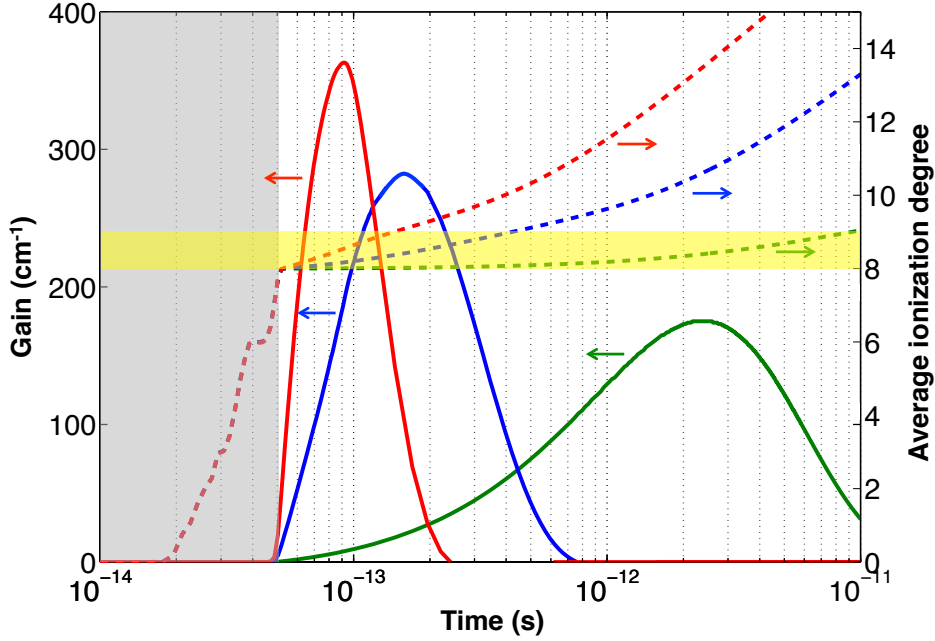


Figure 2.16: Temporal dependence of the  $Kr^{8+}$  plasma amplifier gain coefficient (solid line) and the average ionization degree (dashed line) in case of  $n_e = 6 \times 10^{18} \text{ cm}^{-3}$ ,  $n_e = 1.2 \times 10^{20} \text{ cm}^{-3}$  and  $n_e = 4 \times 10^{20} \text{ cm}^{-3}$

which a population inversion responsible for laser emission of soft X-rays takes place. When the dashed line exceeds an average ionization degree of 9, the population of  $Kr^{8+}$  ions is completely exhausted and at this time, the plasma amplifier gain completely plummets. We can notice that, for instance with  $n_e = 1.2 \times 10^{20} \text{ cm}^{-3}$ , even when the ionization degree surpasses 9, the gain remains non-zero for about 200 fs. This is explained by the fact that the displayed data only report the over-ionization of the  $Kr^{8+}$  ion. In fact, collisional ionization of lower charge species ( $Kr^{7+}$ ) generates a portion of  $Kr^{8+}$  whose laser transition can be pumped. For a high electron density of  $n_e = 1.2 \times 10^{20} \text{ cm}^{-3}$ , this time window is about 550 fs.

When increasing the plasma density, the depletion of the lasing ion population becomes fast enough to provoke an anticipated interruption of amplification in less than a few hundred femtoseconds, consequently shortening the duration of the soft XRL pulse. As shown in numerical calculations from fig. 2.16, increasing the electron density from  $6 \times 10^{18} \text{ cm}^{-3}$  up to  $4 \times 10^{20} \text{ cm}^{-3}$ , the CIG process becomes sufficiently fast to exhaust the gain within a time window from about 10 ps to slightly more than 100 fs.

**Temporal evolution of atomic populations.** As described in section 2.1.3, the pumping efficiency of the laser transition notably depends on the electron temperature of the plasma. Indeed, hot free electrons are required to achieve a large population inversion.

Considering given laser conditions, the increase in electron density enhances the pumping efficiency for two reasons. First, the electron temperature increases because of more electron-electron collisions. The fig. 2.17a illustrates the evolution of the electron temperature as a function of time following the optical field ionization (OFI) of the plasma. Data were calculated using 0D OFIKinRad atomic code (see Appendix A) and are shown for a set of electron densities corresponding to a plasma filled with  $Kr^{8+}$  (i.e. 8 times ionized from the neutral density):  $n_e = 3 \times 10^{18} \text{ cm}^{-3}$ ,  $n_e = 7.9 \times 10^{18} \text{ cm}^{-3}$ ,  $n_e = 3.2 \times 10^{19} \text{ cm}^{-3}$ ,  $n_e = 1.2 \times 10^{20} \text{ cm}^{-3}$ . Second,

the rate of electron-ion collisions also increases, which leads to a larger population inversion.

As a result, over-ionization of the gain medium is more effective at higher electron densities. The faster collisional rate exhausts the population of  $Kr^{8+}$  ions, which become promoted to a higher charge. The fig. 2.17b shows the temporal evolution of the population of the  $Kr^{8+}$  fundamental level for the various electron densities. This population is mainly affected by the laser ionization and the collisional excitation. This figure illustrates a dramatic reduction of the lifetime of  $Kr^{8+}$  ions as the electron densities rises. This lifetime shrinks from over 7 ps at  $n_e = 3 \times 10^{18} \text{ cm}^{-3}$  to about 300 fs at  $n_e = 1.2 \times 10^{20} \text{ cm}^{-3}$ .

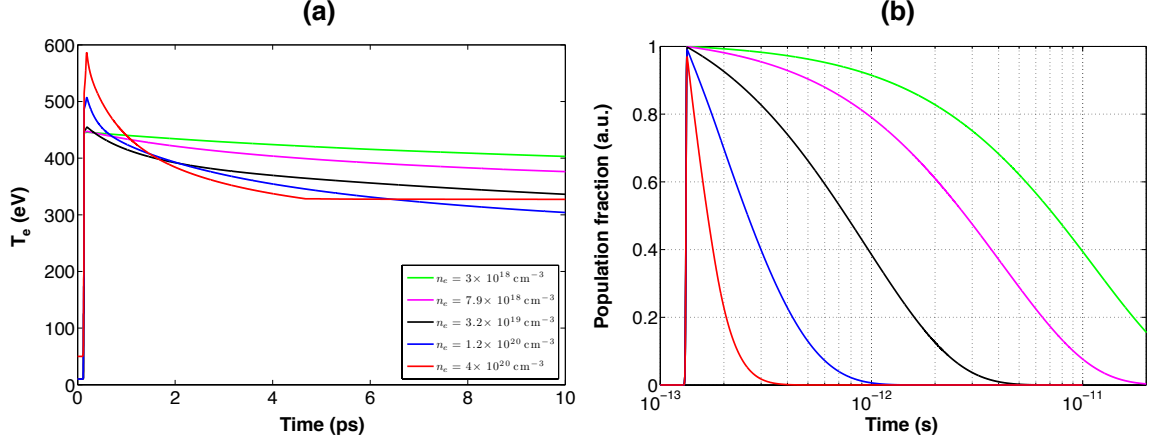


Figure 2.17: (a) Electron temperature  $T_e$  (eV). (b) Lifetime of the fundamental level population of the  $Kr^{8+}$  ion.

The fig. 2.18 shows the evolution of the population of the upper and lower levels of the laser transition. Those populations correspond to the fraction of the fundamental level population of the lasing ion. The populations of the upper and lower levels first increase because of collisional excitation through electron-ion collisions and then decay. The subsequent decrease is due to a diminishing population of the fundamental level (cf. fig. 2.17), which turns unable to compensate collisional ionization depleting these levels. The relative difference of those populations defines the so-called population inversion. Because the small-signal gain coefficient is proportional to the population inversion (see eq. (2.76)), the temporal behavior of those populations is similar to the evolution of the gain depicted in fig. 2.15.

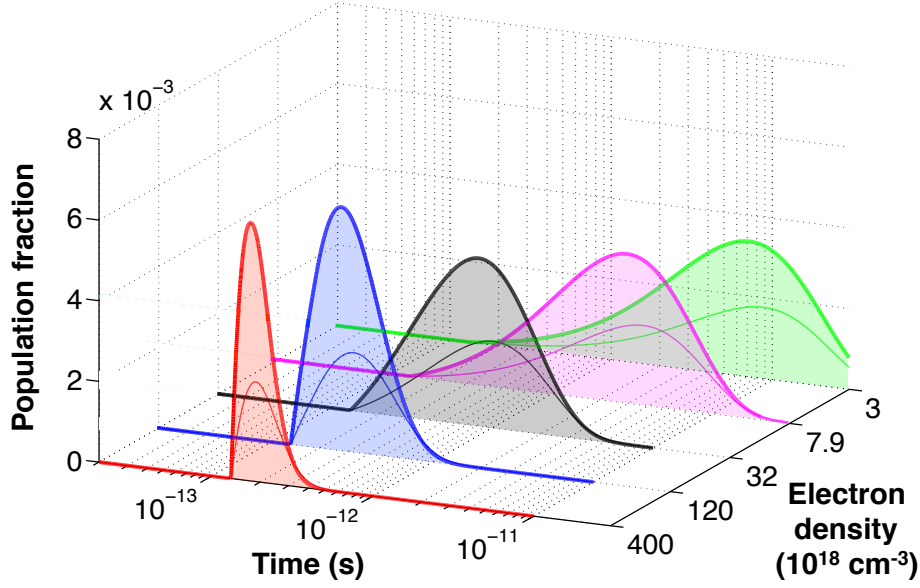


Figure 2.18: Evolution of the population fraction of the upper (bold solid line) and lower (thin solid line) levels of the  $3d^9 4d_{J=0} \rightarrow 3d^9 4p_{J=1}$  laser transition for various electron densities.

### 2.3.3 Saturation intensity

Furthermore, aside from a dramatic reduction of the amplifier gain duration, increasing the density leads to a significant boost of the lasing yield mainly caused by the enhancement of the saturation intensity, thus pushing previous limitations in terms of peak brightness of compact SXRL sources. Actually, increasing the electron density rises the number of emitters. The fig. 2.19 shows the monotonous increase of the saturation intensity and the maximum value of the plasma amplifier gain as the electron density rises.

It should be noticed that the displayed small-signal gain coefficient does not vary significantly with respect to the electron density. Indeed, this coefficient is the product of the population inversion and the cross section. The cross section is affected by the SXRL lineshape, which at high densities is dominated by homogeneous broadening due to collisional excitation and ionization, which alters the lifetime of the level, thus decreasing the cross section. This decrease in the cross section is approximately inversely proportional to the electron density. The parallel increase in the population inversion tends to cancel the decrease from the cross section and thus yields a small signal gain coefficient that is approximately flat versus density. But the OFIKinRad atomic code takes into account collisional broadening effects, which translates into the fact that the reported gain coefficient is not proportional to the electron density. According to fig. 2.16, the maximum gain coefficient rises by a factor of 2 when the electron density is increased by 67. Despite the offsetting effects, a small increase of the gain coefficient is reported and it stems from the fact that the upper level of the laser transition is being populated by the contributions from other excited atomic levels in addition to the direct pumping process.

As a conclusion, the main effects associated with the increase of the electrons density are the hike in saturation intensity and the shortening of the gain duration. Considering  $n_e = 6 \times 10^{18} \text{ cm}^{-3}$  (green) and  $n_e = 4 \times 10^{20} \text{ cm}^{-3}$  (red) in fig. 2.16, the gain duration is reduced by a factor of about 120 and the saturation intensity soars by 2000, whereas the maximum gain coefficients only slightly increases. Furthermore, it should be noticed that the experimental data



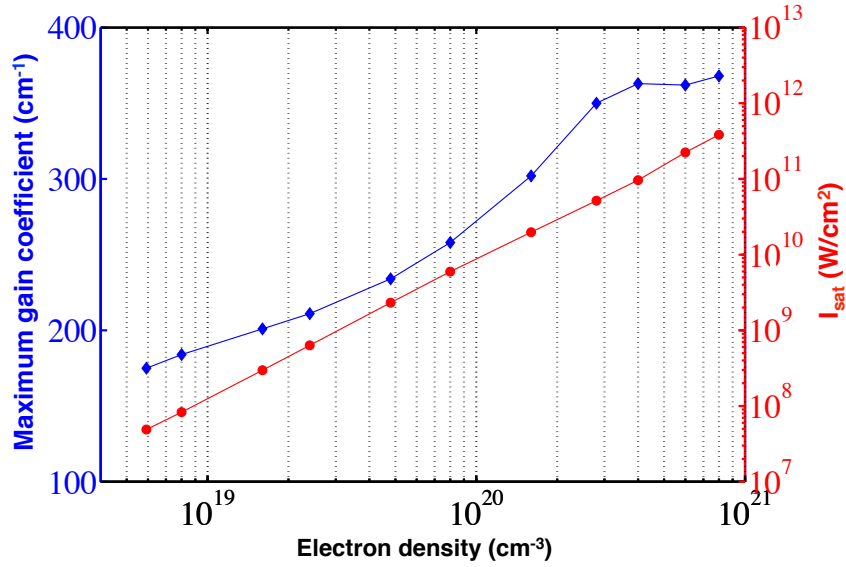


Figure 2.19: Evolution of the saturation intensity (red) and the maximum gain coefficient (blue) for a  $Kr^{8+}$  plasma amplifier as the electron density is increased.

correspond to a strongly saturated regime, where broadening effects do not play any significant role. The main contribution comes from the population rates, which are directly proportional to the electron density. This explains why the amplification factor remains high, while the small-signal gain coefficient only slightly increases and the gain duration significantly shortens.

The previously described data illustrate that driving **high density plasmas** opens a promising path towards the development of **ultrafast** and **energetic** plasma-based soft X-ray lasers [Depresseux et al., 2015b].

## 2.4 Propagation of an ultrashort infrared pulse in plasmas

The implementation of a long plasma amplifier requires to strongly ionize the medium over its whole length in order to generate an elongated medium filled with lasing ions. If this condition is not fulfilled, the resulting soft X-ray emission can be subsequently absorbed by poorly ionized regions of the plasma. This section presents an overview of the propagation of an ultrashort laser pulse in a plasma, along with the associated defocusing effects limiting the effective length over which a lasing medium can be generated.

### 2.4.1 Propagation equation

We consider here a medium displaying dielectric properties, which is the case of a plasma. The microscopic expression of the Maxwell equations yields:

$$\nabla \cdot \mathbf{E} = \frac{\rho}{\epsilon_0} \quad (2.89)$$

$$\nabla \cdot \mathbf{B} = 0 \quad (2.90)$$



$$\nabla \times \mathbf{E} = -\frac{\partial \mathbf{B}}{\partial t} \quad (2.91)$$

$$\nabla \times \mathbf{B} = \mu_0 J + \frac{1}{c^2} \frac{\partial \mathbf{E}}{\partial t} \quad (2.92)$$

where  $\mathbf{E}$  and  $\mathbf{B}$  are respectively the electric and magnetic fields,  $\rho$  the volume charge density,  $\epsilon_0$  the vacuum permittivity and  $\mu_0$  the vacuum magnetic permeability. We can notice that  $\mu_0 \epsilon_0 c^2 = 1$ . Taking the *curl* vector operator of the expression eq. (2.91) and placing its result in equation eq. (2.92), we get:

$$\Delta \mathbf{E} - \frac{1}{c^2} \frac{\partial^2 \mathbf{E}}{\partial t^2} - \nabla(\nabla \cdot \mathbf{E}) - \mu_0 \frac{\partial \mathbf{J}}{\partial t} = 0 \quad (2.93)$$

The gradient of the divergence operator applied to the electric field  $\nabla(\nabla \cdot \mathbf{E})$  in relation eq. (2.93) is equal to zero in vacuum. We will consider in the following a transverse wave, whose electric and magnetic components lie in a plane orthogonal to the propagation direction  $z$ . We will also put aside the temporal dependence of the pulse and focus on the evolution of the field amplitude as the beam propagates. In those conditions, we can write:

$$\mathbf{E}(\mathbf{r}, t) = A(\mathbf{r}) e^{ikz - \omega t} \mathbf{e}_r \quad (2.94)$$

where  $A$  is the amplitude of the transverse field and  $\mathbf{e}_r$  a unit vector defining the polarization direction of the wave. This vector belongs to the plane (x y) orthogonal to the propagation direction  $z$ .

**Propagation in vacuum.** In vacuum, where there is no charges, the equation eq. (2.93) then takes the following shape:

$$(\Delta + k^2) \mathbf{E} = 0 \quad (2.95)$$

with  $k$  the wave vector such as  $k = \omega/c = 2\pi/\lambda$ . Because the variations of the envelope of  $A$  are due to the propagation, these are slow compared to those in the transverse direction and compared to the field oscillations (described by the term  $e^{ikz}$ ). The equation eq. (2.95) can therefore be simplified thanks to the so-called "paraxial approximation":

$$\left| \frac{\partial^2 A}{\partial z^2} \right| \ll 2k \left| \frac{\partial A}{\partial z} \right| \quad \text{and} \quad 2k \left| \frac{\partial A}{\partial r} \right| \quad (2.96)$$

Therefore, the propagation equation reads:

$$\Delta_{\perp} A + 2ik \frac{\partial A}{\partial z} = 0 \quad (2.97)$$

where the operator  $\Delta_{\perp} = \left( \frac{\partial^2}{\partial x^2} + \frac{\partial^2}{\partial y^2} \right)$  refers to the transverse Laplace operator.

In the case of a Gaussian beam, the spherical wave defined by the following equation is a solution to the paraxial equation eq. (2.97):

$$A(r, z) = A_0 \frac{w_0}{w(z)} e^{-\frac{r^2}{w^2(z)}} e^{-ik \frac{r^2}{2R(z)}} e^{-ikz} e^{i\zeta(z)} \quad (2.98)$$

We can then define  $w_0$ , the beam waist, which represents the smallest size of the beam and  $Z_R = \frac{\pi w_0^2}{\lambda}$ , the Rayleigh length. The latter distance corresponds to twice distance from the

beam focus (where the spot radius equals the waist) to the region where the beam size increases by a factor of  $\sqrt{2}$ . The expression eq. (2.98) can be decomposed into 5 contributions:

- $A_0 \frac{w_0}{w(z)}$  is the on-axis field amplitude with  $w(z)$  the beam radius depending on the propagation coordinate  $z$  through the formula:

$$w(z) = w_0 \sqrt{1 + \frac{z^2}{Z_R^2}} \quad (2.99)$$

- $e^{-\frac{r^2}{w^2(z)}}$  defines the transverse profile of the field amplitude.
- $e^{-ik\frac{r^2}{2R(z)}}$  corresponds to the phase in the wave plane, where the radius of curvature  $R(z)$  varies according to the relation:

$$R(z) = z \left( 1 + \frac{Z_R^2}{z^2} \right) \quad (2.100)$$

- $e^{-ikz}$  is a term describing the variation of the wave phase due to propagation.
- $e^{i\zeta(z)}$  is an additional phase term varying by a factor of  $\pi$  when  $z$  varies from  $-\infty$  to  $+\infty$ .  $\zeta$  is the Gouy phase, expressed thanks to the formula:

$$\zeta(z) = \arctan \left( \frac{z}{Z_R} \right) \quad (2.101)$$

This terms describe the  $\pi$ -phase difference the wave takes when crossing the focus region.

From the above-mentioned relations, the angular aperture of the beam can be derived.

$$\theta = \lim_{z \rightarrow \infty} \left( \frac{w(z)}{z} \right) = \frac{\lambda}{\pi w_0} \quad (2.102)$$

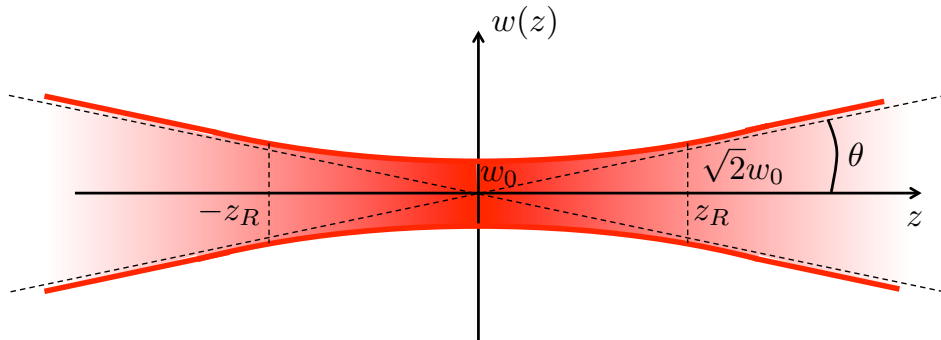


Figure 2.20: Illustration of the evolution of the Gaussian beam size in the focal spot region.

**Propagation in a plasma.** In the case of a charged medium, the current density induced by the electrons stripped from atoms is non-zero. Atoms get further ionized as the laser pulse propagates in the plasma. The resulting ionization map of the medium depends on the intensity distribution profile of the beam, which is affected by its propagation in the plasma.

Considering  $v_i$  and  $v_e$ , as the ions' and electrons' velocities, the current density  $\mathbf{J}$  can be written:

$$\mathbf{J} = -n_e e (\mathbf{v}_e - \mathbf{v}_i) = -n_e e \mathbf{v}_e \quad (2.103)$$

where  $e$  et  $n_e$  are respectively the electron charge and the number of electrons per unit volume. Here, because of the huge mass difference between the ions and the electrons, we neglect the oscillations of ions in the electromagnetic field of the laser. Thus, only the electrons contribute to the current density in the Maxwell equation eq. (2.92). The current density induced by the valence electrons will be also neglected. Thus, taking into account the electrons' collisions, the equation governing the movement of the free electrons can be approximated by the following relation:

$$m_e \frac{\partial \mathbf{v}_e}{\partial t} + m_e \nu_e \mathbf{v}_e = -e \mathbf{E} \quad (2.104)$$

with  $m_e$  is the electron mass and  $\nu_e$ , the electron collision frequency. Besides, the equations eq. (2.103) and eq. (2.104) yield:

$$\mathbf{J} = \frac{e^2 n_e}{m_e (\nu_e - i\omega)} \mathbf{E} \quad (2.105)$$

Considering that the characteristic timescale of collisions is in the order of a few picoseconds, we can write  $\nu_e \ll \omega$  and the expression eq. (2.105) can therefore be simplified:

$$\mathbf{J} = i\epsilon_0 \frac{\omega_p^2}{\omega} \mathbf{E} \quad (2.106)$$

with  $\omega_p = \sqrt{\frac{e^2 n_e}{\epsilon_0 m_e}}$ , the plasma frequency.

Under those conditions, the equation eq. (2.93) reads:

$$\Delta \mathbf{E} + k^2 \left( 1 - \frac{\omega_p^2}{\omega^2} \right) \mathbf{E} = \nabla(\nabla \cdot \mathbf{E}) \quad (2.107)$$

The coefficient  $\eta = \sqrt{1 - \frac{\omega_p^2}{\omega^2}}$  corresponds to the medium refractive index. The right-hand side is called the medium polarization term. It can be neglected in the case where the refractive index inhomogeneities lie in a plane orthogonal to the field  $\mathbf{E}$ . Taking the divergence vector operator of the equation eq. (2.92), one gets:

$$\nabla \cdot \mathbf{E} = -\frac{\mathbf{E} \cdot \nabla(\eta^2)}{\eta^2} \quad (2.108)$$

In particular, as long as  $\eta \neq 0$ , this term vanishes when the inhomogeneity in  $n_e$  lies in a plane perpendicular to  $\mathbf{E}$ . Moreover, it can also be neglected when the fluctuations of  $\eta$  are small compared to its mean value.

We can notice that when the wave frequency becomes lower than  $\omega_p$ , the refractive index becomes purely imaginary and the wave attenuates sharply in the plasma. Hence, a so-called critical density  $n_c$  can be defined for which  $\omega = \omega_p$ :

$$n_c = \frac{m_e \omega^2}{4\pi e^2} \quad (2.109)$$

A wave can thus propagate in the plasma only if the medium electron density is inferior to the critical density, which is related to its wavelength. In a practical case, one can use the formula:

$$n_c \approx 1.74 \times 10^{21} \left( \frac{\lambda_{Ti:sapph}}{\lambda} \right) \text{ cm}^{-3} \quad (2.110)$$

with  $\lambda_{Ti:sapph} = 800 \text{ nm}$ . For wavelengths of 800 and 32.8 nm, the critical density values are respectively  $n_c \simeq 1.74 \times 10^{21} \text{ cm}^{-3}$  and  $n_c \simeq 10^{24} \text{ cm}^{-3}$ .

### 2.4.2 Beam refraction

When a beam is focused into a gas, the field strength is far stronger on axis and therefore, a larger number of electrons are generated on axis. This configuration corresponds to a lower on-axis refractive index, which turns the plasma to behave as a diverging lens. Therefore, the propagation results in a defocusing of the beam combined with a collapse of on-axis intensity. This phenomenon gets stronger as the initial electron density of the plasma gets higher. In case of OFI plasma amplifiers, this situation leads to a drop of the laser intensity below the required threshold to create lasing ions, thus terminating the effective amplifier length. This defocusing effect, illustrated in fig. 2.21 hampering the beam propagation is known as refraction.

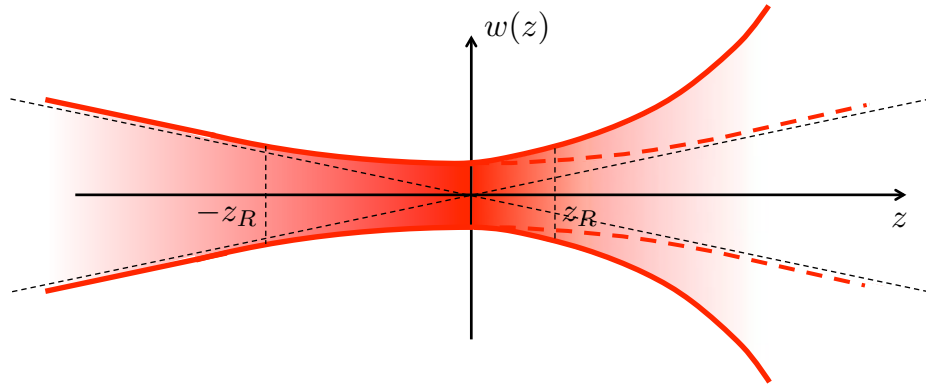


Figure 2.21: Illustration of refraction.

As a first geometrical approach, we consider the ray path in a density varying environment. According to the Fermat principle, the path light takes to get from one point to another corresponds to the quickest one. This principle derives from the variational principle of least action. The optical path of rays is stationary and is written:

$$l = \int \eta ds \quad (2.111)$$

where  $s$  is the curvilinear abscissa.

Considering  $\mathbf{r}$ , a unitary vector of propagation, the ray path is governed by the Eikonal equation:

$$\frac{d}{ds} \left( \eta(\mathbf{r}) \frac{d\mathbf{r}}{dz} \right) = \nabla \eta \quad (2.112)$$

Considering a paraxial wave with a refractive index gradient transverse to the propagation, the equation eq. (2.112) turns:

$$\frac{d^2\eta(x)}{dz^2} = \frac{1}{\eta(x)} \frac{d\eta(x)}{x} \quad (2.113)$$

This equation is valid for a simple 2D case where  $x$  and  $z$  are respectively the transverse and the propagation coordinates. When  $n_e \ll n_c$ , the refractive index can be approximated as following:

$$\eta \approx 1 - \frac{n_e}{2n_c} \quad (2.114)$$

If we assume the laser pulse induces a linear transverse electron density with the shape,

$$n_e(x) = n_{e0} \left( 1 - \frac{x}{x_0} \right) \quad (2.115)$$

then, considering  $\eta \approx 1$ , the equation eq. (2.113) reads:

$$\frac{d^2x}{dz^2} = \frac{1}{2} \frac{n_{e0}}{n_c x_0} \quad (2.116)$$

A gradient transverse to the propagation direction of a beam will deviate the rays towards the zones of lower densities.

If we note  $x(0)$  and  $\theta_0$  the initial position and divergence angle of the ray at  $z=0$ , the ray trajectory is:

$$x(z) = \frac{n_{e0}}{4n_c x_0} z^2 + \theta_0 z + x(0) \quad (2.117)$$

Hence, assuming  $\nabla n_e \approx n_{e0}/x_0$ , the deviation imparted by refraction over a length  $L$  can therefore be derived as:

$$\Delta x[cm] \approx 4.55 \times 10^{-22} L^2[cm] \lambda^2[\mu m] \nabla n_e[cm^{-4}] \quad (2.118)$$

Using another approach, the contribution of the beam refraction can be assessed [Rankin et al., 1991] defining a characteristic length over which the phase of the wave changes by a factor of  $\pi/2$ . This yields:

$$L_D = \frac{\lambda n_c}{2n_e} \quad (2.119)$$

This characteristic length gives a "rule of thumb" for evaluating the significance of refraction. When this length is smaller than the Rayleigh length, refraction overcomes natural diffraction. Refraction gets therefore significant when:

$$n_e > \frac{\lambda^2}{2\pi w_0^2} n_c \quad (2.120)$$

In a practical example, considering a waist size of  $15 \mu m$  and for  $\lambda = 800 \text{ nm}$ , the refraction effects get significant when the electron density reaches  $7.9 \times 10^{17} \text{ cm}^{-3}$ , which corresponds to the conditions with a gas cell pressure of 32 mbar.

### Intensity map and distribution of lasing ions' population

The propagation of an intense IR pulse is hampered by refraction effects that lead to the beam defocusing and therefore to a reduction of the zone of laser-plasma interaction. The duration of ultrashort pulses (30 fs) is significantly shorter than characteristic timescales of the plasma (a few ps for the shortest cases). The effects of plasma collisions have therefore a negligible effect on the beam propagation and only optical field ionization (OFI) is to be considered. Losses from OFI can be neglected. The plasma is considered to be isotropic and thus has no effect on the beam polarization. In the experimental conditions, the main pulse energy is 1.36 J and is focused down to a 32  $\mu\text{m}$  spot thanks to a spherical mirror of focal length 75 cm. In those conditions, the Rayleigh length is 725  $\mu\text{m}$ .

The impact of plasma refraction is brought to the fore thanks to numerical simulations using WAKE-EP particle-in-cell code [Paradkar et al., 2013]. This is an extended version of the quasi-static 2D axisymmetric code WAKE [Mora and Antonsen, 1997]. The code performs moving window simulations describing laser plasma interaction in the short pulse regime as the beam propagates. However, the code contains several approximations limiting its validity.

The code is suitable for low to moderate values of the electron density and remains valid for  $\omega_p \leq 0.15\omega_0$ . This allows saving time by averaging some physical quantities over the inverse of the laser frequency  $\omega_0$ , such as the laser intensity and the particle motion. Second, it is assumed that in the laser frame coordinate, all physical quantities vary slowly with time. The quasistatic approximation is applied for the motion of electrons, which turns the model not relevant for the description of large Raman instabilities. Finally, because of the axi-symmetric considerations, a beam break-up at very high intensities, notably due to filamentation, cannot be properly modeled. The studied experimental conditions, which modeled in the following, lie in the frame of validity of this code.

The fig. 2.22 shows the intensity maps of the pump beam for a 5 mm long plasma under previously described focusing conditions at the entrance of the plasma in case of vacuum (a),  $P_{Kr} = 10 \text{ mbar}$  (b),  $P_{Kr} = 30 \text{ mbar}$  (c) and  $P_{Kr} = 50 \text{ mbar}$  (d). The field is considered to be Gaussian. The intensity maps illustrate the defocusing effects from the plasma that add up to the natural beam diffraction, shown in fig. 2.22a. We clearly see that those effects get stronger as the plasma density increases from 10 mbar to 50 mbar, corresponding to atomic densities of  $2.5 \times 10^{17} \text{ cm}^{-3}$  and  $1.2 \times 10^{18} \text{ cm}^{-3}$  respectively. The waist dimension gets wider and the maximum intensity on axis drops more sharply as the beam propagates in the 5 mm-long plasma. The fig. 2.22c ( $P_{Kr} = 30 \text{ mbar}$ ) & fig. 2.22d ( $P_{Kr} = 50 \text{ mbar}$ ) show an autofocusing effect at about 2.5 mm and 2 mm respectively. This effect is stronger on-axis for the highest density but the beam collapse fails to increase the region where the lasing ions are generated within the field.

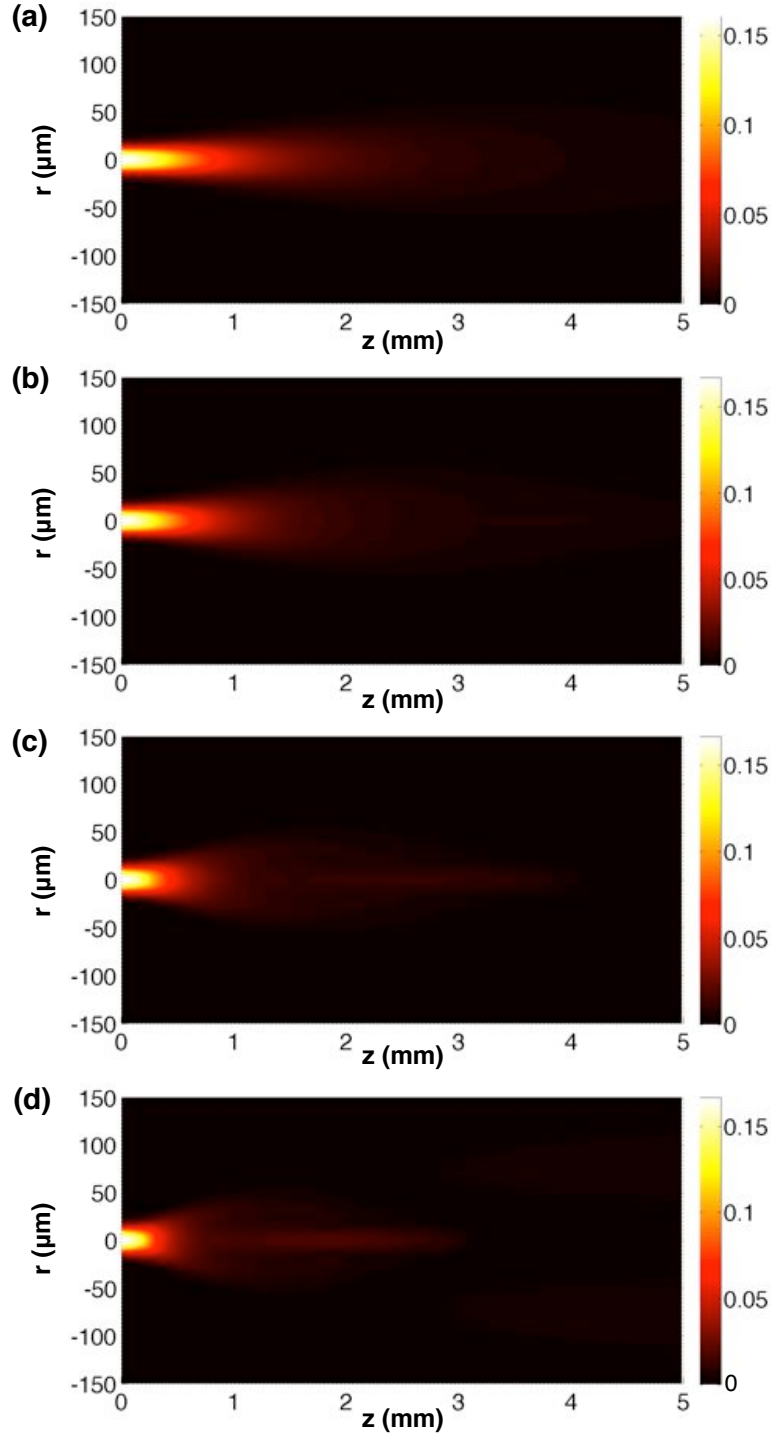


Figure 2.22: Evolution of the IR pump beam vector potential as it propagates in vacuum (a) and in plasmas of electron densities corresponding to  $P_{Kr} = 10$  mbar (b),  $P_{Kr} = 30$  mbar (c) and  $P_{Kr} = 50$  mbar.

The fig. 2.23 shows the maps of the average ionization degree of the generated plasma in case of  $P_{Kr} = 10$  mbar (a),  $P_{Kr} = 30$  mbar (b) and  $P_{Kr} = 50$  mbar (c). Here, we consider that the

plasma properties only depend on the laser intensity and its polarization. The lasing ion species ( $Kr^{8+}$ ) are depicted in pale green. Those maps report a reduction of the plasma amplifier size as the electron density is increased. This means a smaller volume of ion species that can be effectively pumped, which will result in reducing the amplification and may lead to prevent reaching the saturation regime of the amplifier. Furthermore, as far as soft X-rays (32.8 nm) are concerned, lower ionized regions of the plasma (of charge lower than 3) lead to the absorption of emission.

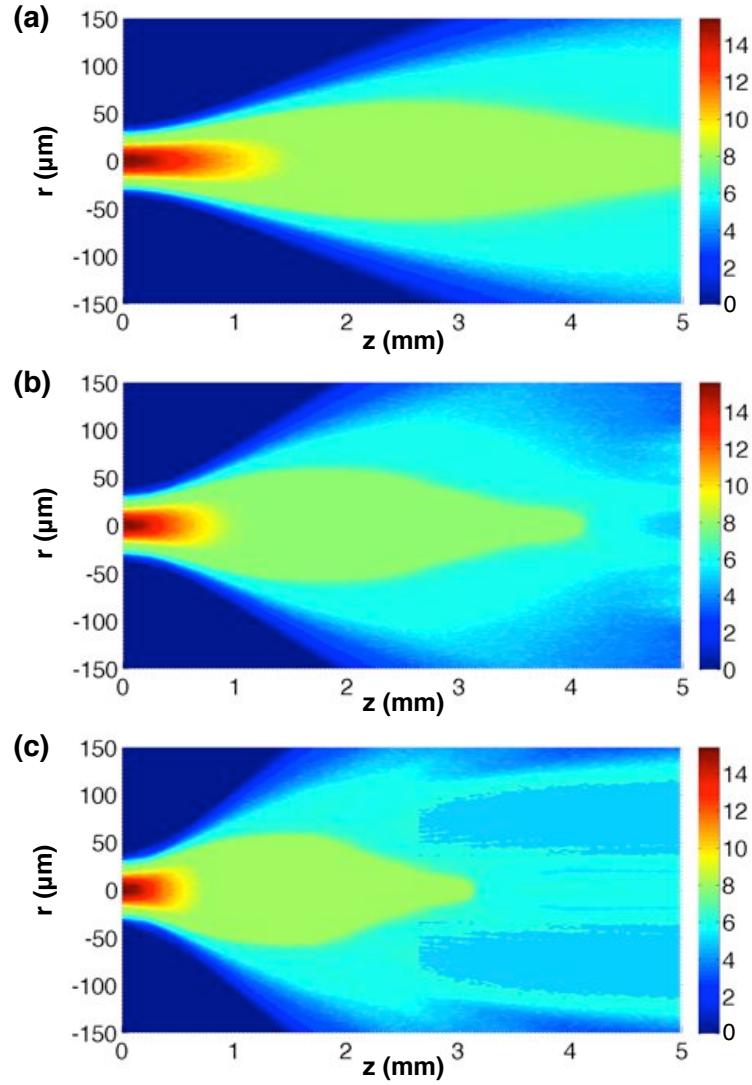


Figure 2.23: Maps of ion species resulting from OFI of a 5 mm-long krypton plasma in vacuum (a) of electron densities corresponding to  $P_{Kr} = 10\text{mbar}$  (b),  $P_{Kr} = 30\text{mbar}$  (c) and  $P_{Kr} = 50\text{mbar}$ .

As a result, increasing the electron density reduces the volume and length of the generated lasing ions' volume, which prevents the implementation of a saturated amplifier at high electron densities.



## 2.5 Modeling the amplification of HH by a plasma amplifier

The radiative transfer equation, describing the amplification of soft X-ray radiation by the plasma amplifier, has been described in section 2.3.1. This approach gives in reality only an approximate view of the underlying physical processes responsible for amplification in the plasma and is based on two main assumptions. The first one is that the kinetics of atomic populations is faster than the characteristic timescale of the temporal envelope of soft X-ray emission. This assumption is called the *adiabatic approximation*. The second one considers the spatial coherence of emission is weak, which means that the field is, at each point in space, the sum of numerous non-coherent contributions whose phases have no relationship with each other. As a consequence, the total intensity can be written as the sum of intensities from all individual contributions. This approach is valid under amplified spontaneous emission (ASE) operating in conditions, where the plasma amplifies its "own noise". Actually, the stochastic nature of spontaneous emission makes ASE weakly coherent. Besides, the temporal envelope of ASE emission is larger than the gain recovery time.

The merits of injection seeded plasma-based soft X-ray lasers [Zeitoun et al., 2004] have demonstrated much improved beam features compared to the ASE operating mode, in terms of duration, spatial coherence and wavefront characteristics. Moreover, the perspective of using this setup to control the polarization of soft X-ray emission appears promising. In this case, the amplification of a coherent resonant field is considered. Furthermore, while the seeded signal (high-harmonics) has a duration of a few tens of femtoseconds, the plasma response characteristic timescale is usually on the order of a few picoseconds. Therefore, none of the previously-stated approximations are valid and a more adequate description of this configuration is needed.

The **Maxwell-Bloch treatment** is an appropriate model for this. It is based on a semi-classical microscopic approach, known as the Lorentz model. This describes the interaction between the laser field and a bound electron in terms of a classical harmonic oscillator, but including quantum effects. The treatment of the electromagnetic field is classical and based on Maxwell equations, whereas the interaction of the field with atoms is described by non-relativistic quantum mechanics. This semi-classical approach is cogent to our experimental conditions, considering the field intensities ( $\approx 10^9 - 10^{12} \text{W/cm}^2$ ). Another approximation is that the model considers only two "effective" atomic levels. This means that the population transfers from and to other levels are taken into account through global "losses" and "gain" terms.

In this thesis, the numerical description corroborating the experimental results (cf. chapter 5) has been performed thanks to *DeepOne* code, which is based a 1D time-dependent model. For the sake of computational efficiency, the plasma amplifier is considered to be uniform. The description of the dynamics of the laser transition populations allows computing a time-dependent gain characterizing the amplification. *Maxwell-Bloch equations* consist in a set of three coupled equations depicting the temporal evolution of three important parameters: the field  $\mathbf{E}$  with its evolution due to propagation, the polarization of the medium  $\mathbf{P}$  illustrating the interaction of the field with atoms and the population inversion between the laser upper and lower levels,  $\Delta N$ , responsible for the rate of stimulated emission.

### 2.5.1 Field equations

Because of the different timescales involved in the amplification process along the plasma amplifier (tens of femtoseconds for HH pulse duration and a few picoseconds for the plasma response), a full time-dependent model is needed. The equation describing the propagation of the soft X-ray field in a non-magnetic plasma is derived from Maxwell equations (see section 2.4.1) and are written eq. (2.121):

$$\Delta \mathbf{E} - \frac{1}{c^2} \frac{\partial^2 \mathbf{E}}{\partial t^2} - \nabla(\nabla \cdot \mathbf{E}) = \mu_0 \frac{\partial \mathbf{J}}{\partial t} \quad (2.121)$$

There are two contributions to the current density  $\mathbf{J} = -n_e e \mathbf{v}_e$ . One is from free electrons. Here, we consider those are only subjected to the field and we neglect the electron-ions collisions that slow down free electrons. This would have actually lead to consider a friction force decreasing the current density  $\mathbf{J}$ . Under this approximation, the current density from free electrons  $\mathbf{J}^{(f)}$  obeys to the relation:

$$\frac{\partial \mathbf{J}^{(f)}}{\partial t} = \frac{1}{\mu_0} \frac{\omega_p^2}{c^2} \mathbf{E} \quad (2.122)$$

The other contribution comes from bound electrons ( $\mathbf{J}^{(b)} = \frac{\partial \mathbf{P}}{\partial t}$ ). The polarization of the medium  $\mathbf{P}$  describes how the bound electrons oscillate in the presence of an electric field:

$$\mathbf{P} = -n_e^{(b)} e \mathbf{r} \quad (2.123)$$

$n_e^{(b)}$  is the electron density of bound electrons and  $\mathbf{r}$  is a vector locating the position of the bound electrons with respect to the atom nucleus.

Besides, the displacement of ions also contribute to the current density. However, because of the great difference of mass between ions and electrons, this contribution can be neglected.

The interaction of the pulse with the medium induces a charge separation through an ambipolar diffusion of species. The induced field providing an opposing force to enforce the charge equilibrium has a low frequency compared to the field. Hence, the high frequency component of the field verifies  $\nabla \cdot \mathbf{E} = 0$ . Therefore the propagation equation eq. (2.121) reads:

$$\Delta \mathbf{E} - \frac{1}{c^2} \frac{\partial^2 \mathbf{E}}{\partial t^2} - \frac{\omega_p^2}{c^2} \mathbf{E} = \mu_0 \frac{\partial^2 \mathbf{P}}{\partial t^2} \quad (2.124)$$

We consider a transverse field propagating along the z-direction. Hence, it can be written  $\mathbf{E} = A \times e^{i(\omega_0 t - kz)}$ , with  $A$  the field amplitude,  $\omega_0$  the laser frequency and  $k = \omega_0/c$  the wave vector value. The polarization vector has the same direction and frequency as the field. Thus, in a similar way,  $\mathbf{P} = P \times e^{i(\omega_0 t - kz)}$ . Therefore, the propagation equation eq. (2.124) can be expanded:

$$\Delta A - 2i \frac{\omega_0}{c} \frac{\partial A}{\partial z} - \frac{\omega_0^2}{c^2} A + \frac{\omega_0^2}{c^2} A - 2i \frac{\omega_0}{c^2} \frac{\partial A}{\partial t} - \frac{1}{c^2} \frac{\partial^2 A}{\partial t^2} - \frac{\omega_p^2}{c^2} A = \mu_0 \left[ -\omega_0^2 P + 2i\omega_0 \frac{\partial P}{\partial t} + \frac{\partial^2 P}{\partial t^2} \right] \quad (2.125)$$

The Laplacian can be written  $\Delta = \Delta_T + \frac{\partial^2}{\partial z^2}$ , where  $\Delta_T$  is the transverse Laplacian. Using the so-called slowly varying envelope approximation,

$$\left| \frac{\partial^2 A}{\partial z^2} \right| \ll \left| 2 \frac{\omega_0}{c} \frac{\partial A}{\partial z} \right| \quad \& \quad \left| \frac{\partial^2 A}{\partial t^2} \right| \ll \left| 2\omega_0 \frac{\partial A}{\partial t} \right| \quad \& \quad \left| \frac{\partial^2 P}{\partial t^2} \right| \ll \left| 2\omega_0 \frac{\partial P}{\partial t} \right| \quad (2.126)$$

and neglecting the local temporal evolution of the polarization as its times scale is in order of magnitude of the plasma response (i.e. much longer compared to the variation of the field amplitude), we get:

$$\Delta_T A - 2i \frac{\omega_0}{c} \frac{\partial A}{\partial z} - 2i \frac{\omega_0}{c^2} \frac{\partial A}{\partial t} - \frac{\omega_p^2}{c^2} A = -\mu_0 \omega_0^2 P \quad (2.127)$$

For the sake of simplicity, a one-dimensional model is used and the transverse Laplacian can thus be neglected. Only the spatial derivatives on the  $z$  coordinate are retained. This simplification allows a significant computational efficiency but the description of refraction and diffraction effects is not accounted. This aspect is independently studied with WAKE-EP numerical code (see chapter 3). All in all, we obtain a first-order advection equation for the electric field:

$$2i \frac{\omega_0}{c^2} \left[ c \frac{\partial A}{\partial z} + \frac{\partial A}{\partial t} \right] = \frac{\omega_0^2}{c^2} \left[ \frac{\omega_p^2}{\omega_0^2} A - \mu_0 c^2 P \right] \quad (2.128)$$

The numerical solution can be more easily obtained solving the propagation equation eq. (2.128) in the reference frame of a photon, introducing a reduced time  $\tau = t - z/c$  and the coordinate change  $\xi = c\tau$ . As a consequence, the second-order partial derivative equation is reduced to a first-order ordinary derivative equation, solvable by standard Runge-Kutta methods:

$$\frac{\partial A}{\partial \xi} = \frac{i\omega_0}{2c} \left[ \mu_0 c^2 P - \frac{\omega_p^2}{\omega_0^2} A \right] \quad (2.129)$$

This equation describes the amplification of soft X-ray emission by the polarization density as the electric field propagates through the plasma. The second term in the right-hand side of equation eq. (2.129) illustrates the damping by the free-electron current, which does not participate in the polarization term. Now, a constitutive relation for the polarization is needed to describe the field interaction with atoms.

### 2.5.2 Atomic description

**Atomic model** The description of the interaction between the soft X-ray laser field and the medium is carried out through a quantum approach. To study incoherent or dissipative processes, the density operator formalism is relevant for a statistical description. The density operator  $\rho$  is defined as the dyadic product of the state with itself:

$$\rho = |\psi\rangle\langle\psi| \quad (2.130)$$

with  $\psi$ , the wave function describing the state. The polarization density is derived from Bloch equations [Sureau and Holden, 1995] and its expectation value is:

$$\mathbf{P} = Tr(\rho \mathbf{d}) = \langle \psi | \mathbf{P} | \psi \rangle \quad (2.131)$$

where  $\rho$  is the density operator,  $Tr()$  the matrix trace, and  $\mathbf{d}$ , the atomic electric dipole. The temporal variation of the matrix elements of the density operator is given by the Bloch equation written in the dipole approximation:

$$\begin{cases} i\hbar \frac{\partial \rho}{\partial t} = [H, \rho] \\ H = H_A - \mathbf{d} \cdot \mathbf{E} \end{cases} \quad (2.132)$$

where  $H_A$  is the atomic Hamiltonian in the absence of electric field. This term determines the structure of an atom or an ion. Considering  $N$  electrons orbiting an atom, the Hamiltonian  $H_A$  is written:

$$H_A = \underbrace{\sum_{i=0}^N \frac{p_i^2}{2}}_{\text{Bound electron kinetic energy}} - \underbrace{\sum_{i=0}^N \frac{Z}{r_i^2}}_{\text{Attraction energy of the atom over electrons}} + \underbrace{\sum_{i < j} \frac{1}{r_{ij}}}_{\text{Repulsive Coulomb energy between electrons}} \quad (2.133)$$

The temporal evolution of the system is given by the Schrödinger equation:

$$i\hbar \frac{\partial \Psi}{\partial t} = H_A \Psi \quad (2.134)$$

The solutions of this equation are wave functions  $\Psi(\mathbf{r}_1, \dots, \mathbf{r}_N, t)$  describing the repartitions of electrons in the atomic structure. The density operator is derived from eq. (2.132) through a perturbation approach.

**Population inversion.** Assuming linearly-polarized light and neglecting the second-order (Zeeman) coherences [Sureau and Holden, 1995], the non-diagonal element of the density matrix  $\rho$  is governed by the equation:

$$\frac{\partial \rho_{ul}}{\partial \tau} = -\gamma \rho_{ul} + \frac{iE}{\hbar} d_{ul} (N_u - N_l) \quad (2.135)$$

where  $\gamma$  is the depolarization rate due to electron-ion collisions (proportional to the electron-ion frequency),  $d_{ul}$  the corresponding dipole matrix element and  $N_u$ ,  $N_l$  the populations of the upper and lower levels of the transition respectively. The equation for the polarization density is obtained by multiplying the equation eq. (2.135) by the dipole matrix element. A stochastic source term  $\Gamma$  [Chandrasekhar, 1943; Larroche et al., 2000] is added to account for spontaneous emission:

$$\frac{\partial P}{\partial \tau} = \Gamma - \gamma P + \frac{iE}{\hbar} d_{ul}^2 (N_u - N_l) \quad (2.136)$$

Then, the populations of upper and lower levels are computed using standard rate equations coupled with the electric field:

$$\begin{cases} \frac{\partial N_u}{\partial \tau} = \sum_k C_{ku} N_k + \frac{1}{2\hbar} \mathcal{I}(E.P^*) \\ \frac{\partial N_l}{\partial \tau} = \sum_k C_{kl} N_k + \frac{1}{2\hbar} \mathcal{I}(E.P^*) \end{cases} \quad (2.137)$$

where  $C_{ij}$  are collisional (de-)excitation and radiative (de-)excitation rates regrouping the depletion rates of levels (u) and (l), as well as the collisional and radiative rates coupling atomic levels.  $\mathcal{I}$  designates the imaginary part of an expression.  $N_k$  are the population of other atomic levels that strongly interact with the lasing ones. This set of equations allows determining the dynamics of population inversion and the resulting temporal evolution of the gain. Several processes determining the amplification of soft X-ray radiation in a plasma can be described.

In chapter 5, we will see that, in a high-harmonic seeding regime, the amplified HH pulses are mixed with a noisy ASE signal and that they display two regimes: a so-called dynamic regime, characterized by Rabi oscillations and an adiabatic regime governed by the evolution of the amplified field envelope.

This model, upon which *DeepOne* code is based, has been benchmarked [Wang et al., 2008] to study the spatio-temporal evolution of an amplified high-harmonic seed throughout a plasma amplifier.

### 2.5.3 Amplification of a HH seed pulse

The fig. 2.24 illustrates the simultaneous temporal profiles of the population inversion, the polarization (through the dipole moment term) and the intensity of the amplified HH field at the beginning of the plasma (0 mm) and after 1, 2, 3 and 5 mm of propagation.

Qualitatively, the amplified HH pulse is composed of a weakly amplified HH and a **wake**, which develops in front of the HH pulse and which embodies the temporal response of the plasma to the HH resonant excitation. This wake starts becoming predominant after 2 mm of propagation. The buildup of the amplified HH pulse leads to emptying the population inversion. This saturation of the population inversion is characterized by **Rabi oscillations** affecting the population inversion, the polarization and the amplified pulse in a similar way.

A more detailed description of this amplification regime and its dependance with respect to the electron density is presented in section 5.3 & section 6.3.2.

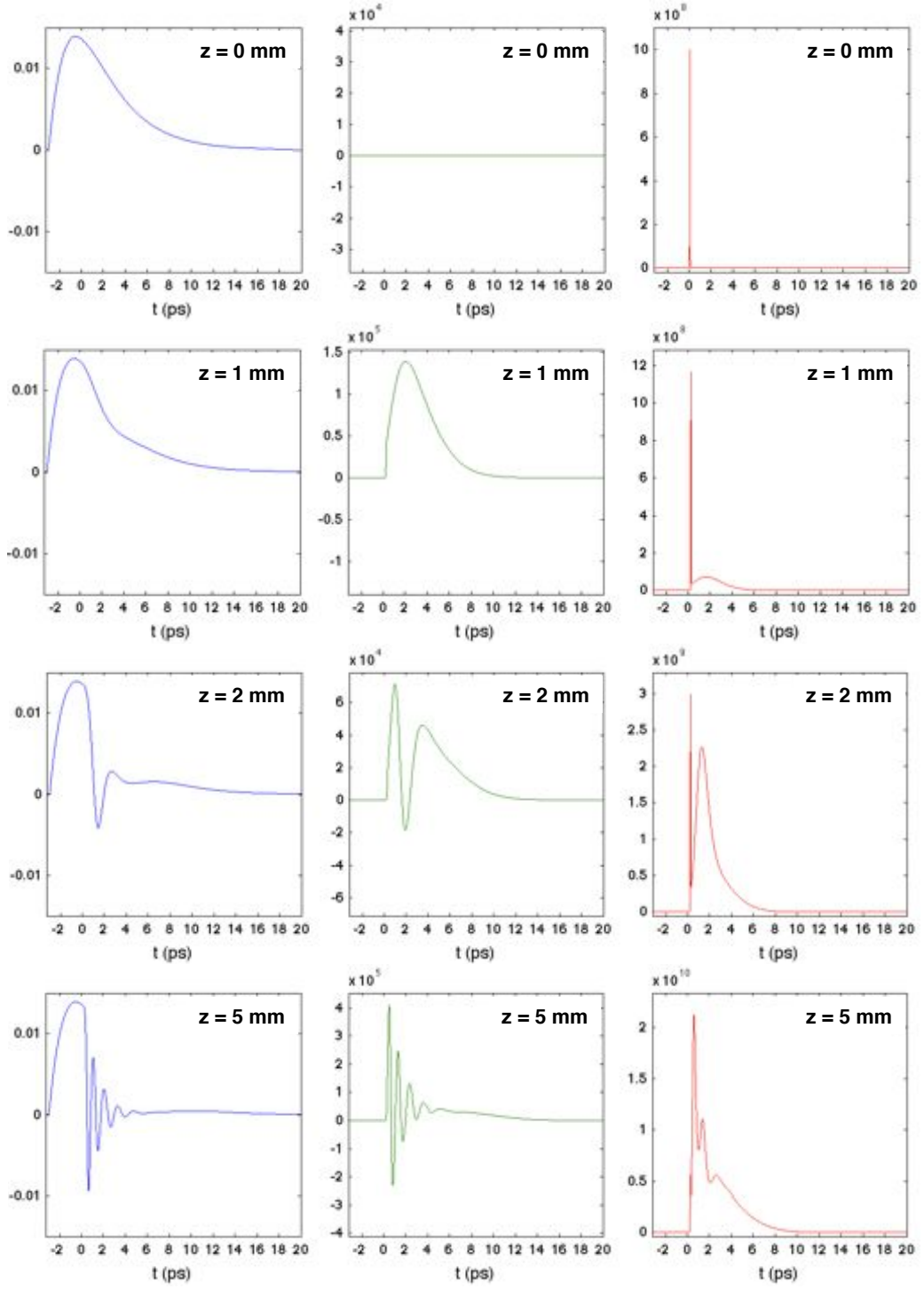


Figure 2.24: Illustration of the amplification over 5 mm of seed HH by a  $Kr^{8+}$  amplifier at an electron density of  $n_e = 6 \times 10^{18} \text{ cm}^{-3}$ . The blue, green and red curves stand for the population inversion (a.u.), the dipole moment (a.u.) and the amplified HH field intensity ( $\text{W}/\text{cm}^2$ ) respectively.

## **2.6 Conclusion**

The description of the physical processes associated with plasma-based soft X-ray lasers is complex as it encompasses a set of inter-disciplinary elements belonging to plasma physics, quantum mechanics and laser physics. The numerical description, based on theoretical models, provides a valuable insight into experimental observations but the latter also provide a valuable feedback to improve the post-processing and understanding of numerical results.

Driving high-density plasma amplifier turns out to be a worthwhile research direction as it promises the generation of ultrashort and intense pulses in the soft X-ray region. Indeed, the increase of the plasma amplifier electron density leads to a temporal gating of the lasing action, while yielding more photons per pulse.

However, the propagation of an intense pump IR laser pulse to implement the lasing medium turns out problematic at very high electron densities. Refraction leads to a defocusing of the beam, which in turn reduces the volume of laser-plasma interaction. Therefore, guiding the pump beam proves to be pivotal for the implementation of saturated ultrashort plasma-based soft X-ray lasers.

## Chapter 3

# Modeling of a high-density krypton plasma waveguide

The development of waveguiding techniques is pivotal to many applications, since it allows increasing the laser-plasma interaction length. This chapter presents an overview of waveguiding techniques and brings into the fore their merits and limitations.

The «ignitor-heater » waveguiding technique has been investigated since it turns well adapted for high-density plasmas. The critical parameters to optimize the guiding conditions are introduced and a numerical modeling [Oliva et al., 2015] is used to describe the complex propagation of an ultrashort and intense infrared driving pulse into an elongated high-density plasma channel.

### Contents

---

<b>3.1</b>	<b>State of the art of waveguiding techniques of high-intensity laser pulses</b>	<b>80</b>
3.1.1	Relativistic self-guiding	80
3.1.2	Capillary discharge plasma waveguide	81
3.1.3	Hollow capillary tube	82
3.1.4	Optically-preformed plasma waveguide using the «ignitor-heater » technique	83
<b>3.2</b>	<b>Numerical modeling of plasma waveguiding</b>	<b>89</b>
3.2.1	Waveguiding conditions	90
3.2.2	Numerical model	94
3.2.3	Numerical investigation of a range of parameters	100
<b>3.3</b>	<b>Conclusion</b>	<b>107</b>

---



### 3.1 State of the art of waveguiding techniques of high-intensity laser pulses

Performances of laser-driven plasma sources, from soft X-ray lasers to particle plasma accelerators, are limited by the length of the laser-plasma interaction. Those limitations are increasingly predominant at higher plasma densities. To overcome this bottleneck stemming from diffraction and refraction defocusing effects, several waveguiding techniques have been demonstrated. Those allow boosting previous performances by increasing the effective length over which a nearly uniform laser intensity can be deposited. Similarly to optical fibers, the waveguiding techniques aim at engineering a radial refractive index profile to counterbalance beam defocusing effects. From the refractive index of a plasma  $\eta = \sqrt{1 - n_e(r)e^2/(m_e\epsilon_0\omega^2)}$ , one can see that lowering the electron density on axis will result in a stronger on-axis refractive index, which offers appropriate conditions for guiding.

#### 3.1.1 Relativistic self-guiding

The propagation of an ultrashort intense pulse in a plasma induces transverse variations of the background plasma density. This generally leads to premature defocusing, which causes the beam propagation to collapse. However, in a uniform fully ionized plasma, *relativistic self-focusing* appears as the laser intensity is increased [Esarey et al., 1997; Chen et al., 1998]. The power threshold from which this phenomenon arises is:

$$P_c \approx 17 \left( \frac{\omega_0}{\omega_p} \right)^2 \quad [GW] \quad (3.1)$$

Considering plasma densities ranging from  $10^{17} - 10^{19} \text{ cm}^{-3}$ , this threshold translates into a 3-300 TW power requirement.

At high intensities, the dispersion relation of a propagating wave is altered due to the effective relativistic mass increase of electrons. Under those conditions, the transverse refractive index  $\eta(r)$  reads [Gibbon, 2005]:

$$\eta(r) = \sqrt{1 - \frac{\omega_p^2}{\omega_0^2 \sqrt{1 + a(r)^2/4}}} \quad (3.2)$$

where  $a(r)$  is the electric field vector potential related to the pulse intensity. When  $d\eta/dr > 0$ , the medium behaves as a converging lens. The phase velocity of the wave fronts passing through the focusing medium can be approximated as following:

$$\frac{v_p(r)}{c} = \frac{1}{\eta} \approx \frac{\omega_p^2}{8\omega_0^2} a_0^2 e^{-r^2/w_0^2} \quad (3.3)$$

Considering a transverse Gaussian beam profile of waist  $w_0$ , we can write a Taylor expansion such as:

$$\frac{\Delta v_p(r)}{c} = \frac{\omega_p^2}{2\omega_0^2} \left( 1 - \frac{a(r)^2}{4} \right) \quad (3.4)$$

Hence, the wave fronts travel faster at the edge of the beam than at its center. From a geometrical point of view, this causes the rays to bend by an amount determined by their relative path difference. The maximum value is given by:

$$\Delta L = | \Delta v_p(r) | t = \left| \frac{\Delta v_p}{c} \right|_{max} z = \alpha_{SF} R \quad (3.5)$$

where  $R$  is the radius of curvature and  $\alpha_{SF}$ , the maximum focusing angle due to self-focusing given by:

$$\alpha_{SF} = \frac{\omega_p^2 a_0^2}{8\omega_0^2} \quad (3.6)$$

Equating  $\alpha_{SF}$  with  $\alpha_d = \lambda/(\pi w_0)$  gives a condition to counterbalance natural diffraction:

$$a_0^2 \geq 8 \left( \frac{c}{\omega_p^2 w_0^2} \right)^2 \quad (3.7)$$

Moreover, the ponderomotive force adds up and is increased for higher pulse intensities. This causes an ejection of electrons out of the optical axis. The on-axis electron density can therefore be depleted, which corresponds to a higher on-axis refractive index. This effect is known as ponderomotive self-channelling. When the laser peak power reaches the critical power, these two relativistic effects counterbalance refraction and allow the beam to propagate over a longer distance than the Rayleigh length.

However, a successful guiding over long distances would require maintaining the pulse intensity over the threshold as the beam propagates, which turns out difficult because of the various competing effects (natural diffraction, over-ionization induced diffraction, instabilities,...). Moreover, nonlinear instabilities and filamentation effects occurring at such high intensities lead to a break-up of the beam and the subsequent drop in intensity.

### 3.1.2 Capillary discharge plasma waveguide

The challenge of preforming the electron density to provide suitable conditions to guide the laser driver has been successfully addressed implementing a capillary discharge waveguide [Spence and Hooker, 2000]. The underlying principle advocates the engineering of a parabolic plasma channel [Bobrova, 2002].

Pre-forming a plasma waveguide is carried out through hydrodynamic compression. This has been done using fast capillary discharges. Such a system is illustrated in fig. 3.1a. In this approach, a capillary of a few millimeters diameter is filled with gas at low pressure. This gas is then ionized by a discharge current with a rise time of a few tens of ns, and a peak intensity of a few kA. Since the current rises rapidly, a skin effect occurs close to the capillary walls and allows the generation of initial electrons. The large magnetic field generated by the current then compresses the plasma thanks to the  $\mathbf{j} \times \mathbf{B}$  force (with  $\mathbf{j}$ , the current density and  $\mathbf{B}$ , the magnetic field) to drive a strong shock wave towards the capillary axis. Under those conditions, a plasma channel is then formed just before the generated annular plasma reaches the axis and collapses. The generated needle-shaped plasma column forms a plasma channel allowing waveguiding (fig. 3.1b). With this shape, the plasma turns out able to guide a Gaussian beam with a nearly constant spot radius over propagation, provided that the spot radius is correctly matched to the curvature of the plasma. In earlier works, guiding of laser pulses with a peak input intensity of  $1.2 \times 10^{17} \text{ W/cm}^2$  over lengths of up to 50 mm was demonstrated with low loss [Spence et al., 2001; Butler et al., 2002].

This guiding technique aroused great interest, notably for electron acceleration [Leemans et al., 2014]. Indeed, high-intensity laser pulses generate longitudinal plasma waves in their

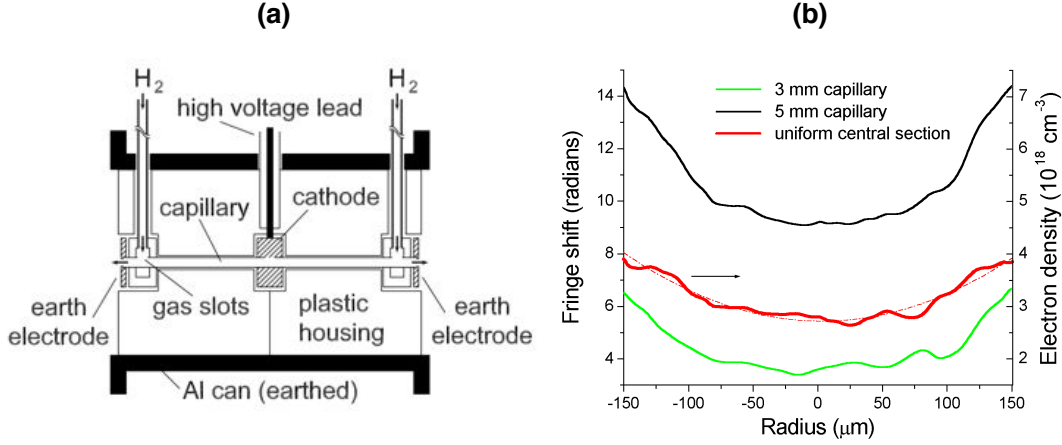


Figure 3.1: (a) Schematic of a hydrogen-filled capillary discharge waveguide [Butler et al., 2002]. (b) Transverse electron density profile [Spence and Hooker, 2000].

wake and long interaction distances are sought to boost the performances of electron beam sources. This technique has also been successfully implemented to emit coherent soft X-ray radiation using electric discharge pumping (see section 1.2.2).

Apart from electrical discharge pumping, the gas-filled capillary discharge waveguide approach has also been successfully implemented in case of collisionally-pumped optical field ionized soft X-ray lasers [Butler et al., 2003]. The experiment demonstrated the successful driving of an ultrashort intense pulse within gas-filled capillary discharge waveguides, with increased energy extraction and reduced beam divergence. This scheme operated the 5d-5p transition of  $Xe^{8+}$  at 41.8 nm. Efficient waveguiding over 30 mm allowed to significantly enhance the photon yield.

Notwithstanding, when implemented for plasma-based soft X-ray lasers, the capillary discharge technique faces intrinsic limitations because of hydrogen used in the gas mixture. Although essential for waveguiding, the electrons from hydrogen have a low energy and decrease the overall electron temperature, which results in both low gain and saturation intensity.

Moreover, this scheme is limited to low gas pressures (below 100 mbar, i.e.  $n_e \leq 2 \times 10^{18} \text{ cm}^{-3}$ ) and thus not relevant for our application.

### 3.1.3 Hollow capillary tube

Guiding laser pulses can be performed by injection into a hollow capillary tube. In this approach, the pulse is being waveguided via total reflections on the capillary boundaries. This technique, illustrated in fig. 3.2, shares common ground with step-index guiding, which is achieved by surrounding a cylindrical core of material by a cladding layer of lower refractive index. In this configuration, light propagating along the core can be totally internally reflected from the core-cladding boundary. However, the solid cladding will have a higher refractive index, thus preventing total internal reflection. Hence the core must be a plasma. The losses can be counterbalanced considering grazing angles of incidence on the boundaries and thanks to ionization of the capillary walls by the laser radiation. With the latter condition, the refractive index can be decreased below unity to allow total internal reflection.

Preliminary works showed the possibility of guiding pulses with a high intensity of  $2 \times 10^{17} \text{ W/cm}^2$  [Jackel et al., 1995; Dorchies et al., 1999]. The transmission over a 126 mm-long capillary tube was assessed at 26 %. This technique has been successfully demonstrated with a

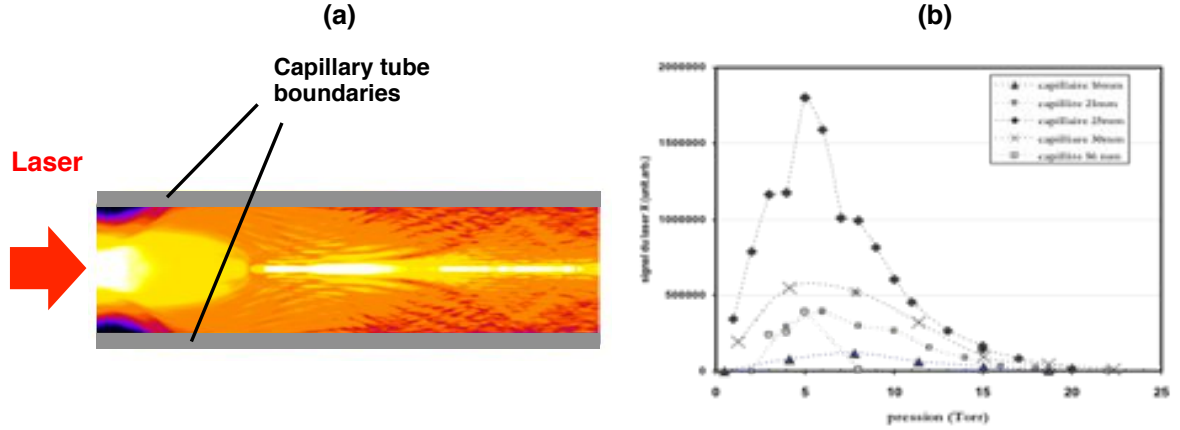


Figure 3.2: (a) Simulation of the waveguiding of a focused beam in a hollow capillary tube with COFIXE code [Cros et al., 2006]. (b) XUV laser signal strength for different capillary tube lengths with various gas pressure [Bettaibi, 2005].

collisionally excited OFI laser using a capillary filled with pure Xe gas [Mocek et al., 2004]. A significant increase of the gain length was reported.

Compared to capillary discharge soft X-ray lasers, higher electron temperatures are available, which bolster the laser transition pumping. Thus, higher gain is demonstrated. However, as reported in fig. 3.2b, the optimum gas densities (about 5 mbar) are low and therefore, the saturation intensity remains low. Other limitations include the great sensitivity of the system to the pointing of the driving laser beam. Indeed, small fluctuations lead to the progressive destruction of the tube by the high-intensity laser pulse. Moreover, because of the poor heat conduction of the capillary tube, such lasers can only operate at a low repetition rate.

#### 3.1.4 Optically-preformed plasma waveguide using the «ignitor-heater» technique

This technique is well adapted to high electron densities. Optically-preformed plasma waveguides are achieved by pre-forming a plasma channel with a transverse electron density profile that increases with radial distance from the axis, thanks to a laser beam. The implemented radially-decreasing refractive index allows waveguiding an intense IR pulse propagating in a plasma, as illustrated in fig. 3.3.

The implementation of an elongated plasma-based amplifier requires that the pump beam propagates over the whole gas jet length at high intensity, over the ionization threshold of the lasing  $Kr^{8+}$  ion. However, at high electron densities, the quickly predominating refraction effects lead to a reduction of the effective volume in which those species can be generated. Furthermore, while the interaction region is basically limited to the Rayleigh length, a tight focus is needed to reach sufficiently high intensity on target. Thus, there is a tradeoff between the interaction length and the intensity. Those difficulties can nevertheless be overcome by guiding the pump beam in the plasma. The underpinning idea behind this approach relies on engineering, prior to the interaction, a higher refractive index on axis in an attempt to counterbalance the radial spreading of the beam due to diffraction. The underlying principle has similarities with optical fibers. The challenge consists in tailoring the waveguide size and its radial density gradient to effectively couple the focused IR beam at its entrance and to subsequently guide the high-intensity IR pulse, minimizing energy losses. Because of its electron density geometry, the

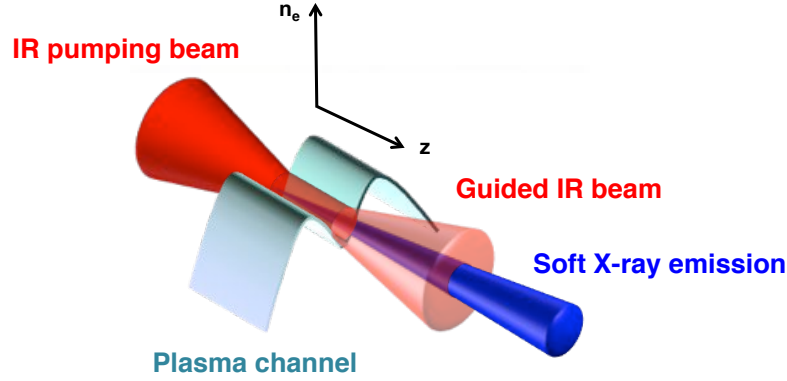


Figure 3.3: Illustration of laser pulse waveguiding by means of a pre-formed plasma channel.

waveguide is referred to the so-called "plasma channel".

The first demonstration of a plasma waveguide for high-intensity laser pulses was achieved by taking advantage of hydrodynamic expansion of a plasma column [Durfee and Milchberg, 1993]. In this approach, 100 ps-long laser pulses of about 100 mJ are focused with an axicon to generate a focal line in a gas at neutral densities of a few  $10^{18} \text{ cm}^{-3}$ . The details of this setup will be illustrated later. The intensity along the focal line ranges between  $10^{13}$  and  $10^{14} \text{ W/cm}^2$ , which is sufficient for both ionizing the gas and heating the resulting plasma by inverse bremsstrahlung. A plasma channel is then being formed as the hot plasma column expands radially over a nanosecond timescale, driving a shock wave into the surrounding cold gas. This approach has been used to guide [Nikitin et al., 1999] 50 mJ, 110 fs laser pulses with a peak input intensity of  $10^{17} \text{ W/cm}^2$  through 15 mm long plasma. The transmission of the channel was found to be slightly greater than 50 %.

Since the waveguide channel is pre-formed, the guiding does not rely on a particular channeled intensity. The method offers more control over the waveguide properties by varying the laser pulse duration and energy, as well as the delay before pulse injection and the channel length. Furthermore, it should be noticed that this technique is non-destructive. Compared to capillary discharge and hollow capillary waveguiding, the plasma channel technique can be implemented for high electron densities and does not compromise the electron temperature. Therefore, a combination of high gain and high saturation intensity to yield a large number of photons is promised.

**Principle.** The implementation of a plasma channel relies on the hydrodynamic expansion of a previously ionized plasma. The waveguide is formed using an IR laser beam propagating collinearly to the pump beam propagation. The method is banking on the ejection of the generated electrons out of the optical axis. This phenomenon is favored by a heating process and the plasma expansion, which takes place on the nanosecond timescale. This leads to the creation of a transverse radial electron density profile on both sides of the optical axis. This configuration is illustrated in fig. 3.4 and offers advantageous conditions to guide ultra-intense IR laser pulses compensating diffraction-induced beam spreading.

To pre-form a plasma channel over the whole length of the high-density gas jet, a particular optical component has been used. It is called an axicon lens [McLeold, 1954]. This optical component focuses light over a long focal line of several Rayleigh lengths. It has a conical shape, whose angular aperture determines the length over which an incoming beam can be tightly

focused.

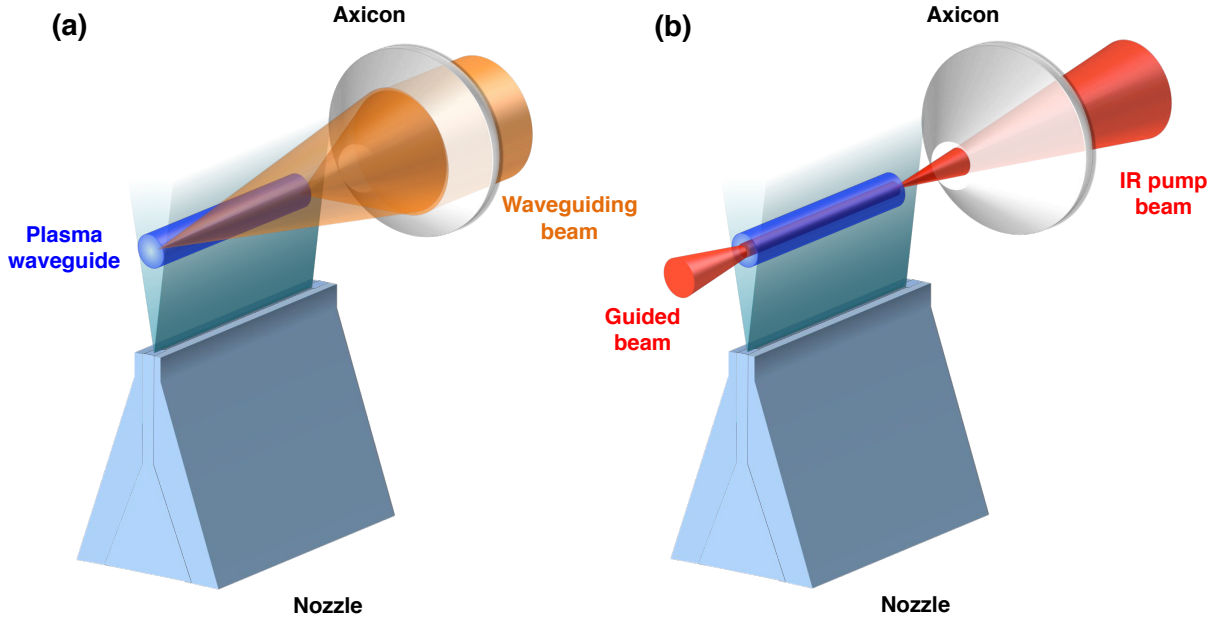


Figure 3.4: Illustration of an intense pulse waveguiding in a high-density plasma. (a) A waveguiding beam focused thanks to an axicon lens produces an annular electron density distribution with lower on-axis density, which provides appropriate conditions for waveguiding. (b) When the plasma channel is formed, the IR pump beam is focused at its entrance and gets guided over the whole gas jet length.

**Axicon.** The axicon lens constitutes a key element regarding plasma channel engineering. This optical component is a conic shape lens, which focuses an incoming beam into a focal line of several millimeters. The intensity profile is presented in fig. 3.5. In case of Gaussian beams, the axicon generates a Bessel-like radial intensity profile where on-axis intensity remains almost uniform over relatively long distances, when compared to focusing properties of conventional lenses. It can be noticed that an axicon is more efficient in concentrating light in a line compared to a cylindrical lens.

Since their introduction [McLeold, 1954], axicons have found applications in numerous fields including optical coherence tomography [Ding et al., 2002], optical tweezers [Manek et al., 1998] and precision laser machining [Rioux et al., 1978].

Its utilization has been notably studied for the formation of extended plasma channels in condensed media [Kosareva et al., 2005]. In particular, using an axicon turned out attractive to generate long plasma channels in gases, including air, through multiphoton absorption. Durfee and Milchberg [Durfee and Milchberg, 1993] have used an axicon to pre-form a plasma channel in argon, which then served as a waveguide for another laser beam.

In the present work, the axicon will allow us to create a transverse optical index profile, suitable for waveguiding the pump beam, over the whole length of the elongated gas jet. The optical component is drilled to avoid hindering the focusing of the pump beam, as illustrated in fig. 3.5. Additional information about the focal line produced by an axicon lens is provided in Appendix C.



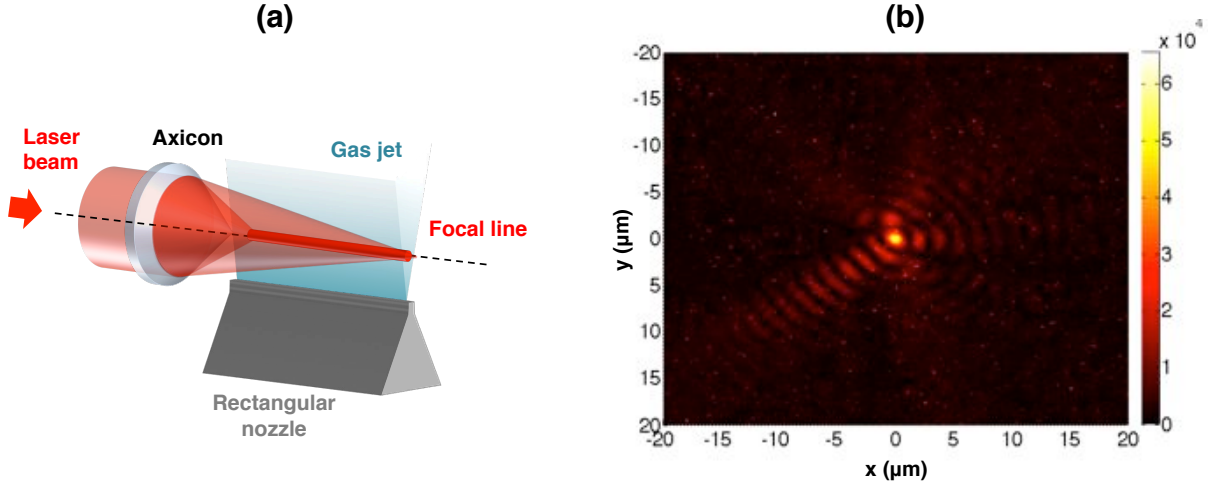


Figure 3.5: (a) Illustration of axicon focusing coupled to a gas jet for the purpose of waveguiding. (b) Radial beam profile of a focal line obtained with a 20 degrees-apex angle axicon. The transverse size is less than 2 microns FWHM.

« Ignitor-heater » scheme. In order to create an elongated high-density plasma amplifier and counterbalance strong refraction effects, a double pulse scheme has been used. This method is known as the « ignitor-heater » technique and was first introduced in 1999 [Volfbeyn et al., 1999] and later experimentally demonstrated [Butler et al., 2004; Chou et al., 2007]. In analogy with the transient pumping scheme for soft X-ray plasma-based lasers, it is based on the consecutive implementation of ionization and plasma heating processes.

Two pulses allow those processes to occur in a decoupled way:

- The first pulse is named « ignitor » is very short (a few tens of fs) and is used to generate the first electrons directly within the laser field.
- The second one, dubbed « heater », is long (a few hundreds of ps) and allows heating the plasma electrons via inverse bremsstrahlung in the field.

The combined action of those two pulses will lead to the formation of a plasma waveguide in the following four steps, summarized in fig. 3.6

1. Pre-plasma generation: The ultrashort first pulse (« ignitor ») snatches the first electrons within the field. The required energy is low and generally of a few tens of milli-joules. This pre-plasma is necessary because the following heating long pulse is not intense enough to generate a sufficiently ionized plasma.
2. Plasma heating: The second pulse (« heater ») initiates an inverse bremsstrahlung heating process over a timescale of several hundreds of picoseconds. In this process, an electron absorbs energy from the laser beam during a collision with an ion. From a classical point of view, the electron that was oscillating in the electric field is knocked out of phase because of the collision. The oscillatory energy is then converted to thermal energy.  
The characteristic distance between an ion and an electron in a plasma is given by the Wigner-Seitz radius:

$$l_{ei} = \sqrt[3]{\frac{3}{4\pi n_e}} \quad (3.8)$$

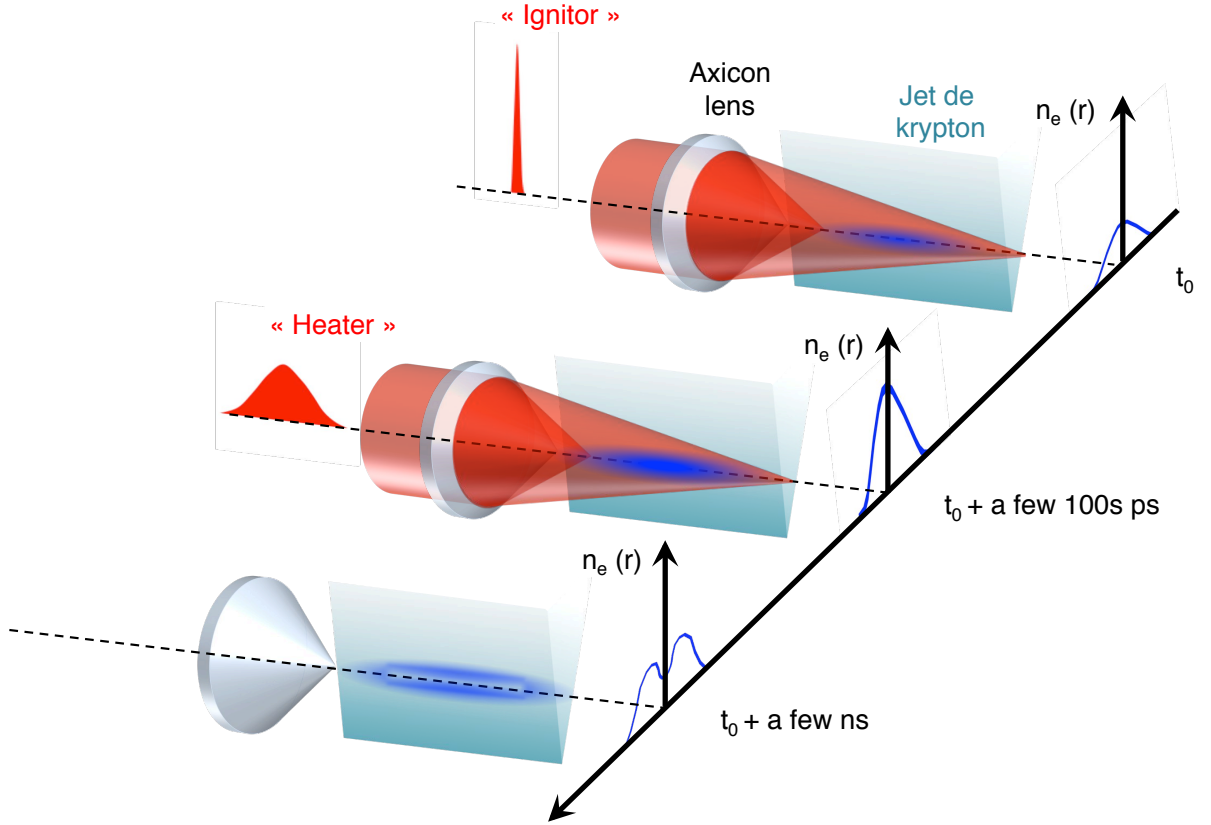


Figure 3.6: Illustration of the « Ignitor-heater » technique.

The thermal electron velocity is given by:

$$v_e = \sqrt{\frac{k_B T_e}{m_e}} \quad (3.9)$$

Where  $k_B$  is the Boltzman constant,  $T_e$  the electron temperature and  $m_e$  the electron mass. If we consider a dense plasma with an electron density and an energy of 10 eV, then the average time between subsequent collisions is a few femtoseconds and therefore, considering a long pulse, the main heating mechanism is inverse bremsstrahlung absorption. Here, we suppose the electron density is sufficiently far from the critical density to neglect parametric heating effects. Hence, we can assess the heating rate.

In the classic Lorentz model, the equation of motion of an electron in an oscillatory electric field is:

$$m_e \frac{d\mathbf{v}}{dt} = e\mathbf{E}_0 e^{i\omega_0 t} - \frac{1}{2} m_e \nu_{ei} \mathbf{v} \quad (3.10)$$

where  $\nu_{ei}$  is the electron-ion collision frequency. We can solve it and derive from it the time-average kinetic energy of the electron:

$$\mathcal{E}_0 = \frac{e^2 E_0^2}{2m_e \omega_0^2} \quad (3.11)$$



Then, the average rate of energy absorption from the electron from the field is [Seely and Harris, 1972]:

$$\frac{d\mathcal{E}}{dt} = \frac{e^2 E_0^2}{2m_e \omega_0^2} \nu_{ei} \quad (3.12)$$

The term  $\frac{e^2 E_0^2}{2m_e \omega_0^2}$  corresponds to the thermal energy during collision. In the strong field limit where the field potential  $U_{field} \gg k_B T_e$ , the effective collision frequency is [Silin, 1965]:

$$\nu_{ei} \simeq \frac{4\pi Z^2 n_i e^4 \ln \Lambda}{\sqrt{m_e T_{eff}^3}} \quad (3.13)$$

where  $n_i$  is the ion density,  $T_{eff}$  the effective temperature such that  $T_{eff} = k_B T_e + U_{field}$ , and  $\ln \Lambda$  the coulomb logarithm defined for elastic collisions:

$$\Lambda = \frac{12\pi n_e \lambda_D^3}{Z} \quad (3.14)$$

with  $\lambda_D = \sqrt{\frac{k_B T_e}{4\pi n_e e^2}}$ , the Debye length.

Considering  $\frac{3}{2} k_B T_e$ , the thermal energy of electron, the heating can be assessed for a rectangular pulse substituting eq. (3.13) and eq. (3.14) into eq. (3.12). The heating imparted by a long pulse can therefore be assessed integrating the obtained equation:

$$\Delta T_e \propto \lambda^{4/5} \mathcal{E}_0^{2/5} \quad (3.15)$$

with  $\mathcal{E}_0$ , the energy of the pulse. For such long pulses, the relation eq. (3.15) illustrates heating is mainly determined by the pulse energy.

Under experimental conditions with a 600 ps long pulse with an energy of about 400 mJ ( $\sim 10^{15} \text{W/cm}^2$ ) focused down to a spot of a few microns, the heating induced by the IR pulse is about 500 eV.

### 3. Avalanche collisional ionization:

The substantial increase in electron temperature resulting from the ongoing inverse bremsstrahlung process leads to trickle-down collisional ionization. Collisional ionization takes place during and after the laser pulse on the timescale of a few nanoseconds. The subsequent increase in electron density is described by the following formula:

$$\frac{dn_e}{dt} = n_e(n_0 - n_e)S(T_e) \quad (3.16)$$

where  $n_0$  is the initial atomic density and  $S(T_e)$  the collisional ionization rate. The characteristic timescale of the evolution of electron density through cascade collisional ionization is in the order of several picoseconds for initial densities as high as  $10^{19} \text{cm}^{-3}$  and lower than the pulse total duration. Hence, the increase of electron density occurs within the "heater" pulse time window and is limited by the heating time of electrons. The time required to reach the saturation of the ionization state depends on the electron density

from which collisional ionization starts. This explains the use of the "ignitor" pulse to generate a pre-plasma.

4. Plasma expansion: After plasma heating and the following substantial production of electrons, the hydrodynamic evolution of the plasma will lead to the formation of a plasma channel. Because of the significant difference in mass between electrons and ions, the displacement of electrons will prevail. Combined with the radial non-uniformity of plasma heating stemming from the pulse transverse profile, this results in creating a depressed density duct through ambipolar diffusion. In particular, hot electrons quickly diffuse out of the axis because of their low mass and hot temperature. The motion of ions being very slow comparatively, these electrons will leave behind a space charge region with a greater population of positively charged species. This results in an outwardly-directed electric field, which tends to enforce plasma neutrality. The consequence will be slowing down the electrons and speeding up the ions. The competition between thermal effects and the action of the electrostatic force will lead to an equilibrium, where both ions and electrons stream outward at the speed of sound:

$$c_s = \sqrt{\langle Z \rangle \frac{k_B T_e}{m_i}} \quad (3.17)$$

Where  $m_i$  is the ion mass and  $\langle Z \rangle$  the average atomic number. This speed is much smaller than electron thermal velocity but much greater than thermal ion velocity. This simultaneous stream of both species at the same rate, or ambipolar diffusion, is referred to plasma expansion. We can notice this speed is actually larger than the sound speed in a neutral gas, which creates a propagating radial shock wave. This speed is in the order of tens of microns per nanosecond (considering an average ionization degree of 3 and electron temperature in the range of 100 eV). A thermal precursor wave propagates in advance of the shock wave, in which the heated electrons further ionize the gas collisionally. This plasma expansion is responsible for the so-called plasma channel with a radial refractive index distribution suitable for waveguiding.

## 3.2 Numerical modeling of plasma waveguiding

The propagation of intense laser pulses in high-density plasmas is not straightforward and involves various mechanisms affecting the intensity distribution of the beam, as well as its duration. The complex propagation of intense IR pulses is characterized by a combination of self-focusing effects, refraction from the waveguide density gradient and refraction due to strong ionization induced by the pulse itself [Monot et al., 1992]. Moreover, in charge-displacement and relativistic regimes, other phenomena add up. For instance, relativistic focusing [Sprangle et al., 1992] can occur for very large peak intensities over  $10^{18} \text{ W/cm}^2$ . However, the pulse leading edge may not be focused since forward charge displacement diffracts the beam, canceling the effect of relativistic focusing. The trailing edge may also be subject to scattering by Raman instabilities [Antonsen and Mora, 1992]. Besides, for very high peak powers, propagation can be further complicated since the high-intensity beam may break up because of filamentation [Sullivan, 1993]. However, those hurdles can be avoided resorting to a pre-formed plasma waveguide and when the intense laser beam does not create its own channel.

Simulations have been used to model those physical phenomena in force during propagation over an elongated plasma waveguide. The model is described in section 3.2.2. In order to

ascertain the regimes governing the evolution of the pulse intensity as it propagates in the plasma channel, a ray-tracing model is described at the end of the section 3.2.1. A parametric study is performed in section 3.2.3 to look at the impact of the waveguide transverse size and the density gradient for various electron densities and account for the conditions suitable for advantageous waveguiding.

The plasma channel is considered to be 5 mm long and its radial density is approximated by a parabolic profile with  $n_{e0}$ , the electron density on-axis and  $n_{e1}$ , the maximum off-axis electron density evaluated at  $r_1$ . Out of the waveguide, the density is considered to drop to 0 for a radial value  $r_2$ .

The radial electron density distribution is shown in fig. 3.7 and described by:

$$\begin{cases} n_e = n_{e0} \times \left(1 + \frac{\Delta n}{n_{e0}} \frac{r^2}{r_1^2}\right) & \text{for } -r_1 < r < r_1 \\ n_e = \frac{n_{e1}}{(r_2 - r_1)} \times (r_2 - r) & \text{for } -r_2 < r < -r_1 \text{ and } r_1 < r < r_2 \end{cases} \quad (3.18)$$

where  $\Delta n = n_{e1} - n_{e0}$ . This shape will be used as input data to simulate the propagation of an ultrashort and intense IR pulse in a high-density plasma (see section 3.2.2).

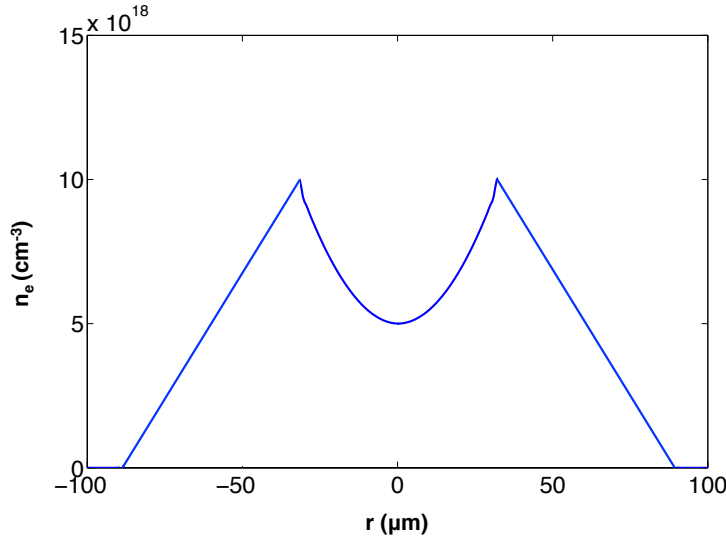


Figure 3.7: Electron density profile model used for simulations. Here,  $n_{e0} = 5 \times 10^{18} \text{cm}^{-3}$ ,  $n_{e1} = 10^{19} \text{cm}^{-3}$ ,  $r_1 = 32 \mu\text{m}$  and  $r_2 = 90 \mu\text{m}$ .

### 3.2.1 Waveguiding conditions

The most important parameters to ensure an efficient coupling of the IR pump beam into the waveguide, as well as convenient guiding are:

- The plasma channel transverse size: It is defined from the optical axis to the off-axis peak electron density, and the radial density gradient. Its size should at least match the waist of the IR pump beam. Some margin should be preserved because of possible slight misalignment of the incoming beam.
- The numerical aperture of the waveguide: The numerical aperture at the entrance of the waveguide defines the acceptance solid angle, under which incoming rays will be efficiently

coupled into the waveguide.

Considering a simple waveguide made of two slices of different refractive index, as illustrated in fig. 3.8, the numerical aperture is defined as:

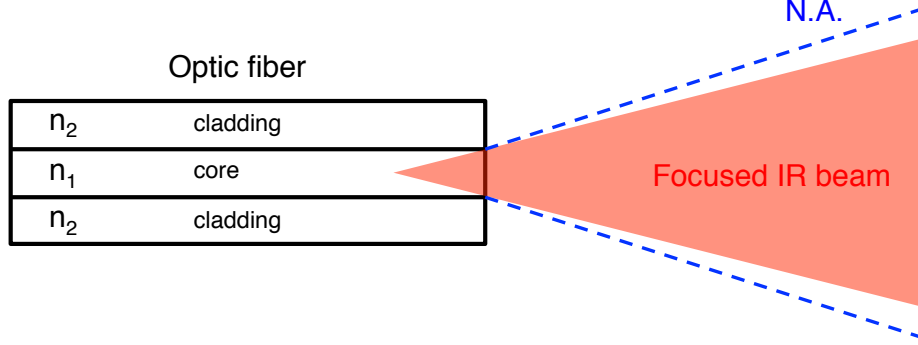


Figure 3.8: Schematic of an optic fiber.

$$N.A. = \sqrt{n_1^2 - n_2^2} \quad (3.19)$$

The aim is to make sure the waveguide numerical aperture encompass the light cone defined by the focusing parameters of the pump beam. This condition is even more important considering the fact that experimentally, the waveguide geometry should care about laser beam stability and possible small misalignments.

As an example, with this "rule of thumb", for an electron density of  $5 \times 10^{18} \text{ cm}^{-3}$  and  $10^{19} \text{ cm}^{-3}$ , the numerical aperture for an IR beam at 800 nm will be 0.068. This radial gradient offers convenient conditions when it comes to focus a 50 mm diameter beam with a focusing optic of focal length 75 cm.

- The electron density gradient: The difference of on- and off-axis electron densities, and thus refractive index, defines the numerical aperture of the waveguide, as previously described. But, aside from its impact on input coupling, it is also of paramount importance for efficiently guiding the coupled IR pulse into the waveguide.

If we consider a graded index waveguide with a refractive index difference  $\Delta\eta = \eta(w_0) - \eta(0)$  between the center and a beam radius  $w_0$ , a Gaussian beam propagating over a length  $\delta z$  will experience both defocusing and focusing. The defocusing stems from diffraction and its contribution to the beam radius of curvature is:

$$R_d = \delta z \left( 1 + \frac{z_R^2}{\delta z^2} \right) \approx \frac{z_R^2}{\delta z} \quad (3.20)$$

Focusing is due to the waveguide graded index and its contribution is [Durfee et al., 1994]:

$$R_w \approx \frac{w_0^2}{2\Delta\eta\delta z} \quad (3.21)$$

The waveguide compensation for the outward curvature of diffraction, which amounts to maintaining a constant beam size, can be written:  $R_w = R_d$ . Hence, the guiding condition is:

$$\Delta\eta \geq \frac{\lambda^2}{2\pi^2 w_0^2 n(0)^2} = \frac{1}{kz_R} \quad (3.22)$$

This condition for a plasma of refractive index  $\eta = \sqrt{1 - n_e/n_c}$  with  $n_c = \frac{m_e \omega_0^2}{4\pi e^2}$ , yields a condition for the electron density difference  $\Delta n_e = n_e(w_0) - n_e(0)$ :

$$\Delta n_e \geq \frac{1}{r_e \pi w_0^2} \quad (3.23)$$

with  $r_e \approx 2.82 \times 10^{-13}$  cm the classical electron radius.

The relation eq. (3.23) gives a rule of thumb for the needed plasma channel geometry. This condition is exact for a radial parabolic profile of electron density. We can notice that the density difference  $\delta n_e$  determines the spot size that may be channeled, independent of the wavelength.

For example, considering a beam size  $w_0 = 16\mu m$ , the required electron density difference should be over  $5 \times 10^{17} cm^{-3}$ .

This condition remains roughly valid for neutral plasma densities below  $10^{18} cm^{-3}$ . However, when considering **high-density plasmas**, over-ionization induced by the pulse becomes very serious. The following ray tracing model proposes to assess the needed density gradient to overcome natural diffraction and overionization-induced diffraction. For this purpose, we consider a parabolic electron density profile generated by overionization. This parabola will modify the transverse structure of the waveguide defined in relation eq. (3.18). This parabola is defined in eq. (3.24) with the parameters  $r_0$  and the on-axis density  $n_{e0}^{O.I.}$ .

$$n_e = n_{e0}^{O.I.} \times \left(1 - \frac{r^2}{r_0^2}\right) \quad \text{for} \quad -r_c < r < r_c \quad (3.24)$$

The radial coordinate  $r_c$  defines the intersection between the parabola eq. (3.24) and eq. (3.18).

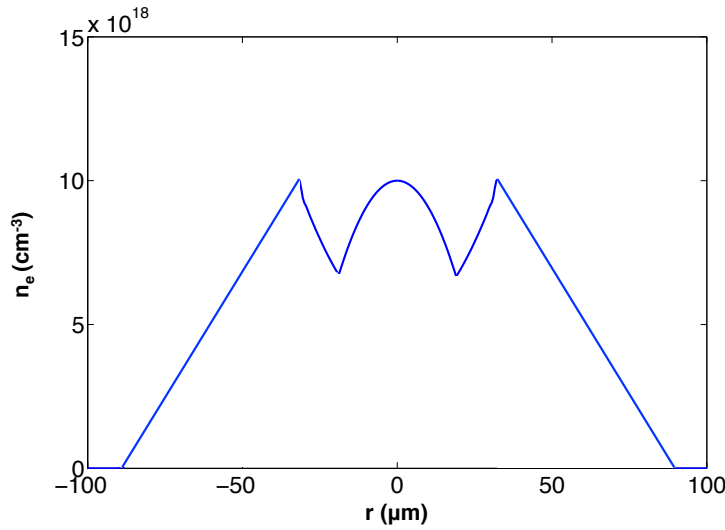


Figure 3.9: Electron density profile taking account of the modification of electron density because of overionization. Here,  $n_{e0} = 5 \times 10^{18} cm^{-3}$ ,  $n_{e1} = 10^{19} cm^{-3}$ ,  $r_1 = 32\mu m$  and  $r_2 = 90\mu m$ .

The ray trajectories of a Gaussian beam diffracting and propagating through a parabolic channel is computed, as following [Fill, 1997]:

$$w(z) = (w_d(z) + w_c(z) + w_{O.I.})/3 \quad (3.25)$$

where  $w_d$ ,  $w_c$  and  $w_{O.I.}$  are the contributions to the beam size from natural diffraction, channelling and overionization-induced diffraction respectively.

$$\begin{cases} w_d = w_0 \sqrt{1 + \left(\frac{z}{z_R}\right)^2} \\ w_c = w_0 \cos\left(\sqrt{\frac{n_1}{n_c}} \times \frac{z}{r_1}\right) \\ w_{O.I.} = w_0 \cosh\left(\sqrt{\frac{n_0}{n_c}} \times \frac{z}{r_0}\right) \end{cases} \quad (3.26)$$

The condition to perfectly guide the rays amounts to turn the first derivative of the trajectory to zero. This is equivalent to say the rays are parallel to the axis. Under those conditions, we can make a Taylor expansion of the ray trajectories in equations eq. (3.26):

$$\begin{cases} w_d \approx w_0 \left[1 + \frac{1}{2} \left(\frac{z}{z_R}\right)^2\right] \\ w_c \approx w_0 \left[1 - \frac{1}{2} \left(\frac{z}{z_1}\right)^2\right] \\ w_{O.I.} \approx w_0 \left[1 + \frac{1}{2} \left(\frac{z}{z_0}\right)^2\right] \end{cases} \quad (3.27)$$

where  $z_0$  and  $z_1$  are the characteristic lengths for overionization-induced refraction and waveguide refraction respectively. Their expression is:

$$\begin{cases} z_0 = r_0 \sqrt{\frac{n_c}{n_{e0}^{O.I.}}} \\ z_1 = r_1 \sqrt{\frac{n_c}{n_{e1}}} \end{cases} \quad (3.28)$$

Guiding is achieved when the sum of the second order terms of relations eq. (3.27) is zero. The fig. 3.10 shows that two different regimes can be identified. The figure illustrates how the characteristic lengths  $z_0$  (red curve) and  $z_1$  (green curve) vary as a function of the electron density at the centre of the waveguide, according to the presented model.

1. At electron densities lower than  $1.8 \times 10^{18} \text{ cm}^{-3}$ ,  $z_R < z_0$ . Natural diffraction dominates and the criterion for waveguiding is similar to the relation eq. (3.22) [Durfee et al., 1994] but in terms of characteristic lengths:

$$z_1 = z_R \quad (3.29)$$

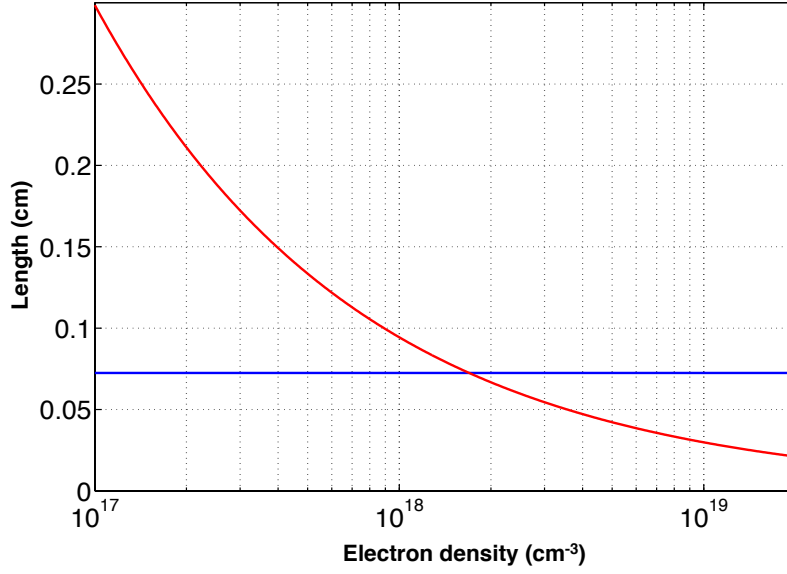


Figure 3.10: Evolution of characteristic length  $z_0$  (red curve) with respect to the electron density. The blue curve stands for the Rayleigh length.

2. At higher densities,  $z_0 < z_R$ . Diffraction resulting from overionization is of primary importance. The waveguiding criterion thus becomes:

$$z_1 = z_0 \quad (3.30)$$

Actually compensating this term as much as possible is critical because strong overionization at the entrance of the waveguide leads to non-negligible coupling losses. Indeed, those initial coupling losses prove to take the major part in overall losses from the unguided pump beam.

### 3.2.2 Numerical model

The influence of the critical parameters affecting the waveguiding efficiency (plasma channel size, electron density and density gradient) has been explored thanks to numerical simulations modeling the interaction and propagation of an ultrashort and intense pulse in a plasma. Simulations were conducted using WAKE-EP particle-in-cell code [Paradkar et al., 2013].

The previously described moving window code (section 2.4.2) simulates laser plasma interaction in the short pulse regime as the beam propagates. The model is suitable for low to moderate values of the electron density and remains valid for  $\omega_p \leq 0.02\omega_0$ , thus limiting the validity of the code to moderate electron densities (about  $5 \times 10^{18} \text{ cm}^{-3}$ ).

The studied plasma channel geometries correspond to realistic experimental conditions reported in chapter 4.

**Initial conditions.** We will see in the section 4.3.1 that the plasma channel electron density, defining the waveguide geometry, was probed using a Mach-Zehnder interferometer. However, it was not possible at this stage to assess the ionization degree of species contained in the waveguide. Nevertheless, some predictions can be done. The plasma channel was found to absorb a HH signal with photon energies below 50 eV (cf. section 5.2). According to table 2.1, summarizing the ionization energies of different krypton ion species, this means that the ionization degree in the waveguide is at most 3. Besides, the ionization degree can also be guessed comparing the probed electron density of the plasma channel with the one when the pump beam propagates in this channel (cf. fig. 4.25). In the latter case, the plasma emits at 32.8 nm and is thus populated with  $Kr^{8+}$  ions. However, the plasma inhomogeneity prevents any precise determination to be made.

The fig. 3.11 shows a typical experimental transverse electron density profile, which allowed strong lasing at 32.8 nm. Those data can be fit using a Padé approximant, with the following parameters:

$$\frac{n_e}{n_{e0}} = \frac{1 + r^2(a + b \times r^2)}{1 + c \times r^6} \quad (3.31)$$

with

$$n_{e0} = 9.2 \times 10^{18} \text{ cm}^{-3} \quad a = -2.2949 \times 10^{-4} \quad b = 1.73762 \times 10^{-6} \quad c = 2.88648 \times 10^{-10} \quad (3.32)$$

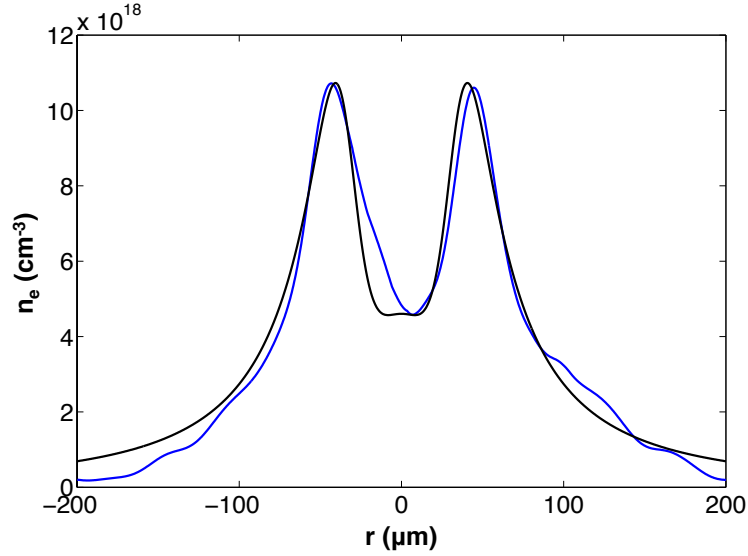


Figure 3.11: Typical experimental (blue) and numerical (black) radial electron density profile of a plasma channel.

The density of ions, essential for modeling, can be derived assuming a constant ionization degree close to the optical axis. We consider a transverse profile of the average ionization degree  $Z^*$  using the function:

$$\frac{Z^*}{Z_0^*} = \frac{1 + \alpha \times r^2}{1 + \alpha \times r^2 + \beta \times r^6} \quad (3.33)$$



with

$$Z_0^* = 3 \quad \alpha = 3 \times 10^{-8} \quad \beta = 1.2 \times 10^{-11} \quad (3.34)$$

The fig. 3.12b illustrates the ion transverse density profile considering the radial electron density and average ionization degree depicted in fig. 3.12a. The small hollow in the density of ions, observed between 75  $\mu\text{m}$  and 80  $\mu\text{m}$  may be provoked by a local heating of the plasma ahead of the shock wave, which drives the plasma hydrodynamic expansion.

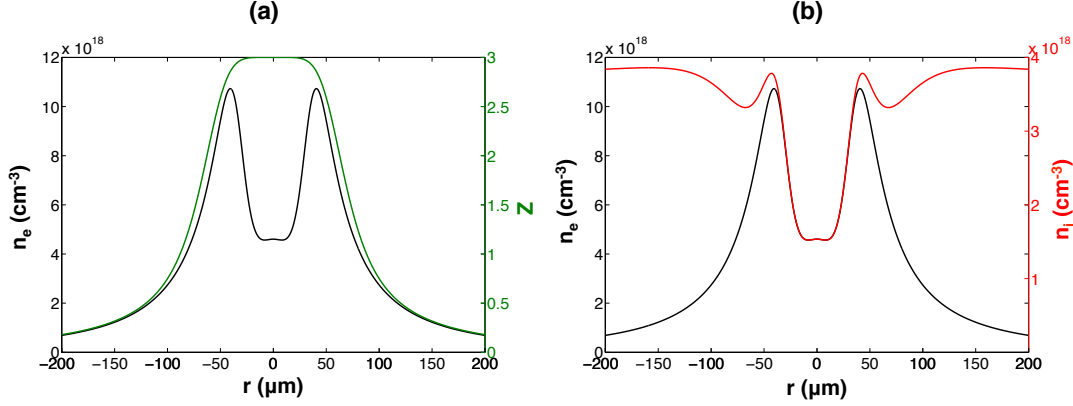


Figure 3.12: Radial electron density (black), average ionization degree (green) and ion density (red) profiles within the plasma waveguide.

**Propagation of the intense IR pulse in the waveguide.** In the following simulations, we considered a 250 mJ, 30 fs FWHM pulse at wavelength 800 nm. The beam is focused into a 16  $\mu\text{m}$  focal spot ( $I \approx 1.4 \times 10^{18} \text{ W cm}^{-2}$ ) at the entrance of the pre-formed plasma channel. Those parameters match experimental conditions. Different values of the transverse waveguide size, radial density gradient and electron densities at the centre of the unperturbed channel were explored to ascertain their respective roles.

The fig. 3.13 illustrates the distribution of intensity, electron density and average ionization degree as a result of waveguiding over a 5 mm krypton plasma. In this representation, the propagation axis is equivalent to the time. The conditions correspond to a waveguide of radius  $r_1 = 2w_0$  and a density gradient such as  $n_{e1}/n_{e0} = 2$  for  $n_{e0} = 5 \times 10^{18} \text{ cm}^{-3}$ .

The fig. 3.13a shows the effects of strong refraction due to over-ionization in the dense plasma. After 1 mm of propagation, the intensity drops sharply and rays deflect before being reflected onto the plasma channel density gradient. The beam refocuses at about 2 mm and diffracts again.

The fig. 3.13b shows the impact of the beam propagation on electron density. The plot reports how the waveguide geometry is being affected by the laser beam. At  $z=0$  mm, we see the strong on-axis ionization generated by the intense IR beam at its focus, at the entrance of the waveguide. The electron distribution generated by the electric field has a feedback effect on the propagation of the ultrashort and intense driving laser pulse. When electron density gets high after focusing and refocusing of the propagating IR pulse, the induced higher electron density leads to a refraction of the pulse.

Finally, the fig. 3.13c depicts the average ionization degree in the plasma amplifier. The figure testifies the fact that  $Kr^{8+}$  lasing ions are effectively created over the whole plasma amplifier.

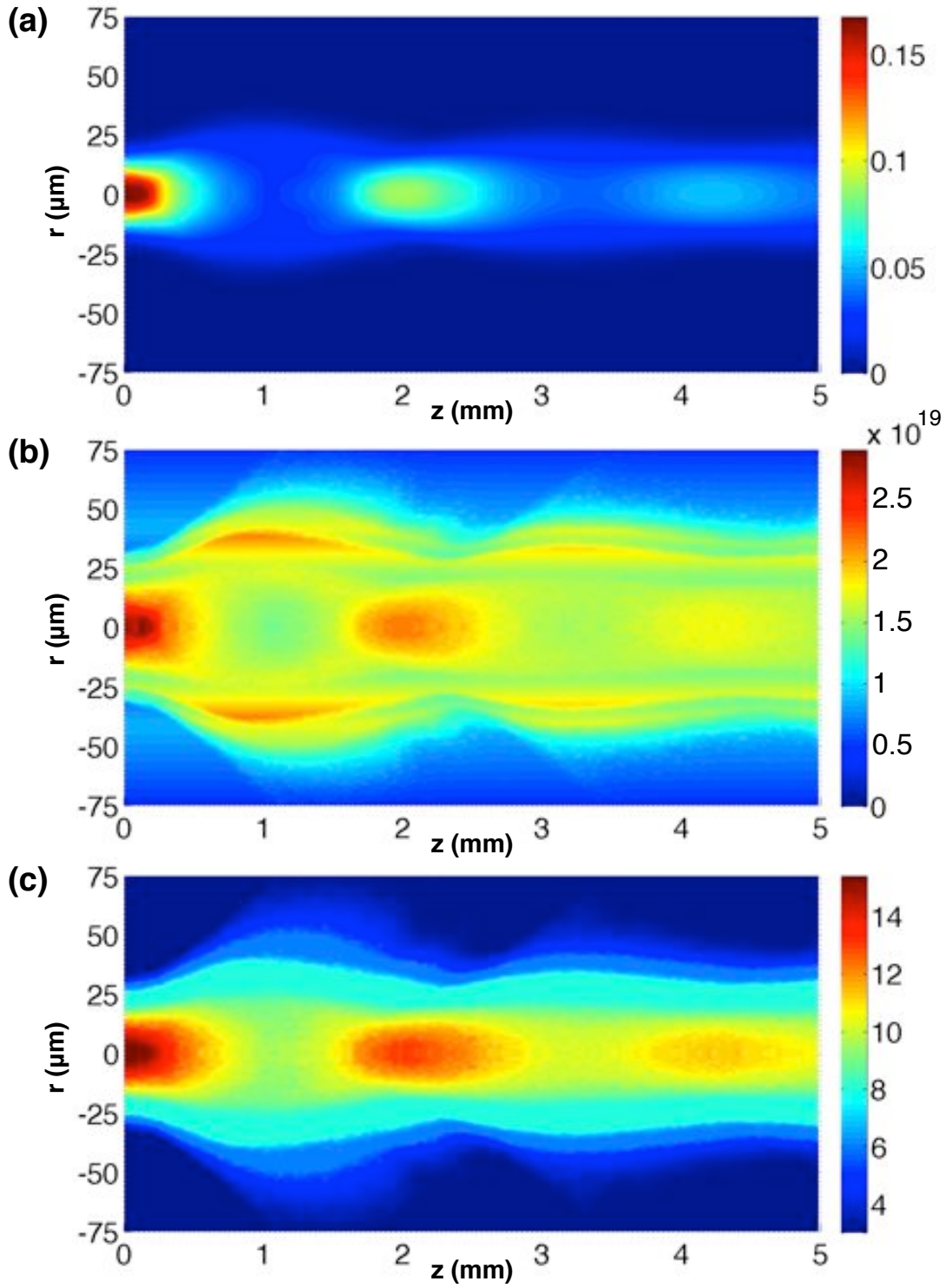


Figure 3.13: Maps of the distributions of intensity (vector potential) (a), electron density (b) and ionization degree (c) as the ultra-intense IR pulse propagates over a 5 mm long plasma amplifier with  $n_{e0} = 5 \times 10^{18} \text{cm}^{-3}$ ,  $n_{e1}/n_{e0} = 2$  and  $r_1 = 2w_0 = 32 \mu\text{m}$ . The maps are observed just after the passage of the IR pulse in the 5 mm-long plasma.

All in all, the fig. 3.13 reveals the competition between overionization-induced refraction and refraction in the plasma waveguide. This behavior allows the propagating beam to remain sufficiently intense to generate  $Kr^{8+}$  lasing ions over the whole amplifier length. Those ions are primarily generated off-axis, therefore creating a lasing volume with an annular cross-section of emission.

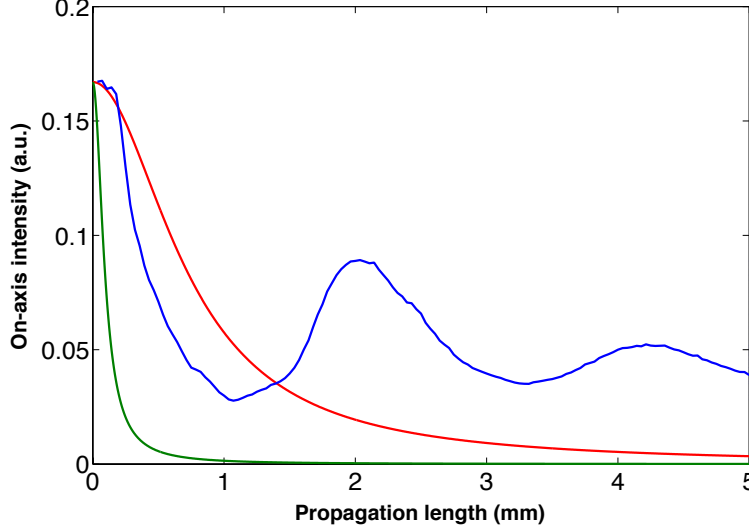


Figure 3.14: On-axis intensity in case of an ultra-intense IR pulse propagates being guided over a 5 mm long plasma amplifier with  $n_{e0} = 5 \times 10^{18} \text{ cm}^{-3}$ ,  $n_{e1}/n_{e0} = 2$  and  $r_1 = 2w_0 = 32 \mu\text{m}$  (blue). This is compared to the pulse propagation in vacuum (red) and without the waveguide (green).

The fig. 3.14 highlights the evolution of the squared potential vector as a function of the propagating length (blue curve). It is brought into comparison with the case of a beam propagating in vacuum (red curve) and also with the case when such a beam propagates without the waveguide (green). This figure emphasizes the pressing need of resorting to waveguiding when operating at high plasma densities.

The fig. 3.15 shows the fraction of total propagating energy that is being effectively waveguided inside the plasma channel (blue curve). The portion of the energy that is not being guided is represented in magenta. The red curve stands for total energy, which means the sum of the blue and magenta curves contributions.

Total energy decreases for two reasons. First, because a small part of the beam is being absorbed by the medium and secondly, because a non-negligible portion of the unguided pulse is moving out of the computation window, as it propagates over 5 mm. The guided component has been computed integrating the beam energy between the plasma channel dimensions, i.e. radially from  $-r_1$  to  $r_1$ . The transmission of the waveguide, i.e. the portion of guided energy, is found to be 57 %.

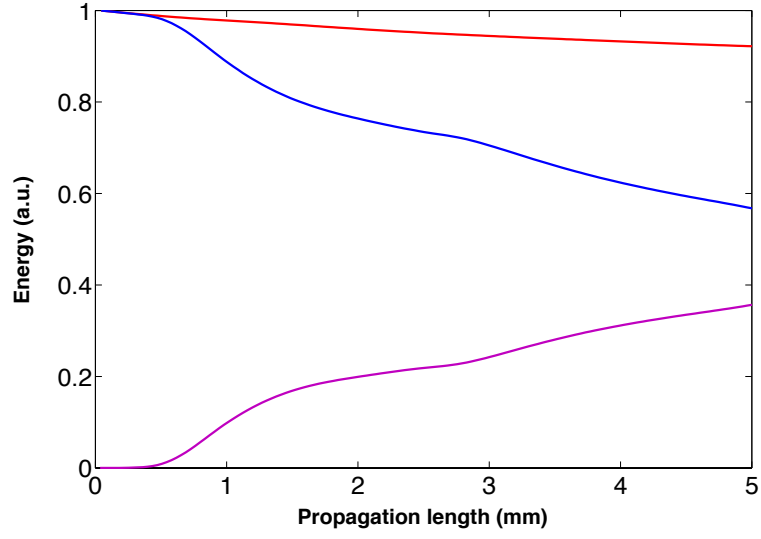


Figure 3.15: Portion of guided (blue) and unguided (magenta) energy in case of an ultra-intense IR pulse propagates being guided over a 5 mm long plasma amplifier with  $n_{e0} = 5 \times 10^{18} \text{ cm}^{-3}$ ,  $n_{e1}/n_{e0} = 2$  and  $r_1 = 2w_0 = 32 \mu\text{m}$ . Total energy is represented by the red curve.

### 3.2.3 Numerical investigation of a range of parameters

1. Waveguide transverse size: The influence of the plasma channel size, defined by the value of  $r_1$ , is studied in this paragraph. Simulations are carried out varying the waveguide transverse size from the previously reported conditions with  $n_{e0} = 5 \times 10^{18} \text{cm}^{-3}$ ,  $n_{e1}/n_{e0} = 2$  and  $r_1 = 2w_0 = 32 \mu\text{m}$ .

As shown in fig. 3.16, a transverse plasma channel size equating the waist of the laser imparts about 10 % losses right at the beginning. Those conditions are unfavorable, as the portion of unguided energy overcomes the guided energy after only 3.4 mm of plasma. The transmission over 5 mm falls to 33.5 %.

For  $r_1 = 1.5w_0$  and  $r_1 = 2w_0$ , the whole beam is coupled in the few hundreds of microns of the amplifier and transmission improves to 51.5 % and 57 % respectively. A further increase in the plasma channel radius to  $r_1 = 2.5w_0$  and  $r_1 = 3w_0$  fails to improve the overall transmission, which stalls at 57.4 % and 57.6 % respectively.

Therefore, increasing the size of the waveguide to values greater than twice the waist does not lead to a significant improvement of the total transmission. Because the plasma expansion is taking place at the expense of the radial density gradient, too large plasma channels would degrade the waveguiding.

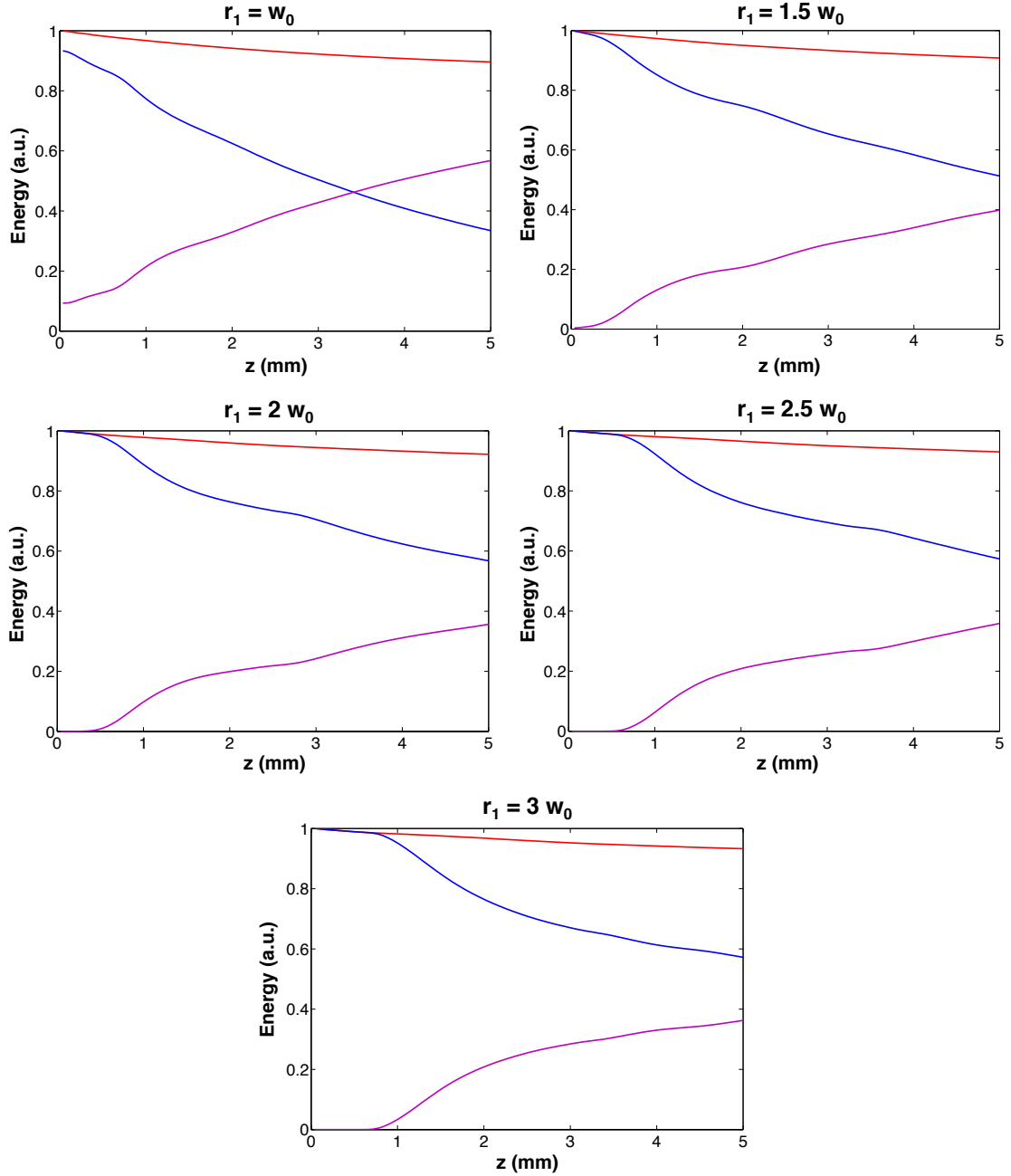


Figure 3.16: Evolution of the portion of guided (blue) and unguided (magenta) energy as the size of the plasma channel is varied. The conditions correspond to the propagation of an ultra-intense IR pulse, guided over a 5 mm long plasma amplifier with  $n_{e0} = 5 \times 10^{18} \text{cm}^{-3}$  and  $n_{e1}/n_{e0} = 2$ . Total energy is represented by the red curve.

2. Radial density gradient: The higher the density gradient, the better the waveguiding. However, this gradient is given by the plasma heating and the subsequent plasma expansion. For fixed experimental parameters (gas density, energies, durations and delays between the "ignitor" and the "heater"), the density gradient depends on the size of the channel. A tradeoff between the plasma channel size and the density gradient is thus needed.

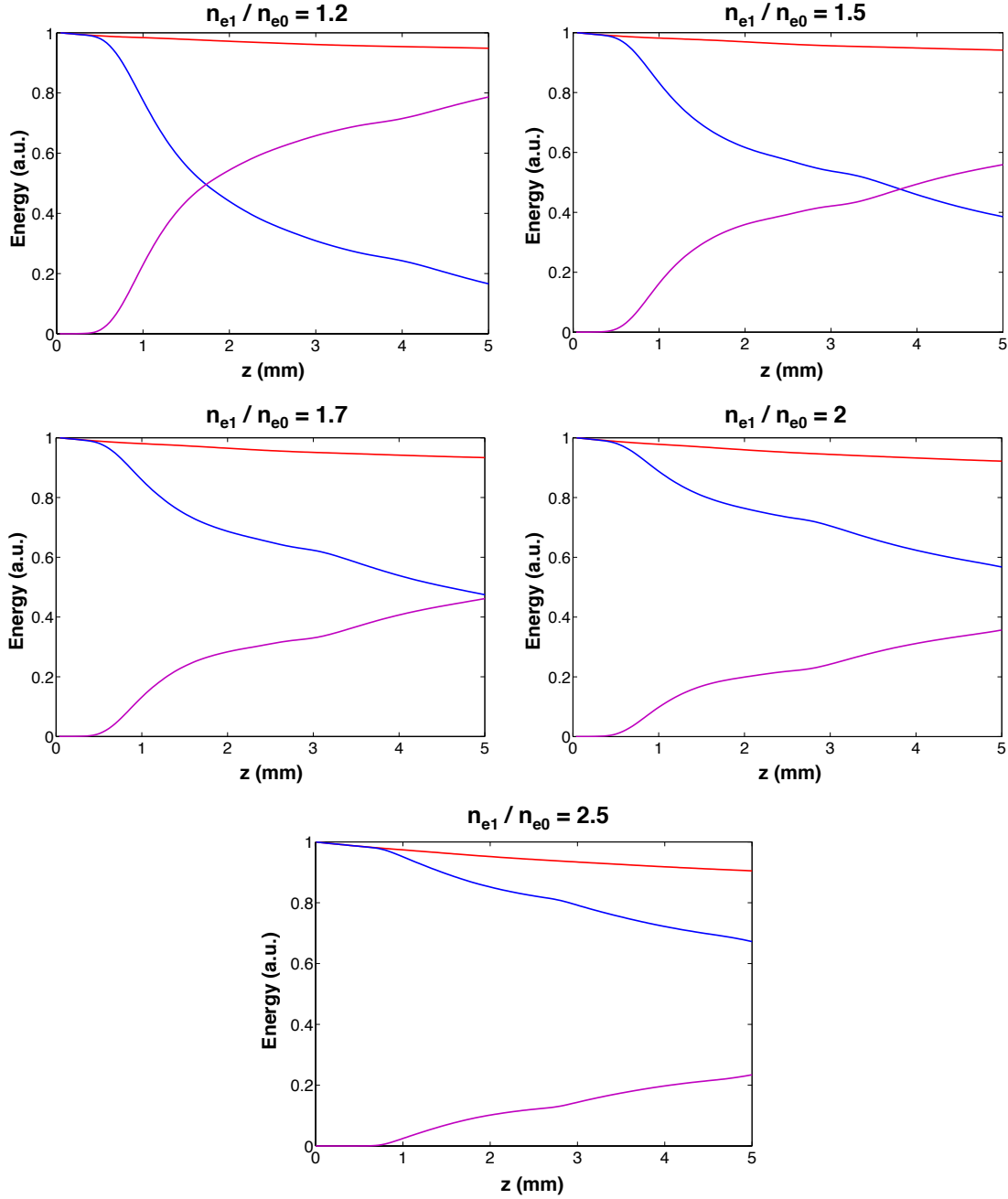


Figure 3.17: Evolution of the portion of guided (blue) and unguided (magenta) energy as the density gradient is altered. The conditions correspond to the propagation of an ultra-intense IR pulse, guided over a 5 mm long plasma amplifier with  $n_{e0} = 5 \times 10^{18} \text{ cm}^{-3}$  and  $r_1 = 2w_0 = 32 \mu\text{m}$ . Total energy is represented by the red curve.

As shown in fig. 3.17, the waveguide transmission monotonously rises as the electron density gradient is increased. For low values of  $n_{e1}/n_{e0} = 1.2, 1.5$  and  $1.7$ , losses outclass the guided part of the beam. Transmissions are respectively 16.8 %, 38.7 % and 47.6 %. For  $n_{e1}/n_{e0} = 2$  and  $2.5$ , transmissions as high as 57 % and 67.2 % are computed.

3. **Electron density:** The fig. 3.18 shows the evolution of the transmission when the electron density is varied. The waveguide transverse dimension corresponds to twice the beam waist, whereas the ratio between axial and off-axis electron density is maintained at 2. For the latter condition, the density gradient decreases as the overall density becomes lower. Thus, the waveguide refraction gets lower but overionization-induced refraction also plummets at lower densities. For axial densities of  $10^{18} \text{cm}^{-3}$ ,  $3 \times 10^{18} \text{cm}^{-3}$ ,  $5 \times 10^{18} \text{cm}^{-3}$  and  $8 \times 10^{18} \text{cm}^{-3}$ , the transmission is found to be 68 %, 61 %, 57 % and 49 % respectively. Those data show a sharper decrease of transmission at higher densities, therefore highlighting the limitations of the optically pre-formed plasma channel technique.

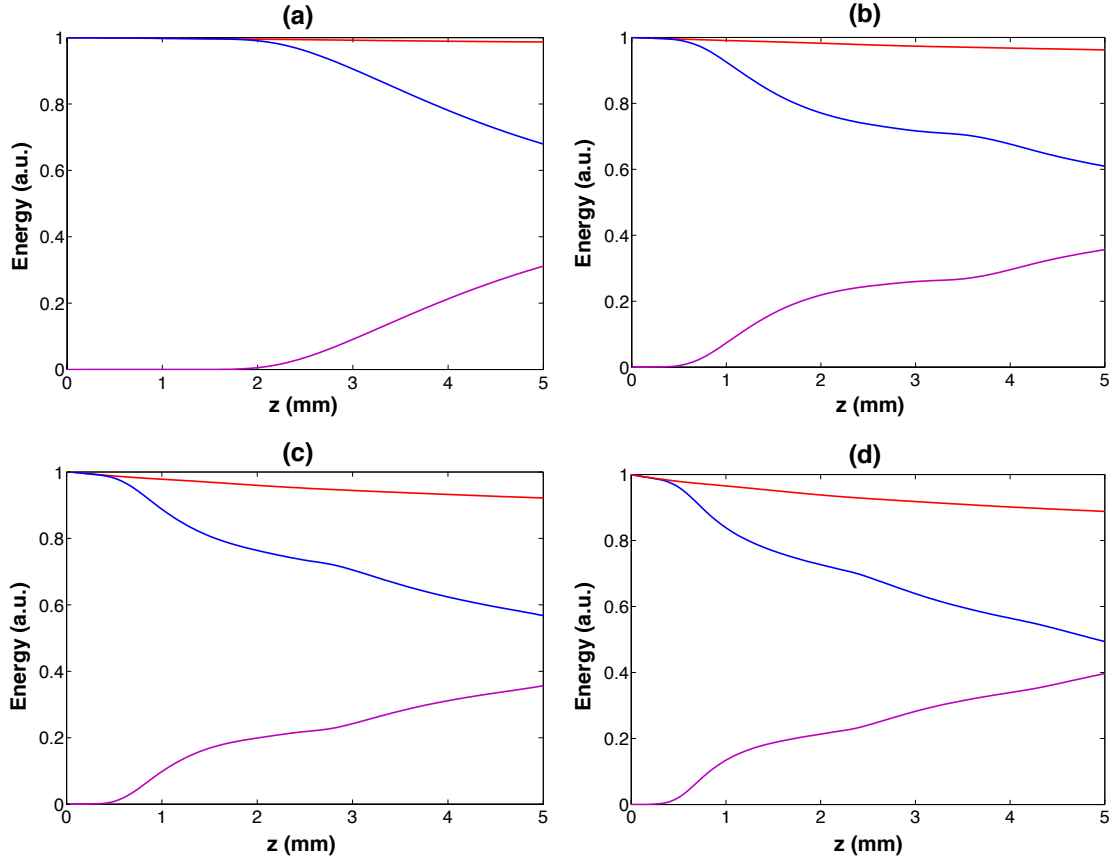


Figure 3.18: Evolution of the portion of guided (blue) and unguided (magenta) energy as the electron density is changed. The conditions correspond to the propagation of an ultra-intense IR pulse, guided over a 5 mm long plasma amplifier with  $n_{e1}/n_{e0} = 2$  and  $r_1 = 2w_0 = 32 \mu\text{m}$ , for  $n_{e0} = 10^{18} \text{cm}^{-3}$  (a),  $n_{e0} = 3 \times 10^{18} \text{cm}^{-3}$  (b),  $n_{e0} = 5 \times 10^{18} \text{cm}^{-3}$  (c) and  $n_{e0} = 8 \times 10^{18} \text{cm}^{-3}$  (d). Total energy is represented by the red curve.

All in all, the numerical study showed that an efficient generation of a high-density plasma amplifier requires the **sharpest density gradients** and a **channel transverse size** with a radius at least **twice** the beam waist.



### Towards higher electron densities

Because WAKE-EP PIC code scope of validity is limited to values of the plasma frequency such as  $\omega_p \leq 0.02\omega_0$ , it was not possible to numerically investigate the guiding conditions at electron densities higher than  $n_{e0} = 5 \times 10^{18} \text{cm}^{-3}$  inside the plasma channel.

In the next chapter, we will see that strong lasing has been observed with a plasma channel of on-axis electron density over  $n_{e0} = 1.5 \times 10^{19} \text{cm}^{-3}$  (cf. fig. 4.25). In this case, the electron density of the plasma amplifier (with the pump beam being guided by the plasma channel) reached electron densities as high as  $1.2 \times 10^{20} \text{cm}^{-3}$ . The very strong soft X-ray signal strength and the good transmission of 45 % of the IR pump beam by the waveguide corroborate the prediction that the elongated medium is efficiently filled with  $Kr^{8+}$  lasing ions.

In these conditions, the simulations have been carried out using a 3D Particle-In-Cell (PIC) code (CalderCirc [Lifschitz et al., 2009]) solving a combination of Maxwell and Vlasov equations, written in cylindrical coordinates. ADK ionization model is considered. The propagation of the IR pulse is complex and characterized by a combination of self-focusing, refraction from the waveguide density gradient and refraction due to strong ionization induced by the pulse itself. Populations of ions with a higher charge are situated in on-axis plasma regions of the plasma. The strong overionization of the medium at the entrance of the plasma explains the absence of lower Z species in this region. The displayed data correspond to an averaged transverse profile of the plasma channel illustrated in fig. 4.25a, considered uniform along the propagation axis. The initial ionization degree in the plasma waveguide is 3.

The fig. 3.19 shows the spatial distribution of the lasing ion species resulting from the guiding of the pump beam over the whole gas jet length, considering the waveguide geometry depicted in fig. 4.25a. The maps are displayed just after the propagation of the intense pulse into the 5 mm-long plasma, which takes over 16.6 ps. The laser pulse propagates from the left to the right of the maps.

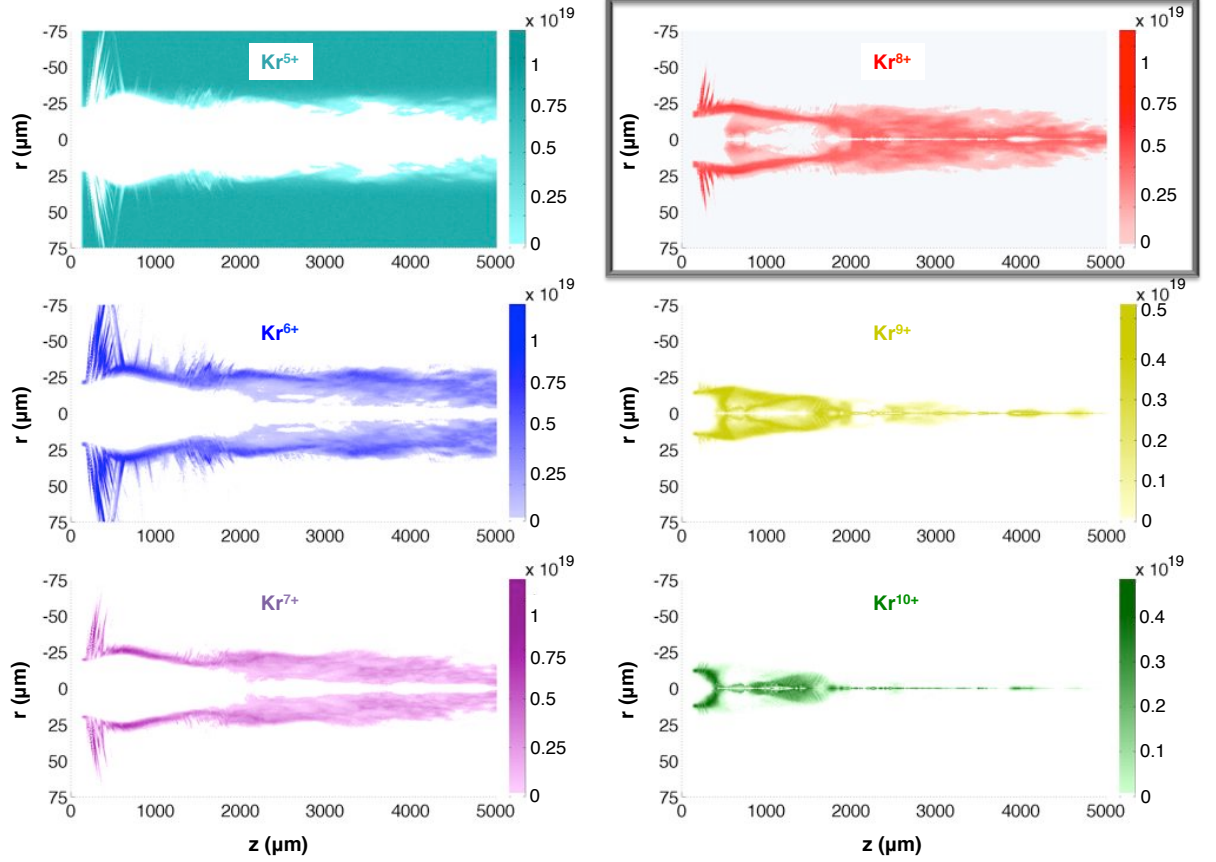


Figure 3.19: Density maps of krypton ions species generated focusing a IR pump beam with  $I = 3 \times 10^{18} \text{ W/cm}^2$  into a high-density 5 mm-long plasma channel, which corresponds to experimental conditions investigated in fig. 4.25a).

The fig. 3.20 shows that lasing ion species are populating the plasma amplifier over the whole length of 5 mm. The stability of  $Kr^{8+}$  to further ionization over a large range of intensities, as reported in fig. 2.3, allows implementing an emitting medium with a large and uninterrupted population of lasing ions over 5 mm. The fig. 3.20 depicts the plasma inhomogeneity, resulting from the complex propagation of the intense IR pulse.

The CalderCirc simulations show that the experimental waveguide geometry allows efficiently filling the whole plasma length with  $Kr^{8+}$  ions, which is consistent with the very strong lasing observed under those conditions. However, the transmission of the IR pump beam by the waveguide was found to be quite bad (slightly over 10 %), which is not in agreement with the experimentally measured transmission of 45 % under those conditions. Two possible reasons can explain this. First, it can be a numerical artifact caused by the fact that the pump beam duration may become longer than the simulation moving window, thus artificially lowering the value of the total energy at the output of the waveguide. Second, the ionization degree of the plasma channel may be higher than expected. Indeed, for a given waveguide electron density profile, the guiding efficiency increases when the initial ionization degree increases.

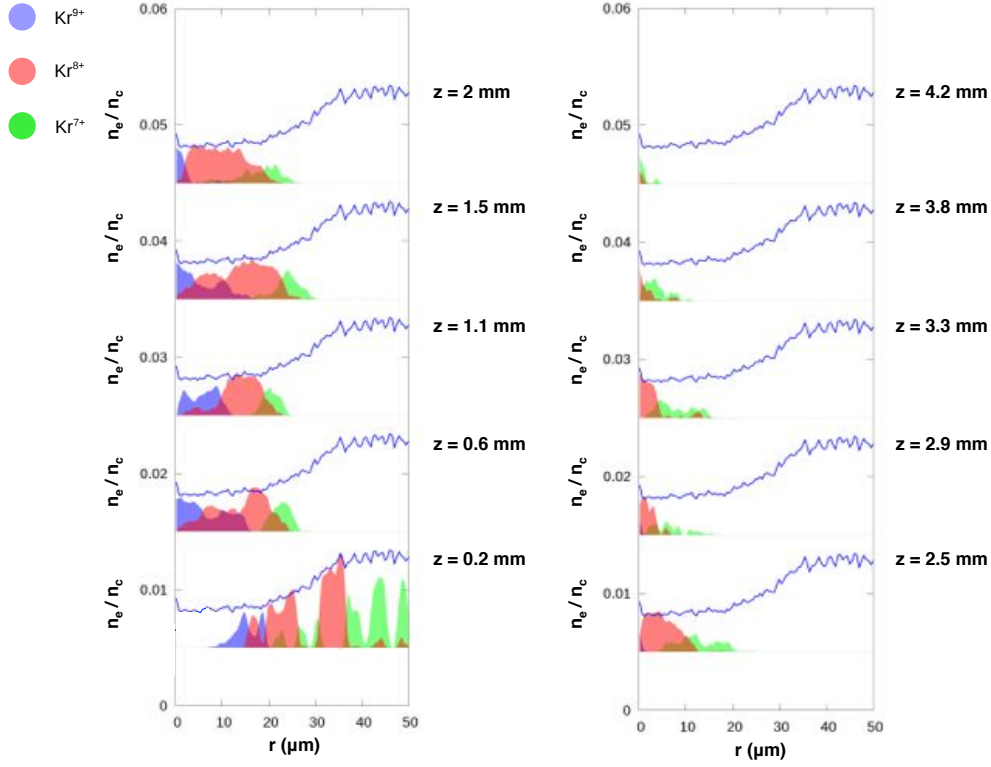


Figure 3.20: Radial distribution of  $Kr^{7+}$ ,  $Kr^{8+}$  and  $Kr^{9+}$  ions at various longitudinal coordinates.

The inconsistency between the experimental observations and the numerical calculations illustrates the need for a better characterization of the plasma channel initial conditions, which proves pivotal to understand how the intense IR driving laser pulse propagates in such an elongated medium.

### 3.3 Conclusion

The « ignitor-heater » waveguiding scheme appears as a very adequate technique to achieve an elongated high-density soft X-ray plasma amplifiers with  $Kr^{8+}$  ions.

Our aim consists in efficiently guiding an ultrashort and intense driving laser pulse into a plasma with the highest possible electron density. The numerical study showed that achieving an amplifier with the highest possible density requires a channel size at least coupled to the beam size (with a radius at least twice the beam waist), along with the sharpest density gradients.

Experimentally, we will see that a tradeoff between the channel transverse size, the density gradients and the electron density is needed. The laser system of « Salle Jaune » at Laboratoire d'Optique Appliquée allows reaching advantageous conditions for guiding at high electron density.

Further work aimed at determining the initial conditions of the plasma channel and the physics of its hydrodynamic expansion should be carried out to better understand how an intense IR driving pulse can be advantageously guided into such high-density plasma.



## Chapter 4

# Experimental investigation of a high-density soft X-ray plasma amplifier

This chapter presents the experimental implementation of the «ignitor-heater» waveguiding technique in a high-density krypton plasma amplifier. The diagnostics used to monitor the waveguiding conditions as well as the properties of the plasma-based soft X-ray laser emission over a range of parameters are described. They report a strong correlation between the emitted signal strength and the waveguiding quality.

### Contents

---

<b>4.1</b>	<b>Experimental arrangement</b>	<b>110</b>
4.1.1	«Salle Jaune» experimental installations	110
4.1.2	Experimental setup	113
<b>4.2</b>	<b>Elongated high-density gas jet target</b>	<b>115</b>
4.2.1	Design of a rectangular nozzle	115
4.2.2	Experimental characterization of rectangular slit nozzles	118
<b>4.3</b>	<b>Diagnostics</b>	<b>122</b>
4.3.1	Waveguide diagnostics	122
4.3.2	Soft X-ray diagnostics	124
<b>4.4</b>	<b>Experimental results</b>	<b>125</b>
4.4.1	Characterization of the plasma waveguide	125
4.4.2	Guiding efficiency	132
4.4.3	Characterization of the soft X-ray laser emission	135
4.4.4	Correlation between waveguiding quality and SXRL signal strength	142
<b>4.5</b>	<b>Conclusion</b>	<b>145</b>

---

## 4.1 Experimental arrangement

### 4.1.1 «Salle Jaune» experimental installations

The experimental work of this thesis coincided with the early stages of the rejuvenation of «Salle Jaune» experimental room at *Laboratoire d'Optique Appliquée*. The IR laser system has been separated from the room where the experiments take place, as illustrated in fig. 4.1. The laser system is installed in a separate room ("Salle Blanche") on the top of the experimental room ("Salle Jaune"), in an environment controlled in hygrometry and temperature to allow stable operation of the laser.

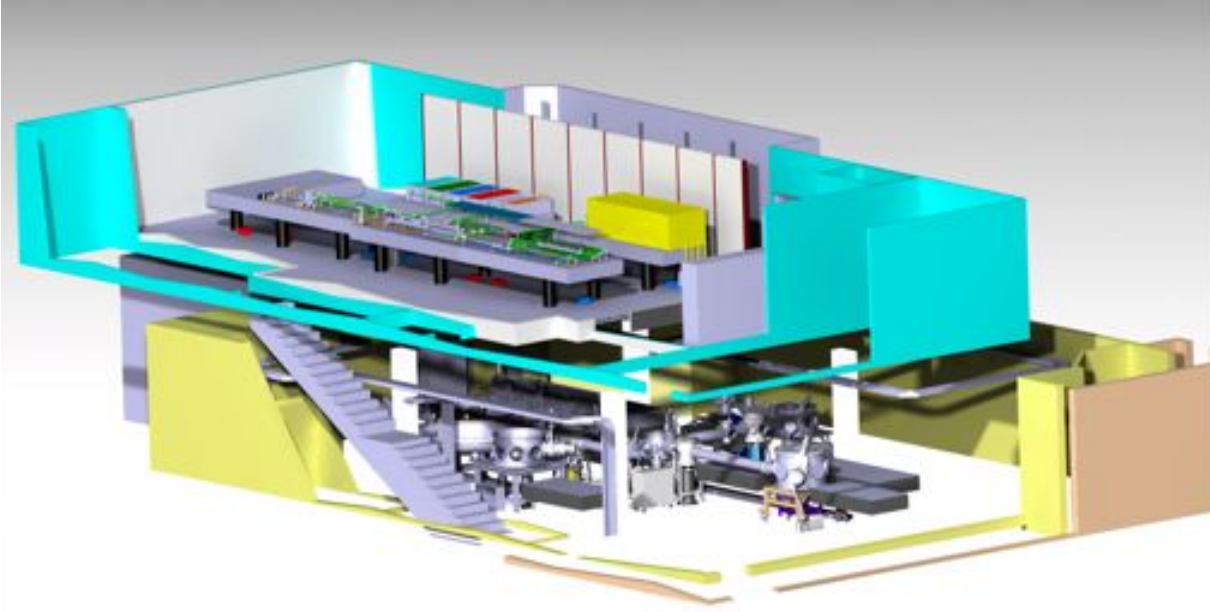


Figure 4.1: Laser and experimental facilities of «Salle Jaune».

The laser system is a 5-stage amplification Ti:sapphire laser chain delivering up to 5 J pulses at 1 Hz operation. Ultrashort pulses as short as 30 fs are obtained implementing a *Chirped Pulse Amplification* technique [Strickland and Mourou, 1985], which consists in stretching out the pulses temporally before amplification and then compress them to their initial duration after amplification. This method allows avoiding parasitic nonlinear phenomena occurring at high peak intensities. The laser amplification is achieved in sapphire crystals doped with titanium ions.

The laser chain is illustrated in fig. 4.2. It starts with a Ti:sapphire oscillator emitting pulses of 4 nJ of duration 9 fs at 88 MHz. Its spectrum is broad with a full width at half-maximum of 150 nm and centered around 800 nm. Those pulses are then stretched out temporally up to a duration of 20 ps and amplified up to 400  $\mu$ J at a rate of 10 Hz. A pre-amplifier increases the energy up to 2 mJ. Those pulses are then compressed down to 20 fs thanks to a diffractive prism. The temporal contrast (ratio between the pulse peak intensity and the ASE level) is enhanced with a XPW (Cross-Polarized Wave) filter [Jullien et al., 2006]. The contrast reaches up to  $10^{10}$ , 100 ps (or  $10^7$  at 10 ps) from the main pulse. The efficiency of the system is about 15 %. Because it sits upstream from the amplification stages, losses induced by the system can be compensated, which is not the case for other contrast improvement techniques involving plasma mirrors. As far as laser-plasma interaction is concerned, a high-contrast is needed to avoid

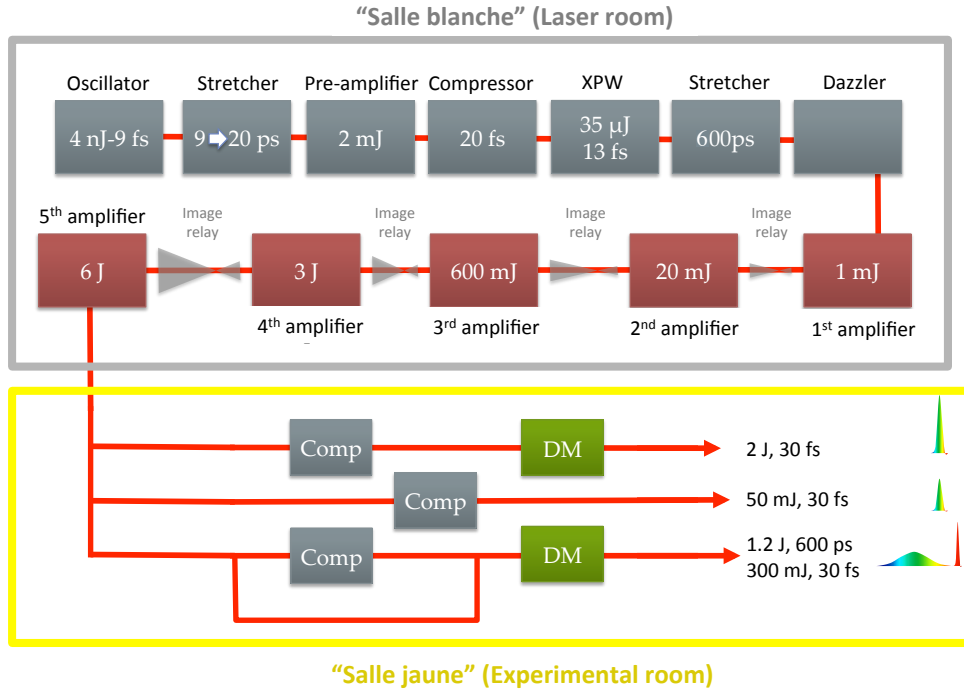


Figure 4.2: Architecture of the laser system from the laser room to the experimental vacuum chambers. The laser beam is splitter into three and arrive in "Salle Jaune" uncompressed. Each of them has its own system of compression consisting of two gratings. "P2" beam is composed of a compressed and uncompressed pulse (see section 4.1.2). Two deformable mirrors (DM) correct the wavefronts of "P1" and "P2".

undesired pre-plasma generation from a pre-pulse or a pedestal. The pulses are then stretched to 600 ps. An AOM (*Acousto-optic modulator*) or *Dazzler* is used to control the spectral phase of the pulses in the aim of pre-compensating the spectral broadening induced by the amplifiers' gain to offer advantageous conditions for the pulse compression [Verluise et al., 2000]. The pulses are then amplified by a series of five amplification stages implemented with Ti:sapphire crystals pumped by Nd:YAG lasers whose frequency have been doubled (532 nm). The amplification stages are multi-pass amplifiers. The first allows reaching 1 mJ and the second 20 mJ, both at 10 Hz. A spatial filter allows then improving the beam quality. It is achieved with a focal system and a hole of a few tens of  $\mu$ m placed at the focus to clean out the focal spot. The third, fourth and fifth amplification stages build up the energy from up to 600 mJ, 3 J and 6 J. The size of the crystal as well as the beam size are increased for further amplification to allow an optimal extraction of energy while keeping the laser fluence below the damage threshold of about  $100 \text{ mJ/cm}^2$ . The crystals are cooled down with water to limit thermal lensing effects. Because of still disturbing thermal lensing effects, the pulse rate has been limited to 1 Hz.

The beam out of the fifth amplification stage is separated in 3 independent beams, named P1, P2 and P3. The main beam is first divided into two by a beamsplitter with 60% in P1 and 40% further splitted with 90% in P2 and 10% in P3. In our experimental setup, P1 is used to generate the plasma amplifier, whereas P2 serves as the waveguiding beam to implement the pre-formed plasma channel (see section 4.1.2 & chapter 5), and while P3 is used both to generate high-harmonics and as a probe beam for electron density diagnostics (see chapter 5).



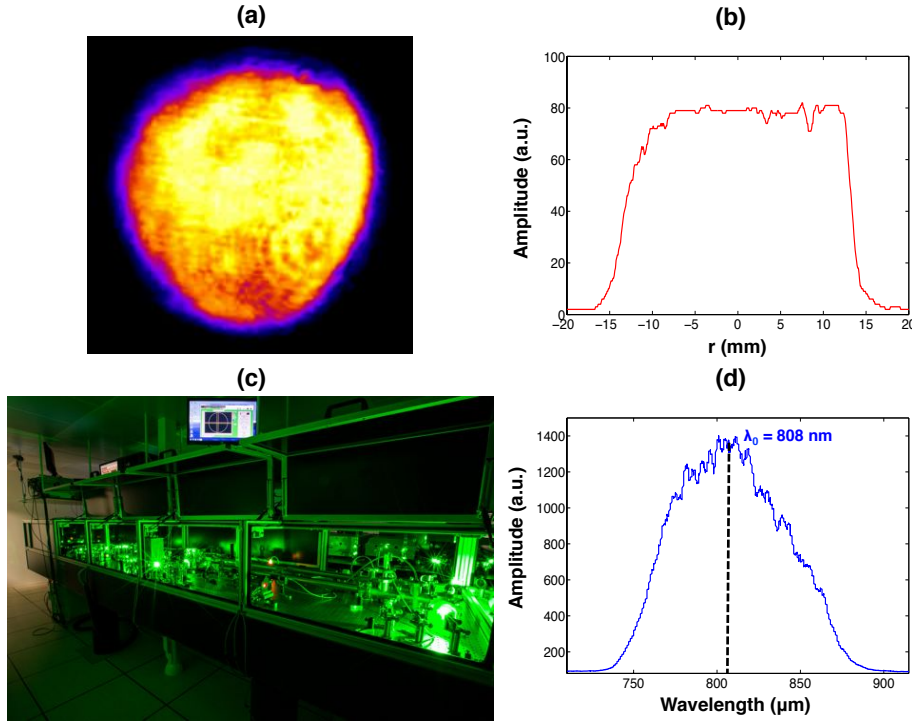


Figure 4.3: (a) Beam profile at the output of the fourth amplification stage. (b) Radial profile of the "top-hat" beam profile. (c) Overview of the laser system in "Salle Blanche". (d) Spectrum shape of the laser oscillator output.

The emission exhibits a broad spectrum and its duration is about 600 ps at the output of the fifth amplification stage. The amplified beam profile and the spectrum at the level of the oscillator are shown in fig. 4.3. The spectrum is centered around 800 nm, but is red-shifted after amplification. The full power laser central wavelength was measured at 808 nm. The laser beam energy distribution exhibits a nearly "top-hat" profile (fig. 4.3a & b) and its polarization is linear along the p-polarization direction.

Afocal systems of lenses are used to relay the image of the output laser beam to the "beam shaping" vacuum chamber and to adapt their transverse size to the desired characteristics. The beam diameters are 60 mm and 30 mm for P1 and P2/P3 respectively. The beams arrive from the top and are sent to the compressor chamber where two systems of double gratings used to compress "P1" and "P2" from 600 ps down to 30 fs sit, whereas "P3" bypasses those optical components.

Deformable mirrors are used to improve the focusing quality of beams "P1" and "P2" after compression. The wavefront of the incoming beams is measured by imaging the surface of deformable mirrors onto a Shack-Hartmann wavefront sensor consisting of an array of microlenses with identical focal lenses. Each one focuses one portion of the beam onto a CCD sensor. Phase aberrations can be approximated by a set of discrete local phase tilts spreading over the whole wavefront. Those local phase tilts across each lens can be calculated from the deviation of the focal spots from the positions of the focus that would produce an aberration-free planar wavefront. Therefore, a map of the actual wavefront can be recovered and decomposed over the orthogonal base of Zernike polynomials, each of them corresponding of a particular type of aberration. The main types of aberrations are tilt, defocusing, astigmatism at  $0^\circ$  and  $45^\circ$ , horizontal and vertical coma, trefoil and spherical aberrations.

### 4.1.2 Experimental setup

The approach to implement *Collisional Ionization Gating* in an elongated high-density plasma consisted in exploiting the "ignitor-heater" plasma channel pre-forming technique (see section 3.1.4) to pre-form a waveguide by radially shaping an optimal profile in electron density, which offers appropriate conditions for guiding an intense IR laser pulse in a high-density plasma.

**High-density plasma amplifier.** The architecture of the high-density collisionally pumped plasma amplifier is presented in fig. 4.4. The waveguiding beam is composed of a sequence of a short (130 mJ, 30 fs) and a long pulse (690 mJ, 600 ps) and is being focused over the whole jet length thanks to an axiconic lens. The following plasma hydrodynamic expansion produces a density channel that is appropriate for guiding the high intensity driving laser pulse. Then, the pump beam (1.36 J, 30 fs) is being focused at the entrance of the channel with a 75 cm-focal length spherical mirror and being guided afterwards. Hence, an amplifier with  $Kr^{8+}$  lasing ion species over the whole gas jet length is implemented. A double-coated plane mirror is used in a  $45^\circ$  configuration to colinearly distribute the waveguiding and pump beams. This mirror, as well as the axicon lens, are drilled to leave free space focusing IR pump beam into the gas jet.

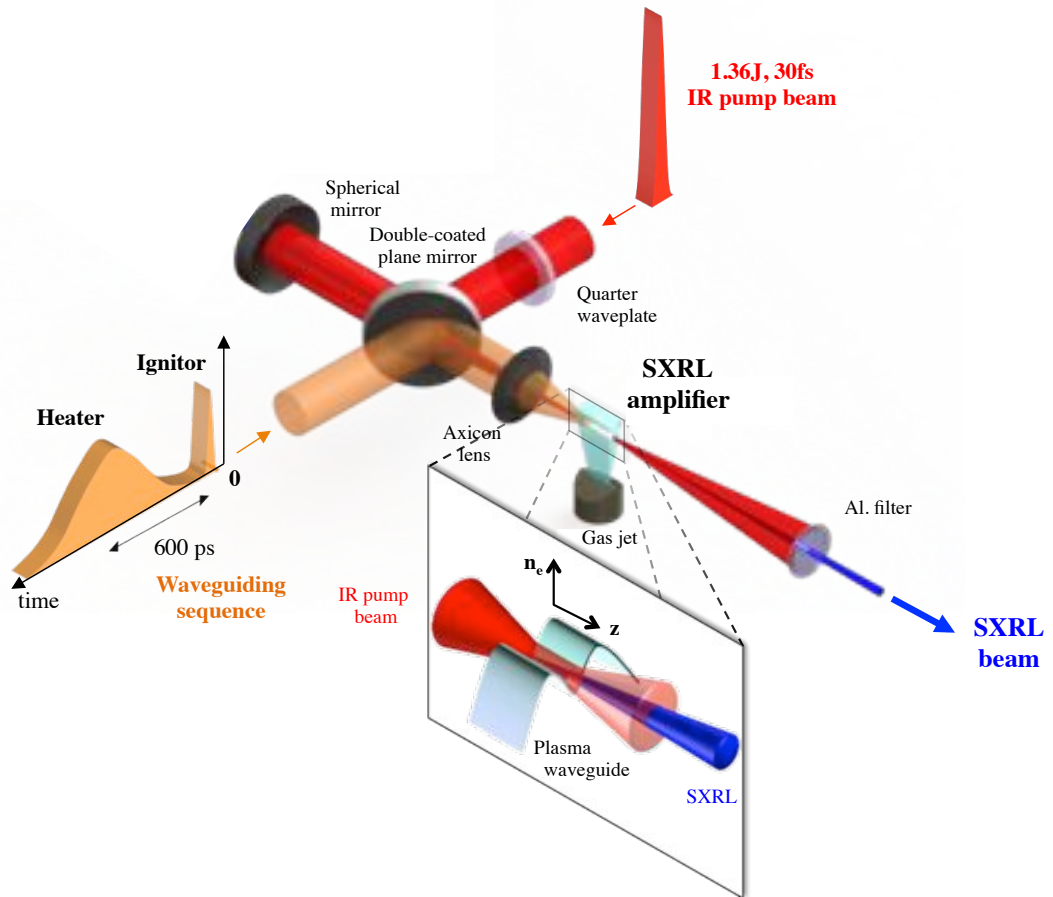


Figure 4.4: Experimental arrangement of the high-density krypton plasma soft X-ray amplifier.

**Waveguiding beam.** The "ignitor-heater technique" (cf. section 3.1.4) is implemented with the beam "P2" of the «Salle Jaune» IR laser. The uncompressed pulse energy is slightly over 1 J and is splitted with 80 % bypassing the gratings system and 20 % being compressed. Both pulses are then recombined into a single beam using a thin plate polarizer working at 72 degrees of incidence, which transmits and reflects cross-polarized beams. The 600 ps and 30 fs pulses are initially both p-polarized. A  $\lambda/2$  wave plate is used to change the polarization direction of the fs pulse to the s-direction to allow it to be reflected on the thin plate polarizer, while the p-polarized ns pulse is transmitted by the device. A  $\lambda/2$  is also placed on the ns beam to control the relative energy of both pulses within the waveguiding beam P2. The setup is illustrated in fig. 4.5. There is a 600 ps delay between the two pulses. The transmission from the laser last amplification stage to the experimental vacuum chamber is 68 %.

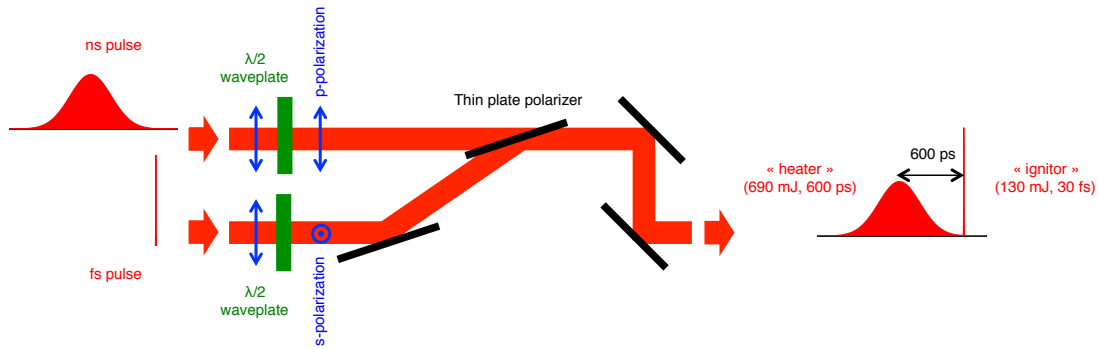


Figure 4.5: Recombination system of the waveguiding beam (P2).  $\lambda/2$  wave plates are used to control the polarization direction of the pulses, as well as their relative energies.

The driving beam "P1" is turned circularly polarized thanks to a quarter-wave plate. This allows catering for hot electrons needed to efficiently pump the laser transition. The measured focal spot is about  $38 \mu m$  in  $1/e^2$ -diameter, as illustrated in fig. 4.6a. In these conditions, intensity on target is about  $3 \times 10^{18} W/cm^2$ . This corresponds to about 43 % energy contained within the  $1/e^2$ -diameter of the spot. The rather low quality of the focal spot is notably due to the two 8 mm on-axis holes on the beam path. For the sake of comparison, the spot size in the diffraction limit is  $29 \mu m$ . The transverse diffraction pattern of the focal line of the waveguiding beam focused with an axicon lens is shown in fig. 4.6b. The transverse intensity pattern has a FWHM size of less than  $2 \mu m$  and exhibits a Bessel function ring structure, as illustrated in fig. 3.5. This pattern has been observed using a x20 microscope objective because of spot small size and also because a high numerical aperture is needed to collect the rays focused by the axicon.

Both pump and waveguiding beams are overlapped. The transverse position and the tilt of the axicon are adjusted to make the focal line collinear to the propagation direction of the pump beam. For this purpose, the pump beam is closed with an iris to increase the confocal parameter in order to be able to overlap the waveguiding beam with the pump beam over the whole gas jet length. The gas jet is then aligned with respect to the focal line direction, as shown in fig. 4.7.

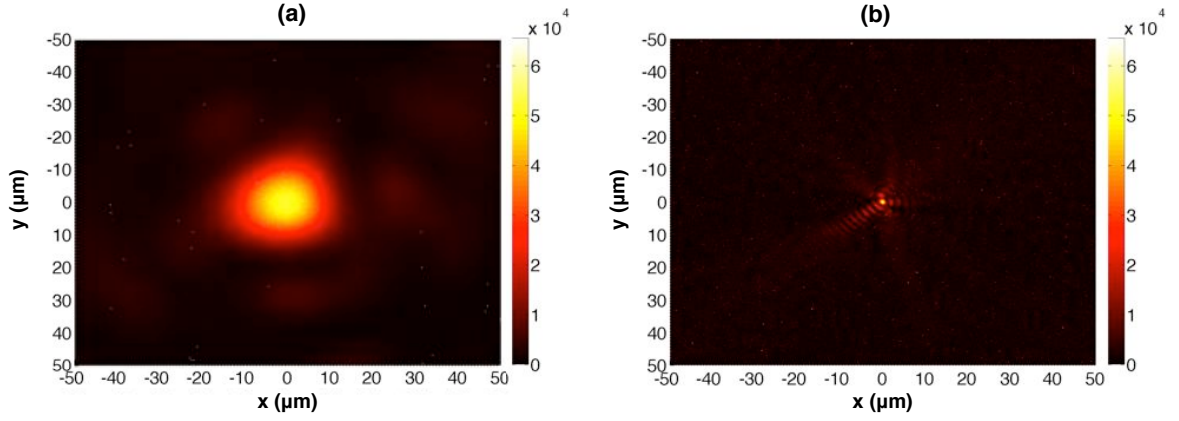


Figure 4.6: (a) Energy distribution (in a.u.) of the pump beam focal spot. (b) Energy distribution (in a.u.) of the diffraction pattern of the waveguiding beam obtained with the axicon lens.

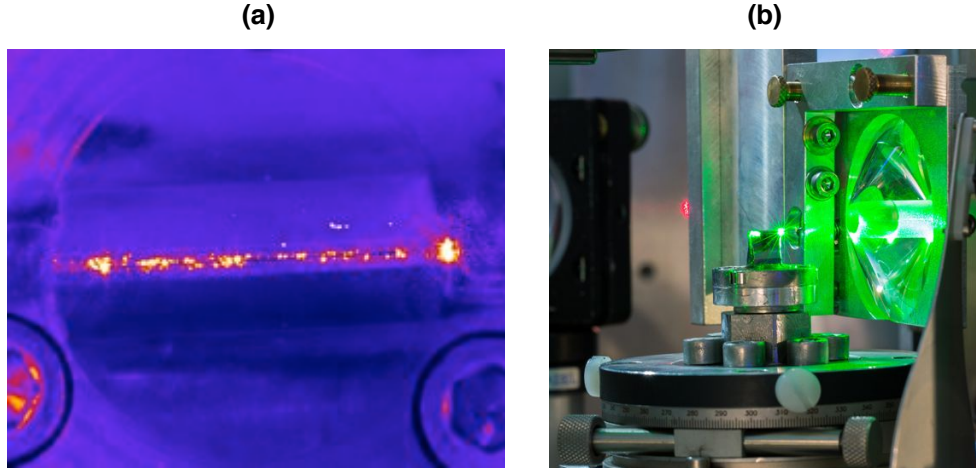


Figure 4.7: (a) "Top view" of a rectangular nozzle slit aligned onto the waveguiding beam focal line. (b) "Side view" of the axicon lens in front of the gas jet nozzle.

## 4.2 Elongated high-density gas jet target

The perspective of quenching the gain lifetime down to the femtosecond duration (see section 2.3.2) hinges on the realization of gas column reaching neutral densities as high as  $10^{19} \text{cm}^{-3}$ . The aim is to generate an elongated homogeneous plasma spreading over several Rayleigh lengths in order to reach the saturation regime of the amplifier, but also to improve the spatial properties of the soft X-ray laser beam.

### 4.2.1 Design of a rectangular nozzle

To generate such high-density plasma amplifiers, rectangular slit nozzles are used and their geometry makes it possible to yield a nearly "top-hat" profile of high-density over several millimeters. The difficulty consists in achieving a long and homogeneous reaching densities over  $10^{19}$  atoms per  $\text{cm}^3$  while displaying sufficiently sharp density gradients to ensure a good laser-plasma coupling.

## Equipment

The nozzles are adapted on the top of a valve, which controls the the gas flow. A small metal ball closes the valve under pressure. The valve has an electro-magnet, which applies a magnetic field on the metallic ball when supplied with a strong current (about 10 A). The ball then undergoes an electro-motive force which deviates it from the valve inlet and liberates the gas flow.

To realize an interaction medium meeting the previously described requirements, a compressor is used between the gas bottle and the valve to increase the backing gas pressure. This apparatus works mechanically boosting the gas pressure thanks an advantageous surface ratios, under the supply of compressed air. A few tens of bar of gas is needed to reach backing pressures exceeding 100 bar. Tuning the pressure is made by controlling the pressure of compressed air over a range of a few bar.

## Nozzle geometry

The investigation of gas jets has been actively researched since the end of the 1930s in the framework of the development of nozzles for aerospace applications. The engaged technical solutions (aiming at maximizing the specific impulse, i.e. the outlet gas speed) were unfortunately not directly transferable to laser plasma interaction, for which efforts are relatively recent.

Actually, to work out gas targets suitable for the needed laser-plasma interaction conditions, a gas density « top hat » profile with sharp gradients requires high Mach numbers, whereas a high-density profile calls for moderate gas flow speeds. The Mach number is an important parameter, characterizing the gas density flow. One talks, respectively, about « subsonic » or « supersonic » nozzles. The combination of high gas density with sharp gradients appears contradictory. Therefore, a tradeoff between those two gas flow regimes [Semushin and Malka, 2001] is needed. The required nozzle geometry has to offer « transsonic » gas flow properties over a length of a few millimeters. Such works were successfully implemented by a team from Taiwan [Xiao et al., 2004; Lin et al., 2007].

The development of such nozzles yielding nearly uniform elongated density profiles has been the subject of significant developments at Laboratoire d'Optique Appliquée and is promoted by a laboratory spinoff, SourceLab.

The design and evaluation of the validity of the nozzle geometry with fluid simulations are presented in Appendix D. Apart from the backing pressure, the density profiles mainly depend upon the opening time of the valve as well as the height with respect to the nozzle.

## Modeled density profiles

The gas flow from the rectangular nozzles was modeled using a fluid dynamics code (see Appendix D) The neutral gas density maps at various heights with respect to the nozzle outlet are presented in fig. 4.8 and fig. 4.9.

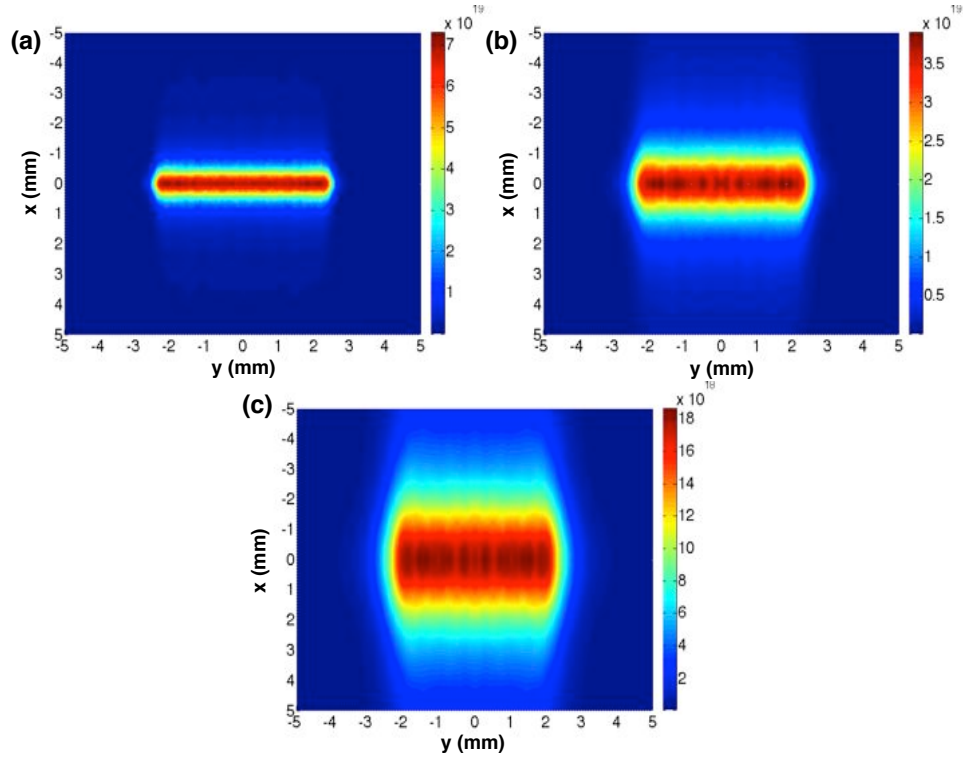


Figure 4.8: Simulated neutral gas density profiles for the  $5\text{mm} \times 500\mu\text{m}$  nozzle at heights  $h = 0.5 \text{ mm}$  (a),  $h = 1 \text{ mm}$  (b) et  $h = 1.5 \text{ mm}$  (c) with  $P_{Kr}=150 \text{ bar}$ .

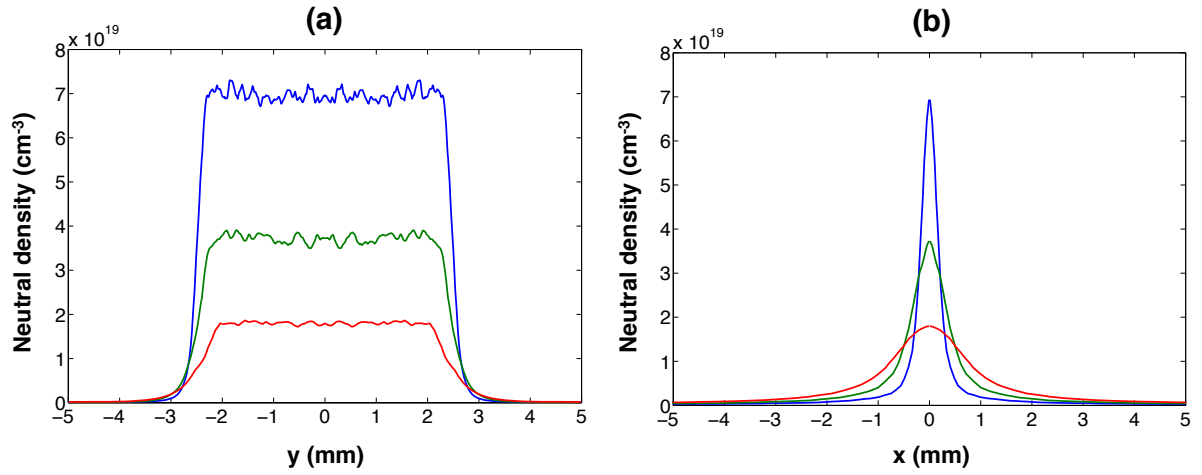


Figure 4.9: Longitudinal (a) and transverse (b) neutral gas density profiles for the  $5 \text{ mm} \times 500 \mu\text{m}$  nozzle at heights  $h = 0.5 \text{ mm}$  (blue),  $h = 1 \text{ mm}$  (green) et  $h = 1.5 \text{ mm}$  (red) with  $P_{Kr}=150 \text{ bar}$ .

The geometry of the  $0.5 \times 5 \text{ mm}$  rectangular slit nozzle, illustrated in fig. D.2 has been adapted to longer slit nozzles of dimensions  $0.5 \times 10 \text{ mm}$  and  $0.5 \times 20 \text{ mm}$ . The density profiles obtained from those nozzles are presented in fig. 4.10 at a height of  $1.5 \text{ mm}$  with respect to the nozzle tip, and compared to the results for the  $5 \text{ mm}$ -long geometry. The figure shows the density drops as the nozzle length is increased by a factor corresponding to the ratio between sectional areas. Similarly, the density gradient decreases with an increase in the nozzle length



but remains decent for laser-plasma coupling, thus confirming the relevance of this rectangular nozzle geometry for longer slits.

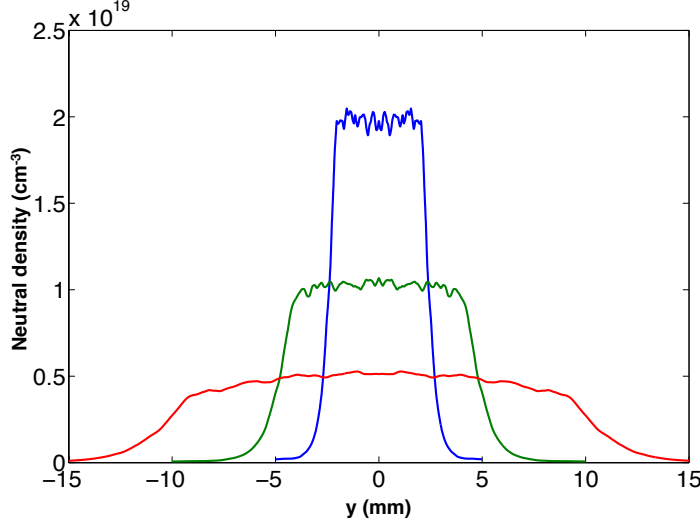


Figure 4.10: Simulated longitudinal density profiles at  $h = 1.5$  mm with  $P_{Kr}=150$  bar for nozzles of sectional areas  $0.5 \times 5$  mm (blue),  $0.5 \times 10$  mm (green) and  $0.5 \times 20$  mm (red).

#### 4.2.2 Experimental characterization of rectangular slit nozzles

**Characterization of the  $5\text{ mm} \times 500\text{ }\mu\text{m}$  rectangular slit nozzle.** The neutral densities of the gas jet at the output of the nozzle has been measured using a tomography technique (see Appendix E). The gas jet system is described in fig. 4.11. The obtained phase maps are presented in fig. 4.12. The longitudinal profile actually shows the consequence of a deformation of the slit on the gas flow. A narrower region of the slit results in a local higher density. The experimental conditions correspond to a backing pressure  $P_{Kr}=150$  bar, a valve opening time  $\Delta t_{ouv}=8$  ms and an acquisition of interferograms 12 ms after the closure of the valve.

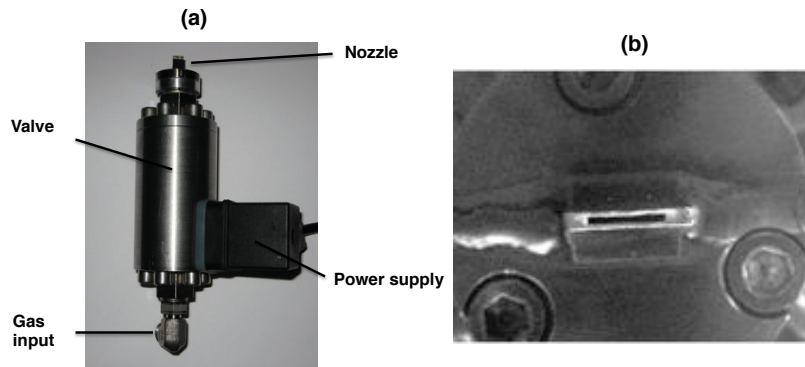


Figure 4.11: High-density gas jet system (a). A small ball closes the valve under pressure. Electro-magnets supplied by a 10 A current generate a sufficiently strong magnetic field to deviate the metallic ball and open the valve, thus liberating the gas flowing through the nozzle. (b) Top view of the  $5\text{ mm} \times 500\text{ }\mu\text{m}$  rectangular slit nozzle.

The fig. 4.13 shows the experimental evolution of the krypton density as a function of the height with respect to the nozzle slit outlet for a parametric study involving a variation of the backing pressure and the valve opening time window.

The fig. 4.14 presents the density profile under experimental soft X-ray lasing conditions. It corresponds to an optical axis located at a distance  $h = 1.5$  mm from the nozzle tip.

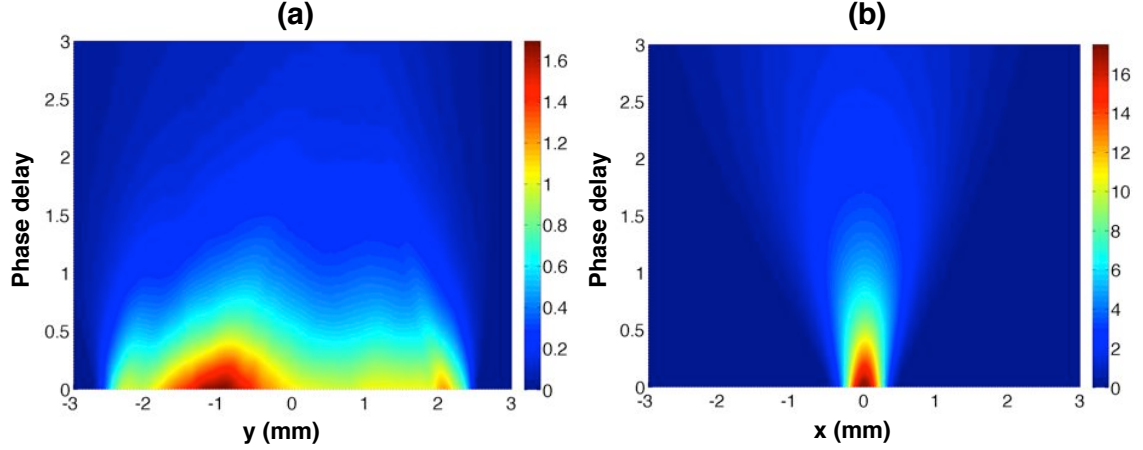


Figure 4.12: Phase maps in longitudinal (a) and transverse directions (b) reconstructed by tomography of the  $5 \text{ mm} \times 500 \text{ } \mu\text{m}$  rectangular slit nozzle, under a backing pressure  $P_{Kr}=150$  bar and for  $\Delta t_{ouv}=8$  ms.

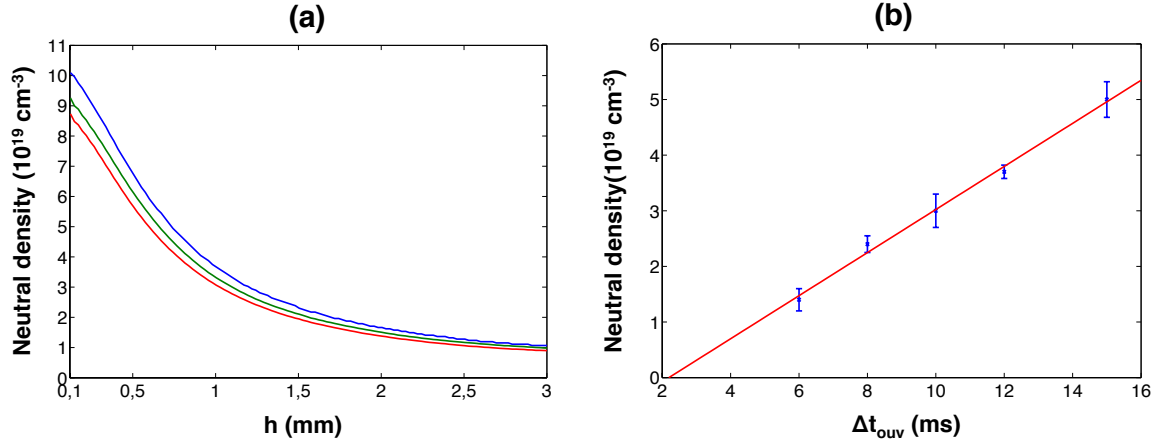


Figure 4.13: (a) Experimental dependence of the neutral krypton density on the height with respect to the nozzle tip for  $P_{Kr}=130$  bar (red), 140 bar (green) et 150 bar (blue) with  $\Delta t_{ouv}=8$  ms. (b) Variation of krypton neutral density as a function of the valve opening time.



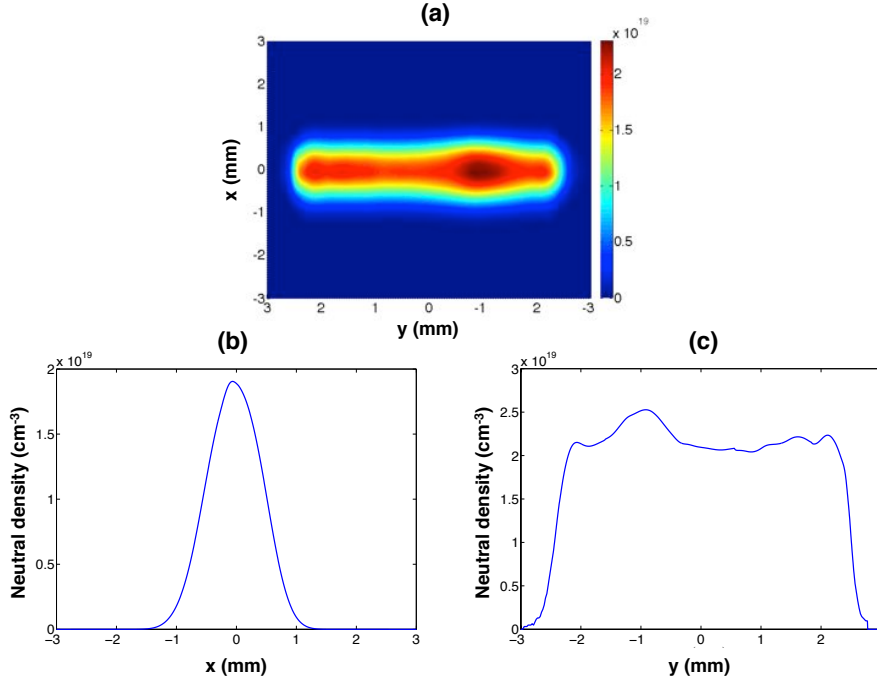


Figure 4.14: (a) Density map of krypton neutral density under nominal experimental conditions (i.e.  $h = 1.5$  mm). Transverse (b) and longitudinal (c) density profiles for  $P_{Kr}=150$  bar and  $\Delta t_{ouv} = 8$  ms.

**Characterization of « long » rectangular slit nozzles.** Working out long plasma amplifiers is an interesting focal area for two reasons. First, it promises an increase of the photon yield. Secondly, ASE emission from those sources is less divergent.

In this perspective, various rectangular slit nozzles have been manufactured and characterized. The fig. 4.15 illustrates the density gas jets for rectangular sectional areas of geometries  $10 \text{ mm} \times 200 \text{ } \mu\text{m}$ ,  $15 \text{ mm} \times 500 \text{ } \mu\text{m}$ ,  $20 \text{ mm} \times 500 \text{ } \mu\text{m}$  and  $30 \text{ mm} \times 500 \text{ } \mu\text{m}$ . Data correspond to a height  $h=1.5$  mm with respect to the nozzle tip. Data are presented using a calibrated color scales spreading in proportion of the nozzle lengths, in an attempt to better compare the expected density levels. The longitudinal profiles of density is homogeneous for nozzle lengths up to 15 mm long. For 20 and 30 mm lengths, the profile maintains relatively sharp density gradient at the input and output edges but exhibits a "cone shape" at the center. For 30 mm, the density at the center is nearly 3 times the value at the edges, thus highlighting the limitation of the used nozzle geometry for more elongated plasmas. Besides, the average density from the nozzles is observed to vary in the proportions of the outlet sections ratios.

All data are presented for a backing pressure  $P_{Kr}=150$  bar, a valve opening time  $\Delta t_{ouv}=8$  ms and acquisition time of 12 ms after the closure of the valve.

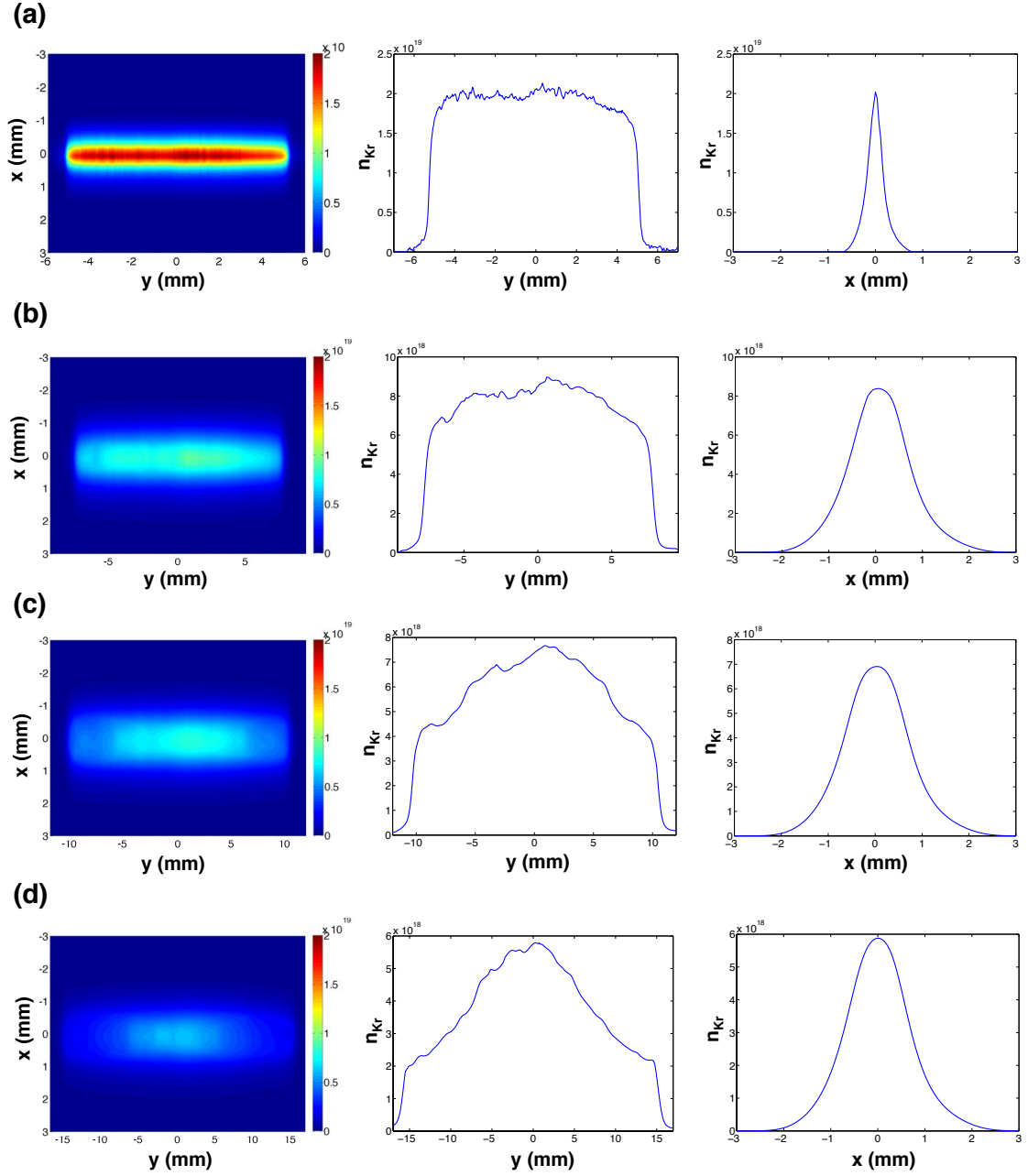


Figure 4.15: (a) Neutral density maps for rectangular slit nozzles of sectional areas  $10 \text{ mm} \times 200 \mu\text{m}$  (a),  $15 \text{ mm} \times 500 \mu\text{m}$  (b),  $20 \text{ mm} \times 500 \mu\text{m}$  (c) and  $30 \text{ mm} \times 500 \mu\text{m}$  (d).

## 4.3 Diagnostics

### 4.3.1 Waveguide diagnostics

#### Electron density diagnostic

The electron density is probed thanks to a Mach-Zehnder interferometer using a phase-retrieval technique (see Appendix E). This measurement, illustrated in fig. 4.16, yields single-shot interferograms displaying local phase shifts, which then allow reconstructing 2D electron density map of the waveguide. Because the transverse and longitudinal sizes of the plasma channel have very different dimensions (about  $100\ \mu\text{m} \times 5\text{mm}$ ), a double-arm system with two different magnifications (1 and 13.3) has been implemented. Due to the high electron density of the plasma, the frequency of the IR probe beam has been doubled using a BBO crystal (400 nm probe beam) to limit the effect of refraction and increase the highest measurable electron density of the plasma (the critical density at 400 nm is about  $7 \times 10^{21}\text{cm}^{-3}$ ). The interferograms are recorded by synchronizing the cameras with the laser.

The electron density profile is reconstructed via the local modification of the refractive index (i.e. of the relative phase between the two arms of the interferometer), which imparts a modification of the interferential pattern. An Abel inversion technique (see Appendix E) is then used to derive the plasma electron density maps from the phase shift maps.

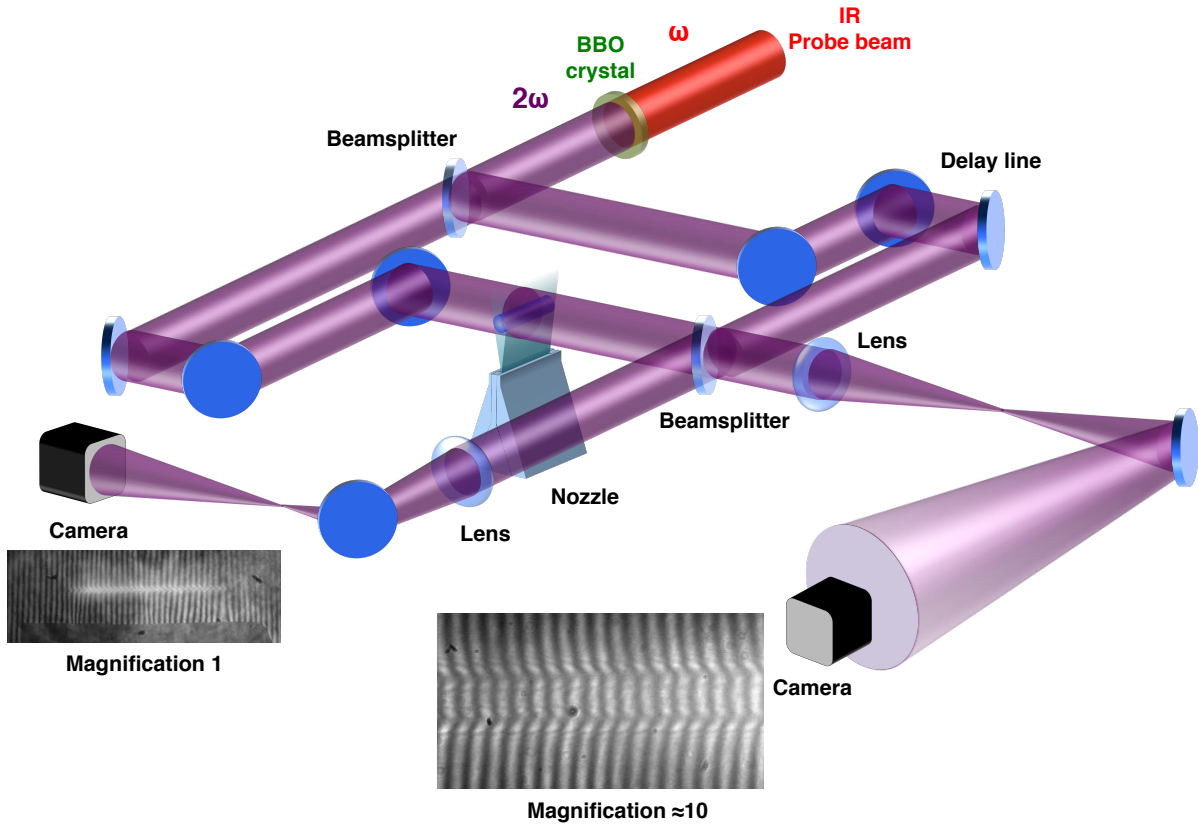


Figure 4.16: Illustration of the Mach-Zehnder interferometer with two imaging arms of different magnifications.

### Guiding efficiency diagnostic

The transmission of the IR pump beam by the plasma waveguide is pivotal to the optimal lasing of the high density elongated plasma. A low transmission due to a bad coupling between the pump beam and the plasma channel promises poor lasing. Indeed, in these conditions, refraction dominates and leads to a shortened medium filled with lasing ions. Furthermore, if the end of the plasma is weakly ionized, the emitted soft X-ray emission will be re-absorbed.

The quality and quantity of the guided driving pulse were assessed thanks to a system imaging the pump beam focus and the output of the waveguide at full energy (over 1 J) under vacuum. The imaging system is illustrated in fig. 4.17. The diameter of the optical components have been chosen be large enough to collect the entire laser signal after propagation through the plasma. The system has been set to avoid the deterioration of the optics and the beam is thus first attenuated using a set of two prismatic uncoated reflecting mirrors ("wedges"). Each mirror have about 4% reflectivity and will reject the main fraction of the laser energy.

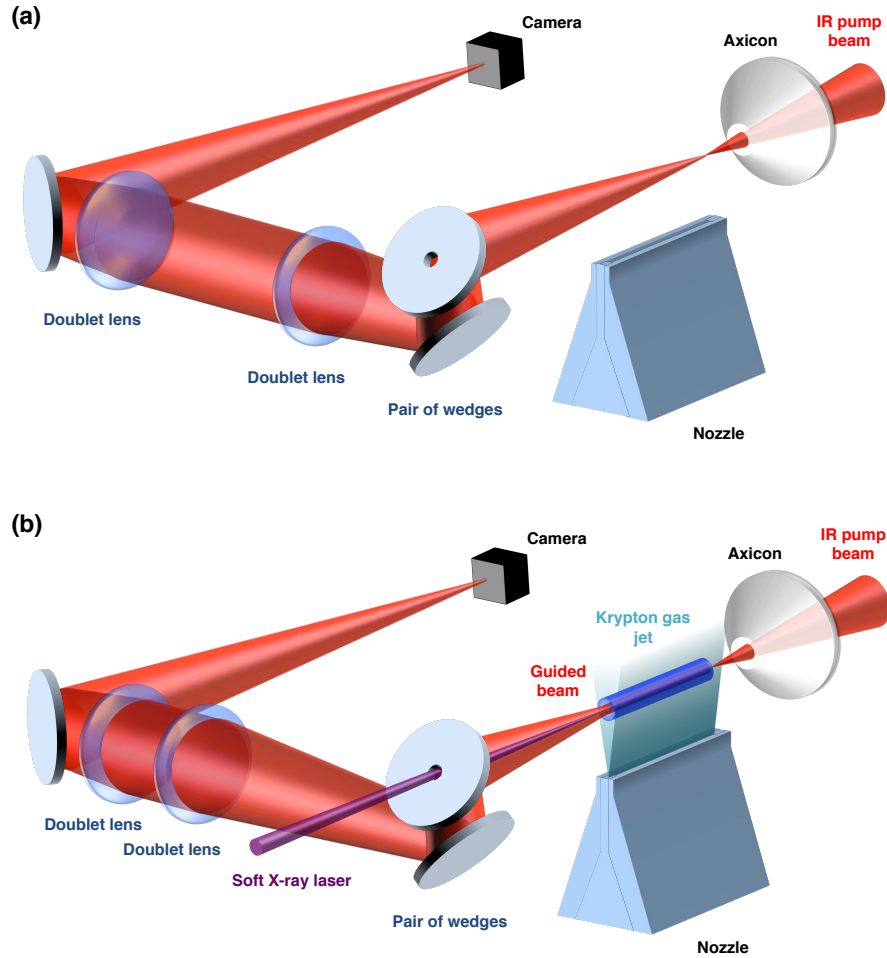


Figure 4.17: Experimental arrangement of the system of two doublet lenses used to successively image the pump beam focal plane and the output of the plasma channel. (a) The focal spot of the pump beam is imaged with no gas. (b) The energy distribution of the pump beam portion transmitted by the plasma channel is imaged translating the first doublet lens by the length of the plasma.

After attenuation, a set of two achromatic doublet lenses of the same focal length are used to image the output of the waveguide at the entrance of microscope objective coupled to a CCD camera. One of them is translatable to successively image the focal spot of the IR pump beam in vacuum and the profile of the guided IR pump beam at the output of the plasma amplifier. As the 1-1 magnification system features a collimated beam between the two lenses, the first doublet can be simply translated by a distance equal to the plasma length to image output profile of the IR beam.

### 4.3.2 Soft X-ray diagnostics

#### Spectra

The soft X-ray spectrometer consists of a  $\text{SiO}_2$  plane mirror, a gold-coated 400 mm-focal length spherical mirror at 77.5 and 80 degrees incidence respectively, along with a  $5\text{mm} \times 5\text{mm}$  grating with 1000 lines/mm and a soft X-ray 16 bit charge-coupled device (CCD) camera of  $2048 \times 2048$  pixels resolution. The spectra are observed at the tangential focus of the spherical mirror. The other direction shows the angular divergence of the source. Two light-tight  $0.16\mu\text{m}$  thickness Luxel aluminum filters each with total transmission of 45% have been used to select the soft X-ray signal from the IR. The setup is illustrated in fig. 4.18. The spectrometer resolution is about  $\Delta\lambda/\lambda \approx 5 \times 10^{-2}$ .

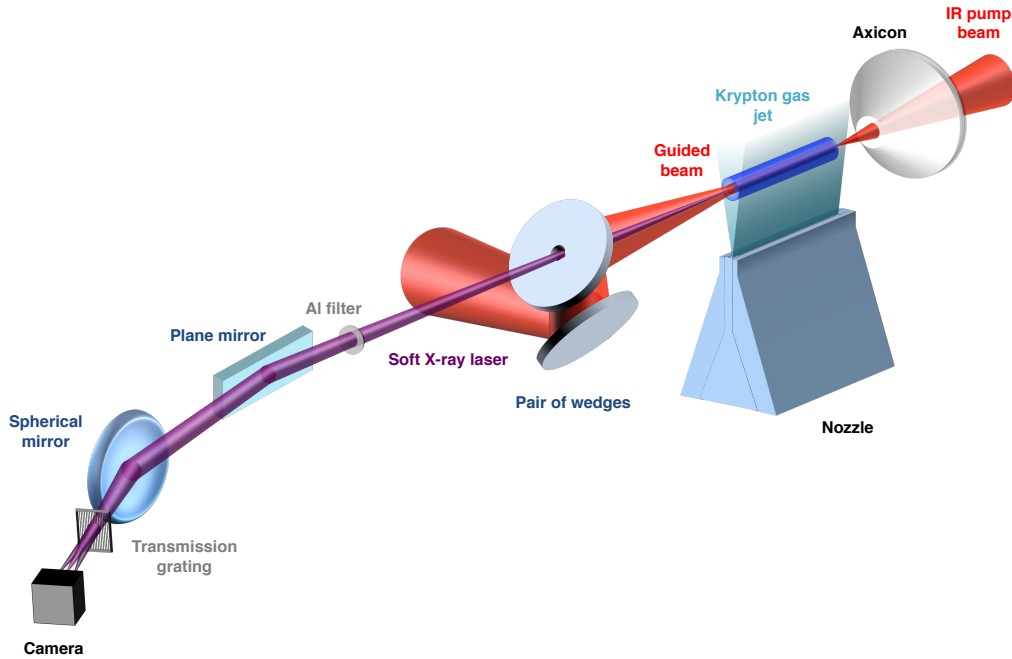


Figure 4.18: Experimental arrangement of the spectrometer.

### Far-field energy distribution

The energy distribution diagnostic is composed of a 25 degrees off-axis parabola of focal length 200 mm, a deflecting plane mirror at 80 degrees incidence and a soft X-ray camera of  $1024 \times 1024$  pixels resolution (see fig. 4.19). The system images a plane situated at the level of the filters, about 1.4 m from the soft X-ray plasma source with a magnification of 0.6. The interferential multilayer coating of the parabola designed to yield high reflectivity at 32.8 nm was deposited at Institut d'Optique, France. The reflectivities of the parabola and the grazing incidence are respectively, 25 and 15 %. Two aluminum filters of  $2 \times 0.4 \mu\text{m}$  and  $0.1 \mu\text{m}$  have been used to isolate soft X-ray radiation from IR radiation. The transmission of each filter has been assessed at 7 %.

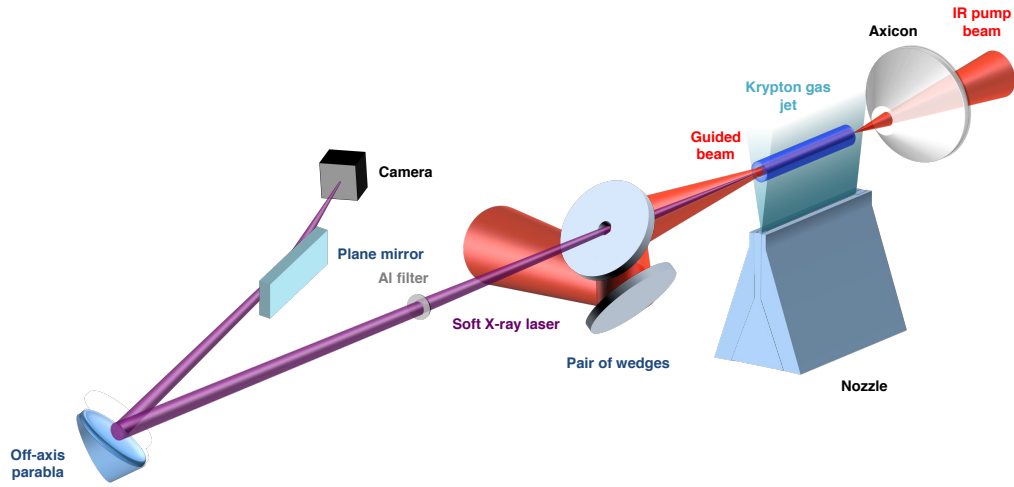


Figure 4.19: Experimental arrangement of the output energy distribution imaging setup.

## 4.4 Experimental results

### 4.4.1 Characterization of the plasma waveguide

#### Formation of the plasma channel

The timeline of the waveguide generation has been recorded for the  $0.5 \mu\text{m} \times 5 \text{ mm}$  slit nozzle under experimental conditions corresponding to a neutral krypton density of about  $10^{19} \text{ cm}^{-3}$ , i.e. at a height  $h=1.5 \text{ mm}$  with respect to the nozzle tip, with a backing pressure of 150 bar. The waveguiding beam is composed of a sequence of a short (130 mJ, 30 fs) and a long pulse (690 mJ, 600 ps). It is focused over the whole jet length thanks to an axiconic lens and creates, a plasma channel following collisional ionization and hydrodynamic expansion. The formation of this channel is being observed thanks to a probe beam at twice the laser frequency for better transmission in the highly dense medium. The electron density is measured with a Mach-Zehnder interferometer and an imaging system with a large magnification (about 13), to be able to resolve the very thin waveguide dimensions.

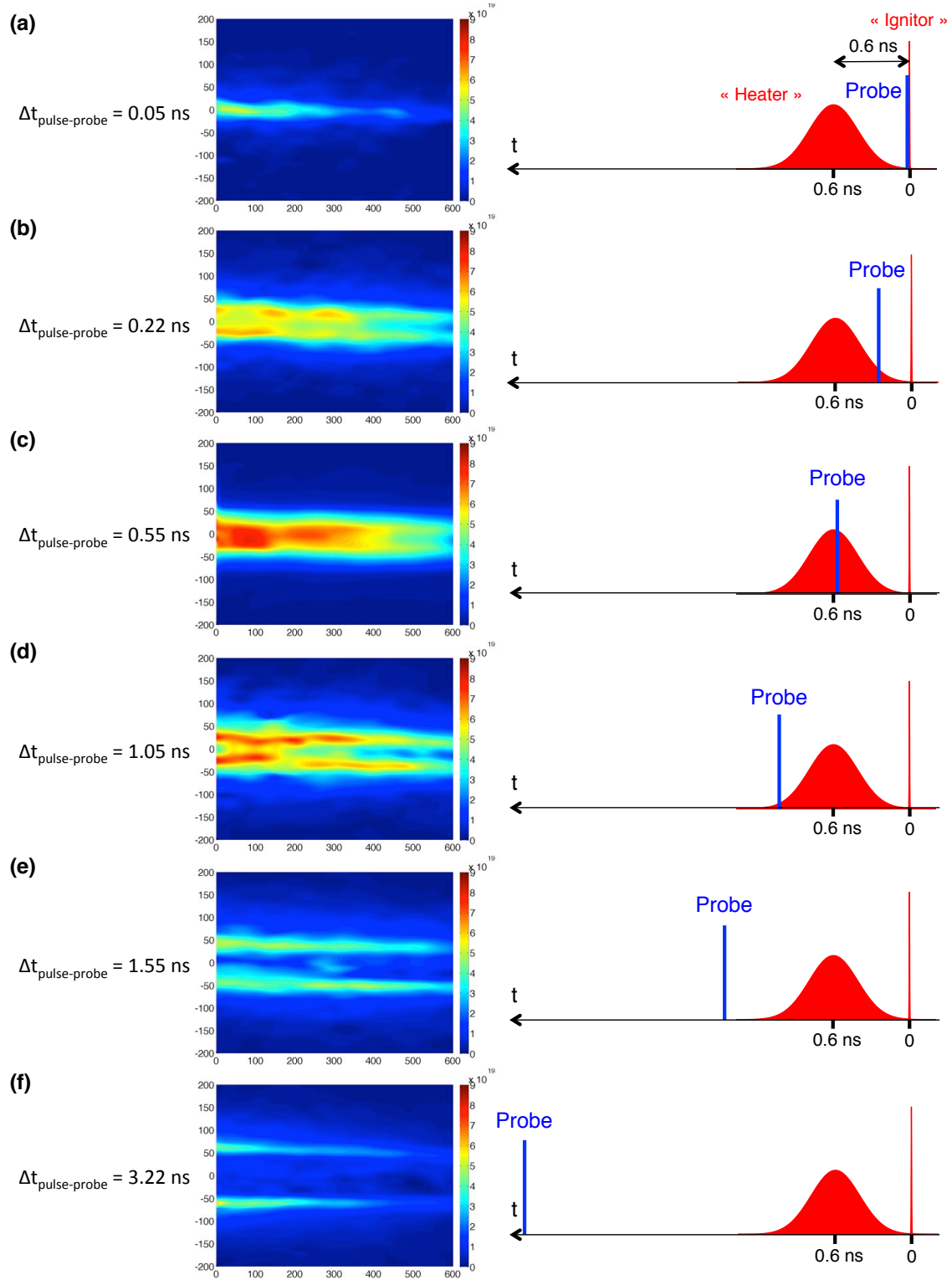


Figure 4.20: Generation of the plasma channel for various delays between the "ignitor" and the probe beam. The plasma region is observed in the middle of the 5 mm-long gas jet.

As illustrated in fig. 4.20, the first electrons are being created within the field (a). Heating and subsequent avalanche collisional ionization lead to an abrupt increase of the number of electrons (cases (b) and (c)). The heating process causes electrons to move out of the optical axis. The formation of the plasma channel is therefore being initiated just after the propagation of the long pulse (d). Then, the plasma expands on the nanosecond timescale (cases (e) and (f)).

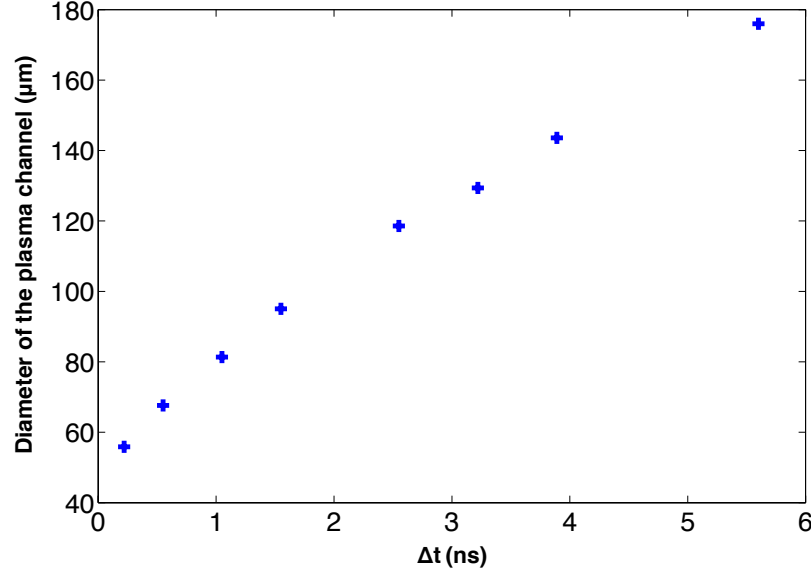


Figure 4.21: Evolution of the diameter of the plasma channel as a function of the delay between the waveguiding beam (i.e. the "ignitor") and the probe beam.

As reported in fig. 4.21, the plasma is found to expand at a speed of about  $23 \mu\text{m}/\text{ns}$ . Considering the acoustic speed of electrons in the medium from equation eq. (3.17), the electron temperature should be:

$$T_e \approx 230\text{eV} \quad (4.1)$$



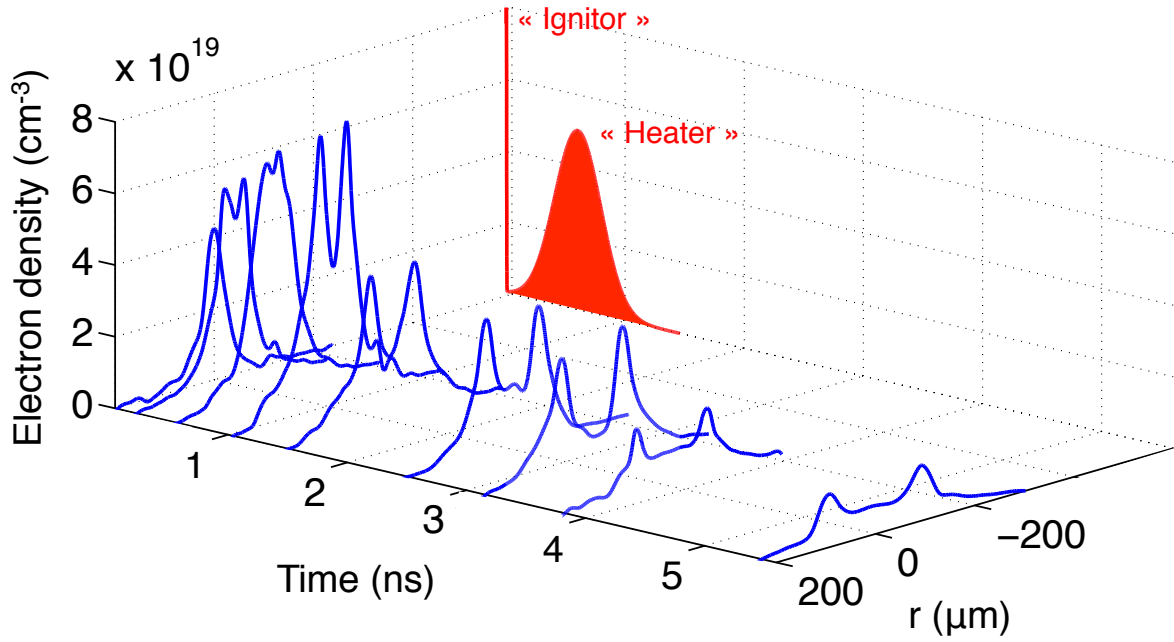


Figure 4.22: Radial distribution of electron density for the following time delays with respect to the "ignitor" pulse:  $\Delta t = 0.05$  ns,  $0.22$  ns,  $0.55$  ns,  $1.05$  ns,  $1.55$  ns,  $2.55$  ns,  $3.22$  ns,  $3.89$  ns and  $5.6$  ns.

The fig. 4.22 illustrates the the average electron density computed from the density maps obtained sampling the plasma at different delays with respect to the "ignitor". The electron density builds up for delays from  $\Delta t = 0.05$  ns to  $0.55$  ns, as first electrons generated by the "ignitor" get heated and foster avalanche collisional ionization. The delay  $\Delta t = 1.05$  ns corresponds to a moment at the end tail of the "heater". Hence, the electron density continues to rise but the central region gets depleted due to the beginning of plasma expansion. After the passage of the sequence of two pulses, the fig. 4.22 shows the expansion of the plasma channel for delays  $\Delta t = 1.05$  ns,  $1.55$  ns,  $2.55$  ns,  $3.22$  ns,  $3.89$  ns and  $5.6$  ns. The plasma channel spreads out and the density gradient plummets. For  $\Delta t = 1.05$  ns, the on-axis electron density is  $4 \times 10^{19} \text{ cm}^{-3}$  and rises up to  $7.7 \times 10^{19} \text{ cm}^{-3}$  off-axis for a channel diameter of about  $50 \mu\text{m}$ . By contrast, for  $\Delta t = 5.6$  ns, the on-axis electron density is  $8 \times 10^{18} \text{ cm}^{-3}$  and rises up to  $1.5 \times 10^{19} \text{ cm}^{-3}$  off-axis for a channel diameter of about  $180 \mu\text{m}$ .

The fig. 4.23 shows how the electron density of the plasma channel varies as the height of the optical axis with respect to the nozzle tip is modified. The plasma region is observed at the center of the gas jet. The black curve corresponds to normal operating conditions at a height  $h = 1.5$  mm with a backing pressure of  $150$  bar for a delay  $\Delta t = 2.55$  ns with between the "ignitor" and the probe beam. The red and blue curves depict the channel transverse density for heights  $h = 1.3$  mm and  $h = 1.1$  mm respectively. As the height decreases and the neutral gas density increases, the off-axis electron density maxima increase faster than the on-axis density and the channel expands to a lesser extent. This leads to a higher density gradient in the channel when shooting closer to the nozzle.

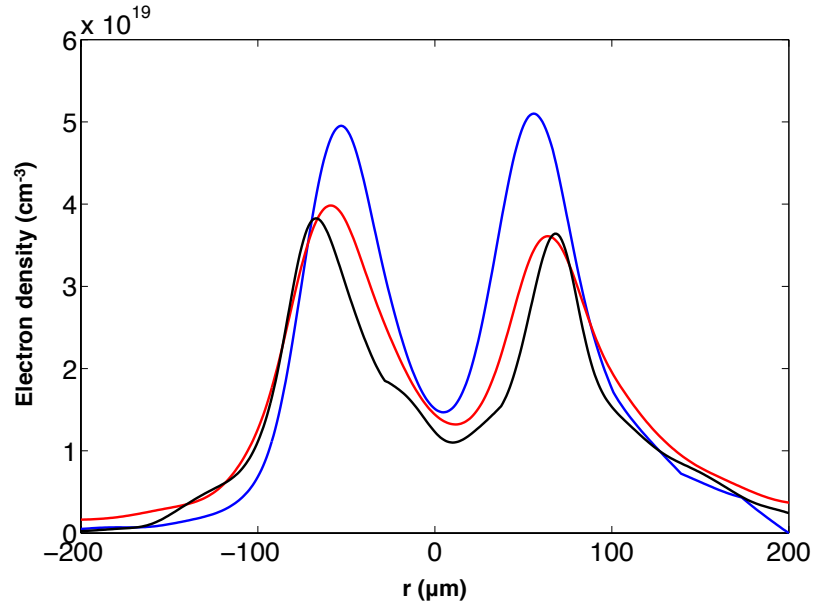


Figure 4.23: Radial distribution of the plasma channels following the hydrodynamic expansion of the waveguide. The data correspond to distances between the nozzle tip and the zone of interaction of 1.5 mm (black), 1.3 mm (red) and 1.1 mm (blue).

### Plasma amplifier density

The fig. 4.24 shows the interferograms obtained using the two different magnifications of the Mach-Zehnder interferometer (see fig. 4.16). The fig. 4.24a shows that a uniform plasma channel is generated over the whole 5 mm gas jet length. Self-emission from the plasma is observed along the channel with white blur on the deflected fringes. This emission has been cut placing a filter isolating the probing wavelength at  $2\omega$ . The fig. 4.24b illustrates the strong over ionization-induced refraction of the pump beam at the beginning of the plasma channel. A large magnification (x13.3) was necessary to resolve the plasma channel transverse dimension along with its sharp density gradients on the edges. The interferograms in fig. 4.24c & d obtained with a large magnification correspond to a zone of about  $400\mu\text{m}$  by  $700\mu\text{m}$  observed at the beginning of the plasma channel.

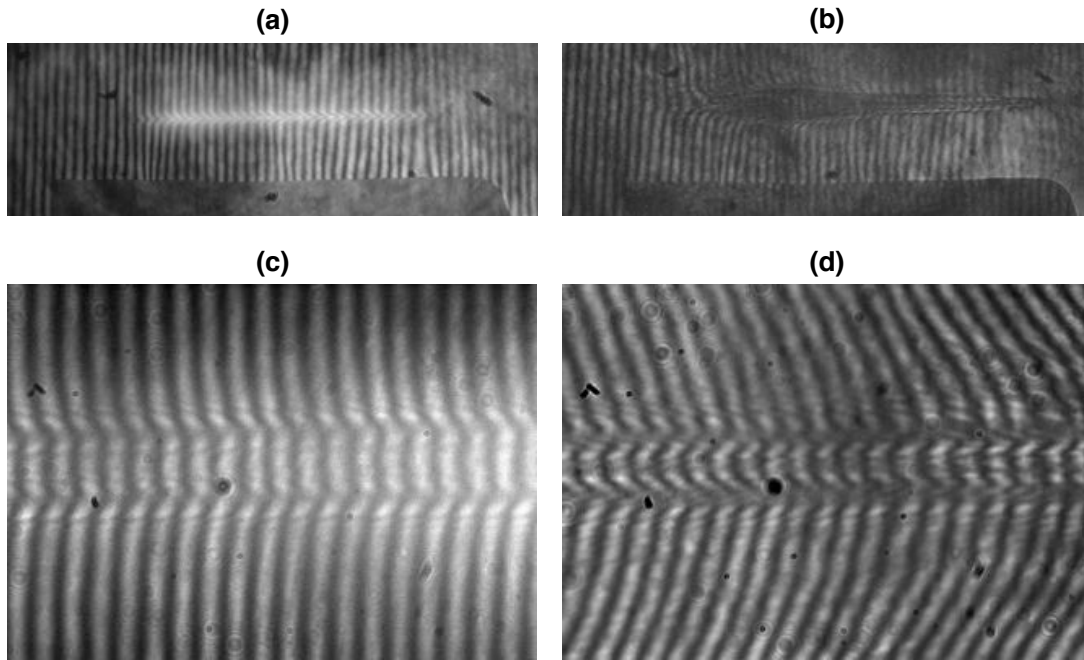


Figure 4.24: Interferograms of the plasma channel with a magnification of 1 (a) and 13 (c). Interferograms of the plasma with the pump beam being guided through the plasma channel with a magnification of 1 (b) and 13 (d). The laser pulses propagate from the left to the right.

The fig. 4.25 shows the electron density maps over a length of  $300\mu\text{m}$  in case of the plasma channel alone (fig. 4.25a) and the plasma amplifier, when the pump beam is guided (fig. 4.25b). Both measurements correspond to the probed zone at the center of the plasma waveguide. Those were obtained for optimal guiding at the highest demonstrated plasma density, i.e. for a pump beam focused about 1.55 ns after the arrival of the "ignitor".

The plasma channel features a parabolic transverse profile with a  $80\mu\text{m}$  wide plasma channel. The electron density varies from  $1.5 \times 10^{19}\text{cm}^{-3}$  on-axis to  $5 \times 10^{19}\text{cm}^{-3}$  off-axis, as shown in fig. 4.25a. The average electron density in the waveguide is considered to be  $2.5 \times 10^{19}\text{cm}^{-3}$ . The average electron density of the amplifier was measured 10 ps after the arrival of the pump beam (fig. 4.25b). We can reasonably consider that  $Kr^{8+}$  lasing ions lie within the waveguide. As the on-axis region is over-ionized, the amplifier electron density is deemed to be the average value and reaches  $2 \times 10^{20}\text{cm}^{-3}$ . Because of on-going collisional ionization, this density corresponds

to an over 60% increase of the actual electron density of  $1.2 \times 10^{20} \text{ cm}^{-3}$  at which the lasing action takes place, because of the on-going collisional ionization reported in fig. 2.16 (dotted blue curve). The "top view" of the electron density map of the plasma amplifier shows that, despite the strong overionization in the first millimeter of propagation, the edges of the plasma channel structure are being maintained, which allows the efficient guiding of the pump beam over the whole gas jet length.

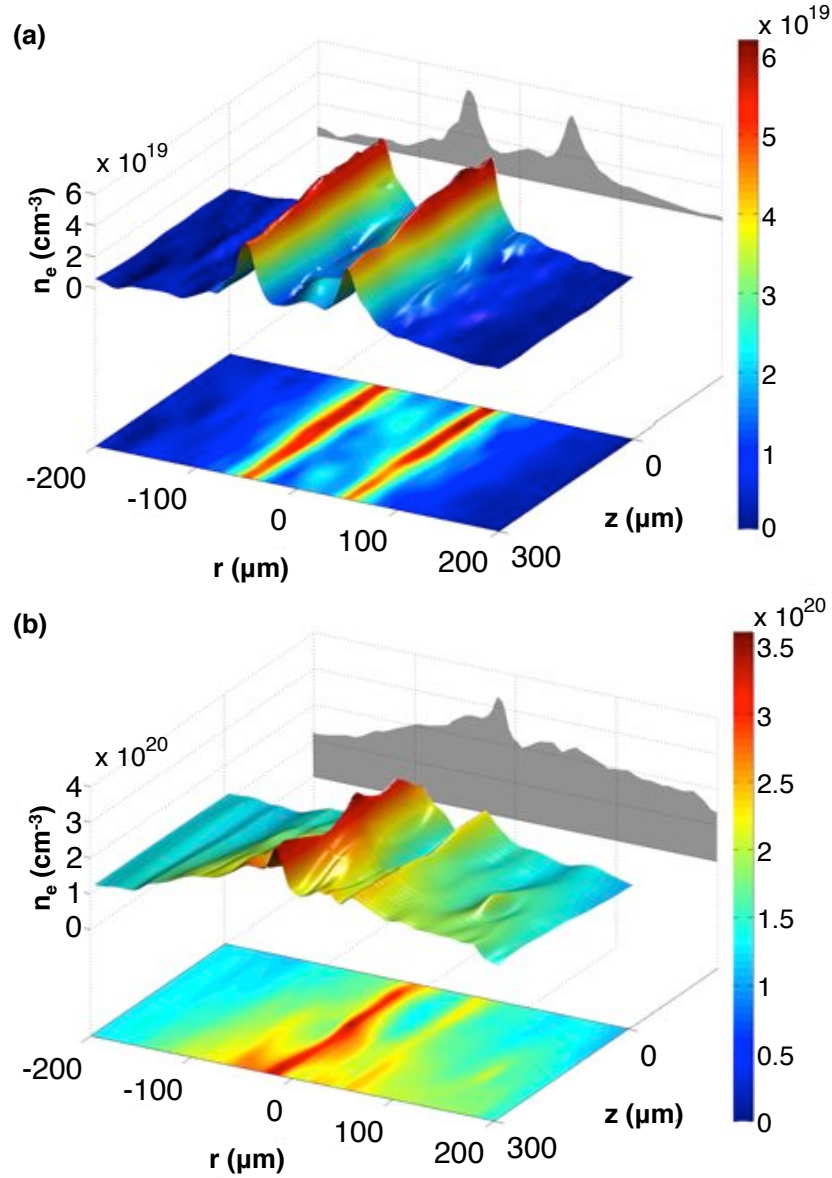


Figure 4.25: Experimental 2D electron density map of the waveguide with a 1.55 ns delay between the main pulse and the "ignitor" (a) and probed 10 ps after the arrival of the pump beam (b).

#### 4.4.2 Guiding efficiency

The fig. 4.26 shows the energy distribution of the pump beam at the focal spot (fig. 4.26a) and at the output of the plasma channel (fig. 4.26c) in the case of the 5 mm-long high-density plasma amplifier illustrated in fig. 4.25. When no waveguide is implemented, the driving beam is strongly refracted and a very weak and divergent IR signal is measured (fig. 4.26b). The transmitted part of the IR pump beam remains more or less collimated after a few Rayleigh lengths. A transmission of about 45% is reported. Losses mainly come from the coupling of the pump beam into the waveguide, as well as the initial strong refraction imparted by the strong ionization at the focus. When there is no waveguide, the pump beam is strongly defocused mainly because of ionization-induced refraction, whose impact is predominant at high electron densities (see fig. 4.26). The transmission is therefore far below 1% and no lasing is observed.

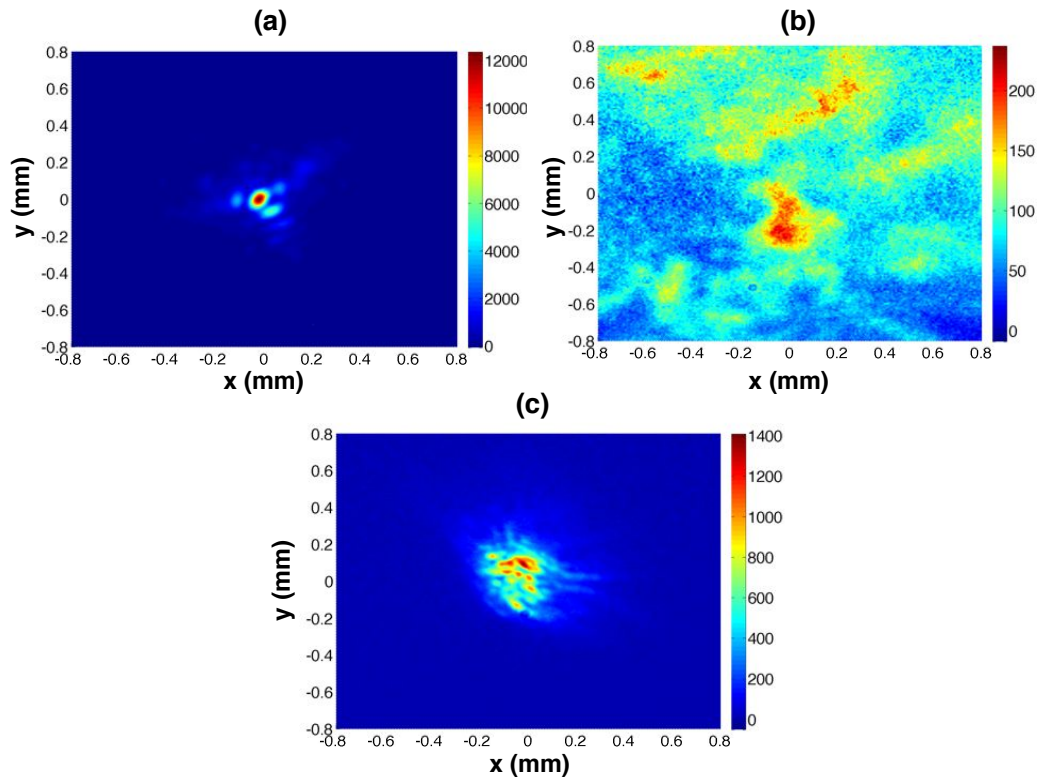


Figure 4.26: Energy distribution of the IR pump beam focal spot at full energy (1.36 J) in vacuum (a) and at the output of the high-density plasma amplifier without (b) and with (c) the waveguide.

The fig. 4.27 shows the value of transmissions corresponding to various delays between the waveguiding beam (i.e. the "ignitor") and the driving laser pulse. For a delay of 1 ns between the "ignitor" and the "pump beam", the plasma channel is at its early stages of hydrodynamic expansion and its transverse diameter is only about  $1.5 w_0$  ( $w_0$ , laser waist). Simulations (section 3.2.3) showed that channel transverse sizes below  $2 w_0$  impart initial coupling losses, thus lowering the transmission of the driving pulse. A high transmission as high as 45 % is measured for a delay of 1.55 ns when the channel transverse size is about  $2 w_0$ . When the plasma channel further expands, the waveguide transmission only slightly increases. Indeed, a larger channel diameter improving the coupling efficiency in size is now counterbalanced by lower density gradients (see fig. 4.22), which decrease the coupling efficiency for the numerical aperture. Therefore, further plasma expansion virtually does not improve the overall waveguiding efficiency and only results in a decrease of the electron density (see fig. 4.22), which decreases the output photon yield.

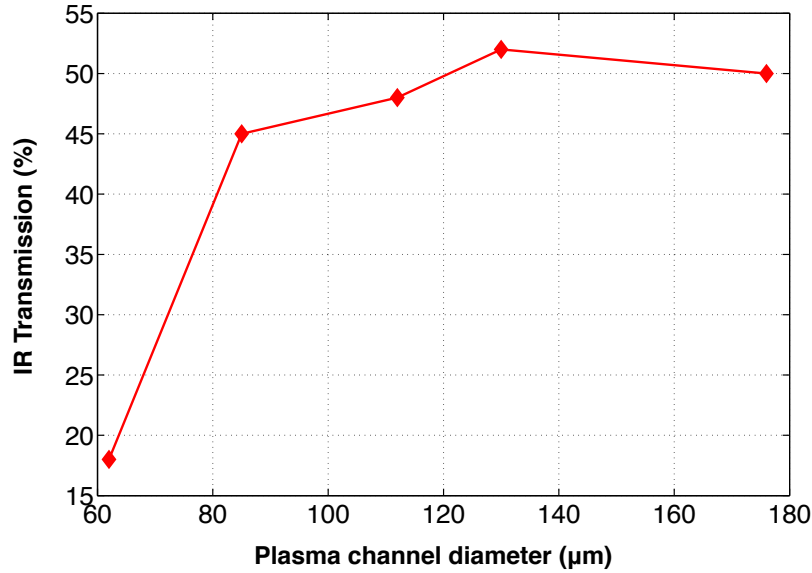


Figure 4.27: Transmission of the pump beam for waveguides corresponding to different transverse diameters of the waveguide.

The fig. 4.28 displays the pump beam transmissions for 5 mm, 10 mm, 15 mm, 20 mm and 30 mm-long waveguides, as well as the patterns of the focal spot and the beam profiles of the IR pump beam at the output of the waveguides. All measurements were carried out with the same axicon lens achieving a 35 mm-long focal line. The delays between the waveguiding and pump beams, along with the gas density (by moving the nozzle closer or further from the optical axis) have been adjusted to maximize the output photon yield (see fig. 4.38). The electron densities for the 5 mm, 10 mm, 15 mm and 20 mm-long plasma channels were respectively  $n_e = 1.2 \times 10^{20} \text{ cm}^{-3}$ ,  $9 \times 10^{19} \text{ cm}^{-3}$ ,  $5.5 \times 10^{19} \text{ cm}^{-3}$ ,  $3.4 \times 10^{19} \text{ cm}^{-3}$  and  $2.6 \times 10^{19} \text{ cm}^{-3}$ .

The output pattern of the pump beam remains fairly collimated for the 5 mm, 10 mm, 15 mm and 20 mm-long channels. The waveguide transmission first significantly decreases to 45 % for the 5 mm-long channel because of the coupling losses. Then, the transmission decreases almost linearly up to a length 20 mm. For the 30 mm-long channel, the transmission drops sharply, probably because the focal line did not well coincide with the gas jet over the whole length. Besides, the pattern looks defocused because it was mechanically not possible to move the doublet lens to image the plane at the output of the 30 mm-long waveguide.

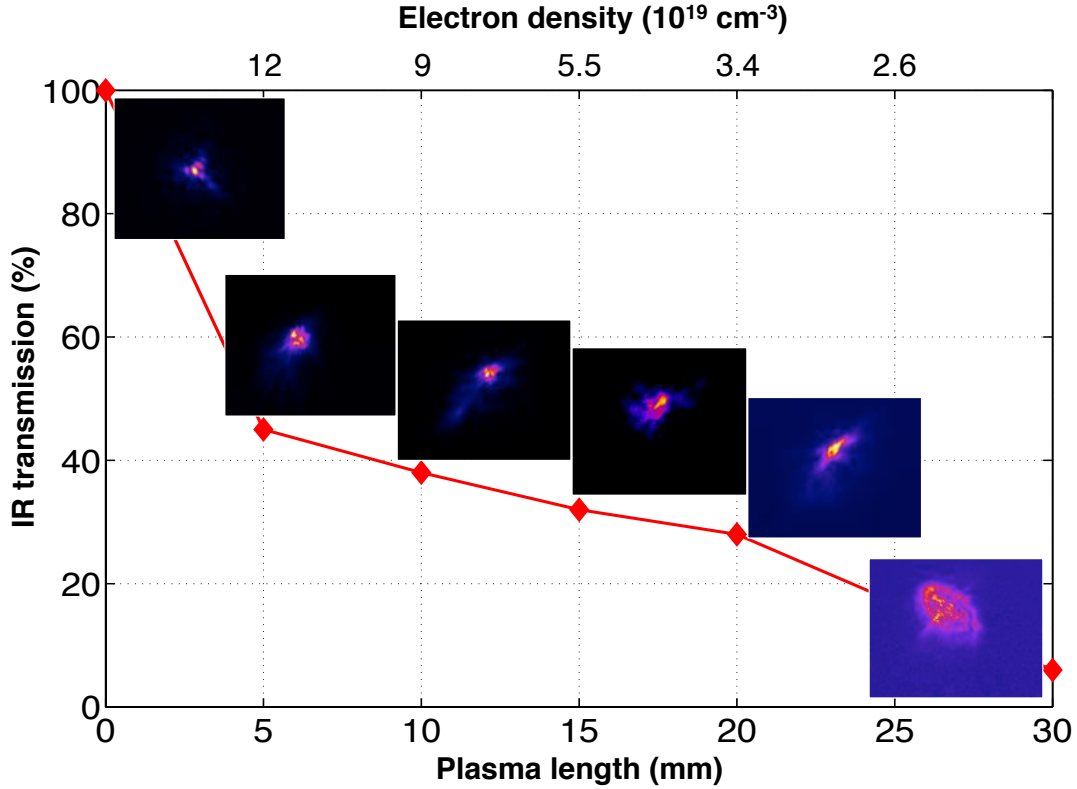


Figure 4.28: Transmissions of waveguides with different lengths.

### 4.4.3 Characterization of the soft X-ray laser emission

#### Spectra

When no plasma channel is used to help the driving beam to propagate into the elongated plasma, no lasing line is observed, as shown in fig. 4.29a. Just a faint zeroth order is recorded, corresponding to emission from a pre-plasma. The end of the plasma is weakly ionized because of the strong refraction of the beam at the beginning. Emission from the beginning of the plasma thus gets absorbed. We can notice the edge of the aluminum filter bandwidth, which cuts the signals below 17 nm. Advantageous guiding conditions allowed strong amplified spontaneous emission from the plasma. The recorded signal is presented in fig. 4.29b. It consists of a saturated zeroth-order emission line and a strong emission line in the grating first order at 32.8 nm. The secondary peaks observed on both sides of the main lines are diffraction patterns from the supporting grid of the grating. This arrangement however does not allow to see the very narrow linewidth of the plasma amplifier ( $\Delta\lambda/\lambda \approx 10^{-5}$ ).

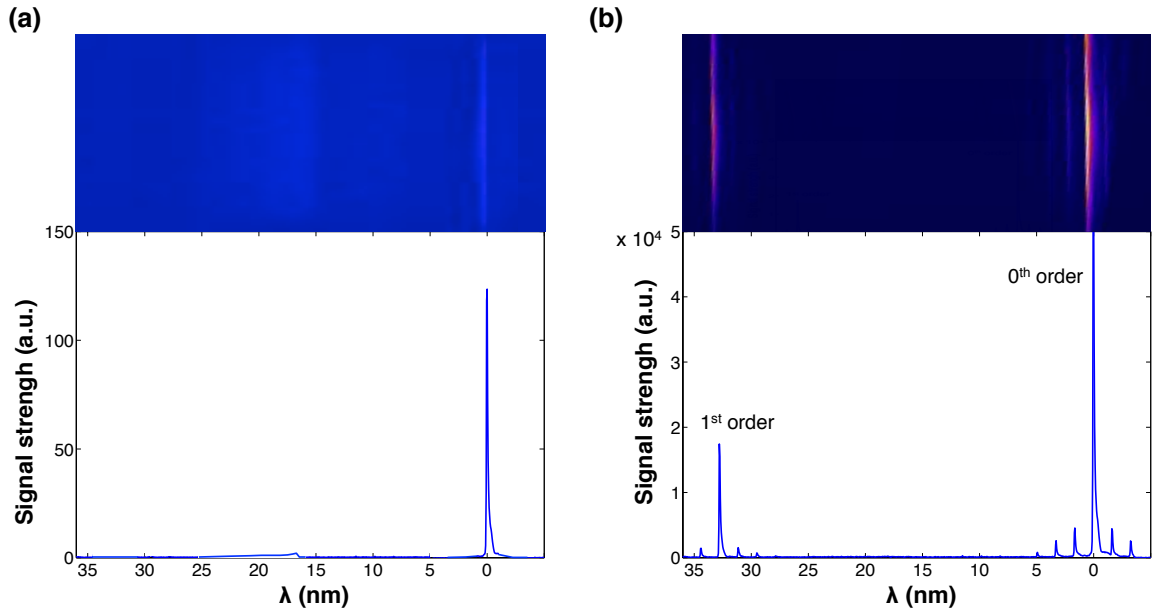


Figure 4.29: Single-shot recorded spectra of the amplified spontaneous emission from a 5 mm-long plasma operating at  $n_e = 1.2 \times 10^{20} \text{ cm}^{-3}$  with no waveguide (a) and with a waveguide (b).



### Far-field energy distribution

The fig. 4.30 depicts the energy distribution of the soft X-ray amplified spontaneous emission from the plasma. The reported beam profile corresponds to an amplifier electron density of  $n_e = 9 \times 10^{19} \text{cm}^{-3}$ . We can notice that the spatial profile is strongly divergent (over 10 mrad) and is cut by the aperture defined by the filters' diameter. Moreover, the ASE emission profile is inhomogeneous and features "hot points". Those are speckle patterns and arise from the fact that the plasma is composed of a set of secondary sources displaying a good temporal but low spatial coherence [Guilbaud, 2005; Guilbaud et al., 2006]. Those secondary sources interfere and give rise to those over-intensity structures.

The annular shape of the far field beam profile can be explained by refraction of the soft X-rays because of the plasma density profile with a higher on-axis density and sharp density gradients on the edges. We can notice that the fact that  $Kr^{8+}$  lasing ions may preferentially populate off-axis zones of the plasma amplifier (as illustrated in simulations in fig. 3.13c) cannot explain the observed profile since far-field emission from an annular zone results in a profile filled in the center.

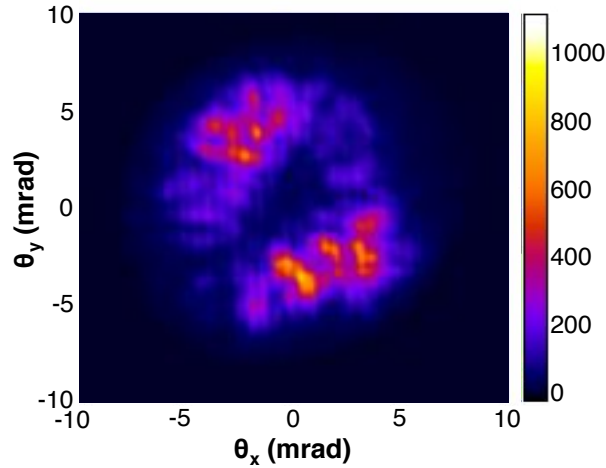


Figure 4.30: Output beam profile of the ASE emission from a 10 mm-long plasma with  $n_e = 9 \times 10^{19} \text{cm}^{-3}$ .

Recording the output spatial profile allows calibrating the photon yield and the energy emitted from the plasma. The number of recorded photons depends on the camera quantum efficiency, its gain, the transmission/reflectivities of the filters/optics and the number of counts on the CCD chip. One electron-hole pair is created with 3.65 eV of incoming energy. The number of photons can be therefore assessed with the following formula:

$$N_{ph} = \frac{3.65gN_c}{\eta RTE_{ph}} \quad (4.2)$$

where  $N_c$  is the number of counts,  $g$  the camera gain,  $\eta$  the quantum efficiency,  $T$  the transmission of the filters,  $R$  the reflection factor of optics used to record the signal and  $E_{ph} = 37.8 \text{ eV}$  the energy of one photon. At this energy, the quantum efficiency  $\eta$  is about 40 %. Counter-intuitively, a high gain corresponds to a bigger recorded signal. For photons at energies of 37.8 eV, 10 electron-hole pairs are created. The integration of the recorded signal in fig. 4.30 leads to a photon yield of  $8.4 \times 10^{11}$  photons per pulse, which corresponds to an energy exceeding  $4.9 \mu\text{J}$ . The source brilliance can be estimated in the order of  $10^{24} \text{phot/s/mrad}^2$ , considering a pulse duration of 100 fs.

### Influence of the pump beam energy, duration and polarization

Aside from the coupling between the pump beam and the pre-formed plasma waveguide, the lasing action strongly depends on the pump beam parameters affecting the laser-plasma interaction, such as its energy, duration and polarization.

- Position of the pump beam focus:

The longitudinal position of the focus strongly determines the output SXRL signal strength. Indeed, an optimal coupling of the pump beam into the pre-formed waveguide should be ensured to minimize losses and thus efficiently fill the whole plasma length with lasing ions. The fig. 4.31 shows the evolution of the ASE signal in case of a 10 mm-long plasma with an electron density of  $n_e = 7 \times 10^{19} \text{ cm}^{-3}$  for different positions of the focus, whose distance is defined from the entrance of the gas jet. When the IR laser beam is focused at the entrance of the gas jet, the pump beam is well coupled into the waveguide and its transmission is optimal. The best lasing configuration is found for a focus situated 3 mm within the gas jet from its entrance. In this position, lasing ions can be created before and after the focus where the medium is overionized, while keeping a good transmission of the IR pump beam by the waveguide. For focus positions over 3 mm, the IR beam at the entrance of the gas jet is large and the waveguide IR transmission thus decreases because of bad laser-plasma spatial coupling.

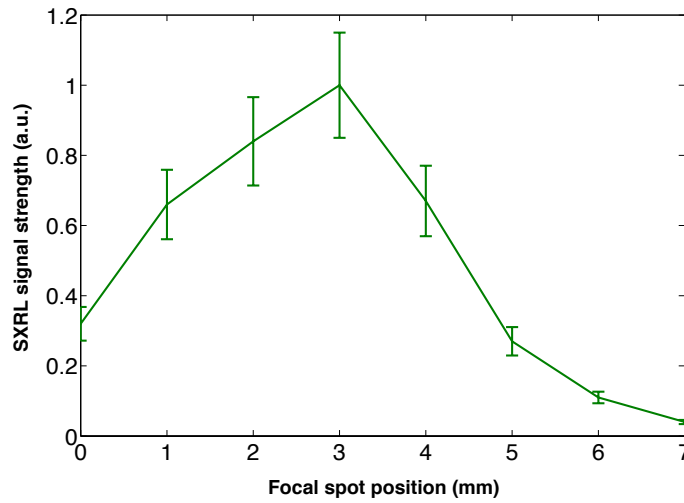


Figure 4.31: Variation of the total ASE signal strength for various positions of the focal spot with respect to the entrance of the gas jet.

The fig. 4.32 displays the energy distribution of the ASE signal as the position of the focus is altered. The beam profile turns out different with various emission divergences ranging from 5 mrad (fig. 4.32e) to 10 mrad (fig. 4.32c). The strongest lasing configuration is found when the ASE emission exhibits the biggest divergence (fig. 4.32c). The beam has an annular shape because of strong on-axis over-ionization or because of high density gradients defocusing the soft X-rays. The lowest divergence for focal positions at 1, 2 and 3 mm from the gas jet entrance can be explained by a geometrical effect. The emission occurs within a cone, whose base at the output has basically the dimensions of the waveguide and whose summit is located at the position of the focus. This solid angle is smaller for focal positions closer to the gas jet entrance. For a focus situated after 3 mm, the divergence

diminishes probably because the waveguide transmission of the pump beam plummets and lasing ions are therefore generated essentially on-axis.

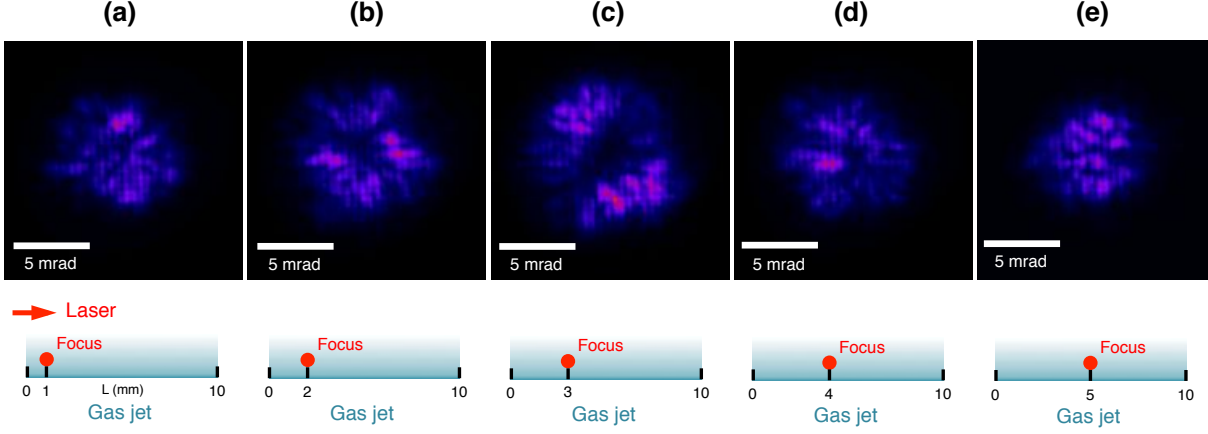


Figure 4.32: Energy distributions of the output ASE signal for a 10 mm-long plasma for a focal spot at 1 mm (a), 2 mm (b), 3 mm (c), 4 mm (d) and 5 mm (e) from the entrance of the gas jet.

- Pump beam energy and polarization: As displayed in fig. 2.3, the ionization threshold of the  $Kr^{8+}$  is  $3.1 \times 10^{16} W/cm^2$ . Regarding the available pulse intensity on target at full power, this means that there is more than one order of magnitude margin on the pump beam energy before lasing action should stop. The fig. 4.33a shows an exponential-like decrease of the recorded signal as the pump beam energy is progressively weakened. As far as the polarization is concerned, a circularly polarized pump beam turns out more efficient at producing a greater amount of hot electrons needed to pump the laser transition (see section section 2.1.3). Hence, a  $\lambda/4$  waveplate is used to get circular polarization from an initially p-polarized beam. The fig. 4.33b shows the dependence of the output SXRL emission with respect to the polarization of the pump beam. The angle "0" corresponds to the optimized signal for circular polarization. The angle "45 degrees" will correspond to linear polarization. Using a circularly polarized pump beam allows increasing the signal by about one order of magnitude.

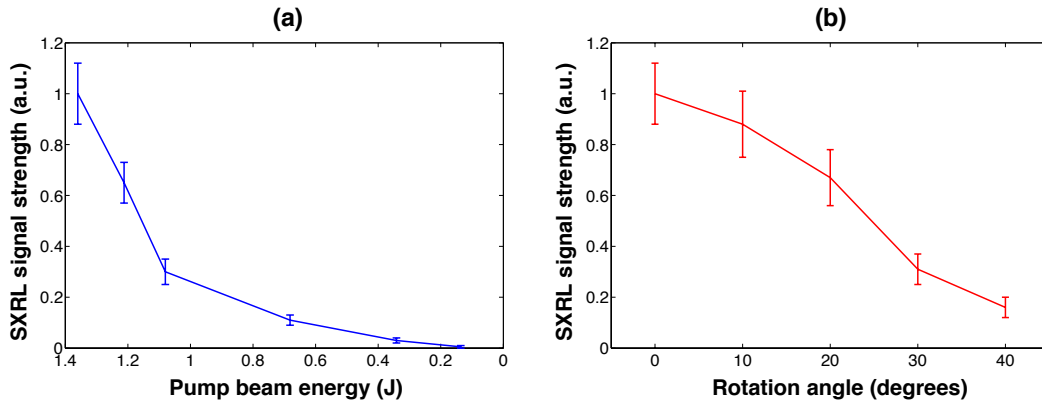


Figure 4.33: (a) Dependence of the SXRL signal strength with respect to the pump beam energy. (b) Influence of the pump beam polarization on the soft X-ray laser emission.

- Chirp of the driving laser:

The duration of the pump beam is obviously very important, as it determines the beam intensity on target. In the best compression conditions, the pump beam pulse duration was 28 fs. The variation of the output SXRL signal strength has been investigated altering the second-order spectral phase of the pulse. This quadratic term corresponds to a linear shift of frequencies, or a so-called "chirp". The various wavelengths within the IR pulse spectrum each have a different propagation time and the duration of the pulse is therefore altered. Chirping the IR pulse was performed by varying the distance between the pair of gratings of the compressor. This results in a change in the pulse duration delaying the spectral components with respect to each other. In case of "positive chirp", when the higher frequencies sit in the leading edge of the laser pulse, the output signal strength was found to be maintained up to an equivalent pulse duration of 295 fs, whereas the signal dropped sharply with "positive chirp". In the former case, the higher frequencies contained in the IR pulse spectrum catch up the lower ones over the propagation in the plasma. As a result, this phenomena can be understood by the fact that a "positive chirp" allows pre-compensating the negative dispersion in the plasma.

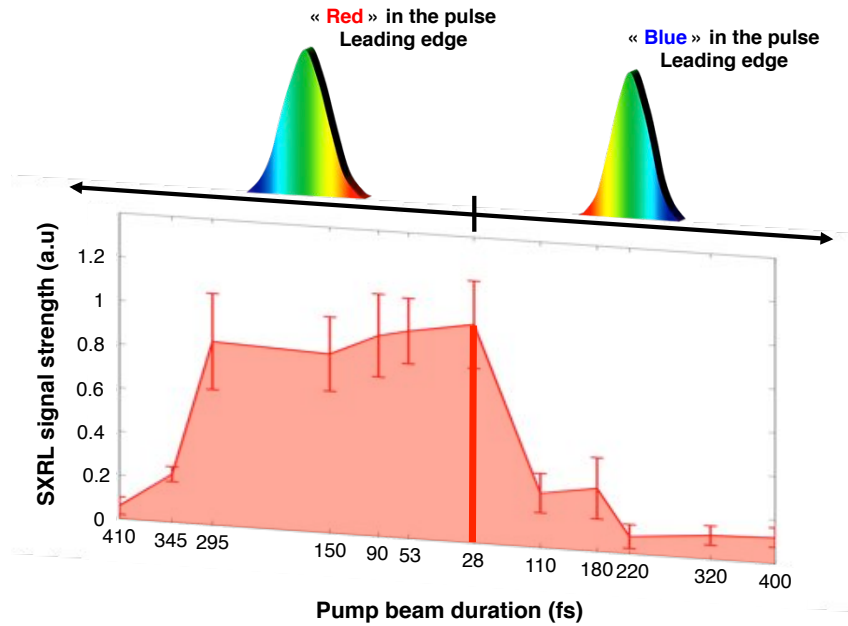


Figure 4.34: Variation of the SXRL signal strength (a.u.) as the pump beam is chirped.

However, this explanation does not fully account for the observed trend. Indeed, the group velocity in plasma for a frequency component at  $\omega$  is given by:

$$v_g = c * \sqrt{1 - \frac{\omega_p^2}{\omega^2}} \quad (4.3)$$

Considering a plasma with a uniform electron density of  $10^{20} \text{ cm}^{-3}$  and a IR spectrum between 760 and 860 nm, the delay between frequency components imparted by the plasma will be 132 fs over a propagation distance of 5 mm. To this extent, the observed optimum

for the minimum duration remains unclear. The maximized SXRL signal strength may not correspond to the shortest pulse duration of the driving laser beam.

### Soft X-ray laser signal strength vs plasma density

According to simulations conducted with OFI-0D code and presented in chapter 2, a rise in electron density is accompanied by an increase in saturation intensity (cf. fig. 2.19) and a small rise of the gain coefficient (cf. fig. 2.16). This results from the increased number of emitters responsible for a higher stimulated emission rate.

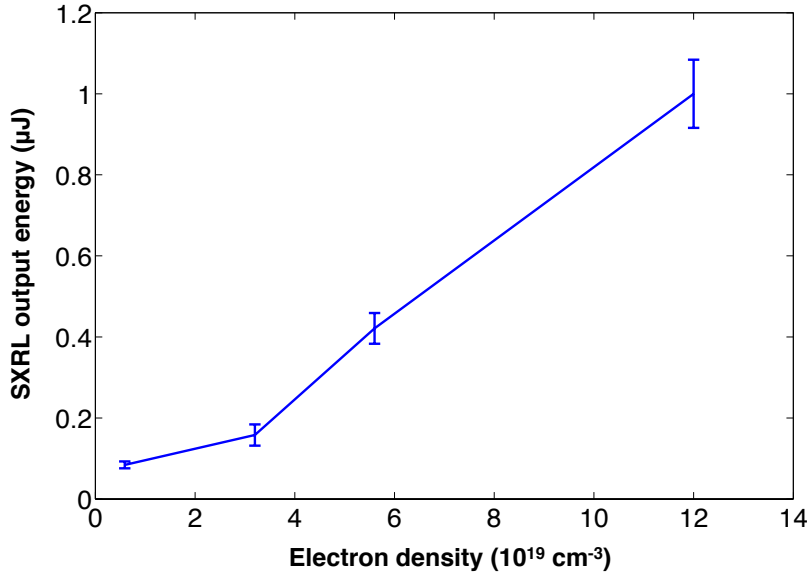


Figure 4.35: Evolution of the plasma amplified spontaneous emission energy as a function of experimentally studied electron densities.

In conformity with expectations from the simulations reporting a boost in gain and saturation intensity as the electron density is increased (fig. 2.19), the fig. 4.35 illustrates the monotonous increase in SXRL output energy regarding a 5 mm plasma for a set of experimental electron densities:  $n_e = 5.9 \times 10^{18} \text{ cm}^{-3}$ ,  $n_e = 3.2 \times 10^{19} \text{ cm}^{-3}$ ,  $n_e = 5.6 \times 10^{19} \text{ cm}^{-3}$  and  $n_e = 1.2 \times 10^{20} \text{ cm}^{-3}$ . It should be noticed that, as the ASE beam is strongly divergent and the collection angle was only about 15 mrad, the signal measurements are underestimated.

### SXRL signal strength vs the medium length

Further increase of the plasma-based soft X-ray laser energy can be achieved resorting to longer amplifying media. The use of an axicon with a low apex angle combined with a diverging waveguiding beam allowed us to create a focal line of over 20 mm long.

The fig. 4.36 shows the energy distribution of the ASE signal for increased length of the amplifying medium. The geometrical confinement of emission due to the elongation of the plasma channel for a fixed transverse size is highlighted with a divergence reduced from over 15 mrad down to about 8 mrad. Soft X-ray emission is essentially confined within a solid angle subtended by a circle with the transverse dimensions of the waveguide at the end of the gas jet at a point located at the gas jet entrance. This cone of emission decreases as the plasma length is expanded.

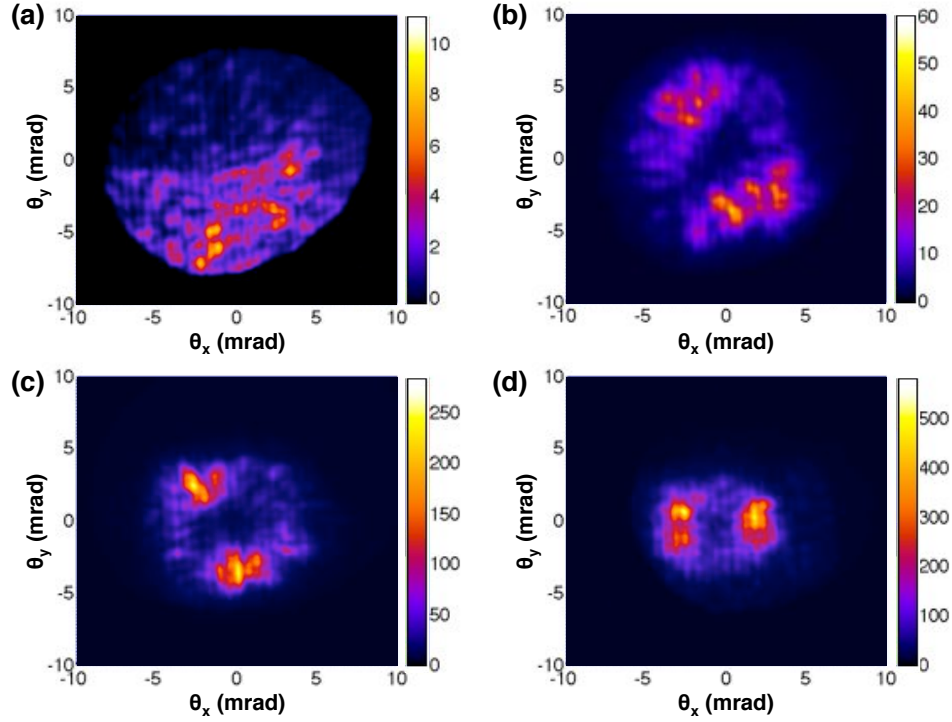


Figure 4.36: Energy distribution profiles (a.u.) of the amplified spontaneous emission in case of 5 mm (a), 10 mm (b), 15 mm (c) and 20 mm (d) gas jets.

The fig. 4.37 provides a geometrical explanation of the change of divergence of the ASE regarding the 10 mm- and 20 mm-long plasma amplifiers displaying 10 and 8 mrad divergence respectively. The profile of the ASE for the 10 mm-long plasma was obtained with a focus of the driving beam (red circle) 3 mm after the entrance of the jet. The corresponding position for the 20 mm-long plasma is 9 mm. Considering a cylindrical volume with emitting  $Kr^{8+}$  ions, those geometrical parameters would correspond to an elongated volume of transverse size of  $70 \mu\text{m}$  and  $90 \mu\text{m}$  for the 10 mm and 20 mm-long plasmas, respectively. The larger transverse dimension for the 20 mm-long plasma is consistent, since this plasma amplifier has a lower electron density compared to the 10 mm-long nozzle and because, according to fig. 4.23, plasma channels expand more for lower densities.

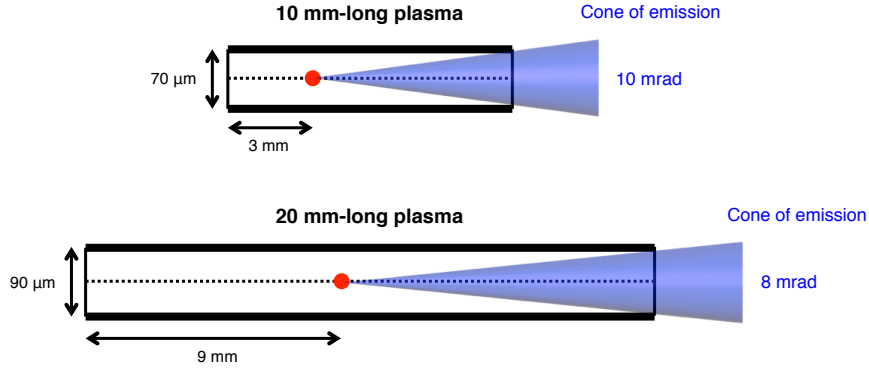


Figure 4.37: Schematic illustrating the conditions affecting the divergence of the ASE for the 10 mm- and 20 mm-long plasma amplifiers. The red circles stand for the positions of the focus.

The fig. 4.38 shows the evolution of the ASE emission energy as a function of the gas jet length. The ASE signal proportionally rises from 1 to 14.4  $\mu\text{J}$  for a gas jet from 5 mm to 15 mm. For the 5 mm, 10 mm, 15 mm and 20 mm-long plasmas, the electron densities were respectively  $n_e = 1.2 \times 10^{20} \text{cm}^{-3}$ ,  $9 \times 10^{19} \text{cm}^{-3}$ ,  $5.5 \times 10^{19} \text{cm}^{-3}$  and  $3.4 \times 10^{19} \text{cm}^{-3}$ , while transmissions of the pump beam by the waveguide were 45 %, 36 %, 32 % and 28 % respectively.

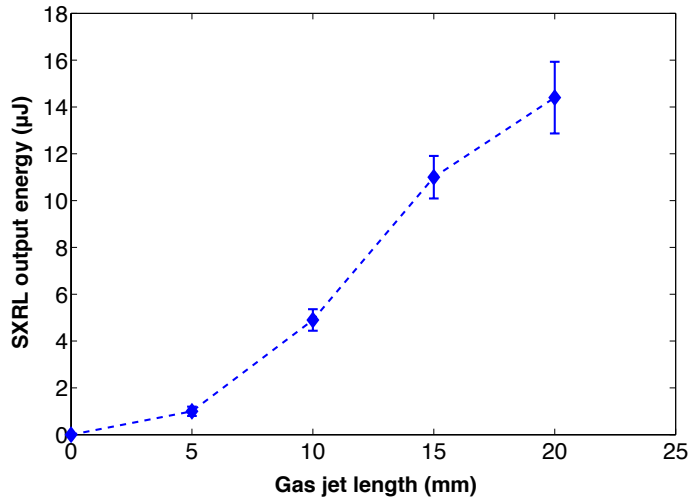


Figure 4.38: Evolution of the plasma ASE output energy with respect to the length of the gas jet.

#### 4.4.4 Correlation between waveguiding quality and SXRL signal strength

##### Plasma channel geometry

The fig. 4.39 shows the value of transmissions corresponding to various delays between the waveguiding beam (i.e. the "ignitor") and the driving laser pulse. For each of these delays, the vertical position of the nozzle has been adjusted to find the optimal configuration providing the maximum photon yield. Indeed, a tradeoff between the electron density and the guiding efficiency has to be found. The figure includes the size and average density defining the geometry

of these plasma channels.

For a delay of 1 ns between the "ignitor" and the "pump beam", the plasma channel is at its early stages of hydrodynamic expansion and its transverse diameter is only about  $1.5 w_0$  ( $w_0$ , diameter of the laser). Simulations (section 3.2.3) showed that channel transverse sizes below  $2 w_0$  impart initial coupling losses, thus lowering the transmission of the driving pulse. The fig. 4.39 shows that, despite the high electron density promising a high photon yield, the low transmission of the pump beam (18 %) reduces the volume of generated lasing ions, which results in a modest soft X-ray laser signal. The optimum for the output SXRL signal strength is found for a channel diameter about twice  $w_0$ . A high transmission of 45 % is measured. When the plasma channel further expands, the plasma channel provides a larger diameter, thus improving the coupling efficiency in size. The transmission only slightly increases and waveguiding is now counterbalanced by lower density gradients (see fig. 4.22), which result in a decrease the coupling efficiency for the numerical aperture. Therefore, further plasma expansion virtually does not improve the overall waveguiding efficiency and only results in a reduction of the electron density (see fig. 4.22), which decreases the output photon yield.

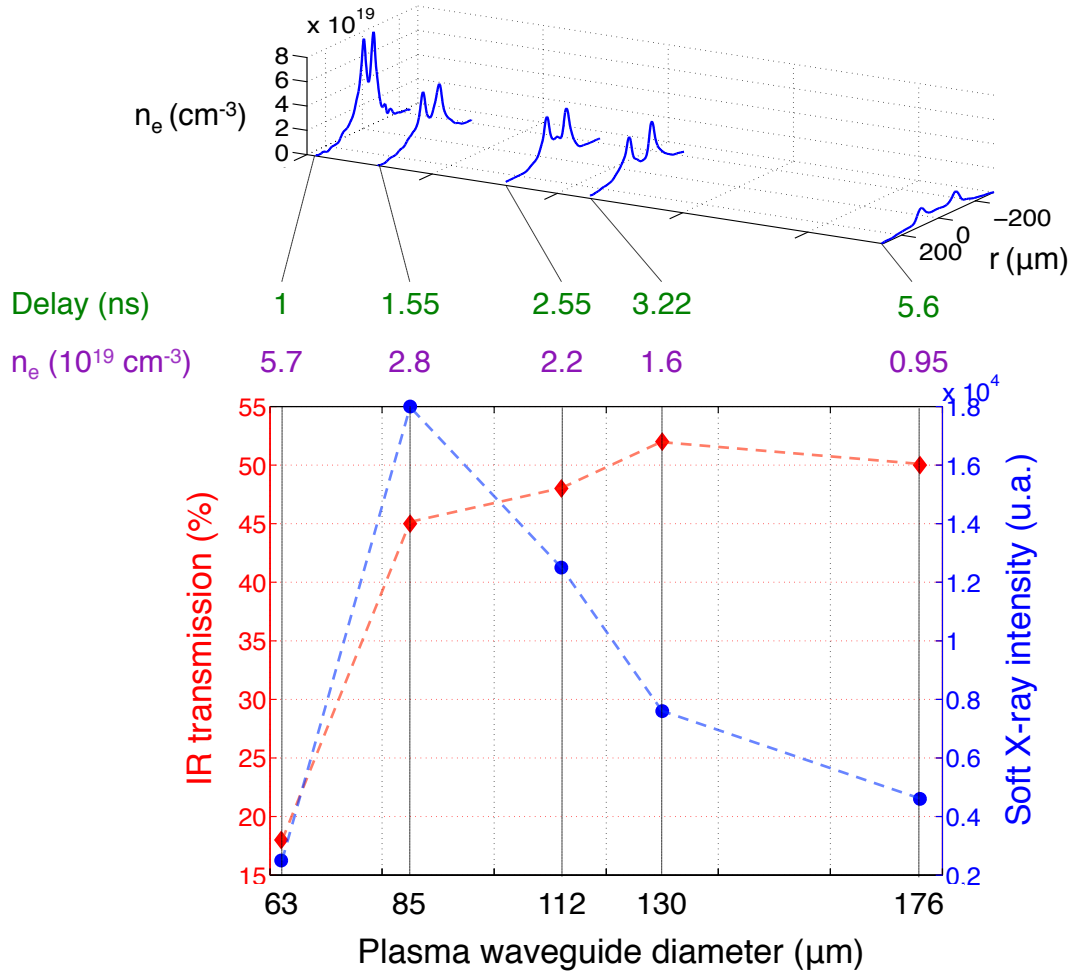


Figure 4.39: Transmission of the pump beam and output soft X-ray laser signal strength in waveguides corresponding to different delays between the waveguiding and the pump beam.



### Plasma channel length

The fig. 4.40 shows the correlation between the ASE energy and the waveguiding efficiency, as the plasma amplifier length is increased from 5 to 30 mm. While the majority of the waveguiding losses are from the coupling at the beginning of the plasma channel, moderate losses are observed for medium lengths increasing from 5 to 20 mm. This allows the soft X-ray laser output signal to monotonously rise. However, in case of the 30 mm-long plasma, because the focal line produced by the axicon was long enough, bad waveguiding occurred at the end of the medium, probably leading to re-absorption of the plasma emission. The output SXRL signal is therefore found to sharply drop.

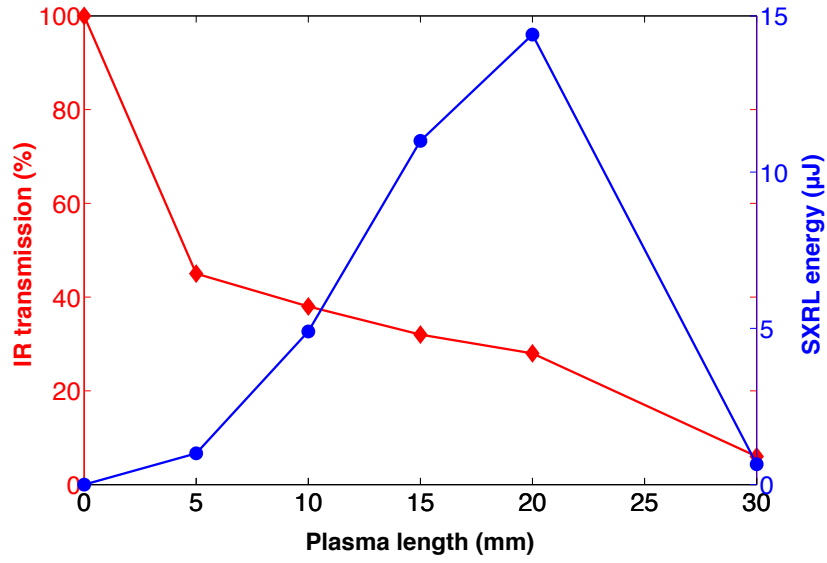


Figure 4.40: Evolution of the plasma ASE output energy and waveguide transmission with respect to the plasma length.

## 4.5 Conclusion

All in all, a tradeoff between the the channel size and its transverse density gradient is needed to yearn for ultrafast collisional ionization gated soft X-ray amplifiers.

The «ignitor-heater » waveguiding scheme has been successfully implemented for a 5 mm-long plasma of a high electron density of  $1.2 \times 10^{20} \text{ cm}^{-3}$ . Longer gain media have been generated and lead to unprecedented energy performances for this type of source (as high as  $14 \mu\text{J}$ ).

Further improvements involve more adequate plasma engineering. Possible solutions would involve varying the absolute and relative amount of energy in the "ignitor" and the "heater", as well as modifying the delay between both pulses. Moreover, more adequate coupling of the pump beam into the plasma channel could be achieved by focusing the pump beam with a spherical mirror of longer focal length.

The spatial quality of ASE beam is low and seeding these amplifiers with a HH source promise a significant improvement. Furthermore the seeding technique can be used to probe the gain dynamics of such high-density plasma amplifiers.



## Chapter 5

# Characterization of a high-density HH-seeded plasma-based soft X-ray laser

This section presents the investigation of the amplification dynamics of a collisional OFI krypton plasma amplifier by seeding it with a high-harmonic (HH) source. The implementation of a waveguiding technique allows increasing electron density without compromising on the volume of emitting ions and leads to a dramatic reduction of the amplification lifetime [Depresseux et al., 2015b]. This HH-seeding configuration can be promoted as a source on its own to deliver ultrashort and energetic pulses exhibiting excellent optical properties.

### Contents

---

<b>5.1</b>	<b>Development of the HH-seeded soft-X-ray laser at 32.8 nm . . . . .</b>	<b>148</b>
5.1.1	Experimental setup . . . . .	149
5.1.2	Spectra . . . . .	153
5.1.3	Far-field Energy distribution and output energy . . . . .	154
5.1.4	Seeding signal strength level . . . . .	157
<b>5.2</b>	<b>Gain dynamics measurement . . . . .</b>	<b>159</b>
<b>5.3</b>	<b>Maxwell-Bloch modeling . . . . .</b>	<b>162</b>
5.3.1	Temporal structure of the amplified HH field . . . . .	163
5.3.2	Regimes of amplification of the resonant HH field . . . . .	165
5.3.3	SXRL pulse buildup . . . . .	166
5.3.4	Final SXRL pulse duration and discussion . . . . .	169
<b>5.4</b>	<b>Extracted energy . . . . .</b>	<b>175</b>
<b>5.5</b>	<b>Conclusion . . . . .</b>	<b>176</b>

---

## 5.1 Development of the HH-seeded soft-X-ray laser at 32.8 nm

In order to improve the spatial features of SXRL emission from high-density plasmas emitting put to  $14.4 \mu\text{J}$  (see section 4.4.3), those amplifiers have been seeded. However, this section only presents the implementation of a 5 mm-long plasma amplifier, as efficient extraction of the medium gain by the seed was not possible for longer plasmas. This can be explained by the impossibility to efficiently counterbalance the growing ASE of those more energetic amplifiers (see section 5.1.4). Nevertheless, a substantial group velocity dispersion at high electron densities between the IR and SXRL pulses leads to a de-synchronization between the longitudinally generated gain and the propagating amplified seed. The fig. 5.1 shows how the time shift between the two pulses evolves for a 10 mm-long plasma at various electron densities. This temporal mismatch reaches 1 ps for  $n_e = 1.2 \times 10^{20} \text{cm}^{-3}$ .

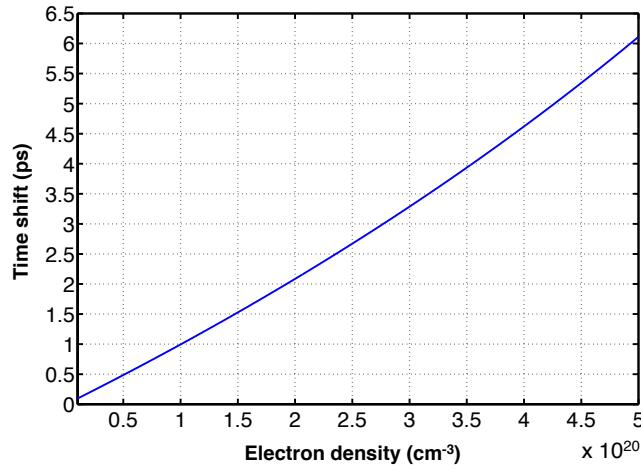


Figure 5.1: Evolution of the temporal shift between the IR and SXRL pulses with the electron density as they propagate in a 10 mm-long plasma.

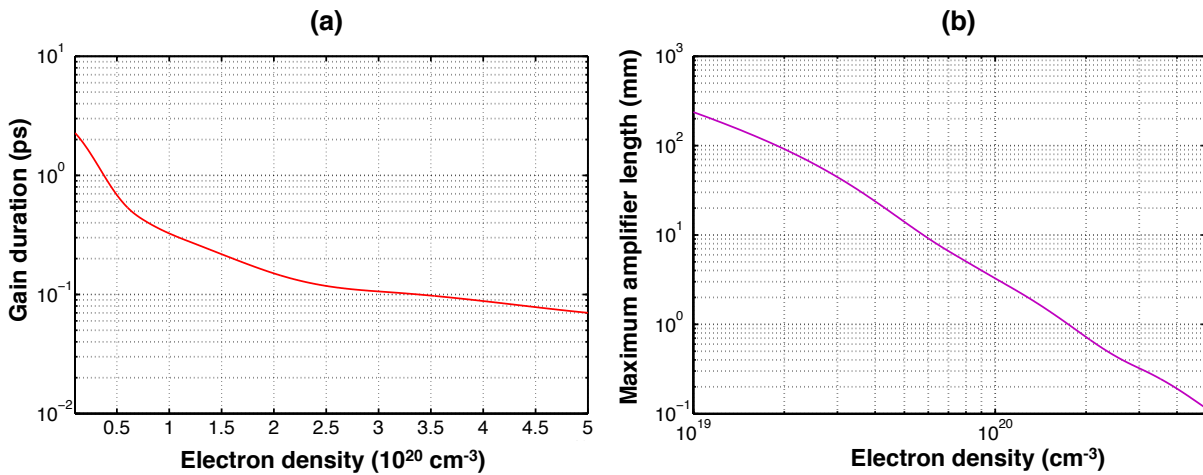


Figure 5.2: (a) Variation of the gain duration (FWHM) with respect to the electron density (data from OFIKinRad code). (b) Maximum amplifier length for which the amplified seed and gain keep synchronized as the electron density is varied.

The fig. 5.2b shows the maximum length of plasma amplifiers, for which the soft X-ray seed is effectively amplified within the FWHM duration of the gain (fig. 5.2a), for various electron densities. For high-density amplifiers reaching a few  $10^{20} \text{ cm}^{-3}$ , the seed stops being amplified after 1 mm of propagation.

### 5.1.1 Experimental setup

The fig. 5.3 displays the experimental arrangement of the HH-seeded plasma-based soft X-ray laser chain. The plasma can be coherently excited using an external source, which works as an "oscillator".

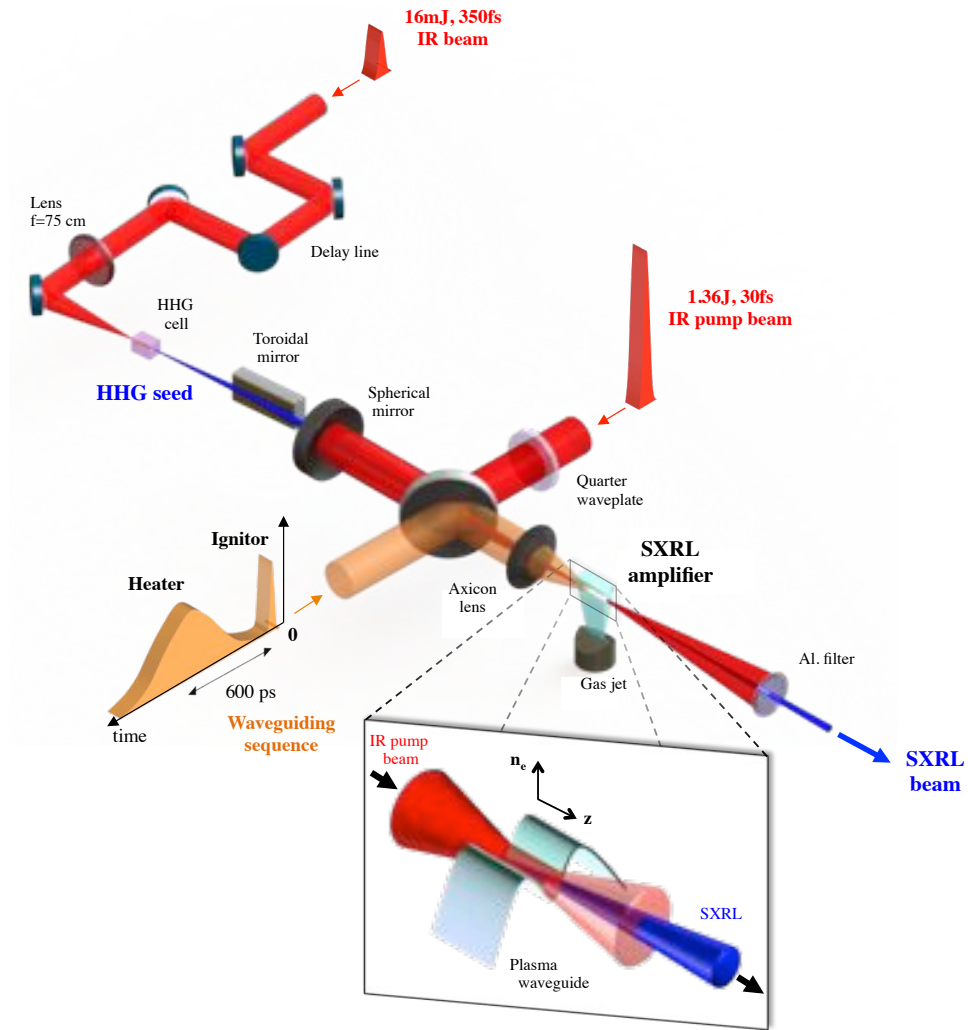


Figure 5.3: Schematic of the experimental arrangement. The waveguiding beam is composed of a sequence of a short (130 mJ, 30 fs) and a long pulse (690 mJ, 600 ps). It is being focused over the whole jet length thanks to an axiconic lens and creates, following collisional ionization and hydrodynamic expansion, a plasma channel. Then, the pump beam (1.36 J, 30 fs) is being focused at the entrance of the channel with a spherical mirror and being guided afterwards. Hence, an amplifier with  $Kr^{8+}$  lasing ion species over the whole gas jet length is implemented. A third IR beam (16 mJ, 350 fs) is used to generate high-harmonics in an argon-filled cell. The latter are image-relayed onto the entrance of the plasma and synchronized with the gain lifetime.

This "seed" source is synchronized with the lifetime of the population inversion achieved within the plasma. In these conditions, the seed gets amplified as it propagates into the plasma and the resulting emission is highly coherent and retains the beam spatial properties of the seed.

The fig. 5.4 depicts this experimental arrangement in «Salle Jaune». The part of the setup corresponding to the plasma amplifier is installed in the "main chamber".

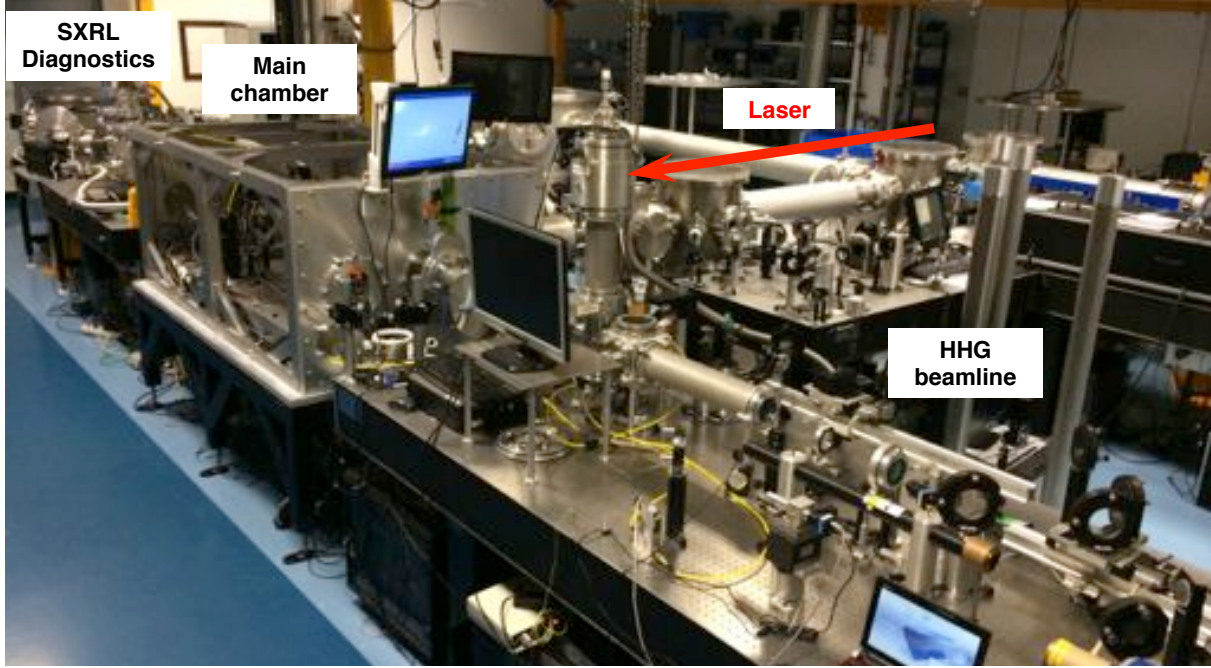


Figure 5.4: Overview of the experimental plasma-based soft X-ray laser chain. The red arrow shows the direction from which the laser beams arrive in the main experimental vacuum chamber.

Because the length of gain region for longitudinally pumped gas target SXRLs is severely limited by ionization-induced refraction, a waveguide is used to maintain sufficient pump intensity over a long distance. The length of gain region for the X-ray lasing can therefore be increased and the length of the under-ionized absorbing region reduced.

The "ignitor-heater" optically preformed plasma waveguide scheme (see section 3.1.4) has been used. The merits of this method involve a high density operation, guiding of pump pulse and the soft X-ray laser pulse simultaneously, and is damage-free, which caters for high-repetition-rate needed for practical applications. The waveguide is implemented focusing a sequence of ignitor (130 mJ, 30 fs) and "heater" pulses (690 mJ, 600 ps) delayed by 600 ps thanks to an axicon lens. The pump beam (1.36 J, 30 fs) was turned circularly polarized thanks to a quarter-wave plate. This allows catering for hot electrons needed to efficiently pump the laser transition. The beam is then focused into the plasma channel using a 75 cm-focal length spherical mirror. The plasma channel was tailored (see fig. 4.22) to operate at the highest possible electron density and thus maximize the output soft X-ray laser signal strength. At the highest reported density, appropriate conditions for guiding in terms of size and transverse density gradient were granted for the pump beam focused about 1.55 ns after the arrival of the "ignitor".

The soft X-ray seed is a high-harmonic (HH) source, implemented focusing an IR driver beam into a gas cell of variable pressure and length, filled with argon. The linearly polarized

beam was focused using a 75 cm- focal length plano-convex lens. The intensity upon target is assessed at about  $4 \times 10^{14} \text{ W/cm}^2$ . The HH source is then image-relayed thanks to a toroidal and a plane mirror onto the plasma amplifier. For this purpose, the spherical, double-coated plane mirror and the axicon have been drilled (8 mm diameter hole). The grazing-incidence plane mirror is placed after the toroidal mirror and is used to control the spatial coupling conditions of the HH beam at the entrance of the plasma.

### Spatial overlap, temporal matching and spectral tuning

- Spatial overlap of the pump beam with the HH-driver: The seeding is fulfilled re-imaging the harmonic output onto the entrance of the amplifying plasma, using a 5 degrees grazing incidence gold-coated toroidal mirror in a 1.5 m - 1 m conjugation and a  $\text{SiO}_2$  plane mirror. The experiment was aligned making the HH beam collinear with the infrared pump and waveguiding beams. The spatial coupling of the HH beam and the SXRL gain region was done with the image of the focal spot of the IR HH-driver beam by the image-relay system composed of the toroidal and plane mirrors. This image is situated on the nozzle gas jet and was overlapped with the focal spot of the pump beam. Because the HH-driver beam defines the optical axis of the experiment, the spherical mirror is finely tilted to overlap the pump beam with the image of the HH-driver focal spot. Because of the low acceptance angles of the image-relay system operating at grazing incidence, the alignment was performed closing the iris of the HH-driving beam. The resulting focal spot image has thus a large diameter of about  $120 \mu\text{m}$  FWHM, as depicted in fig. 5.5, which shows the pump beam focus overlapped with the HH-driver focus image. The image was recorded with a x4 microscope objective.

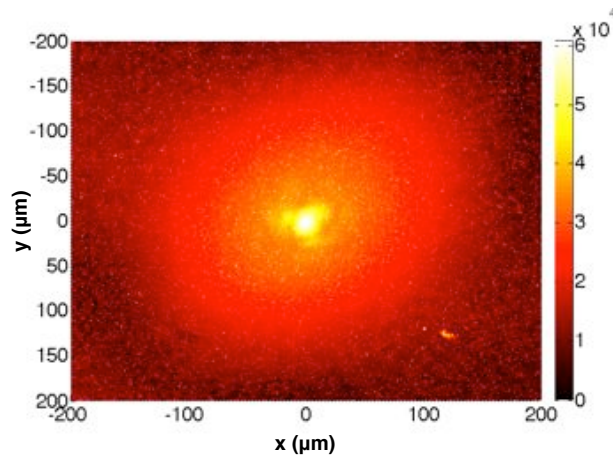


Figure 5.5: Spatial overlapping of the HH-driver focus image with the pump beam focus.

Then, the axicon is moved in the transverse directions to overlap the focal line onto the pump beam focal spot (see fig. 4.6).



- Temporal matching of the HH arrival with the amplifier gain lifetime: The temporal overlap between the HH signal and the SXRL amplification period was approached by synchronizing the HH driver and the pump beams thanks to a 30 fs-accuracy delay line. The synchronization was implemented by placing a piece of sheet in front of the spherical mirror. This sheet is used to center the beam on the spherical mirror and has two holes, one on-axis and the other a few millimeters off-axis. The HH-driver beam passes through the on-axis hole, whereas an edge of the pump beam whose iris has been closed passes through the sheet and is reflected by the spherical mirror. This Young's slits produces a system of fringes when both beams are synchronized. All optical densities on both beams are removed and the  $\lambda/2$  waveplate of the laser polarizing cube attenuator is set to its maximum of transmission to avoid various temporally shifted systems of fringes to be formed. The iris aperture of both beams is then set to equalize the intensities of both overlapped focal spots, in order to yield an optimized fringe contrast, as illustrated in fig. 5.6.

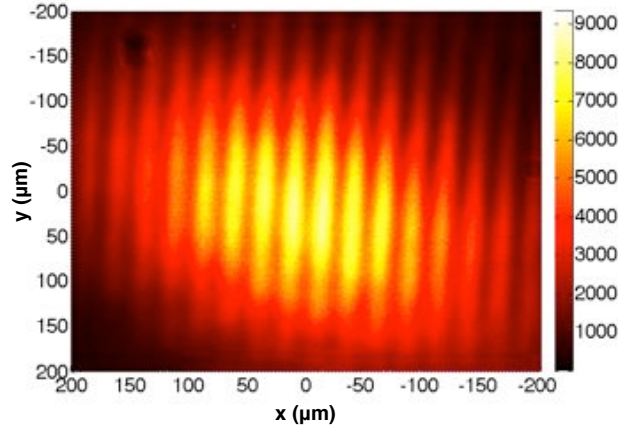


Figure 5.6: Synchronization of the HH-driver beam with the pump beam.

- Spectral tuning of a HH order onto the plasma lasing line: The HH signal can be effectively amplified by the plasma if the seeded signal is spectrally tuned onto the ASE lasing line at 32.8 nm. This was performed altering the second-order spectral phase of the HH driver beam [Lee et al., 2001] by changing the spacing between the pair of gratings of the compressor from their initial position delivering the shortest pulse duration. The 25th harmonic signal was spectrally shifted onto the  $3d^9 4d_{J=0} \mapsto 3d^9 4p_{J=1}$  laser transition of the  $Kr^{8+}$  plasma amplifier. The HH flux was optimized by changing the gas pressure and altering the focusing conditions. Besides, the phase-matching conditions were optimized by fine-tuning the HH driver beam aperture with a motorized iris to adjust the Gouy phase. The appropriate conditions with a 75 cm-focal length lens were found with an iris aperture of 11.8 mm, a pulse of 16 mJ energy and 350 fs duration (chirped IR laser), and for a 6 mm long cell with a pressure of 40 mbar and a focal plane situated about 5 mm after the cell entrance.

### 5.1.2 Spectra

Seeding plasma over 10 mm was not possible, probably because of a too strong ASE signal as compared to the HH signal strength. Consequently, the results regarding the high-density HH-seeded plasma-based soft X-ray laser correspond to a 5 mm-long plasma. The fig. 5.7 reports the spectra for HH, ASE and HH-seeded signals respectively in case of a high-density plasma amplifier with  $n_e = 1.2 \times 10^{20} \text{ cm}^{-3}$ . The arrival of the HH signal was delayed with respect to the pump beam. A strong amplification of the seed pulse was observed when the injection time was synchronized with the gain period. The maximum of amplification was found for a delay of 1.4 ps between the pump and HH-driver beams. The secondary peaks on both sides from central peaks correspond to the diffraction pattern from the grating supporting grid. A factor of about 30 between the HH and the ASE shots and a factor of about 35 between the ASE and the HH-seeded SXRL signal. Overall, the HH signal is amplified by **a factor of about 1000**.

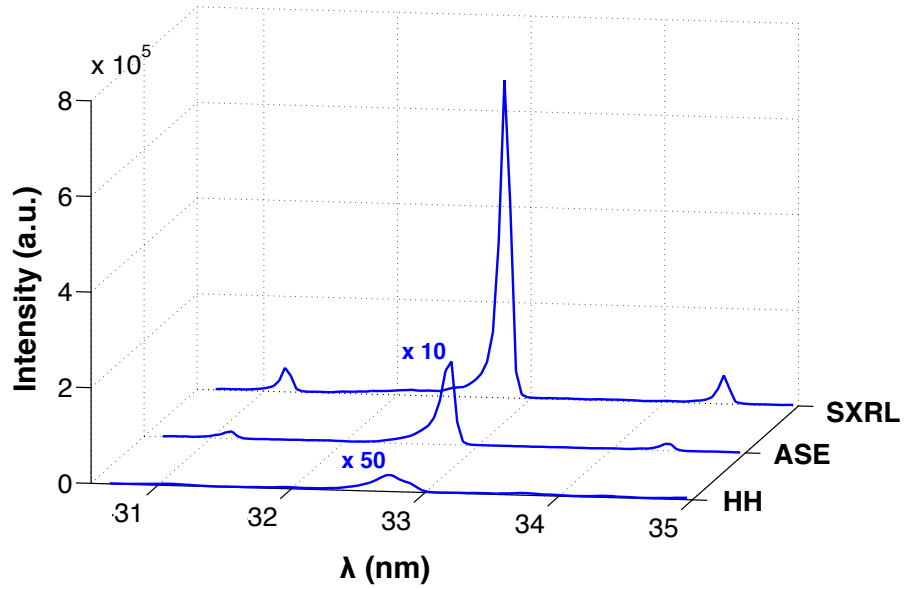


Figure 5.7: Spectra of the high-harmonic signal (a), the ASE (b) and the HH-seeded SXRL (c).

### 5.1.3 Far-field Energy distribution and output energy

The far-field beam profile has also been directly recorded about 4 m from the source. The fig. 5.8 depicts the beam profile of the seeded SXRL in comparison to the HH signal. The  $1 \pm 0.2$  mrad divergence and nearly Gaussian beam profile of HH is maintained over the plasma amplification. A factor of 75 is reported between all HH orders and the seeded SXRL signal, for the highest operated electron density at  $1.2 \times 10^{20} \text{cm}^{-3}$ . The amplification of the HH portion matching the laser transition at 32.8 nm corresponds to more than three orders of magnitude and the resulting SXRL signal yields about  $2 \mu\text{J}$  per shot, which corresponds to over  $3 \times 10^{11}$  coherent photons.

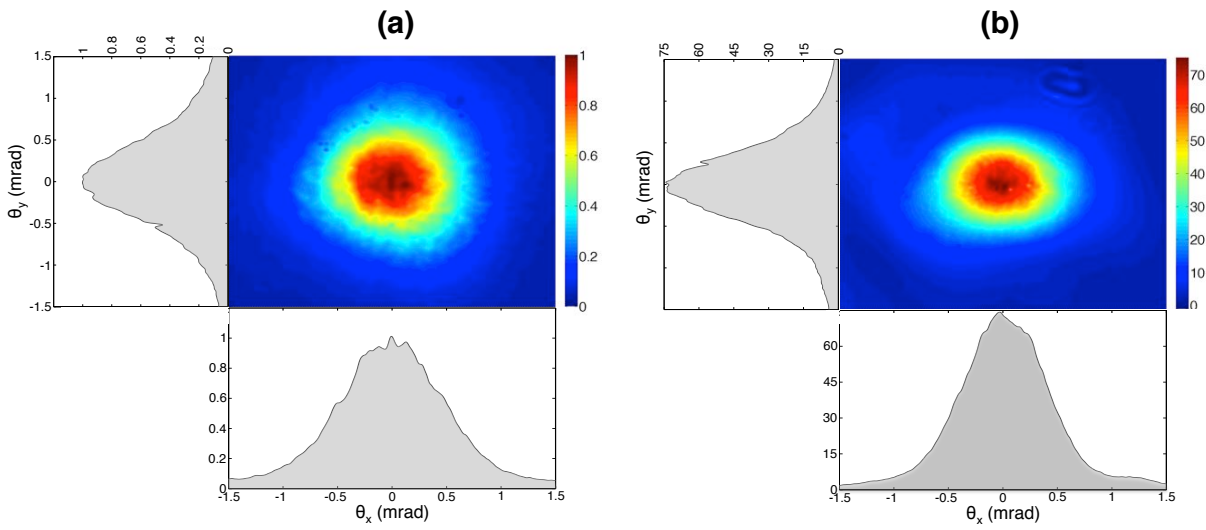


Figure 5.8: Far-field beam profiles of the HH (a) and the seeded SXRL (b) signals in case of  $n_e = 1.2 \times 10^{20} \text{cm}^{-3}$ .

In order to bring into comparison the signal strengths of the highly divergent ASE with low-divergence HH and SXRL signals, the energy distribution of the HH, ASE and HH-seeded soft X-ray signals has been measured using the experimental setup described in fig. 4.19. It allowed imaging the source in a plane lying about 1.40 m from the plasma and collecting photons over an angular aperture of about 15 mrad. The fig. 5.9 illustrates the energy distribution of soft X-ray signal per shot for the HH, ASE and seeded XRL respectively. Data were recorded in the highest density case for  $n_e = 1.2 \times 10^{20} \text{cm}^{-3}$ . Those signals have been observed imaging the filter box with an off-axis parabola. They report an increase in the collected signal for the seeded soft X-ray laser of about 10 compared to ASE signal and about 100 compared to the total HH flux. The ASE signal (fig. 5.9a) is strongly divergent (over 15 mrad) and is actually cut by the filters holder, whereas HH and HH-seeded SXRL display about 1 mrad divergence FWHM. The fig. 5.9c shows that seeding the plasma amplifier with HH lowers the ASE signal (signal level outside the central spot in fig. 5.9c compared to ASE signal in fig. 5.9b) to concentrate photon emission within a spot defined by the solid angle of HH.

Calibrations in energy yield about 25 nJ for whole HH signal comprising all HH orders, over 1  $\mu\text{J}$  for ASE and about 2  $\mu\text{J}$  for the HH-seeded SXRL.

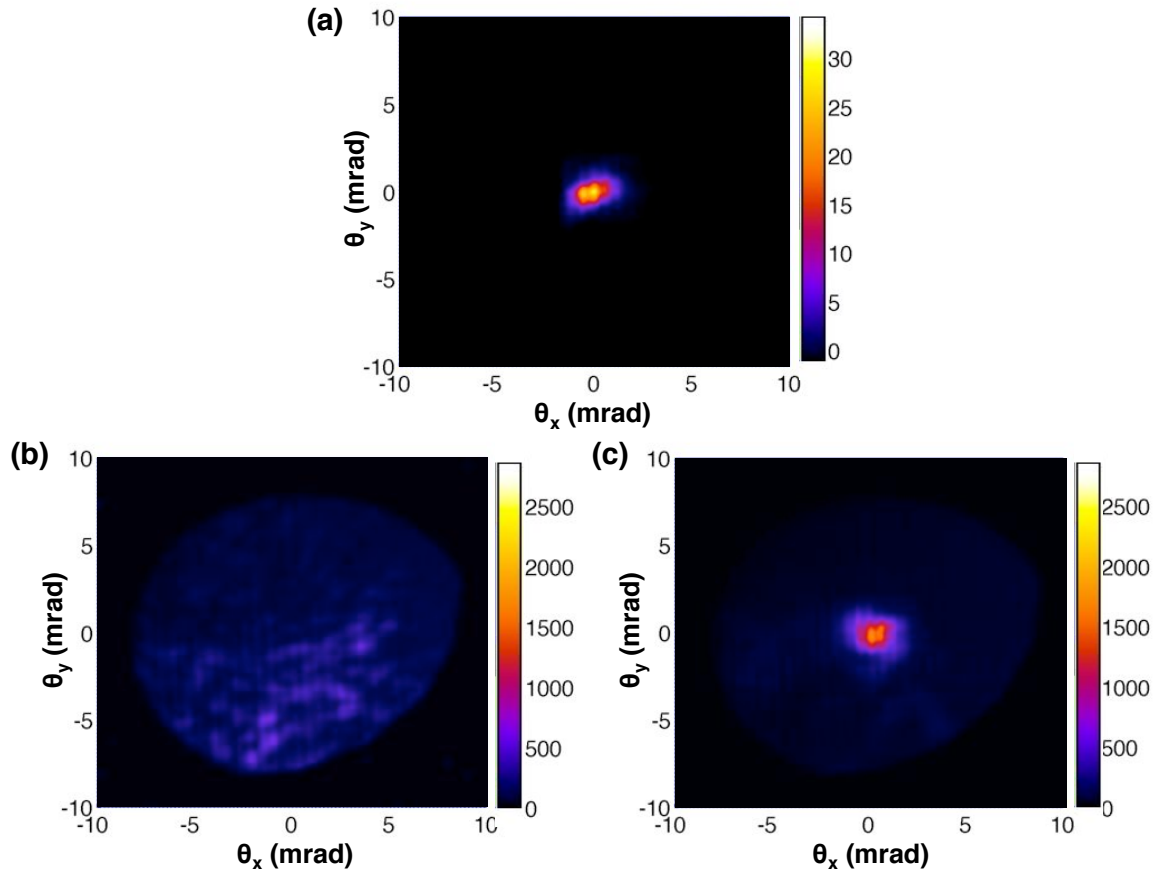


Figure 5.9: Energy distribution of HH (a), ASE (b) and seeded soft X-ray laser signals (c).

In optimal conditions, the HH-seeded SXRL source exhibits a good shot-to-shot stability. The fig. 5.10 illustrates this over 40 shots. The energy fluctuations stand at 6.8 % of the average energy (standard deviation  $\sigma_{RMS} = 0.068$ ). Regarding the beam pointing and beam divergence stabilities, they amount to  $\sigma_{RMS} = 0.116$  mrad and  $\sigma_{RMS} = 0.39$  mrad respectively.

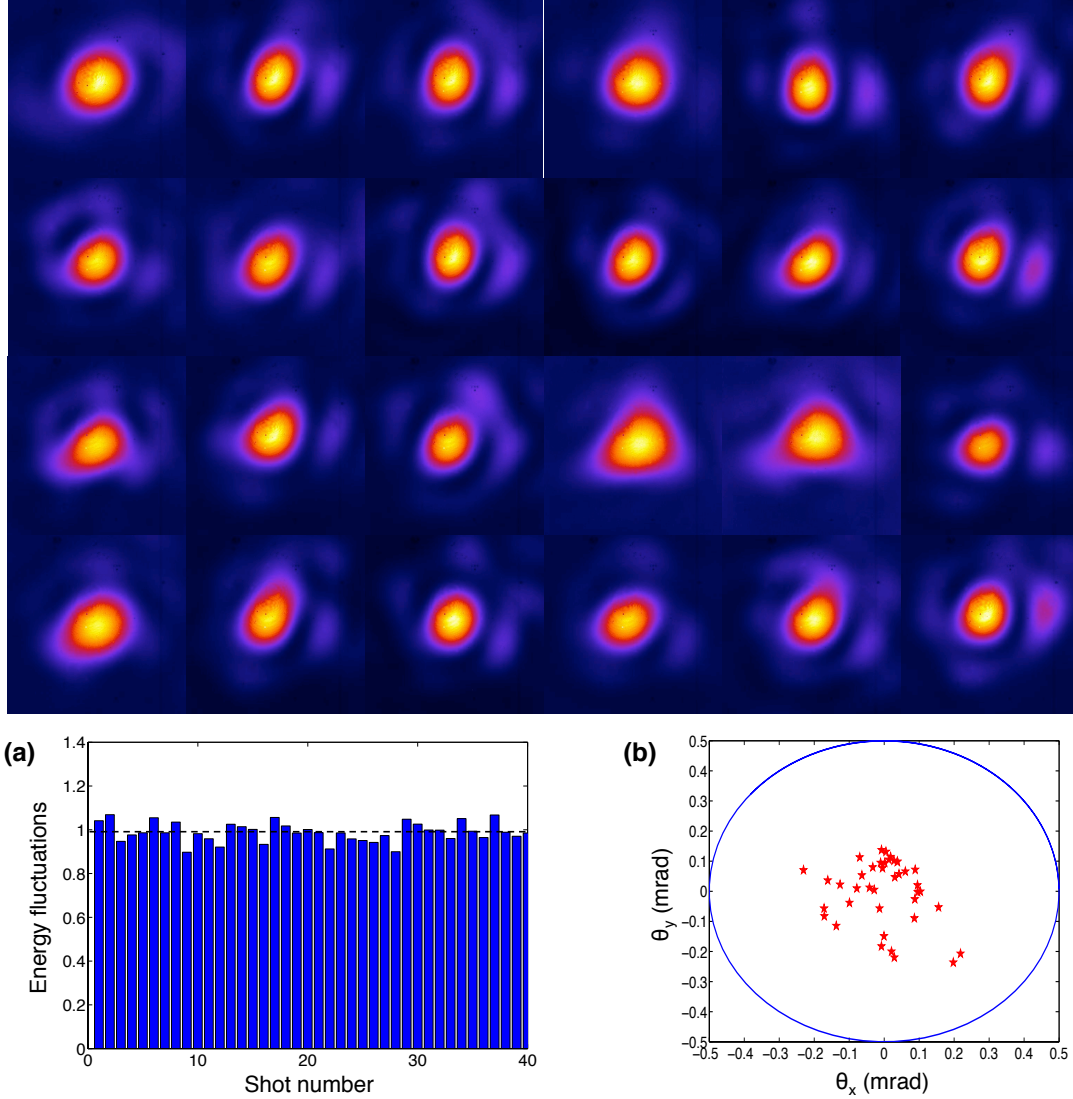


Figure 5.10: Far-field energy distributions of the HH-seeded SXRL signal. (a) Histogram reporting the shot-to-shot stability of the source. The value 1 corresponds to a normalized average energy. (b) Beam pointing stability. The red stars stand for the shots and the blue circle corresponds to the FWHM divergence of those beams.

#### 5.1.4 Seeding signal strength level

The fig. 5.11 illustrates the impact of the spectrally tuned HH seed energy at 32.8 nm on the amplified HH signal strength for  $n_e = 3.2 \times 10^{19} \text{cm}^{-3}$  (black curve) and  $n_e = 7 \times 10^{19} \text{cm}^{-3}$  (orange curve). The optimized HH signal energy has been decreased modifying the polarization of the IR HH driving beam. The HH generation efficiency drops sharply by turning the polarization from linear to circular. For this measurement, neither the focusing conditions of the HH driver into the gas cell nor the intensity of the IR pulse can be modified, as the spatial and spectral coupling of the HH seed into the plasma amplifier would also be changed.

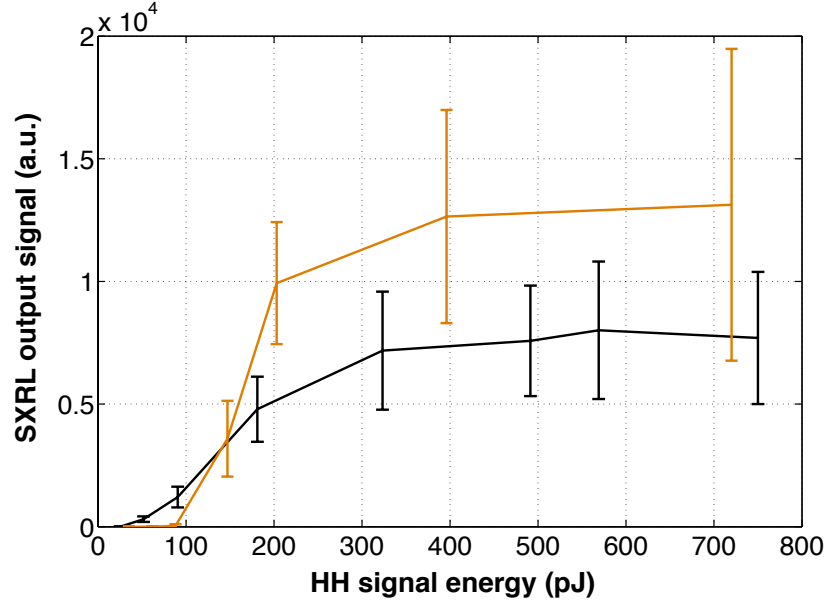


Figure 5.11: Evolution of the amplified HH pulse signal strength as the HH seed energy is varied for a plasma amplifier electron density  $n_e = 3.2 \times 10^{19} \text{cm}^{-3}$  (black) and  $n_e = 7 \times 10^{19} \text{cm}^{-3}$  (orange).

The curve displayed in fig. 5.11 shows a first phase, where the output SXRL signal rapidly rises as the HH seed energy increases. This behavior corresponds to a non-saturated regime of the amplifier. When the HH signal exceeds about 200 pJ, the amplifier saturates and the output SXRL signal increases slower.

The saturation regime is reached earlier for the highest electron density (orange). Furthermore, there is a threshold from which the HH gets amplified. The HH seed signal strength has indeed to overcome the "noisy" ASE signal in order to be efficiently amplified. This threshold is higher at larger densities. The amplification of the seed starts at about 25 pJ for  $n_e = 3.2 \times 10^{19} \text{cm}^{-3}$  and at about 70 pJ at  $n_e = 7 \times 10^{19} \text{cm}^{-3}$ . This behavior moots an additional difficulty when operating at higher near-critical electron densities. In order to efficiently extract the gain of the plasma amplifier, the HH seed signal should be strong enough to overtake the substantially increased amplified spontaneous emission.

The fig. 5.12 illustrates this phenomena when seeding a 5 mm-long plasma amplifier plasma amplifiers displaying an ASE energy of  $1 \mu\text{J}$  (fig. 5.12a) with a high-harmonic seed of different flux. The fig. 5.12b shows the seeded SXRL energy distribution with a seed energy of 25 nJ, whereas fig. 5.12c depicts the result for a seed energy of only 10 nJ. In the former case, the HH beam gets amplified at the expense of the ASE signal, while in the latter case, the ASE remains strong and the seed is less amplified.

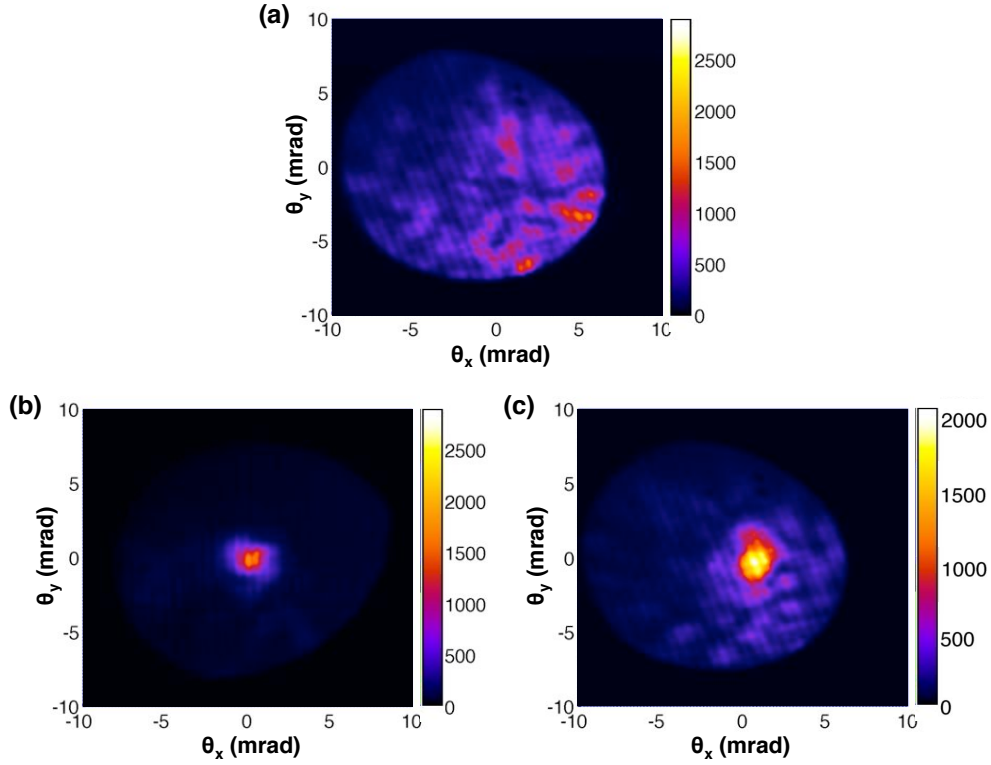


Figure 5.12: (a) Energy distribution of ASE in case of a 5 mm-long plasma with  $n_e = 1.2 \times 10^{20} \text{cm}^{-3}$ . Energy distribution of the seeded soft X-ray laser for a seed with an energy of 25 nJ (b) and 10 nJ (c).

Similarly, fig. 5.13 shows the same phenomena with this time the same strength of HH signal, but in case of two different ASE signal strengths. The fig. 5.13 shows efficient amplification of the HH by a 5 mm-long plasma amplifier (fig. 5.13a), while bad gain extraction is reported when considering a 10 mm-long plasma amplifier (fig. 5.13b). The HH signal strength was about 25 nJ in both cases, whereas ASE was measured to be  $1 \mu\text{J}$  and  $5 \mu\text{J}$  for the 5 mm- and 10 mm-long nozzles.



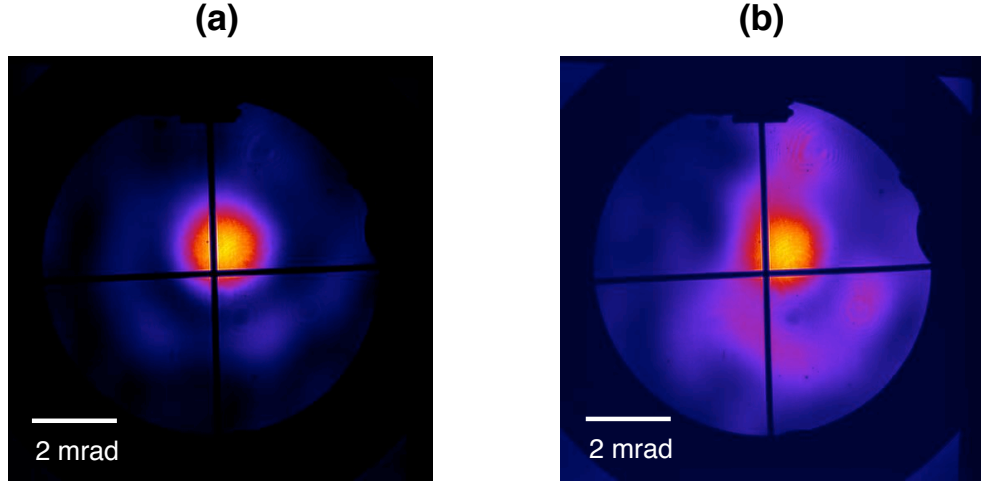


Figure 5.13: Seeded SXRL signal in case of 5 mm-long (a) and 10 mm-long plasma amplifiers.

## 5.2 Gain dynamics measurement

The study of plasma-based soft X-ray sources is carried out with krypton, whose highly-charged and stable  $Kr^{8+}$  ions display a strong lasing line at 32.8 nm for the  $3d^9 4d_{J=0} \mapsto 3d^9 4p_{J=1}$  transition.

As previously reported, in collisionally-pumped plasma amplifiers, the fundamental limit of emission duration is governed by the Fourier transform of the pulse spectral line width. Because of the intrinsic narrow line width of such lasers, femtosecond duration emission is not readily available and spectral broadening techniques have to be envisioned to hope for shorter duration. In this perspective, we will see that increasing the electron density of the plasma amplifier paves the way for ultrashort pulse emission of coherent soft X-rays. The duration of collisionally-pumped plasma-based soft X-ray lasers is ranging between the fundamental limit given by the Fourier transform of the emission linewidth and the lifetime of the amplifier gain [Guilbaud et al., 2010]. Indeed, the HH pulse width is larger than the amplifier narrow linewidth and the HH pulse duration is far shorter compared to the actual plasma temporal response. For more than one decade, collisionally-pumped plasma-based soft X-ray lasers have been limited to the picosecond range. One of the main work of this thesis has been associated with the introduction and the implementation of a technique *Collisional Ionization Gating* (CIG). The method aims at reducing the time window in which the lasing action takes place by quenching the lifetime of the lasing ions. In the OFI plasma soft X-ray lasing scheme [Eder et al., 1992], an ultrashort infrared laser pulse ( $5 \times 10^{18} W/cm^2$ ) was focused onto a krypton gas jet to generate the lasing ion species. The resulting electron distribution permits to achieve a population inversion by collisional pumping leading to the lasing of the transition  $3d^9 4d_{J=0} \mapsto 3d^9 4p_{J=1}$  at 32.8 nm [McGowan et al., 1992b].

**Measurement of the gain dynamics as a function of the electron density.** To evaluate the influence of electron density on the temporal properties of the 32.8 nm lasing emission, the temporal gain dynamics has been measured by seeding the SXRL amplifier using the 25th harmonic of the infrared driving laser. Propitious guiding conditions allowed us to enhance the SXRL yield by one order of magnitude over an electron density range from a few  $10^{18}$  to



over  $10^{20} \text{cm}^{-3}$ , in accordance with our simulations reporting a monotonous increase in gain and saturation intensity (cf. fig. 2.19). By varying the time delay between the amplifier creation and the seed pulse injection, we measured the temporal evolution of the amplification factor, thus revealing the actual temporal profiles of the SXRL gain.

The studied electron densities for plasma amplifiers filled with  $Kr^{8+}$  are  $n_e = 3 \times 10^{18} \text{cm}^{-3}$ ,  $n_e = 7.9 \times 10^{18} \text{cm}^{-3}$ ,  $n_e = 3.2 \times 10^{19} \text{cm}^{-3}$  and  $n_e = 1.2 \times 10^{20} \text{cm}^{-3}$ .

The first two lowest densities correspond to a 5 mm-long gas cell at 15 and 40 mbar respectively. Such low densities did not require a waveguiding beam to counterbalance ionization-induced refraction. In fig. 5.14, the cases (a) and (b) were obtained with a high-density gas jet. Changing the delay between the waveguiding beam and the IR pump beam allowed to alter the electron density of the amplifier. Indeed, as reported in fig. 4.22 in chapter 4, the plasma expansion is characterized by a widening plasma channel with a decreasing average electron density within the waveguide transverse dimensions. The lasing conditions were optimized by tuning the height of the optic axis with respect to the jet nozzle to maximize the IR pump beam transmission by the waveguide. The cases fig. 5.14a & b correspond to delays of 3 ns and 1.55 ns respectively. It should be noted that the electron density of the amplifier fig. 5.14b has been recorded 10 ps after the arrival of the pump beam, whereas for case fig. 5.14a, the electron density was probed just after the propagation of the pump beam.

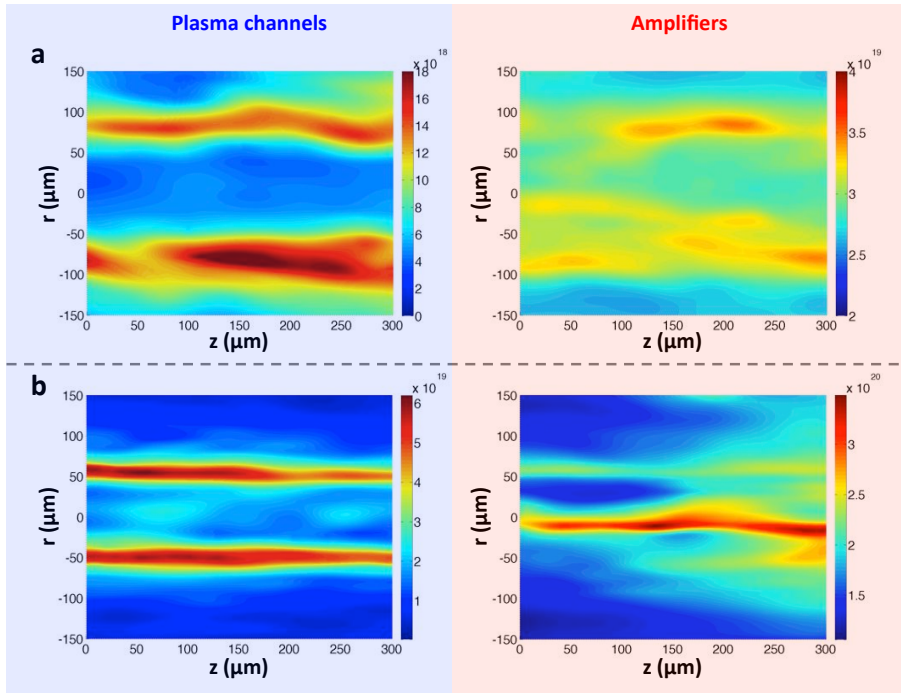


Figure 5.14: Electron density maps in case for amplifiers of average densities  $n_e = 3.2 \times 10^{19} \text{cm}^{-3}$  (a) and  $n_e = 1.2 \times 10^{20} \text{cm}^{-3}$  (b).

The fig. 5.15 shows the temporal dependence of the plasma amplification with respect to the electron density. The experimental behavior of the plasma amplification has been fitted with numerical data (red curve) obtained from a time-dependent Maxwell-Bloch code describing the amplification of HH by the plasma (see section 5.3). The amplification factor,  $A$ , has been computed integrating the energy distribution of the signals using the formula:

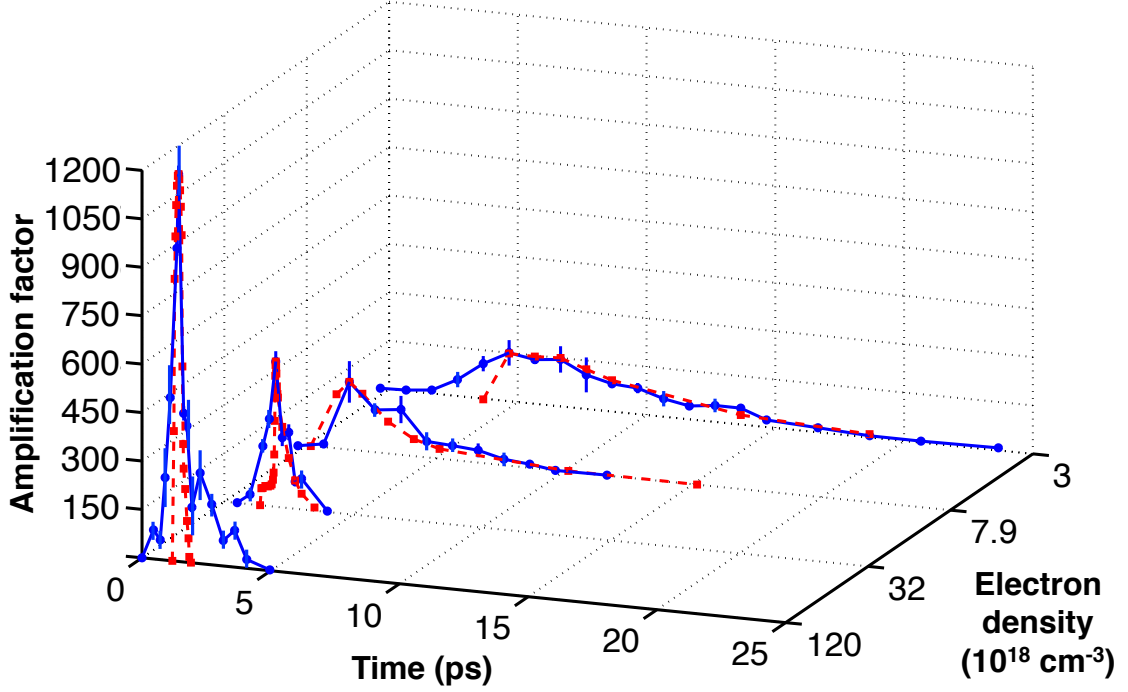


Figure 5.15: Temporal dependence of the amplification factor with respect to the seeding delay. Experimental (blue circles) and Maxwell-Bloch modelling results (red squares) for a scan in plasma density:  $n_e = 3 \times 10^{18} \text{ cm}^{-3}$ ,  $n_e = 7.9 \times 10^{18} \text{ cm}^{-3}$ ,  $n_e = 3.2 \times 10^{19} \text{ cm}^{-3}$  and  $n_e = 1.2 \times 10^{20} \text{ cm}^{-3}$ .

$$A = (N_{XRL} - N_{ASE} - N_{HH})/N_{HH} \quad (5.1)$$

where  $N_{XRL}$ ,  $N_{ASE}$  and  $N_{HH}$  are the number of counts of the seeded XRL, ASE and HH signals respectively, averaged over 3 or 4 shots.

The duration of amplification monotonically decreases from 7 ps to an unprecedented [Wang et al., 2006] shortness of 450 fs full width at half-maximum (FWHM), by increasing the plasma densities from  $3 \times 10^{18} \text{ cm}^{-3}$  up to  $1.2 \times 10^{20} \text{ cm}^{-3}$  respectively. These measurements clearly illustrate the dramatic temporal quenching of the amplification as a result of an increase in electron density. As anticipated from the fig. 2.16, the fast rise of the amplification is due to collisional excitation of the lasing transition taking place after the abrupt field ionization process. The ultrafast decay in amplification brings testimony of the *Collisional Ionization Gating* (CIG) process at high densities. Although vital for pumping, the on-going collisional ionization also mainly contributes to shorten the gain lifetime, the number of lasing ions becoming rapidly scarce due to strong over-ionization. Moreover, the maximum amplification factor increases from 150 to 1200 over nearly two orders of magnitude in electron density, in conformity to expectations (cf. fig. 2.19).

We can notice, especially at the highest electron density, the steep fall of the amplification factor after reaching its peak. This behavior is mainly due to the strong ASE signal, which becomes more predominant when the HH is no more synchronized with the peak of amplification. As a result, ASE exhausts the gain of the amplifier and the HH pulse is less efficiently amplified. The slow increase of the measured amplification factor remains not well understood. As reported in the temporal profiles of amplifier gains in fig. 2.15, one should expect a steeper and earlier rise of the amplification. One possible explanation could be linked to the difference of group

velocities between the HH and the IR pump beam as they propagate in the plasma. However, preliminary calculations show that this cause is not sufficient to explain the discrepancy between the experimental and numerical data.

Besides, a "bounce" in the amplification, right after the main peak is quasi-systematically reported. This "bounce" is clearer at the highest densities and can be explained by the promotion of  $Kr^{6+}$  and  $Kr^{7+}$  species to  $Kr^{8+}$  following collisional ionization, for which the laser transition can be pumped.

### 5.3 Maxwell-Bloch modeling

Using the previously described time-dependent Maxwell-Bloch code *DeepOne* [Oliva et al., 2011; Larroche et al., 2000], the modeling of the radiation transfer in the amplifying SXRL plasma relevant to the experimental conditions has been undertaken. The description of the propagation and amplification of the high harmonic beam is done considering the evolution of plasma parameters, atomic level populations and rates (see section 2.5). Those were computed using an advanced atomic physics model, OFIKinRad, based on the COFIXE code [Cros et al., 2006] taking account of 92 atomic levels of krypton. These data (temporal evolution of the electron density and temperature, atomic collisional radiative rates, population of the lasing ion and population of several atomic levels strongly coupled to the lasing levels) were fed to the time-dependent Maxwell-Bloch code so as to obtain, with its simplified three-level atomic model, the same population inversion as the more complete atomic physics package. The ionization degree in the plasma channel is considered to be initially 3.

As shown in fig. 5.15, our calculations reveal that the amplification lifetime is shorter and starts earlier with steeper slope for higher gas densities, which is in good agreement with the experimental measurements. The Maxwell-Bloch numerical model describes well the atomic processes underpinning the gain temporal quenching over a remarkably large range of electron densities covering nearly two orders of magnitude.

Since the plasma is inhomogeneous as illustrated in fig. 3.19, the amplification profile is a superimposition of different temporal amplification timescales, each corresponding to a particular density. The numerical points (fig. 5.15) correspond to the contribution to amplification from the highest electron densities and describe well the central peak lifetime. Because of the different contributions from various densities that add up to the total amplification, the values of amplification factors have been normalized to match the experimentally measured peak value.

The fig. 5.16 provides a qualitative assessment of the contributions from different densities to the amplification curve and shows the plasma amplification lifetime (blue curve) in case of two electron densities:  $n_e = 1.2 \times 10^{20} \text{cm}^{-3}$  (fig. 5.16a) and  $n_e = 6 \times 10^{19} \text{cm}^{-3}$  (fig. 5.16b). The green-tinted area illustrates, for each case, the time interval where the curve fit is the best. The numerical calculations for  $n_e = 1.2 \times 10^{20} \text{cm}^{-3}$  simulate the amplification peak for  $\Delta t$  between 1.3 and 1.8 ps, whereas those for  $n_e = 6 \times 10^{19} \text{cm}^{-3}$  fit the end tail of the curve between 2 and 3 ps. Regarding fig. 5.16b, a lower normalization factor has been used for the amplification values compared to fig. 5.16a. For delays below 2 ps, the amplification factors from the lower density (black) are dwarfed by those from the highest densities (red), whereas, in the tail of the curve for delays longer than 2 ps, those amplification factors (black) add up to those of intermediate densities.

The numerical calculations have been carried out using *DeepOne* code, based on the model described in section 2.5. This code has been benchmarked [Wang et al., 2008] to study the spatio-temporal evolution of an amplified high-harmonic seed throughout a plasma amplifier.

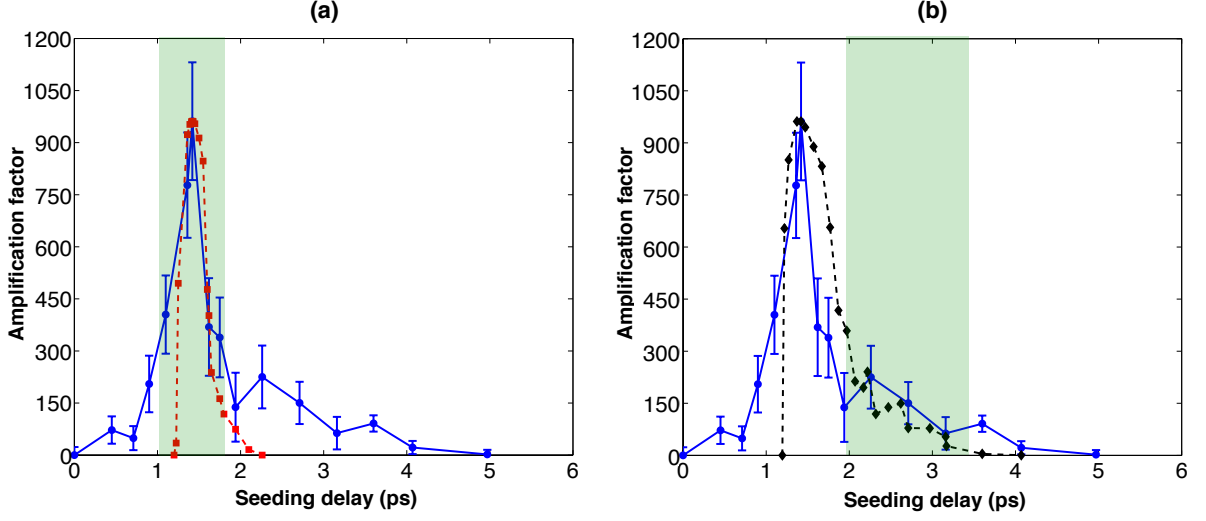


Figure 5.16: Numerical fit of the experimental amplification curve considering  $n_e = 1.2 \times 10^{20} \text{cm}^{-3}$  (a) and  $n_e = 6 \times 10^{19} \text{cm}^{-3}$  (b). The green zone shows the region where numerical data fit experimental data at a particular electron density.

### 5.3.1 Temporal structure of the amplified HH field

Under reasonable considerations, the 1 nJ seed HH pulse FWHM duration is considered to be 60 fs. As the seed signal is well above the plasma spontaneous emission "noise" and much more intense than the ASE, the plasma is immediately coherently polarized. The resulting long-lasting polarization generates and amplifies a **wake** following the HH pulse. The duration of the **wake**, defined as the time interval containing half the total energy of the beam, increases in the first millimeters of the amplifier.

An exact solution of the polarization equation (see eq. (2.136)) at the entrance of the plasma ( $z = 0$ ) can be found assuming the populations are constant within the timescale of the electric field. This approximation is good, as the HH duration is only 60 fs and the populations evolve much slower. This solution can be factorized in three terms, which for an electric field with a Gaussian distribution of standard deviation  $\sigma$  (related to the FWHM duration of the HH pulse) can be written as:

$$P = P_0 \times P_1(t) \times P_2(t) \quad (5.2)$$

$$\text{with } \begin{cases} P_0 = -\frac{iz_{ul}^2}{\hbar} A_s (N_u - N_l) e^{\gamma^2 \sigma^2 / 2} \sigma \sqrt{2\pi} \\ P_1(t) = -\frac{1}{\sigma \sqrt{2\pi}} \int_{-\infty}^t e^{-(\tau - t_s - \gamma \sigma^2)^2 / (2\sigma^2)} d\tau \\ P_2(t) = \begin{cases} e^{-\gamma(t - t_s)} & t \geq t_s \\ 1 & \text{otherwise} \end{cases} \end{cases} \quad (5.3)$$

where  $t_s$  is the time of the maximum seed intensity and  $A_s$ , the amplitude of the electric field at that time. Both terms  $P_1$  and  $P_2$  are normalized to unity (i.e., their maximum value is one) and the numerical value of the polarization is therefore given by  $P_0$ . Polarization is

created by the electric field and thus the rising time is given by  $P_1$ , whereas the decay time, due to collisions, is given by  $P_2$ . This rising time has the same characteristic time as the seed and follows the electric field with a delay depending on the integral of the electric field ( $P_1$ ). On the other hand, the depolarization characteristic time depends only on the plasma properties. In the studied case, the depolarization time ( $\gamma^{-1}$ ) is an order of magnitude greater than the rising time ( $\sigma$ ).

This difference of scale explains the fact that only the **wake** and not the HH is strongly amplified. As shown in fig. 5.17, the seed electric field induces the polarization but due to the intrinsic delay, the HH is barely amplified, as the polarization is still small during their presence. The maximum of the polarization is achieved when the electric field reaches zero and then decays slowly, developing the long-lasting picosecond wake as illustrated in fig. 5.17c.

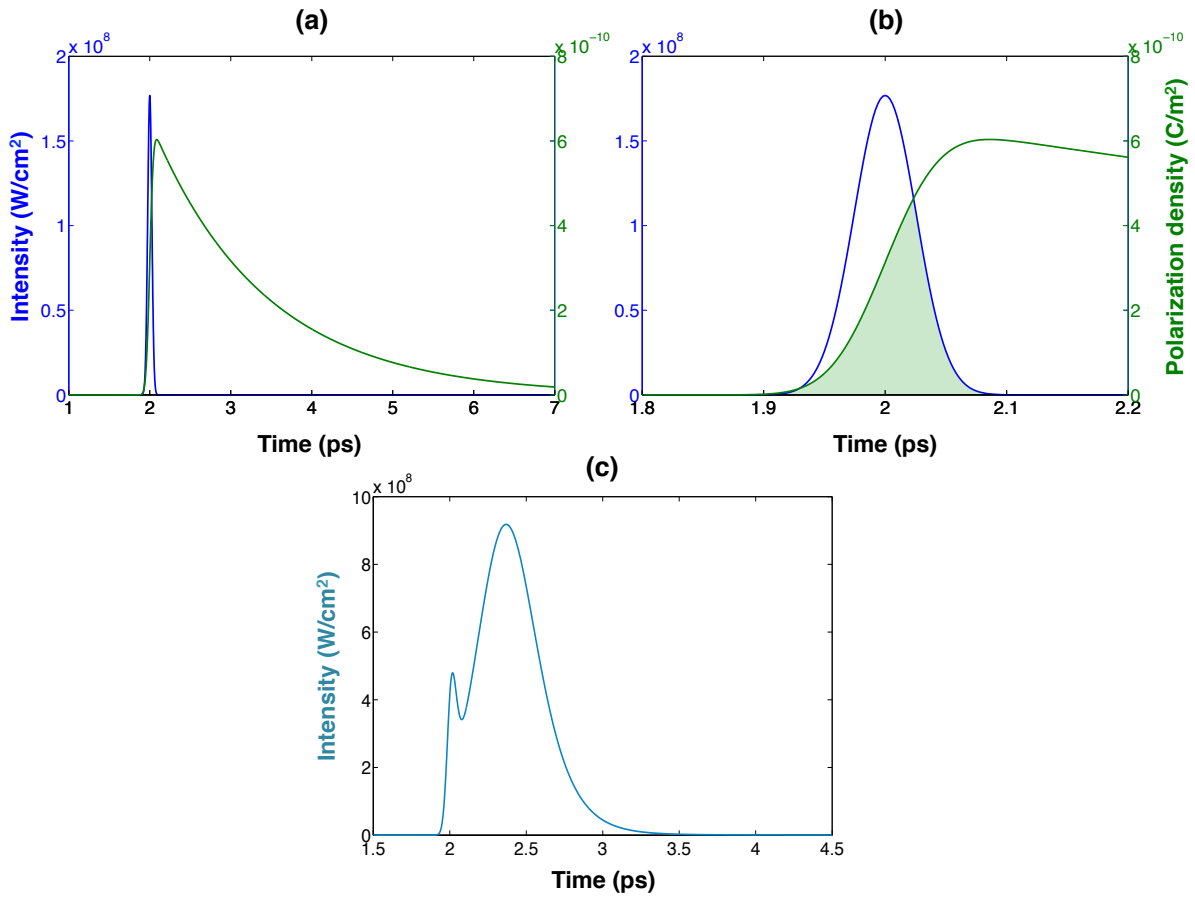


Figure 5.17: (a) Envelope of the HH electric field (blue) and induced polarization density (green) right at the entrance of the plasma amplifier. (b) Close-up. The tinted area depicts the small interaction region, explaining why the wake is amplified at the expense of the HH. (c) Temporal profile of the amplified HH pulse at the output of a plasma amplifier at  $n_e = 6 \times 10^{18} \text{ cm}^{-3}$ .

After 5 mm of amplification, ASE becomes preponderant. The total energy contained in the beam is 100 nJ after 5 mm, which is in good agreement with experimental data. This energy is contained in the wake, whereas the seeded HH pulse is mixed with the ASE.

### 5.3.2 Regimes of amplification of the resonant HH field

The output beam consists in a barely amplified HH pulse preceding a wake displaying **Rabi oscillations** and depolarization-induced decay [Almiev et al., 2007]. The amplified HH pulses are characterized by two regimes: a so-called dynamic regime, characterized by **Rabi oscillations** and an adiabatic regime governed by the evolution of the amplified field envelope [Laroche et al., 2013].

#### 1. Depolarization-induced decay:

The dipole emission is typical of a two-level atomic system subjected to a resonant external field. However, the plasma exhibits a great number of those dipoles and the resulting coherent emission relies on their ability to emit in phase. A single dipole is coupled to external fields, which notably lead to the depolarization of the medium. This depolarization therefore determines the lifetime of the coherent amplification of the resonant HH field.

The oscillating electron radiates and thus loses energy. Hence, the amplitude of an individual dipole momentum decreases. Moreover, electron-ion collisions induce phase shifts between individual dipoles without affecting their amplitude. Because the phases of those individual dipoles cannot be added, the amplitude of the resulting dipole decreases. Electron-ion collisions gradually destroy the macroscopic polarization.

#### 2. Saturated regime and Rabi oscillations:

As the HH pulse propagates through the plasma and gets substantially amplified, its electric field starts saturating the population inversion, which leads to the development of **Rabi oscillations**. As described in section 6.3.2, saturation effects following the strong amplification of the HH field lead to strong oscillations in the population inversion, which can even become negative and turn the medium absorbent. This behavior induces similar oscillations in the medium polarization and the amplified field. Those oscillations are known as **Rabi oscillations** and are observed in case of an isolated two-level system. The coherent external field drives the population of the atomic system between the upper and lower level states with a period  $\pi/\Omega_R$ . Those oscillations can be interpreted by simplifying the set of Maxwell-Bloch equations on field (eq. eq. (2.129)), medium polarization (eq. (2.136)) and the atomic populations (eq. (2.137)). We consider a linearly-polarized HH field and neglect the influence of collisional effects responsible for the dipole and population inversion relaxation, as those occur on a timescale (a few ps) bigger compared to the observed **Rabi oscillations**. In those conditions, we obtain:

$$\frac{\partial P}{\partial \tau} = \frac{iE}{\hbar} d_{ul}^2 \Delta N \quad \text{and} \quad \frac{\partial \Delta N}{\partial \tau} = \frac{i}{2\hbar} E \cdot P \quad (5.4)$$

The variations of the envelope of the field  $\partial E/\partial \tau$  can be neglected compared to  $\partial P/\partial \tau$  and  $\partial \Delta N/\partial \tau$ . Hence, we can write for the population inversion:

$$\frac{\partial^2 \Delta N}{\partial \tau^2} = -\frac{E^2 d_{ul}^2}{2\hbar^2} \Delta N \quad (5.5)$$

In those conditions, the population inversion oscillates at a Rabi frequency  $\Omega_R$ :

$$\Omega_R = \frac{d_{ul}}{2\hbar} \sqrt{I} \quad (5.6)$$

with  $I$ , the intensity of the field. Similarly, the medium polarization and the amplified field display this behavior. This Rabi frequency can be expressed [Robillart, 2010] as a function of characteristic relaxation times  $T_1$  and  $T_2$ :

$$\Omega_R \propto \sqrt{\frac{I}{T_1 T_2}} \quad (5.7)$$

The time constant  $T_1$  is the gain recovery time. It characterizes the relaxation of the population inversion towards its equilibrium value. The time constant  $T_2$  is the phase shift time. It corresponds to the timescale, upon which the emitting dipoles get out of phase with respect to each other, which subsequently destroys the coherent emission.  $T_1$  denotes the energy relaxation and  $T_2$  the phase relaxation.

The long-lasting polarization of the medium, induced by the HH, generates and amplifies a **wake** induced by the HH pulse. The duration of this **wake** increases in the first millimeters of the amplifier. For longer distances, the interaction between the electric field and the atomic populations starts developing **Rabi oscillations**, saturating the gain, and reducing the duration of the **wake**.

### 5.3.3 SXRL pulse buildup

**Amplified pulse temporal profile.** The fig. 5.18 illustrates the HH pulse buildup as it propagates and get amplified in the 5 mm-long plasma for the set of electron densities:  $n_e = 3 \times 10^{18} \text{cm}^{-3}$  (green),  $n_e = 7.9 \times 10^{18} \text{cm}^{-3}$  (magenta),  $n_e = 3.2 \times 10^{19} \text{cm}^{-3}$  (black) and  $n_e = 1.2 \times 10^{20} \text{cm}^{-3}$  (blue). The energy and pulse duration of the HH pulse have been considered to be 1 nJ and 60 fs, respectively.

As illustrated in fig. 5.18, we see that the frequency of Rabi oscillations increases with the intensity of the resonant field. They are anharmonic, as they depend on the field amplitude. The field oscillations decrease at longer times, when the amplified field drops. We can notice that the amplitude of these oscillations increases strongly when the amplification regime is strongly saturated. Moreover, as the electron density is increased, those saturation effects start sooner and the higher dipole phase shifting rate leads to a stronger damping of the Rabi oscillations. Indeed, increasing the electron density causes more electron-ion collisions, which mainly leads to an decrease of the dipole phase shift time constant  $T_2$  (conversely an increase of the associated relaxation rate). As a result, the coherent emission stops sooner. Similarly, the increase of those rates causes a broadening of the laser line, which corresponds to a quenching of the Fourier-limited duration of emission.

As long as the pulse duration (RMS) is concerned, it shrinks from 6.4 ps to 2.9 ps, 645 fs and 64 fs as the electron density rises from  $n_e = 3 \times 10^{18} \text{cm}^{-3}$  to  $n_e = 1.2 \times 10^{20} \text{cm}^{-3}$ . The HH peak intensity is initially  $5.2 \times 10^8 \text{W/cm}^2$ . As the electron density is increased from  $n_e = 3 \times 10^{18} \text{cm}^{-3}$ ,  $n_e = 7.9 \times 10^{18} \text{cm}^{-3}$ ,  $n_e = 3.2 \times 10^{19} \text{cm}^{-3}$  and  $n_e = 1.2 \times 10^{20} \text{cm}^{-3}$ , this peak intensity soars by a factor of 26, 136, 1218 and 12500 respectively after 5 mm of amplification (cf. fig. 5.18). Those pulse profiles include the contribution of ASE within the solid angle of the amplified HH signal (FWHM, i.e. 1 mrad). The coherent amplified pulse totally dominates the stochastic noise from amplified spontaneous emission.



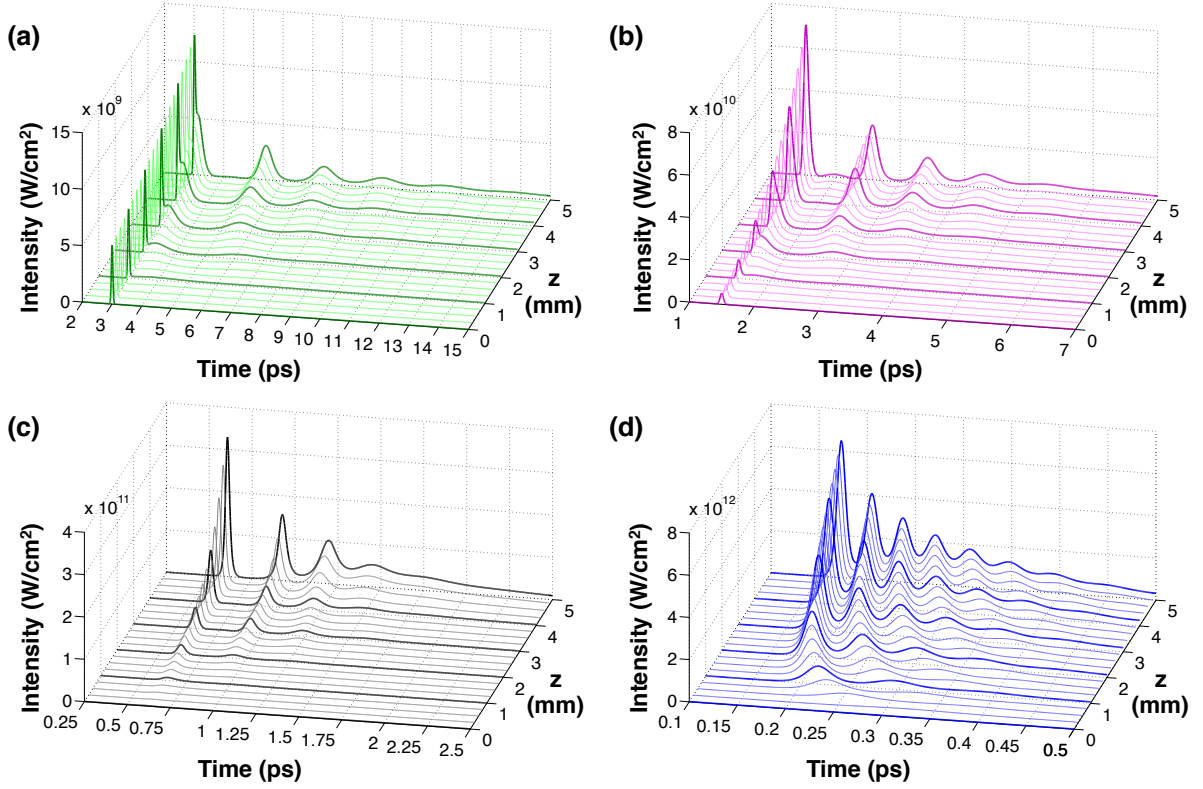


Figure 5.18: HH pulse buildup for a 5 mm-long plasma of electron densities  $n_e = 3 \times 10^{18} \text{cm}^{-3}$  (a),  $n_e = 7.9 \times 10^{18} \text{cm}^{-3}$  (b),  $n_e = 3.2 \times 10^{19} \text{cm}^{-3}$  (c) and  $n_e = 1.2 \times 10^{20} \text{cm}^{-3}$  (d). The HH signal is seeding the plasma at the maximum of amplification.

**Evolution of the population inversion, polarization and amplified field with the electron density.** The fig. 5.19 brings into comparison the temporal evolution of the population inversion between the upper and thrice-degenerate lower level of the  $3d^9 4d_{J=0} \mapsto 3d^9 4p_{J=1}$  transition, with the polarization of the medium (left column) and the amplified HH field (right column). The data are shown after 5 mm of propagation through the plasma. The linearly-polarized electric field of the HH seed involves real and imaginary components of the medium polarization. Therefore, the modulus of the medium polarization is represented. We can see that the variations of the polarization of the medium follow those of the population inversion with a certain delay due to the integration of radiation over the propagation length. The population inversion and the amplified HH field are strongly coupled. We can see that the maxima (conversely minima) of the amplified field correspond to the minima of the population inversion (conversely maxima).



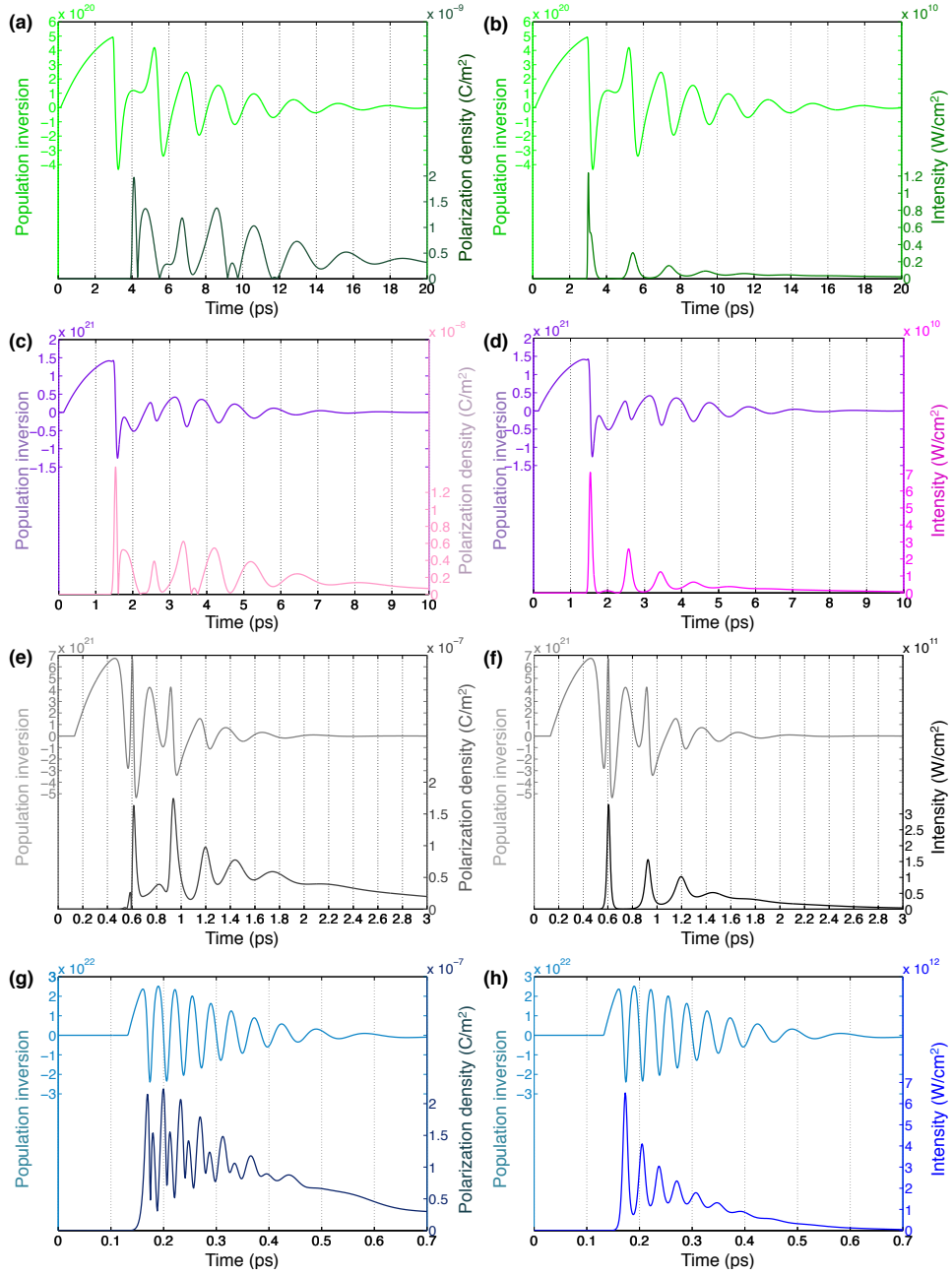


Figure 5.19: Temporal evolution of the population inversion ( $m^{-3}$ ) compared to the polarization density of the medium and the amplified HH field, after 5 mm, for the electron densities:  $n_e = 3 \times 10^{18} cm^{-3}$  (a)&(b),  $n_e = 7.9 \times 10^{18} cm^{-3}$  (c)&(d),  $n_e = 3.2 \times 10^{19} cm^{-3}$  (e)&(f) and  $n_e = 1.2 \times 10^{20} cm^{-3}$  (g)&(h).

#### 5.3.4 Final SXRL pulse duration and discussion

**Extraction of the amplified HH pulse duration.** In plasma-based XRL, the duration of the lasing emission is directly linked to the temporal evolution of the gain. Knowing the gain dynamic permits to infer the SXRL pulse duration with good precision, at the only condition that the plasma dynamic is correctly modeled. The HH-seeded SXRL pulse duration is Fourier-limited [Guilbaud et al., 2010] and therefore shorter than the gain duration. This is due to the fact that the HH pulse width is larger than the amplifier narrow linewidth, but also because the HH pulse duration is far shorter compared to the actual plasma temporal response. As density-induced collisional ionization strongly affects, at high-densities, the broadening of the laser transition levels and the amplification duration in the same way, we can rely on the numerical model to infer the SXRL pulse duration. The HH-seeded SXRL duration only depends on the evolution of the atomic processes regulating the laser transition populations. Therefore, one needs to get a good description of the broadening processes of the laser transition levels to be able to determine its final duration. Those processes include natural, Doppler and collisional broadening. In OFI plasma amplifiers, ions are relatively cool and the contribution of Doppler broadening gets negligible at high electron densities. Hence, both natural and collisional ionization broadening give the full picture of the underlying atomic processes responsible for the SXRL final duration. Experimental data are compared to results from our Maxwell-Bloch numerical modeling, which well reproduce the gain temporal quenching over a remarkably large range of electron densities covering nearly two orders of magnitude (fig. 5.15). The good agreement of the numerical fit with experimental data allows getting, besides electron density measurements (fig. 4.25), a good assessment of the actual electron density, which is pivotal to the description of the broadening effects. As density-induced collisional ionization strongly affects, at high-densities, the broadening of the laser transition levels and the amplification duration in the same way, we can be confident that the numerical model reasonably well describe the atomic processes involved in the laser transition broadening. As a result, the SXRL final duration was extracted from the numerical model.

The fig. 5.20 shows the final duration of the SXRL pulses emitted by the HH-seeded plasma for the four experimentally explored electron density and a prospective one at  $n_e = 4 \times 10^{20} \text{ cm}^{-3}$ . The inferred SXRL pulse duration (RMS) varies from  $6.4 \pm 0.3 \text{ ps}$  for  $n_e = 3 \times 10^{18} \text{ cm}^{-3}$  down to  $23 \pm 6 \text{ fs}$  for  $n_e = 4 \times 10^{20} \text{ cm}^{-3}$ , thus breaking the decade-long picosecond barrier of plasma-based SXRL, and furthermore opening the sub-100 fs range for this type of coherent soft X-ray source.

As shown in fig. 5.20, the temporal structure of the pulse is composed of several periods of Rabi oscillations, induced by the strong amplification of the pulse. Different parts of the beam will induce Rabi oscillations with slight different periods and only the pulse envelope will be observed [Tissandier et al., 2012].

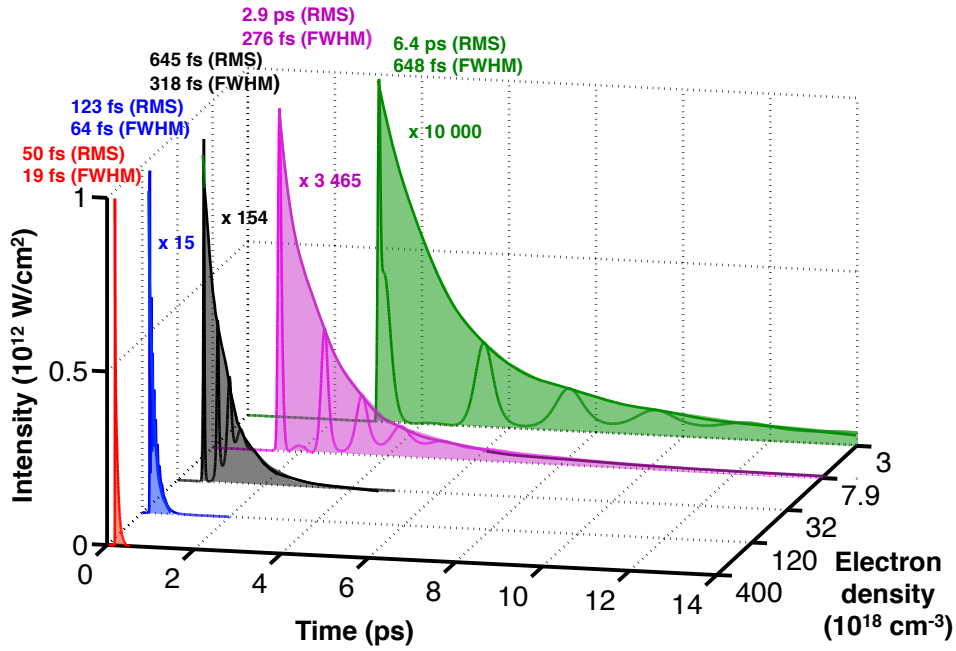


Figure 5.20: Simulated temporal profiles of the amplified SXRL for the set of studied densities and a prospective one of  $n_e = 4 \times 10^{20} \text{ cm}^{-3}$  (red). The duration strongly depends on the density and ranges from  $6.4 \pm 0.3 \text{ ps}$  to  $50 \text{ fs} \pm 18 \text{ fs}$  RMS. The highest experimental density (blue) results in an amplified beam with duration of  $64 \pm 21 \text{ fs}$  FWHM ( $123 \pm 40 \text{ fs}$  RMS). The curves have been normalized to one and their RMS duration specified.

**Illustration of "Collisional Ionization Gating".** The dramatic reduction of the final SXRL pulse duration allowed by the "Collisional Ionization Gating" process, is caused by the anticipated interruption of the gain following the overionization of the medium. To highlight this effect in force at high electron densities, numerical calculations have been carried out artificially fixing the ionization degree of the population of lasing ions.

The fig. 5.21 brings into comparison the amplified HH pulses in the real case, when the plasma ionization degree progressively increases through collisional ionization (blue curve) and in case of an artificially blocked ionization degree (red curve). Those temporal pulse profiles are confronted to the evolution of the average ionization degree of the plasma amplifier over time (data from OFI-0D atomic code). The yellow-tinted area shows the region where  $K\gamma^{8+}$  lasing ions ex-

ist. This region defines a time window (grey-tinted area), in which lasing action occurs (blue curve). When overionization of the lasing ions population is blocked, the SXRL pulse duration is substantially longer (1.15 ps FWHM compared to 123 fs FWHM for the blue curve). Initially, a dynamic regime governed by the oscillating evolution of the population inversion under the influence of a strong amplified HH electric field dominates. Rabi oscillations are therefore observed. After, the profile of the amplified pulse is dominated by the impact of the medium depolarization due to electron-ion collisions. The profile of the red curve shows that the pumping process continues and is not limited by overionization.

The inner envelope of the observed Rabi oscillations is the amplified wake induced by the polarization of the medium by the amplified HH field. When the ionization degree is fixed, the pumping process continues and there is a competition between this polarization induced by the HH and the medium depolarization resulting from electron-ion collisions. This phenomena is materialized by the observed "shoulder" on the red curve.

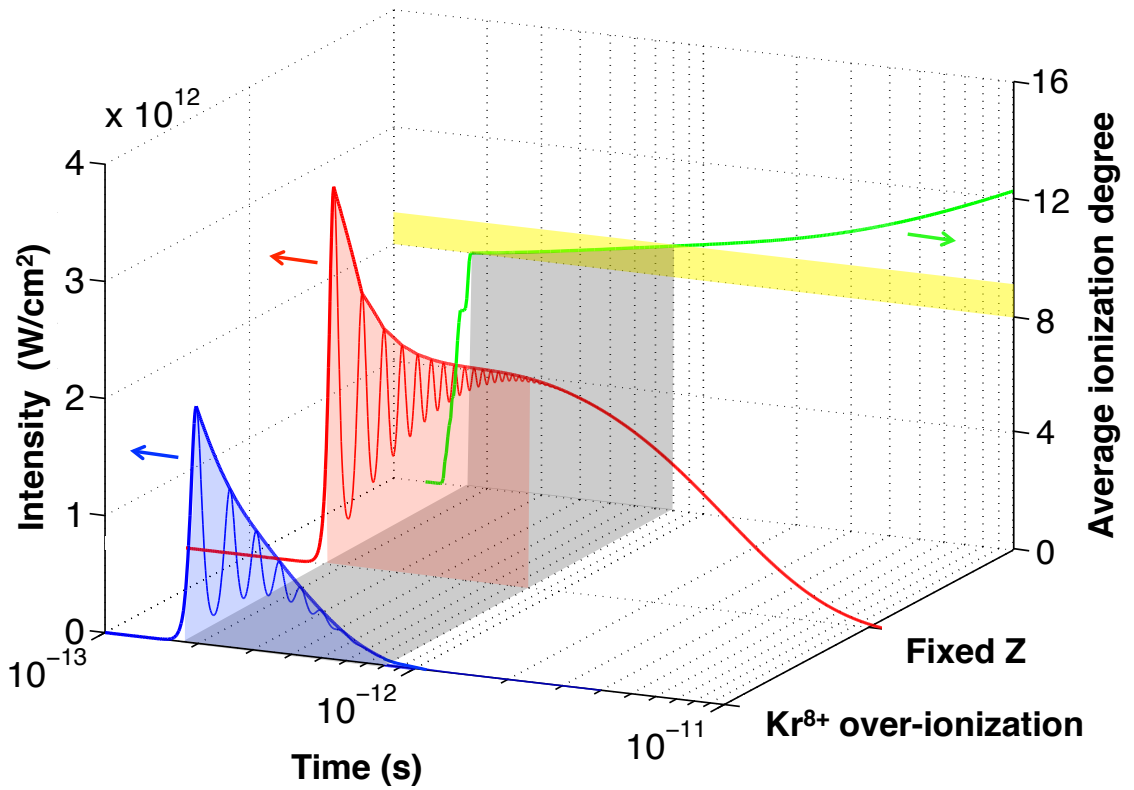


Figure 5.21: Comparison of the HH pulse amplified by a 5 mm-long  $Kr^{8+}$  plasma with  $n_e = 8 \times 10^{19} \text{ cm}^{-3}$  in the real case (blue curve) and when the ionization degree of the lasing ions population is artificially fixed (red curve). The green curve shows the evolution of the average ionization degree and the yellow-tinted area denotes the time region where lasing  $Kr^{8+}$  are present.

**Assessment of the spectral linewidth of the soft X-ray laser emission line.** In case of an OFI collisional plasma amplifiers, the collisional broadening mechanism dominates the other contributions to the soft X-ray laser spectral linewidth (section 2.3.1). As a consequence, the linewidth can be assessed solely from this homogenous broadening source. The electron-ion collision frequency (Hz) used in DeepOne is:

$$\nu_{ei} = 2.63 \times 10^{-6} Z n_e \log(\Lambda) T_e^{-3/2} \quad (5.8)$$

where  $Z$  is the ion charge,  $n_e$  the electron density in  $cm^{-3}$ ,  $T_e$  the electron temperature in eV and  $\log(\Lambda)$ , the Coulomb logarithm:

$$\log(\Lambda) = 23 - \log \left( n_e^{1/2} Z T_e^{-3/2} \right) \quad (5.9)$$

Considering the highest experimentally measured amplifier electron density  $n_e = 1.2 \times 10^{20} cm^{-3}$ , an electron temperature  $T_e = 150$  eV and a charge  $Z=8$ ,  $\log(\Lambda)=5.3195$  and  $\nu_{ei} = 7.3107 \times 10^{12} Hz$ . According to [Whittaker et al., 2010], the FWHM angular frequency bandwidth corresponding to the contribution from collisions is twice the electron-ion collision frequency. Thus, the emission linewidth in the spectral domain,  $\Delta\nu$ , is:

$$\Delta\nu = \frac{\Delta\omega}{2\pi} = 2.3271 \times 10^{12} Hz \quad (5.10)$$

The corresponding Fourier limited duration is difficult to assess as its value strongly depend on the pulse shape. Table 1 of [Sorokin et al., 2000] shows the time-bandwidth product for different pulse shapes. This product is maximized for a Gaussian shape and minimum for a Lorentzian shape. The corresponding duration are:

$$\Delta t_G = \frac{0.4413}{\Delta\nu} = 189 fs \quad \Delta t_L = \frac{0.1420}{\Delta\nu} = 61 fs \quad (5.11)$$

As collisional broadening is the dominating mechanism, it is reasonable to assess that the lineshape is closer to a Lorentzian profile. Thus, the computed value of  $\Delta t_L$  is in very good agreement with the results obtained by the code DeepOne, yielding a 64 fs SXRL pulse duration. As a consequence, we can conclude that this pulse is in Fourier limit. A good match is also achieved for the prospective case of  $n_e = 4 \times 10^{20} cm^{-3}$ , with a FWHM SXRL pulse duration of 20 fs.

Eventually, it is worth to note that no line narrowing correction is needed since an amplification effect is here described and not the intrinsic properties of the amplifier linewidth (ASE).

**SXRL pulse duration versus propagation in the plasma.** The fig. 5.22 shows the variation of the SXRL pulse duration as the HH signal propagates and gets amplified over a 5 mm-long  $Kr^{8+}$  plasma. The data are displayed for a set of electron densities and for the relevant seeding delays corresponding to the maximum in amplification of the HH. As a time-dependent Maxwell-Bloch code is used, the pulses temporal profiles are given by the Fourier transform of the spectra of the emitted radiation. The pulse duration of the HH first increases from its initial value of 60 fs over the first 100s  $\mu\text{m}$  of the plasma. This is due to the fact that coherent excitation of the plasma generates a wake, whose duration corresponds to the characteristic response time of the plasma at a particular electron density (see fig. 5.18). At the highest electron density, the pulse duration decreases after quickly reaching saturation. The pulse duration is then computed from the pulse envelope encompassing the Rabi oscillations. The slight increase of the pulse duration afterwards can be interpreted as a gain-induced narrowing of the HH pulse width.

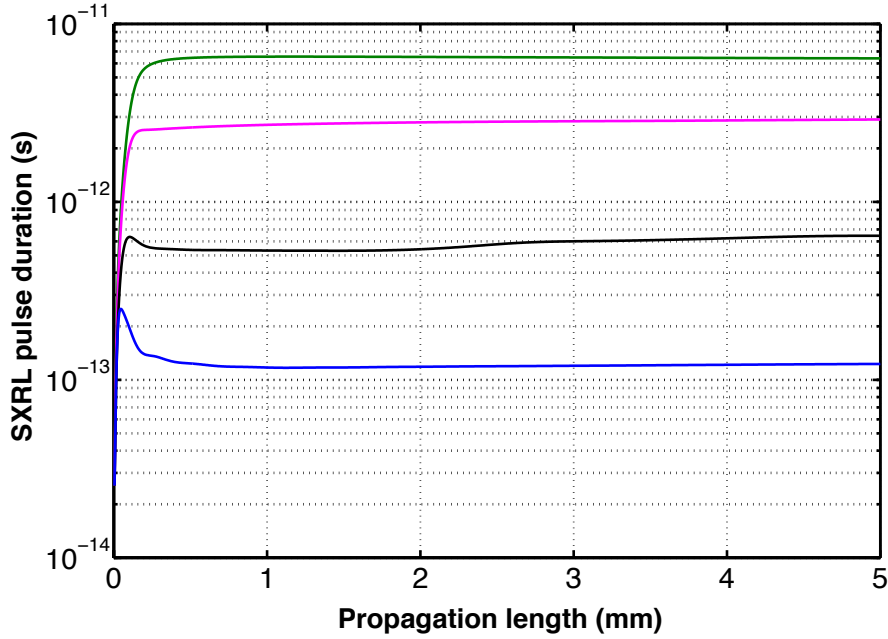


Figure 5.22: Evolution of the amplified HH pulse duration as it propagates in a 5 mm-long  $Kr^{8+}$  plasma amplifier with  $n_e = 3 \times 10^{18} \text{cm}^{-3}$  (green),  $n_e = 7.9 \times 10^{18} \text{cm}^{-3}$  (magenta),  $n_e = 3.2 \times 10^{19} \text{cm}^{-3}$  (black) and  $n_e = 1.2 \times 10^{20} \text{cm}^{-3}$  (blue).

**SXRL pulse duration versus injection delay.** The fig. 5.23 displays the variation of the SXRL pulse duration depending on the injection delay of the HH seed into the plasma amplifier. Calculations were performed in case of the  $Kr^{8+}$  plasma of electron density  $n_e = 1.2 \times 10^{20} \text{cm}^{-3}$ . The evolution of this duration (blue curve) is confronted to the numerically-computed temporal dependence of the amplification factor (aquamarine green). Before 1.2 ps and after 1.9 ps, the plasma does not amplify the HH. The HH pulse duration is therefore only affected by the dispersion of the medium.

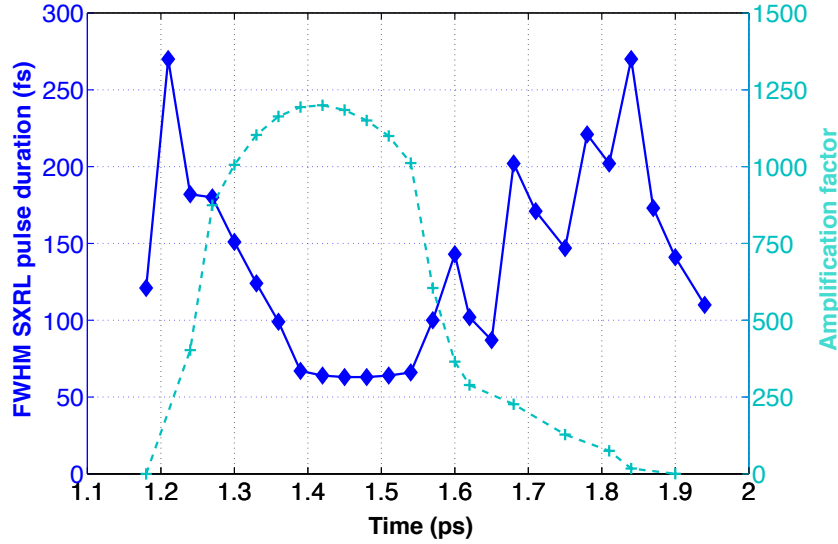


Figure 5.23: Evolution of the amplified HH pulse duration (blue diamonds) for different injection delay times in case of a 5 mm-long  $Kr^{8+}$  plasma amplifier with  $n_e = 1.2 \times 10^{20} \text{cm}^{-3}$ , compared to the amplification factor (aquamarine crosses).

At the early and later injection delays corresponding to the front and end tail of the amplification curve and when the amplification factor is low (below 50), the SXRL pulse duration increases because of the gain narrowing of the linewidth. But, when the HH gets more synchronized with the amplifier gain and the amplification thus increases over both amplification tails, the pulse duration decreases as collisional broadening of the pulse linewidth is stronger. The duration is minimal around the maximum of amplification.

## 5.4 Extracted energy

**Output energy.** Since the Maxwell-Bloch code modeling the HH pulse buildup is 1D, the amplification factor is related to the energy per unit area. Deriving the energy thus requires evaluating the effective emitting surface of the plasma. A HH seed of 1 nJ and 60 fs was considered. For  $n_e = 1.2 \times 10^{20} \text{cm}^{-3}$ , the amplification over 5 mm yielded a SXRL power of  $3.3 \times 10^{12} \text{W/cm}^2$  and a final duration of 64 fs FWHM (Figure 4b). The emitting section was assessed looking at the distribution of  $Kr^{8+}$  ions with WAKE-EP numerical code [Paradkar et al., 2013], which models the propagation of the IR pump beam and the subsequent ionization. The emitting section was found to be an O-ring of  $2.1 \times 10^{-5} \text{cm}^2$  area. This transverse annular surface (defined by circles of diameters 66 and 20  $\mu\text{m}$ ) corresponds to the region populated by  $Kr^{8+}$  ions averaged over the 5 mm-long plasma. Under those considerations, the fig. 5.24 shows the increase of the the amplified HH pulse energy as a function of the plasma length for a set of electron densities. For  $n_e = 3 \times 10^{18} \text{cm}^{-3}$  to  $n_e = 4 \times 10^{20} \text{cm}^{-3}$ , the output energy is 37.6 nJ, 107 nJ, 2.35  $\mu\text{J}$ , 23.8  $\mu\text{J}$  and 118  $\mu\text{J}$ .

Experimentally, for  $n_e = 1.2 \times 10^{20} \text{cm}^{-3}$ , the output beam has been assessed at 2  $\mu\text{J}$  (compared to 23.8  $\mu\text{J}$  in numerical calculations). The discrepancy between the experimental measurement and the numerical calculation comes from the inhomogeneity of the plasma, as illustrated in fig. 3.19. Moreover, in this 1D model, the amplifier has been considered to be uniform and of constant density over 5 mm. However, over-ionization of the plasma at the early stages of the propagation of the IR driving beam is more serious at higher electron densities and lead to shortened effective lengths of the gain region. This can explain why the calculated energy is consistent with measurements at moderate densities while the discrepancy widens at higher electron densities.

Besides, as numerical modeling of propagation at such high electron densities is lacking, the same annular surface of emission obtained at moderate densities has been considered. It should also be noted that plasma channels are wider at moderate densities compared to higher ones (see fig. 5.14). The emission cross section is maybe therefore overestimated at higher electron densities.

The fig. 5.24 also shows the earlier occurrence of the saturation regime as the electron density is increased. For  $n_e = 3 \times 10^{18} \text{cm}^{-3}$ , it starts from about 1 mm whereas it is for  $n_e = 4 \times 10^{20} \text{cm}^{-3}$ , it occurs from about 300  $\mu\text{m}$ .



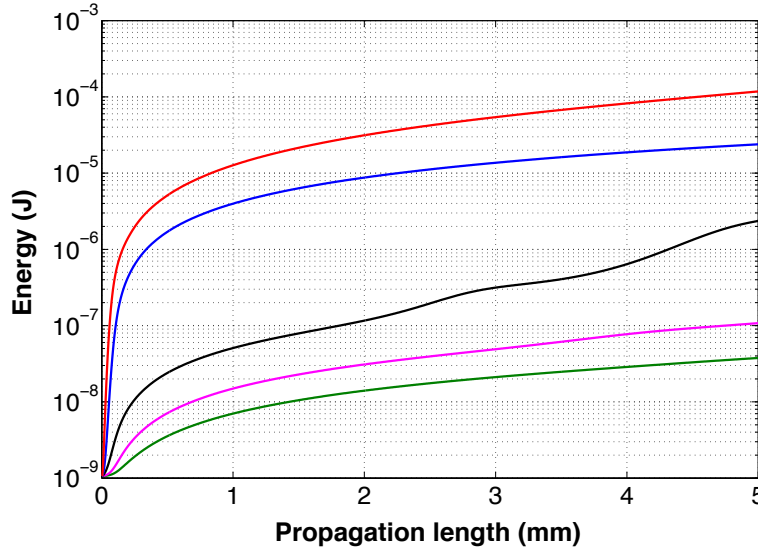


Figure 5.24: Evolution of the amplified HH pulse energy as it propagates into a 5 mm-long  $Kr^{8+}$  plasma of electron density  $n_e = 3 \times 10^{18} cm^{-3}$  (green),  $n_e = 7.9 \times 10^{18} cm^{-3}$  (magenta),  $n_e = 3.2 \times 10^{19} cm^{-3}$  (black),  $n_e = 1.2 \times 10^{20} cm^{-3}$  (blue) and  $n_e = 4 \times 10^{20} cm^{-3}$  (red).

## 5.5 Conclusion

A 5 mm-long plasma amplifier with a density of  $1.2 \times 10^{20} cm^{-3}$  was successfully seeded by a HH source and yielded a  $2 \mu J$  beam displaying a high-quality 1 mrad divergence Gaussian-like beam. The "seeding technique" allowed to sample the gain dynamics of this amplifier and yielded a 450 fs long amplification lifetime, thus breaking the decade-long picosecond range limitation [Depresseux et al., 2015b].

The time-dependent Maxwell-Bloch model was found to be in good agreement with the experimental results over a remarkably wide range of electron density, covering nearly two orders of magnitude. In case of the 5 mm-long plasma amplifier at  $n_e = 1.2 \times 10^{20} cm^{-3}$ , a final SXRL pulse duration was extracted and assessed at  $123 \pm 40 fs$  ( $64 \pm 21 fs$  FWHM).

The generation of longer high density plasmas allowed to reach ASE energies up to  $14 \mu J$  and offers promising prospects. However, the high signal strength of the ASE signal increases the threshold from which the HH seed can be efficiently amplified.

Because of the plasma inhomogeneity, the profile of the final pulse duration is not exactly known at this stage. Further work would require the numerical model to be refined for an adequate description. Qualitatively, the pulse temporal profile is dominated by an intense and ultrashort peak emitted by the highest density regions of the plasma. This peak sits on a longer pedestal corresponding to the emission from the plasma lower densities.

Considering prospective higher densities, up to 100  $\mu J$  pulses of a few tens of femtoseconds are envisioned.

## Chapter 6

# Control of the polarization of plasma-based soft X-ray lasers

Controlling the state of polarization confers an additional source of contrast to probing techniques, thus widening the potential of time-resolved coherent sources at the nanometer scale. Imaging certain samples with a polarization-tunable source can lead to polarization-dependent intensity maps that portrait specific material structures, along with their particular electronic and magnetic properties. Hitherto, the polarization of plasma-based soft X-ray laser has been either undefined or restricted to linear polarization.

This chapter presents the demonstration of a scheme, scalable to different wavelengths, allowing the efficient generation of fully circularly polarized soft X-rays suitable for photon demanding single-shot measurements [Depresseux et al., 2015a]. A numerical code, modeling the amplification of coherent soft X-ray radiation by a plasma has been modified to take account of the polarization of the injected seed signal.

### Contents

---

<b>6.1</b>	<b>Existing circularly-polarized soft X-ray sources</b>	<b>178</b>
6.1.1	Synchrotrons and Free Electron Lasers (FELs)	178
6.1.2	High-harmonic sources	178
<b>6.2</b>	<b>Efficient scheme for a circularly-polarized plasma-based soft X-ray laser</b>	<b>179</b>
6.2.1	Experimental setup	179
6.2.2	Four mirror-phase shifter	180
6.2.3	Rotating analyzer	184
6.2.4	Measurement of the SXRL polarization	185
6.2.5	Output beam profile & energy	189
<b>6.3</b>	<b>Maxwell-Bloch model of amplification of polarized radiation</b>	<b>190</b>
6.3.1	Adaptation of equations to various states of polarization	190
6.3.2	Final energy and duration of the circularly polarized soft X-ray laser	193
6.3.3	Polarization of the amplified HH signal	199
<b>6.4</b>	<b>Conclusion</b>	<b>201</b>

---

## 6.1 Existing circularly-polarized soft X-ray sources

Laser-driven high-order harmonics (HH) or high-energy expensive large-scale facilities, such as synchrotrons and free-electron lasers (FELs) currently spurs on the development of applications using coherent circularly polarized soft X-ray sources. Regarding HH sources, various techniques have been demonstrated to generate circularly polarized soft X-ray sources. However, the generation efficiency of those sources is mostly low compared to their counterparts in linear polarization. As long as synchrotrons and FELs sources are concerned, the operation turns out expensive and complex, thus preventing a flexible and wide-access utilization.

### 6.1.1 Synchrotrons and Free Electron Lasers (FELs)

Coherent circularly polarized soft X-ray radiation has been demonstrated on large-scale facilities. At BESSY synchrotron in Germany, the geometry of the magnets' setup has been modified to generated efficiently circularly-polarized light [Bahrt et al., 1992]. As far as free-electron lasers (FELs) are concerned, circularly-polarized radiation has been demonstrated [Schneidmiller and Yurkov, 2013; Deng et al., 2014] by modifying the configuration of undulators. Under those conditions, circularly-polarized emission can very efficiently generated. Furthermore, FEL emission is characterized by both short wavelength and time duration.

Notwithstanding, such techniques turn out expensive and complex, thus preventing a flexible and wide-access utilization at the laboratory scale.

### 6.1.2 High-harmonic sources

Regarding laser-driven soft X-ray sources, the availability of coherent circularly polarized beam has been limited so far to high-order harmonics (HH).

The polarization of HH is directly governed by the atomic dipole direction determined by the driving laser polarization [Lewenstein et al., 1994]. However, electron recombination probability drops sharply when the driving laser ellipticity increases, thus leading to a very poor radiation efficiency [Dietrich et al., 1994]. Several techniques were proposed to overcome this bottleneck and efficiently generate circularly polarized HH. One promotes the use of pre-aligned molecules as targets for high-harmonic generation [Zhou et al., 2009]. However, while being complex, the setup provides a degree of circular polarization below 40%. Other methods were proposed, notably suggesting sub-optical synchronization between subsequent re-collision processes occurring along different directions in the polarization plane of the driver. This can be implemented by irradiating atoms with a circularly polarized counter-rotating bichromatic driver [Fleischer et al., 2014] or a cross-polarized two-colour laser field [Lambert et al., 2015]. Very recently, resonant high-order harmonic generation [Ferré et al., 2014] was achieved and produced bright quasi-circular pulses in the extreme ultraviolet. Finally, another approach consists in using a reflector phase-shifter [Hochst et al., 1994] to turn circular linearly-generated harmonics. This method allows getting fully circularly polarized X-ray radiation up to about 70 eV, but the efficiency is limited to a few percent, depending on the wavelength [Vodungbo et al., 2011].

However, the photon yield of HH beams remains low, which turns those sources inopportune for single-shot measurements.

## 6.2 Efficient scheme for a circularly-polarized plasma-based soft X-ray laser

To fill the gap between HH sources and large-scale facilities, collisional soft x-ray lasers (SXRL) offer a promising approach for generating compact but photon-rich circularly polarized light allowing photon-demanding measurements at the laboratory scale [Rus et al., 2002]. Despite of one proposal based on Zeeman splitting of the  $3d^9 4d_{J=0} \mapsto 3d^9 4p_{J=1}$  transition of the nickel-like molybdenum ions at 18.895 nm [Hasegawa et al., 2009], the polarization of existing SXRL sources has been either undefined or restricted to be linear so far [Kawachi et al., 1995; Zeitoun et al., 2004]. Seeded soft x-ray lasers (SXRLs) thus offer an alternative approach for generating circularly polarized coherent light, which has not been demonstrated so far and therefore appear as a new milestone in the development of plasma-based soft X-ray lasers. In 2004, it was reported that the high-harmonic seeded soft X-ray laser retains the linear polarization state of the seeded HH [Zeitoun et al., 2004]. The physical processes governing the time-dependent populations of the  $3d^9 4d_{J=0} \mapsto 3d^9 4p_{J=1}$  laser transition atomic levels in Ni-like Krypton ions are described in section 6.3.1. Indeed, the lower level of the electric dipole laser transition has three degenerate sublevels ( $m = -1, 0, 1$ ). Emission from the upper to the ( $m = -1$ ) or ( $m = 1$ ) lower-levels is distinctly characterized by left-handed or right-handed circular polarization respectively. The stimulated emission induced by a circularly polarized HH source is thus expected to control a particular resonant transition. Therefore, the polarization of amplified injection-seeded HH corresponds to the polarization of the seed, whose components preferentially excite a particular transition. As a consequence, seeding a soft X-ray plasma amplifier by a circularly polarized seed is expected to efficiently generate a coherent circularly polarized source.

### 6.2.1 Experimental setup

In this perspective, the present work proposes an original approach based on the integration of a reflector phase-shifter into a 32.8 nm plasma-based soft X-ray laser chain [Zeitoun et al., 2004], as illustrated in fig. 6.1.

Because of low transmission of the polarizer, it was not possible to use a high-density plasma amplifier. Indeed, as previously reported, the low signal strength of seeded circularly-polarized HH causes the seeding signal to be outmatched by the strong ASE. A low-density gas cell has therefore been used. The experiment was done in "Salle Jaune" (see section 4.1.1). The krypton plasma amplifier is implemented by longitudinally pumping a krypton gas cell with a 1.36 J, 30 fs Ti:sapphire laser centered around 813 nm using a 75 cm focal length spherical mirror. The collisional pumping of the generated  $Kr^{8+}$  ions leads to a strong lasing of the  $4d \mapsto 4p$  laser transition at 32.8 nm. The seed beam was obtained by focusing a 20 mJ, 30 fs, infrared laser in a gas cell filled with argon. This seed was image-relayed onto the entrance of the amplifier using a grazing-incidence toroidal mirror. The 25th HH signal was then spectrally tuned onto the amplifier ASE lasing line at 32.8nm chirping [Lee et al., 2001] the driving laser beam while its flux was optimized changing the gas pressure and altering the focusing conditions, notably by fine-tuning the beam aperture with an iris. The seed beam arrives 3 ps after the pump beam.

The phase-shifter consists in four grazing incidence mirrors [Vodungbo et al., 2011], converting linear to circular polarization. This method allows getting fully circularly polarized soft X-ray radiation up to about 70 eV, but the efficiency is limited to the device transmission, which amounts to only a few percent, depending on the wavelength [Vodungbo et al., 2011].

By placing the phase-shifter polarizer before the amplification stage, this architecture promises to leverage the merits of the reflector phase-shifter technique [Hochst et al., 1994] while efficiently

compensating the losses of the system by the amplifying properties of the plasma.

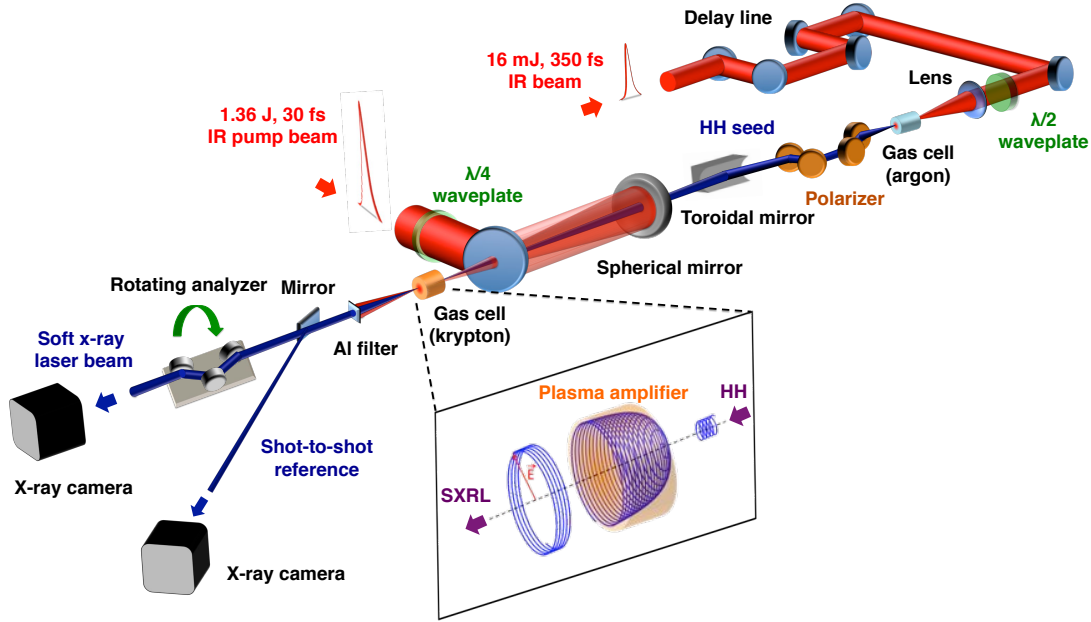


Figure 6.1: Schematic description of the experimental setup. The pump beam (1.36 J, 30 fs) is being focused in a gas cell filled with krypton thanks to a spherical mirror. Thus, an amplifier with  $Kr^{8+}$  lasing ion species over the whole gas cell length is implemented. A second IR beam (16 mJ, 350 fs) is used to generate high-harmonics in another gas cell filled with argon. A downstream four-reflector phase shifter (polarizer) and a  $\lambda/2$  waveplate allow converting HH polarization from linear to circular. HH are then image-relayed onto the entrance of the  $Kr^{8+}$  plasma and synchronized with the pump beam to match the gain lifetime. A rotating analyzer collects the soft X-ray laser signal at the end of the chain, whereas a reference intensity measurement compensates shot-to-shot signal fluctuations.

### 6.2.2 Four mirror-phase shifter

Multiple-mirrors phase-shifters prove to be a very attractive solution to generate various states of polarization from linearly-polarized monochromatic beams in the energy range from 8 to 100 eV.

**Principle.** The use of a set of mirrors in grazing incidence allows altering the polarization of input linearly-polarized radiation by imparting different phase shifts between its p- and s-polarization components. The generation of circularly-polarized light requires a  $\pi/2$  phase delay between p- and s-polarization components. Considering a unique mirror, this phase delay increases for higher grazing incidence angles, however the transmission drops sharply in the soft X-ray range in those conditions. Hence, a tradeoff between the phase delay and the transmission is needed. This can be reached by resorting to lower individual contributions to the total phase delay from multiple reflectors, which can then each afford working in a grazing incidence configuration, thus maximizing the transmission. The use of four grazing-incidence mirrors turns out to be convenient from this point of view, but also because this setup keeps the optical axis unchanged.

**Conditions for generating circularly-polarized light.** A general case of elliptical polarization can be described by the following ellipse:

$$\frac{p^2}{E_p^2} + \frac{s^2}{E_s^2} + \frac{2\cos\phi}{E_p E_s} ps = 0 \quad (6.1)$$

where  $p$  and  $s$  are the coordinates along  $p$ - and  $s$ -polarization directions respectively, and  $E_p$  and  $E_s$  the corresponding values of the field. The phase  $\phi$  is the phase delay between  $p$ - and  $s$ -components. This ellipse determines the shape described by the field over an optical period in a plane transverse to its propagation directions. A Jones vector representation summarizes the amplitudes and phase along polarization directions:

$$J_{ellipse} = \begin{bmatrix} E_p \\ E_s e^{i\phi} \end{bmatrix} \quad (6.2)$$

The figure fig. 6.2 illustrates the parameters defining the polarization ellipse. The amplitudes  $a$  and  $b$  are, respectively, the biggest (major axis) and lowest (minor) amplitudes that the field takes over an optical cycle. The major axis direction is given by  $\alpha$  and is related to the phase difference  $\phi$  through the formula:

$$\tan 2\alpha = \frac{2E_p E_s}{E_p^2 - E_s^2} \cos\phi \quad (6.3)$$

In this case, the amplitudes  $a$  and  $b$  read:

$$\begin{cases} a^2 = E_p^2 \cos^2 \alpha + E_s^2 \sin^2 \alpha + 2E_p E_s \sin \alpha \cos \alpha \cos \phi \\ b^2 = E_p^2 \sin^2 \alpha + E_s^2 \cos^2 \alpha - 2E_p E_s \sin \alpha \cos \alpha \cos \phi \end{cases} \quad (6.4)$$

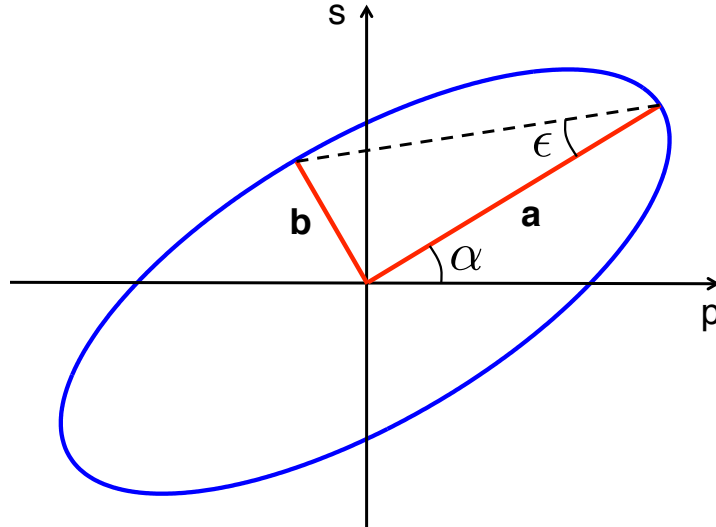


Figure 6.2: Polarization ellipse defining the ellipticity angle  $\epsilon$ .

From equation 6.3 and 6.4, one can derive that circularly-polarized light is characterized by a phase delay of  $\pi/2$  between  $p$ - and  $s$ -polarization components, and equal amplitudes along those two polarization directions. This leads to a helix-shape field distribution, as depicted in fig. 6.3.

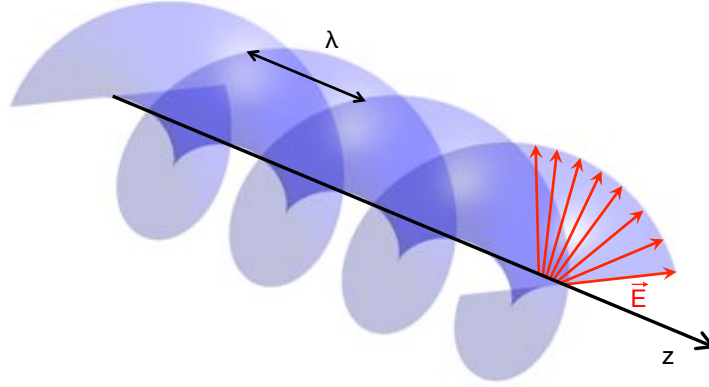


Figure 6.3: Illustration of a circularly polarized field traveling along the z-direction.

The polarizer, consisting of a four-reflector phase-shifter is illustrated in fig. 6.4. In this configuration, the mirrors reflect the input beam under identical angles of incidence  $\theta$ . The direction of the input linearly polarized high-harmonic signal is the same as the polarization direction of the IR driving laser and makes an angle  $\Upsilon$  with respect to the p-direction. The mirror coatings are made of pure gold. Indeed, uncoated gold has the advantage to offer large phase delays between p- and s-polarization components under grazing incidence, while maximizing the overall output transmission.

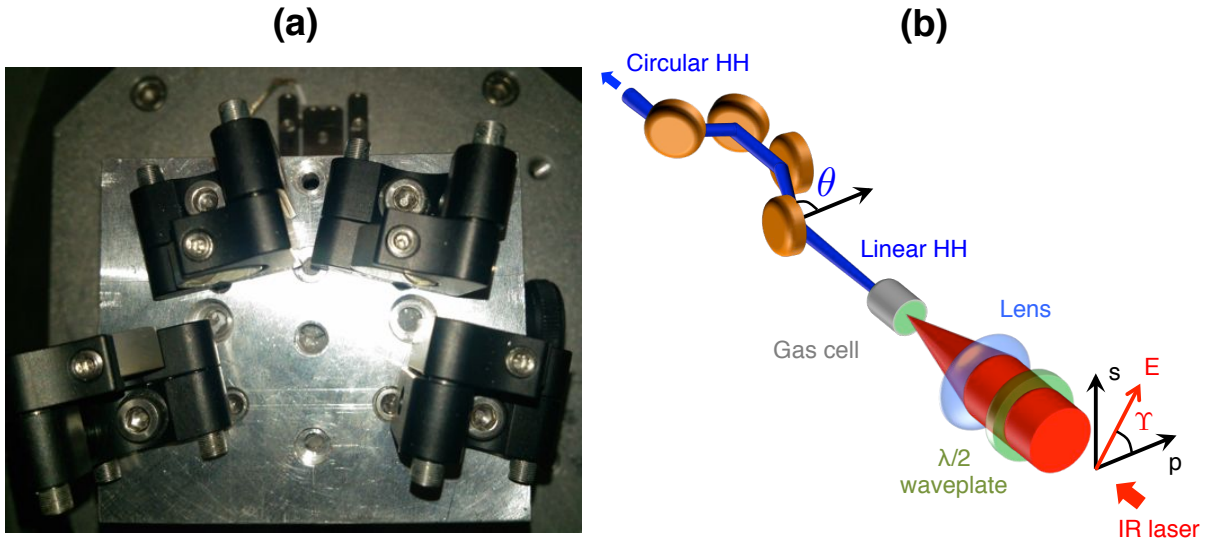


Figure 6.4: (a) Four-reflector phaser shifter. (b) Generation of circularly-polarized HH. The four mirrors are under  $\theta$  incidence angle. The polarization direction of the driving IR laser is determined by the angle  $\Upsilon$ .

The reflectors' angles of incidence are chosen to yield an overall phase shift of  $\pi/2$  between p- and s-polarization components, whereas the polarization direction of the HH driving laser is adopted to equal both components field amplitudes. For the latter purpose, a  $\lambda/2$  waveplate allows controlling the polarization direction of the infrared laser driver.

The Fresnel equations give the amplitude reflectivities for p- and s-polarization components of a



wave being reflected onto a mirror of index  $N = n + i \times k$ , with  $n$  and  $k$  the real and imaginary parts of the refractive index, respectively:

$$\begin{cases} r_p e^{i\delta_p} = \frac{N^2 \cos(\theta) - \sqrt{N^2 - \sin^2(\theta)}}{N^2 \cos(\theta) + \sqrt{N^2 - \sin^2(\theta)}} \\ r_s e^{i\delta_s} = \frac{\cos(\theta) - \sqrt{N^2 - \sin^2(\theta)}}{\cos(\theta) + \sqrt{N^2 - \sin^2(\theta)}} \end{cases} \quad (6.5)$$

Considering an input beam of linear polarization, the phase delay between p- and s-components imparted by the polarizer is  $\Delta = \delta_p - \delta_s$ . The phase shift is evenly imparted by each mirror. Hence, we can write:

$$\Delta = 4 \times \Delta_1 \quad (6.6)$$

with

$$r_p = |r_{p1}|^4 \quad \text{et} \quad r_s = |r_{s1}|^4 \quad (6.7)$$

where  $\Delta_1$ ,  $r_p$  et  $r_s$  are respectively the phase delay and amplitude reflectivities imparted by one mirror.

It should be noticed that the design has to take account of the image-relay system composed of a *Pt*-coated toroidal mirror and a *SiO<sub>2</sub>*-coated plane mirror. Those image-relay optics are both under  $85^\circ$  of incidence. Hence, their contributions amount to:

$$\Delta_{IR} = -0.218 \quad r_p^{IR} = 0.7981 \quad r_s^{IR} = 0.8534 \quad (6.8)$$

Then, the conditions for getting circularly-polarized light translate:

$$\begin{cases} \Delta_1 = \pi/8 - \Delta_{IR}/4 \\ r_p * r_p^{IR} = r_s * r_s^{IR} \times \tan(\Upsilon) \end{cases} \quad (6.9)$$

The fig. 6.5 illustrates the needed configuration for the circular polarizer, taking account of the uncoated gold refractive index defined with the following parameters at 32.8 nm:

$$\begin{cases} n = 0.79003 \\ k = 0.37486 \end{cases} \quad (6.10)$$

The fig. 6.5a shows that the angle  $\theta$ , for which  $|\Delta_1| - \pi/8 + \Delta_{IR}/4$  is equal to zero, is  $11.95^\circ$ . For four mirrors in this configuration, the polarizer total reflectivities are  $r_p = 0.2403$  and  $r_s = 0.4538$ . To equal amplitudes along p- and s-directions, the condition 6.9 yields the needed value for the angle  $\Upsilon$ :

$$\Upsilon = 26.35^\circ \quad (6.11)$$

Considering the driving IR laser is p-polarized, the  $\lambda/2$  wave plate has to be turned by about  $13.1^\circ$  with respect to the p-polarization direction.

Under those conditions, the total transmission of the polarizer is  $T = 2r_s^2 \sin^2(\alpha) = 6.26 \%$ .



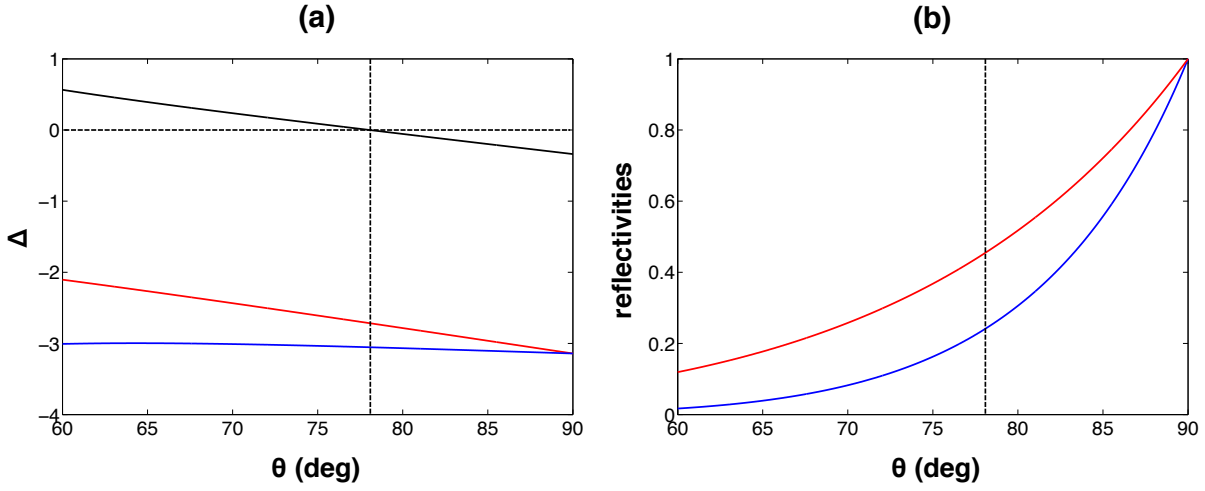


Figure 6.5: (a) Phase delays  $\delta_p$  (blue),  $\delta_s$  (red) and  $|\Delta_1| - \pi/8 + \Delta_{IR}$  (black). (b) Polarizer amplitude reflectivities  $r_p$  (blue) and  $r_s$  (red). The dotted line illustrates the mirrors' configuration to yield circularly polarized HH.

### 6.2.3 Rotating analyzer

The polarization of both harmonics and the seeded soft X-ray signal has been studied with the help of a rotating analyzer consisting of three mirrors. Upstream from it, an off-axis plane mirror collects a part of soft X-rays for a reference measurement to get rid of shot-to-shot signal fluctuations, as reported in fig. 6.1.

The analyzer is made of three multilayer mirrors ( $Mo(35 \text{ nm})/B4C(5 \text{ nm})$ ). Those mirrors are placed on a mount, illustrated in fig. 6.7, which keeps the optical axis unchanged while rotating over  $90^\circ$ . The choice of the mirrors' angles is dictated by a tradeoff between the device contrast and its transmission. Actually, considering a linearly polarized input beam, the signal will oscillate between  $T_p \times I_0$  and  $T_s \times I_0$ , where  $I_0$  is the incident signal intensity and  $T_p = R_p^2(\beta) \times R_p(2\beta)$  with  $T_s = R_s^2(\beta) \times R_s(2\beta)$ , the transmissions along p- and s-polarization directions with  $\beta$ , the grazing incidence angle. A large contrast, allowing clear distinction between polarization states, requires fairly large grazing incidence angles, as shown in fig. 6.6b, which is done at the expense of the analyzer transmission.

The compromise is chosen with a  $20^\circ - 40^\circ - 20^\circ$  grazing incidence configuration. Hence, according to fig. 6.6a, the transmissions for p-, s- and circular polarizations are:

$$T_p \approx 3.5\% \quad T_s \approx 0.4\% \quad T_{circ} \approx 2\% \quad (6.12)$$

The polarization state was studied using a rotating the system of mirrors about the optical axis. Those mirrors are placed on a mount, illustrated in fig. 6.7, which keeps the optical axis unchanged while rotating over  $90^\circ$ .

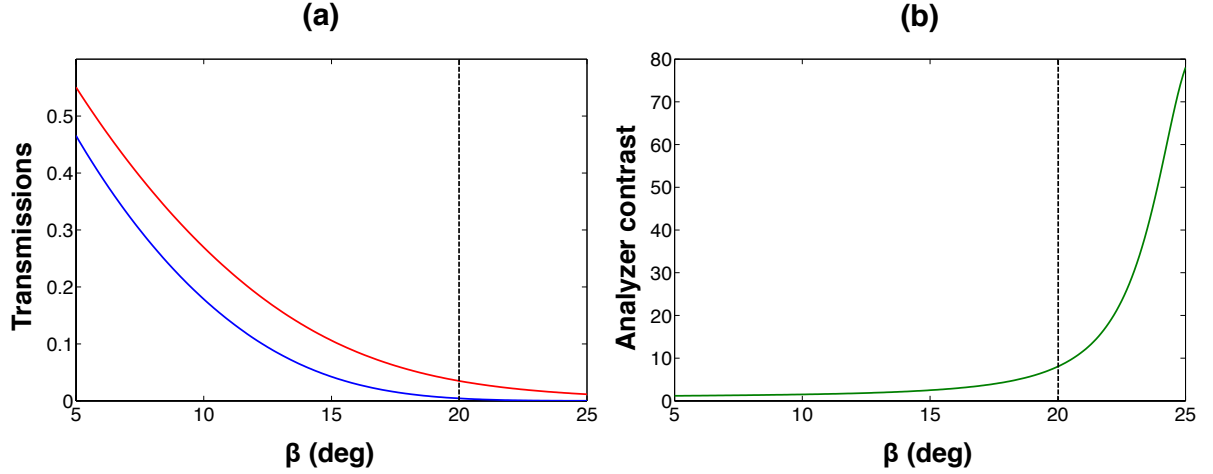


Figure 6.6: (a) Analyzer transmissions  $T_p$  (blue) and  $T_s$  (red). (b) Contrast of the analyzer ( $T_s/T_p$ ). The chosen mirrors' configuration is determined by the dotted line.

#### 6.2.4 Measurement of the SXRL polarization

In case of circularly polarized radiation generation, the effective polarizer and analyser transmissions were found to be 1.5 % and 1 % respectively, resulting in signal accumulation for polarization measurements over one minute.

The fig. 6.8 reports the experimental intensities as a function of the analyzer rotation angle in case of linear and circular polarization, for both HH and SXRL signals. Raw data were corrected by the reference measurements and then presented in fig. 6.8 normalizing the recorders intensities by the value  $(I_{max} + I_{min})/2$  (see Appendix F). For linear polarization, the Malus law [Vodungbo et al., 2011] has been recovered with the same contrast of about 7 between s- and p-transmissions for both the HH (fig. 6.8a) and SXRL (fig. 6.8b) signals, thus testifying the linear polarization of harmonics is being fully maintained over amplification. In case of seeding with circularly polarized harmonics, the signal appears to almost not vary while rotating the analyser. Fluctuations of less than 9% with respect to 1 can be explained by a slight misalignment of the polarizer or shot-to-shot fluctuations of the SXRL beam direction, thus altering the angle under which the signal is collected by the analyzer. As the experimental points distribution turn out mostly flat for the HH (fig. 6.8c) and the SXRL (fig. 6.8d), we can conclude the circular polarization state has been maintained over amplification.

**Polarization state recovery.** The fitting of experimental data was done deriving a theoretical expression of the intensity recorded by the camera at the output of the analyzer. The Stokes vector formalism is used to describe the state of polarization. Considering the general case of elliptical polarization with parameters defined in fig. 6.2, the polarization state can be written:

$$S_{in} = \begin{bmatrix} 1 \\ \cos 2\alpha \cos 2\epsilon \\ \sin 2\alpha \cos 2\epsilon \\ \sin 2\epsilon \end{bmatrix} \quad (6.13)$$

The normalized intensity recorded by the camera can therefore be written as a function of the ellipse parameters and the rotation angle of the analyzer  $\gamma$  (see Appendix F):

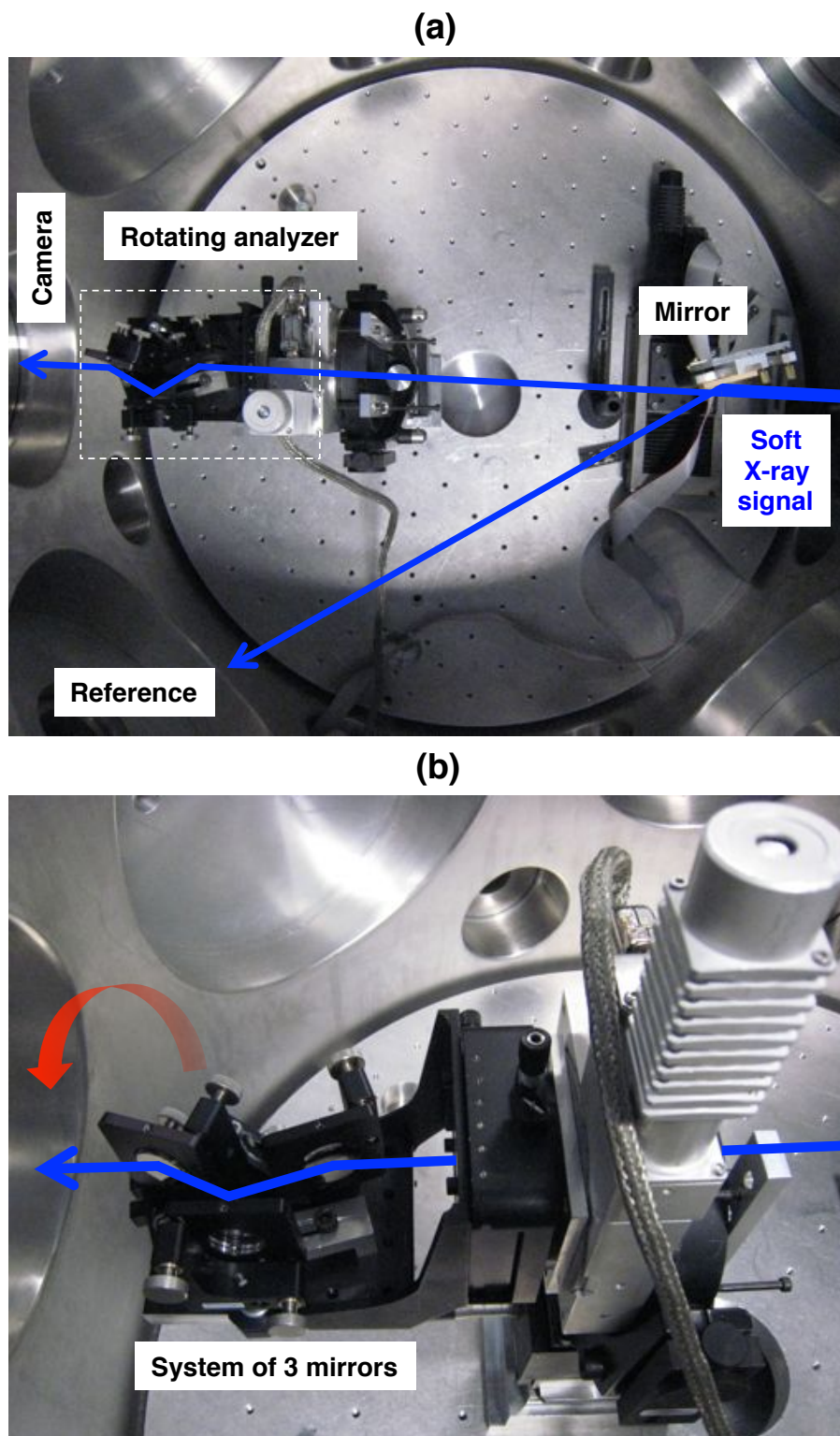


Figure 6.7: (a) Polarization analysis setup composed of a rotating analyzer and a shot-to-shot reference measurement. (b) Close-up of the rotating analyzer composed of 3 mirrors.

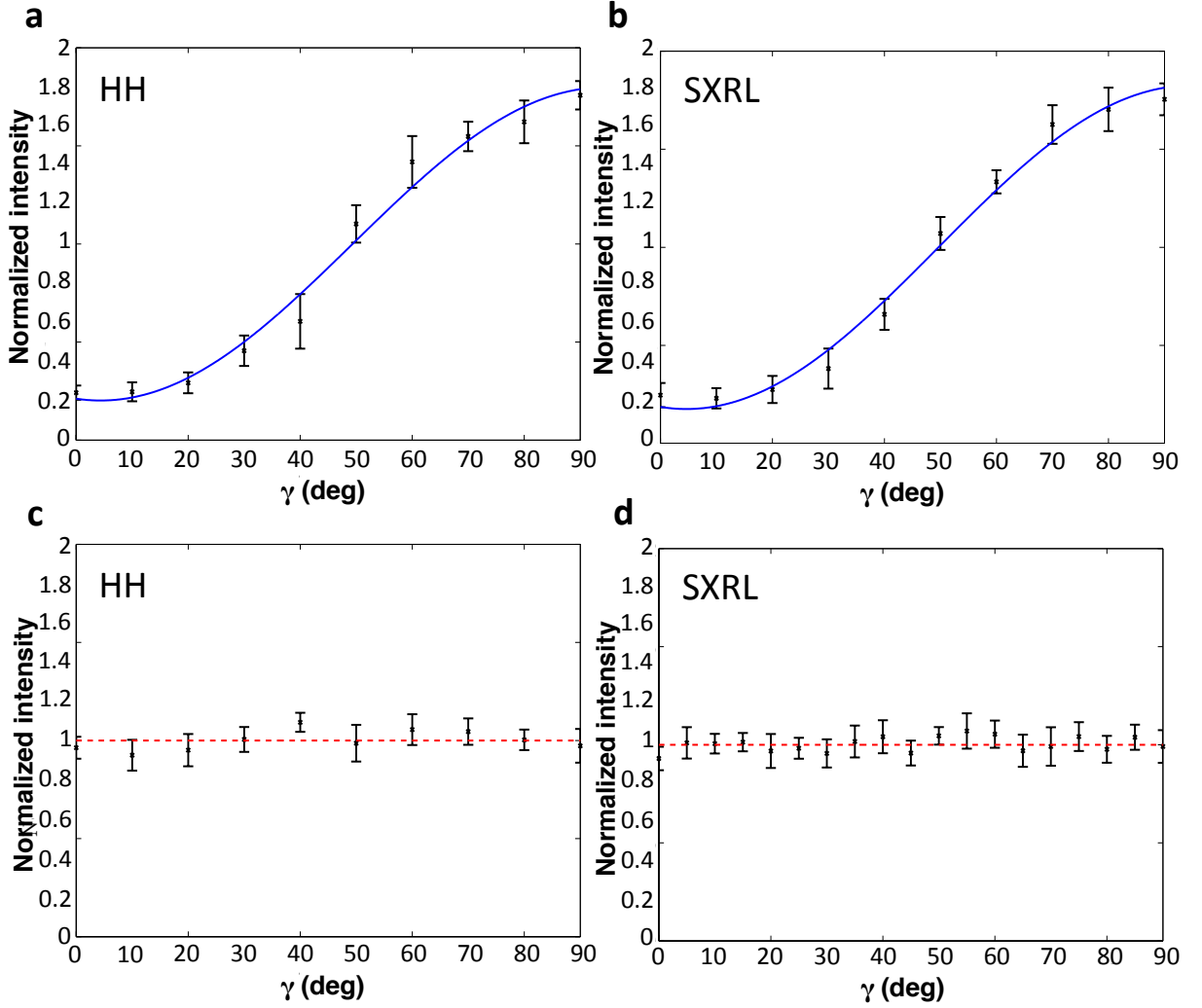


Figure 6.8: Polarization investigation of the HH-seeded SXRL (b & d) in case of linearly (p) and circularly-polarized high-harmonics (a & c) respectively. The signal intensity is measured as a function of the analyzer rotation angle  $\gamma$ . The black crosses indicate the experimental points with their error bars whereas the numerical fits (see Methods) are displayed by a blue and red curve for linear and circular polarizations respectively. In the linear configuration, the Malus law is recovered with the same contrast for the harmonics and the seeded SXRL. In the circular configuration, a very flat profile with values around 1 (red dotted line) is observed for both harmonics and the seeded SXRL.

$$I_{out}^N = 1 - \cos 2\Psi \cos 2\epsilon (\cos 2\alpha \cos 2\gamma - \sin 2\alpha \sin 2\gamma) \quad (6.14)$$

In case of linear polarization,  $\epsilon=0$ . Hence, the relation 6.14 becomes:

$$I_{out}^N = 1 - \cos 2\Psi \cos(2(\alpha + \gamma)) \quad (6.15)$$

In this case, the recorded intensity obeys the so-called Malus law:  $I_{out} = 1 - C \times \cos(2(\alpha + \gamma))$ , with  $C = \cos(2\Psi) = \frac{r_s^2 - r_p^2}{r_s^2 + r_p^2}$ , the effective contrast of the analyzer. The terms  $r_s$  and  $r_p$  stand for the amplitude reflectivities along p- and s- directions. They were calculated calibrating the

analyzer total s- and p-components transmissions. Because of the poor transmissions, the signal was accumulated over 60 seconds.

An attempt at fitting the curve for the circularly-polarized signal indicates an ellipticity angle  $\epsilon = 42^\circ$ , corresponding to a degree of circular polarization of 91 %. Thus, the actual state of polarization is in fact inferred to be slightly elliptic for both harmonics and the SXRL. This small ellipticity can be explained by slight misalignment of the polarizer's mirrors but also by small misalignment of the analyzer as it rotates about the optical axis. This can also come from changes in the beam direction as the measurement is performed. Actually, perfect alignment of the polarizer holds the promise to potentially deliver fully circularly polarized harmonics and therefore coherent X-rays. As the best fit was found to be the same for harmonics (fig. 6.8c) and the SXRL (fig. 6.8d), we can derive the circular polarization state has been maintained over amplification.

In this geometry the p-polarization components are always delayed by a larger amount compared to the s-polarization components. Hence, left-handed circularly polarized soft X-rays have been produced (defined from the point of view of the source). However, it is worthy to note that the handedness of the source can be reversed rotating both the polarizer and the  $\lambda/2$  waveplate by  $90^\circ$ .

Besides, another attractive feature of the demonstrated scheme refers to the polarization tunability of the source. Indeed, the polarization of the SXRL can be controlled from the orientation of the HH driving laser linear polarization thanks to the  $\lambda/2$  waveplate. The fig. 6.9 illustrates this in a configuration close to the one yielding circularly polarized light (the angle of the  $\lambda/2$  waveplate was here a bit detuned from the configuration of circular polarization). The recorded signal thus displays an intermediate behavior between the circular and the linear polarization cases (see fig. 6.8). It appears slightly sensitive to the rotation of the polarizer, thus reporting an elliptical polarization state, close to the circular polarization. The ellipticity,  $\epsilon$ , is here assessed at about  $40^\circ$  ( $45^\circ$  in case of circular polarization). It should be noted that the phase delay between p- and s- components cannot be altered and the ellipticity can only be controlled through a relative adjustment of the field amplitudes along both polarization directions.

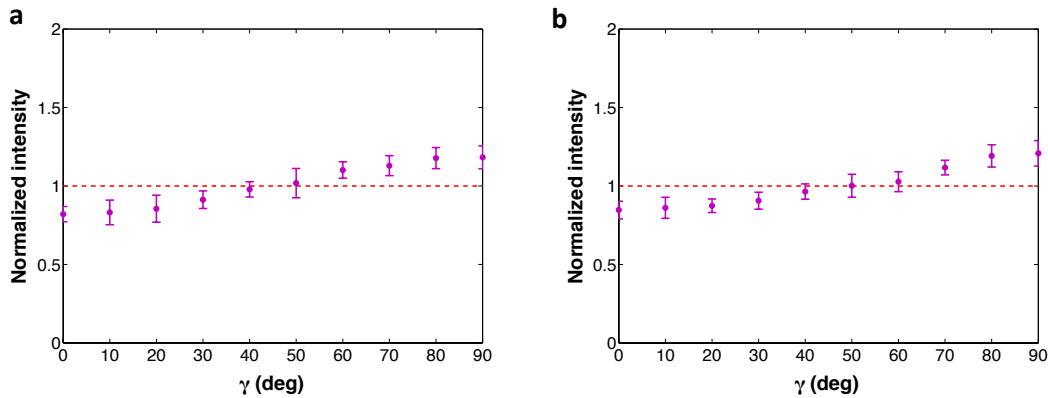


Figure 6.9: Investigation of the polarization state as a function of the analyzer rotation angle  $\gamma$  for the HH-seeded SXRL (b) in case of elliptically-polarized high-harmonics (a).

### 6.2.5 Output beam profile & energy

Energy distributions of the seeded soft X-ray laser are presented in fig. 6.10 with and without the polarizer. The beam profiles are nearly Gaussian and have both a full width at half- maximum (FWHM) divergence of about 1 mrad. In the presence of the polarizer, no alteration of beam spatial distribution is reported, which allows maintaining the good focusing capabilities of the source. The integrated energy distribution of the seeded SXRL is found to yield about  $8 \times 10^9$  fully circularly polarized photons per pulse.

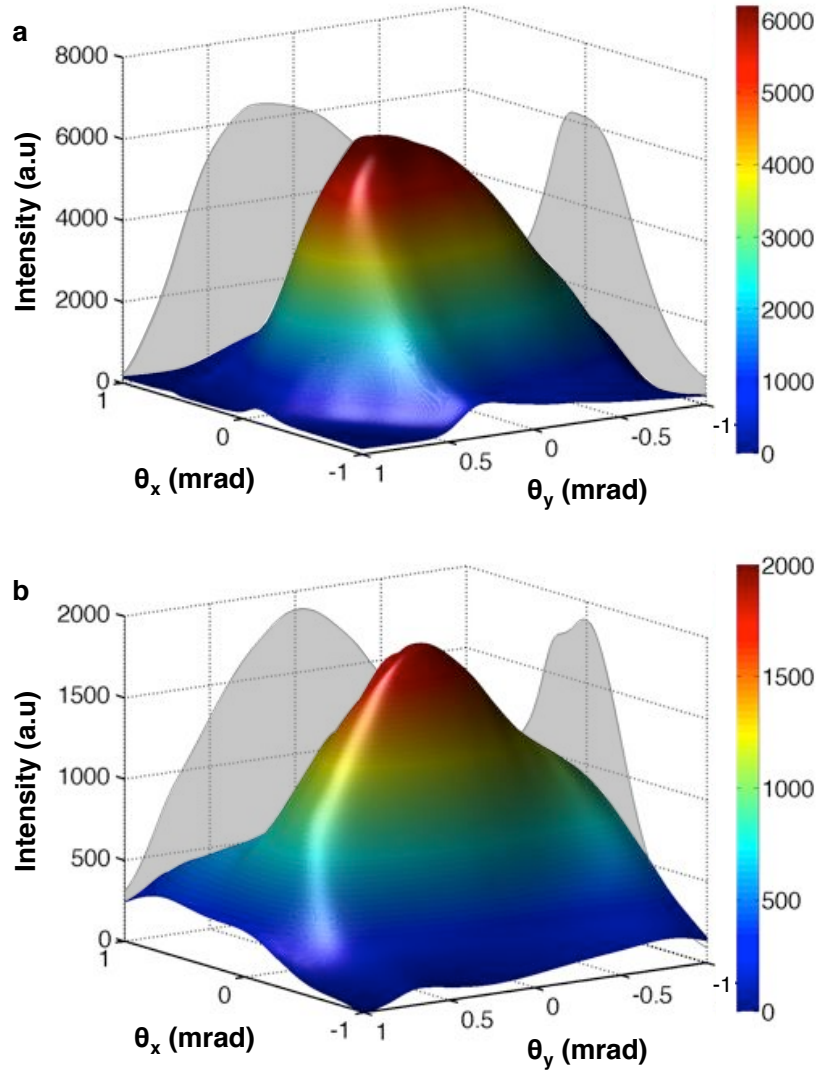


Figure 6.10: Energy distribution of the seeded SXRL in case of linear polarization (without the polarizer) (a) and circular polarization (with the polarizer) (b). The divergence is found to be about 1 mrad (FWHM). A factor of about 3 is lost switching from the linear to the circular configuration with the polarizer.

Despite the poor 1.5% transmission of the polarizer, total energy in case of circular SXRL is found to be about three times less than for linear SXRL. Actually, the amplified HH signal soars exponentially in the first hundreds microns of the amplifier before reaching a saturation



regime and increasing linearly. Compared to the linear polarization seed, because of the lower seeding signal level due to the polarizer low transmission, the amplified circularly-polarized HH reaches saturation later. Nevertheless, a longer plasma amplification length would promise to completely counterbalance these losses. As a consequence, the demonstrated configuration proves to be efficient while being capable of delivering fully circularly polarized SXRL pulses.

## 6.3 Maxwell-Bloch model of amplification of polarized radiation

As introduced in section 5.3, the microscopic approach of the Maxwell-Bloch description is adapted to the characterization of the amplification of an ultrashort HH pulse by a plasma. The long-lasting polarization of the medium generates and amplifies a wake following the HH pulse.

At the output of the plasma, the typical structure of the beam consists in a barely amplified HH pulse preceding a **wake** displaying **Rabi oscillations** and polarization decay [Almiev et al., 2007].

### 6.3.1 Adaptation of equations to various states of polarization

The equations of *DeepOne* time-dependent Maxwell-Bloch code [Oliva et al., 2011; Wang et al., 2014] (see section 2.5) have been modified to take account of the polarization of the seeding HH signal. This procedure aims at including the degenerescence of the lower level of the laser transition. The  $3d^9 4d_{J=0} \mapsto 3d^9 4p_{J=1}$  laser transition of the  $Kr^{8+}$  ion is depicted in fig. 6.11, with all physical processes governing the time-dependent level's populations. The lower level of the electric dipole laser transition has three degenerate sublevels ( $m = -1, 0, 1$ ). Because of the selection rules from quantum theory, each sublevel can only interact with a particular component of the electric field, which can be decomposed into Eigen components, namely left- or right-handed circular polarizations. Besides, the transition between levels (u) and (l,0) is forbidden. The resonant transitions between upper level u and lower levels (l, -1) and (l, 1) involves only the left-handed and right-handed circular polarization component of the electric field, respectively.

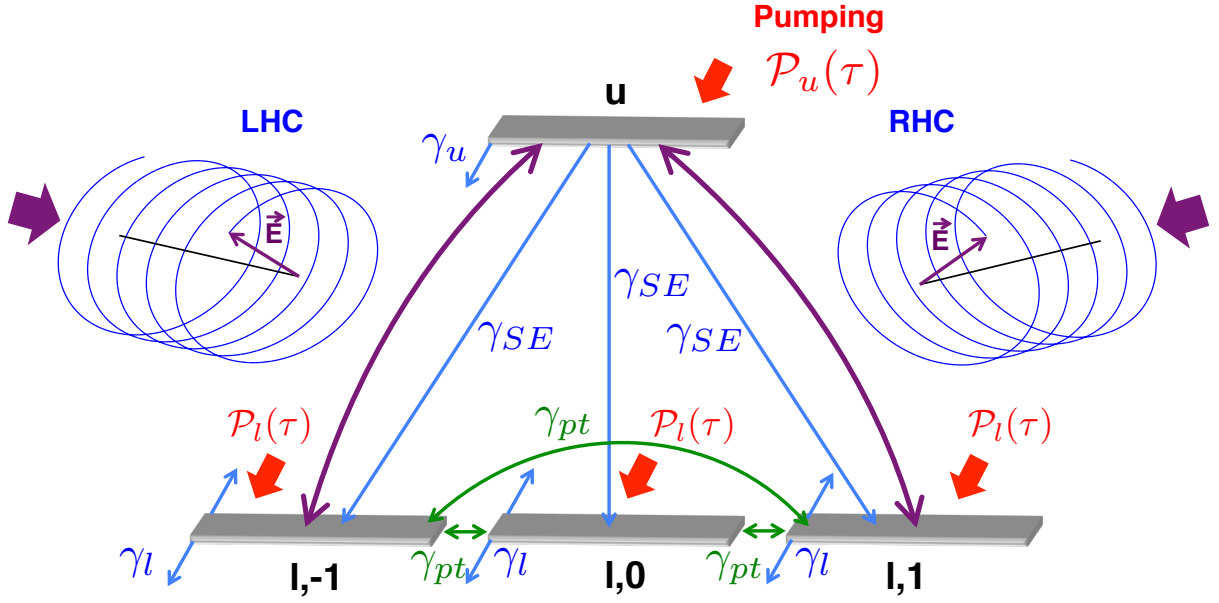


Figure 6.11: Atomic structure of the laser  $Kr^{8+}$  transition with its lower sublevels ( $m = +1, 0, -1$ ) and the associated physical processes. The purple double arrows stand for the resonant transitions that can be preferentially excited with left-handed circular (LHC) or right-handed circular polarization between the upper level ( $u$ ) and the ( $l,-1$ ) or ( $l,1$ ) lower level respectively. The blue arrows illustrates the various depopulation processes whereas the green double arrows describe the population transfers between sublevels.

The rates determining the dynamics of atomic populations can be splitted into three categories:

- Pumping rate: the pumping is made at a rate  $\mathcal{P}(\tau)$  through collisional excitation of ions by hot electrons.
- Relaxation rates: the transition levels relaxation rates are induced by 3 mechanisms:
  1. *Inelastic electron-ion collisions*. They lead to the depletion of the upper level of the laser transition at a rate  $\gamma_u$ .
  2. *Radiative decay*. In the collisional pumping scheme, there is fast radiative decays (of rate  $\gamma_l$ ) from the lower sublevels down to the ground state of the ion [Pert, 1994].
  3. *Spontaneous emission*. The upper level of the laser transition is also depleted by spontaneous emission (at rate  $\gamma_{SE}$ ), but this contribution is minor.
- Population transfer rates: Elastic electron-ion collisions induce population transfer between the degenerate sublevels at a rate of  $\gamma_{pt}$ . They also contribute to dephasing of atomic dipoles (at a rate of  $\gamma_{dp}$ ).

The upper level is populated at a rate  $\mathcal{P}_u(\tau)$  while its relaxation is induced dominantly by inelastic electron-ion collisions with a minor contribution coming from spontaneous emission. As far as the lower sublevels are concerned, they are being populated through collisional excitation and minority through spontaneous emission from the upper level.



Both level depopulation and atomic dipole dephasing determine the decay of medium polarization. The medium polarization decay rate  $\gamma_{ul}$  is given by  $\gamma_{ul} = (\gamma_u^* + \gamma_l^*)/2 + \gamma_{dp}$  for homogeneous broadening [Milonni and Eberly, 2010], with  $\gamma_u^*$  and  $\gamma_l^*$  being the depopulation rates of (u) and (l) levels including  $\gamma_{SE}$ . This decay rate is related to the homogeneously broadened linewidth by the formula  $\gamma_{ul} = \pi \Delta\nu_{FWHM}$  [Yariv, 1989]. As a result of time-dependent pumping, population and depopulation processes, the plasma demonstrates time-dependent gain (*OFI-0d* code), as illustrated in chapter 2.

For the following numerical calculations, the collisional-radiative code *OfiKinRad* [Cros et al., 2006] is used to compute the electron density, temperature, linewidth, radiative and collisional (de-)excitation rates and the populations  $N_k$ . The addition of these levels as sources allows our atomic model (simplified to ensure an affordable computational time) to mimic the results of the complex collisional-radiative code *OfiKinRad* in the absence of the electric field. It is worth noting that the code is fully time-dependent in the sense that all coefficients (plasma frequency  $\omega_p$ , depolarization rate  $\gamma_{ul}$ , collisional (de-)excitation rates  $\gamma$  and populations  $N_k$ ) vary in time. The temporal variation of these coefficients is given by external hydrodynamic and/or collisional-radiative codes (*OfiKinRad*).

The polarization state of a field can be decomposed and expressed as a function of right- and left-handed circular polarization components ( $A_R$  and  $A_L$  respectively). Hence, as the propagation eq. (2.129) in section 2.5 is linear, each components can be propagated independently:

$$\frac{\partial A_{L,R}}{\partial \xi} = \frac{i\omega_0}{2c} \left[ \mu_0 c^2 P_{L,R} - \frac{\omega_p^2}{\omega_0^2} A_{L,R} \right] \quad (6.16)$$

where  $A_R$  and  $A_L$  are the complex amplitudes of the field respectively. Selection rules imply that each field can only interact with a particular coherence [Sureau and Holden, 1995]. Thus, the thrice-degenerate lower level of the lasing transition cannot be modeled as a whole but splitted in three sublevels ( $m = +1, 0, -1$ ) [Kim et al., 2011, 2010]. Elastic electron-ion collisions between sublevels are also considered via a population transfer rate  $\gamma_{pt}$ , following [Kim et al., 2010]. The population rate equations are:

$$\frac{\partial N_u}{\partial \tau} = \mathcal{P}_u(\tau) - \gamma_u N_u - 3\gamma_{SE} N_u + \frac{1}{2\hbar} \mathcal{I}(P_R \cdot A_R^* + P_L \cdot A_L^*) \quad (6.17)$$

$$\frac{\partial N_{l,1}}{\partial \tau} = \mathcal{P}_l(\tau) - \gamma_l N_{l,0} + \gamma_{SE} N_u + \gamma_{pt}(N_{l,-1} + N_{l,0} - 2N_{l,1}) + \frac{1}{2\hbar} \mathcal{I}(P_R \cdot A_R^*) \quad (6.18)$$

$$\frac{\partial N_{l,0}}{\partial \tau} = \mathcal{P}_l(\tau) - \gamma_l N_{l,1} + \gamma_{SE} N_u + \gamma_{pt}(N_{l,-1} - 2N_{l,0} + N_{l,1}) \quad (6.19)$$

$$\frac{\partial N_{l,-1}}{\partial \tau} = \mathcal{P}_l(\tau) - \gamma_l N_{l,-1} + \gamma_{SE} N_u + \gamma_{pt}(-2N_{l,-1} + N_{l,0} + N_{l,1}) + \frac{1}{2\hbar} \mathcal{I}(P_L \cdot A_L^*) \quad (6.20)$$

where  $N_u$  is the population of the upper level of the lasing transition,  $N_{l,m}$  with  $m = 1, 0, -1$  the population of each lower sublevel,  $N_k$  are the population of other atomic levels that strongly interact with the lasing ones and  $C_{ji}$  denote the collisional (de-)excitation and radiative de-excitation rates.

The constitutive relation derived from Bloch equations is written as:

$$\frac{\partial P_L}{\partial \tau} = \Gamma_L - \gamma_{ul} P_L - \frac{iA_L}{\hbar} d_{ul}^2 (N_u - N_{l,-1}) + \frac{iA_R}{\hbar} d_{ul}^2 n_i \rho_{1,-1} \quad (6.21)$$

$$\frac{\partial P_R}{\partial \tau} = \Gamma_R - \gamma_{ul} P_R - \frac{i A_L}{\hbar} d_{ul}^2 (N_u - N_{l,1}) + \frac{i A_L}{\hbar} d_{ul}^2 n_i \rho_{1,-1} \quad (6.22)$$

$$\frac{\partial n_i \rho_{1,-1}}{\partial \tau} = -\gamma_{-1,1} n_i \rho_{1,-1} + \frac{i}{4\hbar} (P_R^* A_L + P_L A_R^*) \quad (6.23)$$

where  $n_i$  is the density of ions,  $\gamma_{ul} = \pi \Delta \nu$  is the full width at half maximum of the transition linewidth,  $z_{ul}$  the dipole matrix element,  $\rho_{1,-1}$  the off-diagonal matrix element of the states  $m = -1, 1$  and  $\gamma_{1,-1}$  its relaxation rate. It is given by the formula  $\gamma_{1,-1} = \gamma_l + \gamma_{dp}$ . The complex functions  $\Gamma_R$  and  $\Gamma_L$  simulate the stochastic behavior of ASE. The atomic levels population, as well as the complex amplitudes of the medium polarization and electric field are functions of propagation distance  $z$  and of the reduced time  $\tau = t - z/c$ .

### 6.3.2 Final energy and duration of the circularly polarized soft X-ray laser

The above-stated Maxwell-Bloch equations were solved self-consistently. Initial conditions are set by the input laser field. The equations giving the evolution of levels populations, medium polarization and density matrix element are then solved to obtain material response to radiation. The resulting medium polarization components are substituted into equations eq. (6.16). These yield the complex amplitudes of the electric field at the next position. By incrementally repeating these steps, the spatiotemporal evolution of the interaction of matter with the laser field is therefore described.

The numerical computations were performed considering a 5 mm-long plasma longitudinally pumped by a 30 fs, 1.36 J IR laser focused down to a  $30\mu$  m-diameter focal spot. This results in creating a gain cross-sectional area of about  $10^{-5} \text{ cm}^2$ , as given by WAKE hydrodynamic code. The seed HH pulse is 60 fs FWHM with an energy of 1 nJ. As the seed signal is well above the plasma spontaneous emission "noise" and much more intense than the ASE, the plasma is immediately coherently polarized.

The amplification of the seeded HH signal over the propagation length exhibits the typical behavior with **two regimes** [Laroche et al., 2013]. Apart from the plasma amplifier gain and HH duration, the parameters affecting the temporal dependence of amplification the characteristic times correspond to the depolarization rate  $\gamma_{ul}$  and the relaxation rate  $\gamma_{1,-1}$  in the equations eq. (6.21), eq. (6.22) and eq. (6.23). The following simulations have been carried out considering a LHC HH pulse.

1. In the first lengths of propagation, the signal is low and the population inversion of the medium is large. The signal grows exponentially until the onset of saturation, where the amplified pulse gets strong enough to deplete the population inversion. The amplified signal then grows linearly.

Before saturation, the equations of the previous section can be simplified. The terms involving  $A_R$  and  $A_L$  can be dropped. In this case, the equations eq. (6.17), eq. (6.18), eq. (6.19) and eq. (6.20) get decoupled and can therefore be solved independently, as well as equations eq. (6.21), eq. (6.21) and eq. (6.23) in case of a uniform plasma. As the density matrix term remains negligible in a low-signal regime, the contributions for right-handed and left-handed circular polarization can be treated independently, solving eq. (6.16) and eq. (6.16) or eq. (6.22) and eq. (6.21), respectively. Thus, for incremented variables  $z + dz$  and  $\tau + d\tau$ , the solutions for those pairs of equations will be:

$$A_{L,R} = i \frac{2\pi\omega_0}{c} \int_0^{z+dz} dz \int_0^{\tau+d\tau} d\tau e^{-\gamma_{ul}d\tau} \times [-id_{ul}^2 E(z, \tau) \Delta N_{L,R} + \Gamma(\Delta N_u(\tau), \tau)] \quad (6.24)$$

where  $\Delta N_L = N_u - N_{l,-1}$  and  $\Delta N_R = N_u - N_{l,1}$ . Both stimulated emission ( $E\Delta N$ ) and ASE ( $\Gamma$ ) build up over propagation, but the more intense seeded HH signal surpasses quickly spontaneous emission from the plasma amplifier.

Those conditions correspond to the plasma amplification behavior over the first two millimeters of plasma.

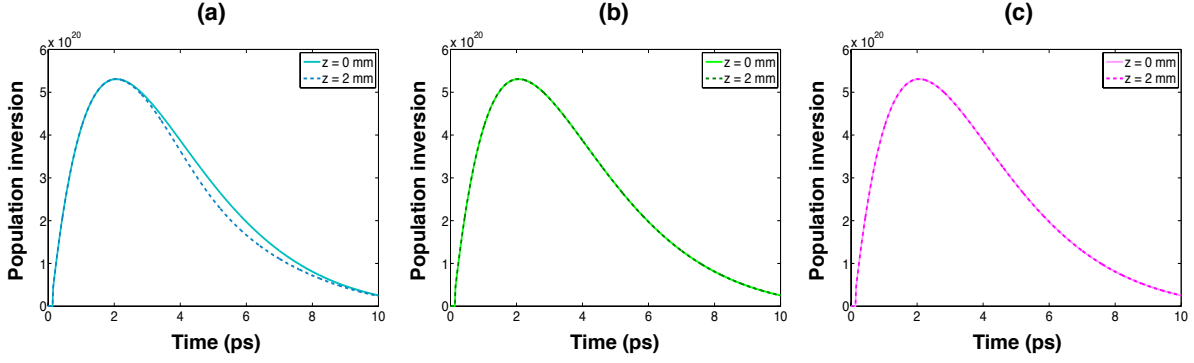


Figure 6.12: Population inversions ( $m^{-3}$ ) between the upper level (u) and the lower sublevels (l,-1) (a), (l,0) (b) and (l,1) (c).

The fig. 6.12 shows the temporal structures of the population inversions of the laser transition levels at the entrance of the plasma amplifier ( $z=0$  mm) and after after 2 mm of amplification. The lower levels are evenly populated by the pump beam. We see the influence of the resonant LHC field on the population inversion that starts being preferentially depopulated between the levels (u) and (l,-1) while the others remain unchanged. Saturation effects start appearing.

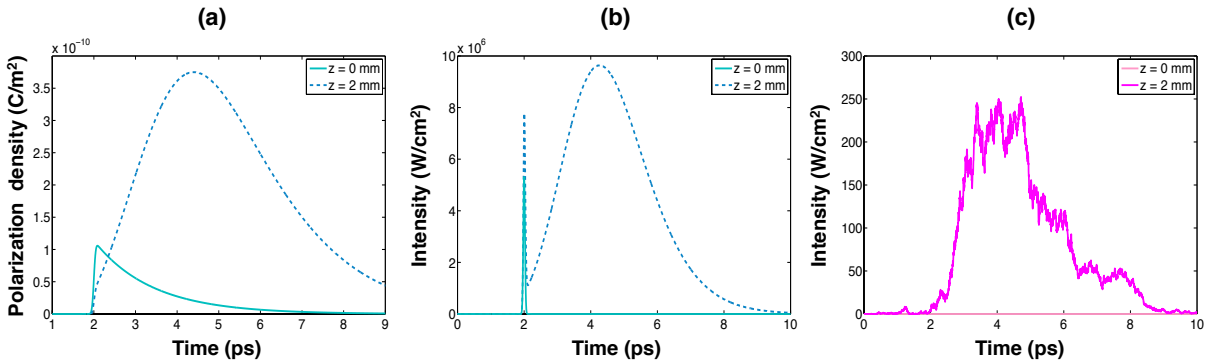


Figure 6.13: (a) Polarization density of the medium for the  $u \mapsto (l, -1)$  transition stimulated by the LHC HH. (b) Amplified HH field resulting from emission from the  $u \mapsto (l, -1)$  transition. (c) Emission from the  $u \mapsto (l, 1)$  transition.

The fig. 6.13 reports the corresponding evolutions of the polarization and the amplified field at  $z = 0$  and 2 mm. The transition  $u \mapsto (l, 0)$  is forbidden because of the selection

rules. As the resonant seeded HH has a LHC polarization, only the medium polarization corresponding to the  $u \mapsto (l, -1)$  transition is non-zero and builds up over propagation (fig. 6.13a). The fig. 6.13b & c show the amplified HH emission resulting from  $u \mapsto (l, -1)$  and  $u \mapsto (l, 1)$  transitions respectively. For the former, we have only the HH of peak intensity about  $5 \times 10^6 \text{ W/cm}^2$  at  $z=0$  mm, and at  $z=2$  mm, an amplified HH reaching  $7.8 \times 10^6 \text{ W/cm}^2$  followed by a long wake lasting for 1.5 ps (FWHM) (fig. 6.13b). For the emission from the  $u \mapsto (l, 1)$  transition, only stochastic amplified spontaneous emission is observed (fig. 6.13c). The appearing saturation effects have not yet impacted the shapes of polarization and the amplified field. The dipoles are generated under the still moderately amplified HH field and emit over a characteristic time defined by  $1/\gamma_{ul}$ . The variations of the medium polarization follow those of the amplified field but with a certain inertia. Considering the amplified field, its shape is, as earlier reported, composed of a weakly amplified HH followed by long dipole-induced emission.

2. After 2 mm of amplification, the amplified HH field becomes strong enough to completely deplete the population inversion and the pumping process does not manage to catch up.

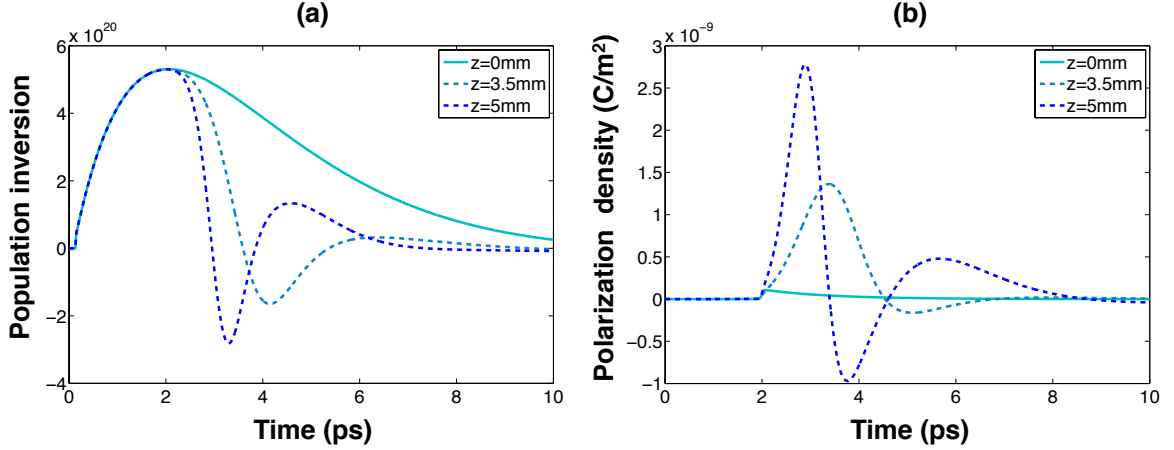


Figure 6.14: (a) Population inversion ( $m^{-3}$ ) of the  $u \mapsto (l, -1)$  transition stimulated by the LHC HH. (b) Polarization density of the medium for the  $u \mapsto (l, -1)$  transition.

The fig. 6.14 shows the evolution of the population inversion and the polarization for the  $u \mapsto (l, -1)$  transition being excited by the resonant LHC HH field. After 3.5 mm of amplification, the population inversion even becomes negative before building up again because of ongoing pumping. The negative population inversion means the plasma becomes momentarily absorbing. The fig. 6.14a shows that the population inversion oscillates about zero. This is due to a competition between population depletion and pumping. The upper state of the laser transition can re-populate because just after the population inversion depletion, the amplified HH is momentarily weaker. This behavior gets increasingly predominant as the HH builds up over propagation. As a consequence, the amplitude and the frequency of oscillations increase.

The fig. 6.15 brings into comparison the temporal evolution of the population inversion of the  $u \mapsto (l, -1)$  transition with the polarization (fig. 6.15a) and the amplified HH field (fig. 6.15b). The variations of the polarization of the medium follow those of the population inversion with a certain delay due to the integration of radiation over the propagated distance. Strong interdependence is reported between the population inversion and the

amplified HH field. The maxima and minima of the amplified field correspond, respectively, to the minima and maxima of the population inversion.

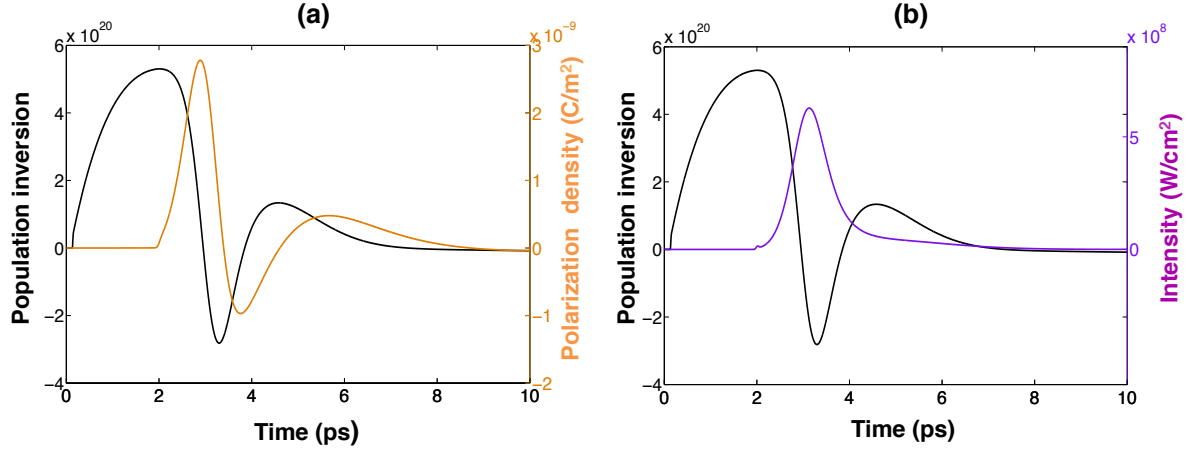


Figure 6.15: (a) Comparison of the temporal evolutions of the population inversion ( $m^{-3}$ ) and the polarization density of the medium at  $z = 5$  mm for the  $u \mapsto (l, -1)$  transition stimulated by the LHC HH. (b) Comparison of the temporal evolutions of the population inversion ( $m^{-3}$ ) and the amplified HH field.

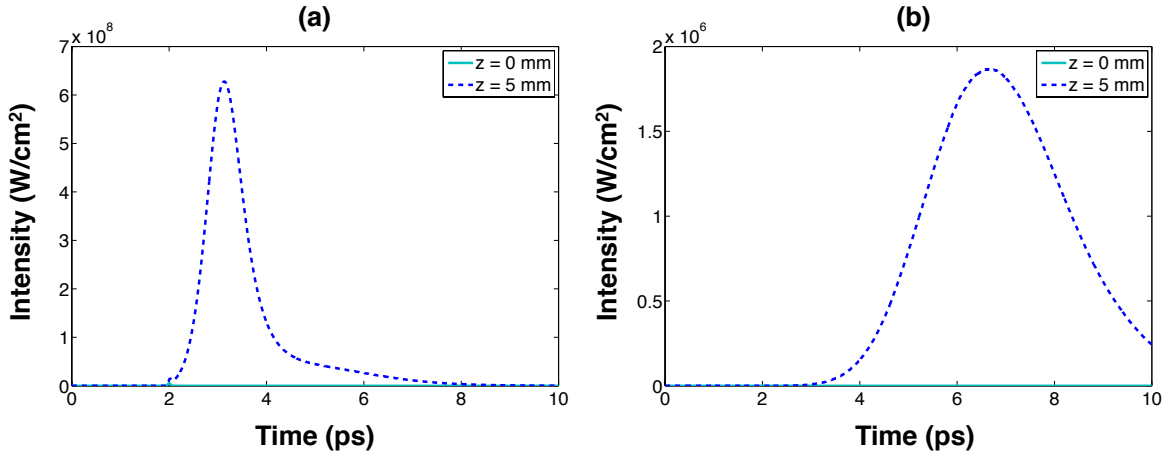


Figure 6.16: (a) Intensity of the amplified field corresponding to the  $u \mapsto (l, -1)$  transition in case of a LHC HH seed. (b) Intensity of the amplified field for the  $u \mapsto (l, -1)$  transition.

The fig. 6.16 illustrates the field resulting from emission from the  $u \mapsto (l, -1)$  transition (fig. 6.16a) and the  $u \mapsto (l, 1)$  transition (fig. 6.16b). In the former case, the seeded LHC HH signal gets amplified, while the latter case corresponds to ASE. The ASE peak intensity is more than two orders of magnitude lower than amplified HH.

**Evolution of the SXRL pulse envelope profile.** As reported in section 5.3, the pulse profile of the amplified HH signal is composed of a weakly amplified HH and an amplified wake, whose duration corresponds to the plasma response characteristic timescale [Oliva et al., 2011]. The fig. 6.18 shows the evolution of the amplified linearly-polarized HH pulse shape as it propagates in the plasma amplifier. The injection signal level of the seed is 1 nJ. After 5 mm of

propagation, the wake structure becomes predominant and dwarves the HH signal by a factor of about 2. The HH signal itself is only amplified by a poor factor of 2.8. As reported earlier, this behavior is due [Almiev et al., 2007] to the temporal shape of the medium polarization induced by the seeded resonant HH field (eq. (5.3)). As illustrated in fig. 6.17a, the HH creates a long-lasting polarization with a significant difference of timescale between its rise and its end tail. The polarization collapses because dephasing between induced dipoles emitters. This depolarization occurs on a characteristic time about one order of magnitude greater than the rising time. Because of the intrinsic delay between HH and the plasma polarization, only the final part of the HH pulse interacts with the dipoles, thus preventing a strong amplification. The medium polarization reaches its maximum well after the peak of the HH pulse. At this moment, the characteristic time scale is no longer given by the seeded beam duration, but by the plasma properties (electron-ion collisions frequency). The higher the collision rate becomes, the faster the depolarization gets.

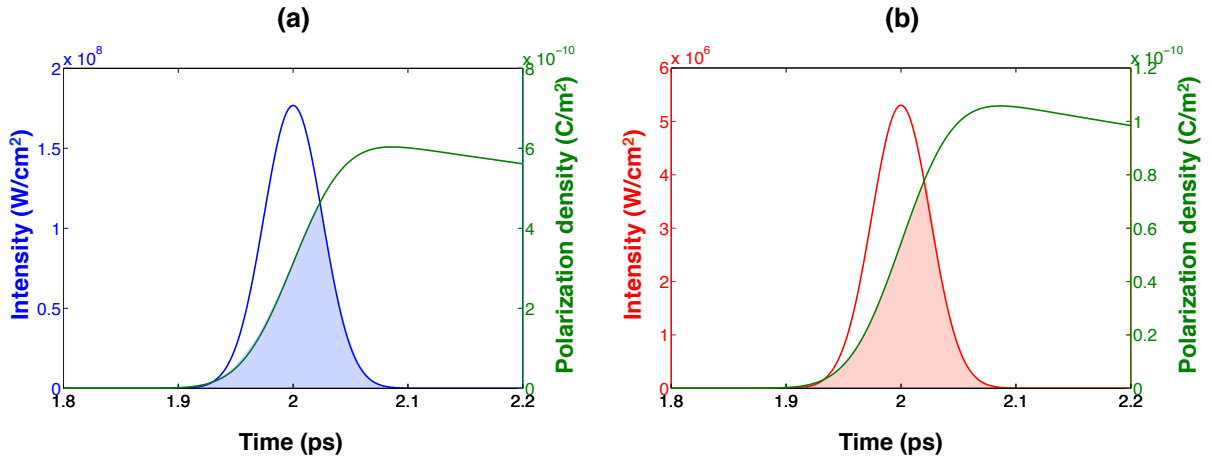


Figure 6.17: Envelope of the HH electric (blue & red) field and polarization density (green) right at the entrance of the plasma amplifier in case of seeding with linearly-polarized HH (a) and circularly-polarized HH with a lower injection signal level (because of the 1.5 % polarizer transmission) (b).

The fig. 6.19 depicts the evolution of the amplified circularly-polarized HH pulse shape as it propagates in the plasma amplifier. Because of the polarizer transmission, the injection signal level of the seed is now reduced from 1 nJ to 15 pJ. The HH itself gets amplified by about the same factor of 2.8 after 5 mm of propagation. Compared to the temporal profile in the linear case in fig. 6.18, the wake structure now dwarves the HH by a factor of about 43. The fig. 6.17b shows that the polarization is now smaller compared to fig. 6.17a because of the weaker field, but the rising and depolarization timescales are the barely the same, which explains why the interaction between the HH and its induced polarization is very similar and remains weak.

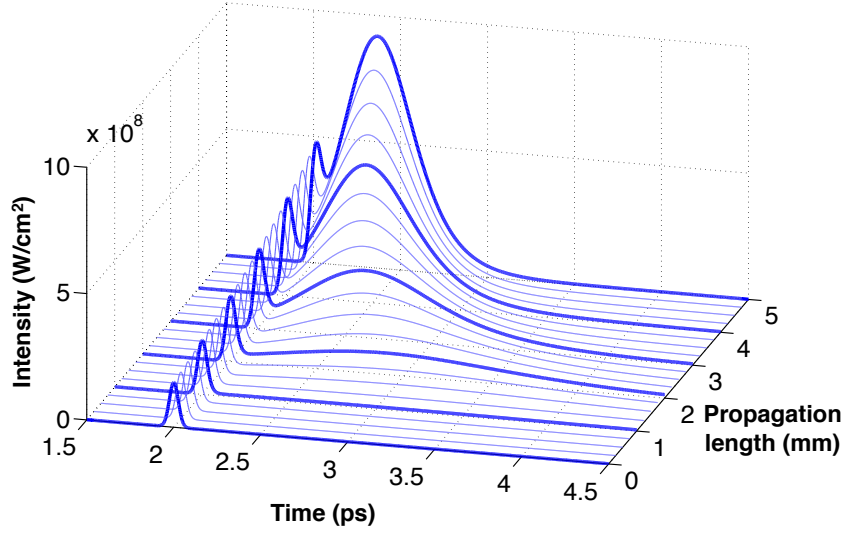


Figure 6.18: Temporal profile of the linearly-polarized HH seeded soft X-ray laser signal as function of the propagation length in case of a  $Kr^{8+}$  amplifier with  $n_e = 6 \times 10^{18} cm^{-3}$ . The injection signal level of the seed is 1 nJ.

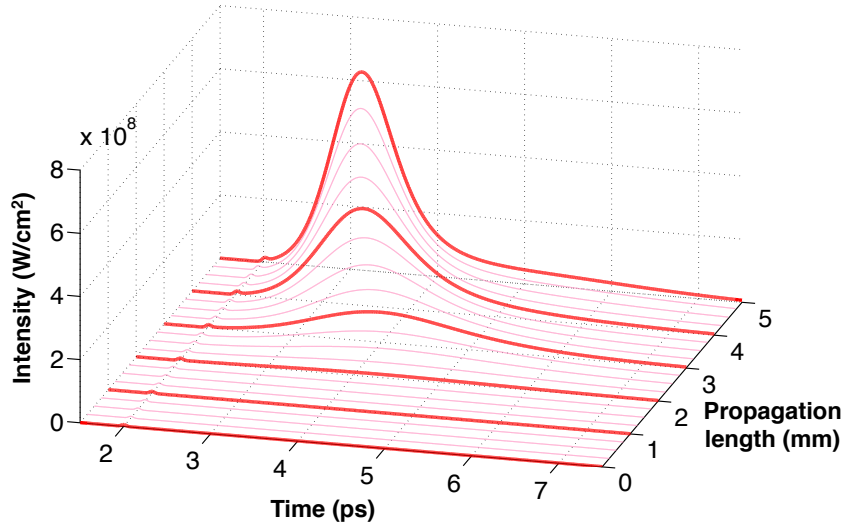


Figure 6.19: Temporal profile of the circularly-polarized HH seeded soft X-ray laser signal as function of the propagation length in case of a  $Kr^{8+}$  amplifier with  $n_e = 6 \times 10^{18} cm^{-3}$ . The injection signal level of the seed is 15 pJ.

**SXRL pulse energy.** The fig. 6.20 shows the build-up of the amplified HH signal over propagation in the plasma. The polarizer allowed generating fully circularly-polarized HH but the signal drops by an amount corresponding to the transmission of the device. The energy of the pulse is computed considering a pulse duration of 5 ps and an O-ring emitting surface of  $3.4 \times 10^{-5} cm^2$  area (defined by circles of diameters 69 and 10  $\mu m$ ) obtained from WAKE-EP simulations.

The amplified HH signal soars exponentially in the first hundreds microns of the amplifier before reaching a saturation regime and increasing linearly. Because of the lower seeding signal

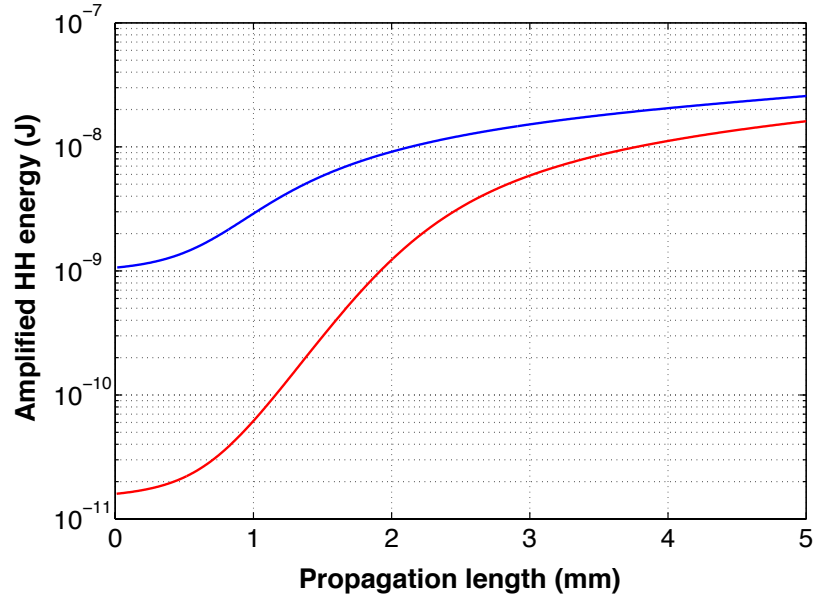


Figure 6.20: Build up of the seeded soft X-ray laser signal in case of a  $Kr^{8+}$  amplifier with  $n_e = 6 \times 10^{18} \text{ cm}^{-3}$ . The blue curve represents the linearly seeded case (p-direction) for a HH signal injection level of 1 nJ, whereas the red one stands for the circularly HH polarization seeding taking account of the 1.5 % transmission of the four-mirror polarizer (15 pJ).

level due to the polarizer low transmission, the amplified circularly-polarized HH gets exponentially amplified over a longer plasma length. To this extent, the saturation properties of the plasma amplifier allow partially compensating the losses induced by the polarizer transmission.

### 6.3.3 Polarization of the amplified HH signal

The model describes the dynamics of the plasma population inversion between the laser transition upper level and its lower polarization-selected levels. The numerical simulations show this scheme maintains both linear and circular polarization of harmonics over amplification.

**Degree of polarization.** Experimentally, the output signal is composed of a low-divergence intense amplified HH spot along with much highly diverging amplified spontaneous emission (ASE). The former is fully polarized while the latter, resulting from the stochastic nature of spontaneous emission, is unpolarized. As a consequence, the numerical results take account of depolarization of the seeded SXRL induced by ASE within its low-divergence solid angle defined at full width at half-maximum (FWHM). The ratio between signal the fully polarized amplified HH and the unpolarized ASE allows us to define a degree of polarization.

**State of polarization.** We saw that the amplification of each right- and left-handed circular polarization contributions of the field can be treated independently. The resulting state of polarization can be easily computed using the Stokes formalism. The Stokes parameters, containing all the information about the polarization state of the amplified HH, are directly obtained from the computed fields  $A_R$  and  $A_L$  as:



$$\begin{cases} I = |A_R|^2 + |A_L|^2 \\ Q = 2\mathcal{R}(A_L^* A_R) \\ U = -2\mathcal{I}(A_R^* A_L) \\ V = |A_R|^2 - |A_L|^2 \end{cases} \quad (6.25)$$

The fig. 6.21 illustrates that the polarization of HH is just slightly altered following amplification in the plasma. The fig. 6.21a reports that the portion of fully polarized light after 5 mm of amplification is over 99.5%. In this fraction, the linearly-seeded SXRL polarization (fig. 6.21b) axis is turned by less than  $0.05^\circ$ , while it gets a very small ellipticity of about 0.04. As far as circularly-seeded SXRL is concerned (fig. 6.21c), the polarization is marginally modified from an initial value of 1 to over 0.98. The slight depolarization effects comes from the contribution of unpolarized ASE. Those are bigger in case of circular polarization because, for the same amount of ASE signal, the amplified signal is three times weaker compared to the linear case. Those very weak alterations of the state of polarization can be explained by coupling effects due to off-diagonal elements of the density matrix (see eq. (6.23)), which induce ASE-SXRL coupling resulting in second-order perturbations of the amplified HH polarization. This alteration is a bit larger in case of linear polarization. Indeed, in case of circular polarization, only the left- or right-handed components of the field and polarization initially exist. After amplification in the plasma, the coupling term in eq. (6.23) creates respectively right- or left-handed components, which alter the polarization state. However, the linear HH field, which is decomposed into left- and right-handed circular polarization components, will already provide for initial "source terms" ( $P_R^*$ ,  $A_L$ ,  $P_L$ ,  $A_R^*$ ) in eq. (6.23).

Thus, these numerical simulations substantiate the experimental demonstration of the first ever circularly-polarized plasma-based soft X-ray laser.

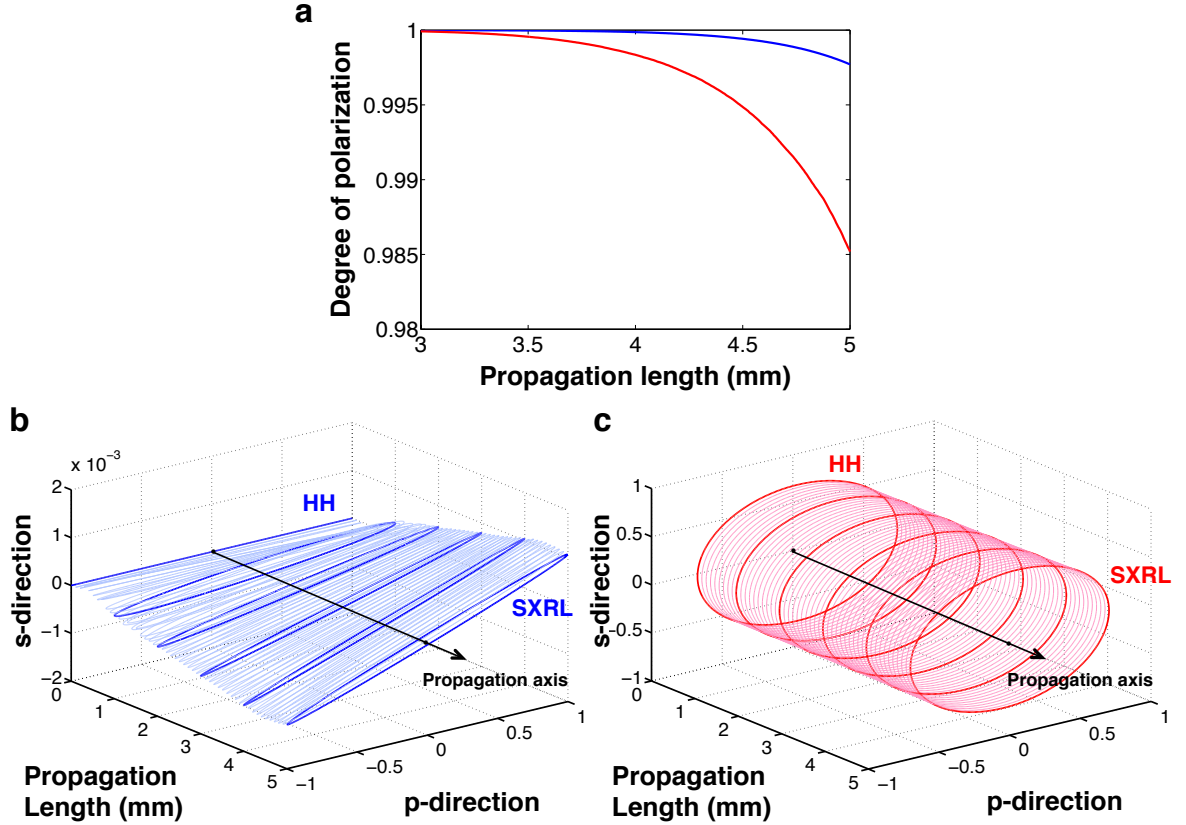


Figure 6.21: Conservation of the polarization state of amplified HH seeding a plasma-based krypton amplifier. (a), the blue and red curves describe the evolution of the degree of polarized light over amplification for linear (along p-direction) and circular (left-handed) respectively. (b)& (c), in the linear (blue) and circular (red) cases, polarization states are depicted as the normalized path described in the space by the electric field over an optical period. The propagation axis intercepts the transverse plane at the point of coordinates (0, 0). Data are shown taking account of the portion of ASE included in the solid angle defined by the amplified HH (FWHM).

## 6.4 Conclusion

The demonstrated [Depresseux et al., 2015a] fills the requirements for a compact and efficient jitter-free fully circularly polarized soft X-ray coherent source combining a very high photon yield with a near diffraction-limited wavefront [Goddet et al., 2009]. A prospective development would consist in using a high-density plasma as an amplifier to achieve shorter durations and higher photon yields (cf. section 2.3.2). However, the low transmission of the four-reflector mirror (polarizer) led to a fall of the HH signal below the injection level, from which amplification is effective (cf. section 5.1.4).

All in all, being scalable to shorter wavelengths [Berril et al., 2010] and adaptable to other pumping schemes [Korobkin et al., 1996], the demonstrated approach holds out hope for delivering intense circularly-polarized soft X-ray pulses suitable for single-shot measurements in holography [Eisebitt et al., 2004], crystallography pump-probe experiments [Boutet et al., 2012], magnetism [Vodungbo et al., 2012] or circular dichroism in molecular structures [Ferré et al., 2014; Garica et al., 2010].



# Conclusion

## Summary of the results

This thesis was focused on the development and characterization of OFI plasma-based soft X-ray lasers using the high-harmonic injection technique. This work allowed significant breakthroughs for this kind of source.

The main focus of the work has been centered on the **reduction of the duration** of plasma-based soft X-ray lasers emission. The collisional pumping scheme, which proved to be the most robust and efficient, has been used to reach this objective. The source has been generated with an OFI plasma made of nickel-like krypton ions, lasing at 32.8 nm. Earlier observations at low plasma densities [Mocek et al., 2005] motivated this thesis work in order to explore the plasma gain dynamics at higher densities. The merits of this approach have been formalized to introduce a « **Collisional Ionization Gating** » (CIG) scheme to quench the gain lifetime and pave the way for sub-picosecond soft X-ray laser plasma amplification at high electron densities [Depresseux et al., 2015b]. However, in those conditions, strong refraction hurdles the propagation of the driving laser pulse and dramatically reduces the relevant laser-plasma interaction length.

To meet the challenge of generating an elongated high density amplifier to reach saturated amplification, an « ignitor-heater » **waveguiding technique** has been used. The guiding conditions have been identified and explored over a range of parameters using a numerical model in order to efficiently guide the driving ultrashort and intense pulse into such a plasma [Oliva et al., 2015]. This scheme has been experimentally implemented and led to efficient guiding over a 5 mm-long plasma at electron densities as high as  $1.2 \times 10^{20} \text{ cm}^{-3}$  and over distances up to 20 mm. Such a high-density plasma-based soft X-ray laser yielded **14  $\mu\text{J}$** , which is unprecedented for this type of source.

Based on the aforementioned achievements, high-density plasma amplifiers were seeded with a high-harmonic source. The « seeding technique » was used to sample temporally the gain lifetime. A time-dependent Maxwell-Bloch code was used to model the amplification of the high-harmonic pulse and was found to be in good agreement with those experimental data over a remarkable wide range of electron densities covering nearly two orders of magnitude. In case of a 5 mm-long plasma at  $1.2 \times 10^{20} \text{ cm}^{-3}$ , a **450 fs gain duration** has been demonstrated, thus breaking the picosecond range for the first time. When the seeded HH signal was synchronized with the maximum of amplification, this source delivered 1 mrad divergence beams of **2  $\mu\text{J}$**  (i.e.  $3.4 \times 10^{11}$  photons) displaying a Gaussian-like profile. Numerical calculations, describing well the amplification lifetime, enabled to infer a **pulse duration in the range of 100 fs**. Compared to previous performances, the « Collisional Ionization Gating » process allowed an overall upsurge of nearly **three orders of magnitude in soft X-ray intensity per shot**. We can also notice that the technique allows remarkably increasing the efficiency of soft X-ray

generation without increasing the pump beam energy.

Finally, we showed that OFI plasma SXRL amplifiers are well adapted to maintain the **polarization** state of the seed. Indeed, the polarization of the seeding resonant field can control the relative excitation of populations of the sub-levels of the laser transition lower level. Whereas, amplified spontaneous emission is unpolarized, the resulting coherently amplified emission fully maintains the polarization state of the seed. An efficient architecture has been demonstrated to efficiently generate a **fully circularly-polarized** HH-seeded soft X-ray laser [Depresseux et al., 2015a].

## Future prospects

These results open up prospects, both regarding the enhancement of the source parameters and the utilization of the high-harmonic seeded plasma-based soft X-ray laser for photon-demanding applications.

Further developments include the **improvement of the guiding efficiency** with the available « Salle Jaune » laser system. The introduced numerical models showed that tailoring of a plasma channel allows guiding an ultrashort and intense driving laser pulse into a high-density plasma. However, experimental and numerical models do not fully agree, especially regarding the plasma waveguide infrared transmission. Additional measurements and modeling are needed to optimally engineer a high-density plasma waveguide in an attempt to improve the guiding efficiency. The initial ionization degree of plasma channel is notably an important parameter to be measured. Besides, a numerical model should be introduced to understand better the conditions of plasma channel generation and the impact of density, as well as the ignitor and heater pulses on the geometry of the waveguide. Furthermore, better coupling conditions between the focused driving laser beam and the plasma waveguide could also improve the IR transmission.

Progress in plasma engineering would also pioneer operation at even higher densities and thus allow achieving **shorter pulse durations**. Indeed, according to our numerical model, driving near-critical plasma densities promises to yield pulse durations in the range of a few tens of femtoseconds. This future achievement is strongly connected to our capability to improve the guiding performance at density of about  $4 \times 10^{20} \text{cm}^{-3}$ .

The optimization of the guiding efficiency also holds promise to further **enhance the SXRL photon yield**. Along with the operation at higher densities, the perspective to generate longer plasmas also fosters promising opportunities. However, during this thesis, it was not possible to efficiently seed and amplify high-harmonics when operating over 10 mm-long plasma amplifiers. The reasons are still not well defined but a too strong ASE signal compared to the signal strength of the seed could be the main cause. Three solutions can be introduced to overcome this issue.

First, the photon yield of the HH source could be enhanced using a long focal length or boosting the conversion efficiency by resorting to quasi-phase matching techniques or a two-color generation scheme.

Second, a multi-stage architecture can be envisioned (cf. fig. 22). This scheme would consist in a first amplifier at low density ( $n_e \approx 10^{18} - 10^{19} \text{cm}^{-3}$ ) and a second one at higher density ( $n_e > 10^{20} \text{cm}^{-3}$ ).

Third, designing long nozzles exhibiting a longitudinal density gradient could be a valuable alternative. The seeding threshold would be lower at the entrance of the jet with a lower density. The HH could then be gradually amplified and outmatch the growing ASE.

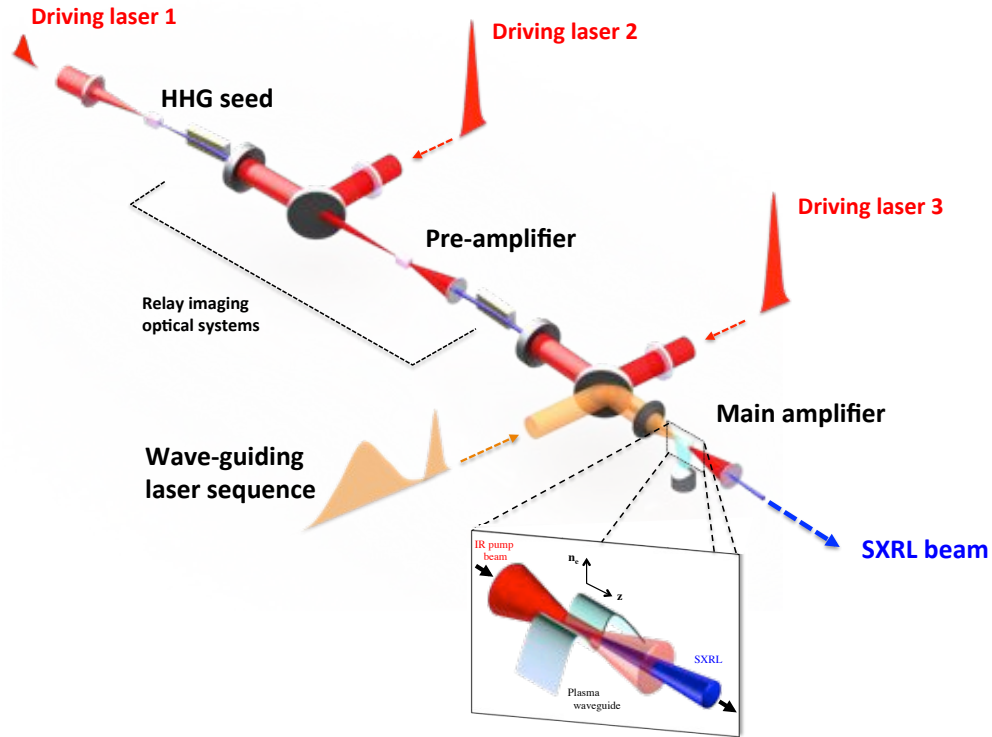


Figure 22: Schematic of a two-stage femtosecond SXRL amplification chain.

Finally, recent numerical calculations [Oliva et al., 2012] proposed a transposition of chirped pulse amplification technique to the soft X-ray range. By stretching a femtosecond HH seed to duration close to the gain lifetime, this scheme would allow continuously and coherently extracting the energy stored in the plasma.

Overcoming those challenges associated with the seeding threshold would also allow extending the demonstrated circularly polarized SXRL scheme to deliver **ultrashort and intense circularly-polarized pulses** as the low transmission of the polarizer prevented the use of a high-density plasma amplifier.

Can we drive those OFI HH-seeded plasma-based soft X-ray lasers at shorter emission wavelengths where better spatial resolutions for imaging are promised? The recent advent of PW-class laser systems (Apollon in France, APRI in Korea or ELI Beamlines in EU) will provide new prospects to pioneer shorter wavelengths using the collisional pumping OFI scheme employing higher charge species, which require very high intensities. For instance, an elongated plasma amplifier made of Ni-like Xe, lasing at 9.96 nm [Li et al., 1998] could be envisioned. However, the collisional scheme turns less and less efficient when considering shorter wavelengths. A more promising path to shorter wavelengths would consist in implementing the OFI recombination scheme. As this scheme requires operation at very high electron densities, applying the demonstrated waveguiding technique turns out auspicious to reach saturated amplification and deliver sub-100 fs lasing down to the so-called « water window » (between 2.3 and 4.4 nm) [Shen et al., 1997]. Moreover, lowering the electron temperature is critical for the success of this scheme. For this purpose, the use of gas mixtures with low-Z species could be used to cool down the plasma thanks to the release of low energy electrons following OFI. Another approach

would consist in doubling or tripling the frequency of the driving laser to generate a high-density amplifier while keeping the electron temperature as low as possible (cf. fig. 23). Good frequency conversion up to 45% for the second harmonic and 30% to the third harmonic are feasible. However, the ultrashort pulse duration should be measured soon to validate this approach.

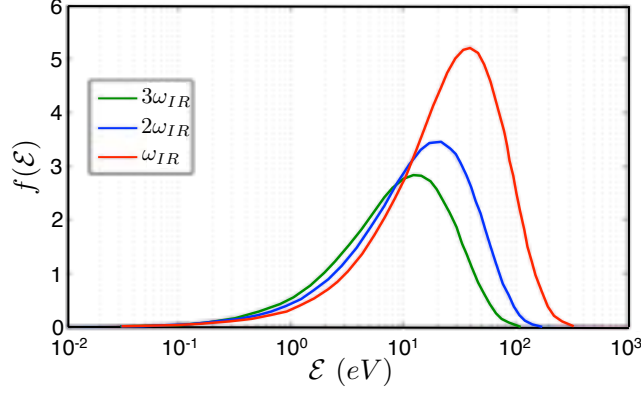


Figure 23: Computed electron distribution following OFI of a  $10^{20} \text{ cm}^{-3}$  Ne gas media for 3 different laser driver wavelengths.

All in all, the achievements of this thesis widen the potential of these sources and promote their relevancy in the framework of **applications** requiring high on-target intensities and regarding the study of ultrafast phenomena or polarization-dependent properties of materials. HH-seeded plasma-based soft X-ray lasers strengthen their place between HH and XFEL sources, by expanding their performances (in terms of photon yield, pulse duration and polarization tuning) and leveraging on their own intrinsic qualities (jitter-free source, and excellent spatial and temporal coherence). The current state of the art performances of HH-seeded soft X-ray lasers ( $2 \mu\text{J}/100 \text{ fs}$  pulses) combined with the prospective developments (a few 10s of  $\mu\text{J}/20 \text{ fs}$  pulses) enhance the maturity of these sources to carry out, at the laboratory scale, applications that were previously restricted to the XFEL community (using  $100 \mu\text{J}/10 \text{ fs}$  pulses). A first application of this source, consisting in soft X-ray diffraction imaging of a sample featuring details of a few tens of nm, has been performed in mid-july 2015 and laid promises for achieving single-shot diffraction-limited resolution (see fig. 24 & fig. 25). To this extent, the CIG approach contributes to substantiate the full-fledged capabilities of this compact source to carry out single-shot high-resolution dynamical studies on the femtosecond time scales, ranging from soft X-ray holography [Chapman et al., 2007] to phase contrast coherent imaging [Sakdinawat and Liu, 2008]. Additionally, the demonstrated circularly polarized SXRL grants access to single-shot measurements in a large range of applications in crystallography [Boutet et al., 2012], magnetism [Vodungbo et al., 2012] or the observation of dichroism in biology [Ferré et al., 2014; Garica et al., 2010].



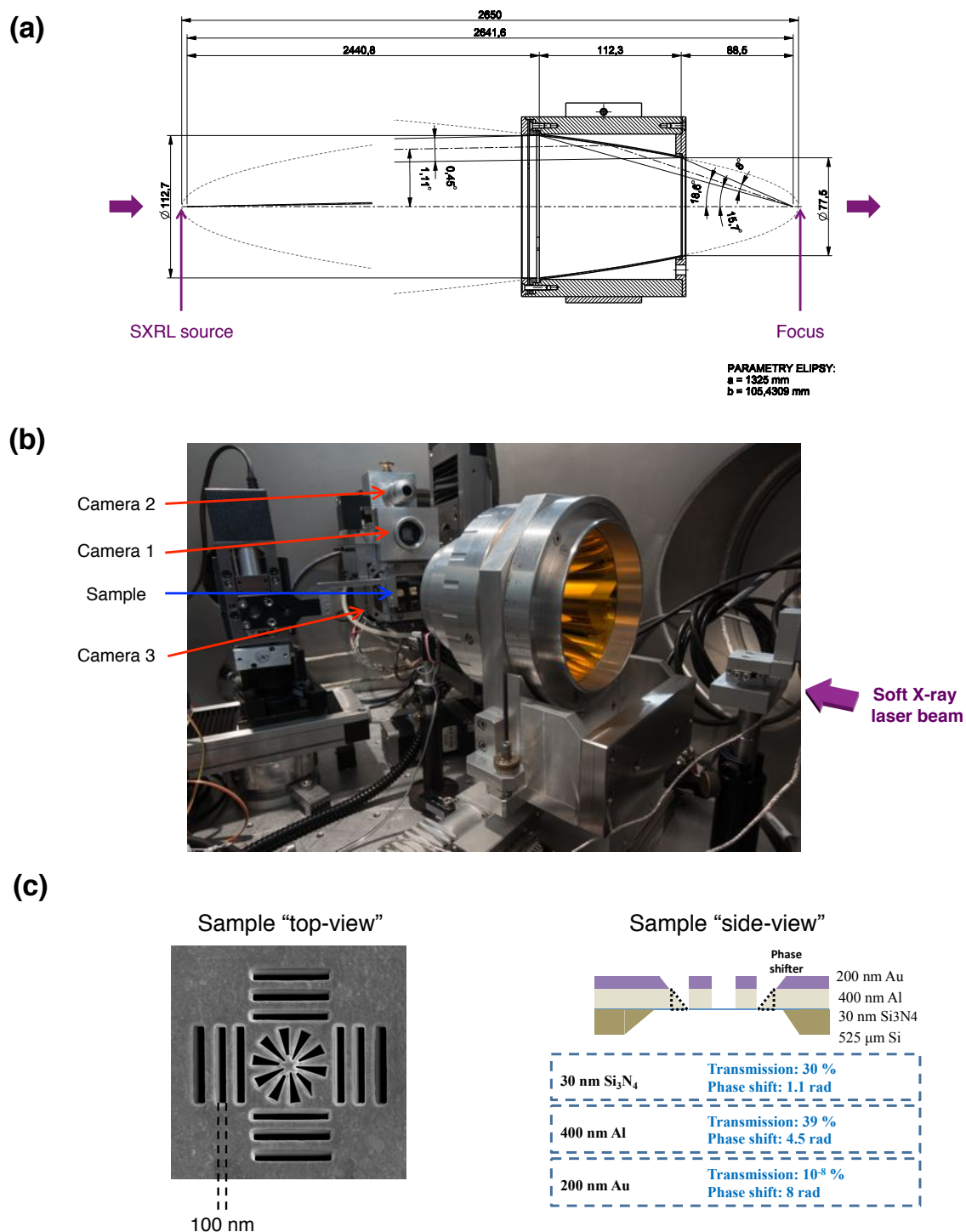


Figure 24: Soft X-ray diffraction imaging experiment: (a) Technical description of the gold-coated *Rigaku* ellipsoidal mirror used to focus soft X-rays onto the sample. (b) Picture of the imaging system. Camera 1 has a phosphor deposited on the CCD chip, which allows pinpointing the longitudinal position of the SXRL focus and correcting its quality thanks to the ellipsoidal mirror actuators under vacuum. Camera 2 is fitted with a microscope objective and images a plane, whose relative position with respect to the camera 1 chip is known. Camera 2 is then used to place the sample in the focal plane of the ellipsoidal mirror. Camera 3 is a soft X-ray camera used to record the diffraction pattern about 3-4 cm away from the sample. (c) SEM image and composition of a sample engineered with an ion beam.



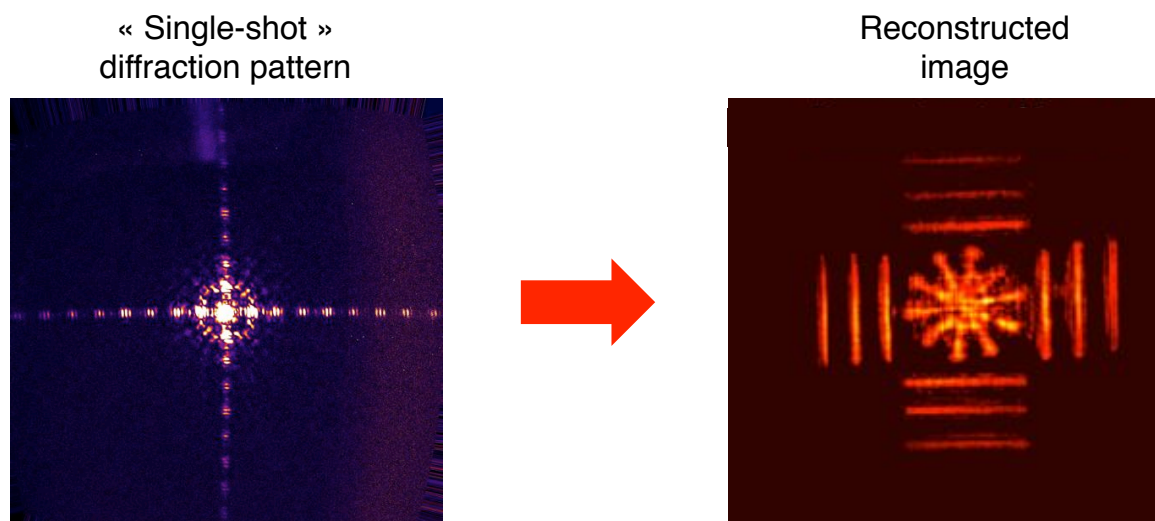


Figure 25: Single-shot diffraction pattern (right) obtained from the sample depicted in fig. 24c and its reconstruction (left). Further effort was needed to improve the resolution by taking account of the soft X-ray focus aberrations.

# Appendix A

## OFIKinRad atomic code

The OFIKinRad atomic code is based on the COFIXE code [Cros et al., 2006]. Instead of Xenon, it considers 36 ionization levels of krypton and 93 atomic levels of  $Kr^{8+}$ . The numerical model takes into account collisional ionization and excitation, along with radiative processes such as spontaneous emission and absorption.

The code computes the energy distribution functions of electrons, the populations of the atomic levels taking part in the lasing transition, the temporal evolution of gain and emissivity at a low signal level, the spectral width and the saturation intensity.

The input parameters are the IR laser intensity, wavelength and polarization, the atomic density of the neutral krypton gas and the plasma initial temperature.

The main approximations of the code are the following:

- The code is 0D and computes the gain in one point in the space. The evolution of the gain only depends on the initial gas composition and the laser intensity temporal profile at this point. The macroscopic hydrodynamic expansion is not properly considered here. In our conditions, as illustrated in chapter 2, the plasma expansion resulting from the large increase in electron temperature due to ionization occurs on tens of microns per ns timescales. As the characteristic timescale of computed parameters (see section 2.3.2) is in the order of tens of ps, the plasma expansion and its induced density variation can be neglected.
- The timescale of interaction with the laser (of duration of a few tens of fs) is shorter than the characteristic time of kinetics. This latter timescale, embodied by the gain duration, is supposed to be far larger compared to the laser pulse duration.
- The resonant transitions between excited and fundamental levels are locally absorbed (thick media considered for these transitions), whereas transitions between excited levels can freely leak. Radiative losses come from the fact that emitted photons are not necessarily reabsorbed by the plasma, thus leading to an energy loss. A loss parameter is introduced into the code to account for them.

As a consequence, the computed local evolution of the gain is entirely determined by the initial state of the plasma and its interaction with the intense laser pulse.

**Initial state of the plasma just after interaction with the intense laser pulse.** The parameters defining the initial state of the plasma are its electron density, temperature and ionization state. The interaction within the ultrashort duration of the intense IR laser field describes the so-called *Optical Field Ionization*. The main underlying mechanism is tunnel ionization, whose rates are computed from the probabilities expressions derived from ADK theory [Ammosov et al., 1986]. The reached ionization state yield the electron density, whereas the ionization rates determine the energy distribution of electrons and thus, the electron temperature.

**Plasma kinetics.** Following interaction with the laser pulse, the plasma parameters evolve. The energy distribution functions of freed electrons are calculated using the model developed by Pert [Pert, 1999]. The knowledge of the temporal dependence of those functions is essential since the collisional rates affecting the variations of populations depend on them. Indeed, considering the excitation of an ion from levels  $i$  to  $j$ , the variation of population of the level  $i$  is:

$$\frac{dn_i}{dt} = \sum C_{ji}n_en_j - C_{ij}n_en_i \quad (\text{A.1})$$

where  $n_e$  is the electron density and  $C_{ij}$  the collisional rate defined as the product between the cross section  $\sigma_{ij}$  and the electron speed  $v_e$  [Salzmann, 1998]:

$$C_{ij} = \langle v_e \sigma_{ij} \rangle = \sqrt{\frac{2}{m_e}} \frac{\int \epsilon \sigma_{ij}(\epsilon) f(\epsilon) d\epsilon}{\int f(\epsilon) d\epsilon} \quad (\text{A.2})$$

The cross section can be expressed as a function of the collisional strength  $\Omega_{ij}$ :

$$\sigma_{ij} = \frac{h^2}{8\pi m_e \epsilon g_i} \Omega_{ij} \quad (\text{A.3})$$

In OFIKinRad code, the cross sections for collisional ionization are derived from Clark & Sampson formulae [Clark and Sampson, 1984], whereas, for collisional excitation, they are computed from expressions used in stellar atmospheres [Van Regemorter, 1962]. Those are then integrated over the electron energy distribution to yield the relevant rates.

The calculation of the temporal evolution of the atomic populations relies on the evolution of those collisional rates, which depend on the variation of those electron energy distribution functions. The kinetics of theses functions is affected by the electron-ion and electron-electron collisions. The former modifies the mean energy and density of electrons, whereas the latter alter the energy distribution. In the studied case of a plasma of hot free electrons, the Boltzmann equation describing the evolution of the states of a collisional plasma can be simplified into the so-called Fokker-Planck equation. The calculation of the relaxation of those energy distribution functions follows closely the work of Pert [Pert, 2001]. Contrary to electron-ion and electron-electron collisions, which play a fundamental role in ion kinetics, the impact of ion-ion collisions is negligible.

---

The atomic processes governing the temporal evolution of atomic populations in the plasma are:

1. Collisional processes (and their counterparts):

- collisional ionization (increase of ion charge thanks to the collision of an electron with the ion and release of an additional electron) and three-body ionization.
- collisional excitation (promotion of an ion into a higher energy state thanks to the transfer of energy from a hot free electron) and deexcitation.
- di-electronic recombination (di-electronic capture of an electron and radiative stabilization with emission of a photon).

2. Radiative processes (and their counterparts):

- spontaneous decay (random deexcitation of an ion into a lower energy level with the release of a photon).
- stimulated emission (stimulated deexcitation of an excited ion thanks to a photon and emission of an additional identical photon) and absorption.
- radiative recombination (decrease of ion charge and excitation with the interaction with an electron and release of a photon) and photoionization.

The plasma resulting from OFI interaction is in a strongly non-equilibrium state and evolves towards a local thermodynamic equilibrium characterized by an ionization degree much larger than the initial one ( $Z = 15 - 20$ ). As a consequence, this means that ionization and excitation display a rate much larger than inverse processes (three-body recombination and de-excitation). Hence, in the code approximation, radiative and three-body recombination processes are not taken into account. The collisional excitation from excited levels is taken into consideration. The data file contains energies and radiative emission rates for each atomic levels, as well as collision rates. The first two are obtained from the SUPERSTRUCTURE code [Eissner and al., 1974], whereas the last one comes from DISTORTED WAVE [Eissner and al., 1998].

It is worthy to note that the code basically considers that the gain is driven by the dynamics of population only for states with a charge of 8. Indeed, the approximation described in the last paragraph leads to the fact that ionization states with a charge over 8 do not play a role in the gain dynamics. Besides, the contribution from states with charges below 8 is minimal. While the ionization state  $Z = 7$  for krypton is not very stable, the contributions from the more stable states with  $Z = 6$  are not expected to have a significant impact on the gain. Actually, for the  $Z = 6$  state, the electrons are cooler and get further cooled down because of the two ionization processes as well as excitation needed to participate to the gain of the laser transition. The lower energy of electrons results in lower gain from this contribution. Furthermore, there are less electrons (6 instead of 8) and the ionization and excitation processes take time, which means that the contribution from those states with a lower charge occurs significantly after the main amplification peak.

The results from the code were found to yield a consistent insight into the gain dynamics of the plasma amplifier with respect to experimental measurements (see section 2.3.2 and section 5.2), over a range of electron densities varying from  $10^{18} \text{ cm}^{-3}$  to just over  $10^{20} \text{ cm}^{-3}$ .



# Appendix B

## Laser spectral lineshape

The broadening mechanisms and their contribution to the gain and emissivity mechanisms are described in section 2.3.1. Those impact the laser spectral lineshape and can be divided into two categories: homogeneous or inhomogeneous broadening.

- **Homogeneous broadening** affects all radiating ions in the same way. Natural and collisional broadening enter in this category. The emission line width profile is the same for all emitters and has a Lorentzian lineshape  $S_L(\nu)$ :

$$S_L(\nu) = \frac{2}{\pi \Delta\nu_L} \frac{1}{1 + \left( \frac{\nu - \nu_0}{\Delta\nu_L/2} \right)^2} \quad (\text{B.1})$$

where  $\nu_0$  is the central frequency and  $\Delta\nu_L$  the full width at half-maximum of the spectral line. It can be written as the inverse of the transition upper level lifetime  $\tau_u$ :

$$\Delta\nu_L = \frac{1}{\tau_u} \quad (\text{B.2})$$

- **Inhomogeneous broadening** comes from Stark and Doppler effects.

Simulations showed that Stark effect has a very small influence in the case of collisionally-pumped plasma-based soft X-ray lasers [Talín et al., 1995]. However, this source of linewidth broadening becomes more significant for recombination pumping schemes [Ben Nessib et al., 1994]. When ion heating gets non-negligible, their thermal velocity induce a Doppler shift of the central frequency of emission for each emitter. Hence, the lineshape gets broadened in an inhomogeneous way. When this phenomena dominates and when considering a maxwellian distribution of ion velocities, the lineshape features a Gaussian profile, such as:

$$S_D(\nu) = \frac{1}{\Delta\nu_D} \frac{2\sqrt{\ln 2}}{\pi} \exp \left[ - \left( \frac{\nu - \nu_0}{\Delta\nu_D/(2\sqrt{\ln 2})} \right)^2 \right] \quad (\text{B.3})$$

where  $\Delta\nu_D$  is the full width at-half maximum Doppler broadening.

$$\Delta\nu_D = \nu_0 \sqrt{\frac{8k_B T_i \ln 2}{m_i c^2}} \quad (\text{B.4})$$

where  $k_B$  is the Boltzmann constant,  $m_i$  the ion mass and  $T_i$  the ion temperature. Compared to the Lorentzian profile, the Gaussian profile is more weighted in the central part and falls more rapidly on the edges.

When both homogeneous and Doppler broadening coexist, the resulting lineshape is a Voigt profile. This is the convolution between both lineshapes:

$$S_V(\nu) = \int_{-\infty}^{\infty} S_L(\nu') S_D(\nu - \nu') d\nu' \quad (\text{B.5})$$

Combining equations eq. (B.1) and eq. (B.3) yields:

$$S_V(\nu) = \frac{2\beta^2}{\pi^{3/2}\Delta\nu_L} \int_{-\infty}^{\infty} \frac{e^{-y}}{(y + \alpha)^2/\beta^2} dy \quad (\text{B.6})$$

with

$$\alpha = 2\sqrt{\ln 2} \frac{\nu_0 - \nu}{\Delta\nu_D} \quad \text{and} \quad \beta = \sqrt{\ln 2} \frac{\Delta\nu_L}{\Delta\nu_D} \quad (\text{B.7})$$

The Voigt profile is similar to the Gaussian distribution at the center of the lineshape, whereas it decreases as a function of  $1/(\nu - \nu_0)^2$ , in a similar way to a Lorentz profile. Its value at the center of the emission line can be expressed as:

$$S_V(\nu_0) = \frac{2\sqrt{\ln 2}}{\pi} \frac{1}{\Delta\nu_D} e^{\beta^2} \text{erfc}(\beta) \quad (\text{B.8})$$

with  $\text{erfc}$ , the complementary error function defined as:

$$\text{erfc}(x) = \frac{2}{\sqrt{\pi}} \int_{-\infty}^{\infty} e^{-u^2} du \quad (\text{B.9})$$

## Appendix C

# Focusing light by means of an axicon lens

This appendix gives information about the focusing properties of an axicon lens. The fig. C.1 depicts the important geometrical parameters defining the axicon focusing properties, such as the length and the position of the focal line, as well as the on-axis peak intensity.

In the following, we assume the incoming beam is Gaussian and that its wavefront is planar. The system is symmetrical about the optical axis. Incoming rays enter the planar side and emerge from the conical shape side to converge on the optical axis with a conical wavefront. We introduce  $\alpha$  the base angle derived from the apex angle,  $\gamma$  the angle of approach to the optical axis,  $n$  the refractive index of the lens and  $\rho$  and  $z$  the radial and axial coordinates respectively. We note  $\rho_0$  the actual radius of the beam.

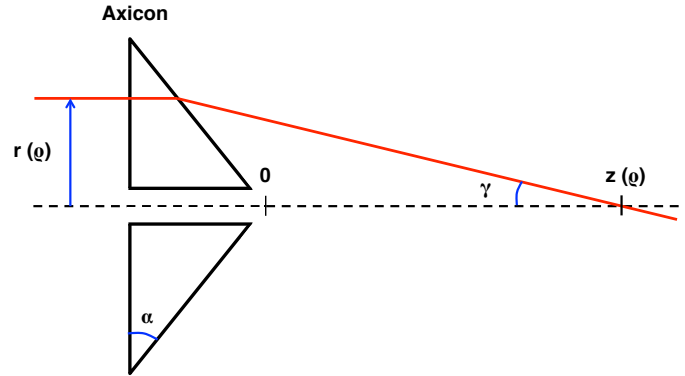


Figure C.1: (a) Schematic of axicon lens parameters.

Assuming, the beam is propagating in perfect vacuum, Snell-Descartes equation imposes:

$$n \sin(\alpha) = \sin(\alpha + \gamma) \quad (\text{C.1})$$

The axial coordinate at which rays are hitting the optical axis is related to the radial coordinate through:

$$z(\rho) = \rho \left( \frac{1}{\tan \gamma} - \tan \alpha \right) = \rho K_{\alpha \gamma} \quad (\text{C.2})$$



Considering a collimated input field  $E_{in}$  polarized in the x direction, an expression of the field near the optical axis can be derived using Kirchoff diffraction integral and the stationary phase method [Durfee et al., 1994]:

$$\begin{cases} E_x(r, z) = \left( \frac{\pi k \sin(\gamma)}{2} \frac{z}{K_{\alpha\gamma}} \right)^{1/2} E_{in}(z) \times \left( \frac{1+\cos(\gamma)}{2} J_0(kr \sin(\gamma)) + \frac{1-\cos(\gamma)}{2} J_2(kr \sin(\gamma)) \right) \\ E_z(r, z) = \left( \frac{\pi k \sin(\gamma)}{2} \frac{z}{K_{\alpha\gamma}} \right)^{1/2} E_{in}(z) \sin(\gamma) J_1(kr \sin(\gamma)) \end{cases} \quad (C.3)$$

where  $k = \frac{2\pi}{\lambda}$  is the wave number. The contribution along z-axis comes from input rays near x-z plane developing a small axial polarization component when refracted toward the optical axis. This contribution can be neglected. Besides, as the angle  $\gamma$  is usually small, the term  $\frac{1-\cos(\gamma)}{2} J_2(kr \sin(\gamma))$  can be neglected. Therefore, the total intensity profile is dominated by the terms  $J_0(kr \sin(\gamma))$  and can be computed as follows:

$$I(z) = \frac{\pi k \sin(\gamma)}{2} \frac{z}{K_{\alpha\gamma}} \frac{(1 + \cos(\gamma))^2}{4} J_0^2(kr \sin(\gamma)) I_{in}(\rho(z)) \quad (C.4)$$

The central spot size  $r_0$  can be derived evaluating the first zero of the Bessel function  $J_0$ :

$$r_0 \approx \frac{2.405}{k \sin(\gamma)} \quad (C.5)$$

The length of the focal line is given by  $z_{max} = z(\rho_0)$  and can be approximated for small angles to:

$$L \approx \frac{\rho_0}{2\alpha(n-1)} \quad (C.6)$$

The peak intensity occurs at a axial position depending on the input beam intensity profile. For a Gaussian beam, it is reached at  $z = L/2$ .

The fig. C.2 illustrates the formula eq. (C.4) for a 50 mm-diameter axicon with  $\alpha = 35$  deg in case of a pulse of 35 fs duration, 150 mJ energy for a Gaussian input beam profile, such that:

$$I_{in}(z) = I_0 \exp \left[ -2 \left( \frac{\rho}{\rho_0} \right)^2 \right] \quad (C.7)$$

A 8 mm central hole, used for focusing the main driving beam, is considered. As a result, the focal line starts in this case about 11.4 mm in front of the axicon tip.

The waist was considered to be  $w_0 = 25 \mu\text{m}$ . For  $\alpha = 25$  deg, the focal line is 32.3 mm long begins 10.4 mm after the tip of the axicon. Its transverse size is  $2.26 \mu\text{m}$ .

The fig. C.3 shows how the focal line changes when the apex angle is bigger (i.e. a lower value of  $\alpha$ ), which corresponds to a "flatter" axicon geometry. In the latter case, the focal line is 51.8 mm long begins 16.6 mm after the tip of the axicon. Its transverse size is  $3.12 \mu\text{m}$ .

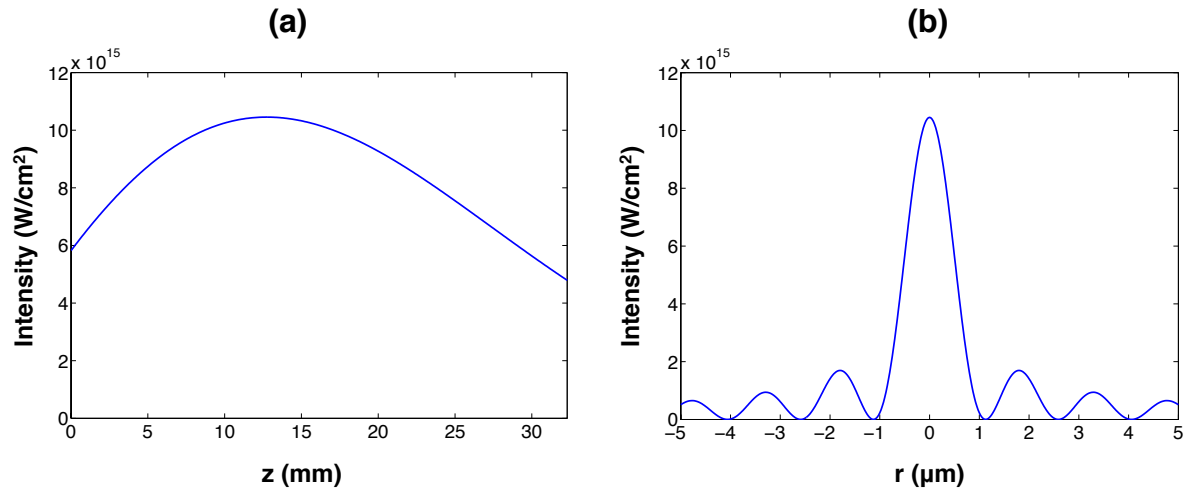


Figure C.2: Axial (a) and transverse (b) intensity profiles for a 50 mm-diameter axicon with  $\alpha = 35^\circ$

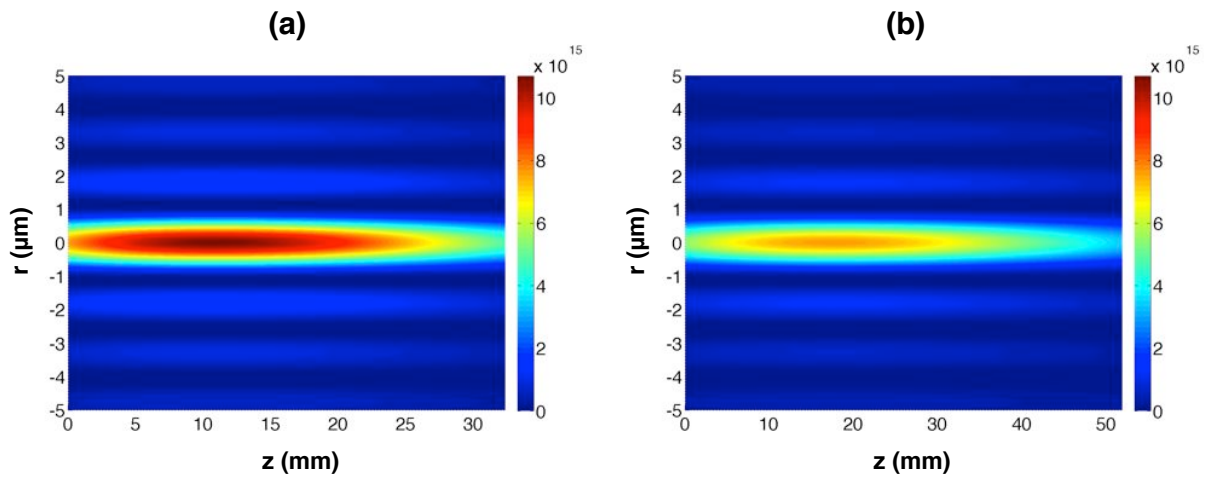


Figure C.3: Intensity map of the focal line for an axicon with  $\alpha = 35^\circ$  (a) and  $\alpha = 25^\circ$  (b).



## Appendix D

# Design of elongated rectangular slit nozzles

This appendix presents fluid simulations of the gas flow in such a convergent-divergent nozzle geometry adapted to an elongated rectangular outlet slit. This modeling is carried out with the software *Ansys Fluent* to validate the geometry of an existing nozzle and to motivate the possibility of manufacturing longer rectangular slit nozzles featuring comparable CDN geometry.

### Compressible fluid flow

This part aims at summing up the basic principles determining the flow behavior of a compressible fluid, while illustrating the correlation between import an parameters of the nozzle geometry and the outlet gas profile.

The gas is here considered to be ideal, thus being completely described by its pressure (Pa), its temperature (K) and its specific mass ( $kg.m^{-3}$ ) thanks to Avogadro-Ampère law:  $P = \rho RT$  with  $R = 8.314 JK^{-1}mol^{-1}$ , the ideal gas constant. The compressibility of the gas implies that its kinematic viscosity is zero and that its specific mass varies in the flow. As a first approach, a one-dimensional approximation is undertaken. Under those conditions, gas flow parameters describing the gas (pressure, specific mass, speed, temperature, gas flow section) are considered to be constant in the transverse direction. This approach is good to the extent that one look at creating a high density amplifier of transverse dimensions comparable to a few focal spots over a length of several millimeters. The rectangular slit geometry will therefore have longitudinal dimensions much bigger than its transverse size.

When considering an elementary section of fluid flowing along a nozzle, one need to link among them the different parameters describing the physical properties of the gas. Those include the pressure (P), the temperature (T), the specific mass ( $\rho$ ), the speed (v) and the section being crossed by the gas flow (S). The knowledge of the gas speed (i.e. its Mach number) when the gas gets out of the nozzle into the vacuum chamber is important. This speed will indeed determine the gas density and its gradients at the outlet of the nozzle [Semushin and Malka, 2001].

To describe the compressible ideal gas flow, four equations need to be considered:

1. Mass continuity equation:

$$\frac{d\rho}{\rho} + \frac{v}{v} + \frac{S}{S} = 0 \quad (\text{D.1})$$

2. Momentum continuity equation:

$$-dp.S = (S.\rho.v).dv \quad (\text{D.2})$$

3. Isentropic transformation equation:

$$\frac{dp}{d\rho} = \gamma.R.T \quad (\text{D.3})$$

with  $\gamma$ , the adiabatic index of the gas defined by the relation:

$$\gamma = \frac{C_P}{C_V} \quad (\text{D.4})$$

where  $C_P$  et  $C_V$  are respectively the calorific capacities at constant pressure and constant volume, describing the gas.

4. Steady flow adiabatic energy equation:

$$\frac{dT}{T} = -(\gamma - 1).M^2.\frac{dv}{v} \quad (\text{D.5})$$

This equation neglects the gravity effects.

The combination of equations eq. (D.1), eq. (D.2), eq. (D.3) and eq. (D.5) yields:

$$\frac{dS}{S} = \left( \frac{M^2 - 1}{1 + \left(\frac{\gamma-1}{2}\right).M} \right) \cdot \frac{dM}{M} \quad (\text{D.6})$$

The equation eq. (D.6) related the variation of the sectional area to that of the Mach number and thus shows how the nozzle geometry affects the gas flow speed.

### Convergent-divergent geometry

To meet the desired characteristics for the gas near-critical density profile with sharp density gradients, a nozzle displaying a convergent-divergent geometry is adopted with a strong backing pressure. This profile has the advantage to provide convenient conditions for efficiently accelerating the gas flow to high Mach numbers.

For this geometry, five different gas flow regimes can be identified. These stages at which each of them occurs are depicted in fig. D.1):

1. The first part of the nozzle consists of a « reservoir » where the gas is being accumulated. When the valve is opened, the gas naturally flows towards the vacuum chamber and fills this part.

2. Then, there is the convergent part of the nozzle, where the section crossed by the gas flow monolithically sharply decreases. The gas flow is subsonic at this stage ( $M < 1$ ). The equation eq. (D.6) show that the convergent geometry is appropriate to accelerate the gas flow until the critical zone, where the flow should reach transsonic speeds.
3. The critical zone consists in a bottleneck delimitating the convergent and the divergent parts.
4. Then comes the divergent part of the nozzle. In this part, equation eq. (D.6) show that the gas flow can be further accelerated up to supersonic speeds only if a transsonic speed is reached at the level of the critical zone. Otherwise, a shock wave is being formed and results in a turbulent gas flow. The divergent part of the nozzle corresponds to a relaxation phase of the gas. The angle defining the increase rate of the sectional area is an important parameter. It has to be maintained to low values to keep gas flow transverse speeds negligible compared to the main propagation speed of the gas flow. Those conditions correspond to so-called « adiabatic » gas flow, which will guarantee sharp density gradients out of the nozzle. In the considered model, the gas flow speed only depends on the ratio of inlet and outlet sections, through the formula:

$$\frac{S}{S_0} = \frac{1}{M} \left( \frac{2 + (\gamma - 1)M^2}{\gamma + 1} \right)^{\frac{\gamma+1}{2(\gamma-1)}} \quad (D.7)$$

This equation is derived from the equations eq. (D.1), eq. (D.2), eq. (D.3) and eq. (D.5) with  $S_0$  the sectional area of the critical zone.

Hence, choosing the surfaces ration is of primary importance to reach the desired Mach number fostering the required density and gradient conditions out of the nozzle.

5. Finally, in the last regime, the gas expands in the vacuum chamber, following the outflow from the nozzle.

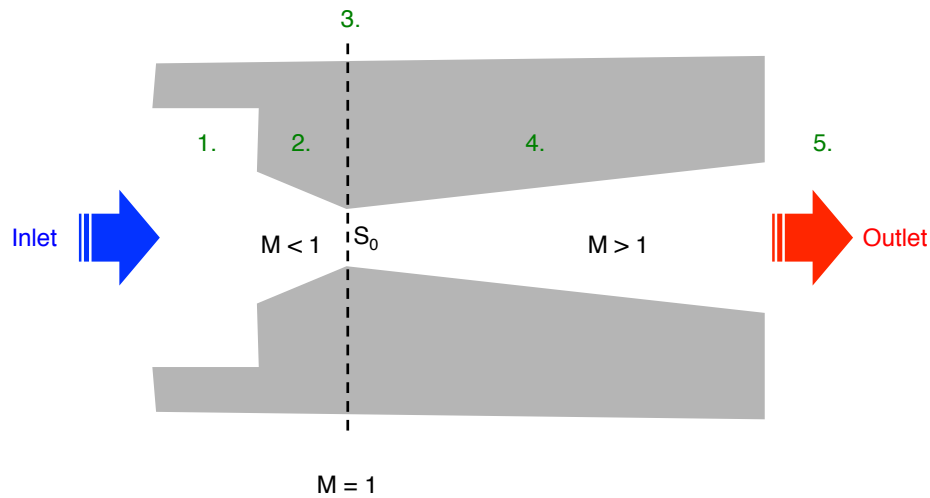


Figure D.1: Scheme of a Convergent-Divergent Nozzle (CDN) illustrating the various gas flow regimes.

### Numerical model.

The software *Ansys Fluent* was used to model the hydrodynamics of turbulent krypton gas flow over a structured mesh. Physical parameters describing the gas properties are teen constant over the elementary volume defined by this mesh. The code solves the Navier-Stokes equations in their integral form in a fixed frame of reference. The turbulence of the gas flow is described by the transport equations. The computation starts under specified initial conditions and is carried out iteratively elementary volume by elementary volume from the inlet. Iterations are performed until stationary operation is reached.

The first modeled rectangular slit nozzle has a  $500\ \mu\text{m}$  by  $5\ \text{mm}$  sectional area. This nozzle has been previously experimentally proven to offer appropriate conditions for plasma soft X-ray generation. Its geometry is described in fig. D.2.

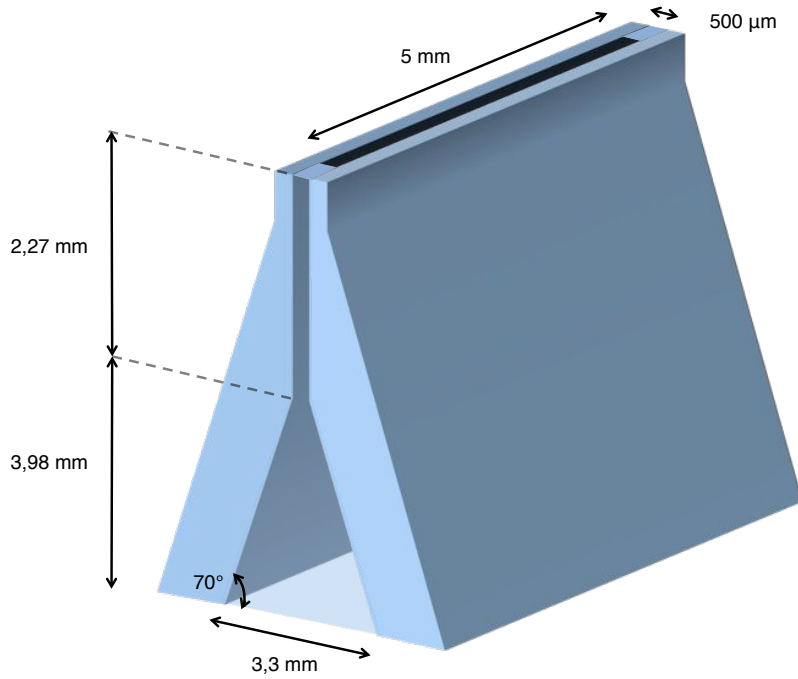


Figure D.2: Geometry of the  $5\text{mm} \times 500\ \mu\text{m}$  slit nozzle used for previous experiments. The transverse section is seen by transparency.

The numerical simulation hinges upon the several following steps:

- The drawing of the three-dimentional nozzle geometry. The rectangular nozzle slit has two axes of symmetry, thus only a quarter of the nozzle need to be modeled. This allows saving calculation time.
- The definition of the physical model. The parameters defining the set of equations are specified. Thus, the adiabatic index of the gas  $\gamma$  (here, krypton), defined by the ratio of thermoelastic coefficients is taken into account.

In order to describe the turbulent gas flow, the software uses a so-called RANS approach (Reynolds Averaged Navier-Stokes). The underlying principle consists in separating the physical parameters between an averaged part and fluctuating one. In this method, new terms appear in the set of equations and have to be taken into account. This formalism

---

yields the turbulent viscosity  $\mu_t$ , whose effects add up to those of the laminar (or molecular) viscosity. Moreover, a thermal diffusion coefficient describes the impact of turbulence on the gas flow heat. The evolution of the thermal diffusion coefficient is linked to the variations of  $\mu_t$ . To compute the latter coefficient, several models can be chosen.

Here, a model composed of two transport equations, dubbed «  $k - \omega$  model » is used. It turns out more adapted to the present configuration involving high pressure gas flow. Two turbulence scales are calculated and those allow computing  $\mu_t$  from an algebraic relation. For this two-equations model, the turbulent viscosity is expressed as a function of two turbulence parameters. A transport equation for each of them is set:

- for  $k$ , the turbulent kinetic energy.
- for  $\omega$ , the turbulence characteristic frequency. The inverse of  $\omega$  represents the characteristic timescale of the kinetic energy dissipation. The turbulent viscosity is written as a function of  $k$  and  $\omega$  :

$$\mu_t = \rho \frac{k}{\omega} \quad (D.8)$$

- The implementation of the numerical algorithm. This step defines the parameters involved in the set of equations, which will be solved. The spatial discretization method, as well as the time integration method (numbers of iterations, time step, numerical convergence model) are applied to the algebraic system. The step by step computation is performed from the nozzle inlet.
- The spatial mesh geometry. The mesh is tuned over the nozzle geometry. Regions where strong and quick variations of physical parameters of the gas flow are expected, such as the nozzle "throat", are covered with smaller elementary volumes. The mesh geometry used to model the gas flow of the  $5mm \times 500\mu m$  slit nozzle is depicted in fig. [D.3](#).

It involves 1 237 244 elementary cells, in which temperature, speed, density, pressure and kinematic viscosity are considered to be constant. The latter parameter (expressed in  $m^2.s^{-1}$ ) is defined by the following formula:

$$\nu = \frac{\eta}{\rho} \quad (D.9)$$

where  $\eta$  is the dynamic viscosity ( $Pa.s$  or  $kg.m^{-1}.s^{-1}$ ) and  $\rho$  the specific mass ( $kg.m^{-3}$ ).

- The boundary conditions. Those are specified for each physical surface of material of the nozzle.
- The initial conditions. The gas pressure and a zero gas flow velocity is imposed at the inlet surface. Very low values ( $10^{-5}$  bar, corresponding to vacuum conditions under experimental conditions) are taken for the surfaces at the boundaries of the simulation volume out of the nozzle
- At last, computation by finite elements is carried out over the pre-defined mesh.



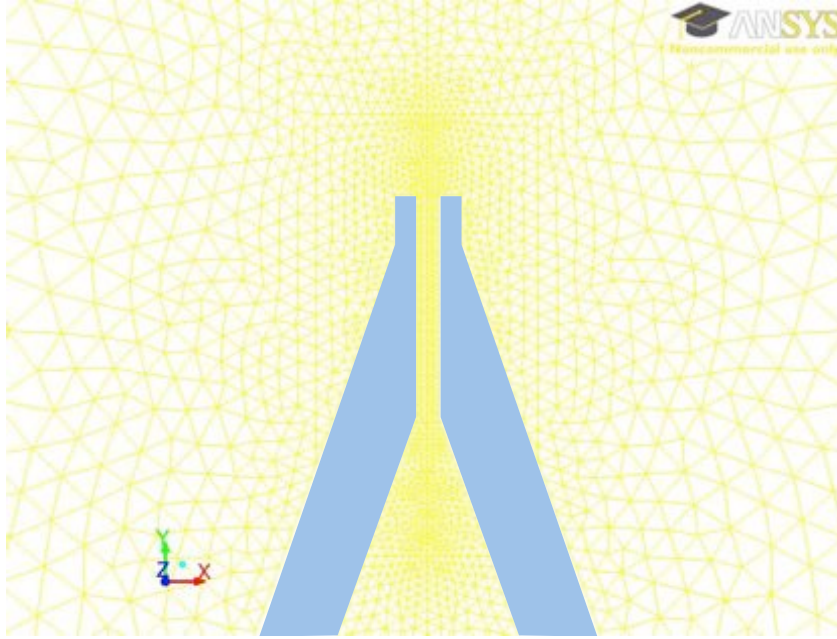


Figure D.3: Transverse profile of the mesh geometry for the  $5\text{mm} \times 500\mu\text{m}$  slit nozzle. The solid edges of the nozzle are materialized by the pale blue lines. A finer mesh is applied in zones where stronger local gradient of physical parameters are expected.

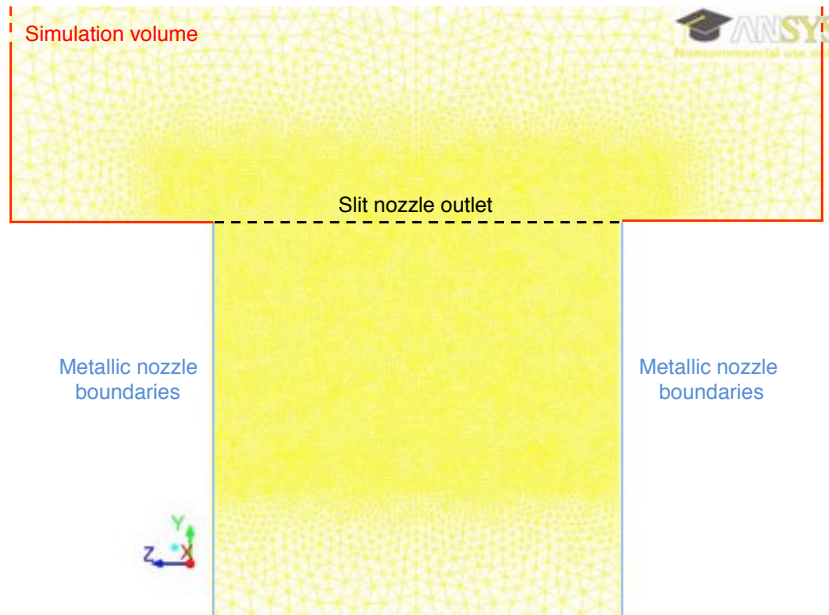


Figure D.4: Longitudinal profile of the mesh geometry for the  $5\text{mm} \times 500\mu\text{m}$  slit nozzle.

### Simulated density profiles.

The simulations were realized considering a 150 bar krypton backing pressure. The distribution of neutral gas density is there studied under stationary operation. The transverse and longitudinal profiles are reported respectively in fig. D.6 and fig. D.7. The evolution of the gas density

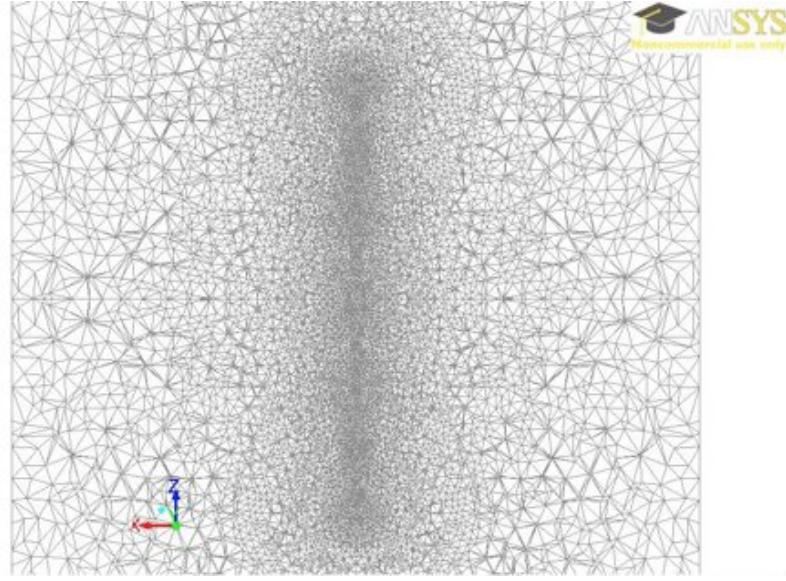


Figure D.5: Profile of the mesh geometry for the  $5\text{mm} \times 500\mu\text{m}$  slit nozzle at the height  $h = 1\text{ mm}$  with respect to the nozzle outlet tip.

from the "reservoir" up to the vacuum chamber out of the nozzle slit outlet is illustrated in fig. D.8. The plots represents the neutral density along a line centered in the nozzle.

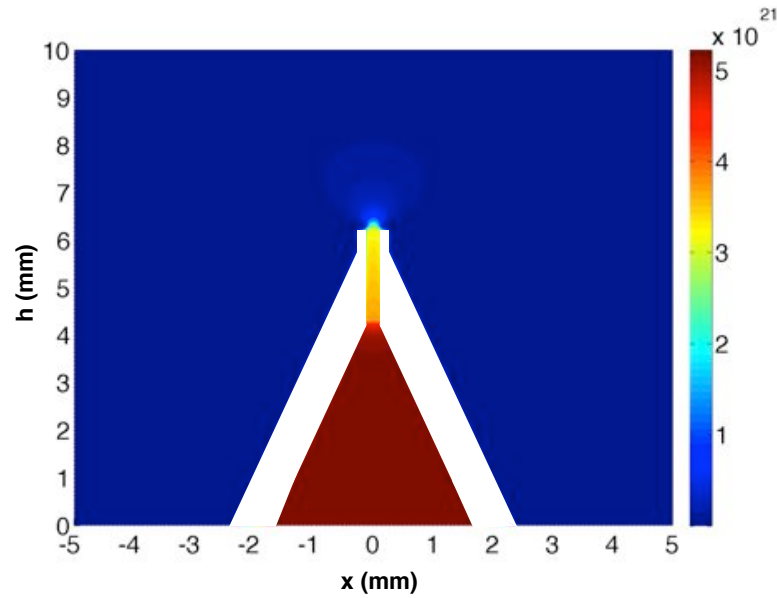


Figure D.6: Transverse krypton neutral density profile for the rectangular slit nozzle of sectional area  $5\text{mm} \times 500\mu\text{m}$  for  $P_{Kr}=150\text{ bar}$ .

The neural gas density exceeds  $5 \times 10^{21}\text{cm}^{-3}$  in the reservoir and slowly decreases as the gas flow velocity increases up to the "throat" zone. The gas then relaxes in a quasi-adiabatic

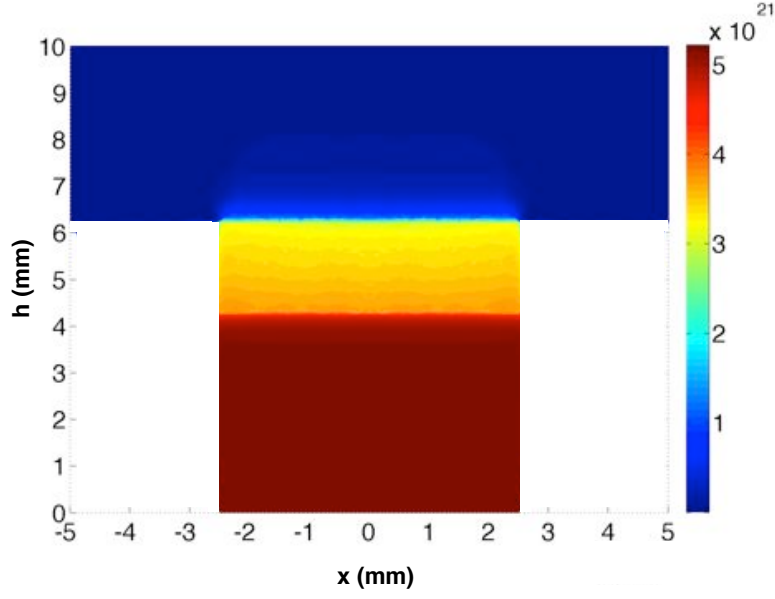


Figure D.7: Longitudinal krypton neutral density profile for the rectangular slit nozzle of sectional area  $5\text{mm} \times 500\mu\text{m}$  for  $P_{Kr}=100$  bar

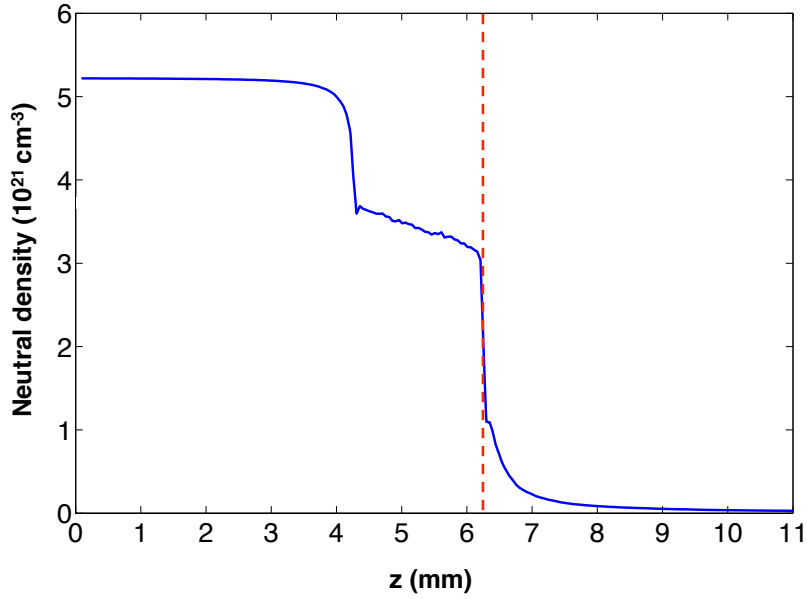


Figure D.8: Neutral density evolution from the "reservoir" to the vacuum chamber along a line centered in the nozzle. The dashed red line shows the nozzle slit outlet.

way, while being modestly further accelerated until the nozzle slit outlet, from which it gets out and expands in the vacuum chamber. Out of the nozzle, the neutral gas density exponentially decreases as the gas expands.

# Appendix E

## Gas and plasma density diagnostics

This appendix presents the techniques associated with probing the gas and plasma density of a flow using a Mach-Zehnder interferometer. The tomography setup used for density diagnostic of a neutral gas is illustrated in the following paragraph, whereas the one used to probe plasma electron densities is showed in fig. [4.16](#).

### Tomography technique

The experimental characterization of neutral gas density out of the rectangular slit nozzles were performed thanks to a phase retrieval technique using a Mach-Zehnder interferometer. This method allows calculating neutral gas or plasma density reconstructing the phase difference imparted by the medium density spatial distribution on the beam wavefront.

The relevant experimental setup is illustrated in fig. [E.1](#). The interferometer splits the laser beam into two part. One is used to probe the gas, whereas the other serves as a reference. The difference of optical path between those two beam parts generates an interferogram. The resulting set of fringes is perturbed when the gas crosses the probing beam. The measurement of the fringe displacement allows reconstructing the density profile.

The diagnostic was performed with a He-Ne laser at 632.8 nm. The valve is controlled by a TTL signal delivered by a delay box, which allows synchronizing the camera acquisition with the gas flow. The signal has a shape of a "temporal gate", which is used to control the opening time window of the valve.

### Phase retrieval

More specifically, the phase delay induced by the gas represents the product of the gas index (depending on the medium, its density, temperature and pressure) and the medium length crossed by the probing beam, from which the « reference » phase without gas is subtracted. Therefore, the measurement of the local variation of phase can be linked to the density profile.

In order to calculate the gas density, at least two measurements of the phase delay at different attacking angles with respect to the gas flow are needed. In the following transverse and longitudinal profiles are considered.

### Gas density computation by tomography

The reconstruction of density profiles by tomography consists in calculating the local phase variation from phase measurements integrated along at least two probing directions. The transverse and longitudinal interferograms actually does not record the absolute phase but rather an

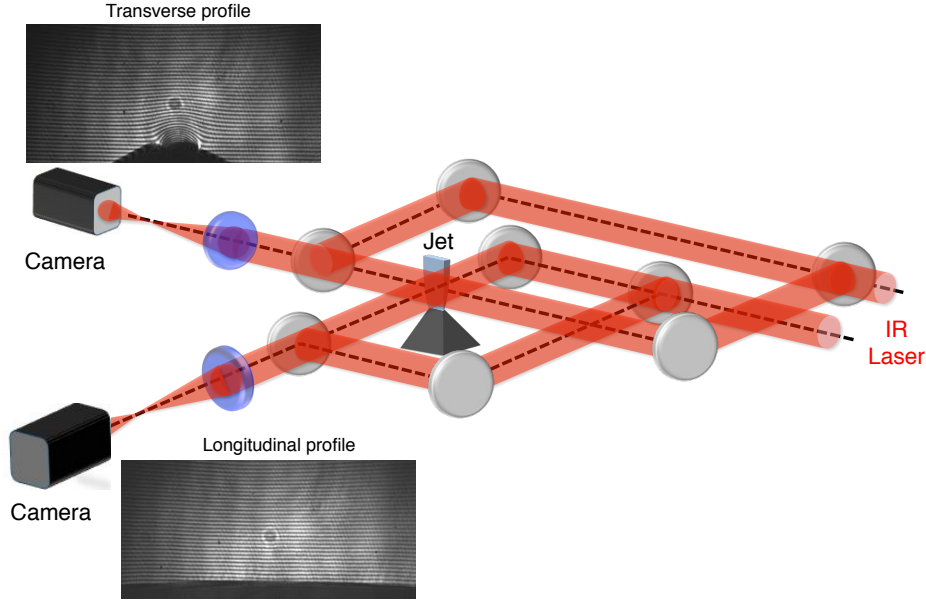


Figure E.1: Schematic of the double Mach-Zehnder interferometer, which allows probing the transverse and longitudinal phase maps. Those are necessary to reconstruct the whole neutral gas density.

integrated phase measurement over a spatial projection.

The combination of those two projection measurements allows deriving a tri-dimensional map of the phase, from which density can be extracted.

A simultaneous algebraic reconstruction technique (SART) [Gordon, 1974; Andersen, 1987] implemented with Matlab allowed reconstructing the phase distribution through a discretization of the space. The phase is then linked to density under the normal conditions of pressure and temperature.

In the following, the axis  $x$  is considered to be the propagation axis of the laser beam probing the medium. The axis  $y$  defines the polarization direction of the laser and the axis  $z$  represents the remaining direction orthogonal to the previous axes. Under those conditions, the optical path difference between the probing beam and the reference is:

$$\delta(y, z) = \int_{x_1}^{x_2} \eta(x, y, z) dx \quad (\text{E.1})$$

The phase delay can therefore be written:

$$\Delta\Phi(y) = \Phi(y) - \Phi_0 = \frac{2\pi}{\lambda} \int_{x_1}^{x_2} (\eta(x, y, z) - 1) dx \quad (\text{E.2})$$

From the measurement of the local fringe displacement, it is possible to derive the local variation of the refractive index of the gas, resorting to an Abel inversion [Whittaker, 1948] of the equation eq. (E.16).

1. **Abel inversion.** This mathematical operation supposes that, for a fixed  $y$  coordinate, the refractive index displays a rotational symmetry. Hence, we consider the radial coordinate  $r = \sqrt{x^2 + z^2}$ .

The phase map corresponds to the projection of the optical index, whose distribution is axisymmetric in a plane orthogonal to the x-axis.

Supposing the gas density has the same axisymmetric distribution, the term  $\eta(r, y) - 1$  can be recovered implementing an Abel inversion of the equation eq. (E.16). Then, the density  $n(r, y)$  is derived from the refractive index  $\eta(r, y)$  using the dispersion relations depending on the nature of the medium (plasma or gas) and the wavelength of the probing beam. The Abel inversion can be easily formulated only in the case of a fringe displacement featuring a Gaussian profile such as:  $\Delta\Phi = 2\pi/\lambda \cdot \exp(x^2/\Delta r)$  (with  $\Delta r$ , the full width at half-maximum of the refractive index profile). In the general case, considering  $F$  and  $f$ , functions related to each other by the following formula:

$$F(y) = \int_{-\infty}^{\infty} f(\sqrt{x^2 + y^2}) dx \quad (\text{E.3})$$

The Abel inversion can be written:

$$f(r) = \mathcal{A}^{-1}[F](r) - \frac{1}{\pi} \int_r^{\infty} \frac{dF}{dx} \frac{1}{\sqrt{x^2 - r^2}} dx \quad (\text{E.4})$$

The details of the Abel inversion calculations are presented in the paragraph E.

2. **Case of a neutral gas.** Derived from the Clausius-Mossotti relation the Lorentz-Lorenz formula allows linking, from a neutral gas, the refractive index  $\eta$ , the gas polarizability  $\alpha$  and the particle density  $n$ :

$$\frac{\eta^2 - 1}{\eta^2 + 2} = \frac{4\pi}{3} n\alpha = A \frac{n}{N_A} \quad (\text{E.5})$$

with  $A = \frac{4\pi}{3} N_A \alpha$ , the molar refractivity of the gas under consideration.

The refractive index  $\eta$  being close to 1, the following approximation can be done:  $\eta^2 + 2 \approx 3$ . Hence, we can write:

$$\eta^2 = 1 + 3A \frac{n}{N_A} \quad (\text{E.6})$$

Thus,

$$\eta \approx 1 + \frac{3An}{2N_A} \quad (\text{E.7})$$

The Matlab program, with which the reconstruction was performed, expresses the refractive index as a function of the gas pressure  $P$ :

$$\eta = 1 + \tilde{\alpha} P \quad (\text{E.8})$$

Considering an ideal gas,  $\eta = 1 + \frac{3A}{2RT} P$  with  $T$ , the temperature and  $R$ , the ideal gas constant. As a consequence, the parameter  $\tilde{\alpha}$  included in the program is written:

$$\tilde{\alpha} = \frac{2\pi}{RT} N_A \alpha \times 10^5 \quad (\text{E.9})$$

for a gas pressure expressed in bar.

The molar refractivity being weakly dependent on the wavelength, acquisitions of data using white light are also relevant.

The following table summarizes the previously described constants for three different gases, which are being used either in the *Matlab* program (neutral gas density measurements with a tomography technique) or with *Neutrino* software (plasma density retrieval).

Gas	$\alpha$ ( $\times 10^{18} m^3$ )	A ( $cm^3/mol$ )	$\tilde{\alpha}$ ( $bar^{-1}$ )
Hélium	0.206	1.3	0.0000343
Argon	1.64	2.3	0.000273
Krypton	2.48	2.3	0.000413

Tab.1: Characteristic coefficient derived from the gas polarizability  $\alpha$  [Forbes, 1977] and being used as input parameters in the programs *reconstruction.m* ( $\tilde{\alpha}$ ) and *Neutrino* ( $A$ ).

3. **Case of a plasma.** As far as plasmas are concerned, the dispersion relation highly depends on the wavelength of the probing beam. A monochromatic beam is thus needed. For probing high-density plasmas, a part of the infrared laser beam is collected and its frequency is doubled thanks to a BBO nonlinear crystal. This allows increasing the transmission, operating away from the critical density at twice the laser frequency. The dispersion relation in a plasma is:

$$\eta = \sqrt{1 - \frac{n_e}{n_c}} \quad (E.10)$$

where  $n_e$  is the electron density in the plasma, and  $n_c = \frac{\omega_L \epsilon_0 m_e}{e^2}$  the critical density with  $\omega_L$  laser frequency,  $\epsilon_0$  the vacuum permitivity and  $m_e$  the electron mass. Hence,  $n_c[cm^{-3}] = \frac{1.1 \times 10^{21}}{\lambda^2[\mu m]}$ . Therefore:

$$n_e[cm^{-3}] = (1 - \eta) \frac{1.1 \times 10^{21}}{\lambda^2[\mu m]} \quad (E.11)$$

4. **Derivation of the actual density from the refractive index.** It was previously reported that, in the case of a plasma, the refractive index  $\eta$  is derived from the Abel inversion of the retrieved phase  $\Delta\Phi = \frac{2\pi}{\lambda} \int_{-\infty}^{\infty} (\eta(r, y) - 1) dx$ . The refractive index can therefore be written:

$$\eta(r, z) = 1 + \frac{\lambda}{2\pi} \mathcal{A}^{-1}(\Delta\Phi) \quad (E.12)$$

Thus, in case of a plasma:

$$n_e = n_c \left[ 1 - \left( 1 + \frac{\lambda}{2\pi} \mathcal{A}^{-1}(\Delta\Phi) \right)^2 \right] \quad (E.13)$$

As far as a neutral gas is concerned,

$$n = \frac{2N_A}{3A} \frac{\lambda}{2\pi} \frac{1}{\Delta r} \mathcal{A}^{-1}(\Delta\Phi) \quad (E.14)$$

Under the normal conditions of temperature and pressure (CNTP), we get:  $n_{CNTP} = \frac{2N_A}{3A} \tilde{\alpha} P_0 = 2.68 \times 10^{19} cm^{-3}$  with  $P_0 = 1.013 bar$ . Hence, the number of particles per unit volume is:

$$n = \frac{n_{CNTP}}{\tilde{\alpha} P_0} \frac{\lambda}{2\pi} \frac{1}{\Delta r} \mathcal{A}^{-1}(\Delta\Phi) \quad (E.15)$$



---

## Abel inversion calculation

This appendix briefly presents the Abel inversion algorithm [Whittaker, 1948] used to reconstruct the neutral and electron density profiles from phase maps. The computation of the Abel inversion suppose that the gas density profile has an axisymmetric distribution.

We assume a phase delay induced by the gas such that:

$$\Delta\Phi(y) = \frac{2\pi}{\lambda} \int_{x_1}^{x_2} (\eta(x, y, z) - 1) dx \quad (\text{E.16})$$

We note  $f$ , the function describing the profile of the refractive index  $\eta$ . We can then introduce a function  $F$ , such that:

$$F(y) = \int_{-\infty}^{\infty} f(\sqrt{x^2 + y^2}) dx \quad (\text{E.17})$$

The Abel inversion can therefore be expressed:

$$f(r) = \mathcal{A}^{-1}[F](r) - \frac{1}{\pi} \int_r^{\infty} \frac{dF}{dx} \frac{1}{\sqrt{x^2 - r^2}} dx \quad (\text{E.18})$$

The computation is being implemented over a discretized space.

The function  $F$  can be written in the following way:

$$F(y) = \int_{-\infty}^{\infty} f(\sqrt{x^2 + y^2}) dx \quad (\text{E.19})$$

Then, for a radial value  $r \geq 0$  :

$$f(r) = -\frac{1}{\pi} \int_r^{\infty} \frac{dF}{dy} \frac{1}{\sqrt{x^2 - r^2}} dx \quad (\text{E.20})$$

The function  $f$  can be discretized over  $N$  points defined by  $r_i = i\Delta r$  such as:

$$f(r_i) = -\frac{1}{\pi} \int_{r_i}^{r_{N-1}} \frac{dF}{dy} \frac{1}{\sqrt{x^2 - r_i^2}} dx \quad (\text{E.21})$$

This integral is not defined for values  $y = r_i$ . Let us suppose that  $dF/dy$  (written  $dF$ ) is sampled by  $N$  points over the interval  $[0..r_{N-1}]$  with  $dF_i = dF/dy(r_i = i\Delta r)$ , the value  $dF_0$  lying on the axis of inversion. To integrate this quantity,  $dF$  is approximated by a line over each interval  $[r_i, r_{i+1}]$ , which means for every  $j \leq N - 1$  et  $y \leq \Delta r$ :

$$dF(r_j + y) = dF_j + y \frac{dF_{j+1} - dF_j}{\Delta r} \quad (\text{E.22})$$

Thus:

$$f(r_i) = -\frac{1}{\pi} \sum_{j=0}^{N-2} \int_{r_j}^{r_{j+1}} [dF_j + (x - r_j) \frac{dF_{j+1} - dF_j}{\Delta r}] \frac{1}{\sqrt{x^2 - r_i^2}} dx \quad (\text{E.23})$$

Hence:

$$f(r_i) = -\frac{1}{\pi} \sum_{j=0}^{N-2} \int_0^1 [dF_j + t(dF_{j+1} - dF_j)] \frac{1}{\sqrt{(j+t)^2 - i^2}} dt \quad (\text{E.24})$$



These integrals are defined for  $j > i$  and  $j = i \neq 0$  and depend only on  $i$  and  $j$ .

Their value is respectively  $B_{i,j}$  and  $A_{i,j} - jB_{i,j}$ . Reorganizing the terms in the addition leads to arranging  $f_i$  in the form [Pretzler, 1991]:

$$f_{i-1} = \sum_{j=1}^N dF_{j-1} D_{i,j} \quad (\text{E.25})$$

$$D_{i,j} = \begin{cases} 0 & \text{if } j = i = 1 \text{ or } j < i \\ \frac{1}{\pi}(A_{i,j} - jB_{i,j}) & \text{if } j = i \text{ and } i \neq 1 \\ \frac{1}{\pi}(A_{i,j} - jB_{i,j} - 1) & \text{if } j > i \text{ and } j = 2 \\ \frac{1}{\pi}(A_{i,j} - A_{i,j-1} - (j-2)B_{i,j-1}) & \text{if } j > i \text{ and } j \neq 2 \end{cases} \quad (\text{E.26})$$

This algorithm was characterized in case of inversions of known analytical expression, such as a Gaussian distribution. It leads to a very small numerical shift compared to the exact expression given by the analytical form. The definition of the symmetrical axis is made by successive iterations. This is done minimizing iteratively the discontinuities of the reconstructed profile.

# Appendix F

## Polarization state recovery

This appendix provides additional information about the recovery of the polarization state of fully polarized light using a multiple-mirror rotating analyzer. The field polarization can be decomposed in a base consisting of left-handed and right-handed polarization eigenvectors. Considering a field with complex amplitudes  $A_R$  and  $A_L$ , its Stokes vector is defined as:

$$\begin{cases} I = |A_R|^2 + |A_L|^2 \\ Q = 2\mathcal{R}(A_L^* \cdot A_R) \\ U = -2\mathcal{I}(A_R^* \cdot A_L) \\ V = |A_R|^2 - |A_L|^2 \end{cases} \quad (\text{F.1})$$

The first term represents the intensity of the field, the second and third ones describe the p- & s-directions and  $-/+ 45^\circ$  linear polarizations, whereas the last term describes the left-handed and right-handed circular polarizations.

Considering the general case of elliptical polarization with parameters defined in fig. 6.2, the polarization state can be written:

$$S_{in} = \begin{bmatrix} 1 \\ \cos 2\alpha \cos 2\epsilon \\ \sin 2\alpha \cos 2\epsilon \\ \sin 2\epsilon \end{bmatrix} \quad (\text{F.2})$$

The modification of the polarization of light by an optical device is modeled using the Mueller matrix formalism. Let us first consider the Jones matrix of the analyzer system  $J_A$ , which applies  $r_p$  and  $r_s$  reflection coefficients as well as phase delays  $\delta_p$  and  $\delta_s$  on the input beam in its frame of reference:

$$J_A = \begin{bmatrix} r_p & 0 \\ 0 & r_s e^{i\Delta} \end{bmatrix} \quad (\text{F.3})$$

with  $\Delta = \delta_p - \delta_s$  the total phase delay.  
The Mueller matrix is derived from eq. (F.3):

$$M_A = A[J_A \otimes J_A^*]A^{-1} \quad (\text{F.4})$$

with

$$A = \begin{bmatrix} 1 & 0 & 0 & 1 \\ 1 & 0 & 0 & -1 \\ 0 & 1 & 1 & 0 \\ 0 & i & -i & 0 \end{bmatrix} \quad \text{and} \quad A^{-1} = \frac{1}{2} \begin{bmatrix} 1 & 1 & 0 & 0 \\ 0 & 0 & 1 & i \\ 0 & 0 & 1 & -i \\ 1 & -1 & 0 & 0 \end{bmatrix} \quad (\text{F.5})$$

The symbol ' $\otimes$ ' means the Kroenecker product between two matrices. Thus, the Mueller matrix of the analyzer  $M_A$  reads:

$$M_A = \frac{1}{2} \begin{bmatrix} r_p^2 + r_s^2 & r_p^2 - r_s^2 & 0 & 0 \\ r_p^2 - r_s^2 & r_p^2 + r_s^2 & 0 & 0 \\ 0 & 0 & 2r_p r_s \cos \Delta & 2r_p r_s \sin \Delta \\ 0 & 0 & -2r_p r_s \sin \Delta & -2r_p r_s \cos \Delta \end{bmatrix} \quad (\text{F.6})$$

If we assume  $\tan \Psi = r_p/r_s$ , then comes:

$$-\cos 2\Psi = \frac{r_p^2 - r_s^2}{r_p^2 + r_s^2} \quad \text{and} \quad \sin 2\Psi = \frac{2r_p r_s}{r_p^2 + r_s^2} \quad (\text{F.7})$$

Therefore, the equation eq. (F.7) can be written:

$$M_A = \frac{(r_p^2 + r_s^2)}{2} \begin{bmatrix} 1 & -\cos 2\Psi & 0 & 0 \\ -\cos 2\Psi & 1 & 0 & 0 \\ 0 & 0 & 2r_p r_s \cos \Delta & 2r_p r_s \sin \Delta \\ 0 & 0 & -2r_p r_s \sin \Delta & -2r_p r_s \cos \Delta \end{bmatrix} \quad (\text{F.8})$$

Considering an input elliptical polarization defined by equation eq. (F.2) and  $\gamma$ , the angle of rotation of the analyzer, the output Stokes vector in the frame of reference of the laboratory is derived by the following expression:

$$S_{out} = R(-\gamma) M_A R(\gamma) S_{in} \quad \text{with} \quad R(\gamma) = \begin{bmatrix} 1 & 0 & 0 & 0 \\ 0 & \cos 2\gamma & \sin 2\gamma & 0 \\ 0 & -\sin 2\gamma & \cos 2\gamma & 0 \\ 0 & 0 & 0 & 1 \end{bmatrix} \quad (\text{F.9})$$

The normalized intensity recorded by the camera can therefore be written as a function of the ellipse parameters and the rotation angle of the analyzer  $\gamma$ :

$$\frac{I_{out}}{I_{norm}} = 1 - \cos 2\Psi \cos 2\epsilon (\cos 2\alpha \cos 2\gamma - \sin 2\alpha \sin 2\gamma) \quad (\text{F.10})$$

where  $I_{norm} = \frac{(r_p^2 + r_s^2)I_0}{2} = \frac{I_{max} + I_{min}}{2}$  is the normalizing intensity factor with  $I_0$  the input intensity. As shown in fig. F.1, a fitting with this function is done for the experimental data obtained for the SXRL seeded with circularly-polarized HH.

The best fit is obtained for an angle  $\epsilon = 42.3^0$  with  $\alpha = 50^0$ . Alternatively, the ellipticity can be determined from the formula:

$$\tan(\epsilon) = \sqrt{\frac{I_{minor}}{I_{major}}} = \sqrt{\frac{\Omega - e}{1 - \Omega e}} \quad (\text{F.11})$$

, which is obtained combining the expressions:

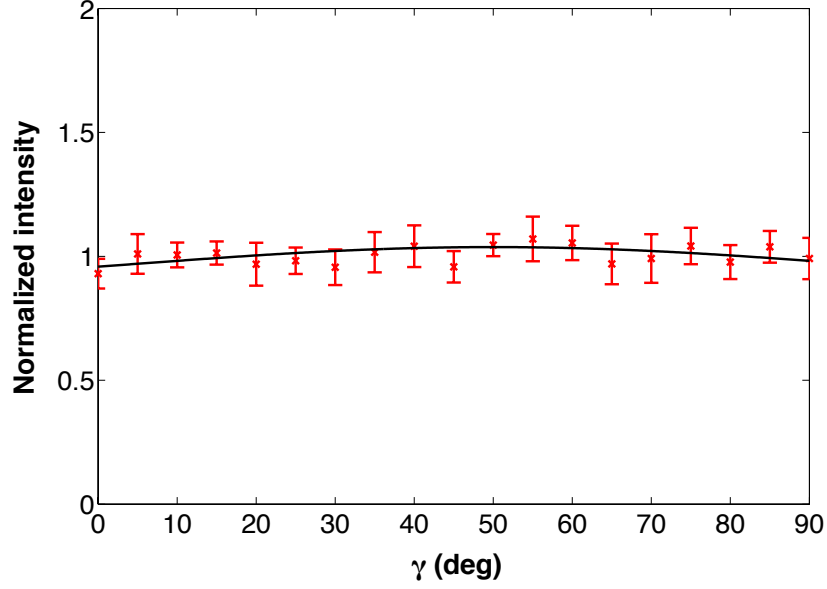


Figure F.1: Evolution of the normalized recorded intensity as the analyzer is rotated by an angle  $\gamma$ . Red points stand for the experimental data whereas the black line corresponds to the fit.

$$\begin{cases} I_{max} = r_s^2 I_{major} + r_p^2 I_{minor} \\ I_{min} = r_p^2 I_{major} + r_s^2 I_{minor} \end{cases} \quad \text{and} \quad \Omega = \frac{I_{min}}{I_{max}} = \frac{e I_{major} + I_{minor}}{I_{major} + e I_{minor}} \quad (\text{F.12})$$

where  $I_{minor}$  and  $I_{major}$  are the intensities along the minor and major axes of the ellipse respectively and  $e = r_p^2/r_s^2$ .  $I_{min}$  and  $I_{max}$  are the minimum and maximum recorded intensities. With the experimental data, we get  $\tan(\epsilon) \approx 0.91$ , which corresponds to the angle  $\epsilon = 42.3^\circ$  used for the fit. The degree of circular polarization can alternatively be defined from Stokes vector components as:

$$D_{circ} = \frac{V}{I} = \sin 2\epsilon \approx 0.98 \quad (\text{F.13})$$



# Appendix G

## List of publications and conference contributions

### Publications

#### **Table-top femtosecond soft X-ray laser by collisional ionization gating**

A. Depresseux, E. Oliva, J. Gautier, F. Tissandier, J. Nejd, M. Kozlova, G. Maynard, J.P. Goddet, A. Tafzi, A. Lifschitz, H. T. Kim, S. Jacquemot, V. Malka, K. Ta Phuoc, C. Thaur, P. Rousseau, G. Iaquaniello, T. Lefrou, A. Flacco, B. Vodungbo, G. Lambert, A. Rousse, P. Zeitoun and S. Sebban

*Nature Photonics* (2015)

#### **Demonstration of a circularly polarized plasma-based soft-X-Ray laser**

A. Depresseux, E. Oliva, J. Gautier, F. Tissandier, G. Lambert, B. Vodungbo, J-P. Goddet, A. Tafzi, J. Nejd, M. Kozlova, G. Maynard, H. T. Kim, K. Ta Phuoc, A. Rousse, P. Zeitoun, and S. Sebban

*Physical Review Letters* 115, 083901 (19 August 2015)

#### **Self-regulation of intense infrared pulses propagating through dense soft X-ray amplifying waveguides**

E. Oliva, A. Depresseux, F. Tissandier, J. Gautier, S. Sebban, and G. Maynard

*Physical Review A* 92, 023848 (26 August 2015)

#### **Modeling of dense injection-seeded Ni-like krypton plasma amplifiers**

E. Oliva, A. Depresseux, F. Tissandier, J. Gautier, S. Sebban, and G. Maynard

*Proc. SPIE 9589, X-Ray Lasers and Coherent X-Ray Sources: Development and Applications XI, 95890E* (September 22, 2015); doi:10.1117/12.2187034

#### **Femtosecond soft x-ray laser by temporal ionization gating**

S. Sebban, A. Depresseux, F. Tissandier, J. Gautier, F. Tissandier

*Proc. 2015 IEEE International Conference on Plasma Sciences* (May 2015); doi:10.1109/PLASMA.2015.7179997

**Modélisation de sources cohérentes de photons XUV créés par interaction laser gaz à haute intensité**

G. Maynard, E. Oliva, A. Boudaa, B. Cros, A. Depresseux, J. Gautier, S. Sebban, F. Tissandier, P. Zeitoun

*Modélisation: atomes, molécules, plasmas et systèmes dynamiques (Presses universitaires Orléans, mai 2013)*

**Development of X-ray sources using PW laser systems at GIST**

H. T. Kim, K.H. Lee, H. Yun, I. J. Kim, C. M. Kim, K. H. Pae, J. H. Sung, S. K. Lee, T. J. Yu, S. Sebban, F. Tissandier, J. Gautier, A. Depresseux, J. Nejd, M. Kozlova, T. M. Jeong and C. H. Nam

*Proc. SPIE 8849, X-Ray Lasers and Coherent X-Ray Sources: Development and Applications X, 88490T (September 30, 2013); doi:10.1117/12.2023922*

## Conference contributions

**Development of an ultrashort plasma-based soft X-ray laser**

A. Depresseux, E. Oliva, J. Gautier, F. Tissandier, G. Lambert, B. Vodungbo, J-P. Goddet, A. Tafzi, J. Nejd, M. Kozlova, G. Maynard, H. T. Kim, K. Ta Phuoc, A. Rousse, P. Zeitoun, and S. Sebban

*Oral presentation - SPIE 2015 Optics & Photonics OP315, San Diego, USA (9-13 May 2015).*

**Recent developments of collisionally pumped soft X-ray laser**

A. Depresseux, E. Oliva, J. Gautier, F. Tissandier, G. Lambert, B. Vodungbo, J-P. Goddet, A. Tafzi, J. Nejd, M. Kozlova, G. Maynard, H. T. Kim, K. Ta Phuoc, A. Rousse, P. Zeitoun, and S. Sebban

*Poster - Laser and Plasma Accelerator Workshop, Deshaies, Guadeloupe (10-15 May 2015).*

**Utilization of gas targetery for the development of plasma-based soft X-ray lasers**

A. Depresseux, E. Oliva, J. Gautier, F. Tissandier, G. Lambert, B. Vodungbo, J-P. Goddet, A. Tafzi, J. Nejd, M. Kozlova, G. Maynard, H. T. Kim, K. Ta Phuoc, A. Rousse, P. Zeitoun, and S. Sebban

*Oral presentation - Laser Plasma Targetery Workshop 2015. Paris, France (20-22 May 2015).*

**Development of a table-top femtosecond soft X-ray laser**

A. Depresseux, E. Oliva, J. Gautier, F. Tissandier, G. Lambert, B. Vodungbo, J-P. Goddet, A. Tafzi, J. Nejd, M. Kozlova, G. Maynard, H. T. Kim, K. Ta Phuoc, A. Rousse, P. Zeitoun, and S. Sebban

*Oral presentation - COST MP1203 Annual General Assembly. Dubrovnik, Croatia (1-4 October 2014).*

---

**Progrès sur les plasmas OFI pompés en regime collisionnel**

A. Depresseux, E. Oliva, J. Gautier, F. Tissandier, G. Lambert, B. Vodungbo, J-P. Goddet, A. Tafzi, J. Nejdl, M. Kozlova, G. Maynard, H. T. Kim, K. Ta Phuoc, A. Rousse, P. Zeitoun, and S. Sebban

*Oral presentation - Conférence UVX, Campus Carnot. Saint-Etienne, France (1-4 July 2014).*

**Lasers à plasmas XUV polarisés circulairement**

A. Depresseux, E. Oliva, J. Gautier, F. Tissandier, G. Lambert, B. Vodungbo, J-P. Goddet, A. Tafzi, J. Nejdl, M. Kozlova, G. Maynard, H. T. Kim, K. Ta Phuoc, A. Rousse, P. Zeitoun, and S. Sebban

*Oral presentation - Groupe de Recherche AppliX, Campus Carnot. Saint-Etienne, France (30 June 2014).*

**Investigation of a circularly-polarized plasma-based soft X-ray laser**

A. Depresseux, E. Oliva, J. Gautier, F. Tissandier, G. Lambert, B. Vodungbo, J-P. Goddet, A. Tafzi, J. Nejdl, M. Kozlova, G. Maynard, H. T. Kim, K. Ta Phuoc, A. Rousse, P. Zeitoun, and S. Sebban

*Oral presentation - Conference on X-ray Lasers, Colorado State University. Fort Collins, Colorado, USA (26 - 30 May 2014).*



# Table-top femtosecond soft X-ray laser by collisional ionization gating

A. Depresseux<sup>1</sup>, E. Oliva<sup>2</sup>, J. Gautier<sup>1</sup>, F. Tissandier<sup>1</sup>, J. Nejd<sup>3</sup>, M. Kozlova<sup>3</sup>, G. Maynard<sup>2</sup>, J. P. Goddet<sup>1</sup>, A. Tafzi<sup>1</sup>, A. Lifschitz<sup>1</sup>, H. T. Kim<sup>4,5</sup>, S. Jacquemot<sup>6,7</sup>, V. Malka<sup>1</sup>, K. Ta Phuoc<sup>1</sup>, C. Thauray<sup>1</sup>, P. Rousseau<sup>1</sup>, G. Iaquaniello<sup>1</sup>, T. Lefrou<sup>1</sup>, A. Flacco<sup>1</sup>, B. Vodungbo<sup>1</sup>, G. Lambert<sup>1</sup>, A. Rousse<sup>1</sup>, P. Zeitoun<sup>1</sup> and S. Sebban<sup>1\*</sup>

**The advent of X-ray free-electron lasers has granted researchers an unprecedented access to the ultrafast dynamics of matter on the nanometre scale<sup>1–3</sup>. Aside from being compact, seeded plasma-based soft X-ray lasers (SXRLs) turn out to be enticing as photon-rich<sup>4</sup> sources (up to  $10^{15}$  per pulse) that display high-quality optical properties<sup>5,6</sup>. Hitherto, the duration of these sources was limited to the picosecond range<sup>7</sup>, which consequently restricts the field of applications. This bottleneck was overcome by gating the gain through ultrafast collisional ionization in a high-density plasma generated by an ultraintense infrared pulse (a few  $10^{18}$  W cm<sup>-2</sup>) guided in an optically pre-formed plasma waveguide. For electron densities that ranged from  $3 \times 10^{18}$  cm<sup>-3</sup> to  $1.2 \times 10^{20}$  cm<sup>-3</sup>, the gain duration was measured to drop from 7 ps to an unprecedented value of about 450 fs, which paves the way to compact and ultrafast SXRL beams with performances previously only accessible in large-scale facilities.**

In plasma-based SXRL systems, the amplifying medium is a hot, highly charged plasma generated by the interaction of an intense laser pulse with a solid<sup>8</sup> or a gas<sup>9</sup> target. Hitherto, in all SXRL amplifiers that operate at saturation, a population inversion between the levels of the lasing ion is induced by electron-collisional excitation, which results in a strong amplification of spontaneous emission (ASE) down to 3.56 nm (ref. 10) with a high temporal coherence<sup>11</sup>. When seeded with a high-order harmonic (HH) beam, the generated soft X-ray beam exhibits excellent spatial properties<sup>6</sup> and an adjustable linear polarization<sup>12</sup>. However, all previous attempts to shorten the duration of plasma-based SXRLs below 1 ps have failed<sup>13,14</sup>, with the fundamental lower limit governed by the very narrow gain bandwidth of collisionally pumped plasma amplifiers. Therefore, a wealth of phenomena that occur on femtosecond timescales, such as molecular dynamics<sup>2</sup> or lattice vibrations<sup>3</sup>, unfortunately remained out of reach for these attractive sources.

To overcome this constraint, recent numerical calculations<sup>15</sup> proposed a transposition of the technique of chirped-pulse amplification to the soft X-ray range. Stretching a femtosecond HH seed to a duration close to the gain lifetime would allow the continuous and coherent extraction of the energy stored in the plasma. After compressing the amplified seed, this scheme theoretically inferred SXRL pulses as short as 200 fs, but has not been demonstrated experimentally to date. Other research directions have been

considered to bring SXRLs in the ultrafast domain, mainly based on a straightforward approach that capitalizes on intrinsically femtosecond population-inversion schemes. The so-called recombination scheme in plasmas is an attractive candidate<sup>16</sup>, but it requires drastic plasma conditions that have not yet been implemented. More recently, the inner-shell ionization scheme demonstrated an ultrafast capability in the kiloelectronvolt range; however, this scheme requires a very intense hard X-ray pump to work efficiently<sup>17,18</sup>.

Our approach is based on the collisional ionization gating (CIG) of the gain media to reduce the time window in which the lasing action takes place. In the present work, an ultrashort infrared laser pulse ( $5 \times 10^{18}$  W cm<sup>-2</sup>) was focused onto a krypton-gas jet to generate the lasing-ion species through optical-field ionization (OFI)<sup>19</sup>. The resulting electron distribution permits a population inversion by collisional pumping that leads to the lasing of the  $3d^9 4d_{j=0} \rightarrow 3d^9 4p_{j=1}$  transition of nickel-like krypton at 32.8 nm (ref. 9). In this scheme, the amplifier lifetime strongly depends on the depletion rate of the lasing-ion population<sup>20</sup> because of collisional ionization during the lasing process.

When the plasma density is increased, this process becomes fast enough to provoke an anticipated interruption of the amplification process and consequently shortens the duration of the soft XRL pulse. As shown in the numerical calculations from Fig. 1, with an increase in the electron density from  $6 \times 10^{18}$  cm<sup>-3</sup> up to  $4 \times 10^{20}$  cm<sup>-3</sup>, the CIG process becomes sufficiently fast to exhaust the gain in less than 100 fs, and thus reveals a promising path towards ultrafast SXRLs. Furthermore, an increase in the density leads to a dramatic boost of the lasing yield caused by the enhancement of the gain coefficient and the saturation intensity (see the Supplementary Information), which pushes previous limitations in terms of peak brightness of compact SXRL sources<sup>7</sup>.

To generate a saturated plasma amplifier, the most serious challenge is the propagation of the driving laser in a near-critical density plasma over several millimetres. In such a dense OFI plasma, diffraction, refraction and self-focusing of the pump beam limit the amplifying length to a few hundreds of micrometres<sup>21</sup>. Our approach overcomes these difficulties by implementing an optically preformed plasma waveguide<sup>22,23</sup>. This is created by a sequence of infrared short ('ignitor', 130 mJ, 30 fs) and long ('heater', 690 mJ, 600 ps) laser pulses focused into a high-density gas jet by an axicon lens (Fig. 2). The ignitor-heater sequence permits us to

<sup>1</sup>LOA, ENSTA ParisTech, CNRS, Ecole Polytechnique, Université Paris-Saclay, 828 bd des Maréchaux, Palaiseau Cedex 91762, France. <sup>2</sup>Laboratoire de Physique des Gaz et des Plasmas, CNRS-Université Paris Sud 11, Orsay 91405, France. <sup>3</sup>ELI Beamlines Project, Institute of Physics of the ASCR, Na Slovance 2, 182 21 Prague 8, Czech Republic. <sup>4</sup>Advanced Photonics Research Institute, GIST, Gwangju 500-712, Korea. <sup>5</sup>Center for Relativistic Laser Science, Institute for Basic Science (IBS), Gwangju 500-712, Korea. <sup>6</sup>LULI – CEA, CNRS, École Polytechnique, Université Paris-Saclay, UPMC Univ Paris 06, Sorbonne Universités, F-91128 Palaiseau cedex, France. <sup>7</sup>CEA, DAM, DIF, F-91297 Arpaçon, France. \*e-mail: [stephane.sebban@ensta-paristech.fr](mailto:stephane.sebban@ensta-paristech.fr)

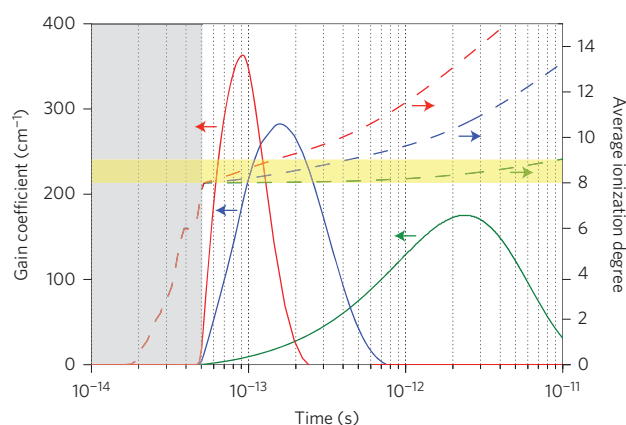


**Figure 1 | Computed temporal dependence of the average charge state and gain coefficient of a krypton-plasma amplifier for  $n_e = 6 \times 10^{18} \text{ cm}^{-3}$  (green),  $n_e = 1.2 \times 10^{20} \text{ cm}^{-3}$  (blue) and  $n_e = 4 \times 10^{20} \text{ cm}^{-3}$  (red).** The grey-tinted part corresponds to the OFI regime that precedes the subsequent collisional ionization. The dotted lines show the increase in ionization rate with density. Therefore, at high densities, the steep depletion in the number of  $\text{Kr}^{8+}$  ions leads to an ultrafast gating of the gain lifetime (CIG process). The yellow area illustrates the region in which  $\text{Kr}^{8+}$  ions are predominant.

pre-ionize the gas first, which generates free electrons that are later heated by the second pulse and then multiplied through cascade-collisional ionization. The following plasma hydrodynamic expansion produces a density channel that is appropriate for guiding the high-intensity driving laser pulse. Advantageous guiding conditions allowed strongly amplified spontaneous emission from the plasma (see the Supplementary Information).

To evaluate the influence of electron density on the temporal properties of the 32.8 nm lasing emission, we measured the temporal gain dynamic by seeding the SXRL amplifier using the 25th harmonic of the infrared driving laser. The seed was obtained by focusing a 20 mJ, 30 fs, 813 nm wavelength laser into a gas cell filled with argon and then image relayed onto the entrance of the SXRL amplifier using a grazing-incidence toroidal mirror. A strong amplification of the seed pulse was observed when the injection time was synchronized with the gain period. For the highest electron density operated here,  $1.2 \times 10^{20} \text{ cm}^{-3}$ , Fig. 3 depicts the far-field beam profile of the seeded SXRL in comparison with the HH signal. Both beams exhibit a nearly Gaussian shape with a full-width at half-maximum (FWHM) divergence of about 1 mrad. The amplification factor for SXRL is 75 if all the HH orders are considered and 1,000 for only the wavelength-matching HH order (see the Supplementary Information). The amplification of the HH portion that matches the laser transition at 32.8 nm corresponds to more than three orders of magnitude

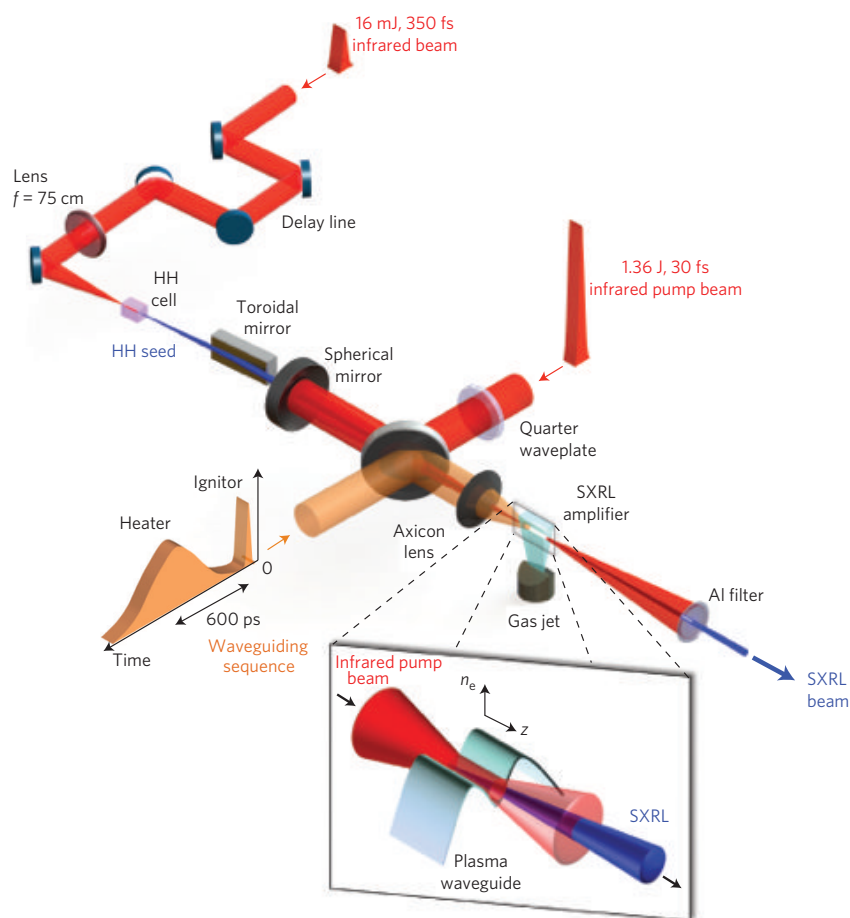


**Figure 2 | Schematic of the experimental arrangement.** The waveguiding beam is composed of a sequence of short (130 mJ, 30 fs) and long (690 mJ, 600 ps) pulses. It is focused over the whole jet length by an axicon lens and creates, after collisional ionization and hydrodynamic expansion, a plasma channel. Then, the pump beam (1.36 J, 30 fs) is focused at the entrance of the channel with a spherical mirror and guided thereafter. Hence, an amplifier with  $\text{Kr}^{8+}$  lasing-ion species over the whole gas-jet length is implemented. A third infrared beam (16 mJ, 350 fs) is used to generate a high-harmonics seed in an argon-filled cell. The latter is image relayed onto the entrance of the plasma and synchronized with the gain lifetime.

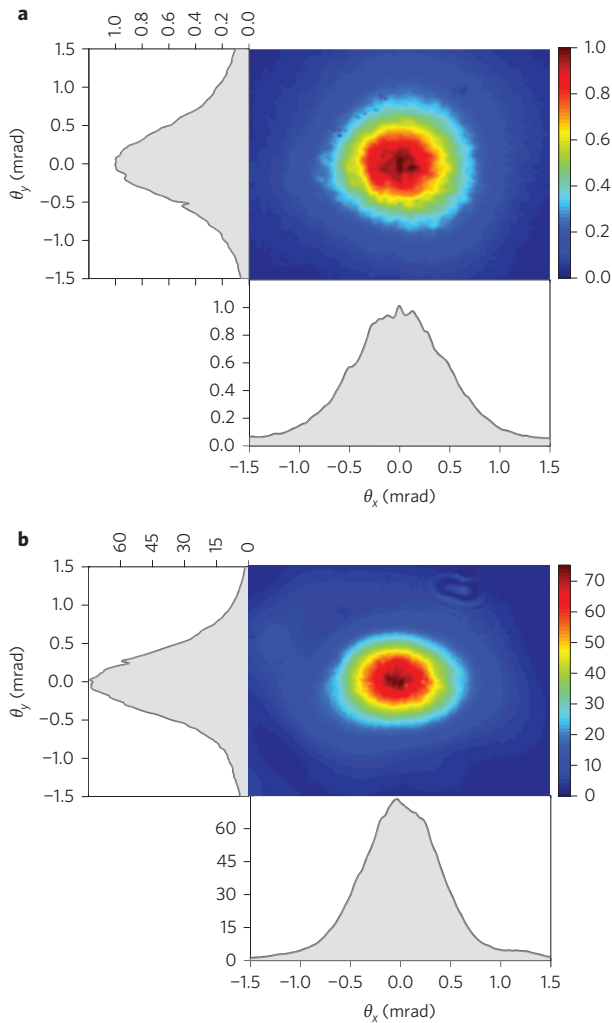


**Figure 3 | Far-field beam profiles.** **a**, HH. **b**, Seeded SXRL for  $n_e = 1.2 \times 10^{20} \text{ cm}^{-3}$ . The SXRL energy is assessed at  $2 \mu\text{J}$ , which corresponds to more than  $3 \times 10^{11}$  coherent photons. The  $1 \pm 0.2 \text{ mrad}$  divergence and nearly Gaussian beam profile of HH is maintained over the plasma amplification. A factor of about 75 is reported between total HH and seeded SXRL signals.

and the resulting SXRL signal yields about  $2 \mu\text{J}$  (over  $3 \times 10^{11}$  photons) per shot. Propitious guiding conditions allowed us to enhance the SXRL yield by one order of magnitude over an electron-density range from a few  $10^{18} \text{ cm}^{-3}$  to over  $10^{20} \text{ cm}^{-3}$ , in accordance with our simulations that reported a monotonous increase in gain and saturation intensity (see the Supplementary Information).

By varying the time delay between the amplifier creation and the seed-pulse injection, we measured the temporal evolution of the amplification factor, and thus revealed the actual temporal profiles of the SXRL gain. As shown in Fig. 4, the gain duration monotonically decreased from 7 ps to an unprecedented<sup>8</sup> shortness of 450 fs FWHM as the amplification peak rose from 150 to 1,200 with an increase of the plasma density from  $3 \times 10^{18} \text{ cm}^{-3}$  up to  $1.2 \times 10^{20} \text{ cm}^{-3}$ . These measurements clearly illustrate the dramatic temporal quenching of the amplification as a result of an increase in electron density. As anticipated from Fig. 1, the fast rise of the amplification is caused by the collisional excitation of the lasing transition that takes place after the abrupt field-ionization process. The ultrafast decay in amplification brings testimony of the CIG process at high densities. Although vital for pumping, the

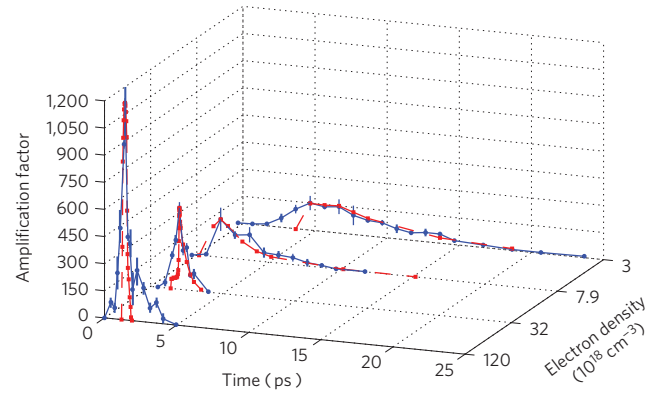


**Figure 4 | Temporal dependence of the amplification factor with respect to the seeding delay.** Experimental (blue circles) and Maxwell-Bloch-modelling results (red squares) for a scan in the plasma densities  $n_e = 3 \times 10^{18} \text{ cm}^{-3}$ ,  $n_e = 7.9 \times 10^{18} \text{ cm}^{-3}$ ,  $n_e = 3.2 \times 10^{19} \text{ cm}^{-3}$  and  $n_e = 1.2 \times 10^{20} \text{ cm}^{-3}$ . Owing to the inhomogeneity of the plasma channel, lower-density regions, for which the gain duration is longer, are accountable for the tail at the end of the experimental curve.

ongoing collisional ionization also mainly contributes to shorten the gain lifetime, as the lasing ions become rapidly scarce because of strong overionization.

Using a time-dependent Maxwell-Bloch code<sup>24</sup>, we undertook to model the radiation transfer in the amplifying SXRL plasma relevant to experimental conditions. As shown in Fig. 4, our calculations reveal that the amplification lifetime is shorter and starts earlier with a steeper slope for higher gas densities, which is in good agreement with our experimental measurements. Our Maxwell-Bloch numerical model describes well the atomic processes that underpin the gain temporal quenching over a remarkably large range of electron densities that covers nearly two orders of magnitude. The final pulse duration of the HH-seeded SXRL is Fourier limited<sup>5</sup> and therefore shorter than the amplification duration (see the Supplementary Information). The duration is thereby determined by the SXRL-transition broadening dominated by electron-ion collisional broadening, particularly strong at the highest densities. The benchmarking of the electron-density values used in our numerical model through the amplification dynamics as well as interferometry measurements brings a high degree of confidence in extracting the SXRL final duration from the numerical model. As shown in Fig. 5, the temporal structure of the pulse is composed of several periods of Rabi oscillations induced by the strong amplification of the pulse. As the plasma is inhomogeneous (see the Supplementary Information), the amplification profile is a superposition of different temporal amplification timescales, each of which corresponds to a particular density. Different parts of the beam induce Rabi oscillations with slightly different periods and only the pulse envelope is observed<sup>25</sup>. From our Maxwell-Bloch modelling, the inferred SXRL pulse duration (root mean square (r.m.s.)) varies from  $6.4 \pm 0.3 \text{ ps}$  for  $n_e = 3 \times 10^{18} \text{ cm}^{-3}$  down to  $123 \pm 40 \text{ fs}$  ( $64 \pm 21 \text{ fs}$  FWHM) for  $n_e = 1.2 \times 10^{20} \text{ cm}^{-3}$ , which thus breaks the decade-long picosecond barrier of plasma-based SXRL.

The achieved combination of a shorter duration and a boost in photon yield demonstrates a more than two orders of magnitude upsurge of plasma-based SXRL output power. Therefore, the prospect of guiding over longer distances and at higher densities fosters opportunities that promise to extend further the current state-of-the-art performances. Although the development of adequate plasma engineering appears necessary, our calculations show that, despite density inhomogeneities and transverse gradients,

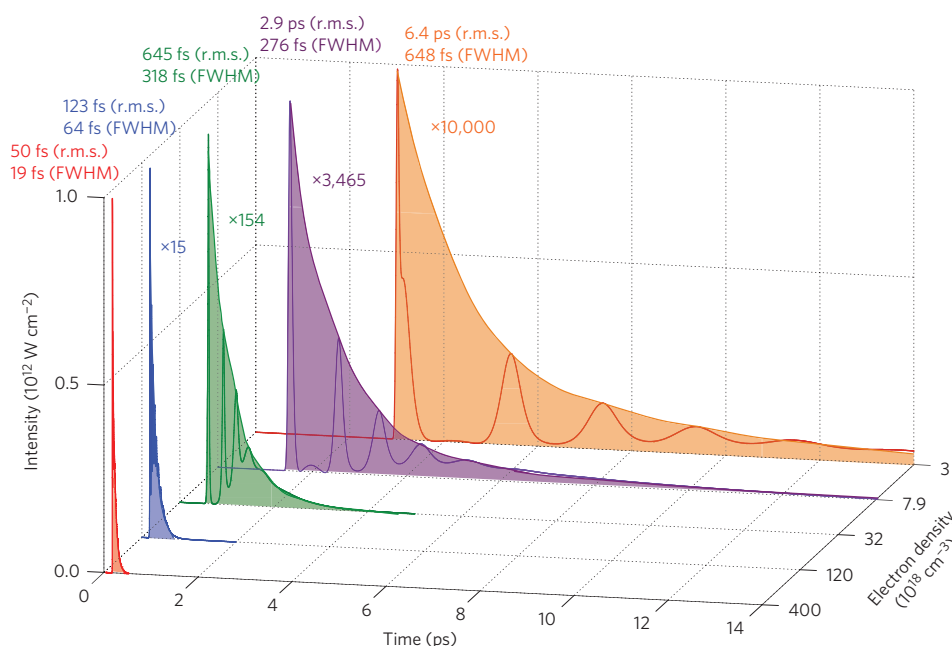


**Figure 5 | Simulated temporal profiles of the amplified SXRL for the set of studied densities and a prospective one for  $n_e = 4 \times 10^{20} \text{ cm}^{-3}$  (red).** The duration strongly depends on the density, and ranges from  $6.4 \pm 0.3 \text{ ps}$  to  $50 \pm 18 \text{ fs}$  r.m.s. The highest experimental density (blue) results in an amplified beam with a duration of  $64 \pm 21 \text{ fs}$  FWHM ( $123 \pm 40 \text{ fs}$  r.m.s.). The curves are normalized to one and their r.m.s. duration is specified.

an SXRL duration as short as 20 fs is expected for  $n_e = 4 \times 10^{20} \text{ cm}^{-3}$  (see Fig. 5). As it combines remarkable beam quality<sup>6</sup> with a full longitudinal coherence<sup>5</sup> and the jitter-free nature of seeded plasma-based SXRLs, the CIG approach contributes to substantiate the fully fledged capabilities of this compact source to carry out, at the laboratory scale, single-shot high-resolution dynamical studies on femtosecond timescales<sup>26,27</sup>.

## Methods

Methods and any associated references are available in the [online version of the paper](#).

Received 10 June 2015; accepted 8 October 2015;  
published online 16 November 2015

## References

- Mancuso, A. P. *et al.* Coherent imaging of biological samples with femtosecond pulses at the free-electron laser FLASH. *New J. Phys.* **12**, 035003 (2010).
- Gagnon, E. *et al.* Soft X-ray-driven femtosecond molecular dynamics. *Science* **317**, 1374–1378 (2007).
- Sokolowski-Tinten, K. *et al.* Femtosecond X-ray measurement of coherent lattice vibrations near the Lindemann stability limit. *Nature* **422**, 287–289 (2003).
- Rus, B. *et al.* Multimillijoule, highly coherent X-ray laser at 21 nm operating in deep saturation through double-pass amplification. *Phys. Rev. A* **66**, 063806 (2002).
- Guilbaud, O. *et al.* Fourier-limited seeded soft X-ray laser pulse. *Opt. Lett.* **35**, 1326–1328 (2010).
- Goddet, J. P. *et al.* Aberration-free laser beam in the soft X-ray range. *Opt. Lett.* **34**, 16 (2009).
- Wang, Y. *et al.* Phase-coherent, injection-seeded, table-top soft-X-ray lasers at 18.9 nm and 13.9 nm. *Nature Photonics* **2**, 94–98 (2008).
- Wang, Y. *et al.* High-brightness injection-seeded soft X-ray laser amplifier using a solid target. *Phys. Rev. Lett.* **97**, 123901 (2006).
- Sebban, S. *et al.* Demonstration of a Ni-like Kr optical-field-ionization collisional soft X-ray laser at 32.8 nm. *Phys. Rev. Lett.* **89**, 253901 (2002).
- MacGowan, B. J. *et al.* Short wavelength X-ray laser research at the Lawrence Livermore Laboratory. *Phys. Fluids B* **4**, 2326 (1992).
- Zeitoun, P. *et al.* A high-intensity highly coherent soft X-ray femtosecond laser seeded by a high harmonic beam. *Nature* **431**, 426–429 (2004).
- Smith, R. F. *et al.* Longitudinal coherence measurements of a transient collisional X-ray laser. *Opt. Lett.* **28**, 2261–2263 (2003).
- Klisnick, A. *et al.* Demonstration of a 2-ps transient X-ray laser. *Phys. Rev. A* **65**, 033810 (2002).
- Sebban, S. *et al.* Progress on collisionally pumped optical-field-ionization soft X-ray lasers. *IEEE J. Sel. Top. Quant. Electron.* **10**, 6 (1992).
- Oliva, E. *et al.* A proposal for multi-tens of GW fully coherent femtosecond soft X-ray lasers. *Nature* **6**, 764–767 (2012).
- Korobkin, D. V., Nam, C. H., Suckewer, S. & Goltsov, A. Demonstration of soft X-ray lasing to ground state in Li III. *Phys. Rev. Lett.* **77**, 5206–5209 (1996).
- Rohringer, N. *et al.* Atomic inner-shell X-ray laser at 1.46 nanometres pumped by an X-ray free-electron laser. *Nature* **481**, 488–491 (2012).
- Kapteyn, H. C. Photoionization-pumped X-ray lasers using ultrashort pulse excitation. *Appl. Opt.* **31**, 4931–4939 (1992).
- Eder, D. C., Amendt, P. & Wilks, S. C. Optical field ionized plasma X-ray lasers. *Phys. Rev. A* **45**, 6761 (1992).
- Lin, P. H. *et al.* Seeding of a soft-X-ray laser in a plasma waveguide by high harmonic generation. *Opt. Lett.* **34**, 3562–3564 (2009).
- Mocek, T. *et al.* Characterization of collisionally pumped optical-field-ionization soft X-ray lasers. *Appl. Phys. B* **78**, 939–944 (2004).
- Chou, M. C. *et al.* Dramatic enhancement of optical-field-ionization collisional-excitation X-ray lasing by an optically preformed plasma waveguide. *Phys. Rev. Lett.* **99**, 063904 (2007).
- Xiao, Y. F. *et al.* Efficient generation of extended plasma waveguides with the axicon ignitor-heater scheme. *Phys. Plasmas* **11**, 21–24 (2004).
- Oliva, E. *et al.* Comparison of natural and forced amplification regimes in plasma-based soft-X-ray lasers seeded by high-order harmonics. *Phys. Rev. A* **84**, 013811 (2011).
- Tissandier, F. *et al.* Three-dimensional Maxwell–Bloch calculation of the temporal profile of a seeded soft X-ray laser pulse. *Appl. Phys. Lett.* **101**, 251112 (2012).
- Chapman, H. N. *et al.* Femtosecond time-delay X-ray holography. *Nature* **448**, 676–679 (2007).
- Sakdinawat, A. & Liu, Y. Phase contrast soft X-ray microscopy using Zernike zone plates. *Opt. Expr.* **13**, 1559–1564 (2008).

## Acknowledgements

We thank J. L. Charles for his technical support. This work was backed by the Agence Nationale de la Recherche through projects ROLEX ANR-06-BLAN-04 023 01 and ANR-10-EQPX-25, and by the European Research Council through the X-five project (Contract No. 339128). We acknowledge funding from project ECOP (Grant No. CZ.1.07/2.3.00/20.0279 and No. CZ.1.07/2.3.00/30.005) and ANR-11-IDEX-0003-02. H.T.K. was supported by the Institute for Basic Science (IBS-CA1306). Finally, we also thank SourceLAB for its contribution to the development of the high-density gas-jet system.

**Author contributions**

S.S. proposed the experiment. S.S., J.G, F.T. and A.D. designed and built the set-up. G.M. developed the code OFI-0D. E.O., G.M. and A.L. performed the numerical simulations. J.P.G. and A.T. designed, built and operated the upgraded laser system of 'Salle Jaune'. K.T.P., C.T. and P.R. provided support for the operation of the facilities. A.F. developed a phase reconstruction and Abel inversion software for the electron-density diagnostic. All the authors contributed to the data analysis and the writing of the paper. P.Z., S.J., V.M. and A.R. supported the project.

**Additional information**

Supplementary information is available in the [online version](#) of the paper. Reprints and permissions information is available online at [www.nature.com/reprints](http://www.nature.com/reprints). Correspondence and requests for materials should be addressed to S.S.

**Competing financial interests**

The authors declare no competing financial interests.



## Methods

**Laser system and target.** The experiment was conducted at the Laboratoire d'Optique Appliquée with the 'Salle Jaune' Ti:Sapphire laser system, which delivers 5 J, 30 fs (FWHM) pulses at 1 Hz centred around a wavelength of 813 nm. The main laser beam is divided into four beams: a pump beam, a waveguiding beam, a HH driver beam and a probe beam. The waveguiding beam is composed of two pulses: the ignitor (130 mJ, 30 fs FWHM), which arrives 600 ps before the heater (690 mJ, 600 ps FWHM). The gas nozzle has a rectangular section of 500  $\mu\text{m} \times 5$  mm. The backing pressure of the krypton-gas jet was set at 150 bar, and the valve was opened over a period of 8 ms, 10 ms before the arrival of the main pulse.

At the highest-reported density, the appropriate conditions for guiding in terms of size and transverse-density gradient were for a pump beam focused about 1.55 ns after the arrival of the 'ignitor'. For investigations at lower densities, for which waveguiding is not needed, a 5 mm long krypton-filled gas cell was used.

**Plasma amplifier.** The amplifying medium was achieved by focusing the pump beam using a 75 cm focal length spherical mirror in the krypton-gas jet. The beam was turned circularly polarized thanks to a quarter-waveplate to cater for the hot electrons needed to pump the laser transition efficiently. The measured focal spot was about 38  $\mu\text{m}$  in a  $1/e^2$  diameter, which corresponds to an intensity on the target of about  $5 \times 10^{18} \text{ W cm}^{-2}$ .

The soft X-ray seed is implemented by focusing the HH driver beam into a gas cell of variable pressure and length, and filled with argon. The linearly polarized beam was focused using a 75 cm focal length planoconvex lens. The intensity on the target was assessed at about  $10^{15} \text{ W cm}^{-2}$ . The 25th harmonic signal was then spectrally tuned onto the amplifier ASE laser line at 32.8 nm, chirping the HH driver beam as its flux was optimized by changing the gas pressure and altering the focusing conditions, notably by fine-tuning the beam aperture with a motorized iris. The appropriate conditions were found for a 12 mm long cell with a pressure of 40 mbar and a focal plane situated about 5 mm after the cell entrance. The seeding was fulfilled by re-imaging the harmonic output onto the entrance of the amplifier plasma, using a  $5^\circ$  grazing-incidence gold-coated toroidal mirror in a 1.5–1 m conjugation. The experiment was aligned by making the HH beam collinear with the infrared pump and waveguiding beams. The spatial coupling of the HH beam and the SXRL gain region was done in the infrared by superimposing the HH driver with the focal spot of the pump. The temporal overlap between the HH signal and the SXRL amplification period was approached by synchronizing the HH driver and the pump beams with a delay line accurate to 30 fs.

The waveguide transmission was assessed between 40 and 50% by integrating the whole energy of the beam profile imaged at the entrance and the output of the plasma channel.

**X-ray beam diagnostics.** The extreme ultraviolet (XUV) spectrometer consists of a removable on-axis deflecting soft X-ray plane mirror and a gold-coated 400 mm focal length spherical mirror at  $77.5^\circ$  and  $80^\circ$  incidence angles, respectively, along with a 5 mm  $\times$  5 mm grating with 1,000 lines  $\text{mm}^{-1}$  and a soft X-ray 16-bit charge-coupled device (CCD) camera of resolution  $2,048 \times 2,048$  pixels. The energy-distribution measurement was performed using a  $25^\circ$  off-axis parabola of focal length 200 mm, a deflecting plane mirror at an  $80^\circ$  incidence angle and a soft X-ray camera of resolution  $1,024 \times 1,024$  pixels. The interferential multilayer coating of the

parabola designed to yield a high reflectivity at 32.8 nm was deposited at the Institut d'Optique, France. Two aluminium filters of  $2 \times 0.15 \mu\text{m}$  and  $0.1 \mu\text{m}$  were used to isolate the XUV spectrometer from infrared radiation. The amplification factor,  $A$ , was computed by integrating the energy distribution of the signals (see the Supplementary Information) using the formula:

$$A = (N_{\text{XRL}} - N_{\text{ASE}} - N_{\text{HH}}) / N_{\text{HH}}$$

where  $N_{\text{XRL}}$ ,  $N_{\text{ASE}}$  and  $N_{\text{HH}}$  are the number of counts of the seeded XRL, ASE and HH signals, respectively, averaged over three or four shots.

**Electron-density mapping.** A Mach–Zehnder interferometer allowed us to measure the plasma electron density. The infrared beam was frequency-doubled using a beta barium borate crystal to limit the effect of refraction within the medium and increase the highest-measurable electron density. The interferograms were recorded using a 16-bit CCD camera with a 13.3 magnification optical set-up that imaged a plasma zone of 700  $\mu\text{m}$  long by 500  $\mu\text{m}$  at the entrance of the waveguide.

**Numerical modelling.** The field and collisional ionization of the krypton plasma was characterized using the OFI-0D code (Fig. 1), which was derived from the COFIXE code<sup>28</sup> taking into account 92 atomic levels of krypton. This allowed us to model the plasma amplifier at one point in space in terms of ion population, gain, emissivity and saturation intensity with respect to key parameters, such as gas pressure, laser intensity and field polarization. Macroscopic phenomena, such as hydrodynamic expansion, along with radiative losses and transfer were not considered here. The calculations were performed for a krypton-plasma amplifier generated by a circularly polarized laser beam with a peak intensity of  $5 \times 10^{18} \text{ W cm}^{-2}$ .

The propagation and amplification of the high-harmonic beam within the plasma amplifier was modelled with our time-dependent Maxwell–Bloch model DeepOne<sup>29</sup>. The evolution of the plasma parameters and atomic-level populations and rates were computed using an advanced atomic physics model. These data (temporal evolution of the electron density and temperature, atomic collisional radiative rates, population of the lasing ion and population of several atomic levels strongly coupled to the lasing levels) were fed into our time-dependent Maxwell–Bloch code so as to obtain, with its simplified three-level atomic model, the same population inversion as the more-complete atomic physics package. The ASE was taken into account consistently via a stochastic source term. Owing to the induced stochasticity, each point in Fig. 5 was averaged over 50 simulations. As a consequence of the uncertainty in the energy of the seed beam, the amplification given by our model was normalized to the experimental data using the maximum amplification point. The duration of the amplified pulse is taken to be the FWHM of the pulse envelope (as shown in Fig. 5). In addition to this, because of the complex temporal profile of the pulse, the r.m.s. duration was also computed.

## References

28. Cros, B. Characterization of the collisionally pumped optical field-ionized soft X-ray laser at 41.8 nm driven in capillary tubes. *Phys. Rev. A* **73**, 033801 (2006).
29. Larroche, O. *et al.* Maxwell–Bloch modelling of X-ray-laser-signal buildup in single- and double-pass configurations. *Phys. Rev. A* **62**, 043815 (2000).

## Table-top femtosecond soft X-ray laser by collisional ionization gating

### Plasma electron density

The electron density has been measured retrieving the phase change imparted by the plasma with a Mach-Zehnder interferometer. The phase profile has been assumed to have a cylindrical symmetry about the axis of propagation to perform an Abel inversion.

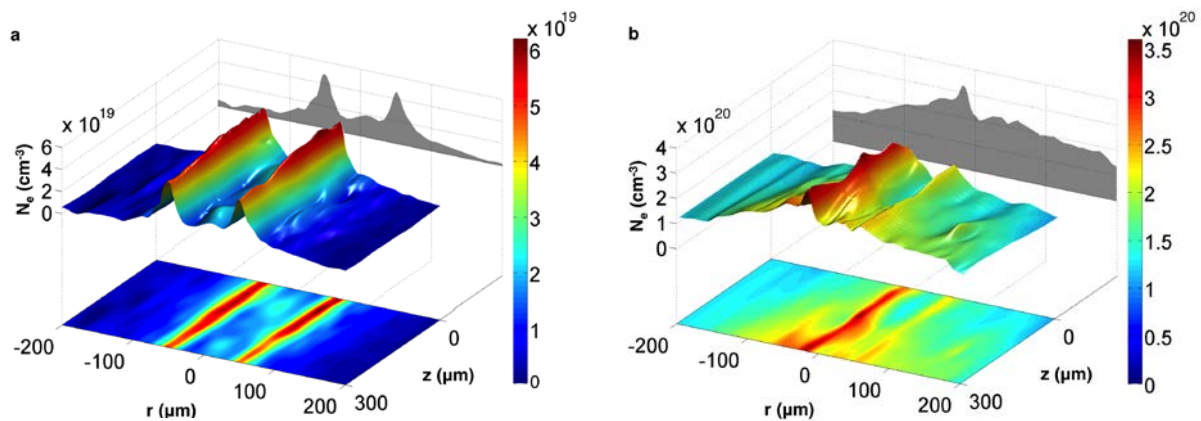


**Figure S1.** Experimental bidimensional electron density map of the waveguide in the lasing conditions with a 1.55 ns delay between the main pulse and the "ignitor" (a) and for the soft X-ray amplifier about 10 ps after the arrival of the pump beam (b). The plasma channel is found to have a parabolic transverse profile. When pumped, the amplifier is observed to somehow retain the waveguide structure, thus enabling compensation for strong diffraction. Both measurements correspond to the same zone of the plasma column probed at entrance of the channel.

At the highest operated density, optimal lasing conditions were met for a 80  $\mu\text{m}$  wide plasma channel with an electron density varying from  $1.5 \times 10^{19} \text{ cm}^{-3}$  on-axis to  $5 \times 10^{19} \text{ cm}^{-3}$  off-axis, as shown in Figure S1. We consider the average electron density in the waveguide to be  $2.5 \times 10^{19} \text{ cm}^{-3}$ . The average electron density of the amplifier was measured 10 ps after the arrival of the pump beam (Figure S1b) and reaches  $2 \times 10^{20} \text{ cm}^{-3}$ . This density corresponds to an over 60% increase of the actual electron density of  $1.2 \times 10^{20} \text{ cm}^{-3}$  at which the lasing action takes place, because of the on-going collisional ionization reported in Figure 1 (dotted blue curve). Under these conditions, a transmission of the IR pump beam of about 45% is reported. Losses mainly come from the coupling of the pump beam into the waveguide, as well as the initial strong

refraction imparted by the strong ionization at the focus.

## Spectra

Figure S2 reports the spectra for HH, ASE and HH-seeded signals respectively. The latter is illustrated for a delay with respect to the pump beam that corresponds to the maximum of the gain. These spectra have been obtained with a grazing-incidence spherical mirror and a transmission grating. The driving laser used to generate the high-harmonic signal has been chirped to match the 25<sup>th</sup> harmonic onto the ASE wavelength of the plasma amplifier at 32.8 nm. The secondary peaks on both sides from central peaks correspond to the diffraction pattern from the grating supporting grid.

A factor of about 30 between the HH and the ASE shots and a factor of about 35 between the ASE and the HH-seeded SXRL signal. Overall, the wavelength-matching HH signal is amplified by a factor of about 1000.

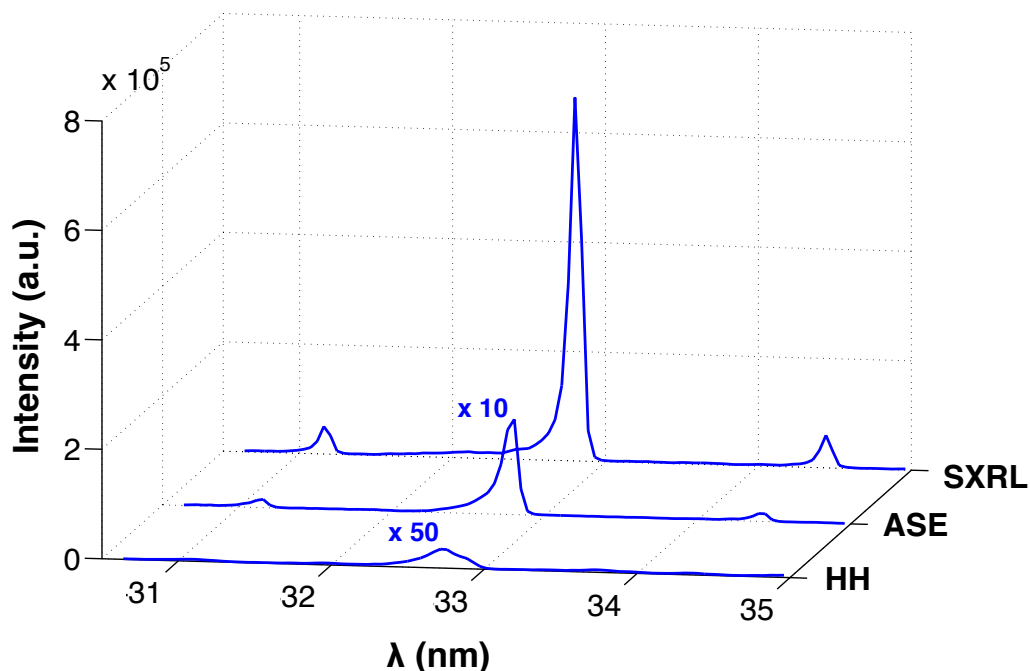


**Figure S2.** Spectra of the high-harmonic signal (a), the ASE (b) and the HH-seeded SXRL (c).



### Ion density map of the plasma channel

Figure S3 shows the density map of the lasing ion species resulting from the guiding of the pump beam over the whole gas jet length, considering the waveguide geometry depicted in Figure S1 ( $n_e = 1.2 \times 10^{20} \text{ cm}^{-3}$ ). This simulation has been carried out using a 3D PIC code (CalderCirc [1]) solving a combination of Maxwell and Vlasov equations, written in cylindrical coordinates. ADK ionization model is considered. The propagation of the IR pulse is complex and characterized by a combination of self-focusing, refraction from the waveguide density gradient and refraction due to strong ionization induced by the pulse itself.

Figure S3 shows that lasing ion species are populating the plasma amplifier over the whole length of 5 mm. Besides, Figure S3 depicts the plasma inhomogeneity, responsible for different amplification duration regimes.

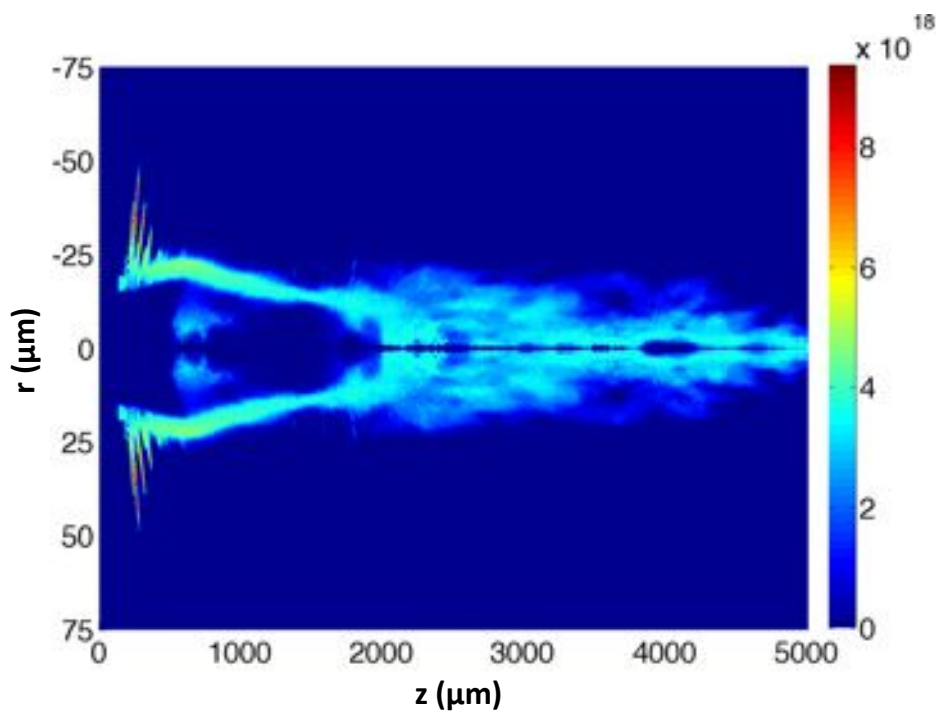


**Figure S3.** Ion density map of  $\text{Kr}^{8+}$  species ( $\text{cm}^{-3}$ )

### Benefit in SXRL energy with increased electron density

The Figure S4 reports an increase of the small signal gain coefficient and the saturation intensity as the electron density of the amplifier is augmented. The data were derived from numerical simulations performed using OFI-0D code (see Methods). The main effect of the increase in electron density is associated with the fast rise in saturation intensity and the significant quenching of the gain lifetime. The small signal gain coefficient is the product of the population inversion and the cross section and is virtually independent of the density. Indeed, the increase in electron density leads to a reduction of the cross section, which offsets the rise in population inversion. The small increase of the gain coefficient is caused by the fact that the upper level of the laser transition is being populated by the contributions from other excited atomic levels in addition to the direct pumping process.

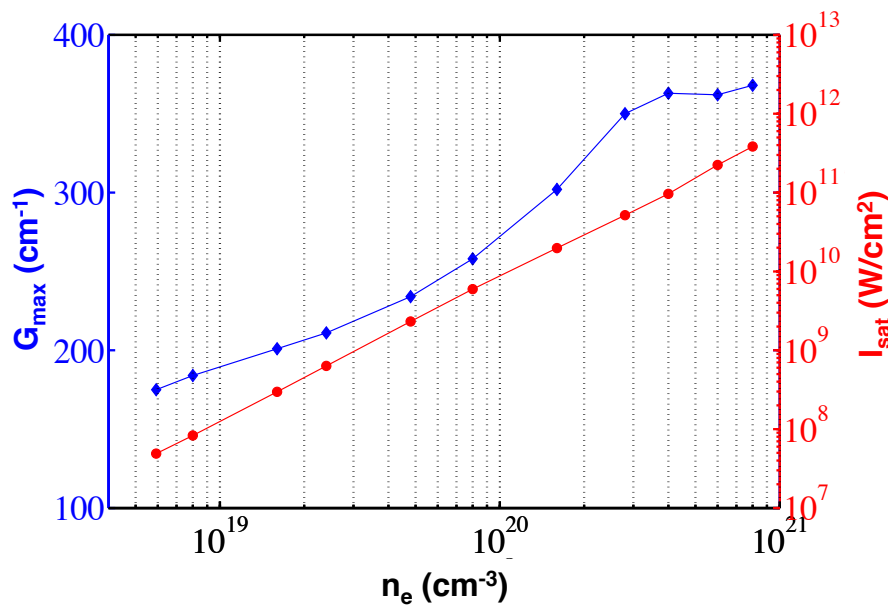


**Figure S4.** Evolution of both saturation intensity and maximum value of the gain coefficient with respect to the electron density of  $\text{Kr}^{8+}$  plasma.

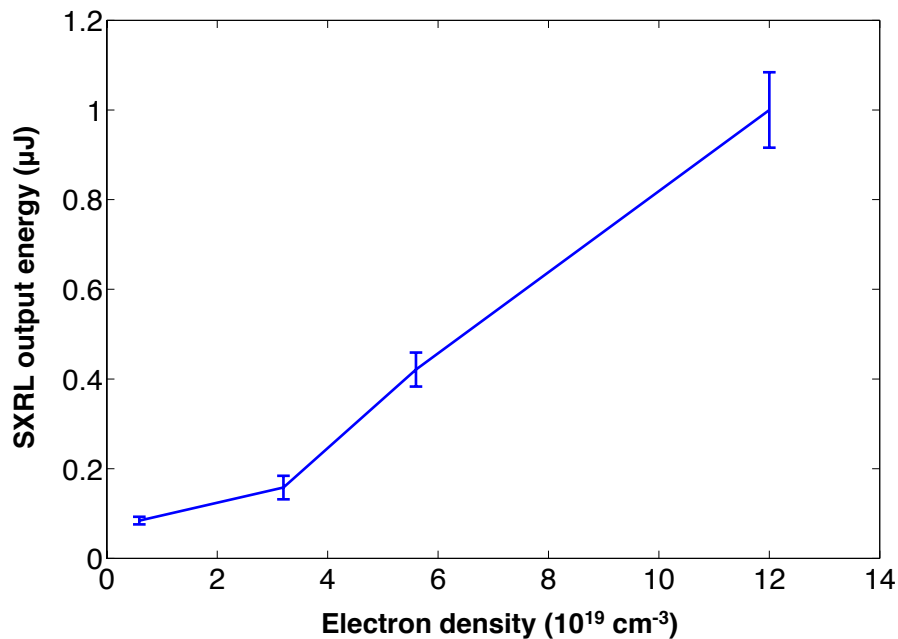


**Figure S5.** Evolution of the plasma amplified spontaneous emission energy as a function of experimentally studied electron densities.

In conformity with expectations from our numerical calculations in Figure S4, the Figure S5 illustrates the monotonous increase in SXRL output energy regarding a 5 mm plasma for a set of experimental electron densities:  $n_e = 5.9 \times 10^{18} \text{ cm}^{-3}$ ,  $3.2 \times 10^{19} \text{ cm}^{-3}$ ,  $n_e = 5.6 \times 10^{19} \text{ cm}^{-3}$  and  $n_e = 1.2 \times 10^{20} \text{ cm}^{-3}$ . When seeding the plasma amplifier in the latter case, the SXRL beam profile is yields 2  $\mu\text{J}$  (see Figure 3). As the ASE beam is strongly divergent and the collection angle is about 15 mrad, the ASE signal is in reality stronger than the measurement yielding 1  $\mu\text{J}$ .

### Towards higher energies

Further increase of the plasma-based soft X-ray laser energy can be achieved resorting to longer amplifying media. The use of an axicon with a low apex angle combined with a diverging waveguiding beam allowed us to create a focal line of over 20 mm long. Figure S6 shows the evolution of the measured ASE emission energy as a function of the gas jet length. The ASE signal proportionally rises for a gas jet from 5 mm to 15 mm.

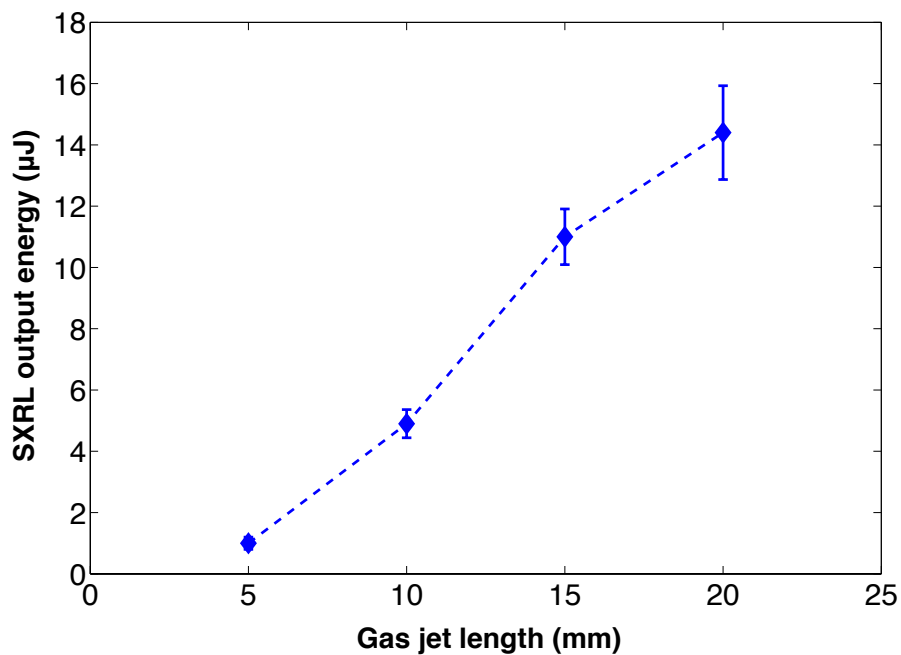


**Figure S6.** Evolution of the plasma ASE output energy with respect to the length of the gas jet.

### Maxwell-Bloch Model

We performed numerical simulations of the amplification of HH using our time-dependent Maxwell-Bloch code DeepOne [3]. This code solves the 1D paraxial Maxwell equation for the electric field in the slowly varying envelope approximation.

$$\frac{\partial E}{\partial \xi} = \frac{i\omega_0}{2c} \left[ \mu_0 c^2 P - \left( \frac{\omega_p}{\omega_0} \right)^2 E \right] \quad (1)$$

where  $\omega_0$  is the frequency of the HH,  $\omega_p$  the plasma frequency,  $P$  the polarization density and  $\zeta = c\tau$  with  $\tau = t - z/c$ , being the so-called reduced time.

This equation is supplemented with a constitutive relation for the polarization density, derived from Bloch equations  $\mathbf{P} = \text{Tr}(\rho \mathbf{d})$ , where  $\rho$  is the density operator and  $\mathbf{d}$  the atomic electric dipole. Spontaneous emission is modelled as a stochastic source term  $\Gamma$  [4].

$$\frac{\partial P}{\partial \tau} = \Gamma - \gamma P - \frac{iz_{ul}^2}{\hbar} E(N_u - N_l) \quad (2)$$

where  $\gamma = \pi\Delta\nu$  is the depolarization rate,  $z_{ul}$  the dipole matrix element and  $N_u, N_l$  are respectively the population of the upper and lower level of the lasing transition.

The population of the lasing levels are modelled with standard rate equations.

$$\begin{aligned} \frac{\partial N_u}{\partial \tau} &= \sum_k C_{ku} N_k + \frac{1}{2\hbar} \text{Im}(PE^*) \\ \frac{\partial N_l}{\partial \tau} &= \sum_k C_{kl} N_k - \frac{1}{2\hbar} \text{Im}(PE^*) \end{aligned} \quad (3)$$

where  $C_{ji}$  denote the collisional (de)excitation and radiative deexcitation rates and  $N_k$  are the population of other atomic levels that strongly interact with the lasing ones. We use the collisional-radiative code OFI-0D [5] to compute the electron density, temperature, linewidth, radiative and collisional (de)excitation rates and the populations  $N_k$ . The addition of these levels as sources allows our atomic model (simplified to ensure an affordable computational time) to mimic the results of the complex collisional-radiative code OFI-0D in the absence of the electric field.

It is worth to note that the code is fully time-dependent in the sense that all coefficients (plasma frequency  $\omega_p$ , depolarization rate  $\gamma$ , collisional (de)excitation rates  $C_{ji}$  and populations  $N_k$ ) vary in time. The temporal variation of these coefficients is given by external hydrodynamic and/or collisional-radiative codes (OFI-0D [5] in this article).

## Derivation of the final SXRL pulse duration from the amplification dynamics

In plasma-based XRL, the duration of the lasing emission is directly linked to the temporal evolution of the gain. Knowing the gain dynamic permits to infer the SXRL pulse duration with good precision, at the only condition that the plasma dynamic is correctly modelled.

The HH-seeded SXRL pulse duration is Fourier-limited and therefore shorter than the gain duration. This is due to the fact that the HH pulse width is larger than the amplifier narrow linewidth, but also because the HH pulse duration is far shorter compared to the actual plasma temporal response. As density-induced collisional ionization strongly affects, at high-densities, the broadening of the laser transition levels and the amplification duration in the same way, we can rely on the numerical model to infer the SXRL pulse duration.

The HH-seeded SXRL duration only depends on the evolution of the atomic processes regulating the laser transition populations. Therefore, one needs to get a good description of the broadening processes of the laser transition levels to be able to determine its final duration. Those processes include natural, Doppler and collisional broadening. In OFI plasma amplifiers, ions are relatively cool and the contribution of Doppler broadening gets negligible at high electron densities. Hence, both natural and collisional ionization broadening give the full picture of the underlying atomic processes responsible for the SXRL final duration.

Experimental data are compared to results from our Maxwell-Bloch numerical modelling, which well reproduce the gain temporal quenching over a remarkably large range of electron densities covering nearly two orders of magnitude (Figure 4). The good agreement of the numerical fit with experimental data allows getting, besides electron density measurements (Figure S1), a good assessment of the actual electron density, which is pivotal to the description of the broadening effects.

As density-induced collisional ionization strongly affects, at high-densities, the broadening of the laser transition levels and the amplification duration in the same way, we can be confident that the numerical model reasonably well describe the atomic processes involved in the laser transition broadening.

As a result, we extracted the SXRL final duration from the numerical model (see Figure 5). The inferred SXRL pulse duration (RMS) varies from  $6.4 \pm 0.3$  ps for  $n_e = 3 \times 10^{18} \text{ cm}^{-3}$  down to  $123 \pm 40$  fs ( $123 \pm 40$  fs FWHM) for  $n_e = 1.2 \times 10^{20} \text{ cm}^{-3}$ , thus breaking the decade-long picosecond

barrier of plasma-based SXRL, and furthermore opening the sub-100 fs range for this type of coherent soft x-ray source.

## References

- [1] Lifschitz, A.F. *et al.* Particle-in-Cell modelling of laser-plasma interaction using Fourier decomposition, *J. Comput. Phys.* 228 1803, 2009.
- [2] Sebban, S. *et al.* Demonstration of a Ni-like Kr Optical Field Ionization Collisional Soft X-ray Laser at 32.8 nm. *Phys. Rev. Lett.* 89, 25 (2002).
- [3] Oliva, E. *et al.* Comparison of natural and forced amplification regimes in plasma-based soft-x-ray lasers seeded by high-order harmonics. *Phys. Rev. A*, 84(1):013811, Jul 2011.
- [4] Larroche, O. *et al.* Maxwell-bloch modeling of x-ray-laser-signal buildup in single- and double-pass configurations. *Phys. Rev. A*, 62(4):043815, Sep 2000.
- [5] Cros, B. *et al.* Characterization of the collisionally pumped optical-field-ionized soft-x-ray laser at 41,8 nm driven in capillary tubes. *Phys. Rev. A*, 73:033801, Mar 2006.



## Demonstration of a Circularly Polarized Plasma-Based Soft-X-Ray Laser

A. Depresseux,<sup>1</sup> E. Oliva,<sup>2</sup> J. Gautier,<sup>1</sup> F. Tissandier,<sup>1</sup> G. Lambert,<sup>1</sup> B. Vodungbo,<sup>1</sup> J-P. Goddet,<sup>1</sup> A. Tafzi,<sup>1</sup> J. Nejd,<sup>3</sup> M. Kozlova,<sup>3</sup> G. Maynard,<sup>2</sup> H. T. Kim,<sup>4,5</sup> K. Ta Phuoc,<sup>1</sup> A. Rousse,<sup>1</sup> P. Zeitoun,<sup>1</sup> and S. Sebban<sup>1</sup>

<sup>1</sup>Laboratoire d'Optique Appliquée, ENSTA ParisTech, CNRS, École Polytechnique, Université Paris-Saclay, 828 boulevard des Maréchaux, 91762 Palaiseau, France

<sup>2</sup>Laboratoire de Physique des Gaz et des Plasmas, CNRS Université Paris-Sud 11, 91405, Orsay, France

<sup>3</sup>ELI Beamlines Project, Institute of Physics of the ASCR, Na Slovance 2, 182 21 Prague 8, Czech Republic

<sup>4</sup>Advanced Photonics Research Institute, GIST, Gwangju 500-712, Korea

<sup>5</sup>Center for Relativistic Laser Science, Institute for Basic Science (IBS), Gwangju 500-712, Korea

(Received 27 May 2015; published 19 August 2015)

We report the first experimental demonstration of a laser-driven circularly polarized soft-x-ray laser chain. It has been achieved by seeding a 32.8 nm Kr IX plasma amplifier with a high-order harmonic beam, which has been circularly polarized using a four-reflector polarizer. Our measurements testify that the amplified radiation maintains the initial polarization of the seed pulse in good agreement with our Maxwell-Bloch modeling. The resulting fully circular soft-x-ray laser beam exhibits a Gaussian profile and yields about  $10^{10}$  photons per shot, fulfilling the requirements for laboratory-scale photon-demanding application experiments.

DOI: 10.1103/PhysRevLett.115.083901

PACS numbers: 42.55.Vc, 42.50.Md, 42.65.Ky

Controlling the state of polarization of soft-x-ray sources is a powerful approach for probing material structures, along with their electronic and magnetic properties. In this framework, areas of study involve dichroism [1], magnetization dynamics in matter [2], or chiral domains in biology and molecular physics [3,4]. In the soft-x-ray range, the availability of coherent circularly polarized light has been limited so far to a few large-scale facilities and more recently to high-order harmonic (HH) generation. Regarding HH, several techniques have successfully been demonstrated, including the use of prealigned molecules as targets [5], a circularly polarized counterrotating bichromatic driver [6], a cross-polarized two-color laser field [7], or resonant high-order harmonic generation [8]. However, the photon yield remains low, which turns those sources inopportune for single-shot measurements. Higher photon flux has been demonstrated on large-scale facilities, such as synchrotrons [9] and free-electron lasers [10–12], by modifying the configuration of the undulators. Notwithstanding, such techniques turn out to be expensive and complex, thus preventing a flexible and wide-access utilization. To fill the gap between HH sources and large-scale facilities, collisional soft-x-ray lasers (SXRLs) offer a promising approach for generating compact but photon-rich circularly polarized light allowing photon-demanding measurements at the laboratory scale [13]. Despite one proposal based on Zeeman splitting of the  $3d^9 4d_{J=0} \rightarrow 3d^9 4p_{J=1}$  transition of the nickel-like molybdenum ions at 18.895 nm [14], the polarization of existing SXRL sources has been either undefined or restricted to be linear so far [15,16].

For generating circularly polarized SXRL beams, we propose here a new approach based on the seeding of a

laser-driven optical field ionization soft-x-ray plasma amplifier by a circularly polarized HH at 32.8 nm. Figure 1 shows the Kastler diagram of the SXRL using the Ni-like krypton ions. The XRL is generated between the  $3d^9 4d_{J=0} \rightarrow 3d^9 4p_{J=1}$  levels. The lower level of the electric dipole laser transition has three degenerate sub-levels ( $m = -1, 0, 1$ ). Because of the selection rules from quantum theory, each sublevel can interact only with a particular component of the electric field, which can be decomposed into eigencomponents, namely, left- or right-handed circular polarizations. The resonant transitions between the upper level ( $u$ ) and lower levels ( $l, -1$ ) and ( $l, 1$ ) involves only the left-handed and right-handed circular polarization components of the electric field, respectively. The purple double arrows stand for the resonant transitions that can be preferentially excited with left-handed circular (LHC) or right-handed circular

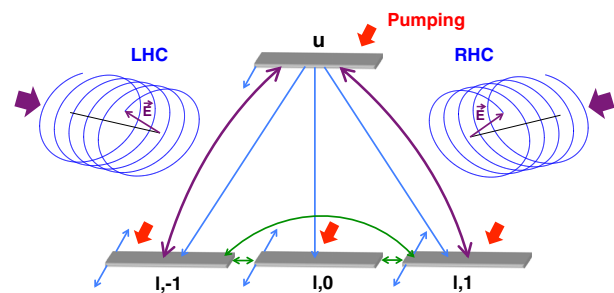


FIG. 1 (color online). Atomic structure of the laser  $\text{Kr}^{8+}$  transition with its lower sublevels ( $m = +1, 0, -1$ ) and the associated physical processes.



polarization between the upper level ( $u$ ) and the ( $l, -1$ ) or ( $l, 1$ ) lower level, respectively. The blue arrows illustrate the various depopulation processes, whereas the green double arrows describe the population transfers between sublevels. In an amplified spontaneous emission (ASE) mode, emission is unpolarized. However, the polarization of amplified injection-seeded HH corresponds to the polarization of the seed, whose components preferentially excite a particular transition. As a consequence, one could expect to efficiently generate a coherent circularly polarized soft-x-ray laser beam (CPSXRL) [17] when seeding the  $3d^9 4d_{J=0} \mapsto 3d^9 4p_{J=1}$  SXRL transition by circularly polarized light.

In this Letter, we report the first experimental demonstration of a circularly polarized plasma-based soft-x-ray laser by implementing a grazing incidence phase shifter into a soft-x-ray laser chain composed by a HH seed and a 32.8 nm population-inverted plasma amplifier (Fig. 2). The experiment has been carried out at the Laboratoire d'Optique Appliquée. To generate the soft-x-ray amplifier, a circularly polarized 1.36 J, 30 fs pump beam is focused into a gas cell filled with 30 mbar of krypton using a 75 cm focal length spherical mirror. The laser intensity at the focus is of the order of  $2 \times 10^{18}$  W/cm<sup>2</sup>. A 5-mm-long optical field ionized amplifying plasma column is therefore generated and pumped through collisional excitation [18]. A second laser beam (16 mJ, 350 fs) is used to generate the high-order harmonics seed in another gas cell filled with 30 mbar argon. The 25th harmonic signal has been spectrally tuned to match the  $3d^9 4d_{J=0} \mapsto 3d^9 4p_{J=1}$  transition at 32.8 nm by chirping [19] the laser driver. The seed beam is image relayed onto the entrance of the Kr<sup>8+</sup> plasma using a grazing incidence toroidal mirror and synchronized with the pump beam to match the gain lifetime. In standard operation conditions, the amplified emission is composed by a highly collimated Gaussian-like beam with a divergence of about 1 mrad. Previous measurements have shown that the wave front is better than  $\lambda/10$  [20] and that the duration of the amplified pulse is a few picoseconds [21].

To convert the HH polarization from linear to circular, a grazing incidence four-reflector phase shifter (polarizer) [22] and a  $\lambda/2$  wave plate have been implemented between the HH seed and the amplifier. The phase shifter consists in four uncoated gold mirrors operating at 12° grazing incidence [23], which convert polarization from linear to circular. This method allows getting fully circularly polarized soft-x-ray radiation with an efficiency of about 1.5% at 32.8 nm [23]. The reflector angles of incidence are chosen to yield an overall phase shift of  $\pi/2$  between  $p$ - and  $s$ -polarization components, whereas the polarization direction of the HH driving laser is adopted at 26.3° with respect to the  $p$ -polarization direction to equal both component field amplitudes. Its polarization direction is controlled thanks to a  $\lambda/2$  wave plate on the infrared driver. The geometry takes into account the contributions from the

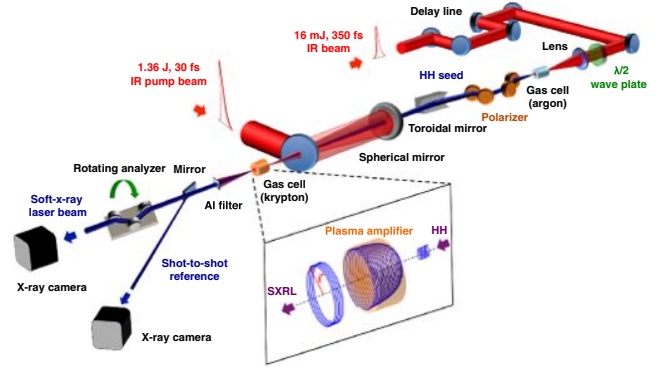


FIG. 2 (color online). Schematic description of the experimental setup.

image-relay system composed of a Pt-coated toroidal mirror and a SiO<sub>2</sub>-coated plane mirror.

The polarization of both the harmonics and the seeded soft-x-ray signal has been studied with the help of an analyzer consisting of three Mo(35 nm)/B4C(5 nm) multi-layer mirrors in a 20°-40°-20° grazing incidence configuration. This motorized device could be rotated under vacuum from 0° to 90°. In the case of circularly polarized radiation generation, the analyzer transmission was found to be 1%, resulting in signal accumulation over 60 shots for polarization measurements. To measure the soft-x-ray yield of HH and seeded SXRL sources, we monitored the far-field emission using an on-axis 16-bit soft-x-ray CCD camera disposed 4.5 m away from the Kr<sup>18</sup> plasma amplifier. The collection angle was about 5 mrad. We placed a 320 nm thin aluminum filter in the soft-x-ray beam path in order to block the infrared driving laser. Moreover, a plane mirror collected a part of soft x rays for a reference measurement to take into account the shot-to-shot signal fluctuations.

Figure 3 reports the measured output for both HH and seeded SXRL signals as a function of the analyzer rotation angle  $\gamma$ , in the cases of linear and circular polarization. The black crosses indicate the experimental measurements with their error bars, whereas the numerical fits are displayed by a blue and a red curve for linear and circular polarization, respectively. For linear polarization, the Malus law [23] has been recovered with the same contrast of about 7 between  $s$  and  $p$  transmissions for both the HH [Fig. 3(a)] and SXRL [Fig. 3(b)] signals, despite weak fluctuations that might originate from shot-to-shot pointing variations of the HH and SXRL. In the case of seeding with circularly polarized harmonics, the experimental results are shown in Figs. 3(c) and 3(d). Similarly to HH, the SXRL signal appears insensitive to the rotation of the analyzer, thus bearing testimony to either circularly polarized or unpolarized light.

We modeled the plasma amplification using a modified time-dependent Maxwell-Bloch code [24,25] taking into account the polarization of the seeding HH and including the transition lower sublevels. Our model

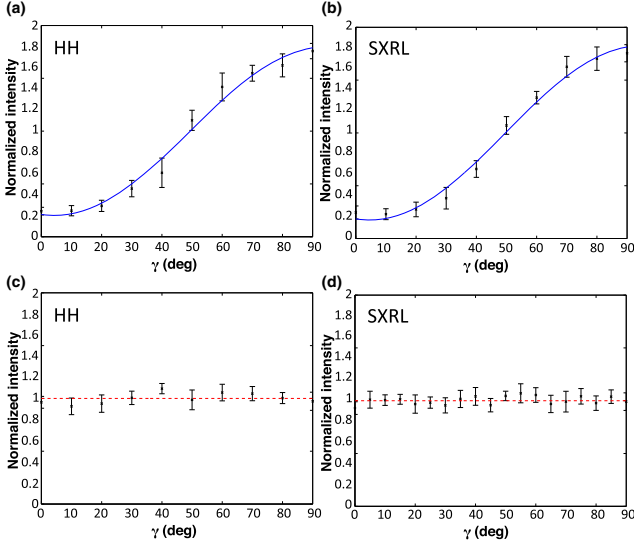


FIG. 3 (color online). Polarization investigation of the HH-seeded SXRL [(b),(d)] in the case of linearly ( $p$ ) and circularly polarized high-order harmonics [(a),(c)], respectively.

describes the dynamics of the plasma population inversion between the laser transition upper level and its lower polarization-selected levels (see Fig. 1). This code solves the 1D paraxial Maxwell equation for the electric field in the slowly varying envelope approximation. This equation is supplemented with a constitutive relation for the polarization density, derived from Bloch equations  $\mathbf{P} = \rho \mathbf{d}$ , where  $\rho$  is the density operator and  $\mathbf{d}$  the atomic electric dipole. Spontaneous emission is described as a stochastic source term  $\Gamma$  [26], and the populations of the lasing levels are modeled with standard rate equations. We use the collisional-radiative code OFIKINRAD [27] to compute the radiative and collisional (de)excitation rates as long as the population of other atomic levels that strongly pump the lasing levels. To study the polarization of the amplified beam, the electric field is decomposed as a superposition of the right-handed and left-handed circularly polarized fields ( $E_L$  and  $E_R$ , respectively):

$$\frac{\partial E_{L,R}}{\partial \xi} = \frac{i\omega_0}{2c} \left[ \mu_0 c^2 P_{L,R} - \frac{\omega_p^2}{\omega_0^2} E_{L,R} \right], \quad (1)$$

where  $\omega_0$  and  $\omega_p$  are the HH and plasma frequencies, respectively,  $P_{L,R}$  the polarization density, and  $\xi = c\tau$ , with  $\tau = t - z/c$  the so-called reduced time. Selection rules imply that each field can interact only with a particular coherence [28]. Thus, the thrice-degenerate lower level of the lasing transition cannot be modeled as a whole but is split in three sublevels ( $m = +1, 0, -1$ ) [29,30]. Elastic electron-ion collisions between sublevels are also considered via a population transfer rate  $\gamma_{PT}$  [30]:

$$\frac{\partial N_u}{\partial \tau} = \sum_k C_{k,u} N_k + \frac{1}{2\hbar} \text{Im}(P_R E_R^* + P_L E_L^*), \quad (2)$$

$$\frac{\partial N_{l,1}}{\partial \tau} = \sum_k C_{k,1} N_k + \gamma_{PT}(N_{l,-1} + N_{l,0} - 2N_{l,1}) + \text{Im}(P_R E_R^*)/(2\hbar), \quad (3)$$

$$\frac{\partial N_{l,0}}{\partial \tau} = \sum_k C_{k,0} N_k + \gamma_{PT}(N_{l,-1} - 2N_{l,0} + N_{l,1}), \quad (4)$$

$$\frac{\partial N_{l,-1}}{\partial \tau} = \sum_k C_{k,-1} N_k + \gamma_{PT}(-2N_{l,-1} + N_{l,0} + N_{l,1}) + \text{Im}(P_L E_L^*)/(2\hbar), \quad (5)$$

where  $N_u$  is the population of the upper level of the lasing transition,  $N_{l,m}$  (with  $m = 1, 0, -1$ ) the population of each lower sublevel, and  $N_k$  the population of other atomic levels that strongly interact with the lasing ones. The coefficients  $C_{j,i}$  denote the collisional (de)excitation and radiative deexcitation rates. The constitutive relation derived from Bloch equations is written as

$$\frac{\partial P_L}{\partial \tau} = \Gamma_L - \gamma P_L - \frac{iE_L}{\hbar} z_{ul}^2 (N_u - N_{l,-1}) + \frac{iE_R}{\hbar} z_{ul}^2 n_i \rho_{1,-1}, \quad (6)$$

$$\frac{\partial P_R}{\partial \tau} = \Gamma_R - \gamma P_R - \frac{iE_L}{\hbar} z_{ul}^2 (N_u - N_{l,1}) + \frac{iE_L}{\hbar} z_{ul}^2 n_i \rho_{1,-1}, \quad (7)$$

$$\frac{\partial n_i \rho_{-1,1}}{\partial \tau} = -\gamma_{-1,1} n_i \rho_{1,-1} + \frac{i}{4\hbar} (P_R^* E_L + P_L E_R^*), \quad (8)$$

where  $n_i$  is the density of ions,  $\gamma = \pi\Delta\nu$  the full width at half maximum of the transition linewidth,  $z_{ul}$  the dipole matrix element,  $\rho_{1,-1}$  the off-diagonal matrix element of the states  $m = -1, 1$ , and  $\gamma_{1,-1}$  its relaxation rate. The Stokes parameters, containing all the information about the polarization state of the amplified HH, are directly obtained from the computed fields  $E_R$  and  $E_L$  with the following formulas:

$$\begin{aligned} I &= |E_R|^2 + |E_L|^2, & Q &= 2\text{Re}(E_L^* E_R), \\ U &= -2\text{Im}(E_R^* E_L), & V &= |E_R|^2 - |E_L|^2. \end{aligned} \quad (9)$$

Figure 4 shows the calculated evolution of the degree of polarized light and the polarization as the HH pulse propagates and gets amplified in the plasma. Data are taking into account the contribution of the unpolarized ASE collected into the solid angle defined by the amplified HH divergence (FWHM). Polarization states are depicted as the normalized path described in the space by the electric field over an optical period. Figure 4(a) reports that the portion

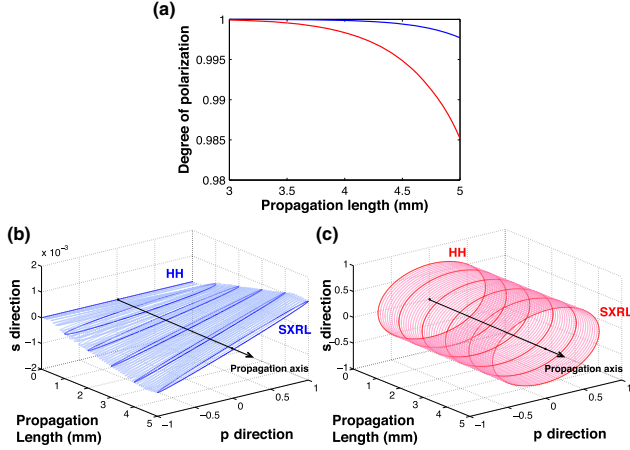


FIG. 4 (color online). (a) Degree of polarized light of amplified HH seeding a plasma-based krypton amplifier. (b) and (c) Evolution of the amplified HH polarization in the case of seeding with linear (blue) and circular (red) polarizations.

of fully polarized light after 5 mm of amplification is over 99.5%. In this fraction, the linearly seeded SXRL polarization [Fig. 4(b)] axis is turned by less than  $0.05^\circ$ , while it gets a very small ellipticity of about 0.04. As far as circularly seeded SXRL is concerned [Fig. 4(c)], the polarization is marginally modified from an initial value of 1 to over 0.98. Those very weak depolarization effects can be explained by off-diagonal elements of the density matrix [Eqs. (6)–(8)], which induce ASE-SXRL coupling resulting in second-order perturbations of the amplified HH polarization. Finally, our numerical modeling is in reasonable agreement with our experimental measurements, substantiating the validity of our approach. Because both HH and SXRL are polarized, the insensitivity of the SXRL signal to the rotation of the analyzer [Figs. 3(c) and 3(d)] provides evidence that the circular polarization state has been maintained over amplification of the 32.8 nm seed HH pulse.

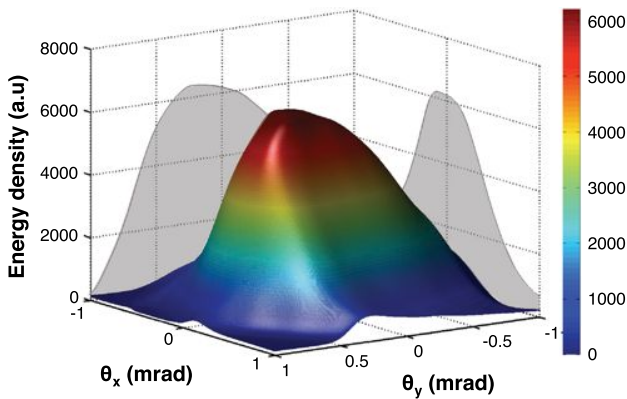


FIG. 5 (color online). Energy distribution of the CPSXRL.

The energy distribution of the 32.8 nm CPSXRL is presented in Fig. 5. The far-field beam profile is nearly Gaussian and has a FWHM divergence of about 1 mrad. The good quality of beam spatial distribution should allow maintaining the advantageous focusing capabilities of the source, as previously measured [20]. The integrated energy distribution of the CPSXRL is found to yield about  $10^{10}$  fully circularly polarized photons, when seeding with about  $10^6$  circularly polarized photons at 32.8 nm, which corresponds to an amplification factor of nearly 4 orders of magnitude. Despite the low seeding level caused by the poor transmission efficiency of the soft-x-ray polarizer (1.5%), the amplifying properties of the plasma allow efficiently compensating the losses induced by the polarizer transmission.

In conclusion, the demonstrated scheme fills the requirements for a laboratory-scale, jitter-free, and fully circularly polarized photon-rich soft-x-ray coherent source. Being scalable to shorter wavelengths [31] and adaptable to femtosecond SXRL schemes [32,33], the demonstrated approach holds out hope for delivering intense circularly polarized soft-x-ray pulses suitable for photon-demanding measurements in holography [34], crystallography pump-probe experiments [35], and magnetism [36] or circular dichroism in molecular structures [4,8].

We thank J. L. Charles for his technical support. This work was supported by the Agence Nationale de la Recherche, through Projects No. ROLEX ANR-06-BLAN-04 023 01 and No. ANR-10-EQPX-25. We acknowledge funding from project ECOP (Grants No. CZ.1.07/2.3.00/20.0279 and No. CZ.1.07/2.3.00/30.005) and COST Action MP1203.

- [1] N. Greenfield, *Nat. Protoc.* **1**, 2876 (2007).
- [2] H. Stoll, A. Puzic, B. Van Waeyenberge, P. Fischer, J. Raabe, M. Buess, T. Haug, R. Hollinger, C. Back, D. Weiss, and G. Benbeaux, *Appl. Phys. Lett.* **84**, 3328 (2004).
- [3] G. Contini, S. Turchini, S. Sanna, D. Catone, J. Fujii, I. Vobornik, T. Prosperi, and N. Zema, *Phys. Rev. B* **86**, 035426 (2012).
- [4] G. Garica, L. Nahon, S. Daly, and I. Powis, *Nat. Commun.* **4**, 2132 (2010).
- [5] X. Zhou, R. Lock, N. Wagner, W. Li, H. C. Kapteyn, and M. M. Murnane, *Phys. Rev. Lett.* **102**, 073902 (2009).
- [6] A. Fleischer, O. Kfir, T. Diskin, P. Sidorenko, and O. Cohen, *Nat. Photonics* **8**, 543 (2014).
- [7] G. Lambert, B. Vodungbo, J. Gautier, B. Mahieu, V. Malka, S. Sebban, P. Zeitoun, J. Luning, J. Perron, A. Andreev, S. Stremoukhov, F. Ardane-Lamas, A. Dax, C. Hauri, A. Sardinha, and M. Fajardo, *Nat. Commun.* **6**, 6167 (2015).
- [8] A. Ferré, C. Handschin, D. Dumergue, F. Burgy, A. Comby, D. Deschamps, B. Fabre, G. Garcia, R. Gréneaux, L. Merceron, E. Mével, L. Nahon, S. Petit, B. Pons, D. Staedter, S. Weber, T. Ruchon, V. Blanchet, and Y. Mairesse, *Nat. Photonics* **9**, 93 (2014).

- [9] J. Bahrt, A. Gaupp, W. Gudat, M. Mast, K. Molter, W. Peatman, M. Scheer, T. Schroter, and C. Wang, *Rev. Sci. Instrum.* **63**, 339 (1992).
- [10] E. A. Schneidmiller and M. V. Yurkov, *Phys. Rev. ST Accel. Beams* **16**, 110702 (2013).
- [11] H. Deng, T. Zhang, L. Feng, C. Feng, B. Liu, X. Wang, T. Lan, G. Wang, W. Zhang, X. Liu, J. Chen, M. Zhang, G. Lin, M. Zhang, D. Wang, and Z. Zhao, *Phys. Rev. ST Accel. Beams* **17**, 020704 (2014).
- [12] E. Allaria, B. Diviacco, C. Callegari, P. Finetti, B. Mahieu, J. Viehhaus, M. Zangrando, G. De Ninno, G. Lambert, E. Ferrari, J. Buck, M. Ilchen, B. Vodungbo, N. Mahne, C. Svetina, C. Spezzani, S. Di Mitri, G. Penco, M. Trovó, W. M. Fawley *et al.*, *Phys. Rev. X* **4**, 041040 (2014).
- [13] B. Rus, T. Mocek, A. R. Prag, M. Kozlova, G. Jamelot, A. Carillon, D. Ros, D. Joyeux, and D. Phalippou, *Phys. Rev. A* **66**, 063806 (2002).
- [14] N. Hasegawa, A. Sasaki, H. Yamatani, M. Kishimoto, M. Tanaka, Y. Ochi, M. Nishikino, Y. Kuneida, and T. Kawachi, *J. Opt. Soc. Korea* **13**, 60 (2009).
- [15] T. Kawachi, K. Murai, G. Yuan, S. Ninomiya, R. Kodama, H. Daido, Y. Kato, and T. Fujimoto, *Phys. Rev. Lett.* **75**, 3826 (1995).
- [16] P. Zeitoun, G. Faivre, S. Sebban, T. Mocek, A. Hallou, M. Fajardo, A. Aubert, P. Balcou, F. Burgy, D. Douillet, S. Kazamias, G. de Lachèze-Murel, T. Lefrou, S. le Pape, P. Mercière, H. Merdji, A. Morlens, J. Rousseau, and C. Valentin, *Nature (London)* **431**, 426 (2004).
- [17] Y. Wang, E. Granados, M. A. Larotonda, M. Berrill, B. M. Luther, D. Patel, C. S. Menoni, and J. J. Rocca, *Phys. Rev. Lett.* **97**, 123901 (2006).
- [18] S. Sebban, T. Mocek, D. Ros, L. Upcraft, P. Balcou, R. Haroutunian, G. Grillon, B. Rus, A. Klisnick, A. Carillon, G. Jamelot, C. Valentin, A. Rousse, J. P. Rousseau, L. Notebaert, M. Pittman, and D. Hulin, *Phys. Rev. Lett.* **89**, 253901 (2002).
- [19] D. G. Lee, J.-H. Kim, K.-H. Hong, and C. H. Nam, *Phys. Rev. Lett.* **87**, 243902 (2001).
- [20] J. Goddet, S. Sebban, J. Gautier, P. Zeitoun, C. Valentin, F. Tissandier, T. Marchenko, G. Lambert, M. Ribieres, D. Douillet, T. Lefrou, G. Iaquaniello, F. Burgy, G. Maynard, B. Cros, B. Robillard, T. Mocek, J. Nejd, M. Kozlova, and K. Jakubczak, *Opt. Lett.* **34**, 2438 (2009).
- [21] T. Mocek, S. Sebban, G. Maynard, P. Zeitoun, G. Faivre, A. Hallou, M. Fajardo, S. Kazamias, B. Cros, D. Aubert, G. de Lachèze-Murel, J. P. Rousseau, and J. Dubau, *Phys. Rev. Lett.* **95**, 173902 (2005).
- [22] P. Hochst, R. Patel, and F. Middleton, *Nucl. Instrum. Methods Phys. Res., Sect. A* **347**, 107 (1994).
- [23] B. Vodungbo, A. Barszczak Sardinha, J. Gautier, G. Lambert, C. Valentin, M. Lozano, G. Iaquaniello, F. Delmotte, S. Sebban, J. Luning, and P. Zeitoun, *Opt. Express* **19**, 4346 (2011).
- [24] E. Oliva, P. Zeitoun, M. Fajardo, G. Lambert, D. Ros, S. Sebban, and P. Velarde, *Phys. Rev. A* **84**, 013811 (2011).
- [25] Y. Wang, S. Wang, E. Oliva, L. Li, M. Berrill, L. Yin, Y. Nejd, B. Luther, C. Proux, T. Le, J. Dunn, D. Ros, P. Zeitoun, and J. Rocca, *Nat. Photonics* **8**, 381 (2014).
- [26] O. Larroche, D. Ros, A. Klisnick, A. Sureau, C. Moller, and H. Guennou, *Phys. Rev. A* **62**, 043815 (2000).
- [27] B. Cros, T. Mocek, I. Bettaibi, G. Vieux, M. Farinet, J. Dubau, S. Sebban, and G. Maynard, *Phys. Rev. A* **73**, 033801 (2006).
- [28] A. Sureau and P. B. Holden, *Phys. Rev. A* **52**, 3110 (1995).
- [29] C. M. Kim, J. Lee, and K. A. Janulewicz, *Phys. Rev. Lett.* **104**, 053901 (2010).
- [30] C. M. Kim, K. A. Janulewicz, and J. Lee, *Phys. Rev. A* **84**, 013834 (2011).
- [31] M. Berrill, D. Alessi, Y. Wang, S. Domingue, D. Martz, B. Luther, Y. Liu, and J. Rocca, *Opt. Lett.* **35**, 2317 (2010).
- [32] D. V. Korobkin, C. H. Nam, S. Suckewer, and A. Goltsov, *Phys. Rev. Lett.* **77**, 5206 (1996).
- [33] S. J. Moon and D. C. Eder, *Phys. Rev. A* **57**, 1391 (1998).
- [34] S. Eisebitt, J. Luning, F. Schlotter, M. Lorgen, O. Hellwig, W. Eberhardt, and J. Stohr, *Nature (London)* **432**, 885 (2004).
- [35] S. Boutet, L. Lomb, G. Williams, T. Barends, A. Aquila, R. Doak, U. Weierstall, D. DePonte, J. Steinbrener, R. Schoeman, M. Messerschmitt, A. Barty, T. White, S. Kassemayer, R. Kirian, M. Steibert, P. Montanez, C. Kenney, R. Herbst, P. Hart *et al.*, *Chirality* **337** (2012).
- [36] B. Vodungbo, J. Gautier, G. Lambert, A. Barszczak Sardinha, M. Lozano, S. Sebban, M. Ducouso, W. Boutu, K. Li, B. Tudu, M. Tortarolo, R. Hawaldar, R. Delaunay, V. Lopez-Flores, J. Arabski, C. Boeglin, H. Merdji, P. Zeitoun, and J. Luning, *Nat. Commun.* **3**, 999 (2012).



**Self-regulated propagation of intense infrared pulses in elongated soft-x-ray plasma amplifiers**Eduardo Oliva,<sup>1,\*</sup> Adrien Depresseux,<sup>2</sup> Fabien Tissandier,<sup>2</sup> Julien Gautier,<sup>2</sup> Stéphane Sebban,<sup>2</sup> and Gilles Maynard<sup>1</sup><sup>1</sup>*Laboratoire de Physique des Gaz et des Plasmas, Université Paris Sud, CNRS, UMR8578, 91405 Orsay, France*<sup>2</sup>*Laboratoire d'Optique Appliquée, ENSTA ParisTech, École Polytechnique ParisTech, CNRS, UMR7639, 91761, Palaiseau, France*

(Received 7 April 2015; published 26 August 2015)

Increasing the electron density of collisionally pumped plasma-based soft-x-ray lasers offers promising opportunities to deliver ultrashort pulses. However, strong nonlinear effects, such as overionization-induced refraction and self-focusing, hinder the propagation of the laser beam and thus the generation of elongated volume of lasing ions to be pumped. Using a particle-in-cell code and a ray-tracing model we demonstrate that optically preformed waveguides allow for addressing those issues through a self-regulation regime between self-focusing and overionization processes. As a result, guiding intense pulses over several millimeters leads to the implementation of saturated plasma amplifiers.

DOI: [10.1103/PhysRevA.92.023848](https://doi.org/10.1103/PhysRevA.92.023848)

PACS number(s): 42.15.Dp, 42.55.Vc, 52.38.Hb, 52.38.Ph

**I. INTRODUCTION**

The development and the applications of ultraintense and ultrashort radiation from XUV to x rays have experienced a dramatic expansion in the past few years with the emergence of free-electron lasers (FELs). The excellent optical properties of these sources opened new ways in such important fields as material science and biology by means of coherent imaging (diffraction [1] and holography [2]). However, since few FELs are available, the number of projects that can be carried out in these facilities and the allotted beam time are limited. The access to complementary small-scale facilities delivering x-ray pulses not only would ensure the conduction of experiments that do not need the extreme FEL performances, but also would help to prepare and increase the success of FELs experiments.

Among these complementary sources, plasma-based seeded soft-x-ray lasers (SXRL) [3,4] offer a promising approach. These sources demonstrated energetic picosecond pulses [5] with full spatial and temporal coherences and good wavefronts [6]. In addition to this, different techniques to deliver subpicosecond pulses [7–10] have been proposed. Most of these techniques rely on increasing the density of the plasma amplifier, broadening the lasing transition linewidth [11].

In order to get optimized spatial and temporal properties, the SXRL should reach the saturated amplification regime. This requires achieving plasma amplifiers of a few millimeters length. Elongated optical field ionized [12,13] plasmas filled with lasing ions are generated focusing an ultrashort intense infrared (IR) pulse onto a target. When the plasma is created from a solid target, the IR pump beam takes advantage of the refraction induced by the density gradient to efficiently deposit the laser energy at the optimum density [14]. In the case of a gas target, the pump pulse has to propagate through the full length of the amplifier, which becomes a quite problematic issue when the electron density is increased (i.e.,  $n_e \approx 10^{19} \text{ cm}^{-3}$ ).

Intense IR pulses can be guided over several Rayleigh lengths using a preformed plasma waveguide. In Ref. [15], the

propagation of a moderate intensity ( $I = 2.5 \times 10^{15} \text{ W cm}^{-2}$ ) IR pulse through a partially ionized hydrogen plasma channel is studied. The total density has a truncated parabolic profile with  $n_0 = 5 \times 10^{17} \text{ cm}^{-3}$  at the center and  $0.89 \times 10^{18} \text{ cm}^{-3}$  at  $r = 66 \mu\text{m}$ . It is found that the performance of the waveguide depends strongly on the initial degree of ionization. A high initial degree of ionization is needed in order to guide the pulse, thus hinting that refraction plays a fundamental role. Guiding at moderate intensities ( $10^{13}$ – $10^{14} \text{ W cm}^{-2}$ ) was achieved in argon, nitrogen, and xenon using plasma channels [16]. Guiding at higher intensities ( $I = 4 \times 10^{18} \text{ W cm}^{-2}$ ) using a capillary discharge waveguide filled with hydrogen has also been experimentally demonstrated in relation with laser wakefield acceleration of relativistic electrons [17].

The situation is much more complex in dense plasma-based soft-x-ray lasers. In these amplifiers, an intense ( $I > 10^{18} \text{ W cm}^{-2}$ ) IR pulse must propagate over several millimeters or even centimeters of a partially ionized high- $Z$  (i.e., krypton) plasma [18,19]. At such high intensities, further ionization of the plasma is not uniform but strongly depends on the IR beam intensity [20,21]. Therefore, the physics of the propagation becomes highly nonlinear, the initial electron-density profile inside the channel being strongly perturbed by the laser beam. Note also that nonlinear relativistic effects may also play a role, leading to the well-known relativistic self-focusing effect [22]. Relativistic self-focusing appears when the beam power is higher than the threshold power [23]  $P_{\text{th}}(W) \approx 1.7 \times 10^{10} \frac{n_c}{n_e}$ , where  $n_c$  is the plasma critical density and  $n_e$  is the electron density. Thus, new challenges arise when modeling these kinds of waveguides.

In this paper we analyze this propagation regime (intense IR pulse through a dense plasma channel that can be multiply ionized) using the particle-in-cell (PIC) code WAKE-EP (extended performances) [24], an upgrade of the quasistatic two-dimensional axisymmetric particle code WAKE [25]. The study is carried out in the case of  $\text{Kr}^{8+}$  plasma amplifiers [26]. We will show that a self-regulating mechanism (with similarities with laser filamentation of intense IR pulses propagating through gases, liquids, and solids [27]) appears in which overionization-induced refraction (due to relativistic self-focusing) is compensated by plasma guiding. The pump pulse waveguiding combined with the prevalence of  $\text{Kr}^{8+}$

\*Present address: Instituto de Fusión Nuclear, Universidad Politécnica de Madrid, 28006, Madrid, Spain; [eduardo.oliva@upm.es](mailto:eduardo.oliva@upm.es)

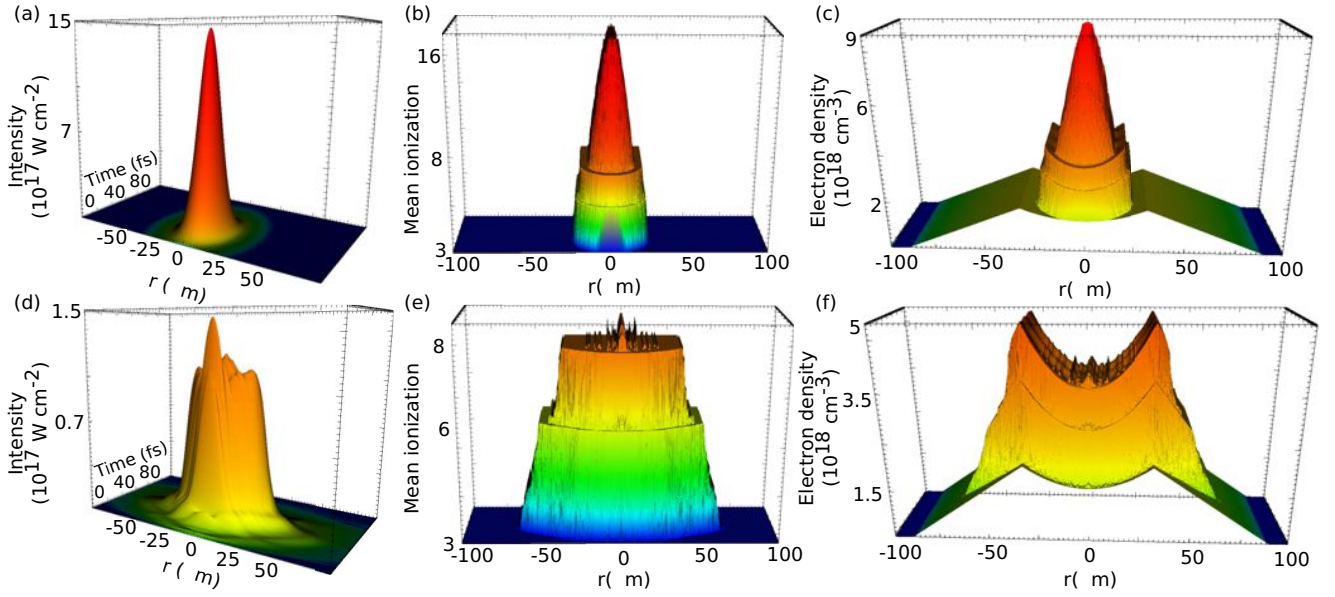


FIG. 1. (Color online) (a) Intensity, (b) mean ionization, and (c) electron density at  $z = 0$ . (d) Intensity, (e) mean ionization, and (f) electron density at  $z = 1.5Z_R$ .  $Z_R = 0.0725$  cm. The temporal scale is the same in all six figures, but it is only depicted in (a) and (d) for the sake of visualization.

lasing ions due to its superior stability allows efficiently filling plasmas of several Rayleigh lengths (more than ten). This opens the way for centimeter-scale dense soft-x-ray amplifiers while promising ultrashort ( $\Delta t \approx 100$ -fs) pulses.

## II. SIMULATIONS

In this paper we model the propagation of an intense IR pulse through a  $\text{Kr}^{3+}$  plasma channel created with the ignitor-heater technique using an axicon lens [19,28]. The IR pulse should be efficiently guided through the plasma to fill properly the whole plasma length with  $\text{Kr}^{8+}$  ions and to generate a population inversion via collisions of hot electrons with lasing ions.

The parameters of the simulations are chosen to match recent experimental conditions [18,29,30]. The IR laser pulse  $\lambda = 800$  nm,  $E = 250$  mJ,  $\Delta t = 30$  fs FWHM was focalized into a  $16 \mu\text{m}$  focal spot ( $I \approx 1.4 \times 10^{18} \text{ W cm}^{-2}$ ) at the entrance of the preformed plasma channel. The plasma channel density has a truncated parabolic radial shape, decreasing linearly afterwards,

$$N_n(r) = N_0 \left( 1 + \frac{r^2}{R_0^2} \right), \quad r < R_c, \quad (1)$$

$$N_n(r) = N_0 \left( 1 + \frac{R_c^2}{R_0^2} \right) \left( \frac{R_v - r}{R_v - R_c} \right), \quad R_c < r < R_v, \quad (2)$$

where  $N_n$  is the atomic density and  $N_0, R_0$  are the parameters of the parabola [ $N_0$  being the density at  $r = 0$  and  $R_0$  being the radial coordinate where  $N_n(R_0) = 2N_0$ ].  $R_c$  is the radius of the channel where the density attains its maximum, and  $R_v$  is the point where vacuum starts. We assume that the plasma is initially ionized three times ( $\text{Kr}^{3+}$ ), and thus the initial electron density is  $n_e(r, t = 0) = 3N_n(r)$ . In this article, these parameters are adjusted to experimental data [29,30]

taking the values  $R_0 = 50.6$ ,  $R_c = 32.0$ , and  $R_v = 90.0 \mu\text{m}$ . Different values of the electron density at the center of the unperturbed channel, ranging from  $n_e(r = 0, t = 0) = 1.4 \times 10^{16}$  to  $n_e(r = 0, t = 0) = 4.1 \times 10^{18} \text{ cm}^{-3}$ , were explored to ascertain the role played by the density.

Figure 1(a) shows the initial intensity profile of the laser pulse when entering the plasma channel with an initial electron density of  $n_e(r = 0, t = 0) = 1.4 \times 10^{18} \text{ cm}^{-3}$ . The intensity is so high that the mean ionization [shown in Fig. 1(b)] reaches  $\bar{Z} = 16$ , which is much greater than the desired  $\bar{Z} = 8$  that roughly corresponds to the lasing ion  $\text{Kr}^{8+}$ . This overionization induces a steep electron-density gradient at the center of the channel, depicted in Fig. 1(c). This overionization-induced gradient strongly defocuses the IR beam, thus overcoming the guiding of the plasma channel.

After one and a half Rayleigh lengths, the maximum intensity has been reduced one order of magnitude [Fig. 1(d)] to a value that cannot produce the  $\text{Kr}^{9+}$  ion. Thus, most of the channel is composed of  $\text{Kr}^{8+}$  [Fig. 1(e)]. This ion proliferates because of its increased stability deriving from its closed subshell. At this moment, the defocusing gradients have disappeared [Fig. 1(f)], and the plasma channel starts guiding the pulse as Fig. 2(a) shows. The intensity of the pulse increases steadily due to the guiding effect until the self-focusing threshold is attained. From this point ( $z \approx 3Z_R$ ), the intensity of the pulse increases faster [Fig. 2(a)] and produces an overionization at the center of the plasma [Fig. 2(b)], triggering refraction effects that defocus the beam which then gets reflected onto the density gradient of the waveguide. In this way, there is a competition between overionization refraction and refocusing from the waveguide density gradient, which leads to an elongated gain medium filled with lasing ions over its whole length as shown in Fig. 2(b). This mechanism allows for the propagation of a pulse intense enough to produce the  $\text{Kr}^{8+}$  ion but not the  $\text{Kr}^{9+}$  along more than ten Rayleigh lengths as Fig. 2(b) depicts.

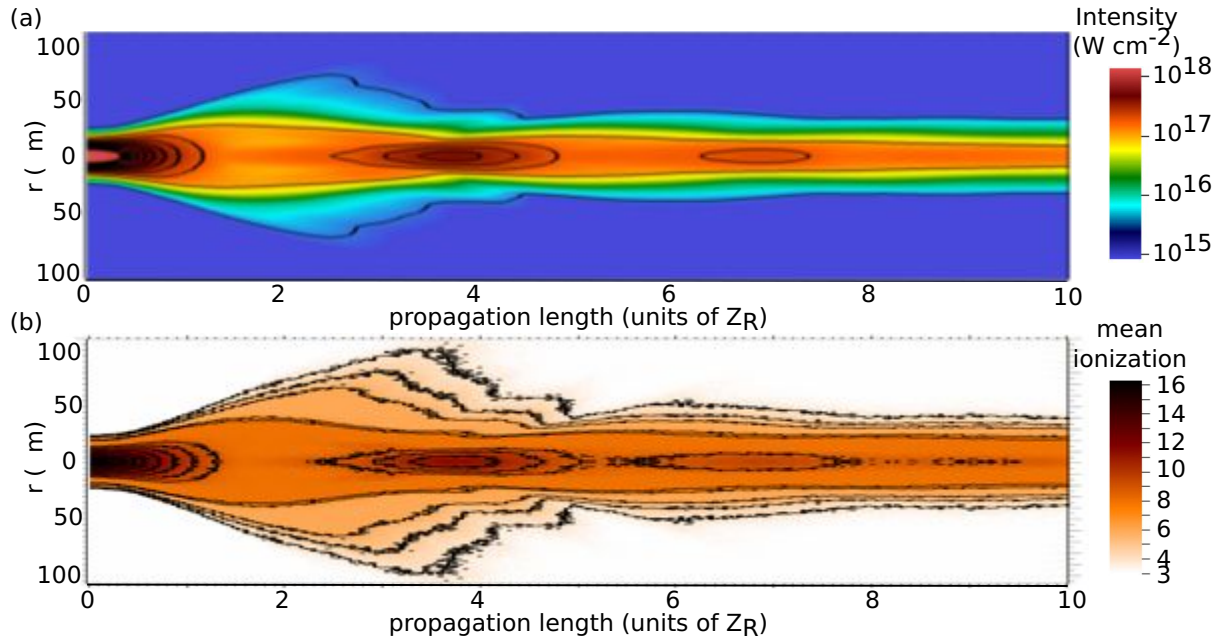


FIG. 2. (Color online) (a) Maximum intensity along the plasma channel. (b) Mean ionization along the plasma channel.  $Z_R = 0.0725$  cm.

### III. RAY-TRACING MODEL

The predominance of channel guiding, overionization defocusing, or diffraction can be ascertained with a simple model. In an ideal case of paraxial approximation, the ray trajectories of a Gaussian beam diffracting and propagating through a parabolic channel are easily computed [31]. When the electron-density profile of the channel is

$$n_e(r) = n_{e1} \left( 1 + \frac{r^2}{r_{e1}^2} \right), \quad 0 < r < R_c, \quad (3)$$

they are given by

$$w_d(z) = w_0 \sqrt{1 + \frac{z^2}{Z_R^2}}, \quad (4)$$

$$w_c(z) = w_0 \cos \left( \left[ \frac{n_{e1}}{n_c} \right]^{1/2} \frac{z}{r_{e1}} \right), \quad (5)$$

where  $w_0$  denotes the initial radial coordinate of the ray,  $n_c$  is the critical density,  $n_{e1}$  is the density at  $r = 0$ , and  $r_{e1}$  is the coordinate where  $n_e(r_{e1}) = 2n_{e1}$ . These parameters are depicted in Fig. 3.

The condition for perfect guiding is that the first derivative of the trajectory is zero (i.e., the rays are parallel to the axis). Then, when our system is near perfect guiding, we can perform a Taylor expansion of the trajectories,

$$w_d(z) \approx w_0 \left[ 1 + \frac{1}{2} \frac{z^2}{Z_R^2} \right], \quad (6)$$

$$w_c(z) \approx w_0 \left[ 1 - \frac{1}{2} \frac{z^2}{Z_1^2} \right], \quad (7)$$

where  $Z_1 = r_{e1} \sqrt{\frac{n_c}{n_{e1}}}$  is the channel refraction characteristic length.

Guiding is achieved when the sum of the second-order terms in both equations is zero, obtaining the same criterion given in Ref. [16] but in terms of the parameters of the channel and the Rayleigh length,

$$Z_R = Z_1. \quad (8)$$

The criterion given by Eq. (8) is a balance between two characteristic lengths, diffraction ( $Z_R$ ) and the deviation induced by the parabolic channel ( $Z_1$ ). Whether diffraction

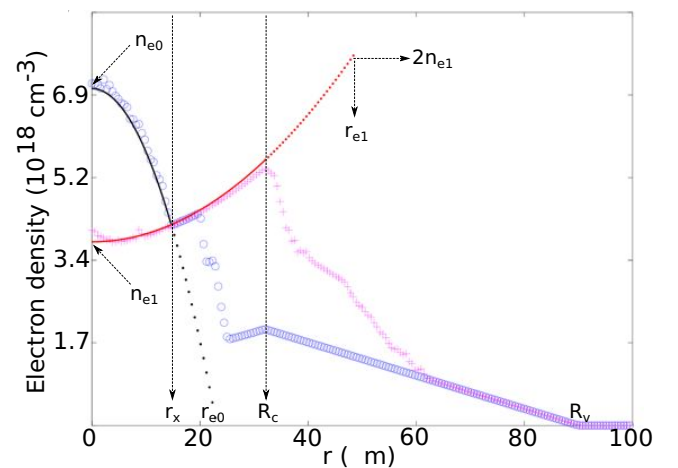


FIG. 3. (Color online) Parameters for the two-parabola ray-tracing model [Eqs. (9) and (3)]. The electron-density radial profile at  $z = 0$  (blue circles) and  $z = 1.5Z_R$  (magenta crosses) as given by the PIC code are depicted. Continuous lines (red and black) represent the parabolas that approximate the computed electron-density profile.

TABLE I. Electron density ( $\text{cm}^{-3}$ ) at the center of the unperturbed  $\text{Kr}^{3+}$  channel (first row). Refraction characteristic length (cm) of the ideal guiding  $\text{Kr}^{8+}$  channel (second row) and of the overionized profile at the center of the channel (third row). The Rayleigh length is  $Z_R = 0.0725$  cm. The shortest characteristic length ( $Z_R, Z_1, Z_0$ ) determines which mechanism dominates: diffraction, channel guiding, or overionization-induced refraction, respectively.

$n_{e1}^{3+} (\times 10^{17})$	0.14	0.57	1.3	2.3	3.6	5.2	7.0	14.3	41.4
$Z_1$	1.1	0.54	0.36	0.27	0.21	0.18	0.15	0.11	0.06
$Z_0$	0.33	0.17	0.11	0.08	0.07	0.06	0.05	0.04	0.02

or refraction predominates depends on which of these lengths is shorter.

After interaction with the intense IR pulse, the plasma is ionized to  $\text{Kr}^{8+}$  in most of the channel and to higher ionization states at the central part where the intensity of the IR pulse is stronger as shown in Fig. 2(b). The overionized region at the center of the channel is adjusted by Eq. (9) (black line in Fig. 3),

$$n_e(r) = n_{e0} \left( 1 - \frac{r^2}{r_{e0}^2} \right), \quad r < r_x, \quad (9)$$

$$n_e(r) = n_{e1} \left( 1 + \frac{r^2}{r_{e1}^2} \right), \quad r_x < r < R_c. \quad (10)$$

The parameters of the parabola are  $n_{e0} = n_e(0)$  and  $r_{e0}$ , which is the coordinate where  $n_e(r_{e0}) = 0$ . Both parabolas intercept at  $r_x$ . All these parameters are depicted in Fig. 3. The increasing parabola, adjusted by Eq. (10) (red line in Fig. 3) models the  $\text{Kr}^{8+}$  plasma channel since the low intensity region of the radial profile of the pulse is intense enough to attain this level of ionization [as shown in Fig. 2(b)]. The characteristic length of the defocusing induced by this overionization  $Z_0 = r_{e0} \sqrt{\frac{n_c}{n_{e0}}}$  is obtained Taylor expanding the corresponding hyperbolic cosine ray trajectory as done with Eq. (5).

Table I shows the refraction characteristic lengths of the focusing induced by the plasma channel and defocusing induced by overionization after interaction with the IR pulse. For lower electron densities, diffraction is the predominant effect. Only in the densest cases  $Z_1 \approx Z_R$ , which is the condition for an efficient guiding. However, as the third row of Table I shows, in these cases overionization-induced refraction dominates both guiding and diffraction ( $Z_0 < Z_1, Z_R$ ). The predominance of this defocusing refraction implies that the criterion given by Eq. (8) is no longer valid. Since we are interested in the densest cases where refraction predominates, ray-tracing techniques can be used to study the evolution of the pulse as refraction dominates diffraction.

A ray starting parallel to the  $Z$  axis at  $r = \rho_0 < r_x$  will follow this trajectory [31],

$$r(z) = \begin{cases} \rho_0 \cosh \left[ \frac{z}{Z_0} \right], & r < r_x, \\ \rho_1 \cos \left[ \frac{z}{Z_1} + \phi_1 \right], & r > r_x, \end{cases} \quad (11)$$

where  $\rho_1$  and  $\phi_1$  are chosen so as to ensure the continuity of the trajectory and its first derivative. Defining  $z_c = Z_0 \cosh^{-1} \frac{r_x}{\rho_0}$

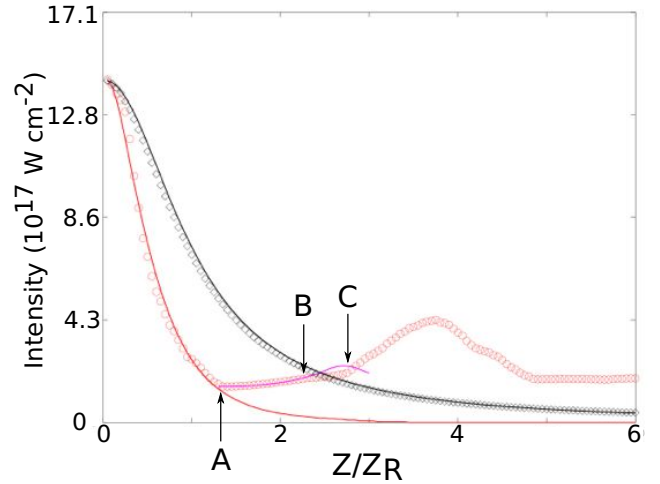


FIG. 4. (Color online) Maximum intensity as given by the PIC simulation for  $n_{e1} = 1.4 \times 10^{16} \text{ cm}^{-3}$  (black diamonds) and  $n_{e1} = 1.4 \times 10^{18} \text{ cm}^{-3}$  (red circles) compared with the propagation of a Gaussian beam in vacuum (black line) and our ray-tracing model (red and magenta curves). Points A–C indicate a switch on the driving mechanism (overionization-induced refraction, channel guiding, diffraction, and relativistic self-focusing, respectively).

[i.e.,  $r(z_c) = r_x$ ] we can compute the parameters as

$$\phi_1 = \arctan \left( -\frac{Z_1}{Z_0} \tanh \frac{z_c}{Z_0} \right) - \frac{z_c}{Z_0},$$

$$\rho_1 = \frac{\rho_0 \cosh \frac{z_c}{Z_0}}{\cos \left[ \arctan \left( -\frac{Z_1}{Z_0} \tanh \frac{z_c}{Z_0} \right) \right]}.$$

A ray will be confined in the channel if its maximum radial deviation  $\rho_1$  is smaller than the channel radius  $R_c$ ,

$$\rho_1 = \frac{\rho_0 \cosh \frac{z_c}{Z_0}}{\cos \left[ \arctan \left( -\frac{Z_1}{Z_0} \tanh \frac{z_c}{Z_0} \right) \right]} \leq R_c.$$

The observed behavior is explained with our composite model. Figure 4 shows the maximum intensity as given by the PIC simulation (red circles) and our ray-tracing model (red and magenta curves). The points named A–C indicate a switch on the mechanism that drives the temporal evolution of the intensity (overionization-induced refraction, channel guiding, diffraction, and relativistic self-focusing). During the first one and a half Rayleigh length the strong density gradient created by the overionization of the plasma refracts the pulse, reducing its intensity. The two parabola model [Eqs. (9) and (10)] mimics this behavior (depicted as a red line in Fig. 4) from  $Z = 0$  until  $Z \approx 1.5Z_R$  (i.e., point A). From this point (A), the intensity is low, and only the  $\text{Kr}^{8+}$  ion is maintained in the channel [Fig. 2(b)]. The mechanism that drives the propagation of the pulse is the channel guiding, modeled with one parabola [Eq. (3)] and depicted as a magenta line in Fig. 4. Between points B and C, the one parabola model focuses the beam more than observed in the PIC simulation. As shown in Table I, diffraction and refraction focusing both play a role in the unperturbed channel ( $Z_R = 0.0725$  and  $Z_1 = 0.11$  cm). However, our model does not take into account diffraction. Thus, the origin of this discrepancy is the switch



of the channel-guiding mechanism (between points A and B) to a competition between guiding and diffraction. At point C ( $Z \approx 3Z_R$ ) the threshold for self-focusing is attained, and the intensity increases (driven by another mechanism, relativistic self-focusing) until overionization again refracts the pulse. Then, the intensity adjusts itself to the value that is guided in the channel, i.e., the one sustaining only  $\text{Kr}^{8+}$  ions [Figs. 2(a) and 2(b)].

Figure 4 (black diamonds) shows for comparison the case where  $n_{e1} = 1.4 \times 10^{16} \text{ cm}^{-3}$ . In this case, the refraction characteristic length for both overionization refraction ( $Z_0 = 0.33 \text{ cm}$ ) and channel focusing ( $Z_1 = 1.1 \text{ cm}$ ) are much larger than the Rayleigh length ( $Z_R = 0.0725 \text{ cm}$ ), and thus the propagation is dominated by diffraction. The comparison with a Gaussian beam propagating in vacuum is shown in Fig. 4 (black line).

The *breathing* effect described above has several similarities and differences with the laser filamentation of intense IR pulses propagating through different media [27,32]. Both mechanisms rely on a focusing effect (optical Kerr effect in the case of laser filamentation and guiding and relativistic self-focusing in this article) and a defocusing effect (ionization induced by the field via multiphoton absorption or tunneling). The differences appear in the range of power and intensities involved on these effects. Whereas both the optical Kerr effect and the relativistic self-focusing are threshold effects, their threshold power and thus the propagated intensity are different by orders of magnitude. The self-focusing threshold in laser filamentation is [33]  $P_{\text{th}} = 3.72 \frac{\lambda_0^2}{8\pi n_0 n_2}$ , where  $n_0$  is the linear index of refraction and  $n_2$  is the second-order nonlinear index coefficient. For a  $\lambda_0 = 800 \text{ nm}$  laser propagating in air at atmospheric pressure,  $P_{\text{th}} = 3.2 \text{ GW}$ , and the propagated intensity is on the order of  $4 \times 10^{13} \text{ W/cm}^2$  [32,34]. On the other hand, the relativistic self-focusing threshold is [23]  $P_{\text{th}} \approx 17 \frac{n_c}{n_e} \text{ GW}$ . Since usually  $n_e \ll n_c$  the latter threshold will be greater than the former (i.e., for  $n_e = 0.1n_c$ , a relatively high electron density  $P_{\text{th}} = 0.17 \text{ TW}$ ). Figures 2(a) and 4 show that the propagated intensity is greater than  $10^{17} \text{ W/cm}^2$ .

#### IV. CONCLUSIONS

In this paper we model the propagation of intense ( $I > 10^{18} \text{ W cm}^{-2}$ ) IR pulses through dense plasma channels formed by partially ionized high- $Z$  elements (krypton in this article). The propagation of these pulses is highly nonlinear since they are intense enough to locally ionize several times ( $\bar{Z} \approx 16$ ) the atoms, creating steep density gradients. In addition to this, the high electron density achieved reduces the self-focusing threshold, adding complexity to the problem. Unlike in other applications, both high- $Z$  elements and high electron density are required to achieve ultrashort and energetic plasma-based soft-x-ray lasers, and thus a thorough study is needed.

We have shown that efficient guiding of intense IR pulses through dense plasma channels is regulated by two counterbalancing effects. Overionization-induced refraction decreases the intensity of the IR beam over the first Rayleigh length such that only  $\text{Kr}^{8+}$  ions are present afterwards. From this moment, feedback between waveguide refraction and self-focusing on one side and overionization-induced refraction on the other allows for the guiding of the IR beam and the creation of an almost uniform population of  $\text{Kr}^{8+}$  ions during several Rayleigh lengths. A better understanding of the waveguide formation along with a thorough parametric study of its experimental implementation should feed the ambition to guide at higher densities and over longer distances. The perspective of guiding at higher densities holds the promise of developing plasma-based x-ray lasers as a worthwhile complementary, and possibly alternative, tool for large-scale and expensive facilities delivering ultraintense coherent x rays.

#### ACKNOWLEDGMENTS

This work was supported by the Agence Nationale de la Recherche, through Project No. ROLEX ANR-06-BLAN-04 023 01.

- 
- [1] H. N. Chapman and K. A. Nugent, Coherent lensless X-ray imaging, *Nat. Photonics* **4**, 833 (2010).
  - [2] A. P. Mancuso, T. Gorniak, F. Staier, O. M. Yefanov, R. Barth, C. Christophis, B. Reime, J. Gulden, A. Singer, M. E. Pettit, T. Nisius, T. Wilhein, C. Gutt, G. Grübel, N. Guerassimova, R. Treusch, J. Feldhaus, S. Eisebitt, E. Weckert, M. Grunze, A. Rosenhahn, and I. A. Vartanyants, Coherent imaging of biological samples with femtosecond pulses at the free-electron laser FLASH, *New J. Phys.* **12**, 035003 (2010).
  - [3] P. Zeitoun, G. Faivre, S. Sebban, T. Mocek, A. Hallou, M. Fajardo, D. Aubert, P. Balcou, F. Burgy, D. Douillet, S. Kazamias, G. de Lachèze-Muriel, T. Lefrou, S. le Pape, P. Mercère, H. Merdji, A. S. Morlens, J. P. Rousseau, and C. Valentin, A high-intensity highly coherent soft x-ray femtosecond laser seeded by a high harmonic beam, *Nature (London)* **431**, 426 (2004).
  - [4] Y. Wang, E. Granados, F. Pedaci, D. Alessi, B. M. Luther, M. Berrill, and J. J. Rocca, Phase-coherent, injection-seeded, tabletop soft-x-ray lasers at 18.9 nm and 13.9 nm, *Nat. Photonics* **2**, 94 (2008).
  - [5] Y. Wang, M. Berrill, F. Pedaci, M. M. Shakya, S. Gilbertson, Z. Chang, E. Granados, B. M. Luther, M. A. Larotonda, and J. J. Rocca, Measurement of 1-ps soft-x-ray laser pulses from an injection-seeded plasma amplifier, *Phys. Rev. A* **79**, 023810 (2009).
  - [6] L. Li, Y. Wang, S. Wang, E. Oliva, L. Yin, T. T. T. Le, S. Daboussi, D. Ros, G. Maynard, S. Sebban, B. Hu, J. J. Rocca, and P. Zeitoun, Wavefront improvement in an injection-seeded soft x-ray laser based on a solid-target plasma amplifier, *Opt. Lett.* **38**, 4011 (2013).
  - [7] E. Oliva, M. Fajardo, L. Li, S. Sebban, D. Ros, and P. Zeitoun, Soft x-ray plasma-based seeded multistage amplification chain, *Opt. Lett.* **37**, 4341 (2012).

- [8] E. Oliva, M. Fajardo, L. Li, M. Pittman, T. T. T. Le, J. Gautier, G. Lambert, P. Velarde, D. Ros, S. Sebban, and P. Zeitoun, A proposal for multi-tens of GW fully coherent femtosecond soft x-ray lasers, *Nat. Photonics* **6**, 764 (2012).
- [9] F. Tissandier, S. Sebban, J. Gautier, P. Zeitoun, E. Oliva, A. Rousse, and G. Maynard, Three-dimensional Maxwell-Bloch calculation of the temporal profile of a seeded soft x-ray laser pulse, *Appl. Phys. Lett.* **101**, 251112 (2012).
- [10] O. Larroche and A. Klisnick, Two-dimensional Maxwell-Bloch simulation of quasi- $\pi$ -pulse amplification in a seeded XUV laser, *Phys. Rev. A* **88**, 033815 (2013).
- [11] D. S. Whittaker, M. Fajardo, P. Zeitoun, J. Gautier, E. Oliva, S. Sebban, and P. Velarde, Producing ultrashort, ultraintense plasma-based soft-x-ray laser pulses by high-harmonic seeding, *Phys. Rev. A* **81**, 043836 (2010).
- [12] B. E. Lemoff, C. P. J. Barty, and S. E. Harris, Femtosecond-pulse-driven, electron-excited XUV lasers in eight-times-ionized noble gases, *Opt. Lett.* **19**, 569 (1994).
- [13] B. E. Lemoff, G. Y. Yin, C. L. Gordon III, C. P. J. Barty, and S. E. Harris, Demonstration of a 10-Hz Femtosecond-Pulse-Driven XUV Laser at 41.8 nm in Xe IX, *Phys. Rev. Lett.* **74**, 1574 (1995).
- [14] R. Keenan, J. Dunn, P. K. Patel, D. F. Price, R. F. Smith, and V. N. Shlyaptsev, High-Repetition-Rate Grazing-Incidence Pumped X-Ray Laser Operating at 18.9 nm, *Phys. Rev. Lett.* **94**, 103901 (2005).
- [15] R. Rankin, N. H. Burnett, P. B. Corkum, and C. E. Capjack, Refraction effects associated with multiphoton ionization and ultrashort-pulse laser propagation in plasma waveguides, *Opt. Lett.* **16**, 835 (1991).
- [16] C. G. Durfee and H. M. Milchberg, Light pipe for high intensity laser pulses, *Phys. Rev. Lett.* **71**, 2409 (1993).
- [17] W. P. Leemans, B. Nagler, A. J. Gonsalves, C. Tóth, K. Nakamura, C. G. R. Geddes, E. Esarey, C. B. Schroeder, and S. M. Hooker, GeV electron beams from a centimetre-scale accelerator, *Nat. Phys.* **2**, 696 (2006).
- [18] M.-C. Chou, P.-H. Lin, C.-A. Lin, J.-Y. Lin, J. Wang, and S.-Y. Chen, Dramatic Enhancement of Optical-Field-Ionization Collisional-Excitation X-Ray Lasing by an Optically Preformed Plasma Waveguide, *Phys. Rev. Lett.* **99**, 063904 (2007).
- [19] P.-H. Lin, M.-C. Chou, C.-A. Lin, H.-H. Chu, J.-Y. Lin, J. Wang, and S.-Y. Chen, Optical-field-ionization collisional-excitation x-ray lasers with an optically preformed plasma waveguide, *Phys. Rev. A* **76**, 053817 (2007).
- [20] A. M. Perelomov, V. S. Popov, and M. V. Terent'ev, Ionization of atoms in an alternating electric field, *J. Exp. Theor. Phys.* **23**, 924 (1966).
- [21] M. V. Ammosov, N. B. Delone, and V. P. Krainov, Tunnel ionization of complex atoms and of atomic ions in an alternating electromagnetic field, *J. Exp. Theor. Phys.* **64**, 1191 (1986).
- [22] C. E. Max, J. Arons, and A. B. Langdon, Self-Modulation and Self-Focusing of Electromagnetic Waves in Plasmas, *Phys. Rev. Lett.* **33**, 209 (1974).
- [23] P. Sprangle, C.-M. Tang, and E. Esarey, Relativistic Self-Focusing of Short-Pulse Radiation Beams in Plasmas, *IEEE Trans. Plasma Sci.* **15**, 145 (1987).
- [24] B. S. Paradkar, B. Cros, P. Mora, and G. Maynard, Numerical modeling of multi-GeV laser wakefield electron acceleration inside a dielectric capillary tube, *Phys. Plasmas* **20**, 083120 (2013).
- [25] P. Mora and T. M. Antonsen, Jr., Kinetic modeling of intense, short laser pulses propagating in tenuous plasmas, *Phys. Plasmas* **4**, 217 (1997).
- [26] S. Sebban, T. Mocek, D. Ros, L. Upcraft, P. Balcou, R. Haroutunian, G. Grillon, B. Rus, A. Klisnick, A. Carillon, G. Jamelot, C. Valentin, A. Rousse, J. P. Rousseau, L. Notebaert, M. Pittman, and D. Hulin, Demonstration of a Ni-Like Kr Optical-Field-Ionization Collisional Soft X-Ray Laser at 32.8 nm, *Phys. Rev. Lett.* **89**, 253901 (2002).
- [27] A. Couairon and A. Mysyrowicz, Femtosecond filamentation in transparent media, *Phys. Rep.* **441**, 47 (2007).
- [28] Y.-F. Xiao, H.-H. Chu, H.-E. Tsai, C.-H. Lee, J.-Y. Lin, J. Wang, and S.-Y. Chen, Efficient generation of extended plasma waveguides with the axicon ignitor-heater scheme, *Phys. Plasmas* **11**, L21 (2004).
- [29] F. Tissandier, Caractérisation spatio-temporelle d'une chaîne laser à 32.8 nm par plasma laser et perspectives vers une source untrabève et intense, Ph.D. thesis, Ecole Polytechnique, 2011.
- [30] F. Tissandier, S. Sebban, M. Kozlova, J. Gautier, P. Zeitoun, A. Klisnick, and G. Maynard, High Density Optical-Field-Ionization Soft X-Ray Lasers, in *X-Ray Lasers 2012*, edited by S. Sebban, J. Gautier, D. Ros, and P. Zeitoun, Springer Proceedings in Physics Vol. 147 (Springer, Berlin, 2014), pp. 243–255.
- [31] E. E. Fill, Ray trajectories in line-focused laser plasmas, *J. Opt. Soc. Am. B* **14**, 1505 (1997).
- [32] S. L. Chin, The physics and the challenge of the propagation of powerful femtosecond laser pulses in optical media, *Phys. Canada* **60**, 273 (2004).
- [33] J. Marburger, Self-focusing: Theory, *Progr. Quantum Electron.* **4**, 35 (1975).
- [34] J. Kasparian, R. Sauerbrey, and S. Chin, The critical laser intensity of self-guided light filaments in air, *Appl. Phys. B* **71**, 877 (2000).



# Bibliography

- Ackerman, W., Asova, G., Ayvazyan, and al. (2007). Operation of a free-electron laser from the extreme ultraviolet to the water window. *Nat. Phot.*, 1:336–342. [29](#)
- Afanasev, Y. and Shlyaptsev, V. (1989). Formation of a population inversion of transitions in ne-like ions in steady-state and transient plasmas. *Sov. J. Quantum Electron.*, 16:1606. [19](#), [22](#)
- Agostini, P., Barjot, G., Bonnal, J., Mainfray, G., Manus, C., and Morellec, J. (1968). Multi-photon ionization of hydrogen and rare gases. *J. Quantum Electron.*, 4:667–669. [33](#)
- Almiev, I., Larroche, O., Benredjem, D., Bubau, J., Kazamias, S., Moller, C., and Klisnick, A. (2007). Dynamical de-scription of transient x-ray lasers seeded with high-order harmonic radiation through maxwell-bloch numerical simulations. *Phys. Rev. Lett.*, 99:123902. [165](#), [190](#), [197](#)
- Amann, J., Berg, W., Blank, V., Decker, F. J., Ding, Y., Emma, P., Feng, Y., Frisch, J., Fritz, D., Hastings, J., Huang, Z., Krzywinski, J., Lindberg, R., Loos, H., Lutman, A., Nuhn, H., Ratner, D., Rzepiela, J., Shu, D., Shvydko, Y., Spampinati, S., Stoupin, S., Terentyev, S., Trakhtenberg, E., Walz, D., Welch, J., Wu, J., Zholents, A., and Zhu, D. (2012). Demonstration of self-seeding in a hard-x-ray free-electron laser. *Nat. Phot.*, 6(10):693–698. [7](#)
- Ammosov, M., Delone, N., and Krainov, V. (1986). Tunnel ionization of complex atoms and atomic ions by an alternating electromagnetic field. *Sov. Phys. JETP*, 64:1191. [37](#), [210](#)
- Andersen, A. (1987). Tomography transform and inverse in geometrical optics. *J. Opt. Soc. Am.*, 4(8):1385. [228](#)
- Andreev, N., Nishida, Y., and Yagumi, N. (2002). Propagation of short intense laser pulses in gas-filled capillaries. *Phys. Rev. E*, 65:056407. [50](#)
- Antonsen, T. and Mora, P. (1992). Self-focusing and raman scattering of laser pulses in tenuous plasmas. *Phys. Rev. Lett.*, 69:2204. [89](#)
- Augst, S., Meyerhofer, D., Strickland, D., and Chint, S. (1991). Laser ionization of noble gases by coulomb-barrier suppression. *J. Opt. Soc. Am. B*, 8(4):858–867. [35](#)
- Bahrt, J., Gaupp, A., Gudat, W., Mast, M., Molter, K., Peatman, W., Scheer, M., Schroter, T., and Wang, C. (1992). Circularly polarized synchrotron radiation from the crossed undulator at bessy. *Rev. Sci. Instrum.*, 63:339. [178](#)
- Basov, N. and Prokhorov, A. (1958). *Journal for Experimental and Theoretical Physics*, 27:433–438. [1](#)

- Becker, A. and Faisal, F. (2005). Intense-field many-body s-matrix theory. *J. Phys. B.: At., Mol. Opt. Phys.*, 38(3):1. [32](#)
- Ben Nessib, N., Ben Lakhdar, Z., Nguyen, H., and Arranz, J. (1994). Modélisation de l'élargissement stark dans les lasers x. *Annales de Physique-Colloque C1*, 5(19). [213](#)
- Berril, M., Alessi, D., Wang, Y., Domingue, S., Martz, D., Luther, B., Liu, Y., and Rocca, J. (2010). Improved beam characteristics of solid-target soft x-ray laser amplifiers by injection seeding with high-harmonic pulses. *Opt. Lett.*, 35(14):2317. [201](#)
- Bethe, H. and Salpeter, E. (1957). Quantum mechanics of one- and two-electron atoms. *Plenum*, New York. [35](#)
- Bettaibi, I. (2005). Développement et caractérisation des lasers xuv créés par laser femtoseconde. *Thèse de doctorat*. [22](#), [83](#)
- Bobrova, N. (2002). Simulations of a hydrogen-filled capillary discharge waveguide. *Phys. Rev. E*, 65:016407. [81](#)
- Born, M. and Wolf, E. (1959). Principles of optics. *Pergamon Press*. [25](#)
- Boutet, S., Lomb, L., Williams, G., Barends, T., Aquilla, A., Doak, R., Weierstall, U., DePonte, D., Steinbrener, J., Schoeman, R., Messerschmitt, M., Barty, A., White, T., Kassemayer, S., Kirian, R., Steibert, M., Montanez, P., Kenney, C., Herbst, R., Hart, P., Pines, J., Haller, G., Gruner, S. M., P. S., , Tate, M., Hromalik, M., Koerner, L., van Bakel, N., Morse, J., Ghonsalves, W., Arnlund, D., Bogan, M., Coleman, C., Fromme, R., Hampton, C., Hunter, M., Johansson, L., Katona, G., Kupitz, C., Liang, M., Martin, A., Nass, K., Redecke, L., Stellato, F., Timneanu, N., Wang, D., Zatsepin, N., Schafer, D., Defever, J., Neutze, R., Fromme, P., Spence, J., Chapman, H., and Schlichting, I. (2012). High-resolution protein structure determination by serial femtosecond crystallography. *Chirality*, 337. [30](#), [201](#), [206](#)
- Brunel, F. (1987). Not-so-resonant, resonant absorption. *Phys. Rev. Lett.*, 59:52–55. [9](#)
- Burnett, N. H.; Baldis, H. A. R. M. C. E. G. D. (1977). Harmonic generation in co2 laser target interaction. *Appl. Phys. Lett.*, 31:172–174. [8](#)
- Butler, A., Gonwales, A., McKenna, C., Spence, D., Hooker, S., Sebban, S., Mocek, T., Bettaibi, I., and Cros, B. (2003). Demonstration of a collisionally excited optical-field-ionization xuv laser driven in a plasma waveguide. *Phys. Rev. Lett.*, 92(20):205001. [22](#), [82](#)
- Butler, A., Gonwales, A., McKenna, C., Spence, D., Hooker, S., Sebban, S., Mocek, T., Bettaibi, I., and Cros, B. (2004). 41.8 nm xe 8+ laser driven in a plasma waveguide. *Phys. Rev. A*, 70(2):023821. [86](#)
- Butler, A., Spence, D., and Hooker, S. (2002). Guiding of high-intensity laser pulses with a hydrogen-filled capillary discharge waveguide. *Phys. Rev. Lett.*, 89:185003. [81](#), [82](#)
- Calisti, A., Ferri, S., Mossé, C., Talin, B., Klisnick, A., Meng, L., Benredjem, D., and Guilbaud, O. (2013). Line profiles of ni-like collisional xuv laser amplifiers: Particle correlation effects. *High Energy Density Physics*, 9:516–522. [57](#)

- Carillon, A., Chen, H., Dhez, P., Dwivedi, L., Jacoby, J., Jaeglé, Jamelot, G., Zhang, J., Key, M., Kidd, A., Klisnick, A. Kodama, R., Krishnan, J., Lewis, C., Neely, D., Norreys, P., O'Neill, D., Pert, D., Ramsden, S., Raucourt, J., Tallents, G., and Uthmaniyah, J. (1992). Saturated and near-diffraction-limited operation of an xuv laser at 23.6 nm. *Phys. Rev. Lett.*, 68:2917–2920. [16](#)
- Carman, R. L., Rhodes, C. K., and Benjamin, R. F. (1981). Observation of harmonics in the visible and ultraviolet created in co<sub>2</sub>-laser-produced plasmas. *Phys. Rev. A*, 24:2649–2663. [8](#)
- Ceglio, N., Stearns, D., Gaines, D., Hawryluk, A., and Trebes, J. (1988). Multipass amplification of soft x-rays in a laser cavity. *Opt. Lett.*, 13(2):108–110. [18](#)
- Chandrasekhar, S. (1943). Stochastic problems in physics and astronomy. *Rev. Mod. Phys.*, 15:1–89. [75](#)
- Chang, Z., Rundquist, A., Wang, H., Murnane, M. M., and Kapteyn, H. C. (1997). Generation of coherent soft x rays at 2.7 nm using high harmonics. *Phys. Rev. Lett.*, 79:2967–2970. [10](#)
- Chapman, H., Hau-Riege, S., Bogan, M., Bajt, S., Bary, A., Boutet, S., Marchesini, S., Frank, M., Woods, B., Benner, W., London, R., Rohner, U., Szoke, A., Spiller, E., Moller, T., Bostedt, C., Shapiro, D., Khukmann, M., Treusch, R., Plonjes, E., Burmeister, F., Bergh, M., Caleman, C., Huidt, G., Seibert, M., and Hajdu, J. (2007). Femtosecond time-delay x-ray holography. *Nature*, 448:676–679. [206](#)
- Chen, S., Sarkisov, G., Maksimchuk, A., and Unstadter, D. (1998). Evolution of a plasma waveguide created during relativistic ponderomotive self-channeling of an intense laser pulse. *Phys. Rev. Lett.*, 80:2610–2613. [80](#)
- Chou, M., Lin, P., Lin, C., Lin, Y., Wang, J., and Chen, S. (2007). Dramatic enhancement of optical-field-ionization collisional-excitation x-ray lasing by an optically preformed plasma waveguide. *Phys. Rev. Lett.*, 99(6):063904. [22](#), [86](#)
- Clark, R. and Sampson, D. (1984). Ionisation from the sub levels nl with n=5 and 6 in highly charged ions. *J. Phys. B: At. Mol. Phys.*, 17:3311–3320. [210](#)
- Contini, G., Turchini, S., Sanna, S., Catone, D., Fujii, J., Vobronik, I., Prosperi, T., and Zema, N. (2012). Transfer of chirality from absorbed chiral molecules to the substrate highlighted by circular dichroism in angle-resolved valence photoelectron spectroscopy. *Phys. Rev. B*, 86:035426. [29](#)
- Corkum, P. (1993). Plasma perspective on strong field multiphoton ionization. *Phys. Rev. Lett.*, 71:1994–1997. [10](#)
- Corkum, P., Burnett, N., and Brunel, F. (1989). Above-threshold ionization in the long-wavelength limit. *Phys. Rev. Lett.*, 62:1259–1262. [21](#)
- Cros, B., Mocek, T., Bettaibi, I., Vieux, G., Farinet, M., Dubau, J., Sebban, S., and Maynard, G. (2006). Characterization of the collisionally pumped optical field-ionized soft x-ray laser at 41.8nm driven in capillary tubes. *Phys. Rev. A*, 73:033801. [83](#), [162](#), [192](#), [209](#)
- Daido, H. (2002). *Rev. Prog. Phys.*, 65:1513–1576. [17](#)



- Dattoli, G., Renieri, A., and Torrer, A. (1993). Lecture on the free-electron laser: Theory and related topic. *World Scientific*. 7
- de Aldana, J. and Roso, L. (2001). High-order harmonic generation in atomic clusters with a two-dimensional model. *J. Opt. Soc. Am. B.*, 18:325–330. 8
- Delacroix, J. (1994). Physique des plasmas. *Inter-editions CNRS*. 45
- Delone, N. and Krainov, V. (1998). Tunneling and barrier-suppression ionization of atoms and ions in a laser radiation field. *Physics-Uspenki*, 41(5):469. 32
- Deng, H., Zhang, T., Feng, L., Feng, C., Liu, B., Wang, X., Lan, T., Wang, G., Zhang, W., Liu, X., Chen, J., Zhang, M., Lin, G., Zhang, M., Wang, D., and Zhao, Z. (2014). Polarization switching demonstration using crossed-planar undulators in a seeded free- electron laser. *Phys. Rev. ST Accel. Beams*, 17:020704. 178
- Depresseux, A., Oliva, E., Gautier, J., Tissandier, F., Lambert, G., Vodungbo, B., Goddet, J.-P., Tafzi, A., Nejdl, J., Kozlova, M., Maynard, G., Kim, H. T., Phuoc, K. T., Rousse, A., Zeitoun, P., and Sebban, S. (2015a). Demonstration of a circularly polarized plasma-based soft-x-ray laser. *Phys. Rev. Lett.*, 115:083901. 177, 201, 204
- Depresseux, A., Oliva, E., Gautier, J., Tissandier, F., Nejdl, J., Kozlova, M., Maynard, G., Goddet, J., Tafzi, A., Lifschitz, A., Kim, H., Jacquemot, S., Malka, V., Ta Phuoc, K., Thauray, C., Rousseau, P., Iaquaniello, G., Lefrou, T., Flacco, A., Vodungbo, B., Lambert, G., Rousse, A., Zeitoun, P., and Sebban, S. (2015b). Table-top femtosecond soft x-ray laser by collisional ionization gating. *Nature Photonics*, doi: 10.1038/nphoton.2015.225. 58, 63, 147, 176, 203
- Dietrich, P., Burnett, N., Ivanov, M., and Corkum, P. (1994). High-harmonic generation and correlated two-electron multiphoton ionization with elliptically polarized light. *Phys. Rev. A*, 50:3585–3588. 178
- Ding, Z., Ren, H., Zhao, Y., Nelson, J., and Chen, Z. (2002). High-resolution optical coherence tomography over a large depth range with an axicon lens. *Optics Lett.*, 27(4):243–245. 85
- Ditmire, T., Gumbrell, E., Smith, R., Tish, J., Meyerhofer, D., and Hutchinson, M. (1996). Spatial coherence measurement of soft x-ray radiation produced by high order harmonic generation. *Phys. Rev. Lett.*, 77:4756. 11, 26
- Dorchies, F., Marques, J., Cros, B., Matthieussent, G., Courtois, C., Velikoroussov, T., Audevert, P., Geindre, J., Redibo, S., Hamoniaux, G., and Amiranoff, F. (1999). Monomode guiding of  $1\text{e}16\text{ w/cm}^2$  laser pulses over 100 rayleigh lengths in hollow capillary dielectric tubes. *Phys. Rev. Lett.*, 82:4655. 82
- Duguay, M. and Rentzepis, P. (1967). Some approaches to vacuum uv and x-ray lasers. *Applied Physics Letters*, 10. 13
- Dunn, J., Osterheld, A., Shepherd, R., White, W., Shlyaptsev, V., and Stewart, R. (1998). Demonstration of x-ray amplification in transient gain nickel-like palladium scheme. *Phys. Rev. Lett.*, 80:2825–2828. 19
- Dunne, M., Afshar-Rad, T., Edwards, J., MacKinnon, A., Viana, S., Willi, O., and Pert, G. (1994). Experimental observations of the expansion of an optical-field-induced ionization channel in a gas jet target. *Phys. Rev. Lett.*, 72:1024–1027. 46

- Durfee, C., Lynch, J., and Milchberg, H. (1994). Development of a plasma waveguide for high-intensity laser pulses. *Phys. Rev. E*, 51(3):2368–2389. [91](#), [93](#), [216](#)
- Durfee, C. and Milchberg, H. (1993). Light pipe for high intensity laser pulses. *Phys. Rev. Lett.*, 71:2409. [84](#), [85](#)
- Durfee, C. G., Rundquist, A. R., Backus, S., Herne, C., Murnane, M. M., and Kapteyn, H. C. (1999). Phase matching of high-order harmonics in hollow waveguides. *Phys. Rev. Lett.*, 83:2187–2190. [10](#)
- Eder, D., Amendt, P., DaSilva, P., London, R., McGowan, B., Matthews, D., Penetrante, B., Rosen, M., Wilks, S., Donnelly, T., Falcone, R., and Strobel, G. (1994). Table-top x-ray lasers. *Physics of Plasmas*, 1:1744. [14](#)
- Eder, D., Amendt, P., and Wilks, S. (1991). X-ray lasing by optical-field-induced ionization. *Phys. Rev. Lett.*, 66:2589–2592. [15](#)
- Eder, D., Amendt, P., and Wilks, S. (1992). Optical field ionized plasma x-ray lasers. *Phys. Rev. A*, 45:6761. [159](#)
- Einstein, A. (1917). *Phys. Zs.*, 18:121. [52](#)
- Eisebitt, S., Luning, J., Schlotter, F., Lorgen, M., Hellwig, O., Eberhardt, W., and Stohr, J. (2004). Lensless imaging of magnetic nanostructures by x-ray spectro-holography. *Nature*, 432:885–888. [30](#), [201](#)
- Eissner, W. and al. (1974). Techniques for the calculation of atomic structures and radiative data including relativistic corrections. *Comput. Phys. Commun.*, 8(4):270–306. [211](#)
- Eissner, W. and al. (1998). The ucl distorted wave code. *Comput. Phys. Commun.*, 114(1-3):295–341. [211](#)
- Eliezer, S. (2002). The interaction of high-power lasers with plasmas. *IOP Publishing*. [47](#)
- Elouga Bom, L. B., Ganeev, R. A., Abdul-Hadi, J., Vidal, F., and Ozaki, T. (2009). Intense multimicrojoule high-order harmonics generated from neutral atoms of in2o3 nanoparticles. *Applied Physics Letters*, 94(11):–. [10](#)
- Elton, R. (1975). Extension of 3p - 3s ion lasers into the vacuum ultraviolet region. *Appl. Opt.*, 14(1):97–101. [16](#)
- Emma, P., Akre, R., Arthur, J., Bionta, R., Bostedt, C., Bozek, J., Brachmann, A., Bucksbaum, P., Coffee, R., Decker, F. J., Ding, Y., Dowell, D., Edstrom, S., Fisher, A., Frisch, J., Gilevich, S., Hastings, J., Hays, G., Hering, P., Huang, Z., Iverson, R., Loos, H., Messerschmidt, M., Miahnahri, A., Moeller, S., Nuhn, H., Pile, G., Ratner, D., Rzepiela, J., Schultz, D., Smith, T., Stefan, P., Tompkins, H., Turner, J., Welch, J., White, W., Wu, J., Yocky, G., and Galayda, J. (2010). First lasing and operation of an angstrom-wavelength free-electron laser. *Nat. Phot.*, 4(9):641–647. [7](#)
- Esarey, E., Sprangle, P., Krall, J., and Ting, A. (1997). Self-focusing and guiding of short laser pulses in ionizing gases and plasmas. *J. Quant. Electron.*, 33:1879–1914. [80](#)



- Ferré, A., Handschin, C., Dumergue, D., Burgy, F., Comby, A., Deschamps, D., Fabre, B., Garcia, G., Gréneaux, R., Merceron, L., Mével, E., Nahon, L., Petit, S., Pons, B., Staedter, D., Weber, S., Ruchon, T., Blanchet, V., and Mairesse, Y. (2014). A table-top ultrashort light source in the extreme ultraviolet for circular dichroism experiments. *Nat. Phot.*, 9:93–98. [178](#), [201](#), [206](#)
- Fill, E. (1997). Ray trajectories in line-focused laser plasmas. *J. Opt. Soc. Am. B*, 14(6):1505. [93](#)
- Fleischer, A., Kfier, O., Diskin, T., Sidorenko, P., and O., C. (2014). Spin angular momentum and tunable polarization in high-harmonic generation. *Nat. Phot.*, 8:543–549. [11](#), [178](#)
- Forbes, R. (1977). *Surface Science*, 64:367–371. [230](#)
- Fortov, V., Iakubov, I., and Kharpak, A. (2006). Physics of strongly coupled plasma. *Oxford Science Publications*. [50](#)
- Gagnon, E., Sandhu, A., Paul, A., Hagen, K., Czasch, A., Jahnke, T., Ranitovic, P., Cocke, C., Walker, B., Murnane, M., and Kapteyn, H. (2008). Time-resolved momentum imaging system for molecular dynamics studies using a tabletop ultrafast extreme-ultraviolet light source. *Rev. Sci. Instr.*, 79:063102. [28](#)
- Garica, G., Nahon, L., Daly, S., and Powis, I. (2010). Vibrationally induced inversion of photoelectron forward-backward asymmetry in chiral molecule photoionization by circularly polarized light. *Nat. Comm.*, 4:2132. [201](#), [206](#)
- Gautier, J., Zeitoun, P., Hauri, C., Morlens, A., Rey, G., Valentin, C., Papalarazou, E., Goddet, J., Sebban, S., Burgy, F., Mercière, P., Idir, M., Dovillaire, G., Levecq, X., Bucourt, S., Fajardo, M., Merdji, H., and Cumes, J. (2008). Optimization of the wave front of high-order harmonics. *Eur. Phys. J. D.*, 48:459–463. [11](#), [25](#)
- Gibbon, P. (1996). Harmonic generation by femtosecond laser-solid interaction: a coherent water-window light source. *Phys. Rev. Lett.*, 76:50–53. [8](#)
- Gibbon, P. (2005). Short pulse interactions with matter. *Imperial College Press*, 33:1879–1914. [80](#)
- Goddet, J., Sebban, S., Gautier, J., Zeitoun, P., Valentin, C., Tissandier, F., Marchenko, T., Lambert, G., Ribieres, M., Douillet, D., Lefrou, T., Iaquaniello, G., Burgy, F., Maynard, G., Cros, B., Robillard, B., Mocek, T., Nejd, J., Kozlova, M., and Jakubczak, K. (2009). Aberration-free laser beam in the soft x-ray range. *Opt. Lett.*, 34(16):2438–2440. [1](#), [25](#), [29](#), [201](#)
- Gordon, J., Zeiger, H., and C.H., T. (1954). Molecular microwave oscillator and new hyperfine structure in the microwave spectrum of nh<sub>3</sub>. *Physical Review A*, 95:282–284. [1](#)
- Gordon, R. (1974). Tutorial on art. *IEEE Transactions on Nuclear Science*, 21. [228](#)
- Greenfield, N. (2006). Using circular dichroism spectra to estimate protein secondary structure. *Nat. Protoc.*, 1:2876–2890. [29](#)
- Griem, H. (1974). Spectral line broadening by plasmas. *Academic Press*. [56](#)

- Griem, H. R. (1986). Line profiles of soft-x-ray laser gain coefficients. *Phys. Rev. A*, 33:3580–3583. [56](#)
- Gudzenko, L. and Shelepin, L. (1965). *Sov. Phys. Doklady*, 10(147). [14](#)
- Guilbaud, O. (2005). Etudes et applications des propriétés de cohérence des lasers x-uv à pompage transitoire. *PhD thesis*. [136](#)
- Guilbaud, O., Klisnick, A., Cassou, K., Kazamias, S., Ros, D., Jamelot, G., Joyeux, D., and Phalippou, D. (2006). Origin of microstructures in picosecond x-ray laser beams. *Europhys. Lett.*, 75(5):823. [136](#)
- Guilbaud, O., Tissandier, F., Goddet, J., Ribiere, M., Sebban, S., Gautier, J., Joyeux, D., Ros, D., Cassou, K., Kazamias, S., Klisnick, A., Habib, J. ans Zeitoun, P., Benredjem, D., Mocek, T., Neijdl, J., De Rossi, S., Maynard, G., Cros, B., and Boudaa, A. C. (2010). Fourier-limited seeded soft x-ray laser pulse. *Optics Lett.*, 35(9):1326–1328. [27](#), [159](#), [169](#)
- Hasegawa, N., Sasaki, A., Yamatani, H., Kishimoto, M., Tanaka, M., Ochi, Y., Nishikino, M., Kuneida, Y., and Kawachi, T. (2009). High-resolution spectroscopy of nickel-like molybdenum x-ray laser toward the generation of circularly polarized x-ray laser. *Journal of the Optical Society of Korea*, 13(1):60–64. [179](#)
- Hawkes, J. and Latimer, I. (1995). *Lasers - Theory and practice*, page Prentice Hall International Series in Optoelectronics. [53](#)
- Hochst, P., Patel, R., and Middleton, F. (1994). Multiple-reflection phase shifter: a viable alternative to generate circular-polarized synchrotron radiation. *Nucl. Instrum. Methods Phys. Res A*, 347:107–114. [178](#), [179](#)
- Hulin, S. (2001). Thèse de doctorat de l’université paris vii. [15](#)
- Jackel, S., Burris, R., Grun, J., Ting, A., Manka, C., Eavns, K., and Kosakowskii, J. (1995). Channeling of terawatt laser pulses by use of hollow waveguides. *Opt. Lett.*, 20:1086–1088. [82](#)
- Jaeglé, P., Carillon, A., Dhez, P., Jamelot, G., Sureau, A., and Cukier, M. (1971). *Phys. Lett. A*, 36:167. [12](#)
- Jaeglé, P., Carillon, A., Klisnick, A., Jamelot, G., Guennou, H., and Sureau, A. (1986). Amplification of soft-x-ray spontaneous emission in aluminium and magnesium plasma. *Europhys. Lett.*, 1(11). [14](#)
- Joyeux, D., Pollack, F., Svatos, J., and Phalippou, D. (1995). Applications of wavefront division interferometers in soft x-rays. *Rev. Sci. Instr.*, 66(2). [26](#)
- Jullien, A., Kourtev, S., Albert, O., Chériaux, G., Etchepare, J., Minkovski, N., and Saltiel, S. (2006). Highly efficient temporal cleaner for femtosecond pulses based on cross-polarized wave generation in a dual crystal scheme. *Appl. Phys. B*, 84(3):409–414. [110](#)
- Kalashnikov, M., Nickles, P., Schnurer, M., Sandner, W., Shlyaptsev, V., Danson, C., Neely, D., Wolfrum, E., Zhang, J., Behjat, A., Demir, A., Tallents, G., Warwick, P., and Lewis, C. (1998). Two-color transient pumping in ni-like silver at 13.9 and 16.1 nm. *Phys. Rev. A*, 57:4778–4783. [19](#)

- Kapteyn, H. (1992). Photoionization-pumped x-ray lasers using ultrashort-pulse excitation. *Applied Optics*, 31(24):4931–4939. [13](#), [58](#)
- Kawachi, T., Murai, K., Yuan, G., Ninomiya, S., Kodama, R., Daido, H., Kato, Y., and Fujimoto, T. (1995). Observation of polarization of the soft x-ray laser line in neonlike germanium ions. *Phys. Rev. Lett.*, 75:3826. [179](#)
- Keenan, R., Dunn, J., Patel, P., Price, D., Smith, R., Shlyaptsev, V., Danson, C., Neely, D., Wolfrum, E., Zhang, J., Behjat, A., Demir, A., Tallents, G., Warwick, P., and Lewis, C. (2005). High-repetition-rate grazing-incidence pumped x-ray laser operating at 18.9 nm. *Phys. Rev. Lett.*, 94:103901. [20](#)
- Keldysh, S. (1965). Ionization in the field of a strong electromagnetic wave. *Sov. Phys. JETP*, 20(5). [32](#)
- Kim, C., Janulewicz, K., and Lee, J. (2011). Pulse buildup from noise and intrinsic polarization of plasma-based x-ray lasers. *Phys. Rev. A*, 84:013834. [192](#)
- Kim, C., Lee, J., and Janulewicz, K. (2010). Coherent amplification of an ultrashort pulse in a high- and swept-gain medium with level degeneracy. *Phys. Rev. L*, 104:053901. [192](#)
- Kim, D., Skinner, C., Umesh, D., and Suckewer, S. (1989). Gain measurements at 18.22 nm in c vi generated by a nd:glass laser. *Optics Lett.*, 14:665. [15](#)
- Kim, H., Choi, I., Hafz, N., Sung, J., Yu, T., Hong, K., Jeong, T., Noh, Y., Ko, D., Janulewicz, A., Tummler, A., Nickles, P., Sandner, W., and Lee, J. (2008). Demonstration of a saturated ni-like ag x-ray laser pumped by a single profiled laser pulse from a 10-hz ti :sapphire laser system. *Phys. Rev. A*, 77:023807. [20](#)
- Klisnick, A. and Kuba, J., Ros, D., Smith, R., Jamelot, G., Chenais-Popovics, C., Keenan, R., Topping, S., Lewis, C., Strati, F., Tallents, G., Neely, D., Clarke, R., Collier, J., MacPhee, A., Bortolotto, F., Nickles, P., and Janulewicz, K. A. (2002). Demonstration of a 2-ps transient x-ray laser. *Physical Review A*, 65(033810). [20](#), [27](#)
- Koch, J., MaxGowan, B., Da Silva, L., Matthews, D., Underwood, J., Batson, P., Lee, R., London, R., and Mrowka, S. (1994). Experimental and theoretical investigation of neonlike selenium x-ray laser spectral linewidths and their variation with amplification. *Phys. Rev. A*, 50(2):1877–1889. [57](#)
- Korobkin, D., Nam, C., Suckewer, S., and Goltsov, A. (1996). Demonstration of soft x-ray lasing to ground state in li iii. *Phys. Rev. Lett.*, 77(26):5206–5209. [58](#), [201](#)
- Kosareva, O., Grigorevsjii, A., and Kandidov, V. (2005). Formation of extended plasma channels in a condensed medium upon axicon focusing of a femtosecond laser pulse. *Phys. Rev. A*, 35:1013. [85](#)
- Krainov, V. (1999). Energy and angular distributions of relativistic electrons in the tunneling ionization of atoms by circularly polarized light. *J. Phys. B*, 32:1607. [43](#)
- Kuba, J., Klisnick, A., Ros, D., Fourcade, P., Jamelot, G., Miquel, J., Blanchot, N., and Wyart, J. (2000). Two-color transient pumping in ni-like silver at 13.9 and 16.1 nm. *Phys. Rev. A*, 62:043808. [19](#)

- Kungwirth, K. (2001). The prague asterix laser system. *Phys. Plasmas*, 8:2495. [22](#)
- Kuwata-Gonokami, M., Saito, N., Ino, Y., Kauranen, M., Jefimovs, K., Vallius, T., Turunen, J., and Svirko, Y. (2005). Giant optical activity in quasi-two-dimensional planar nanostructures. *Phys. Rev. Lett.*, 95:227401. [29](#)
- Lambert, G., Hara, T., Garzella, D., Tanikawa, T., Labat, M., Carre, B., Kitamura, H., Shintake, T., Bougeard, M., Inoue, S., Tanaka, Y., Salieres, P., Merdji, H., Chubar, O., Gobert, O., Tahara, K., and Couprie, M. (2008). Injection of harmonics generated in gas in a free-electron laser providing intense and coherent extreme-ultraviolet light. *Nat. Phys.*, 4(4):296–300. [7](#)
- Lambert, G., Vodungbo, B., Gautier, J., Mahieu, B., Malka, V., Sebban, S., Zeitoun, P., Luning, J., Perron, J., Andreev, A., Stremoukhov, S., Ardana-Lamas, F., Dax, A., Hauri, C., Sardinha, A., and Fajardo, M. (2015). Towards enabling femtosecond helicity-dependent spectroscopy with high-harmonic sources. *Nat. Comm.*, 6:6167. [178](#)
- Landau, L. and Lifchitz, E. (1969). Electrodynamique des milieux continus. *Editions Mir*, Moscou. [46](#)
- Laroche, O., Meng, O., Le Marec, A., and Klisnick, A. (2013). Inversion density threshold for rabi oscillations and modified small-signal gain in extreme-ultraviolet lasers. *Optics Lett.*, 38(14):2505–2508. [165](#), [193](#)
- Larroche, O., Ros, D., Klisnick, A., Sureau, A., Moller, C., and Guennou, H. (2000). Maxwell-bloch modeling of x-ray-laser-signal buildup in single- and double-pass configurations. *Phys. Rev. A*, 62(4):043815. [75](#), [162](#)
- Lee, D., Kim, J., Hong, K., and Nam, C. (2001). Coherent control of high-order harmonics with chirped femtosecond laser pulses. *Phys. Rev. Lett.*, 97:243902. [152](#), [179](#)
- Leemans, W. P., Gonsalves, A. J., Mao, H.-S., Nakamura, K., Benedetti, C., Schroeder, C. B., Tóth, C., Daniels, J., Mittelberger, D. E., Bulanov, S. S., Vay, J.-L., Geddes, C. G. R., and Esarey, E. (2014). Multi-gev electron beams from capillary-discharge-guided subpetawatt laser pulses in the self-trapping regime. *Phys. Rev. Lett.*, 113:245002. [81](#)
- Lemoff, B., Barty, C., and Harris, S. (1994). Femtosecond-pulse-driven, electron-excited xuv lasers in eight-times-ionized noble gases. *Opt. Lett.*, 19(8):569–571. [21](#)
- Lemoff, B., Yin, G., Gordon, C., Barty, C., and Harris, S. (1995). Demonstration of a 10-hz femtosecond-pulse-driven xuv laser at 41.8 nm in xe ix. *Phys. Rev. Lett.*, 74:1574–1577. [21](#)
- Lewenstein, M., Balcou, P., Ivanov, M., Lhuillier, A., and Corkum, P. (1994). Theory of high-harmonic generation by low-frequency laser fields. *Phys. Rev. A*, 49:2117–2132. [11](#), [178](#)
- Lewis, C., Neely, D., O Neill, D. ad Uhomoihi, J., Key, M., Al Hadithi, Y., Tallents, G., and Ramsden, S. (1992). An injector/amplifier double target configuration for the ne-like ge x-ray laser scheme. *Opt. Commun.*, 91:71–76. [18](#)
- L’huillier, A., Schafer, K., and Kulander, K. (1991). Theoretical aspects of intense field harmonic generation. *J. Phys. B : At., Mol. Opt. Phys.*, 24(15):3315–3341. [8](#)
- Li, Y., Nilsen, J., Dunn, J., Osterheld, A. L., Ryabtsev, A., and Churilov, S. (1998). Wavelengths of the ni-like  $4d^1S_0 \sim 4p^1P_1$  x-ray laser line. *Phys. Rev. A*, 58:R2668–R2671. [205](#)

- Lichters, R., Meyer-ter Vehn, J., and Pukhov, A. (1996). Short-pulse laser harmonics from oscillating plasma surfaces driven at relativistic intensity. *Phys. Plasmas*, 3(9):3425. [9](#)
- Lifschitz, A., Davoine, X., Lefebvre, E., Faure, J., Rechatin, C., and Malka, V. (2009). Particle-in-cell modelling of laser-plasma interaction using fourier decomposition. *J. Comput. Phys.*, 228:1803. [104](#)
- Lin, P., Chou, M., Jiang, M., Tseng, P., Chu, H., Lin, J., Wang, J., and Chen, S. (2009). Seeding of a soft-x-ray laser in a plasma waveguide by high harmonic generation. *Optics Lett.*, 34(22):3562. [58](#)
- Lin, P., Chou, M., Lin, C., Chu, H., Lin, J., Wang, J., and Chen, S. (2007). Optical-field-ionization collisional- excitation x-ray lasers with an optically preformed plasma waveguide. *Phys. Rev. A.*, 76:053817. [22](#), [116](#)
- Linford, G., Peressini, E., Sooy, W., and Spaeth, M. (1974). Very long lasers. *Appl. Opt.*, 13(2):379–390. [55](#)
- Liu, X., Miao, Q., Gel'mukhanov, F., Patenen, M., Travnikova, O., Nicholas, C., Agren, H., Ueda, K., and Miron, C. (2014). Einstein-bohr recoiling double-slit gedanken experiment performed at the molecular level. *Nat. Phot.*, 9:120–125. [28](#)
- Louisell, W. (1973). *Quantum Statistical Properties of Radiation*, (Wiley):New York – London. [53](#)
- Lu, P., Kawachi, T., Kishimoto, M., Sukegawa, K., Tanaka, M., Hasegawa, N., Suzuki, M., Tai, R., Kado, M., Nagashima, K., Daido, H., and Kato, Y. (2002). Demonstration of a transient-gain nickel-like xenon-ion x-ray laser. *Opt. Lett.*, 27(21):1911–1913. [20](#)
- Lynga, C., LHuillier, A., and Wahlstrom, C. (1996). High-order harmonic generation in molecular gases. *Phys. B : At., Mol. Opt. Phys.*, 29(14):3293. [8](#)
- Macchietto, C., Benware, B., and Rocca, J. (1999). Generation of millijoule-level soft-x-ray laser pulses at a 4-hz repetition rate in a highly saturated tabletop capillary discharge amplifier. *Opt. Lett.*, 24(16):1115–1117. [23](#)
- Maiman, T. (1960). Stimulated optical radiation in ruby. *Nature*, 187:493. [1](#), [12](#)
- Manek, I., Ovchinnikov, Y., and Grimm, R. (1998). Generation of a hollow laser beam for atom trapping using an axicon. *Opt. Comm.*, 147:67–70. [85](#)
- Matthews, D., Hagelstein, P., Rosen, M., Eckart, M., Ceglio, N., Hazi, A., Medeck, H., MacGowan, B., Trebes, J., Whitten, B., Campbell, E., Hatcher, C., Hawryluk, A., Kauffman, R., Pleasance, L., Rambach, G., Scofield, J., Stone, G., and Weaver, T. (1985). Demonstration of a soft x-ray amplifier. *Phys. Rev. Lett.*, 54:110–113. [16](#), [17](#)
- Maynard, G., Lambert, F., Andreev, N., Robillart, B., Boudaa, A., Clerouin, J., Cros, B., Lenglet, A., Mocek, T., and Sebban, S. (2007). Determination of the ion temperature in a plasma created by optical field ionization. *Contrib. Plasma Phys.*, 47(4-5):352–359. [44](#), [49](#), [50](#), [51](#)
- McGowan, B., Da Silva, L., Fields, D., Keane, C., and Koch, J. (1992a). Short wavelength x-ray laser research at the lawrence livermore laboratory. *Phys. Fluids B.*, 4:2326. [18](#)

- McGowan, B., Da Silva, L., Fields, D., Keane, C., Koch, J., London, R., Matthews, D., Maxon, S., Mrowka, S., Osterheld, A., Scofield, J., Shinkaveg, G., Trebes, J., and Walling, R. (1992b). Short wavelength x-ray laser research at the lawrence livermore laboratory. *Phys. Fluids B*, 4:2326. [159](#)
- McLeod, J. (1954). The axicon : A new type of optical element. *J. Opt. Soc. Am.*, 44(8):592. [84](#), [85](#)
- McNeil, B. and Thompson, N. (2010). X-ray free electron lasers. *Nature Phot.*, 4:814–821. [7](#)
- Micali, N., Engelkamp, H., Van Rhee, P., Christianen, P., Monsu Scolaro, L., and Maan, J. (2012). Selection of supramolecular chirality by application of rotational and magnetic forces. *Nat. Chem.*, 4:201–207. [29](#)
- Milonni, P. and Eberly, J. (2010). Laser physics. *Wiley*, (Hoboken). [192](#)
- Mocek, T., McKenne, C., Cros, B., Sebban, S., Spence, D., Maynard, G., Bettaibi, I., Vorontsov, V., Gonsalves, A., and Hooker, S. (2004). Dramatic enhancement of xuv laser output using a multimode gas-filled capillary waveguide. *Phys. Rev. A*, 71(1):013804. [22](#), [83](#)
- Mocek, T., Sebban, S., Maynard, G., Zeitoun, P., Faivre, G., Hallou, A., Fajardo, M., Kazamias, S., Cros, B., Aubert, D., de Lachèze-Murel, G., Rousseau, J. P., and Dubau, J. (2005). Absolute time-resolved x-ray laser gain measurement. *Phys. Rev. Lett.*, 95:173902. [27](#), [28](#), [203](#)
- Monot, P., Auguste, T., Lompre, L., Mainfray, G., and Manus, C. (1992). Focusing limits of a terawatt laser in an under dense plasma. *J. Opt. Soc. Am. B*, 9:1579. [89](#)
- Mora, P. and Antonsen, T. (1997). Kinetic modeling of intense, short laser pulses propagating in tenuous plasmas. *Phys. Plasmas*, 4(217). [69](#)
- New, G. H. C. and Ward, J. F. (1967). Optical third-harmonic generation in gases. *Phys. Rev. Lett.*, 19:556–559. [10](#)
- Nickles, P., Shlyaptsev, V., Kalashnikov, M., Schnurer, M., Will, I., and Sandner, W. (1997). Short pulse x-ray laser at 32.6 nm based on transient gain in ne-like titanium. *Phys. Rev. Lett.*, 78:2748–2751. [19](#)
- Nikitin, S., Alexeev, I., Jan, J., and Milchberg, H. (1999). High efficiency coupling and guiding of intense femtosecond laser pulses in preformed plasma channels in an elongated gas jet. *Phys. Rev. E*, 59:3839–3842. [84](#)
- Nomura, Y., Horlein, R., Tzallas, P., Dromey, B., Rykovanov, S., Major, Z., Osterhoff, J., Karsch, S., Veisz, L., Zepf, M., Charalambidis, D., Krausz, F., and Tsakiris, G. D. (2009). Attosecond phase locking of harmonics emitted from laser-produced plasmas. *Nat. Phys.*, 5:124–128. [8](#)
- Ochi, Y., Hasegawa, N., Kawachi, T., and Nagashima, K. (2007). Development of a chirped pulse amplification laser with zigzag slab and glass amplifiers dedicated to x-ray laser research. *Appl. Opt.*, 46(9):1500–1506. [20](#)
- Oliva, E., Depresseux, A., Tissandier, F., Gautier, J., Sebban, S., and Maynard, G. (2015). Self-regulated propagation of intense infrared pulses in elongated soft-x-ray plasma amplifiers. *Phys. Rev. A*, 92:023848. [79](#), [203](#)



- Oliva, E., Fajardo, M., Li, L., Pittman, M., Le, T., Gautier, J., Lambert, G., Velarde, P., Ros, D., Sebban, S., and Zeitoun, P. (2012). A proposal for multi-tens of gw fully coherent femtosecond soft x-ray lasers. *Nat. Photonics*, 6:764–767. [58](#), [205](#)
- Oliva, E., Zeitoun, P., Fajardo, M., Lambert, G., Ros, D., Sebban, S., and Velarde, P. (2011). Comparison of natural and forced amplification regimes in plasma-based soft x-ray lasers seeded by high-order harmonics. *Phys. Rev. A*, 84:013811. [162](#), [190](#), [196](#)
- Oliva, E., Zeitoun, P., Sebban, S., Fajardo, M., Velarde, P., Cassou, K., and Ros, D. (2009). Optimization of soft x-ray amplifier by tailoring plasma hydrodynamics. *Opt. Lett.*, 34(17):2640–2642. [24](#)
- Paradkar, B., Cros, B., Mora, P., and Maynard, G. (2013). Numerical modeling of multi-gev laser wakefield electron acceleration inside a dielectric capillary tube. *Phys. Plasmas*, 20:083120. [69](#), [94](#), [175](#)
- Paul, P., Toma, E., Breger, P., Mullot, G., Auge, F., Balcou, P., Muller, H., and Agostini, P. (2001). Observation of a train of attosecond pulses from high harmonic generation. *Science*, 292(5522):1689–1692. [11](#)
- Penetrante, B. and Bardsley, J. (1991). Evaporative cooling of highly charged dysprosium ions in an enhanced electron-beam ion trap. *Phys. Rev. A*, 43:4873. [15](#)
- Perelomov, A., Popov, V., and Terent'ev, M. (1966). Ionization of atoms in an alternating electric field. *Sov. Phys. JETP*, 23:924. [37](#)
- Pert, G. (1976). Model calculations of xuv gain in rapidly expanding cylindrical plasmas. *J. Phys. B: At. Mol. Phys.*, 9(18):3301. [14](#), [15](#)
- Pert, G. (1994). Collisional-cross-relaxation effects in amplified-spontaneous-emission lasers. *Phys. Rev. A*, 50:4412. [191](#)
- Pert, G. (1995). Inverse bremsstrahlung in strong radiation fields at low temperatures. *Phys. Rev. E*, 51(5):4778–4789. [41](#), [42](#)
- Pert, G. (1999). Electron distributions generated by tunnelling ionization during gas breakdown by high intensity laser radiation. *J. Phys. B : At., Mol. Opt. Phys.*, 32(1):27–52. [37](#), [42](#), [47](#), [210](#)
- Pert, G. (2001). The calculation of the electron distribution function following tunnel ionization using a fokker planck method. *J. Phys. B*, 34:881. [47](#), [210](#)
- Popov, V. (2004). Tunnel and multiphoton ionization of atoms and ions in a strong laser field. *Physics-Uspenki*, 47(9):855. [32](#)
- Pretzler, G. (1991). A new method for numerical abel-inversion. *Z. Naturforsch.*, 46a:639–641. [232](#)
- Quéré, F., Thaury, C., Monot, P., Dobosz, S., Martin, P., Geindre, J.-P., and Audebert, P. (2006). Coherent wake emission of high-order harmonics from overdense plasmas. *Phys. Rev. Lett.*, 96:125004. [9](#)

- Raines, K., Salha, S., Sandberg, R., Jiang, H., Rodriguez, J., Fahimian, B., Kapteyn, H., Du, J., and Miao, J. (2010). Three-dimensional structure determination from a single view. *Nature*, 463:214–217. [29](#)
- Rankin, R., Capjack, C., Burnett, N., and Corkum, P. (1991). Refraction effects associated with multiphoton ionization and ultrashort-pulse laser propagation in plasma waveguides. *Opt. Lett.*, 16(11):835–837. [68](#)
- Ribière, M., Jacquemot, S., Sebban, S., Corde, S., Ta Phuoc, K., Valentin, C., Gautier, J., Zeitoun, P., Lambert, G., Tissandier, F., and Rousse, A. (2010). Femtosecond coherent pulses in the kev range from inner-shell transitions pumped by a betatron source. *Applied Physics B*, 101(4):753–759. [13](#)
- Rioux, M., Tremblay, R., and Bélanger, P. (1978). Linear, annular, and radial focusing with axicons and applications to laser machining. *Appl. Opt.*, 17(10):1532–1536. [85](#)
- Robillart, B. (2010). Modélisation de la physique atomique et du transfert radiatif pour le laser xuv. *Thèse de Doctorat de l'Université Paris-Sud*. [166](#)
- Rocca, J.J. Shlyaptsev, V., Tomasel, F., Cortazar, O., Hartshorn, D., and J.L.A., C. (1994). Demonstration of a discharge pumped table-top soft-x-ray laser. *Phys. Rev. Lett.*, 73(16):2192–2195. [22](#)
- Rohringer, N., Ryan, D., Londond, R., Purvis, M., Albert, F., Dunn, J., Bozek, J., Bostedt, C., Graf, A., Hill, R., Hau-Riege, S., and Rocca, J. (2012). Atomic inner-shell x-ray laser at 1.46 nanometres pumped by an x-ray free-electron laser. *Nature*, 481:488–491. [13](#), [58](#)
- Ros, D. (1999). *Thesis*, Université Paris Sud(Orsay). [18](#)
- Rosenbluth, M., MacDonald, W., and Judd, D. (1957). Fokker-planck equation from an inverse square force. *Phys. Rev.*, 107:1. [47](#)
- Rus, B., Carillon, A., Dhez, P., Jaeglé, P., Jamelot, G., Klisnick, A., Nantel, M., and Zeitoun, P. (1997). Efficient, high-brightness soft-x-ray laser at 21.2 nm. *PRA*, 55(5):3858–3873. [18](#)
- Rus, B., Mocek, T., Prag, A., Kozlova, M., Jamelot, G., Carillon, A., Ros, D., Joyeux, D., and Phalippou, D. (2002). Multimillijoule, highly coherent x-ray laser at 21 nm operating in deep saturation through double-pass amplification. *Phys. Rev. A.*, 66:063806. [1](#), [24](#), [29](#), [179](#)
- Sakdinawat, A. and Liu, Y. (2008). Phase contrast soft x-ray microscopy using zernike zone plates. *Opt. Expr.*, 13(3):1559. [206](#)
- Salzmann, D. (1998). Atomic physics in hot plasmas. *Oxford University Press*. [210](#)
- Schneidmiller, E. and Yurkov, M. (2013). Obtaining high degree of circular polarization at x-ray free electron lasers via a reverse undulator taper. *Phys. Rev. ST Accel. Beams*, 16:110702. [178](#)
- Schutz, G., Wagner, W., Wilhem, W., Kienle, P., Zeller, R., Frahm, R., and Materlik, G. (1987). Absorption of circularly polarized x rays in iron. *Phys. Rev. Lett.*, 58:737. [29](#)
- Schwartz, A. (2004). The european x-ray free electron laser project at desy. *Proc. of FEL 2004*. [7](#)



- Sebban, S., Haroutunian, R., Balcou, P., Grillon, G., Rousse, A., Kazamias, S., Marin, T., Rousseau, J., Notebaert, L., Pittman, M., Chambaret, J., Antonetti, A., Hulin, D., Ros, D., Klisnick, A., Carillon, A., Jaeglé, P., J. G., and Wyart, J. (2001). Saturated amplification of a collisionally pumped optical-field-ionization soft x-ray laser at 41.8 nm. *Phys. Rev. Lett.*, 86(14):3004–3007. [21](#)
- Sebban, S., Mocek, T., Bettaibi, I., Cros, B., Maynard, G., Butler, A., Gonzalves, A., McKenna, C., Spence, D., Hooker, S., Upcraft, L., Breger, P., Agonosti, P. Le Papa, S. Z. P. V. C. B. P., Ros, D., Kazamias, S., Klisnick, A., Jamelot, G., Rus, B., and Wyart, J. (2004). Progress on collisionally pumped optical-field-ionization soft x-ray lasers. *Journal of Selected Topics in Quantum Electronics*, 10(6). [58](#)
- Sebban, S., Mocek, T., Ros, D., Upcraft, L., Balcou, P., Haroutunian, R., Grillon, G., Rus, B., Klisnick, A., Carillon, A., Jamelot, G., Valentin, C., Rousse, A., Rousseau, J., Notebaert, L., Pittman, M., and Hulin, D. (2002). Demonstration of a ni-like kr optical-field-ionization collisional soft x-ray laser at 32.8 nm. *Phys. Rev. Lett.*, 89:253901. [21](#)
- Sebban, S., Upcraft, L., Balcou, P., Pittman, M., Haroutunian, R., Grillon, G., Valentin, C., Rousse, A., Rousseau, J., Notebaert, L., Hulin, D., Mocek, T., Rus, B., Ros, D., Klisnick, A., Carillon, A., and Jamelot, G. (2003). Investigations of collisionally pumped optical field ionization soft- x-ray lasers. *J. Opt. Soc. Am. B*, 20:195–202. [42](#)
- Seely, J., Brown, C., Feldman, U., Richardson, M., Yaakobi, B., and Behring, W. (1985). Evidence for gain on the c vi 182 Å transition in a radiation-cooled selenium/formvar plasma. *Opt. Comm.*, 54(5):289–294. [14](#)
- Seely, J. and Harris, E. (1972). Heating of a plasma by multi photon inverse brehmstrahlung. *Phys. Rev. A*, 7(3):1064–1067. [88](#)
- Semushin, S. and Malka, V. (2001). High density gas jet nozzle design for laser target production. *Rev. Sci. Instr.*, 72(7):2961. [116](#), [219](#)
- Seres, J., Seres, E., Verhoef, A. J., Tempea, G., Streli, C., Wobrauschek, P., Yakovlev, V., Scrinzi, A., Spielmann, C., and Krausz, F. (2005). Laser technology: Source of coherent kiloelectronvolt x-rays. *Nature*, 433(7026):596–596. [10](#)
- Shen, B., Xu, Z., Zhang, Z., and Yu, W. (1997). Recombination x-ray lasers of helium-like nitrogen ions in a plasma waveguide. *J. Opt. Soc. Am. B*, 12(4):970–973. [205](#)
- Shintake, T. (2006). Status of japanesexfelprojectandscs test accelerator. *Proc. of FEL 2006*. [7](#)
- Silin, V. (1965). *JETP*, 20:1510. [88](#)
- Smirnov, B. and Chibisov, M. (1966). The breaking up of atomic particles by an electric field and by electron collisions. *Sov. Phys. JETP*, 22:585. [37](#)
- Smirnov, M. and Krainov, V. (1998). Hot electrons in the tunneling ionization of atoms. *J. Phys. B*, 31:519. [42](#)
- Sorokin, E., Tempea, G., and Brabec, T. (2000). Measurement of the root-mean-square width and the root-mean-square chirp in ultrafast optics. *J. Opt. Soc. Am. B*, 17(1)(146-150). [172](#)

- Spence, D., Butler, A., and Hooker, S. (2001). First demonstration of guiding of high-intensity laser pulses in a hydrogen-filled capillary discharge waveguide. *J. Phys. B: At., Mol. Opt. Phys.*, 34:4103. [81](#)
- Spence, D. J. and Hooker, S. M. (2000). Investigation of a hydrogen plasma waveguide. *Phys. Rev. E*, 63:015401. [81](#), [82](#)
- Spitzer, L. (1962). Physics of fully ionized gases. *John Wiley*. [45](#)
- Sprangle, P., Esarey, E., Krall, J., and Joyce, G. (1992). Propagation and guiding of intense laser pulses in plasmas. *Phys. Rev. Lett.*, 69:2200. [89](#)
- Stoll, H., Puzic, A., Van Waeyenberge, B., Fischer, P., Raabe, J., Buess, M., Haug, T., Hollinger, R., Back, C., Weiss, D., and Benbeaux, G. (2004). High-resolution imaging of fast magnetization dynamics in magnetic nanostructures. *Appl. Phys. Lett.*, 84:3328. [29](#)
- Strickland, D. and Mourou, G. (1985). Compression of amplified chirped optical pulses. *Opt. Commun.*, 56:219. [110](#)
- Suckewer, S., Skinner, C., Milchberg, H., Keane, C., and Voorhees, D. (1985). Amplification of stimulated soft x-ray emission in a confined plasma column. *Phys. Rev. Lett.*, 55:1753. [15](#), [17](#)
- Sullivan, A. (1993). *Proceedings on Short wavelength V: Physics with Intense Laser Pulses*, page 40. [89](#)
- Sureau, A. and Holden, P. (1995). From amplification of spontaneous emission to saturation in x-ray lasers: A maxwell-bloch treatment. *Phys. Rev. A*, 52(4):3110–3125. [74](#), [75](#), [192](#)
- Takahashi, E., Kanai, T., Ishikawa, K., Nabekawa, Y., and Midorikawa, K. (2008). Coherent water window x ray by phase-matched high-order harmonic generation in neutral media. *Phys. Rev. Lett.*, 101:253901. [11](#)
- Takahashi, E. J., Kanai, T., Ishikawa, K. L., Nabekawa, Y., and Midorikawa, K. (2007). Dramatic enhancement of high-order harmonic generation. *Phys. Rev. Lett.*, 99:053904. [10](#)
- Talin, B., Calisti, A., Godbert, L., Stamm, R., Lee, R., and Klein, L. (1995). Frequency-fluctuation model for line-shape calculations in plasma spectroscopy. *Phys. Rev. Lett.*, 51(3):1918–1928. [213](#)
- Thaury, C. and Quéré, F. (2010). High-order harmonic and attosecond pulse generation on plasma mirrors: basic mechanisms. *J. Phys. B: Atom. Mol. Opt. Phys.*, 43(21):213001. [9](#)
- Tiedtke, K., Azima, A., von Barga, N., Bittner, L., Bonfigt, S., Dusterer, S., Faatz, B., Fruhling, U., Gensch, M., Gerth, C., Guerassimova, N., Hahn, U., Hans, T., Hesse, M., Honkavaar, K., Jastrow, U., Juranic, P., Kapitzki, S., Keitel, B., Kracht, T., Kuhlmann, M., Li, W., Martins, M., Nunez, T., Plonjes, E., Redlin, H., Saldin, E. L., Schneidmiller, E., Schneider, J., Schreiber, S., Stojanovic, N., Tavella, F., Toleikis, S., Treush, R., Weigelt H. and, Wellhofer, M., Wabnitz, H., Yurkov, M., , and Feldhaus, J. (2009). The soft x-ray free-electron laser flash at desy : beamlines, diagnostics and end-stations. *New J. Phys.*, page 11 :023029. [7](#)
- Tissandier, F. (2011). Caractérisation d’une chaîne laser à 32,8 nm par plasma laser et perspectives vers une source ultrabrève et intense. *Thèse de doctorat*. [25](#)

- Tissandier, F., Sebban, F., Ribière, M., Gautier, J., Zeitoun, P., Lambert, G., Barszczak Sardinha, A., Goddet, J., Burgy, F., Lefrou, T., Valentin, C., Rousse, A., G. O., Klisnick, A., Nejd, J., Mocek, T., and Maynard, G. (2010a). Observation of spectral gain narrowing in a high-order harmonic seeded soft-x-ray amplifier. *Phys. Rev. A*, 81:063833. [27](#), [57](#)
- Tissandier, F., Sebban, S., Gautier, J., Zeitoun, P., Oliva, E., Rousse, A., and Maynard, G. (2012). Three-dimensional maxwell-bloch calculation of the temporal profile of a seeded soft x-ray laser pulse. *Appl. Phys. Lett.*, 101(25):251112. [170](#)
- Tissandier, F., Sebban, S., Ribière, M., Gautier, J., P. Zeitoun, Lambert, G., Goddet, J., Burgy, F., Rousse, A., Nejd, J., Mocek, T., and Maynard, G. (2010b). Bessel spatial profile of a soft x-ray laser beam. *Appl. Phys. Lett.*, 97(23):231106. [25](#)
- Tommasini, R. and Fill, E. (2000). Generalized lindford formula. *JOSA B*, 17(1665-1670):Prentice Hall International Series in Optoelectronics. [55](#)
- Usui, T., Tanaka, Y., Nakajima, H., Taguchi, M., Chainani, A., Oura, M., Shin, S., Katayama, N., Sawa, H., Wakabayashi, Y., and Kimura, T. (2014). Observation of quadrupole helix chirality and its domain structure in dyfe3(bo3)4. *Nat. Materials*, 13:611–618. [29](#)
- Van Regemorter, H. (1962). Rate of collisional excitation in stellar atmospheres. *Astrophys. J.*, 136:906–915. [210](#)
- Verluse, F., Laude, V., Cheng, Z., Spielmann, C., and Tournois, P. (2000). Amplitude and phase control of ultrashort pulses by use of an acousto-optic programmable dispersive filter : pulse compression and shaping. *Opt. Lett.*, 25(8):575–577. [111](#)
- Vinogradov, A. and Rocca, J. (2003). Repetitively pulsed x-ray laser operating on the 3p-3s transition of the ne-like argon in a capillary discharge. *Phys. Rev. A*, 33(1):7–17. [22](#)
- Vodungbo, B., Barszczak Sardinha, A., Gautier, J., Lambert, G., Valentin, C., Lozano, M., Iaquaniello, G., Delmotte, F., Sebban, S., Luning, J., and Zeitoun, P. (2011). Polarization control of high-order harmonics in the euv photon energy range. *Opt. Expr.*, 19(5):4346–4356. [178](#), [179](#), [185](#)
- Vodungbo, B., Gautier, J., Lambert, G., Barszczak Sardinha, A., Lozano, M., Sebban, S., Ducouso, M., Boutu, W., Li, K., Tudu, B., Tortarolo, M., Hawaldar, R., Delaunay, R., Lopez-Flores, V., Arabski, J., Boeglin, C., Merdji, H., Zeitoun, P., and Luning, J. (2012). Laser-induced ultrafast demagnetization in the presence of a nanoscale magnetic domain network. *Nat. Comm.*, 3:999. [28](#), [29](#), [201](#), [206](#)
- Volfbeyn, P., Esarey, E., and Leemans, W. (1999). Guiding of laser pulses in plasma channels created by the ignitor-heater technique. *40th annual meeting of the division of plasma physics of the american physical society*, 6:2269–2277. [86](#)
- Wang, Y., Granados, E., Larotonda, M. A., Berrill, M., Luther, B. M., Patel, D., Menoni, C. S., and Rocca, J. J. (2006). High-brightness injection-seeded soft x-ray laser amplifier using a solid targe. *Phys. Rev. Lett.*, 97(12):123901. [26](#), [161](#)
- Wang, Y., Kuba, J., Ros, D., Smith, R., Jamelot, G., Chenais-Popovics, C., Keenan, R., Topping, S., Lewis, C., Strati, F., Tallents, G., Neely, D., Clarke, R., Collier, J., MaxPhee, A.,

- Bortolotto, F., Nickles, P., and Janulewicz, K. (2008). Phase-coherent, injection-seeded, tabletop soft-x-ray lasers at 18.9 nm and 13.9 nm. *Nature Photonics*, 2:94–98. [20](#), [24](#), [27](#), [29](#), [58](#), [76](#), [162](#)
- Wang, Y., Larotonda, M. A., Luther, B. M., Alessi, D., Berrill, M., Shlyaptsev, V. N., and Rocca, J. J. (2005). Demonstration of high-repetition-rate tabletop soft-x-ray lasers with saturated output at wavelengths down to 13.9 nm and gain down to 10.9 nm. *Phys. Rev. A*, 72:053807. [20](#)
- Wang, Y., Wang, S., Oliva, E., Li, L., Berrill, M., Yin, L., Nejd, Y., Luther, B., Proux, C., Le, T., Dunn, J., Ros, D., Zeitoun, P., and Rocca, J. (2014). Gain dynamics in a soft x-ray laser amplifier perturbed by a strong injected x-ray field. *Nature Phot.*, 8:381–384. [20](#), [190](#)
- Wheeler, J. A., Borot, A., Monchoce, S., Vincenti, H., Ricci, A., Malvache, A., Lopez-Martens, R., and Quere, F. (2012). Attosecond lighthouses from plasma mirrors. *Nat. Phot.*, 6(12):829–833. [10](#)
- Whittaker, D. S., Fajardo, M., Zeitoun, P., Gautier, J., Oliva, E., Sebban, S., and Velarde, P. (2010). Producing ultrashort, ultraintense plasma-based soft-x-ray laser pulses by high-harmonic seeding. *Phys. Rev. A*, 81:043836. [172](#)
- Whittaker, T. (1948). A course in modern analysis. *Macmillan*. [228](#), [231](#)
- Xiao, Y., Chu, H., Tsai, H., Lee, C., Lin, J., Wang, J., and Chen, S. (2004). Efficient generation of extended plasma waveguides with the axicon ignitor-heater scheme. *Phys. Plasmas*, 11:21. [116](#)
- Yariv, A. (1989). Quantum electronics. *Wiley*, (New York). [192](#)
- Zeitoun, P. (1994). Thèse de doctorat de l’université paris vii. [14](#)
- Zeitoun, P., Faivre, G., Sebban, S., Mocek, T., Hallou, A., Fajardo, M., Aubert, A., Balcou, P., Burgy, F., Douillet, D., Kazamias, S., de Lachèze-Murel, G., Lefrou, T., le Pape, S., Mercière, P., Merdji, H., Morlens, A., Rousseau, J., and Valentin, C. (2004). A high-intensity highly coherent soft x-ray femtosecond laser seeded by a high harmonic beam. *Nature*, 431:426–429. [1](#), [24](#), [28](#), [72](#), [179](#)
- Zepf, M., Dromey, B., Landreman, M., Foster, P., and Hooker, S. M. (2007). Bright quasi-phase-matched soft-x-ray harmonic radiation from argon ions. *Phys. Rev. Lett.*, 99:143901. [10](#)
- Zhang, J., MacPhee, M., Nilsen, J. Lin, J., Barbee, T., Danson, J., Key, M., Lewis, C., Neely, D., O Rourke, R., Pert, G., Smith, R., Tallents, G., Wark, J., and Wolfrum, E. (1997). Demonstration of saturation in a ni-like ag x-ray laser at 14 nm. *Phys. Rev. Lett.*, 78:3856–3859. [18](#)
- Zhang, P., Mehta, K., Rehman, S., and Chen, N. (2014). Imaging single chiral nanoparticles in turbid media using circular-polarization optical coherence microscopy. *Scient. Rep.*, 4:4979. [29](#)
- Zhang, X., Lytle, A. L., Popmintchev, T., Zhou, X., Kapteyn, H. C., Murnane, M. M., and Cohen, O. (2007). Quasi-phase-matching and quantum-path control of high-harmonic generation using counterpropagating light. *Nat. Phys.*, 3(4):270–275. [10](#)

- Zhang, X., Wu, T., Zhao, J., Li, C., and You, X. (2013). Circular dichroism spectroscopy study of crystalline-to-amorphous transformation in chiral platinum(ii) complexes. *Chirality*, 25(7):384–392. [29](#)
- Zhao, J., Dong, Q., Wand, S., Zhang, L., and Zhang, J. (2008). X-ray lasers from inner-shell transitions pumped by the free-electron laser. *Optics Express*, 16(6):3546–3559. [13](#)
- Zhou, X., Lock, R., Li, W., Wagner, N., Murnane, M., and Kapteyn, H. (2008). Molecular recollision interferometry in high harmonic generation. *Phys. Rev. Lett.*, 100:073902. [28](#)
- Zhou, X., Lock, R., Wagner, N., Li, W., Kapteyn, H., and Murnane, M. (2009). Elliptically polarized high-order harmonic emission from molecules in linearly polarized laser fields. *Phys. Rev. Lett.*, 102:073902. [178](#)
- Zimmer, D., Zielbauer, B., Pittman, M., Guilbaud, O., Habib, J., Kazamias, S., Ros, D., Bagnoud, V., and Kuehl, T. (2010). Optimization of a tabletop high-repetition-rate soft x-ray laser pumped in double- pulse single-beam grazing incidence. *Opt. Lett.*, 35(4):450–452. [20](#)

« Voici mon secret. Il est très simple: on ne voit bien qu'avec le cœur. L'essentiel est invisible pour les yeux. »

Antoine de Saint-Exupéry, *Le Petit Prince*. Chap. XXI, 1943.

« Here is my secret. It is very simple: it is only with the heart that one can see rightly. What is essential is invisible to the eye. »

Antoine de Saint-Exupéry, *The Little Prince*. Chap. XXI, 1943.

# Résumé

Les lasers XUV collisionnels dit « OFI » sont réalisés en focalisant une impulsion laser infrarouge ultra-intense dans un milieu gazeux. L'interaction qui en résulte permet la génération d'une colonne de plasma en inversion de population, constituée d'ions multi-chargés et d'électrons énergétiques. Nous nous intéressons à l'émission de la transition  $3d^9 4d_{J=0} \mapsto 3d^9 4p_{J=1}$  du krypton IX (nickeloïde) à 32,8 nm. Lorsque ce plasma amplificateur est injecté par une source harmonique externe, l'émission résultante montre d'excellentes propriétés spatiales tout en offrant, à la longueur d'onde considérée, un nombre de photons bien supérieur.

Bien que compacts et démontrant d'excellentes propriétés spatiales, les lasers XUV collisionnels font face à des limites inhérentes à leur schéma de pompage. En effet, ceux-ci produisaient jusqu'ici des impulsions relativement longues (quelques picosecondes). L'axe majeur de cette thèse a consisté à repousser cette limite pour atteindre une durée d'émission de l'ordre de la centaine de femtosecondes, en mettant en oeuvre une « fenêtre temporelle sur le gain » de l'amplificateur plasma par sur-ionisation collisionnelle (*Collisional Ionization Gating*). Ceci est rendu possible en opérant à des densités électroniques très élevées (autour de  $10^{20} \text{ cm}^{-3}$ ), ce qui nécessite l'utilisation de techniques de guidage optique. Le régime d'injection d'harmoniques a été utilisé pour sonder la dynamique temporelle du gain d'un tel amplificateur plasma. Un modèle numérique Maxwell-Bloch à dépendance temporelle a permis de décrire cette dynamique d'amplification et d'en extraire une durée d'émission XUV. D'autre part, la méthode permet également la génération d'un plus grand nombre de photons par tir (jusqu'à  $14 \mu\text{J}$ ), offrant ainsi une augmentation de l'intensité des impulsions XUV émises de près de trois ordres de grandeurs. Un autre axe important de la thèse a consisté en la réalisation d'un laser XUV polarisé circulairement. La source a été réalisée avec succès en amplifiant une source harmonique résonante et polarisée circulairement par un plasma de Krypton IX. Conformément aux mesures expérimentales, notre modèle numérique Maxwell-Bloch confirme la conservation de l'état de polarisation des harmoniques au cours de l'amplification ainsi que l'efficacité du schéma de génération, ce qui ouvre ainsi la voie vers l'acquisition de mesures en un seul tir.

# Abstract

Collisionally-pumped OFI plasma-based soft X-ray lasers are achieved by focusing an ultra-intense infrared laser pulse into a gas. The optical field ionization (OFI) of the medium and the subsequent laser-plasma interaction results in the generation of an amplifier populated by hot electrons and highly charged ions. We are interested in the  $3d^9 4d_{J=0} \mapsto 3d^9 4p_{J=1}$  atomic transition of Nickel-like krypton at 32.8 nm, which can be pumped in these conditions via electron-ion collisions. When the plasma operates in a so-called « seeded regime » of amplification of an external high-harmonic source, the resulting emission maintains the latter excellent spatial properties and displays a two to three orders of magnitude higher photon yield at the relevant wavelength.

Although being compact and exhibiting numerous attractive characteristics, collisional plasma-based X-ray lasers face limitations intrinsic to their pumping scheme and therefore used to deliver quite long pulses (a few picosecond). The main focus of this thesis has been associated with the implementation of an original technique aimed at achieving 100 fs-range duration of emission by quenching the plasma amplifier gain lifetime through collisional over-ionization (*Collisional Ionization Gating*). This required operating at very high electron densities (over  $10^{20} \text{ cm}^{-3}$ ), which involved the implementation of optical waveguiding techniques. The « seeded regime » has been used to sample the ultrafast gain lifetime of such a plasma amplifier. A time-dependent Maxwell-Bloch code allowed describing the ultrashort amplification dynamics and deriving a final soft X-ray pulse duration. The method additionally allows a larger photon yield (over  $14 \mu\text{J}$ ), thus promising a nearly three orders of magnitude surge in soft X-ray pulse intensity compared to previous performances. Another focus of the work dealt with the implementation of a circularly polarized plasma-based X-ray laser. The demonstrated source has been generated by seeding a plasma amplifier by a resonant circularly polarized high-harmonic signal. In accordance with the experimental measurements, simulations confirmed the conservation of the high-harmonic polarization over amplification in the plasma and the efficiency of the scheme, which paves the way for prospective single-shot measurements.